Boussinesq Modeling of Waves, Currents and Sediment Transport

by

Wen Long and James T. Kirby

RESEARCH REPORT NO. CACR-06-02
April, 2006

CENTER FOR APPLIED COASTAL RESEARCH

Ocean Engineering Laboratory
University of Delaware
Newark, Delaware 19716

REPORT DOCUMENTATION PAGE

Form Approved
OMB No. 0704-0188

1. REPORT DATE *(DD-MM-YYYY)*	2. REPORT TYPE	3. DATES COVERED *(From - To)*
April 2006	Final	02/01/2204 - 12/31/2005

4. TITLE AND SUBTITLE

Boussinesq Modeling of Waves, Currents and Sediment Transport

5a. CONTRACT NUMBER

Award No. N00014-04-1-0219

5b. GRANT NUMBER

5c. PROGRAM ELEMENT NUMBER

6. AUTHOR(S)

Wen Long and James T. Kirby

5d. PROJECT NUMBER

5e. TASK NUMBER

5f. WORK UNIT NUMBER

7. PERFORMING ORGANIZATION NAME(S) AND ADDRESS(ES)

Center for Applied Coastal Research
University of Delaware
Newark, DE 19716

8. PERFORMING ORGANIZATION REPORT NUMBER

CACR-06-02

9. SPONSORING/MONITORING AGENCY NAME(S) AND ADDRESS(ES)

Office of Naval Research

10. SPONSOR/MONITOR'S ACRONYM(S)

ONR

11. SPONSOR/MONITOR'S REPORT NUMBER(S)

12. DISTRIBUTION/AVAILABILITY STATEMENT

Public

13. SUPPLEMENTARY NOTES

14. ABSTRACT

New Boussinesq-type equatioins are derived for surface water wave propagation and currents in relatively shallow water regions.

15. SUBJECT TERMS

16. SECURITY CLASSIFICATION OF:			17. LIMITATION OF ABSTRACT	18. NUMBER OF PAGES	19a. NAME OF RESPONSIBLE PERSON
a. REPORT	b. ABSTRACT	c. THIS PAGE			19b. TELEPHONE NUMBER *(Include area code)*

Boussinesq Modeling of Waves, Currents and Sediment Transport

by

Wen Long and James T. Kirby

RESEARCH REPORT NO. CACR-06-02
April, 2006

Center for Applied Coastal Research
Ocean Engineering Laboratory
University of Delaware
Newark, DE 19716

ACKNOWLEDGEMENTS

This study was partially supported by the Office of Naval Research under Grant Nos. N00014-99-1-1051 and N00014-04-1-0219, and by the National Oceanic and Atmospheric Administration Office of Sea Grant, Department of Commerce, under Grant No. NA96RG0029.

TABLE OF CONTENTS

LIST OF FIGURES . . . . . **xi**
LIST OF TABLES . . . . . **xxv**
ABSTRACT . . . . . **xxvi**

Chapter

1 INTRODUCTION **1**

1.1 Wave and Current Modeling 4
1.2 Sediment Transport and Morphology 7

2 DERIVATION OF NEW BOUSSINESQ EQUATIONS **11**

2.1 Previous Sets of Boussinesq Equations 13

2.1.1 Equations of Wei et al. (1995), $O(\mu^2)$ 13
2.1.2 Equations of Kennedy et al. (2001), $O(\mu^2)$ 14
2.1.3 Equations of Chen et al. (2003) , $O(\mu^2)$ 15

2.2 Derivations of Gobbi et al. (2000) Equations and New Equations 17

2.2.1 Derivation from potential flow theory following Gobbi et al. (2000), $O(\mu^4)$ 18
2.2.2 Kinematics of potential theory 30
2.2.3 Definition of reference levels z_α, z_β 34
2.2.4 Derivations from Euler equation with vertical vorticity retained $O(\mu^2)$ 34

2.2.4.1 Governing equations and assumptions 35
2.2.4.2 Consistency of kinematics between Euler theory and potential theory 36

2.2.4.3 Boussinesq equation with vertical vorticity retained . . 40

2.2.4.3.1 Continuity equation (COM) 40
2.2.4.3.2 Momentum equation evaluated at $z = \delta\eta$ . . . 40
2.2.4.3.3 Momentum equation evaluated at arbitrary level $z = z_c$ 44

2.3 Derivation of Boussinesq Equation Incorporating Undertow 46

2.3.1 Derivation from shallow water equation 47
2.3.2 Derivation from Boussinesq theory 52

2.4 Final Form of Boussinesq Equation 58

3 SEDIMENT TRANSPORT 60

3.1 Various Transport Formulas 62

3.1.1 Sediment transport formulas for steady flow 62
3.1.2 Sediment transport formulas for wave current climate 65

3.2 Ad-hoc Modifications to Bagnold (1966) and Bailard (1981) Formulas . . 67
3.3 Meyer-Peter Müller Formula with Shear Stress by Boundary Layer Model 69

4 NUMERICAL SOLUTION OF BOUSSINESQ EQUATIONS 71

4.1 Equations in Generalized Coordinate System 72

4.1.1 Vector form of equations 72
4.1.2 Additional effects for actual implementation 72
4.1.3 Some notes on curvilinear coordinates 77
4.1.4 COM and depth integrated EOM in generalized coordinate system 78
4.1.5 Curvilinear representation of shoreline boundary condition 88

4.2 Grid System and Discretization 91

4.2.1 Grid system 91
4.2.2 Spatial discretization 93
4.2.3 Temporal integration 93

4.2.3.1 Adams explicit and implicit schemes 93

4.2.3.2 Implementation of Adams schemes 94

4.2.4 Hot-Start problem 98

4.3 Obtaining $\tilde{u}$ from $\tilde{M}_w$ 99
4.4 Iteration Error Control and Under-relaxation 100
4.5 Calculation of Near Bottom Velocity 101
4.6 Wet-Dry Algorithm 101

5 MORPHOLOGICAL SCHEMES 108

5.1 Model Equation for Bed Elevation in Sediment Transport 110
5.2 Classical Schemes for Shock Capturing 111

5.2.1 Central difference schemes 112
5.2.2 Upwind schemes 113

5.3 Modern Schemes for Shock Capturing 114

5.3.1 WENO schemes 114
5.3.2 TVD schemes 118

5.4 Euler-WENO Scheme for Generalized Coordinate System 119
5.5 Morphology Updating Scheme Tests 120

5.5.1 Numerical Simulation Results and Comparisons for a Gaussian Hump Test 120
5.5.2 Application of the Euler-WENO scheme to sand bar deformation due to waves 136
5.5.3 Application of the Euler-WENO scheme to 2D channel stability problem 142

6 BOTTOM BOUNDARY LAYER SOLUTIONS 146

6.1 Analytical Solutions of Oscillatory Boundary Layer Flows 146
6.2 Numerical Solutions Using Finite Difference Method 149

6.2.1 Free stream velocity and pressure 149
6.2.2 2DHV boundary layer solution 150

6.2.2.1 Linear wave boundary layer 153

6.2.2.2 Nonlinear wave boundary layer 155

6.2.3 3D boundary layer solution 156

6.3 Bottom Boundary Layer Model Test 157

6.3.1 Linear laminar wave boundary layer 157
6.3.2 Wave boundary layer experiment by Jensen et al. (1989) 158

7 MODEL TESTS I: WAVE CURRENT SIMULATION TEST 165

7.1 Mase and Kirby (1992) Flume Test 165
7.2 Stive and Wind (1986) Undertow Test 171
7.3 Solitary Wave Run up Test 173
7.4 Waves in a Circular Channel 177
7.5 Wave Field on a Sloping Beach with Periodic Groins 178

8 MODEL TESTS II: SEDIMENT TRANSPORT TEST 191

8.1 Duck'94 Field Experiment Test 193

8.1.1 Layout of the experiments and wave conditions 193
8.1.2 Model Setup 208
8.1.3 Wave and mean Current test 213
8.1.4 Onshore bar migration events 245

8.1.4.1 Data driven model by Hsu et al. (2005) 245
8.1.4.2 Model results by FUNSEDI1D1.0 251

8.1.5 Offshore bar migration events 252

8.1.5.1 Data driven model by Hsu et al. (2005) 252
8.1.5.2 Model results by FUNSEDI1D1.0 254

8.2 LIP11D Lab Experiment Test 260

8.2.1 Layout of the experiments and wave conditions 260
8.2.2 Model data comparison of waves and currents 261
8.2.3 Erosional case: Test 1b 269
8.2.4 Accretional case: Test 1c 270

9 CONCLUSION AND FUTURE DEVELOPMENT 276

9.1 Conclusion 276
9.2 Perspective on Proposition of New Transport Formulas 277
9.3 Comments on Future Development 280

Appendix

A 283

A.1 Wave Maker Theory 283
A.2 Algorithms for Surface Roller Detection 286
A.3 Cyclically Tridiagonal Matrix Solver 295
A.4 Notes on Generalized Curvilinear Coordinate System 299
A.5 Numerical Estimation of Bedform Phase Speed 304

BIBLIOGRAPHY 306

LIST OF FIGURES

2.1 Schematic system layout 12

2.2 Spilling breaker roller 48

2.3 Horizontal velocity split 49

4.1 Cartesian coordinate and curvilinear coordinate 77

4.2 Covariant basis and contravariant basis 77

4.3 Shoreline boundary condition 88

4.4 Staggered grid system 92

4.5 Wet-dry cells 104

4.6 $f_b - f_{b0}$ as a function of H/δ_R 106

4.7 R_1 (solid) and $IDwetdry$ (dash) as a function of H_{max}/δ_R 106

4.8 R_f as a function of H/δ_R 106

5.1 Initial bed level z_b of Gaussian hump test 122

5.2 Simulation of Gaussian hump evolution using the Lax-Wendroff scheme. 124

5.3 Simulation of Gaussian hump evolution using the Richtmyer scheme. . 125

5.4 Simulation of Gaussian hump evolution using the MacCormack scheme. 126

5.5 Comparison of the model results with the analytical results at $t = 600s$; Lax-Wendroff scheme (stars), Ritchmyer scheme (triangles); MacCormack scheme (circles); analytical (solid line) 127

5.6 Simulation of Gaussian hump evolution using the Lax-Wendroff scheme and filtering. 128

5.7 Simulation of Gaussian hump evolution using the FTBS scheme. . . . 129

5.8 Simulation of Gaussian hump evolution using the Warming-Beam scheme 130

5.9 Comparison of the model results with the analytical results at $t = 600s$; FTBS (stars), Warming-Beam scheme (triangles); Lax-Wendroff scheme with filtering (circles); analytical (solid line) 131

5.10 Simulation of Gaussian hump evolution using the Euler-WENO scheme. 132

5.11 Simulation of Gaussian hump evolution using the TVD-RK-WENO scheme. 133

5.12 Comparison of the model results with the analytical results at $t = 600s$; Euler-WENO scheme (stars); TVD-RK-WENO scheme (triangles); analytical (solid line) 134

5.13 Comparison of the model results of the Euler-WENO scheme (dash) with the TVD-RK-WENO scheme (solid) at time $t = 0s$, $t = 2000s$, $t = 4000s$, $t = 6000s$, $t = 8000s$ and $t = 10000s$ from the left to the right 135

5.14 Relative error of the Gaussian hump volume by different schemes; (thin solid line: Lax-Wendroff; thin dash line: Lax-Wendroff with filtering; circles: Richtmyer; triangles: MacCormack; thick solid line: FTBS; thick dash line: Warming-Beam; squares: Euler-WENO; stars: TVD-RK-WENO) 137

5.15 Initial bed level (red) and still water surface level (blue) 139

5.16 Bed level (b, f, d, h) and surface wave envelop (a, c, e, g) at different times. 140

5.17 Bed level change with respect to time. 141

5.18 Bed evolution of a straight channel (arrow: flow field $\mathbf{u}$, averaged velocity about 1 m/s; contour: bed level) 145

6.1 Vertical discretization grids for boundary layer 153

6.2 Flow structure for laminar boundary layer computation; model: dash; analytical solution: circles 159

6.3 Bottom shear stress for laminar boundary layer computation; model: dash; analytical solution: circles; free stream velocity U: solid 160

6.4 Flow structure for smooth wall boundary layer computation; model: solid; data: circles; Mellor (2002): dash 162

6.5 Bottom shear stress for smooth wall boundary layer computation; model: solid; data: circles; Foti and Scandura (2004): dash; Mellor (2002): dot-dash 162

6.6 Flow structure for smooth wall boundary layer computation; model: solid; data: circles 163

6.7 Bottom shear stress for smooth wall boundary layer computation; model: solid; data: circles; Foti and Scandura (2004): dash; Mellor (2002): dot-dash 164

7.1 Experiment layout of Mase and Kirby (1992) 166

7.2 Time series comparison of gages a) $h = 35cm$ to $15cm$; dash : data; solid: model 167

7.3 Time series comparison of gages b) $h = 12.5$ to $2.5cm$; dash : data; solid: model 168

7.4 Model data comparison of wave spectra; model: thick solid line; data: thin solid line 169

7.5 Wave height comparison 169

7.6 Wave set up comparison 170

7.7 Comparison of skewness and asymmetry 170

7.8 Stive and Wind 1986 undertow test 171

7.9 Model and data comparison of the Stive and Wind (1986) undertow test: free surface η (solid), bottom elevation z_b (solid), model undertow $< u_b >$ (plus), measured undertow $< u_b >$ (circle) model wave height (triangle), measured wave height (square) and model set up $< \eta >$ (dash-dot) 172

7.10 Snap shot of bottom velocity and surface elevation; solid : FUNWAVE1D2.0 model; dash: Long and Kirby (2003) 173

7.11 The climb of a solitary wave with $H/d = 0.019$ up a $1 : 19.85$ beach; corresponding to Synolakis (1987) figure 6; (a) $t/\sqrt{g/d} = 25$, (b) $t/\sqrt{g/d} = 30$, (c) $t/\sqrt{g/d} = 35$, (d) $t/\sqrt{g/d} = 40$, (e) $t/\sqrt{g/d} = 45$, (f) $t/\sqrt{g/d} = 50$, (g) $t/\sqrt{g/d} = 55$, (h) $t/\sqrt{g/d} = 60$, (i) $t/\sqrt{g/d} = 65$, (k) $t/\sqrt{g/d} = 70$; dots: measured value ; solid line: model value; dash-line: nonlinear shallow water wave theory by Synolakis (1987) 175

7.12 The climb of a solitary wave with $H/d = 0.04$ up a $1 : 19.85$ beach; corresponding to Synolakis (1987) figure 9; (a) $t/\sqrt{g/d} = 20$, (b) $t/\sqrt{g/d} = 26$, (c) $t/\sqrt{g/d} = 32$, (d) $t/\sqrt{g/d} = 38$, (e) $t/\sqrt{g/d} = 44$, (f) $t/\sqrt{g/d} = 50$, (g) $t/\sqrt{g/d} = 56$, (h) $t/\sqrt{g/d} = 62$; dots: measured value ; solid line: model value; dash-line: nonlinear shallow water wave theory by Synolakis (1987) 176

7.13 Curvilinear grid system for the circular channel test 178

7.14 Computed surface elevation $\eta(m)$ 179

7.15 Computed wave height distribution normalized by the incident wave height (H/H_0) 179

7.16 Wave field on a sloping beach with periodic groins, case a) $\theta_0 = 30°$; The shore parallel solid lines show the depth contours of $-4m$, $-3m$, $-2m$, $-1m$, $0m$ respectively from the left to the right; Still water level shoreline is located at $x = 180m$. 181

7.17 Wave field on a sloping beach with periodic groins, case b) $\theta_0 = 45°$; The shore parallel solid lines show the depth contours of $-4m$, $-3m$, $-2m$, $-1m$, $0m$ respectively from the left to the right; Still water level shoreline is located at $x = 180m$. 182

7.18 Surface elevation and bathymetry of case a) $\theta_0 = 30°$ 183

7.19 Surface elevation and bathymetry of case b) $\theta_0 = 45°$ 184

7.20 Normalized wave height distribution H/H_0 of 6 horizontal sections of case a) $\theta_0 = 30°$ 186

7.21 Normalized wave height distribution H/H_0 of 6 vertical sections of case a) $\theta_0 = 30°$ 187

7.22 Normalized wave height distribution H/H_0 of 6 horizontal sections of case b) $\theta_0 = 45°$ 188

7.23 Normalized wave height distribution H/H_0 of 6 vertical sections of case b) $\theta_0 = 45°$ 189

7.24 Depth and time averaged current between the groins for case a) $\theta_0 = 30°$ 190

8.1 Duck 94 experiment layout (open squares: pressure gages; circles: sonar altimeters; from Stauble and Cialone, 1997) 194

8.2 Bar migration history (bar crest location indicated by thick solid curve, modified from Elgar et al., 2001) 194

8.3 Peak wave period (circles) and significant wave height (triangles) at gage p19 in Sept., 1994 198

8.4 Peak wave period (circles) and significant wave height (triangles) at gage p19 in Oct., 1994 198

8.5 Mean current and bed elevation on day 09/21/94 199

8.6 Mean current and bed elevation on day 09/22/94 199

8.7 Mean current and bed elevation on day 09/23/94 200

8.8 Mean current and bed elevation on day 09/24/94 200

8.9 Mean current and bed elevation on day 09/25/94 201

8.10 Mean current and bed elevation on day 09/26/94 201

8.11 Mean current and bed elevation on day 10/10/94 202

8.12 Mean current and bed elevation on day 10/11/94 202

8.13 Mean current and bed elevation on day 10/12/94 203

8.14 Mean current and bed elevation on day 10/13/94 203

8.15 Mean current and bed elevation on day 10/14/94 204

8.16 Mean current and bed elevation on day 10/15/94 204

8.17 Mean current and bed elevation on day 10/16/94 205

8.18 Mean current of bar trough gage p12 in September, 1994; Upper panel: cross shore mean current (positive onshore); Lower panel: alongshore mean current (positive toward south) 206

8.19 Mean current of bar trough gage p13 in September, 1994; Upper panel: cross shore mean current (positive onshore); Lower panel: alongshore mean current (positive toward south) 206

8.20 Mean current of bar trough gage p12 in October, 1994; Upper panel: cross shore mean current (positive onshore); Lower panel: alongshore mean current (positive toward south) 207

8.21 Mean current of bar trough gage p13 in October, 1994; Upper panel: cross shore mean current (positive onshore); Lower panel: alongshore mean current (positive toward south) 207

8.22 Time series of wave signal η at gage p19 from 09/23/94 to 09/29/94; The time axis is from 1:00am of each day to 1:00am of the next day 209

8.23 Time series of tidal level signal at gage p19 from 09/23/94 to 09/29/94 (relative to NGVD datum); The time axis is from 1:00am of each day to 1:00am of the next day 209

8.24 Time series of wave signal η at gage p19 from 10/10/94 to 10/16/94; The time axis is from 1:00am of each day to 1:00am of the next day; The measurements from 13:00 to 16:00 on day 10/15/94 are missing due to gage malfunction, and they are shown as repeated signal from 10:00 to 13:00 210

8.25 Time series of tidal level signal at gage p19 from 10/10/94 to 10/16/94 (relative to NGVD datum); The time axis is from 1:00am of each day to 1:00am of the next day; The measurements from 13:00 to 16:00 on day 10/15/94 are missing due to gage malfunction, and they are shown as repeated signal from 10:00 to 13:00 211

8.26 Measured cross shore bathymetry from Sept. 21 to Sept. 30 (relative to NGVD datum) 212

8.27 Measured cross shore bathymetry from Oct. 10 to Oct. 16 (relative to NGVD datum) 212

8.28 Model data comparison of velocity power spectra at different gages on 09/23/94, 1:00am (data: thin-line; model: thick-line) 214

8.29 Model data comparison of velocity power spectra at different gages on 09/24/94, 1:00am (data: thin-line; model: thick-line) 215

8.30 Model data comparison of velocity power spectra at different gages on 09/25/94, 1:00am (data: thin-line; model: thick-line) 215

8.31 Model data comparison of velocity power spectra at different gages on 09/26/94, 1:00am (data: thin-line; model: thick-line) 216

8.32 Model data comparison of velocity power spectra at different gages on 09/27/94, 1:00am (data: thin-line; model: thick-line) 217

8.33 Model data comparison of velocity power spectra at different gages on 09/28/94, 1:00am (data: thin-line; model: thick-line) 217

8.34 Model data comparison of velocity power spectra at different gages on 09/29/94, 1:00am (data: thin-line; model: thick-line) 218

8.35 Model data comparison of velocity power spectra at different gages on 09/30/94, 1:00am (data: thin-line; model: thick-line) 218

8.36 Model data comparison of velocity variance at different velocity gages on 09/23/94, (data: circles; model: pluses) 219

8.37 Model data comparison of velocity variance at different velocity gages on 09/24/94, (data: circles; model: pluses) 219

8.38 Model data comparison of velocity variance at different velocity gages on 09/25/94, (data: circles; model: pluses) 220

8.39 Model data comparison of velocity variance at different velocity gages on 09/26/94, (data: circles; model: pluses) 220

8.40 Model data comparison of velocity variance at different velocity gages on 09/27/94, (data: circles; model: pluses) 221

8.41 Model data comparison of velocity variance at different velocity gages on 09/28/94, (data: circles; model: pluses) 221

8.42 Model data comparison of velocity variance at different velocity gages on 09/29/94, (data: circles; model: pluses) 222

8.43 Model data comparison of velocity variance at different velocity gages on 09/30/94, (data: circles; model: pluses) 222

8.44 Model data comparison of velocity mean at different velocity gages on 09/23/94, (data: circles; model: pluses) 223

8.45 Model data comparison of velocity mean at different velocity gages on 09/24/94, (data: circles; model: pluses) 223

8.46 Model data comparison of velocity mean at different velocity gages on 09/25/94, (data: circles; model: pluses) 224

8.47 Model data comparison of velocity mean at different velocity gages on 09/26/94, (data: circles; model: pluses) 224

8.48 Model data comparison of velocity mean at different velocity gages on 09/27/94, (data: circles; model: pluses) 225

8.49 Model data comparison of velocity mean at different velocity gages on 09/28/94, (data: circles; model: pluses) 225

8.50 Model data comparison of velocity mean at different velocity gages on 09/29/94, (data: circles; model: pluses) 226

8.51 Model data comparison of velocity mean at different velocity gages on 09/30/94, (data: circles; model: pluses) 226

8.52 Model data comparison of velocity skewness at different velocity gages on 09/23/94, (data: circles; model: pluses) 227

8.53 Model data comparison of velocity skewness at different velocity gages on 09/24/94, (data: circles; model: pluses) 227

8.54 Model data comparison of velocity skewness at different velocity gages on 09/25/94, (data: circles; model: pluses) 228

8.55 Model data comparison of velocity skewness at different velocity gages on 09/26/94, (data: circles; model: pluses) 228

8.56 Model data comparison of velocity skewness at different velocity gages on 09/27/94, (data: circles; model: pluses) 229

8.57 Model data comparison of velocity skewness at different velocity gages on 09/28/94, (data: circles; model: pluses) 229

8.58 Model data comparison of velocity skewness at different velocity gages on 09/29/94, (data: circles; model: pluses) 230

8.59 Model data comparison of velocity skewness at different velocity gages on 09/30/94, (data: circles; model: pluses) 230

8.60 Model data comparison of velocity power spectra at different gages on 10/10/94, 1:00am (data: thin-line; model: thick-line) 231

8.61 Model data comparison of velocity power spectra at different gages on 10/11/94, 1:00am (data: thin-line; model: thick-line) 231

8.62 Model data comparison of velocity power spectra at different gages on 10/12/94, 1:00am (data: thin-line; model: thick-line) 232

8.63 Model data comparison of velocity power spectra at different gages on 10/13/94, 1:00am (data: thin-line; model: thick-line) 232

8.64 Model data comparison of velocity power spectra at different gages on 10/14/94, 1:00am (data: thin-line; model: thick-line) 233

8.65 Model data comparison of velocity power spectra at different gages on 10/15/94, 1:00am (data: thin-line; model: thick-line) 233

8.66 Model data comparison of velocity power spectra at different gages on 10/16/94, 1:00am (data: thin-line; model: thick-line) 234

8.67 Model data comparison of velocity variance at different velocity gages on 10/10/94, (data: circles; model: pluses) 234

8.68 Model data comparison of velocity variance at different velocity gages on 10/11/94, (data: circles; model: pluses) 235

8.69 Model data comparison of velocity variance at different velocity gages on 10/12/94, (data: circles; model: pluses) 235

8.70 Model data comparison of velocity variance at different velocity gages on 10/13/94, (data: circles; model: pluses) 236

8.71 Model data comparison of velocity variance at different velocity gages on 10/14/94, (data: circles; model: pluses) 236

8.72 Model data comparison of velocity variance at different velocity gages on 10/15/94, (data: circles; model: pluses) 237

8.73 Model data comparison of velocity variance at different velocity gages on 10/16/94, (data: circles; model: pluses) 237

8.74 Model data comparison of velocity mean at different velocity gages on 10/10/94, (data: circles; model: pluses) 238

8.75 Model data comparison of velocity mean at different velocity gages on 10/11/94, (data: circles; model: pluses) 238

8.76 Model data comparison of velocity mean at different velocity gages on 10/12/94, (data: circles; model: pluses) 239

8.77 Model data comparison of velocity mean at different velocity gages on 10/13/94, (data: circles; model: pluses) 239

8.78 Model data comparison of velocity mean at different velocity gages on 10/14/94, (data: circles; model: pluses) 240

8.79 Model data comparison of velocity mean at different velocity gages on 10/15/94, (data: circles; model: pluses) 240

8.80 Model data comparison of velocity mean at different velocity gages on 10/16/94, (data: circles; model: pluses) 241

8.81 Model data comparison of velocity skewness at different velocity gages on 10/10/94, (data: circles; model: pluses) 241

8.82 Model data comparison of velocity skewness at different velocity gages on 10/11/94, (data: circles; model: pluses) 242

8.83 Model data comparison of velocity skewness at different velocity gages on 10/12/94, (data: circles; model: pluses) 242

8.84 Model data comparison of velocity skewness at different velocity gages on 10/13/94, (data: circles; model: pluses) 243

8.85 Model data comparison of velocity skewness at different velocity gages on 10/14/94, (data: circles; model: pluses) 243

8.86 Model data comparison of velocity skewness at different velocity gages on 10/15/94, (data: circles; model: pluses) 244

8.87 Model data comparison of velocity skewness at different velocity gages on 10/16/94, (data: circles; model: pluses) 244

8.88 Onshore bar migration predicted using measured velocities during 09/23/1994 1:00am to 09/28/1994 1:00am; circles: measured bathymetry; triangles: predicted bathymetry using total transport $q_c + q_w$ by (8.3); pluses: predicted bathymetry using current-related transport q_c only; stars: predicted bathymetry using wave-related transport q_w only . 246

8.89 Onshore bar migration predicted using measured velocities during 09/23/1994 1:00am to 09/28/1994 1:00am; circles: measured bathymetry (dash line indicates the measured bathymetry on 09/23/1994 1:00am, solid line indicates the measured bathymetry on 09/28/1994 1:00am); triangles: predicted bathymetry using total transport $q_c + q_w$ by (8.3); pluses: predicted bathymetry using current-related transport q_c only; stars: predicted bathymetry using wave-related transport q_w only); . . . 247

8.90 Onshore bar migration predicted using Boussinesq model velocities during 09/23/1994 1:00am to 09/28/1994 1:00am; circles: measured bathymetry; triangles: predicted bathymetry using total transport $q_c + q_w$ by (8.3); pluses: predicted bathymetry using current-related transport q_c only; stars: predicted bathymetry using wave-related transport q_w only . 249

8.91 Onshore bar migration predicted using Boussinesq model velocities during 09/23/1994 1:00am to 09/28/1994 1:00am, circles: measured bathymetry (dash line indicates the measured bathymetry on 09/23/1994 1:00am, solid line indicates the measured bathymetry on 09/28/1994 1:00am); triangles: predicted bathymetry using total transport $q_c + q_w$ by (8.3); pluses: predicted bathymetry using current-related transport q_c only; stars: predicted bathymetry using wave-related transport q_w only); 250

8.92 Bedform change using coupled Boussinesq model and sediment transport model (dash-dotted line: measured bathymetry at 09/23/94 1:00am; thin solid line: measured bathymetry at 09/30/94 1:00am; dash line: model A bathymetry at 09/30/94 1:00am; thick solid line: model B bathymetry at 09/30/94 1:00am) 253

8.93 Offshore bar migration predicted using measured velocities during 10/10/1994 1:00am to 10/15/1994 1:00am; circles: measured bathymetry; triangles: predicted bathymetry using total transport $q_c + q_w$ by (8.3); pluses: predicted bathymetry using current-related transport q_c only; stars: predicted bathymetry using wave-related transport q_w only . 255

8.94 Offshore bar migration predicted using measured velocities during 10/10/1994 1:00am to 10/15/1994 1:00am, circles: measured bathymetry (dash line indicates the measured bathymetry on 10/10/1994 1:00am, solid line indicates the measured bathymetry on 10/15/1994 1:00am); triangles: predicted bathymetry using total transport $q_c + q_w$ by (8.3); pluses: predicted bathymetry using current-related transport q_c only; stars: predicted bathymetry using wave-related transport q_w only; 256

8.95 Offshore bar migration predicted using Boussinesq model velocities during 10/10/1994 1:00am to 10/15/1994 1:00am; circles: measured bathymetry; triangles: predicted bathymetry using total transport $q_c + q_w$ by (8.3); pluses: predicted bathymetry using current-related transport q_c only; stars: predicted bathymetry using wave-related transport q_w only . 257

8.96 Offshore bar migration predicted using Boussinesq model velocities during 10/10/1994 1:00am to 10/15/1994 1:00am, circles: measured bathymetry (dash line indicates the measured bathymetry on 10/10/1994 1:00am, solid line indicates the measured bathymetry on 10/15/1994 1:00am); triangles: predicted bathymetry using total transport $q_c + q_w$ by (8.3); pluses: predicted bathymetry using current-related transport q_c only; stars: predicted bathymetry using wave-related transport q_w only; . 258

8.97 Bedform change using coupled Boussinesq model and sediment transport model (dash-dotted line: measured bathymetry at 10/10/94 1:00am; thin solid line: measured bathymetry at 10/16/94 1:00am; dash line: model A bathymetry at 10/16/94 1:00am; thick solid line: model B bathymetry at 10/16/94 1:00am) 259

8.98 Schematic layout of the LIP11D experiments. 261

8.99 Bed profiles during Test 1b; top panel: overall bed profile; bottom panel: closer view of the offshore bar movement from wavehour 7 to wavehour 18 262

8.100 Bed profiles during Test 1c; top panel: overall bed profile; bottom panel: closer view of the onshore bar movement from wavehour 1 to wavehour 10 263

8.101 Model data comparison of wave height and setup for Test 1b 265

8.102 Model data comparison of wave height and setup for Test 1c 266

8.103 Model data comparison of the vertical structure of undertow for Test 1b; data (o); model (Δ) 267

8.104 Model data comparison of the vertical structure of undertow for Test 1c; data (o); model (Δ) 268

8.105 Bedlevel change by model A for test 1b; (a) bedlevel due to both Bagnold formula and acceleration term; (b) bedlevel due to Bagnold formula; (c)bedlevel due to acceleration term; model bedlevel (solid line); measured initial bedlevel (dash-dotted line); measured final bedlevel (dash line) 271

8.106 Bedlevel change by model B for test 1b; (a) bedlevel due to both q_w and q_c; (b) bedlevel due to q_w; (c)bedlevel due to q_c; model bedlevel (solid line); measured initial bedlevel (dash-dotted line); measured final bedlevel (dash line) 272

8.107 Bedlevel change by model A for test 1c; (a) bedlevel due to both Bagnold formula and acceleration term; (b) bedlevel due to Bagnold formula; (c) bedlevel due to acceleration term; model bedlevel (solid line); measured initial bedlevel (dash-dotted line); measured final bedlevel (dash line) . 274

8.108 Bedlevel change by model B for test 1c; (a) bedlevel due to both q_w and q_c; (b) bedlevel due to q_w; (c) bedlevel due to q_c; model bedlevel (solid line); measured initial bedlevel (dash-dotted line); measured final bedlevel (dash line) 275

A.1 Roller geometry for a spilling breaker 287

LIST OF TABLES

8.1 Sonar altimeter gage locations during September 21 to September 30 and October 10 to October 16 in the Duck'94 field experiments 195

8.2 Pressure gage locations during September 21 to September 30 in the Duck'94 field experiments 195

8.3 Pressure gage locations during October 10 to October 16 in the Duck'94 field experiments 196

8.4 Near bed cross shore current meter (u-gage) locations during September 21 to October 16 in the Duck'94 field experiments; (alongshore current meters (v-gage) are co-located with the cross shore current meters) . . . 196

8.5 Gage locations where bathymetry data are obtained 208

8.6 Test conditions of LIP11D experiment 260

8.7 EMF current meter locations during different test wavehours 262

ABSTRACT

New Boussinesq-type equations are derived for surface water wave propagation and currents in relatively shallow water regions. The new equations are fully nonlinear and accurate to $O(\mu^2)$, with μ the indicator of wave dispersion. 1-D and 2-D computer models (FUNWAVE1D2.0 and FUNWAVE2D2.0) are developed based on the new Boussinesq equations for wave current modeling. The new Boussinesq models are based on a staggered grid system. The FUNWAVE2D2.0 model is also based on generalized curvilinear coordinate to fit complex nearshore geometries. Wave breaking introduced undertow currents are included in the dependent reference velocities automatically. The new equations retain vertical vorticity generated by wave breaking and bottom friction to the second order of dispersion. Wetting and drying algorithm is developed to model wave run up and run down and track shoreline change instantaneously. Phase resolving sediment transport is integrated into the Boussinesq wave current model to investigate nearshore morphological change due to wave and current forces (FUNSEDI1D1.0 and FUNSEDI2D1.0). A non-oscillatory Euler-WENO morphological scheme is developed to model the interaction between hydrodynamics and morphological change accurately and stably as compared to classical Lax-Wendroff schemes. 1-D vertical wave current bottom boundary layer models are developed to calculate the bottom shear stresses instantaneously. Classical sediment transport formulas are implemented and compared to investigate their performance for unsteady, transient flow as well as skewed and asymmetric waves introduced sediment transport in nearshore region. The model is applied to simulate DUCK'94 field measurement to investigate both accretional and erosional events of sand bar migration. The LIP11 lab experiment is also simulated to further test

the performance of the model. The present sediment transport model can also be used to examine future transport formulas for unsteady flow system.

Chapter 1

INTRODUCTION

We can not overestimate the importance of the understanding of nearshore hydrodynamics and morphodynamics. The reason is that our civilization up to date has presented us extensive and intensive interactions within the coastal areas where we have a vast diversity of life and natural processes as well as economical operations. "Along this dynamically active intersection of land and the oceans, humans have been building structures throughout history. Ports and harbors have always served as bases for naval forces and as commercial egresses to upland trade routes or major centers of society. As recreation and tourism at the shoreline have become more and more important economically, coastal development, has increased to such an extent that over 50 percent of the U.S. population now lives within 50 miles of the coastline" (Dean and Dalrymple, 2002). As coastal engineers, we are aiming at understanding of coastal processes and developing strategies to cope effectively with shoreline erosion and building coastal structures to better serve our community. With the pressure of population on the shoreline and the threat of sea level rise, tsunamis and coastal storms, we are in great need of more advanced knowledge of coastal processes such as waves, currents, sediment transport mechanics and ecology.

Ocean surface waves are the dominant feature of the nearshore region. Waves are generated by the interaction between the atmosphere and ocean surface water in relatively deep region and propagate to shoreline shallow water areas, where the wave energy is dissipated. "The energy associated with these waves is surprisingly large and it is to a

large degree expended in the nearshore region through the process of wave breaking. The rate at which energy is expended in the surf when the breakers are about 1 m high is approximately equivalent to 3kW /m of beach, i.e. the rate at which energy is dissipated along 400 km of this beach is equivalent to the rate of energy production of a nuclear power plant" (Madsen, 1976). With this tremendous amount of wave energy, it is not surprising that waves can change the appearance of the shoreline and nearshore bottom bathymetry drastically and constantly.

During the propagation from the deep ocean to the shore, waves undergo many changes because of the changing depth. When the water is sufficiently deep, the waves are unaware of the presence of the bottom. As the depth decreases the waves start to feel the bottom and sediments on the bottom start to feel the waves. The oscillatory water motion associated with the waves exerts an oscillatory shear stress on the bottom, which may be shown to be several times larger than the shear stress associated with a steady current of comparable magnitude due to the acceleration and deceleration of fluid particles within a wave cycle. The water velocity, immediately above the bed, associated with the waves is to the first approximation purely oscillatory, i.e. it moves back and forth without any net motion, resulting to purely oscillatory shear stress on the bottom and purely oscillatory sediment movement. Though the magnitude of shear stress associated with the wave motion where capable of setting the bottom sediment in motion, the net movement of sediment would be still small. The importance of the wave motion is evident when there is a superposed slowly varying current which can be generated by various reasons. The larger shear stress exerted on the bottom by the wave motion can stir up the sediment which then can be moved even by a current, which by itself would have been incapable of causing any near bed sediment transport. This is a qualitative description of sediment transport processes on continental shelf.

In the nearshore region, various effects modify the wave features. Wave skewness is mainly due to nonlinearity of wave-wave interaction and presents sharp and peaky wave

crests along with wide and flat wave troughs. Wave shoaling is the gain of wave height due to the decrease of water depth. Wave asymmetry results from the nonlinear transfer of energy from lower to higher harmonics as waves shoal and the waves become pitched forward with a steep slope in the front of a wave crest and a mild slope on the back. Wave skewness and asymmetry will lead to non-purely oscillatory bottom shear stress and again result to a non-purely oscillatory movement of bottom sediments which overall can give a net transport of sediment toward the direction of wave propagation, even when there is no superposed current.

Waves shoal, skew and pitch forward until they finally break drastically. This wave breaking phenomenon involves a number of new features not seen offshore of the breaker zone (surf zone). The dominant effects of wave breaking inside the surf zone are the wave setup, undertow and longshore currents. Wave setup is the time averaged water level increase in front of the shore face with a slope about 10 to 100 times larger than a river surface. This slope of wave setup helps develop a pressure gradient pointing in the offshore direction which helps develop a return current near the bottom of the vertical water column toward the ocean. This return flow is called undertow. With the help of various beach bathymetry features, such as a cut in the middle of a sand bar, the undertow will show three dimensional personalities and develop concentrated jets toward the ocean known as rip currents which cause about 150 life losses per year to swimmers in the United States. More often, waves approach the shoreline at an angle, which will exert a shearing force parallel to the shoreline and results in currents flowing downstream along the shoreline. These longshore currents greatly account for sediment transport along the shoreline and its spatial and temporal variations are responsible for the change of coast lines over long period of time (shoreline recession, shoreline advance, beach erosion and accretion).

Wave skewness and asymmetry will introduce more sediment transport toward the direction of wave propagation in the forward phase of a wave cycle than the amount in

the counter direction of wave propagation in the backward phase. The overall effect for a non-breaking but skewed and asymmetric wave motion in nearshore generally will lead to sediments moving toward shoreline until the surf zone where undertow and alongshore currents change the scenario to be much more sophisticated.

The coastal environment is further complicated by the presence of river estuaries, tidal inlets and man-made coastal structures. Powerful wave breaking will also introduce dramatic water motion such as plunging breakers which can greatly impinge on shallow water bed and suspend a lot of sediments to be transported by the whole vertical column of water. Sometimes the movable bottom behaves as an unstable system which could develop various bed forms such as ripples, mega ripples, dunes and sand bars. The presence of relatively large bed forms will affect the behavior of waves, and also develop form drag that will further introduce sediment movements in addition to shear stresses.

The interactions between water wave, current motion and morphological bed forms go on and on. However sometimes equilibrium states are reached and the geometry of nearshore system stays relatively stable.

In the present research, we focus on computer modeling of nearshore waves and currents and sediment transport as well as morphological changes based on advanced wave theories and bottom boundary layer models along with high-order non-oscillatory morphological schemes.

1.1 Wave and Current Modeling

We have an abundant heritage of observations, experiments and mathematics of water wave mechanics. It has been developed over centuries along with the flourishing of general fluid mechanics, measurement techniques, experimental instruments and advanced by computer science and technology in the last 50 years. Computer modeling becomes an important and efficient tool to explore the world of nearshore hydrodynamics.

Gerstner (1802) published the first deep water wave theory followed by Airy (1841) of linear wave theory, Stokes (1847) for higher order nonlinear wave, long wave

theories by Boussinesq (1871) as well as waves of limiting heights by Michell (1893) and McCowan (1894).

Wave transformations including shoaling, refraction and diffraction can be modeled by mild slope equation theory by Berkhoff (1972) and its parabolic versions (Radder, 1979; Tsay and Liu, 1982; Kirby and Dalrymple, 1984). The University of Delaware Center for Applied Coastal Research REF/DIF model is one of the well recognized wave models for relatively large scale open ocean wave simulation based on parabolic mild slope equations.

Parabolic mild slope models can not cope with complicated coastal regions where islands, breakwaters, jetties and other structures are involved, due to neglect of wave reflection from structures. On the other hand, phase resolving wave models have been developed based on Boussinesq (1871) theory with the extension to variable depth by Peregrine (1967) and further extended to relatively deep water dispersive waves (Witting, 1984; Madsen and Sorensen, 1992; Nwogu, 1993) and higher order nonlinearity by Wei et al. (1995) and Gobbi et al. (2000). The Boussinesq models can provide much more detailed information of wave motion. An extensive review is available in Kirby (2003).

Different numerical methods have been used to solve the Boussinesq-type equations. Abbott et al. (1978) used an alternating-direction-implicit (ADI) finite difference method (FDM) to solve 2D Boussinesq equations which later became the standard method used in DHI MIKE 21 system (DHI, 2002). Walkley and Berzins (2002) and Sorensen et al. (2003) applied finite element method (FEM) and Wei et al. (1995) used the 3rd order Adams-Bashforth predictor and the 4th order Adams-Moulton corrector method (ABM) for higher order nonlinearity Boussinesq model FUNWAVE (Kirby et al., 1998). Shi et al. (2001, 2003) solved the Wei et al. (1995) equation in generalized curvilinear coordinates also using ABM finite difference method.

The numerical model FUNWAVE1.0 produced by the Center for Applied Coastal Research, University of Delaware (Kirby et al., 1998), is capable of simulating surface

waves in coastal region including the outer surf zone and inner surf zone. The model is based on theoretical research of Wei et al. (1995) in which a fully nonlinear Boussinesq equation is set up by extending Nwogu (1993)'s Boussinesq equation with higher order nonlinear dispersive terms fully retained. The Wei et al. (1995) equation can be applied to both intermediate water depth and strong nonlinearity interaction in practical engineering.

After FUNWAVE1.0 was released, further work has been continuously done by Gobbi et al. (2000), Kennedy et al. (2001), Chen et al. (2003), Shi et al. (2001) and Chawla and Kirby (2000). In Gobbi et al. (2000), the equation is extended to fourth order accuracy of dispersion and multi-reference-level is introduced compared to Nwogu (1993) and Wei et al. (1995). In Kennedy (2001), the reference level of Wei et al. (1995) is extended to be moving with the surface elevation. In Chen et al. (2003), a second order vertical vorticity term is further incorporated in the equation which is capable of simulating eddies in the horizontal plane generated after wave breaking in the surf zone. In Shi et al. (2001), the Wei et al. (1995) equation is solved on curvilinear coordinate system and implemented on staggered grids to give better accuracy and convergence rate, so that it can simulate waves with complex geometries. In Chawla and Kirby (2000) a one-way wave maker theory for the model is established by adding a pressure term to the momentum equation compared to Wei et al. (1999), in which a two-way numerical wave maker is developed by including a source term in the continuity equation.

In the present research, we derive a set of Boussinesq equations that can cover all existing Boussinesq equations based on Nwogu (1993) and Wei et al. (1995) mentioned above (Madsen et al., 1992; Nwogu, 1993; Wei et al., 1995; Kennedy et al., 2001; Chen et al., 2003; Gobbi et al., 2000) to second order in dispersion. The new equation is extended to include breaking wave induced undertow automatically in the reference velocity, based on the roller model of spilling breaker (Svendsen, 1984, Schäffer et al., 1993) and the recent work of Lynett (2005).

The new equation system is solved in generalized curvilinear coordinates as in

Shi et al. (2001). Internal boundaries of islands and breakwaters are included in the model, as well as a new but quite simple wetting and drying algorithm developed to model the moving shoreline in the swash zone. This research effort finally resulted into a new version of FUNWAVE model here named FUNWAVE2.0, available for public under the GNU General Public License agreement.

In summary, the following are the new features in FUNWAVE2.0: 1) staggered grid system; 2) generalized curvilinear coordinate system; 3) Multi-reference-levels and moving reference levels included; 4) vertical vorticity term retained; 5) one-way wave maker; 6) internal boundaries for structures; 7) undertow included automatically; 8) new wetting-drying algorithm for wave runup;

In addition, the new model can output more kinematic and dynamic quantities such as temporal wave gage, spatial wave gage, pressure, mean current, set-up/set-down, wave heights, potential vorticity.

The wave breaking simulation, subgrid-mixing, bottom friction and sponge layers are kept the same as in version 1.0. Detailed derivations, numerical methods and examples will be shown in later chapters of this dissertation.

1.2 Sediment Transport and Morphology

In comparison to the hydrodynamic processes of waves and currents, the field of coastal sediment transport and morphology is still as much an art as a science and requires a good deal of future investigation. At this time, the mathematical and statistical equations governing the behavior of sediments are not yet fully known. Our knowledge and ability to model the process of sediment transport are limited by the following remaining difficulties: turbulent bottom boundary layer of waves and currents, turbulent flow of heterogeneous mixture composed of sands, mud and water, the limited power of computer resources and the limited techniques available for measuring the sediment flow and forcing.

Earlier studies of sediment transport started from the investigation of rivers, channels and pipelines with which the flow are dominantly one directional and relatively steady in time. In Chanson (1999), eight different empirical and semi-empirical correlations of bed load transport for open channel flow are nicely summarized. They are Du Boys (1879), Schoklitsch (1930), Shields (1936), Einstein (1942), Meyer-Peter (1948, 1951), Einstein (1950), Schoklitsch (1950) and Nielson (1992). Other formulas for bedload sediment transport or total load sediment transport (bedload plus suspended load) are given by Bagnold (1966), Grass (1981), Van Rijn (1984) and many other contributors. For sediment transport due to waves or combined waves and currents, up to date formulas are mostly based on the quasi-steady assumption (assume the sediment particles respond to the fluid flow as if the flow were steady when the flow changes from one state to another), which include Einstein (1972), Madsen and Grant (1976) and Bailard (1981). Recently developed transport formulas are also available from Dibajnia and Watanabe (1998) and Soulsby and Damgaard (2005).

The assumption of quasi-steady state employed before has been recently seriously questioned based on both experimental and theoretical results. A significant amount of evidence has shown that sediment transport under waves calls for models which reflect the effects of unsteadiness of the driving flow field, as it is the nature of waves, especially when mean currents are weak relative to wave-orbital velocities and wave skewness and asymmetry that are prominent as waves approach shoreline.

Very fine scale discrete particle simulations by Drake and Calantoni (2001) show that Bagnold, Bowen and Bailard (abbreviated as BBB hereafter) type of sediment transport models, which were derived under steady flow or quasi-steady flow assumption, miss important effects due to flow acceleration. The Bailard (1981) formula was then modified in an ad-hoc manner to improve its capability for capturing the flow acceleration-related transport. This approach was applied to fields measurement of bar migration in the DUCK94 experiment by Hoefel and Elgar (2003).

Another important feature of sediment transport under waves is the phase lag between the sediment motion and wave fluid motion. The sediments lying on the bottom feel the shear stress exerted by waves instead of the orbital velocity of waves. Due to the viscous nature of fluid and turbulence within a thin bottom boundary layer, the shear stress has a significant phase difference with the wave motion. This phase lag can not be modeled by traditional bottom shear stress parameterizations which rely on a wave-current friction coefficient and the orbital velocity. The phase lag effect becomes important especially for skewed and asymmetric waves and when the currents are relatively weak. The importance of phase lag and its effect on sediment transport rate is also shown in Dohmen-Janssen et al. (2002) experiments.

There is still a large room to improve our grasp on sediment transport for highly variable wave current environment with both free stream flow acceleration, phase lag, and other effects.

In Drake and Calantoni (2001), the free stream flow is prescribed based on superposition of sinusoidal wave orbital velocities. Advances made in the past two decade on time-domain modeling of waves and currents across the surfzone have enabled us to obtain improved estimates of instantaneous near bottom fluid velocities. Rakha et al. (1997) and Karambas and Koutitas (2002) have both used Boussinesq models to obtain predictions of surfzone hydrodynamics, and have then used averages of the instantaneous quantities to obtain the statistical moments needed to drive wave-averaged transport models. In contrast, Long and Kirby (2003) have used Boussinesq model predictions to drive an instantaneous transport model, allowing morphology changes to accumulate on a wave by wave basis. Qualitatively accurate representation of onshore bar migration movement was achieved. Similar success with a calibrated transport formula in a wave-averaged setting has been demonstrated by Hoefel and Elgar (2003).

While the results obtained by Long and Kirby (2003) are encouraging, the formula used there has no specific mechanical underpinning. Recently, in a small-scale

two-phase sheet flow model, Hsu et al. (2003) and Hsu and Hanes (2004) demonstrated that the instantaneous sediment transport rate under unsteady forcing follows the instantaneous bed shear stress closely. Motivated by the work of Hsu et al. (2004), the goal of the present work is to use a more appropriate, mechanically-based model for the local boundary layer structure and sediment transport rate over the vertical, integrated with the Boussinesq model in order to provide a profile evolution model. As is pointed out by recent work in Hsu et al. (2004), major transport of sediments occurs within a very concentrated layer near the bed so that bedload transport rate is our main concern here. Previous work such as Ribberink (1998), Hsu and Hanes (2004) and Long and Kirby (2003) tried to estimate bedload transport rate using instantaneous bed shear stress estimated through simple power laws, and their model accuracy relies strongly on the bed shear stress prediction.

This part of research in this dissertation incorporates the newly developed Boussinesq model FUNWAVE2.0 and a wave boundary layer model (Hsu et al., 2004, Justesen, 1988) so that advantages of both of them are exploited. The final goal of this research is to provide an advanced hydrodynamic and sediment transport model in nearshore region. Specific tasks include:

1. Couple the Boussinesq model with a boundary layer model to provide accurate phase-resolving hydrodynamic quantities including velocity profiles and bottom shear stress

2. Propose a reasonable phase-resolving bedload sediment transport model based on more physical grounds

3. Model the morphology change due to sediment transport introduced scour and deposition in space

4. Couple the morphology change with the Boussinesq hydrodynamic model in order to calculate evolution over extended time periods.

Chapter 2

DERIVATION OF NEW BOUSSINESQ EQUATIONS

In this chapter, we derive a set of Boussinesq equations that can cover all versions of equations related to FUNWAVE1.0 systematically, and further extend them to include more new features such as arbitrary vertical level choices of momentum equation as well as inclusion of undertow in the reference velocities. The new equations are derived both from potential flow theory and the Euler equations.

With the schematic layout of the system shown in Figure 2.1, the following coordinates and definition of symbols will be used for mathematical description of 3-D flow system typically in the nearshore area. Cartesian coordinates (x, y, z) are defined as right-hand coordinate system with (x, y) for horizontal dimensions, and z perpendicularly upward. The origin of z is defined at a datum level or still water level (SWL). Topography of the sea bottom is defined by function $z_b(x, y, t)$, and free surface elevation is defined by $\eta(x, y, t)$. Flow field is defined by vector $\mathbf{u}(x, y, z, t) = (u(x, y, z, t), v(x, y, z, t), w(x, y, z, t))$ with u, v, w the velocity component in x, y, z direction respectively. Total depth is denoted by $H = \eta - z_b = \eta + h$, where still water depth is denoted by $h = -z_b$.

The following non-dimensional variables are also defined

$$x' = k_0 x, y' = k_0 y, z' = z/h_0, t' = k_0 C_0 t \tag{2.1}$$

$$\eta' = \eta/a_0, h' = h/h_0 \tag{2.2}$$

where ()' means nondimensional quantities, and () means dimensional quantities. Then,

$$\phi' = \frac{\phi}{\phi_0}; \phi_0 = \frac{a_0 C_0}{k_0 h_0}; (u', v') = \frac{h_0}{a_0 C_0}(u, v); w' = \frac{k_0 h_0^2}{a_0 C_0} w; p' = \frac{p}{\rho g a_0} \tag{2.3}$$

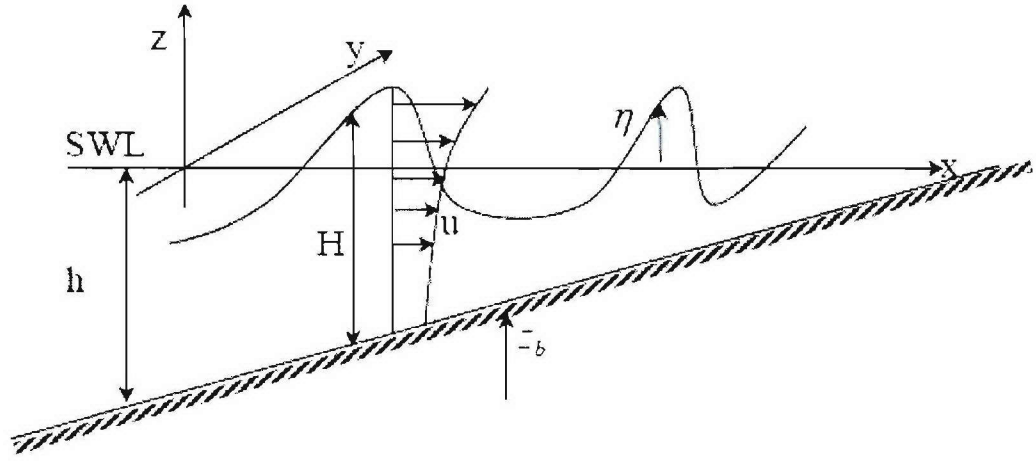

Figure 2.1: Schematic system layout

where l_0 is typical wave length, $l_0 = 2\pi/k_0$; C_0 is typical phase speed, $C_0 = \sqrt{gh_0}$; h_0 is typical water depth: a_0 is typical wave amplitude; k_0 is typical wave number. $p = p(x, y, z, t)$ is pressure field, g is gravitational acceleration.

Two important dimensionless parameters are identified here: $\mu = k_0 h_0$ and $\delta = a_0/h_0$. μ indicates the degree of dispersion, and δ indicates the degree of nonlinearity in the wave field.

We proceed by first listing equations that has already been coded in FUNWAVE1.0, which include Wei et al. (1995), and new developments by Kennedy et al. (2001) and Chen et al. (2003). Then we present the derivation of Gobbi et al. (2000) to obtain a set of Boussinesq equations in which the representative velocity is based on weighted average of two representative velocities defined at two reference levels, with derivations from potential flow theory as in Nwogu (1993) and Wei et al. (1995). Next, the equation of Gobbi et al. (2000) is re-derived from the Euler equation at the same time rendering a new set of equations, in which the momentum equation is physically the momentum balance of fluid

on an arbitrary level other than the free surface elevation. Further, we present a depth integrated momentum equation, which include the effects of wave breaking introduced undertow based on the roller model (Svendsen, 1984; Schäffer et al., 1993) and Lynett (2005).

2.1 Previous Sets of Boussinesq Equations

2.1.1 Equations of Wei et al. (1995), $O(\mu^2)$

The equation system given by Wei et al. (1995) is written as a conservation of mass equation (COM)

$$\eta_t + \nabla \cdot \mathbf{M} = 0 \tag{2.4}$$

where

$$\begin{aligned} \mathbf{M} = \quad & (h+\delta\eta)\{\mathbf{u}_\alpha + \mu^2[\frac{1}{2}z_\alpha^2 - \frac{1}{6}(h^2 - h\delta\eta + \delta^2\eta^2)]\nabla(\nabla\cdot\mathbf{u}_\alpha) \\ + \quad & \mu^2[z_\alpha + \frac{1}{2}(h-\delta\eta)]\nabla[\nabla\cdot(h\mathbf{u}_\alpha)]\} + O(\mu^4) \end{aligned} \tag{2.5}$$

and an equation of motion (EOM)

$$\mathbf{u}_{\alpha t} + \delta(\mathbf{u}_\alpha\cdot\nabla)\mathbf{u}_\alpha + \nabla\eta + \mu^2\mathbf{V}_1 + \delta\mu^2\mathbf{V}_2 = O(\mu^4) \tag{2.6}$$

where

$$\mathbf{V}_1 = \frac{1}{2}z_\alpha^2\nabla(\nabla\cdot\mathbf{u}_{\alpha t}) + z_\alpha\nabla[\nabla\cdot(h\mathbf{u}_{\alpha t})] - \nabla[\frac{1}{2}(\delta\eta)^2\nabla\cdot\mathbf{u}_{\alpha t} + \delta\eta\nabla\cdot(h\mathbf{u}_{\alpha t}] \tag{2.7}$$

$$\begin{aligned} \mathbf{V}_2 = \quad & \nabla\{(z_\alpha - \delta\eta)(\mathbf{u}_\alpha\cdot\nabla)[\nabla\cdot(h\mathbf{u}_\alpha)] + \frac{1}{2}(z_\alpha^2 - \delta^2\eta^2)(\mathbf{u}_\alpha\cdot\nabla)(\nabla\cdot\mathbf{u}_\alpha)\} \\ + \quad & \frac{1}{2}\nabla\{[\nabla\cdot(h\mathbf{u}_\alpha) + \delta\eta\nabla\cdot\mathbf{u}_\alpha]^2\}, \end{aligned} \tag{2.8}$$

with

$$z_\alpha = [(1+2\alpha)^{1/2} - 1]h \approx -0.531h \tag{2.9}$$

$$\alpha = \frac{1}{2}(\frac{z_\alpha}{h})^2 + \frac{z_\alpha}{h} \approx -0.390. \tag{2.10}$$

$\mathbf{u}_\alpha$ is velocity at $z = z_\alpha$: $\mathbf{u}_\alpha = (\nabla\phi)_{z=z_\alpha}$.

2.1.2 Equations of Kennedy et al. (2001), $O(\mu^2)$

The conservation of mass (COM) equation is

$$\eta_t + \nabla \cdot \mathbf{M} = 0 \tag{2.11}$$

where

$$\begin{aligned} \mathbf{M} = (h+\delta\eta)\{\mathbf{u}_\alpha &+ \mu^2[\frac{1}{2}z_\alpha^2 - \frac{1}{6}(h^2 - h\delta\eta + \delta^2\eta^2)]\nabla(\nabla\cdot\mathbf{u}_\alpha) \\ &+ \mu^2[z_\alpha + \frac{1}{2}(h-\delta\eta)]\nabla[\nabla\cdot(h\mathbf{u}_\alpha)]\}. + O(\mu^4) \end{aligned} \tag{2.12}$$

Equations (2.11) (2.12) are identical to equations (2.4) (2.5).

The equation of motion (EOM) is

$$\mathbf{u}_{\alpha t} + \delta(\mathbf{u}_\alpha\cdot\nabla)\mathbf{u}_\alpha + \nabla\eta + \mu^2\mathbf{V}_1 + \delta\mu^2\mathbf{V}_2 = O(\mu^4), \tag{2.13}$$

where

$$\mathbf{V}_1 = [\frac{1}{2}z_\alpha^2\nabla(\nabla\cdot\mathbf{u}_\alpha) + z_\alpha\nabla[\nabla\cdot(h\mathbf{u}_\alpha)]]_t - \nabla[\frac{1}{2}(\delta\eta)^2\nabla\cdot\mathbf{u}_{\alpha t} + \delta\eta\nabla\cdot(h\mathbf{u}_{\alpha t})] \tag{2.14}$$

$$\begin{aligned} \mathbf{V}_2 = \quad & \nabla\{(z_\alpha - \delta\eta)(\mathbf{u}_\alpha\cdot\nabla)[\nabla\cdot(h\mathbf{u}_\alpha)] + \frac{1}{2}(z_\alpha^2 - \delta^2\eta^2)(\mathbf{u}_\alpha\cdot\nabla)(\nabla\cdot\mathbf{u}_\alpha)\} \\ + \quad & \frac{1}{2}\nabla\{[\nabla\cdot(h\mathbf{u}_\alpha) + \delta\eta\nabla\cdot\mathbf{u}_\alpha]^2\}. \end{aligned} \tag{2.15}$$

Equation (2.14) is different from (2.7) by the presence of time derivatives are outside of the square bracket due to the representative water level z_α that is moving in time according to

$$z_\alpha = \rho_0 h + \beta_0\delta\eta, \tag{2.16}$$

and

$$z_{\alpha t} = \beta_0\delta\eta_t \tag{2.17}$$

For a special case ($\rho_0 = \beta_0 - 1$), we have

$$z_\alpha = (\beta_0 - 1)h + \beta_0\delta\eta. \tag{2.18}$$

By setting $\beta_0 = \sqrt{1/5}$, we obtain the Padé [2,2] dispersion relation.

Equation (2.18) is referred as datum invariant version of the Boussinesq equation (Kennedy et al., 2001), for

$$\frac{h + z_\alpha}{h + \delta\eta} = \beta_0 = \text{const.}$$

When

$$\begin{cases} \rho_0 = (1 + 2\alpha)^2 - 1 = -0.531, \\ \beta_0 = 0, \end{cases} \tag{2.19}$$

we recover the Wei et al. (1995) model. When

$$\begin{cases} \rho_0 = \beta_0 - 1 = \sqrt{1/5} - 1 \approx -0.5528; \\ \beta_0 = \sqrt{1/5}, \end{cases} \tag{2.20}$$

we recover the Kennedy et al. (2001) datum invariant model.

2.1.3 Equations of Chen et al. (2003) , $O(\mu^2)$

The continuity of mass (COM) equation is

$$\eta_t + \nabla \cdot \mathbf{M} = 0 \tag{2.21}$$

where

$$\begin{aligned} \mathbf{M} = \quad & (h + \delta\eta)\{\mathbf{u}_\alpha + \mu^2[\frac{1}{2}z_\alpha^2 - \frac{1}{6}(h^2 - h\delta\eta + \delta^2\eta^2)]\nabla(\nabla \cdot \mathbf{u}_\alpha) \\ + \quad & \mu^2[z_\alpha + \frac{1}{2}(h - \delta\eta)]\nabla[\nabla \cdot (h\mathbf{u}_\alpha)]\} + O(\mu^4) \end{aligned} \tag{2.22}$$

The equation of motion (EOM) is

$$\mathbf{u}_{\alpha t} + \delta(\mathbf{u}_\alpha \cdot \nabla)\mathbf{u}_\alpha + \nabla\eta + \mu^2\mathbf{V}_1 + \delta\mu^2\mathbf{V}_2 + \delta\mu^2\mathbf{V}_3 = O(\mu^4) \tag{2.23}$$

where

$$\mathbf{V}_1 = \frac{1}{2}z_\alpha^2\nabla(\nabla \cdot \mathbf{u}_{\alpha t}) + z_\alpha\nabla[\nabla \cdot (h\mathbf{u}_{\alpha t})]] - \nabla[\frac{1}{2}(\delta\eta)^2\nabla \cdot \mathbf{u}_{\alpha t} + \delta\eta\nabla \cdot (h\mathbf{u}_{\alpha t})] \tag{2.24}$$

$$\begin{aligned}\mathbf{V}_2 = \quad & \nabla\{(z_\alpha - \delta\eta)(\mathbf{u}_\alpha \cdot \nabla)[\nabla \cdot (h\mathbf{u}_\alpha)] + \frac{1}{2}(z_\alpha^2 - \delta^2\eta^2)(\mathbf{u}_\alpha \cdot \nabla)(\nabla \cdot \mathbf{u}_\alpha)\} \\ + \quad & \frac{1}{2}\nabla\{[\nabla \cdot (h\mathbf{u}_\alpha) + \delta\eta\nabla \cdot \mathbf{u}_\alpha]^2\} \end{aligned} \tag{2.25}$$

and

$$\mathbf{V}_3 = (V_3^x, V_3^y) = \mathbf{\Omega}_1 \times \mathbf{u}_\alpha \tag{2.26}$$

$$V_3^x = -v_\alpha\omega_1;\ V_3^y = u_\alpha\omega_1 \tag{2.27}$$

$$\mathbf{\Omega}_1 = (0, 0, \omega_1) \tag{2.28}$$

$$\begin{aligned}\omega_1 \quad = \quad & z_{\alpha x}\{[\nabla \cdot (h\mathbf{u}_\alpha)]_y + z_\alpha(\nabla \cdot \mathbf{u}_\alpha)_y\} \\ - \quad & z_{\alpha y}\{[\nabla \cdot (h\mathbf{u}_\alpha)]_x - z_\alpha(\nabla \cdot \mathbf{u}_\alpha)_x\} \end{aligned} \tag{2.29}$$

The Chen et al. (2003) equation has an extra term $\mathbf{V}_3$ compared to Wei et al. (1995) due to the inclusion of the second order correction of vertical vorticity evaluated at $z = z_\alpha$

$$\omega|_{z=z_\alpha} = \omega_0 + \mu^2\omega_1 = (\nabla \times \mathbf{u})|_{z=z_\alpha} \tag{2.30}$$

where

$$\omega_0 = \nabla \times \mathbf{u}_\alpha \tag{2.31}$$

$$\omega_1 = \{\nabla \times (\mathbf{u} - \mathbf{u}_\alpha)\}|_{z=z_\alpha} \tag{2.32}$$

$$\begin{aligned}\mathbf{u} \quad = \quad & \mathbf{u}_\alpha + \mu^2\{(z_\alpha - z)\nabla[\nabla \cdot (h\mathbf{u}_\alpha)] \\ + \quad & (\frac{z_\alpha^2}{2} - \frac{z^2}{2})\nabla(\nabla \cdot \mathbf{u}_\alpha)\} \end{aligned} \tag{2.}$$

The Chen et al. (2003) equation is also equivalent to the results of Liu (1994), where the vorticity term is obtained by rearranging the convection term in the free surface dynamic boundary condition.

2.2 Derivations of Gobbi et al. (2000) Equations and New Equations

In this section, we first re-derive Gobbi et al. (2000) 4-th order equations based on two reference levels, where the two references are extended to be moving as in Kennedy et al. (2001), from potential flow theory. Then we derive the same set of equations from the Euler equations such that the inclusion of vertical vorticity by Chen et al. (2003) is naturally done since the Euler equation doesn't assume zero vertical vorticity even though the horizontal vorticity components are assumed to be zero in the derivation. During the derivation from Euler equation, we will further extend the momentum equation by introducing an arbitrary level z_c on which the momentum equation can be represented unlike the previous equations of Wei et al. (1995), Gobbi et al. (2000) and Kennedy et al. (2001) where the momentum equations are all based on Bernoulli equation of the free surface or the momentum balance of particles on the free surface. The inclusion of z_c gives an additional free parameter that can aid in obtaining better shoaling and nonlinear interaction modeling performance of the resulting equations.

In the derivation, we assume the bottom topography $(z_b(x, y, t))$ is not moving or moving very slowly compared to the water wave motion so that we will neglect time derivative of z_b and still water depth h. In the later chapters for sediment transport, we will include the motion of bottom into the continuity equation and first order terms in the momentum equations but not in the high order dispersive terms for simplicity. This is a reasonable assumption for gravity waves with a time scale much smaller than the morphology change. In some extreme cases such as swash tip of wave run up, the morphology change can be of the same rate as fluid flow, then the effect of h_t should be included.

2.2.1 Derivation from potential flow theory following Gobbi et al. (2000), $O(\mu^4)$

The Gobbi et al. (2000) 4th order Boussinesq equation is derived based on potential flow theory with introduction of two fixed reference levels z_α and z_β. Here we repeat the derivations while further assuming that the two reference levels z_α and z_β are moving according to Kennedy et al. (2001). We start from the following well established mathematical description of the irrotational flow system:

COM (depth integrated continuity equation)

$$\eta_t + \nabla \cdot \mathbf{M} = 0,\ \mathbf{M} = \int_{-h}^{\delta\eta} \nabla\phi dz \tag{2.34}$$

Laplace equation for flow potential

$$\phi_{zz} + \mu^2\nabla^2\phi = 0; \quad -h \le z \le \delta\eta \tag{2.35}$$

Bottom Boundary Condition (BBC)

$$\phi_z + \mu^2\nabla h \cdot \nabla\phi = 0; \quad z = -h \tag{2.36}$$

Dynamic Free Surface Boundary Condition (DFSBC)

$$\eta + \phi_t + \frac{1}{2}\delta[(\nabla\phi)^2 + \frac{1}{\mu^2}(\phi_z)^2] = 0; \quad z = \delta\eta \tag{2.37}$$

Kinematic Free Surface Boundary Condition (KFSBC)

$$\eta_t + \delta\nabla\phi \cdot \nabla\eta - \frac{1}{\mu^2}\phi_z = 0; \quad z = \delta\eta \tag{2.38}$$

The vertical distribution of flow potential $\phi(x, y, z, t)$ can be expressed by a Taylor expansion with $\xi = h + z$ being the distance from bottom to z:

$$\phi(x, y, z, t) = \sum_{n=0}^{N} \xi^n \phi_n(x, y, t). \tag{2.39}$$

From BBC, we obtain

$$\phi_1 = -\mu^2 G\nabla h \cdot \nabla\phi_0 \tag{2.40}$$

where

$$G = \frac{1}{1+\mu^2|\nabla h|^2} \tag{2.41}$$

From Laplace's equation, we have

$$\begin{aligned}(n+2)(n+1)\phi_{n+2} &+ \mu^2[(n+2)(n+1)|\nabla h|^2\phi_{n+2} + (n+1)\nabla^2 h\phi_{n+1} \\ &+ 2(n+1)\nabla h\cdot\nabla\phi_{n+1} + \nabla^2\phi_n] = 0 \ \ (n=0,1,2,...)\end{aligned} \tag{2.42}$$

From the last 3 equations above, we obtain

$$\phi_2 = -\frac{\mu^2}{2}G\nabla^2\phi_0 + \mu^4[\frac{G^2}{2}\nabla^2 h\nabla h\cdot\nabla\phi_0 + G\nabla h\cdot\nabla(G\nabla h\cdot\nabla\phi_0)] + O(\mu^6) \tag{2.43}$$

$$\phi_3 = \mu^4[\frac{G^2\nabla^2 h\nabla^2\phi_0}{6} + \frac{1}{3}G\nabla h\cdot\nabla(G\nabla^2\phi_0) + \frac{1}{6}G\nabla^2(G\nabla h\cdot\nabla\phi_0)] + O(\mu^2) \tag{2.44}$$

$$\phi_4 = \frac{\mu^4}{24}G\nabla^2(G\nabla^2\phi_0) + O(\mu^6) \tag{2.45}$$

so,

$$\begin{aligned}\phi &= \phi_0 + \phi_1\xi + \phi_2\xi^2 + \phi_3\xi^3 + \phi_4\xi^4 + ... \\ &= \phi_0 - \mu^2 G\nabla h\cdot\nabla\phi_0\xi - \frac{\mu^2}{2}G\nabla^2\phi_0\xi^2 \\ &+ \mu^4[\frac{G^2}{2}\nabla^2 h\nabla h\cdot\nabla\phi_0 + G\nabla h\cdot\nabla(G\nabla h\cdot\nabla\phi_0)]\xi^2 \\ &+ \mu^4[\frac{G^2\nabla^2 h\nabla^2\phi_0}{6} + \frac{1}{3}G\nabla h\cdot\nabla(G\nabla^2\phi_0) + \frac{1}{6}G\nabla^2(G\nabla h\cdot\nabla\phi_0)]\xi^3 \\ &+ [\frac{\mu^4}{24}G\nabla^2(G\nabla^2\phi_0) + O(\mu^6)]\xi^4 \\ &+ O(\mu^6).\end{aligned} \tag{2.46}$$

Now we introduce the following representative potential $\tilde{\phi}$ based on a weighted average of flow potential functions on two reference levels z_α and z_β

$$\tilde{\phi} = \beta\phi_\alpha + (1-\beta)\phi_\beta \tag{2.47}$$

where ϕ_α, ϕ_β are ϕ evaluated at z_α, z_β respectively.

In Gobbi et al. (2000), the definitions of z_α, z_β are fixed levels

$$z_\alpha = \{[\frac{1}{9} - \{\frac{8\beta}{567(1-\beta)}\}^{1/2} + \{\frac{8}{567\beta(1-\beta)}\}^{1/2}]^{1/2} - 1\}h \tag{2.48}$$

$$z_\beta = \{[\frac{1}{9} - \{\frac{8\beta}{567(1-\beta)}\}^{1/2}]^{1/2} - 1\}h, \tag{2.49}$$

$$\beta \approx 0.2, \tag{2.50}$$

but in the derivations here, we let z_α and z_β move with time according to Kennedy et al. (2001). Substituting ϕ_α and ϕ_β into $\tilde{\phi}$, one obtains

$$\begin{aligned}
\tilde{\phi} = \phi_0 \quad &- \quad \mu^2(AhG\nabla h \cdot \nabla\phi_0 + \frac{1}{2}Bh^2G\nabla^2\phi_0) \\
&+ \quad \mu^4\{Bh^2[\frac{1}{2}G^2\nabla^2 h\nabla h \cdot \nabla\phi_0 + G\nabla h \cdot \nabla(G\nabla h \cdot \nabla\phi_0)] \\
&+ \quad Ch^3[\frac{1}{6}G^2\nabla^2 h\nabla^2\phi_0 + \frac{1}{3}G\nabla h \cdot \nabla(G\nabla^2\phi_0) + \frac{1}{6}G\nabla^2(G\nabla h \cdot \nabla\phi_0)] \\
&+ \quad Dh^4\frac{1}{24}G\nabla^2(G\nabla^2\phi_0)\} \\
&+ \quad O(\mu^6)
\end{aligned} \tag{2.51}$$

where

$$\begin{cases}
A = \frac{1}{h}[\beta(h+z_\alpha) + (1-\beta)(h+z_\beta)] \\
B = \frac{1}{h^2}[\beta(h+z_\alpha)^2 + (1-\beta)(h+z_\beta)^2] \\
C = \frac{1}{h^3}[\beta(h+z_\alpha)^3 + (1-\beta)(h+z_\beta)^3] \\
D = \frac{1}{h^4}[\beta(h+z_\alpha)^4 + (1-\beta)(h+z_\beta)^4]
\end{cases} \tag{2.52}$$

Inverting the equation above, we obtain ϕ_0 in terms of $\tilde{\phi}$

$$\begin{aligned}
\phi_0 = \tilde{\phi} \quad &+ \quad \mu^2[AhG\nabla h \cdot \nabla\tilde{\phi} + \frac{1}{2}Bh^2G\nabla^2\tilde{\phi}] \\
&+ \quad \mu^4[AhG\nabla h \cdot \nabla(AhG\nabla h \cdot \nabla\tilde{\phi} + \frac{1}{2}Bh^2G\nabla^2\tilde{\phi}) \\
&+ \quad \frac{1}{2}Bh^2G\nabla^2(AhG\nabla h \cdot \nabla\tilde{\phi} + \frac{1}{2}Bh^2G\nabla^2\tilde{\phi})] \\
&- \quad \mu^4\{Bh^2[\frac{1}{2}G^2\nabla^2 h\nabla h \cdot \nabla\tilde{\phi} + G\nabla h \cdot \nabla(G\nabla h \cdot \nabla\tilde{\phi})]
\end{aligned}$$

$$
\begin{aligned}
&+ \quad Ch^3[\frac{1}{6}G^2\nabla^2 h\nabla^2\tilde{\phi} + \frac{1}{3}G\nabla h\cdot\nabla(G\nabla^2\tilde{\phi}) + \frac{1}{6}G\nabla^2(G\nabla h\cdot\nabla\tilde{\phi})] \\
&+ \quad Dh^4\frac{1}{24}G\nabla^2(G\nabla^2\tilde{\phi})\} \\
&+ \quad O(\mu^6)
\end{aligned} \tag{2.53}
$$

Substituting into (2.46) gives

$$
\begin{aligned}
\phi = \quad & \tilde{\phi} + \mu^2[(Ah-\xi)F_1 + (Bh^2-\xi^2)F_2] \\
+ \quad & \mu^4[(Ah-\xi)F_3 + (Bh^2-\xi^2)F_4 + (Ch^3-\xi^3)F_5 + (Dh^4-\xi^4)F_6]
\end{aligned} \tag{2.54}
$$

where

$$
\left\{
\begin{array}{l}
F_1 = G\nabla h\cdot\nabla\tilde{\phi} \\
F_2 = \frac{1}{2}G\nabla^2\tilde{\phi} \\
F_3 = \nabla h\cdot\nabla(Ah\nabla h\cdot\nabla\tilde{\phi}) + \frac{1}{2}\nabla h\cdot\nabla(Bh^2\nabla^2\tilde{\phi}) \\
F_4 = \frac{1}{2}\nabla^2(Ah\nabla h\cdot\nabla\tilde{\phi}) + \frac{1}{4}\nabla^2(Bh^2\nabla^2\tilde{\phi}) \\
-\frac{1}{2}\nabla^2 h\nabla h\cdot\nabla\tilde{\phi} - \nabla h\cdot\nabla(\nabla h\cdot\nabla\tilde{\phi}) \\
F_5 = -\frac{1}{6}\nabla^2 h\nabla^2\tilde{\phi} - \frac{1}{3}\nabla h\cdot\nabla(\nabla^2\tilde{\phi}) - \frac{1}{6}\nabla^2(\nabla h\cdot\nabla\tilde{\phi}) \\
F_6 = -\frac{1}{24}\nabla^2(\nabla^2\tilde{\phi})
\end{array}
\right. \tag{2.55}
$$

The horizontal velocity is then given by

$$
\begin{aligned}
\mathbf{u} = \nabla\phi \quad = \quad & \nabla\tilde{\phi} \\
& + \quad \mu^2[(\nabla(AhF_1) - \xi\nabla F_1 - F_1\nabla h) \\
& + \quad (\nabla(Bh^2F_2) - \xi^2\nabla F_2 - 2\xi F_2\nabla h)] \\
& + \quad \mu^4[(\nabla(AhF_3) - \xi\nabla F_3 - F_3\nabla h) \\
& + \quad (\nabla(Bh^2F_4) - \xi^2\nabla F_4 - 2\xi F_4\nabla h) \\
& + \quad (\nabla(Ch^3F_5) - \xi^3\nabla F_5 - 3\xi^2F_5\nabla h) \\
& + \quad (\nabla(Dh^4F_6) - \xi^4\nabla F_6 - 4\xi^3F_6\nabla h)]
\end{aligned} \tag{2.56}
$$

The volume flux of fluid per unit width can be calculated by integrating the velocity over the depth,

$$
\mathbf{M} = \int_{-h}^{\delta\eta}\nabla\phi dz = \int_0^H \nabla\phi d\xi
$$

which gives

$$\begin{aligned}
\mathbf{M} &= H\nabla\tilde{\phi} \\
&+ \mu^2 H\{\nabla(AhF_1) - \frac{H}{2}\nabla F_1 - F_1\nabla h \\
&+ \nabla(Bh^2F_2) - \frac{H^2}{3}\nabla F_2 - HF_2\nabla h\} \\
&+ \mu^4 H\{\nabla(AhF_3) - \frac{H}{2}\nabla F_3 - F_3\nabla h \\
&+ \nabla(Bh^2F_4) - \frac{H^2}{3}\nabla F_4 - HF_4\nabla h \\
&+ \nabla(Ch^3F_5) - \frac{H^3}{4}\nabla F_5 - H^2F_5\nabla h \\
&+ \nabla(Dh^4F_6) - \frac{H^4}{5}\nabla F_6 - H^3F_6\nabla h\} \qquad (2.57)
\end{aligned}$$

Substituting equation (2.54) into DFSBC, we get the following Bernoulli equation

$$\begin{aligned}
\eta &+ \tilde{\phi}_t + \frac{1}{2}\delta|\nabla\tilde{\phi}|^2 \\
&+ \mu^2[(A_thF_1 + (Ah - H)F_{1t}) + (B_th^2F_2 + (Bh^2 - H^2)F_{2t})] \\
&+ \delta\mu^2[\nabla\tilde{\phi}\cdot\{\nabla((Ah - H)F_1) + F_1\nabla\delta\eta \\
&+ \nabla((Bh^2 - H^2)F_2) + 2F_2H\nabla\delta\eta\} \\
&+ \frac{1}{2}(F_1 + 2HF_2)^2] \\
&+ \mu^4[(A_thF_3 + (Ah - H)F_{3t}) + (B_th^2F_4 + (Bh^2 - H^2)F_{4t}) \\
&+ (C_th^3F_5 + (Ch^3 - H^3)F_{5t} + (D_th^4F_6 + (Dh^4 - H^4)F_{6t})] \\
&+ \delta\mu^4[\frac{1}{2}|\nabla((Ah - H)F_1) + F_1\nabla\delta\eta + \nabla((Bh^2 - H^2)F_2) + 2F_2H\nabla\delta\eta|^2 \\
&+ \nabla\tilde{\phi}\cdot[\nabla((Ah - H)F_3) + F_3\nabla\delta\eta + \nabla((Bh^2 - H^2)F_4) - 2F_4H\nabla\delta\eta \\
&+ \nabla((Ch^3 - H^3)F_5) + 3F_5H^2\nabla\delta\eta + \nabla((Dh^4 - H^4)F_6) - 4F_6H^3\nabla\delta\eta] \\
&+ (F_1 + 2HF_2)(F_3 + 2HF_4 + 3H^2F_5 + 4H^3F_6)\} \\
&= O(\mu^6) \qquad (2.58)
\end{aligned}$$

Next, we introduce representative velocity $\tilde{\mathbf{u}}$ based on reference velocity on the two reference levels

$$\begin{aligned}\tilde{\mathbf{u}}(x,y,t) &= \beta\mathbf{u}_\alpha + (1-\beta)\mathbf{u}_\beta \\ &= \beta[\nabla\phi]|_{z=z_\alpha} + (1-\beta)[\nabla\phi]|_{z=z_\beta} \end{aligned} \tag{2.59}$$

where

$$\begin{aligned}[\nabla\phi]|_{z=z_\alpha} &= \nabla\tilde{\phi} \\ &+ \mu^2[(\nabla(AhF_1) - (h+z_\alpha)\nabla F_1 - F_1\nabla h) \\ &+ (\nabla(Bh^2F_2) - (h+z_\alpha)^2\nabla F_2 - 2(h+z_\alpha)F_2\nabla h)] \\ &+ \mu^4[(\nabla(AhF_3) - (h+z_\alpha)\nabla F_3 - F_3\nabla h) \\ &+ (\nabla(Bh^2F_4) - (h+z_\alpha)^2\nabla F_4 - 2(h+z_\alpha)F_4\nabla h) \\ &+ (\nabla(Ch^3F_5) - (h+z_\alpha)^3\nabla F_5 - 3(h+z_\alpha)^2F_5\nabla h) \\ &+ (\nabla(Dh^4F_6) - (h+z_\alpha)^4\nabla F_6 - 4(h+z_\alpha)^3F_6\nabla h)] \end{aligned} \tag{2.60}$$

$[\nabla\phi]|_{z=z_\beta}$ is similar. Thus, we have $\tilde{\mathbf{u}}$ in terms of $\tilde{\phi}$,

$$\begin{aligned}\tilde{\mathbf{u}} &= \beta\mathbf{u}_\alpha + (1-\beta)\mathbf{u}_\beta \\ &= \nabla\tilde{\phi} + \mu^2[F_1\nabla(Ah-h) + F_2(\nabla(Bh^2) - 2Ah\nabla h)] \\ &+ \mu^4[F_3\nabla(Ah-h) + F_4(\nabla(Bh^2) - 2Ah\nabla h) \\ &+ F_5(\nabla(Ch^3) - 3Bh^2\nabla h) + F_6(\nabla(Dh^4) - 4h^3(\nabla h)] \\ &+ O(\mu^6). \end{aligned} \tag{2.61}$$

By inverting this equation, we get

$$\begin{aligned}\nabla\tilde{\phi} &= \tilde{\mathbf{u}} \\ &- \mu^2[F_{21}(\nabla(Ah) - \nabla h) + F_{22}(\nabla(Bh^2) - 2Ah\nabla h)] \\ &- \mu^4[(F_{41}+F_{43})(\nabla(Ah) - \nabla h) + (F_{42}+F_{44})(\nabla(Bh^2) - 2Ah\nabla h) \\ &+ F_{45}(\nabla(Ch^3) - 3Bh^2\nabla h) + F_{46}(\nabla(Dh^4) - 4Ch^3\nabla h)] \end{aligned} \tag{2.62}$$

where

$$F_{21} = G\nabla h \cdot \tilde{\mathbf{u}} \tag{2.63}$$

$$F_{22} = \frac{1}{2} G\nabla \cdot \tilde{\mathbf{u}} \tag{2.64}$$

$$F_{41} = \nabla h \cdot \mathbf{L} \tag{2.65}$$

$$F_{42} = \frac{1}{2}\nabla \cdot \mathbf{L} \tag{2.66}$$

$$F_{43} = \nabla h \cdot \nabla(Ah\nabla h \cdot \tilde{\mathbf{u}}) + \frac{1}{2}\nabla h \cdot \nabla(Bh^2\nabla \cdot \tilde{\mathbf{u}}) \tag{2.67}$$

$$F_{44} = \frac{1}{2}\nabla^2(Ah\nabla h \cdot \tilde{\mathbf{u}}) + \frac{1}{4}\nabla^2(Bh^2\nabla \cdot \tilde{\mathbf{u}}) - \frac{1}{2}\nabla^2 h\nabla h \cdot \tilde{\mathbf{u}} - \nabla h \cdot \nabla(\nabla h \cdot \tilde{\mathbf{u}}) \tag{2.68}$$

$$F_{45} = -\frac{1}{6}\nabla^2 h\nabla \cdot \tilde{\mathbf{u}} - \frac{1}{3}\nabla h \cdot \nabla(\nabla \cdot \tilde{\mathbf{u}}) - \frac{1}{6}\nabla^2(\nabla h \cdot \tilde{\mathbf{u}}) \tag{2.69}$$

$$F_{46} = -\frac{1}{24}\nabla^2(\nabla \cdot \tilde{\mathbf{u}}) \tag{2.70}$$

$$\mathbf{L} = -[\nabla h \cdot \tilde{\mathbf{u}}(\nabla(Ah) - \nabla h) + \frac{1}{2}\nabla \cdot \tilde{\mathbf{u}}(\nabla(Bh^2) - 2Ah\nabla h)] \tag{2.71}$$

Substituting $\nabla\tilde{\phi}$ into (2.57), the depth integrated flow rate $\mathbf{M}$ becomes

$$\begin{aligned}
\mathbf{M} &= H\tilde{\mathbf{u}} \\
&+ \mu^2 H\{\mathbf{L} + \nabla(AhF_{21}) - \frac{H}{2}\nabla F_{21} - F_{21}\nabla h \\
&+ \nabla(Bh^2F_{22}) - \frac{H^2}{3}\nabla F_{22} - HF_{22}\nabla h\} \\
&- \mu^4 H\{\mathbf{L}_{41} + \mathbf{L}_{43} + \mathbf{L}_{42} + \mathbf{L}_{44} + \mathbf{L}_{45} + \mathbf{L}_{46}\} \\
&+ \mu^4 H\{\nabla(Ah\nabla h \cdot \mathbf{L}) - \frac{H}{2}\nabla(\nabla h \cdot \mathbf{L}) - (\nabla h \cdot \mathbf{L})\nabla h \\
&+ \nabla(Bh^2\frac{1}{2}\nabla \cdot \mathbf{L}) - \frac{H^2}{3}\nabla(\frac{1}{2}\nabla \cdot \mathbf{L}) - \frac{H}{2}(\nabla \cdot \mathbf{L})\nabla h\} \\
&+ \mu^4 H\{\nabla(AhF_{43}) - \frac{H}{2}\nabla F_{43} - F_{43}\nabla h \\
&+ \nabla(Bh^2F_{44}) - \frac{H^2}{3}\nabla F_{44} - HF_{44}\nabla h \\
&+ \nabla(Ch^3F_{45}) - \frac{H^3}{4}\nabla F_{45} - H^2F_{45}\nabla h \\
&+ \nabla(Dh^4F_{46}) - \frac{H^4}{5}\nabla F_{46} - H^3F_{46}\nabla h\} \\
&+ O(\mu^6)
\end{aligned} \tag{2.72}$$

where

$$\mathbf{L}_{41} = F_{41}\mathbf{A}_1 \ ; \ \mathbf{L}_{42} = F_{42}\mathbf{B}_1$$

$$\mathbf{L}_{43} = F_{43}\mathbf{A}_1 \ ; \ \mathbf{L}_{44} = F_{44}\mathbf{B}_1$$

$$\mathbf{L}_{45} = F_{45}\mathbf{C}_1 \ ; \ \mathbf{L}_{46} = F_{46}\mathbf{D}_1$$

$$\mathbf{A}_1 = \nabla(Ah) - \nabla h \ ; \ \mathbf{B}_1 = \nabla(Bh^2) - 2Ah\nabla h$$

$$\mathbf{C}_1 = \nabla(Ch^3) - 3Bh^2\nabla h \ ; \ \mathbf{D}_1 = \nabla(Dh^4) - 4Ch^3\nabla h$$

$$\mathbf{L}_{21} = F_{21}\mathbf{A}_1 \ ; \ \mathbf{L}_{22} = F_{22}\mathbf{B}_1$$

$$\mathbf{L} = -(\mathbf{L}_{21} + \mathbf{L}_{22})$$

$$\nabla h \cdot \mathbf{L} = F_{41} \ ; \ \nabla h \cdot \mathbf{L} = F_{42} \tag{2.73}$$

Simplification leads to

$$\begin{aligned}
\mathbf{M} &= H\{\tilde{\mathbf{u}} \\
&+ \mu^2[(Ah - \frac{H}{2})(2\nabla hF_{22} + \nabla F_{21}) + (Bh^2 - \frac{H^2}{3})\nabla F_{22}] \\
&+ \mu^4[(Ah - \frac{H}{2})(2\nabla hF_{42} + \nabla F_{41} + 2\nabla hF_{44} + \nabla F_{43}) \\
&+ (Bh^2 - \frac{H^2}{2})(\nabla F_{42} + 3\nabla hF_{45} + \nabla F_{44}) \\
&+ (Ch^3 - \frac{H^3}{4})(4\nabla hF_{46} + \nabla F_{45}) + (Dh^4 - \frac{H^4}{5})\nabla F_{46}]\} \\
&+ O(\mu^6)
\end{aligned} \tag{2.74}$$

By taking gradient to Bernoulli equation [1](2.58) (i.e. the DFSBC), we obtain

$$\nabla\eta \ + \ (\nabla\tilde{\phi})_t + \frac{1}{2}\delta\nabla|\nabla\tilde{\phi}|^2$$

[1] Note that this treatment automatically leaves out the vorticity term given by Chen et al. (2003) and Liu (1994). In Liu (1994), the gradient of the convection term in DFSBC is written as $(\nabla\phi \cdot \nabla)\nabla\phi$ to retain the vorticity term. The vorticity term is important for simulating nearshore shear waves generated by wave breaking, bottom friction and lateral mixing.

$$
\begin{aligned}
&+ \mu^2[\nabla(A_t h F_1) + \nabla((Ah - H)F_{1t}) \\
&+ \nabla(B_t h^2 F_2) + \nabla((Bh^2 - H^2)F_{2t})] \\
&+ \delta\mu^2\{\nabla[\nabla\tilde{\phi}\cdot[\nabla((Ah - H)F_1 + F_1\delta\eta \\
&+ \nabla((Bh^2 - H^2)F_2) + 2F_2 H\nabla\delta\eta]] \\
&+ \frac{1}{2}\nabla(F_1 + 2HF_2)^2\} \\
&+ \mu^4[\nabla(A_t h F_3 + (Ah - H)F_{3t}) + \nabla(B_t h^2 F_4 + (Bh^2 - H^2)F_{4t}) \\
&+ \nabla(C_t h^3 F_5 + (Ch^3 - H^3)F_{5t}) + \nabla(D_t h^4 F_6 + (Dh^4 - H^4)F_{6t})] \\
&+ \frac{1}{2}\delta\mu^4\nabla|\nabla((Ah - H)F_1) + F_1\nabla\delta\eta \\
&+ \nabla((Bh^2 - H^2)F_2) + 2F_2 H\nabla\delta\eta|^2 \\
&+ \delta\mu^4\nabla\{\nabla\tilde{\phi}\cdot[\nabla((Ah - H)F_3) + F_3\nabla\delta\eta \\
&+ \nabla((Bh^2 - H2)F_4) + 2F_4 H\nabla\delta\eta \\
&+ \nabla((Ch^3 - H^3)F_5) + 3F_5 H^2\nabla\delta\eta \\
&+ \nabla((Dh^4 - H^4)F_6) + 4F_6 H^3\nabla\delta\eta]\} \\
&+ \delta\mu^4\nabla\{(F_1 + 2HF_2)(F_3 + 2HF_4 + 3H^2F_5 + 4H^3F_6)\} \\
&= O(\mu^6)
\end{aligned}
\tag{2.75}
$$

Substitute the expression of $\nabla\tilde{\phi}$, which is (2.62), into this equation, we have a momentum equation in terms of $\tilde{\mathbf{u}}$ physically describing the momentum balance of fluid particles on the free surface

$$
\begin{aligned}
\tilde{\mathbf{u}}_t &- \mu^2[-\mathbf{L}_t] \\
&+ \mu^2[\nabla(A_t h F_{21}) + \nabla((Ah - H)F_{21t}) \\
&+ \nabla(B_t h^2 F_{22}) + \nabla((Bh^2 - H^2)F_{22t})] \\
&+ \mu^4[\mathbf{L}_{41t} + \mathbf{L}_{43t} + \mathbf{L}_{42t} + \mathbf{L}_{44t} + \mathbf{L}_{45t} + \mathbf{L}_{46t}] \\
&- \mu^4[-\nabla(A_t h\nabla h\cdot\mathbf{L}) - \nabla((Ah - H)\nabla h\cdot\mathbf{L}_t) \\
&- \nabla(B_t h^2\frac{1}{2}\nabla\cdot\mathbf{L}) - \nabla((Bh^2 - H^2)\frac{1}{2}\nabla\cdot\mathbf{L}_t)]
\end{aligned}
$$

$$
\begin{aligned}
&+ \mu^4[\nabla(A_t h F_{43} + (Ah - H)F_{43t}) + \nabla(B_t h^2 F_{44} + (Bh^2 - H^2)F_{44t}) \\
&+ \nabla(C_t h^3 F_{45} + (Ch^3 - H^3)F_{45t}) + \nabla(D_t h^4 F_{46} + (Dh^4 - H^4)F_{46t})] \\
= &- \nabla\eta - \frac{1}{2}\delta\nabla|\tilde{\mathbf{u}}|^2 + \delta\mu^2[-\nabla(\tilde{\mathbf{u}} \cdot \mathbf{L})] \\
&- \delta\mu^2\{\nabla[\tilde{\mathbf{u}} \cdot [\nabla((Ah - H)F_{21}) + \nabla((Bh^2 - H^2)F_{22}) \\
&+ F_{21}\nabla\delta\eta + 2HF_{22}\nabla\delta\eta]] + \frac{1}{2}\nabla(F_{21} + 2HF_{22})^2\} \\
&- \delta\mu^4\{\frac{1}{2}\nabla|\mathbf{L}|^2 \\
&- \nabla(\tilde{\mathbf{u}} \cdot [\mathbf{L}_{41} + \mathbf{L}_{43} + \mathbf{L}_{42} + \mathbf{L}_{44} + \mathbf{L}_{45} + \mathbf{L}_{46}])\} \\
&- \delta\mu^4\{\nabla\{\tilde{\mathbf{u}} \cdot [\nabla((Ah - H)\nabla h \cdot \mathbf{L}) + \nabla h \cdot \mathbf{L}\nabla\delta\eta \\
&+ \nabla \cdot ((Bh^2 - H^2)\frac{1}{2}\nabla \cdot \mathbf{L}) + \nabla \cdot \mathbf{L}H\nabla\delta\eta]\} \\
&+ \nabla\{\mathbf{L} \cdot [\nabla((Ah - H)F_{21} + F_{21}\nabla\delta\eta \\
&+ \nabla((Bh^2 - H^2)F_{22} + 2HF_{22}\nabla\delta\eta]\} \\
&+ \frac{1}{2}\nabla\{2F_{21}\nabla h \cdot \mathbf{L} + 4H^2F_{22}\nabla \cdot \mathbf{L} \\
&+ 2HF_{21}\nabla \cdot \mathbf{L} + 4HF_{22}\nabla h \cdot \mathbf{L}\}\} \\
&- \frac{1}{2}\delta\mu^4\nabla|\nabla((Ah - H)F_{21}) + F_{21}\nabla\delta\eta \\
&+ \nabla((Bh^2 - H^2)F_{22}) + 2HF_{22}\nabla\delta\eta|^2 \\
&- \delta\mu^4\nabla\{\tilde{\mathbf{u}} \cdot [\nabla((Ah - H)F_{43}) + F_{43}\nabla\delta\eta \\
&+ \nabla((Bh^2 - H^2)F_{42}) + 2F_{44}H\nabla\delta\eta \\
&+ \nabla((Ch^3 - H^3)F_{45}) + 3F_{45}H^2\nabla\delta\eta \\
&+ \nabla((Dh^4 - H^4)F_{46}) + 4F_{46}H^3\nabla\delta\eta]\} \\
&- \delta\mu^4\nabla\{(F_{21} + 2HF_{22})(F_{43} + 2HF_{44} + 3H^2F_{45} + 4H^3F_{46})\} \\
&+ O(\mu^6)
\end{aligned}
\tag{2.76}
$$

By utilizing $F_{42} = \frac{1}{2}\nabla \cdot \mathbf{L}$, $F_{41} = \nabla h \cdot \mathbf{L}$, the upper equation can be simplified to

$$
\mathbf{U}_t = -\nabla\eta - \frac{\delta}{2}\nabla(|\tilde{\mathbf{u}}|^2) + \mathbf{\Gamma}_1 + \mathbf{\Gamma}_2 \tag{2.77}
$$

where

$$\begin{aligned}
\mathbf{U} &= \tilde{\mathbf{u}} \\
&+ \mu^2[(A-1)h(2\nabla hF_{22} + \nabla F_{21}) + (B-1)h^2\nabla F_{22}] \\
&+ \mu^4[(A-1)h(2\nabla hF_{42} + \nabla F_{41} + 2\nabla hF_{44} + \nabla F_{43}) \\
&+ (B-1)h^2(\nabla F_{42} + 3\nabla hF_{45} + \nabla F_{44}) \\
&+ (C-1)h^3(4\nabla hF_{46} + \nabla F_{45}) \\
&+ (D-1)h^4\nabla F_{46}] \qquad (2.78)
\end{aligned}$$

$$\begin{aligned}
\mathbf{\Gamma}_1 &= \mu^2\nabla[\delta\eta F_{21t} + (2h\delta\eta + \delta^2\eta^2)F_{22t}] \\
&+ \mu^4\nabla[\delta\eta(F_{41t} + F_{43t}) + (2h\delta\eta + \delta^2\eta^2)(F_{42t} + F_{44t}) \\
&+ (3h^2\delta\eta + 3h\delta^2\eta^2 + \delta^3\eta^3)F_{45t} \\
&+ (4h^3\delta\eta + 6h^2\delta^2\eta^2 + 4h\delta^3\eta^3 + \delta^4\eta^4)F_{46t}] \qquad (2.79)
\end{aligned}$$

$$\begin{aligned}
\mathbf{\Gamma}_2 &= -\delta\mu^2\nabla\{\tilde{\mathbf{u}}\cdot[(Ah - H)(\nabla F_{21} + 2\nabla hF_{22}) \\
&+ (Bh^2 - H^2)\nabla F_{22}] + \frac{1}{2}(F_{21} + 2HF_{22})^2\} \\
&- \delta\mu^4\nabla\{\tilde{\mathbf{u}}\cdot[(Ah - H)(\nabla F_{41} + 2\nabla hF_{42} + \nabla F_{43} + 2\nabla hF_{44}) \\
&+ (Bh^2 - H^2)(\nabla F_{42} + \nabla F_{44} + 3\nabla hF_{45}) \\
&+ (Ch^3 - H^3)(\nabla F_{45} + 4\nabla hF_{46}) + (Dh^4 - H^4)\nabla F_{46}] \\
&+ \frac{1}{2}|(Ah - H)(\nabla F_{21} + 2\nabla hF_{22}) + (Bh^2 - H^2)\nabla F_{42}|^2 \\
&+ \frac{1}{2}[(F_{21} + 2HF_{22})(F_{41} + 2HF_{42} \\
&+ F_{43} + 2HF_{44} + 3H^2F_{45} + 4H^3F_{46})]\} \qquad (2.80)
\end{aligned}$$

Mass conservation equation (2.74) and momentum equation (2.77) are the 4th order Boussinesq equations with multiple moving reference levels.

The second order equation sets are $O(\mu^2)$

$$\eta_t + \nabla\cdot\mathbf{M} = 0 \qquad (2.81)$$

$$\mathbf{U}_t = -\nabla\eta - \frac{\delta}{2}\nabla(|\tilde{\mathbf{u}}|^2) + \mu^2\mathbf{\Gamma}_1 + \delta\mu^2\mathbf{\Gamma}_2 \tag{2.82}$$

$$\begin{aligned}\mathbf{M} &= H\{\tilde{\mathbf{u}}\} \\ &+ \mu^2 H\{(Ah - \frac{H}{2})(2\nabla hF_{22} + \nabla F_{21}) + (Bh^2 - \frac{H^2}{3})\nabla F_{22}\}\end{aligned} \tag{2.83}$$

$$\mathbf{U} = \tilde{\mathbf{u}} + \mu^2[(A-1)h(2\nabla hF_{22} + \nabla F_{21}) + (B-1)h^2\nabla F_{22}] \tag{2.84}$$

$$\mathbf{\Gamma}_1 = \nabla[\delta\eta F_{21t} + (2h\delta\eta + \delta^2\eta^2)F_{22t}] \tag{2.85}$$

$$\begin{aligned}\mathbf{\Gamma}_2 &= -\nabla\{\tilde{\mathbf{u}} \cdot [(Ah - H)(\nabla F_{21} + 2\nabla hF_{22}) \\ &+ (Bh^2 - H^2)\nabla F_{22}] + \frac{1}{2}(F_{21} + 2HF_{22})^2\}.\end{aligned} \tag{2.86}$$

In dimensional form

$$\eta_t + \nabla \cdot \mathbf{M} = 0 \tag{2.87}$$

$$\mathbf{U}_t = -g\nabla\eta - \frac{1}{2}\nabla(|\tilde{\mathbf{u}}|^2) + \mathbf{\Gamma}_1 + \mathbf{\Gamma}_2 \tag{2.88}$$

$$\begin{aligned}\mathbf{M} &= H\{\tilde{\mathbf{u}}\} \\ &+ H\{(Ah - \frac{H}{2})(2\nabla hF_{22} + \nabla F_{21}) + (Bh^2 - \frac{H^2}{3})\nabla F_{22}\}\end{aligned} \tag{2.89}$$

$$\mathbf{U} = \tilde{\mathbf{u}} + [(A-1)h(2\nabla hF_{22} + \nabla F_{21}) + (B-1)h^2\nabla F_{22}] \tag{2.90}$$

$$\mathbf{\Gamma}_1 = \nabla[\eta F_{21t} + (2h\eta + \eta^2)F_{22t}] \tag{2.91}$$

$$\begin{aligned}\mathbf{\Gamma}_2 &= -\nabla\{\tilde{\mathbf{u}} \cdot [(Ah - H)(\nabla F_{21} + 2\nabla hF_{22}) \\ &+ (Bh^2 - H^2)\nabla F_{22}] + \frac{1}{2}(F_{21} + 2HF_{22})^2\}\end{aligned} \tag{2.92}$$

where

$$F_{21} = G\nabla h \cdot \tilde{\mathbf{u}}, \tag{2.93}$$

$$F_{22} = \frac{1}{2}G\nabla \cdot \tilde{\mathbf{u}}, \tag{2.94}$$

$$G = \frac{1}{1 + |\nabla h|^2}. \tag{2.95}$$

When setting $\beta = 1$, then

$$Ah = h + z_\alpha;\ \ Bh^2 = (h + z_\alpha)^2;\ \ Ch^3 = (h + z_\alpha)^3;\ \ Dh^4 = (h + z_\alpha)^4$$

$$\tilde{\mathbf{u}} = \tilde{\mathbf{u}}_\alpha$$

$$F_{21} = G\nabla h \cdot \tilde{\mathbf{u}} = \nabla h \cdot \tilde{\mathbf{u}}_a + O(\mu^4)$$

$$F_{22} = \frac{1}{2}\nabla \cdot \tilde{\mathbf{u}}_a + O(\mu^4),$$

and equation (2.87) and equation (2.88) recovers Kennedy et al. (2001) equation (2.11) and (2.13) and further recovers Wei et al. (1995) equation by setting $z_\alpha = -0.531h$. These equations do not include the effect of vorticity advection when there are wave breaking, bottom friction and lateral mixing, so that corrections are needed. Derivations from the Euler equations will automatically include the vertical vorticity term by Chen et al. (2003) and Liu (1994), and this is done in a later section. From a pure potential flow point of view, these equations are correct since no vorticity exists in a potential flow wave field.

2.2.2 Kinematics of potential theory

It is important for a model to be able to calculate kinematics of the flow field for engineering concerns and sediment transport. We summarize the kinematics included in the Boussinesq equations presented above.

(1) Horizontal velocity $\mathbf{u}(x, y, z, t)$

Substituting (2.62) into (2.56), the horizontal velocity can be written as

$$\begin{aligned}
\mathbf{u} &= \tilde{\mathbf{u}} \\
&+ \mu^2\{(Ah - \xi)(\nabla F_{21} + 2\nabla h F_{22}) + (Bh^2 - \xi^2)\nabla F_{22}\} \\
&+ \mu^4\{(Ah - \xi)(\nabla F_{41} + \nabla F_{43} + 2\nabla h F_{42} + 2\nabla h F_{44}) \\
&+ (Bh^2 - \xi^2)(\nabla F_{42} + \nabla F_{44} + 3\nabla h F_{45}) \\
&+ (Ch^3 - \xi^3)(\nabla F_{45} + 4\nabla h F_{46})
\end{aligned}$$

$$
\begin{aligned}
&+ \quad (Dh^4 - \xi^4)\nabla F_{46}\} \\
&+ \quad O(\mu^6) \qquad (2.96)
\end{aligned}
$$

(2) Vertical velocity $w(x, y, z, t)$

$$
\begin{aligned}
w(x, y, z, t) &= \phi_z \\
&= \mu^2(-F_1 - 2\xi F_2) \\
&+ \mu^4(-F_3 - 2\xi F_4 - 3\xi^2 F_5 - 4\xi^3 F_6) \qquad (2.97)
\end{aligned}
$$

where $F_1, F_2, F_3, F_4, F_5, F_6$ are all in terms of $\nabla\tilde{\phi}$. Substitute (2.62) into the upper equation, we have

$$
\begin{aligned}
w(x, y, z, t) = &- \mu^2(F_{21} + 2\xi F_{22}) \\
&- \mu^4(F_{41} + F_{43} + 2\xi F_{42} + 2\xi F_{44} + 3\xi^2 F_{45} + 4\xi^3 F_{46}) \qquad (2.98)
\end{aligned}
$$

(3) Pressure $p(x, y, z, t)$

The pressure field can be derived from vertical component of Euler momentum equation

$$
w_t + \delta u w_x + \delta v w_y = -p_z - \frac{1}{\delta} \qquad (2.99)
$$

i.e.

$$
-p_z = \frac{1}{\delta} + w_t + \delta \mathbf{u} \cdot \nabla w \qquad (2.100)
$$

Considering (2.96)(2.98), we have

$$
\begin{aligned}
-p_z &= \frac{1}{\delta} \\
&- \mu^2[F_{21t} + 2\xi F_{22t} + \delta\tilde{\mathbf{u}} \cdot (\nabla F_{21} + 2\xi\nabla F_{22} + 2F_{22}\nabla h)] \\
&- \mu^4\{(F_{41t} + F_{43t} + 2\xi F_{42t} + 2\xi F_{44t} + 3\xi^2 F_{45t} + 4\xi^3 F_{46t}) \\
&+ \delta\tilde{\mathbf{u}} \cdot (\nabla F_{41} + \nabla F_{43} + 2\xi\nabla F_{42} + 2\xi\nabla F_{44} + 3\xi^2\nabla F_{45} \\
&+ 4\xi^3\nabla F_{46} + 6\xi F_{45}\nabla h + 12\xi^2 F_{46}\nabla h)
\end{aligned}
$$

$$
\begin{aligned}
&+ \quad \delta(Ah-\xi)(\nabla F_{21}+2\nabla h F_{22})\cdot(\nabla F_{21}+2F_{22}\nabla h) \\
&+ \quad \delta 2(Ah-\xi)\xi(\nabla F_{21}+2\nabla h F_{22})\cdot\nabla F_{22} \\
&+ \quad \delta(Bh^2-\xi^2)\nabla F_{22}\cdot(\nabla F_{21}+2\nabla h F_{22}) \\
&+ \quad \delta 2\xi(Bh^2-\xi^2)\nabla F_{22}\cdot\nabla F_{22}\} \\
&+ \quad O(\mu^6)
\end{aligned} \tag{2.101}
$$

After integrating from surface to z, we obtain

$$
\begin{aligned}
p-p_a &= \eta-\frac{z}{\delta} \\
&- \quad \mu^2\{(H-\xi)F_{21t}+(H^2\xi^2)F_{22t} \\
&+ \quad \delta\tilde{\mathbf{u}}\cdot[\nabla F_{21}(H-\xi)+\nabla F_{22}(H^2-\xi^2)+2F_{22}\nabla h(H-\xi)]\} \\
&- \quad \mu^4\{(F_{41t}+F_{43t})(H-\xi)+(F_{42t}+F_{44t})(H^2-\xi^2) \\
&+ \quad 2(H-\xi)(F_{42}+F_{44})\nabla h \\
&+ \quad F_{45t}(H^3-\xi^3)+F_{46t}(H^4-\xi^4) \\
&+ \quad \delta\tilde{\mathbf{u}}\cdot[(H-\xi)(\nabla F_{41}+\nabla F_{43}) \\
&+ \quad (H^2-\xi^2)(\nabla F_{42}+\nabla F_{44}) \\
&+ \quad (H^3-\xi^3)\nabla F_{45}+(H^4-\xi^4)\nabla F_{46} \\
&+ \quad 3(H^2-\xi^2)F_{45}\nabla h+4(H^3-\xi^3)F_{46}\nabla h] \\
&+ \quad \delta[Ah(H-\xi)-\frac{(H^2-\xi^2)}{2}](\nabla F_{21}+2\nabla h F_{22}) \\
&\cdot \quad (\nabla F_{21}+2F_{22}\nabla h) \\
&+ \quad \delta[Ah(H^2-\xi^2)+Bh^2(H-\xi)-(H^3-\xi^3)]\nabla F_{22} \\
&\cdot \quad (\nabla F_{21}+2\nabla h F_{22}) \\
&+ \quad \delta[Bh^2(H^2-\xi^2)+\frac{1}{2}(H^4-\xi^4)]\nabla F_{22}\cdot\nabla F_{22}\} \\
&+ \quad O(\mu^6)
\end{aligned} \tag{2.102}
$$

where p_a is the atmospheric pressure on the surface.

Briefly, for a second order approximation,

$$\mathbf{u} = \tilde{\mathbf{u}} + \mu^2\{(Ah - \xi)(\nabla F_{21} + 2\nabla h F_{22}) + (Bh^2 - \xi^2)\nabla F_{22}\} \tag{2.103}$$

$$w(x, y, z, t) = -\mu^2(F_{21} + 2\xi F_{22}) \tag{2.104}$$

$$\begin{aligned} p &= p_a + \eta - \frac{z}{\delta} \\ &- \mu^2\{(\delta\eta - z)F_{21t} + (H^2 - \xi^2)F_{22t} \\ &+ \delta\tilde{\mathbf{u}} \cdot [\nabla F_{21}(\delta\eta - z) + \nabla F_{22}(H^2 - \xi^2) + 2F_{22}\nabla h(\delta\eta - z)]\} \end{aligned} \tag{2.105}$$

In dimensional form, we have

$$\mathbf{u} = \tilde{\mathbf{u}} + \{(Ah - \xi)(\nabla F_{21} + 2\nabla h F_{22}) + (Bh^2 - \xi^2)\nabla F_{22}\} \tag{2.106}$$

$$w(x, y, z, t) = -(F_{21} + 2\xi F_{22}) \tag{2.107}$$

$$\begin{aligned} p &= p_a + \rho g(\eta - z) \\ &- \rho\{(\eta - z)F_{21t} + (H^2 - \xi^2)F_{22t} \\ &+ \tilde{\mathbf{u}} \cdot [\nabla F_{21}(\eta - z) + \nabla F_{22}(H^2 - \xi^2) + 2F_{22}\nabla h(\eta - z)]\} \end{aligned} \tag{2.108}$$

(4) Flux per unit width

The depth integrated flux per unit width is expressed by

$$\mathbf{M} = \int_{-h}^{\delta\eta} \mathbf{u} dz \equiv (P, Q), \tag{2.109}$$

where P is flux per unit width in the x direction and Q is flux per unit width in the y direction.

(5) Wave averaged current field

Wave averaged and depth averaged current is calculated by

$$\overline{\mathbf{U}} = \frac{\overline{\mathbf{M}}}{h + \delta\eta} \equiv (\overline{U}, \overline{V}), \tag{2.110}$$

where the $\overline{()}$ denotes time average.

(6) Potential vorticity

Potential vorticity is defined by

$$q = \frac{\nabla \times \frac{\mathbf{M}}{h+\delta\eta}}{h+\delta\eta} \tag{2.111}$$

(7) Set up and set down

The wave set up and set down is simply the time averaged free surface elevation

$$\overline{\eta} = \frac{1}{T}\int_t^{t+T} \eta dt, \tag{2.112}$$

where T is the averaging time period.

2.2.3 Definition of reference levels z_α, z_β

The definition of z_α, z_β in this research is quite general such that it can be both fixed or moving to recover all equations included in FUNWAVE1.0.

$$z_\alpha = \rho_1 h + \beta_1 \delta\eta \tag{2.113}$$

$$z_\beta = \rho_2 h + \beta_2 \delta\eta \tag{2.114}$$

$$\tilde{\mathbf{u}} = \beta \mathbf{u}_\alpha + (1-\beta)\mathbf{u}_\beta \tag{2.115}$$

$$\tilde{\phi} = \beta \phi_\alpha + (1-\beta)\phi_\beta \tag{2.116}$$

The optimization of $\rho_1, \beta_1, \rho_2, \beta_2, \beta$ needs further investigation. In Gobbi et al. (2000), z_α, z_β, β are defined by (2.48) to (2.50) which are fixed reference levels with $\beta_1 = \beta_2 = 0$.

2.2.4 Derivations from Euler equation with vertical vorticity retained $O(\mu^2)$

Boussinesq equations can be also derived from Euler equation as shown in Nwogu (1993). The advantage of the derivation from Euler equation is that it gives us another perspective based on the primitive equations instead of equations of a derived field such as the flow potential. Also, the assumption of vanishing vertical vorticity inherently contained in potential theory can be released since here we can only use vanishing horizontal

vorticity components when doing depth integration. Chen et al. (2003) extended Wei et al. (1995) by retaining vertical vorticity that enables the derived Boussinesq equations to simulate production, convection and mixing of eddies in the horizontal plane. Here we re-derive the equations of the previous section from Euler equations by showing that kinematics are exactly same. The vertical vorticity is retained as Chen et al. (2003), plus a new set of equations resulted from momentum balance of fluid particles on an arbitrary and moving z_c level instead of the previous equations from potential theory which are about momentum balance of fluid particles on free surface only.

2.2.4.1 Governing equations and assumptions

The governing equations from Eulerian point of view for inviscid and incompressible flow are

(1) COM

$$\nabla \cdot \mathbf{u} + w_z = u_x + v_y + w_z = 0 \tag{2.117}$$

(2) EOM

$$x - direction: \; u_t + uu_x + vu_y + wu_z = -\frac{1}{\rho}p_x \tag{2.118}$$

$$y - direction: \; v_t + uv_x + vv_y + wv_z = -\frac{1}{\rho}p_y \tag{2.119}$$

$$z - direction: \; w_t + uw_x + vw_y + ww_z = -\frac{1}{\rho}p_z - g \tag{2.120}$$

The non-dimensional forms of the above equations are written as

(1) COM

$$\mu^2 \nabla \cdot \mathbf{u} + w_z = \mu^2 u_x + \mu^2 v_y + w_z = 0 \tag{2.121}$$

(2) EOM

$$\frac{D\mathbf{u}}{Dt} + \nabla p = 0 \tag{2.122}$$

$$\frac{Dw}{Dt} + p_z + 1/\delta = 0 \tag{2.123}$$

where

$$\frac{D}{Dt} = \frac{\partial}{\partial t} + \delta(\mathbf{u} \cdot \nabla) + \frac{\delta}{\mu^2} w \frac{\partial}{\partial z} \tag{2.124}$$

$$\mathbf{u} = (u, v);\ \nabla = (\frac{\partial}{\partial x}, \frac{\partial}{\partial y}) \tag{2.125}$$

The boundary conditions on the bottom and the free surface are

(1) KFSBC

$$\mu^2 \frac{\partial \eta}{\partial t} + \delta \mu^2 \mathbf{u} \cdot \nabla \eta - w = 0;\ z = \delta \eta \tag{2.126}$$

(2) DFSBC

$$p = p_a = 0;\ z = \delta \eta \tag{2.127}$$

(3) BBC

$$\mu^2 \mathbf{u} \cdot \nabla h + w = 0;\ z = -h \tag{2.128}$$

Horizontal vorticity components are assumed to be zero for the convenience of integration in the vertical direction, leading to a non-horizontal-vorticity condition:

$$\frac{\partial \mathbf{u}}{\partial z} - \nabla w = 0;\ -h \leq z \leq \delta \eta. \tag{2.129}$$

2.2.4.2 Consistency of kinematics between Euler theory and potential theory

Here, we show that the kinematic flow structure from the Euler equation and potential theory are exactly the same when the non-horizontal-vorticity assumption is applied.

The COM integrated from $z = -h$ to z gives

$$\int_{-h}^{z} \mu^2 \nabla \cdot \mathbf{u} dz + \int_{-h}^{z} \frac{\partial w}{\partial z} dz = 0 \tag{2.130}$$

Utilizing Leibniz's Rule, this equation becomes

$$\mu^2\nabla\cdot\int_{-h}^{z}\mathbf{u}dz+w|_z-[\mu^2(\mathbf{u}\cdot\nabla h)|_{-h}+w|_{-h}]=0 \tag{2.131}$$

The square bracket is BBC (2.128), then this equation is reduced to

$$w(x,y,z,t)=-\mu^2\nabla\cdot\int_{-h}^{z}\mathbf{u}dz \tag{2.132}$$

We can introduce a Taylor expansion of $\mathbf{u}$ at $z=-h$

$$\mathbf{u}=\mathbf{u}_b+\frac{\partial\mathbf{u}}{\partial z}|_{z=-h}(h+z)+\frac{\partial^2\mathbf{u}}{\partial z^2}|_{z=-h}\frac{(h+z)^2}{2}+\frac{\partial^3\mathbf{u}}{\partial z^3}|_{z=-h}\frac{(h+z)^3}{6}+\ldots \tag{2.133}$$

where $\mathbf{u}_b$ is velocity at bottom $z=-h$.

In order to express (2.133) in terms of $\mathbf{u}_b$, the terms $\frac{\partial\mathbf{u}}{\partial z}|_{-h}$ and $\frac{\partial^2\mathbf{u}}{\partial z^2}|_{-h}$ can be obtained from the non-horizontal-vorticity condition (2.129).

$$\begin{aligned}
\frac{\partial\mathbf{u}}{\partial z}|_{-h} &= \nabla w|_{-h}\\
&= -\mu^2\{\nabla[\nabla\cdot\int_{-h}^{z}\mathbf{u}dz]\}|_{z=-h}\\
&= -\mu^2\{\nabla[\int_{-h}^{z}\nabla\cdot\mathbf{u}dz+\mathbf{u}\cdot\nabla h]\}|_{z=-h}\\
&= -\mu^2\{\int_{-h}^{z}\nabla(\nabla\cdot\mathbf{u})dz+(\nabla\cdot\mathbf{u})_{z=-h}\nabla h+\nabla(\mathbf{u}_b\cdot\nabla h)\}|_{z=-h}\\
&= -\mu^2[(\nabla\cdot\mathbf{u})|_{z=-h}\nabla h+\nabla(\mathbf{u}_b\cdot\nabla h)]+O(\mu^4)
\end{aligned} \tag{2.134}$$

Here, in order to calculate $(\nabla\cdot\mathbf{u})|_{z=-h}$ in terms of $\mathbf{u}_b$, we need $\nabla\cdot\mathbf{u}$. By integrating the no-horizontal-vorticity condition (2.129) from $-h$ to z , we have

$$\mathbf{u}=\int_{-h}^{z}\nabla w dz+\mathbf{u}_b. \tag{2.135}$$

So,

$$\begin{aligned}
\nabla\cdot\mathbf{u} &= \nabla\cdot\int_{-h}^{z}\nabla w dz-\nabla\cdot\mathbf{u}_b\\
&= \int_{-h}^{z}\nabla^2 w dz+(\nabla w)|_{z=-h}\nabla h+\nabla\cdot\mathbf{u}_b
\end{aligned} \tag{2.136}$$

and

$$\begin{aligned}(\nabla \cdot \mathbf{u})|_{z=-h} &= \int_{-h}^{-h} \nabla^2 w dz + (\nabla w)|_{z=-h} \cdot \nabla h + \nabla \cdot \mathbf{u}_b \\ &= (\nabla w)|_{z=-h} \cdot \nabla h + \nabla \cdot \mathbf{u}_b, \end{aligned} \tag{2.137}$$

where $(\nabla w)|_{z=-h}$ is again (2.134). Substituting (2.134) into the upper equation, it becomes

$$(\nabla \cdot \mathbf{u})|_{z=-h} = -\mu^2[(\nabla \cdot \mathbf{u})|_{z=-h}\nabla h + \nabla(\mathbf{u}_b \cdot \nabla h)] \cdot \nabla h + \nabla \cdot \mathbf{u}_b. \tag{2.138}$$

The equation (2.138) is now an iterative formula for $(\nabla \cdot \mathbf{u})|_{-h}$. By iterating it once, we have

$$(\nabla \cdot \mathbf{u})|_{z=-h} = -\mu^2[\nabla \cdot \mathbf{u}_b \nabla h + \nabla(\mathbf{u}_b \cdot \nabla h)]\nabla h + \nabla \cdot \mathbf{u}_b + O(\mu^4) \tag{2.139}$$

Substitution of (2.139) into (2.134) yields

$$\begin{aligned}\frac{\partial \mathbf{u}}{\partial z}|_{-h} &= (\nabla w)|_{-h} \\ &= -\mu^2[\nabla \cdot \mathbf{u}_b \nabla h + \nabla(\mathbf{u}_b \cdot \nabla h)] + O(\mu^4) \end{aligned} \tag{2.140}$$

Substituting (2.133) into (2.132) and utilizing (2.140) and (2.138),

$$\begin{aligned} w(x, y, z, t) = \quad & -\mu^2 \nabla \cdot [(h + z)\mathbf{u}_b] \\ & + \mu^4 \nabla \cdot \{\frac{(h+z)^2}{2}[\nabla(\mathbf{u}_b \cdot \nabla h) + \nabla \cdot \mathbf{u}_b \cdot \nabla h]\} \\ & - \mu^2 \nabla \cdot [\frac{(h+z)^3}{6}\frac{\partial^2 \mathbf{u}}{\partial z^2}|_{-h}] \\ & + O(\mu^6) \end{aligned} \tag{2.141}$$

In the upper equation, $\frac{\partial^2 \mathbf{u}}{\partial z^2}|_{-h}$ is unknown. However, we can use it to obtain a second order expression for $\mathbf{u}$. Substituting (2.141) into (2.135), we obtain

$$\mathbf{u} = \mathbf{u}_b - \mu^2(h + z)\nabla[\nabla \cdot (h\mathbf{u}_b)] - \mu^2(\frac{z^2}{2} - \frac{h^2}{2})\nabla(\nabla \cdot \mathbf{u}_b) + O(\mu^4) \tag{2.142}$$

Equation (2.142) is the same as Nwogu (1993). Then, we have

$$\frac{\partial^2 \mathbf{u}}{\partial z^2}|_{-h} = -\mu^2 \nabla(\nabla \cdot \mathbf{u}_b) + O(\mu^4) \tag{2.143}$$

Finally, by substituting (2.143) into (2.141), we obtain the expression for $w(x, y, z, t)$

$$\begin{aligned} w = & - \mu^2 \nabla \cdot [(h+z)\mathbf{u}_b] \\ & + \mu^4 \nabla \cdot \{\frac{(h+z)^2}{2}[\nabla(\mathbf{u}_b \cdot \nabla h) + \nabla \cdot \mathbf{u}_b \nabla h]\} \\ & + \mu^4 \nabla \cdot \{\frac{(h+z)^3}{6}\nabla(\nabla \cdot \mathbf{u}_b)\} \\ & + O(\mu^6) \end{aligned} \tag{2.144}$$

The equations (2.142) and (2.144) give kinematics in terms of bottom velocity $\mathbf{u}_b$. Now we can re-express them into terms of $\tilde{\mathbf{u}}$. Let $\mathbf{u}_\alpha = (\mathbf{u})|_{z=z_\alpha}$, $\mathbf{u}_\beta = (\mathbf{u})|_{z=z_\beta}$, from (2.142), we obtain

$$\mathbf{u}_\alpha = \mathbf{u}_b - \mu^2(h + z_\alpha)\nabla[\nabla \cdot (h\mathbf{u}_b)] - \mu^2(\frac{z_\alpha^2}{2} - \frac{h^2}{2})\nabla(\nabla \cdot \mathbf{u}_b). \tag{2.145}$$

Similarly,

$$\mathbf{u}_\beta = \mathbf{u}_b - \mu^2(h + z_\beta)\nabla[\nabla \cdot (h\mathbf{u}_b)] - \mu^2(\frac{z_\beta^2}{2} - \frac{h^2}{2})\nabla(\nabla \cdot \mathbf{u}_b). \tag{2.146}$$

Let

$$\tilde{\mathbf{u}} = \beta \mathbf{u}_\alpha + (1 - \beta)\mathbf{u}_\beta \tag{2.147}$$

Substituting (2.145), (2.146) into (2.147), we have

$$\tilde{\mathbf{u}} = \mathbf{u}_b - \mu^2 Ah\nabla[\nabla \cdot (h\mathbf{u}_b)] - \mu^2(\frac{B}{2} - A)h^2\nabla(\nabla \cdot \mathbf{u}_b) + O(\mu^4). \tag{2.148}$$

Equation (2.148) can be inverted to get

$$\mathbf{u}_b = \tilde{\mathbf{u}} + \mu^2 Ah\nabla[\nabla \cdot (h\tilde{\mathbf{u}})] + \mu^2 \frac{B - 2A}{2} h^2 \nabla(\nabla \cdot \tilde{\mathbf{u}}) + O(\mu^4). \tag{2.149}$$

Substituting (2.149) into (2.142) and (2.144), we immediately have

$$\mathbf{u} = \tilde{\mathbf{u}} + \mu^2(Ah - \xi)\nabla[\nabla \cdot (h\tilde{\mathbf{u}})] + \mu^2(\frac{B - 2A}{2}h^2 - \frac{\xi^2}{2} + h\xi)\nabla(\nabla \cdot \tilde{\mathbf{u}}) + O(\mu^4) \tag{2.150}$$

and

$$w(x,y,z,t) = -\mu^2 \nabla \cdot (\xi \tilde{\mathbf{u}}) + O(\mu^4) \tag{2.151}$$

where $\xi = (h+z)$, and A, B are defined as (2.52). It is easy to prove that (2.150) and (2.151) are the same as (2.103) and (2.98). Therefore the kinematics from Euler theory and potential theory are identical and the same conclusion applies to the pressure distribution (2.105).

2.2.4.3 Boussinesq equation with vertical vorticity retained

2.2.4.3.1 Continuity equation (COM)

Integration of COM (2.121) from $-h$ to $\delta\eta$ gives

$$\int_{-h}^{\delta\eta} \mu^2 \nabla \cdot \mathbf{u} dz + \int_{-h}^{\delta\eta} \mu^2 \frac{\partial w}{\partial z} dz = 0. \tag{2.152}$$

Utilizing Leibniz's rule while considering BBC (2.128) and KFSBC (2.126), it is then

$$\frac{\partial \eta}{\partial t} + \nabla \cdot \int_{-h}^{\delta\eta} \mathbf{u} dz = 0. \tag{2.153}$$

This is the same as (2.34). Because $\mathbf{u}$ is the same as potential theory, the continuity equation is finally the same as potential theory too.

2.2.4.3.2 Momentum equation evaluated at $z = \delta\eta$

Integrating (2.123) from z to $\delta\eta$ gives

$$\int_z^{\delta\eta} \frac{\partial p}{\partial z} dz = -\int_z^{\delta\eta} \frac{Dw}{Dt} dz - \int_z^{\delta\eta} \frac{1}{\delta} dz \tag{2.154}$$

or

$$p|_{\delta\eta} - p(x,y,z,t) = -\int_z^{\delta\eta} \frac{Dw}{Dt} dz - \frac{\delta\eta - z}{\delta} \tag{2.155}$$

Consider DFSBC (2.127) which is $p|_{\delta\eta} = 0$, and taking horizontal gradient to the upper equation gives

$$\begin{aligned} \nabla p &= \nabla \int_z^{\delta\eta} \frac{Dw}{Dt} dz + \nabla\eta \\ &= \int_z^{\delta\eta} \nabla[\frac{Dw}{Dt}] dz + \frac{Dw}{Dt}|_{z=\delta\eta} \delta \nabla\eta + \nabla\eta \end{aligned} \tag{2.156}$$

Substituting (2.156) into (2.122) gives

$$\frac{D\mathbf{u}}{Dt} + \int_z^{\delta\eta} \nabla[\frac{Dw}{Dt}]dz + \nabla\eta[\delta\frac{Dw}{Dt}|_{z=\delta\eta} + 1] = 0. \tag{2.157}$$

This is the momentum equation valid for any z level.

The derivation of momentum equation (2.77) is from DFSBC. Now, we set $z = \delta\eta$ in (2.157) for the purpose of consistency. In (2.157) , we evaluate the three terms one by one.

i) $\frac{D\mathbf{u}}{Dt}$

$$\frac{D\mathbf{u}}{Dt} = \frac{\partial\mathbf{u}}{\partial t} + \delta(\mathbf{u}\cdot\nabla)\mathbf{u} + \frac{\delta}{\mu^2}w\frac{\partial\mathbf{u}}{\partial z} \tag{2.158}$$

where $\frac{\partial\mathbf{u}}{\partial t}$ can be obtained from(2.103)

$$\begin{aligned}
\frac{\partial\mathbf{u}}{\partial t} = & \quad \tilde{\mathbf{u}}_t \\
& + \mu^2\{(Ah-\xi)(\nabla F_{21} + 2\nabla h F_{22}) + (Bh^2 - \xi^2)\nabla F_{22}\}_t \\
= & \quad \tilde{\mathbf{u}}_t \\
& + \mu^2\{[Ah(\nabla F_{21} + 2\nabla h F_{22})_t] - \xi(\nabla F_{21} + 2\nabla h F_{22})_t \\
& + (Bh^2\nabla F_{22})_t - \xi^2(\nabla F_{22})_t\}.
\end{aligned} \tag{2.159}$$

Set $\xi = h + \delta\eta$, then

$$\begin{aligned}
\frac{\partial\mathbf{u}}{\partial t}|_{\delta\eta} = & \quad \{\tilde{\mathbf{u}} \\
& + \mu^2[(A-1)h(\nabla F_{21} + 2\nabla h F_{22}) + (B-1)h^2\nabla F_{22}]\}_t \\
& - \mu^2[\delta\eta(\nabla F_{21t} + 2\nabla h F_{22t}) + (\delta^2\eta^2 + 2h\delta\eta)\nabla F_{22t}] \\
= & \quad \mathbf{U}_t \\
& - \mu^2[\delta\eta(\nabla F_{21t} + 2\nabla h F_{22t}) + (\delta^2\eta^2 + 2h\delta\eta)\nabla F_{22t}]
\end{aligned} \tag{2.160}$$

where

$$\begin{aligned}
\mathbf{U} = & \quad \tilde{\mathbf{u}} + \mu^2[(A-1)h(\nabla F_{21} + 2\nabla h F_{22}) + (B-1)h^2\nabla F_{22}] \\
& + O(\mu^4)
\end{aligned} \tag{2.161}$$

is the same as (2.84).

The second term in (2.158) is $\delta(\mathbf{u}\cdot\nabla)\mathbf{u}$. From (2.103), we have

$$\begin{aligned}
\delta(\mathbf{u}\cdot\nabla)\mathbf{u} &= \delta(\tilde{\mathbf{u}}\cdot\nabla)\tilde{\mathbf{u}} \\
&+ \delta\mu^2(\tilde{\mathbf{u}}\cdot\nabla)[(Ah-\xi)(\nabla F_{21} \\
&+ 2\nabla hF_{22}) + (Bh^2-\xi^2)\nabla F_{22}] \\
&+ \delta\mu^2([(Ah-\xi)(\nabla F_{21}+2\nabla hF_{22}) + (Bh^2-\xi^2)\nabla F_{22}]\cdot\nabla)\tilde{\mathbf{u}} \\
&+ O(\delta\mu^4) \\
&= \delta(\tilde{\mathbf{u}}\cdot\nabla)\tilde{\mathbf{u}} \\
&+ \delta\mu^2(\tilde{\mathbf{u}}\cdot\nabla[(Ah-(H+(z-\delta\eta)))(\nabla F_{21}+2\nabla hF_{22}) \\
&+ (Bh^2-(H+(z-\delta\eta)^2))\nabla F_{22}] \\
&+ \delta\mu^2\{[(Ah-(H+(z-\delta\eta)))(\nabla F_{21}+2\nabla hF_{22}) \\
&+ (Bh^2-(H+(z-\delta\eta)^2))\nabla F_{22}]\cdot\nabla\}\tilde{\mathbf{u}} \qquad (2.162)
\end{aligned}$$

By setting $z=\delta\eta$, the upper equation gives

$$\begin{aligned}
\delta(\mathbf{u}\cdot\nabla)\mathbf{u}|_{\delta\eta} &= \delta(\tilde{\mathbf{u}}\cdot\nabla)\tilde{\mathbf{u}} + \delta\mu^2(\tilde{\mathbf{u}}\cdot\nabla)\tilde{\mathbf{u}}_1 + \delta\mu^2(\tilde{\mathbf{u}}_1\cdot\nabla)\tilde{\mathbf{u}} \\
&+ \delta\mu^2\tilde{\mathbf{u}}\cdot\nabla\eta(\nabla F_{21}+2\nabla hF_{22}+2H\nabla F_{22}) \qquad (2.163)
\end{aligned}$$

where

$$\tilde{\mathbf{u}}_1 = (Ah-H)(\nabla F_{21}+2\nabla hF_{22}) + (Bh^2-H^2)\nabla F_{22} \qquad (2.164)$$

$\tilde{\mathbf{u}}_1$ is the second order $(O(\mu^2))$ part of $\mathbf{u}$ at $z=\delta\eta$ (See equation(2.103)).

The third term in (2.158) is $\frac{\delta}{\mu^2}w\frac{\partial\mathbf{u}}{\partial z}$. Substitue (2.103)(2.104) into it, then

$$\frac{\delta}{\mu^2}w\frac{\partial\mathbf{u}}{\partial z} = \delta\mu^2\{(F_{21}+2\xi F_{22})(\nabla F_{21}+2\nabla hF_{22}+2\xi\nabla F_{22})\} + O(\mu^4) \qquad (2.165)$$

By setting $\xi = h+\delta\eta = H$, it gives

$$\frac{\delta}{\mu^2}w\frac{\partial\mathbf{u}}{\partial z} = \delta\mu^2\{(F_{21}+2HF_{22})(\nabla F_{21}+2\nabla hF_{22}+2H\nabla F_{22})\} + O(\mu^4) \qquad (2.166)$$

ii)$\int_z^{\delta\eta} \nabla[\frac{Dw}{Dt}]dz$

This term is zero when setting $z = \delta\eta$, i.e.

$$\int_z^{\delta\eta} \nabla[\frac{Dw}{Dt}]dz|_{z=\delta\eta} = 0 \tag{2.167}$$

iii)$\delta\frac{Dw}{Dt}|_{z=\delta\eta}$

$$\delta\frac{Dw}{Dt} = \frac{\partial w}{\partial t} + \delta(\mathbf{u}\cdot\nabla)w + \frac{\delta}{\eta^2}w\frac{\partial w}{\partial z} \tag{2.168}$$

where the first term is calculated by (2.104)

$$\frac{\partial w}{\partial t} = -\mu^2(F_{21t} + 2F_{22t}\xi). \tag{2.169}$$

Substitute $\xi = H$ into it, then

$$\frac{\partial w}{\partial t}|_{z=\delta\eta} = -\mu^2(F_{21t} + 2HF_{22t}). \tag{2.170}$$

The second term is calculated by (2.103) and (2.104)

$$\begin{aligned}\delta(\mathbf{u}\cdot\nabla)w = &- \delta\mu^2(\tilde{\mathbf{u}}\cdot\nabla)F_{21} - \delta\mu^2 2(\tilde{\mathbf{u}}\cdot\nabla h)F_{22} \\ &- \delta\mu^2 2\xi\tilde{\mathbf{u}}\cdot\nabla F_{22} + O(\mu^4)\end{aligned} \tag{2.171}$$

Setting $\xi = H$ gives

$$\delta(\mathbf{u}\cdot\nabla)w = -\delta\mu^2\tilde{\mathbf{u}}\cdot(\nabla F_{21} + 2\nabla h F_{22} + 2H\nabla F_{22}) + O(\mu^4). \tag{2.172}$$

The third term can also be obtained from (2.104)

$$\frac{\delta}{\mu^2}w\frac{\partial w}{\partial z}|_{z=\delta\eta} = \delta\mu^2(F_{21} + 2HF_{22})2F_{22} + O(\mu^4) \tag{2.173}$$

Substitute i) ii) and iii) into (2.157), utilizing the following identities,

$$(\tilde{\mathbf{u}}\cdot\nabla)\tilde{\mathbf{u}}_1 + (\tilde{\mathbf{u}}_1\cdot\nabla)\tilde{\mathbf{u}} = \nabla(\tilde{\mathbf{u}}\cdot\tilde{\mathbf{u}}_1) + (\nabla\times\tilde{\mathbf{u}}_1)\times\tilde{\mathbf{u}} + (\nabla\times\tilde{\mathbf{u}})\times\tilde{\mathbf{u}}_1$$

$$(\tilde{\mathbf{u}}\cdot\nabla)\tilde{\mathbf{u}} = \frac{1}{2}\nabla(\tilde{\mathbf{u}}\cdot\tilde{\mathbf{u}}) + (\nabla\times\tilde{\mathbf{u}})\times\tilde{\mathbf{u}},$$

we obtain

$$\mathbf{U}_t = -\nabla\eta - \frac{1}{2}\delta\nabla(\tilde{\mathbf{u}}\cdot\tilde{\mathbf{u}}) + \mu^2\Gamma_1 + \delta\mu^2\Gamma_2 + \Gamma_3 \tag{2.174}$$

where

$$\Gamma_1 = \nabla[\delta\eta F_{21t} + (2h\delta\eta + \delta^2\eta^2)F_{22t}] \tag{2.175}$$

$$\Gamma_2 = -\nabla\{\tilde{\mathbf{u}}\cdot\tilde{\mathbf{u}}_1 + \frac{1}{2}(F_{21} + 2HF_{22})^2\} \tag{2.176}$$

$$\begin{aligned}\Gamma_3 = & - [\delta(\nabla\times\tilde{\mathbf{u}})\times\tilde{\mathbf{u}} + \delta\mu^2(\nabla\times\tilde{\mathbf{u}}_1)\times\tilde{\mathbf{u}} + \delta\mu^2(\nabla\times\tilde{\mathbf{u}})\times\tilde{\mathbf{u}}_1 \\ & + \delta\mu^2\tilde{\mathbf{u}}\cdot\nabla\delta\eta(\nabla F_{21} + 2\nabla h F_{22} + 2H\nabla F_{22}) \\ & - \delta\mu^2\nabla\delta\eta\tilde{\mathbf{u}}\cdot(\nabla F_{21} + 2\nabla h F_{22} + 2H\nabla F_{22})]\end{aligned} \tag{2.177}$$

Γ_1 , Γ_2 are the same as results from potential theory (2.85) and (2.86). Γ_3 can be proved to be $-\delta(\nabla\times\mathbf{u})|_{z=\delta\eta}\times\mathbf{u}|_{z=\delta\eta}$, i. e.

$$\begin{aligned}\Gamma_3 &= -\delta(\nabla\times\mathbf{u})|_{z=\delta\eta}\times\mathbf{u}|_{z=\delta\eta} \\ &= -\delta\boldsymbol{\Omega}|_{z=\delta\eta}\times\mathbf{u}|_{z=\delta\eta}\end{aligned} \tag{2.178}$$

$\mathbf{U}$ is the horizontal velocity $\mathbf{u}$ at still water level $z = 0$; Γ_3 is contribution due to vertical vorticity on the surface.

2.2.4.3.3 Momentum equation evaluated at arbitrary level $z = z_c$

Equation (2.157) can also be evaluated at an arbitrary level

$$z = z_c(x,y,t) \equiv \rho_c h(x,y) + \beta_c\delta\eta(x,y,t) \tag{2.179}$$

and an optimized z_c may lead to better modeling results.

In this case,

$$\begin{aligned}\Gamma_1 &= \nabla[z_c F_{21t} + (2hz_c + z_c^2)F_{22t}] \\ &+ \nabla[(\delta\eta - z_c)(F_{21t} + (\delta\eta + z_c)F_{22t})] \\ &+ \nabla[2h(\delta\eta - z_c)F_{22t}] \\ &= \nabla[\delta\eta 2F_{23t} + \delta^2\eta^2 F_{22t}]\end{aligned} \tag{2.180}$$

$$\begin{aligned}\Gamma_2 = & - \nabla\{\tilde{\mathbf{u}}\cdot\tilde{\mathbf{u}}_{1c} + \frac{1}{2}(F_{21}+2HF_{22})^2 \\ & + \frac{(z_c^2-\delta^2\eta^2)}{2}(\tilde{\mathbf{u}}\cdot\nabla)(2F_{22}) \\ & + (z_c-\delta\eta)(\tilde{\mathbf{u}}\cdot\nabla)(2F_{23})\}\end{aligned} \tag{2.181}$$

$$\begin{aligned}\Gamma_3 &= -[\delta(\nabla\times\tilde{\mathbf{u}})\times\tilde{\mathbf{u}} + \delta\mu^2(\nabla\times\tilde{\mathbf{u}}_{1c})\times\tilde{\mathbf{u}} + \delta\mu^2(\nabla\times\tilde{\mathbf{u}})\times\tilde{\mathbf{u}}_{1c} \\ &+ \delta\mu^2\nabla z_c\cdot\tilde{\mathbf{u}}(\nabla F_{21} + 2\nabla h F_{22} + 2H_c\nabla F_{22}) \\ &- \delta\mu^2\nabla z_c\tilde{\mathbf{u}}\cdot(\nabla F_{21} + 2\nabla h F_{22} + 2H_c\nabla F_{22})] \\ &= -\delta(\nabla\times\mathbf{u})|_{z=z_c}\times\mathbf{u}_{z=z_c} \\ &= -\delta\boldsymbol{\Omega}|_{z=z_c}\times\mathbf{u}_{z=z_c}\end{aligned} \tag{2.182}$$

where

$$H_c = h + z_c \tag{2.183}$$

$$\tilde{\mathbf{u}}_{1c} = (Ah - H_c)(\nabla F_{21} + 2\nabla h F_{22}) + (Bh^2 - H_c^2)\nabla F_{22} \tag{2.184}$$

It is seen from (2.103) that $\tilde{\mathbf{u}}_{1c}$ is the second order part of velocity at $z = z_c$. The level z_c is free to choose, such as

$$\begin{cases} z_c = \delta\eta & \text{on the surface} \\ z_c = 0 & \text{on the still water level} \\ z_c = -h & \text{on the bottom} \end{cases}$$

The optimization of z_c to get better dispersion and nonlinear properties is left for further investigation.

The result that we have in (2.182), $\Gamma_3 = -\delta(\nabla\times\mathbf{u})|_{z=z_c}\times\mathbf{u}_{z=z_c}$, is very natural, because the horizontal Euler equation

$$\frac{\partial\mathbf{u}}{\partial t} + \delta(\mathbf{u}\cdot\nabla)\mathbf{u} + \frac{\delta}{\mu^2}w\frac{\partial\mathbf{u}}{\partial z} = -\nabla p$$

can always be written as

$$\frac{\partial \mathbf{u}}{\partial t} + \frac{\delta}{2}\nabla(\mathbf{u}\cdot\mathbf{u}) + \delta(\nabla\times\mathbf{u})\times\mathbf{u} + \frac{\delta}{\mu^2}w\frac{\partial \mathbf{u}}{\partial z} = -\nabla p$$

and the above equation is valid at any vertical level. One may ask, given that the kinematics between Euler theory (with assumption of zero-horizontal-vorticity) and potential theory are identical, why one has the vertical vorticity retained while the other does not? The answer is that only non-horizontal vorticity condition is used to derive the kinematics. But in potential theory, the vertical vorticity is assumed to be zero by introducing flow potential ϕ. If we rewrite the DFSBC (2.37) as

$$\eta + \phi_t + \frac{1}{2}\delta[\nabla\phi\cdot\nabla\phi + \frac{1}{\mu^2}(\phi_z)^2] = 0; \quad z = \delta\eta \tag{2.185}$$

where $\nabla\phi$ is horizontal velocity $\mathbf{u} = \tilde{\mathbf{u}} + \tilde{\mathbf{u}}_1$, then as we take a gradient of this equation to obtain the momentum equation in the derivations from potential theory, we can see that

$$\frac{1}{2}\nabla(\nabla\phi\cdot\nabla\phi) = \frac{1}{2}\nabla(\mathbf{u}\cdot\mathbf{u}) = (\mathbf{u}\cdot\nabla)\mathbf{u} - (\nabla\times\mathbf{u})\times\mathbf{u}. \tag{2.186}$$

The last term gives the vorticity term accordingly when $\nabla\times\mathbf{u} \neq 0$, yet potential theory assumes $\nabla\times\mathbf{u} = 0$, which is why Wei et al. (1995), Kennedy et al. (2001) and Gobbi et al. (2000) did not have the vertical vorticity term pointed out by Chen et al. (2003) and Liu (1994). Since here $\mathbf{u}$ is only horizontal velocity, doing so doesn't harm the no-horizontal-vorticity condition in the potential flow, but the no-vertical-vorticity condition is released.

2.3 Derivation of Boussinesq Equation Incorporating Undertow

Boussinesq equations can provide instantaneous wave and current information for sediment transport models, many of which rely on detailed predictions of bottom shear stress. This gives us an opportunity to examine existing sediment transport rate formulas based on "quasi-steady" assumption or further examine new formulas being developed.

The Boussinesq equation can give correct free stream velocity skewness estimate when there is no plunging wave breaking (Long and Kirby, 2003; Long et al., 2004).

When in the surfzone, wave introduced undertow will contribute mainly to offshore transport of bedload and suspended load sediments. Hence, it is important to have undertow included for phase resolving sediment transport models to predict offshore transport correctly. Existing undertow models are mostly based on time averaged approaches (Stive and De Vriend, 1994; Stive and Wind, 1986; Svendsen and Putrevu, 1990; Cox and Kobayashi, 1997; Kuriyama and Nakatsukasa, 2000) and also rely on assumptions of bottom friction/stress which is what we are trying to predict and use in the sediment transport calculation.

In this research, we try to predict instantaneous free stream velocity with undertow automatically included. The basic idea is to use roller modeling for description of breakers and include the impact of the roller to the mass conservation and momentum equations for the underlying water column.

The alpha-level representation of velocity $\mathbf{u}_\alpha$ by Nwogu (1993) is used for vertical distribution of velocity. In contrast to Nwogu (1993) and the previous sections, here the momentum equation of water particles is integrated from bottom to free surface, while, in Nwogu (1993) and FUNWAVE version 1.0, the momentum equation only stands for one particular water level with pressure integrated from free surface to that level. In comparison to Nwogu (1993), the new equations arrived here are still in terms of $\mathbf{u}_\alpha$, but more compact and easier to solve numerically.

In summary, the new equation is: 1) using same vertical structure of irrotational flow field; 2) written in terms of $\mathbf{u}_\alpha$; 3) more compact looking than previous equations; 4) fully nonlinear; 5) undertow included.

2.3.1 Derivation from shallow water equation

The key idea of this research is to split the fluid velocity into wave component (irrotational in the vertical plane) and rotational component. Then we elaborate the idea using Boussinesq theory for the irrotational component. For the purpose of illustration, we present the derivation for shallow water system since the fact that entire surfzone and

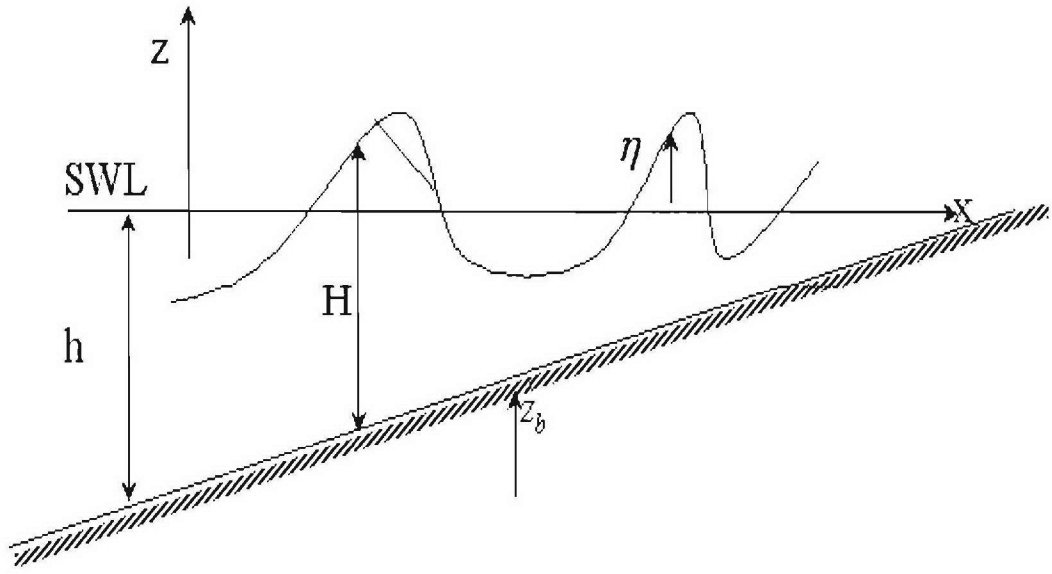

Figure 2.2: Spilling breaker roller

undertow system is a shallow water system. For the sake of simplicity, we derive the equations for a 1-D constant water depth problem. Figure 2.2 shows a schematic picture of spilling breaker with a conceptual roller (Schäffer et al., 1993). Figure 2.3 shows the split of horizontal velocity.

Let

1. $z_b = -h$: bed level
2. η : free surface elevation
3. r : thickness of roller, $r \geq 0$
4. $u(x, z, t)$: fluid velocity
5. $u_w(x, z, t)$: wave component including undertow
6. $u_r(x, z, t)$: component due to roller

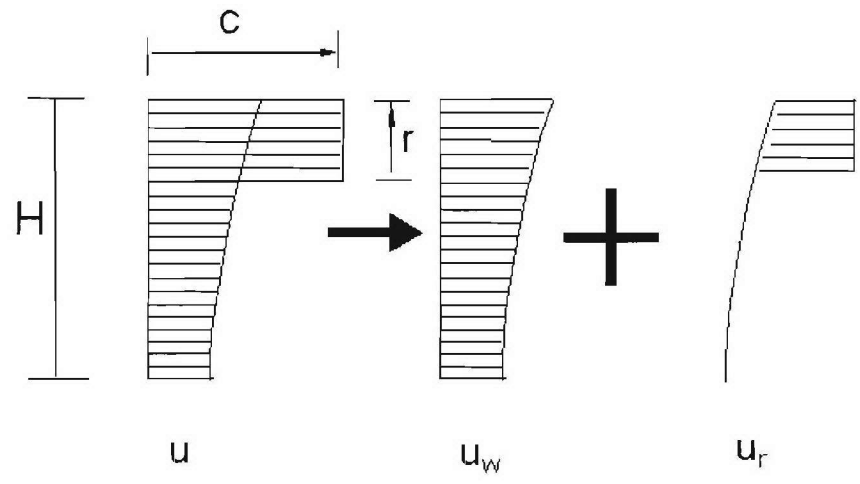

Figure 2.3: Horizontal velocity split

For shallow water system, assume $u_w = u_w(x,t)$, i.e. wave current velocity is uniform in z direction. Figure 2.3 shows the u_w and u_r (Schäffer et al., 1993) decomposition which can be written as

$$u(x,z,t) = u_w(x,z,t) + u_r(x,z,t) \tag{2.187}$$

with (for shallow water)

$$u_w(x,z,t) = u_w(x,t) \tag{2.188}$$

and

$$u_r = \begin{cases} C - u_w & \eta - r \leq z \leq \eta \\ 0 & -h \leq z \leq \eta - r \end{cases}$$

where C is the wave phase speed.

We make the following assumptions: 1) vertical velocity w is the same as in irrotational flow theory; 2) pressure is hydrostatic.

The 2-D vertical (2DV) governing equations for the fluid are given by the continuity equation

$$\frac{\partial u}{\partial x} + \frac{\partial w}{\partial z} = 0 \tag{2.189}$$

and the Euler equation of motion

$$\frac{\partial u}{\partial t} + u\frac{\partial u}{\partial x} + w\frac{\partial u}{\partial z} = -\frac{1}{\rho}\frac{\partial p}{\partial x} \tag{2.190}$$

$$0 = -\frac{1}{\rho}\frac{\partial p}{\partial z} - g \tag{2.191}$$

where in (2.191), w is assumed to be of 2nd order and neglected. It's obvious from (2.191) that

$$p = \rho g(\eta - z), \tag{2.192}$$

where $p = 0$ at free surface is utilized. From (2.192), we have

$$\frac{\partial p}{\partial x} = \rho g\frac{\partial \eta}{\partial x} \tag{2.193}$$

and (2.190) becomes

$$\frac{\partial u}{\partial t} + u\frac{\partial u}{\partial x} + w\frac{\partial w}{\partial z} = -g\frac{\partial \eta}{\partial x} \tag{2.194}$$

with the following boundary conditions (for horizontal bottom problem)

$$w = 0 \quad at \quad z = -h \tag{2.195}$$

$$\frac{\partial \eta}{\partial t} + u\frac{\partial \eta}{\partial x} = w \quad at \quad z = \eta \tag{2.196}$$

$$p = 0 \quad at \quad z = \eta \tag{2.197}$$

Integrate (2.189) from bottom to free surface and utilizing the boundary conditions to obtain the following continuity equation

$$\frac{\partial \eta}{\partial t} + \frac{\partial}{\partial x}\int_{-h}^{\eta} u dz \tag{2.198}$$

Considering $u = u_w + u_r$, we get

$$\frac{\partial \eta}{\partial t} + \frac{\partial M_w}{\partial x} + \frac{\partial M_r}{\partial x} = 0, \tag{2.199}$$

where

$$M_w = \int_{-h}^{\eta} u_w dz = H u_w, \tag{2.200}$$

$$M_r = \int_{-h}^{\eta} u_r dz = (C - u_w) r = u_r r. \tag{2.201}$$

Here, M_w is the volume flux due to wave, M_r is volume flux due to the roller.

Next, we look for integrated horizontal momentum equation. (2.194) plus ((2.189) multiplied by u gives

$$\frac{\partial u}{\partial t} + \frac{\partial u^2}{\partial x} + \frac{\partial uw}{\partial z} = -g\frac{\partial \eta}{\partial x}. \tag{2.202}$$

Integrate this equation from bottom to free surface to obtain

$$\frac{\partial}{\partial t}\int_{-h}^{\eta} u dz + \frac{\partial}{\partial x}\int_{-h}^{\eta} u^2 dz = -g(h+\eta)\frac{\partial \eta}{\partial x}, \tag{2.203}$$

where boundary conditions have been used and

$$\int_{-h}^{\eta} u dz = M_w + M_r \tag{2.204}$$

$$\int_{-h}^{\eta} u^2 dz = \int_{-h}^{\eta} (u_w + u_r)^2 dz = {u_w}^2 H + {u_r}^2 r + 2u_w u_r r. \tag{2.205}$$

Equation (2.203) becomes

$$\frac{\partial M_w}{\partial t} + \frac{\partial M_r}{\partial x} + \frac{\partial {u_w}^2 H}{\partial x} + \frac{\partial {u_r}^2 r}{\partial x} + \frac{\partial 2 u_w u_r r}{\partial x} = -gH\frac{\partial \eta}{\partial x} \tag{2.206}$$

Since $M_w = H u_w$, $M_r = u_r r$, the upper equation can be written as

$$\frac{\partial H u_w}{\partial t} + \frac{\partial H {u_w}^2}{\partial x} + gH\frac{\partial \eta}{\partial x} + \frac{\partial M_r}{\partial t} + \frac{\partial (M_r)^2/r}{\partial x} + \frac{\partial 2 u_w M_r}{\partial x} = 0 \tag{2.207}$$

We see that (2.207) has contribution due to the roller, where $\frac{\partial M_r}{\partial t}$ is inertia of the roller; $\frac{\partial {M_r}^2/r}{\partial x}$ is the convection of the roller by itself $\frac{\partial u_w M_r}{\partial x}$ is the advection of the roller by wave current velocity u_w

Equation (2.207) can be also rewritten as

$$\begin{aligned} \frac{\partial u_w}{\partial t} &+ u_w\frac{\partial u_w}{\partial x} + g\frac{\partial \eta}{\partial x} \\ &+ \frac{1}{H}\left(\frac{\partial M_r}{\partial t} + \frac{\partial {M_r}^2/r}{\partial x} + M_r\frac{\partial u_w}{\partial x}\right) \\ &= 0 \end{aligned} \tag{2.208}$$

We see that (2.208) is an equation in terms of the depth averaged irrotational velocity u_w. u_w should contain undertow information when the roller is present. In equation 2.208, division by $H = \eta + h$ will introduce difficulty near shoreline. In the next section, we will derive the momentum equation from Boussinesq theory and it will be seen that it is better to keep the resulting equation in the form of (2.207) so that the equation is more compact.

2.3.2 Derivation from Boussinesq theory

In the previous section, the shallow water equation is improved to incorporate undertow. Now we proceed to improve our Boussinesq model by incorporating undertow as well. Before we start, we emphasize the assumptions here:

(1) Fluid velocity

$$\mathbf{u} = \mathbf{u}_w + \mathbf{u}_r \tag{2.209}$$

$$w = w_w \tag{2.210}$$

i.e., horizontal velocity is split into an irrotational component $\mathbf{u}_w$ and the roller component u_r, vertical velocity is assumed to have only an irrotational component meaning that vertical component of rotational flow is assumed to be small relative to irrotational flow.

(2) Hydrodynamic pressure $p(x, y, z, t)$ is only determined by vertical momentum equation when $\mathbf{u}_r = 0$, i.e., assume that $\mathbf{u}_r$ does not affect pressure.

(3) Irrotational velocity $\mathbf{u}_w$ can be expressed as a 2nd order polynomial function of z in terms of representative levels: alpha level $\mathbf{u}_{w\alpha}$ and beta level $\mathbf{u}_{w\beta}$, where

$$\mathbf{u}_{w\alpha} = \mathbf{u}_w(x, t, z = z_\alpha) \tag{2.211}$$

$$\mathbf{u}_{w\beta} = \mathbf{u}_w(x, t, z = z_\beta) \tag{2.212}$$

with

$$z_\alpha = \rho_1 h + \beta_1 \eta \tag{2.213}$$

$$z_\beta = \rho_2 h + \beta_2 \eta \tag{2.214}$$

and define

$$\tilde{\mathbf{u}} \equiv \beta \mathbf{u}_{w\alpha} + (1-\beta)\mathbf{u}_{w\beta} \tag{2.215}$$

When $\beta = 1$, equation (2.215) recovers Nwogu (1993) representation. The FUNWAVE2D2.0 developed here use (2.215) as dependent velocity. Kennedy et al. (2001) uses (2.213) with $\beta_1 \neq 0$ to achieve datum invariant version of Boussinesq equation as a special case as is also pointed out in previous sections.

We start derivation from Euler equation in 3-D. The dimensional form of the conservation of mass (COM) equation is

$$\nabla \cdot \mathbf{u} + w_z = \frac{\partial u}{\partial x} + \frac{\partial v}{\partial y} + \frac{\partial w}{\partial z} = 0. \tag{2.216}$$

The dimensional form of the equations of motion (EOM) are

$$\text{x-direction: } \frac{\partial u}{\partial t} + u\frac{\partial u}{\partial x} + v\frac{\partial u}{\partial y} + w\frac{\partial u}{\partial z} = -\frac{1}{\rho}\frac{\partial p}{\partial x} \tag{2.217}$$

$$\text{y-direction: } \frac{\partial v}{\partial t} + u\frac{\partial v}{\partial x} + v\frac{\partial v}{\partial y} + w\frac{\partial v}{\partial z} = -\frac{1}{\rho}\frac{\partial p}{\partial y} \tag{2.218}$$

$$\text{z-direction: } \frac{\partial w}{\partial t} + u\frac{\partial w}{\partial x} + v\frac{\partial w}{\partial y} + w\frac{\partial w}{\partial z} = -\frac{1}{\rho}\frac{\partial p}{\partial z} - g \tag{2.219}$$

In dimensionless form, we have

COM

$$\mu^2\frac{\partial u}{\partial x} + \mu^2\frac{\partial v}{\partial y} + \frac{\partial w}{\partial z} = 0 \tag{2.220}$$

and EOM

$$\frac{D\mathbf{u}}{Dt} + \nabla p = 0 \tag{2.221}$$

$$\frac{Dw}{Dt} + \frac{\partial p}{\partial z} + \frac{1}{\delta} = 0 \tag{2.222}$$

where

$$\frac{D}{Dt} = \frac{\partial}{\partial t} + \delta(\mathbf{u}\cdot\nabla) + \frac{\delta}{\mu^2}w\frac{\partial}{\partial z} \tag{2.223}$$

$$\mathbf{u} = (u, v), \quad \nabla = (\frac{\partial}{\partial x}, \frac{\partial}{\partial y}) \tag{2.224}$$

Boundary conditions are

$$\mu^2\frac{\partial\eta}{\partial t}+\delta\mu^2\mathbf{u}\cdot\nabla\eta-w=0;\quad z=\delta\eta \tag{2.225}$$

$$p=p_a=0;\quad z=\delta\eta \tag{2.226}$$

$$\mu^2\mathbf{u}\cdot\nabla h+w=0;\quad z=-h \tag{2.227}$$

The irrotation condition for wave velocity is given by

$$\frac{\partial\mathbf{u}_w}{\partial z}-\nabla w_w=0;\quad h\le z\le\delta\eta \tag{2.228}$$

Following the derivation in the previous sections, we can express the velocity $(\mathbf{u}_w, w_w)$ in terms of $\tilde{\mathbf{u}}$ as

$$\begin{aligned}\mathbf{u}_w=\tilde{\mathbf{u}} &+ \mu^2(Ah-\xi)\nabla[\nabla\cdot(h\tilde{\mathbf{u}})]\\ &+ \mu^2(\frac{B-2A}{2}h^2-\frac{\xi^2}{2}+h\xi)\nabla(\nabla\cdot\tilde{\mathbf{u}})+O(\mu^4)\end{aligned} \tag{2.229}$$

$$w_w(x,y,z,t)=-\mu^2\nabla\cdot(\xi\tilde{\mathbf{u}}) \tag{2.230}$$

where

$$\xi=h+z \tag{2.231}$$

is distance above the bed.

$$A=\frac{1}{h}[\beta(h+z_\alpha)+(1-\beta)(h+z_\beta)] \tag{2.232}$$

$$B=\frac{1}{h^2}[\beta(h+z_\alpha)^2+(1-\beta)(h+z_\beta)^2] \tag{2.233}$$

The roller component of velocity is given by

$$\mathbf{u}_r=\mathbf{C}-\mathbf{u}_w,\quad \delta\eta-r\le z\le\delta\eta \tag{2.234}$$

$$w_r=0 \tag{2.235}$$

$$\mathbf{C}\approx\sqrt{gh}\mathbf{n} \tag{2.236}$$

where $\mathbf{n}$ is the wave direction unit vector $\mathbf{n} = (n_1, n_2)$.

(1) Continuity Equation

Integrate COM from bottom to free surface to obtain

$$\frac{\partial \eta}{\partial t} + \nabla \cdot \mathbf{M}_w + \nabla \cdot \mathbf{M}_r = 0 \tag{2.237}$$

where $\mathbf{M}_w$ is volume flux due to irrotational flow $\mathbf{u}_w$ and also defined as

$$\mathbf{M}_w \equiv \int_{-h}^{\delta\eta} \mathbf{u}_w dz \tag{2.238}$$

$$\mathbf{M}_w = H\tilde{\mathbf{u}} + \mu^2 H\{2(Ah - \frac{H}{2})\nabla F_{23} + (Bh^2 - \frac{H^2}{3} - 2Ah^2 + hH)\nabla F_{22}\} \tag{2.239}$$

$$\begin{aligned} \mathbf{M}_r &\equiv \int_{-h}^{\delta\eta} \mathbf{u}_r dz & (2.240)\\ &= \int_{-h}^{\delta\eta - r} 0 dz + \int_{\delta\eta - r}^{\delta\eta} (\mathbf{C} - \mathbf{u}_w) dz \\ &= (\mathbf{C} - \tilde{\mathbf{u}})r + O(\mu^2 r) & (2.241) \end{aligned}$$

where r is assumed to be less than δ, i.e., a roller only occurs within a fractional layer of the thickness of a wave front. We see that (2.239) is exactly the same as the previous Boussinesq equations.

(2) Momentum Equation

Derivation of momentum equation here is a bit different than the previous sections. In Nwogu (1993) and Wei et al. (1995), the momentum equation is basically (2.221) evaluated at $z = \delta\eta$. In previous sections, we have the Boussinesq momentum equation being (2.221) evaluated at $z_c = \rho_c h + \beta_c \delta\eta$ level. Here, in order to take account of roller momentum balance we need to integrate (2.221) from the bottom $z = -h$ to the free surface $z = \delta\eta$. We'll see that this approach actually yields an equation that is more compact.

Integration of (2.221) from $z = -h$ to $z = \delta\eta$ and using bottom and surface BC, we have

$$\frac{\partial}{\partial t}\int_{-h}^{\delta\eta} \mathbf{u} dz + \delta\nabla \cdot \int_{-h}^{\delta\eta} \mathbf{u}\mathbf{u} dz + \delta\nabla \int_{-h}^{\delta\eta} p dz - p|_{z=-h}\nabla h = 0 \tag{2.242}$$

This equation (2.242) has the same assumptions in the Euler equation. The physical meaning of each term is apparent: 1) the first is the inertia of the water column; 2) the second term is the convection of the water column; 3) the third term is the pressure gradient of the water column; 4) the fourth term is the bottom pressure projected onto horizontal direction due to the bottom slope.

Integrating the vertical momentum equation (2.222) from z to $z = \delta\eta$, we can obtain pressure field which is the same as (2.105)

$$\begin{aligned} p(x,y,z,t) &= p_a + \eta - \frac{\tilde{z}}{\delta} \\ &- \mu^2\{(\delta\eta - z)F_{21t} + (H^2 - \xi^2)F_{22t} \\ &+ \delta\tilde{\mathbf{u}} \cdot [\nabla F_{21}(\delta\eta - z) + \nabla F_{22}(H^2 - \xi^2) + 2F_{22}\nabla h(\delta\eta - z)]\} \end{aligned} \tag{2.243}$$

where

$$F_{21t} = \frac{\partial F_{21}}{\partial t};\ F_{22t} = \frac{\partial F_{22}}{\partial t} \tag{2.244}$$

and

$$F_{21} = \nabla h \cdot \tilde{\mathbf{u}} \tag{2.245}$$

$$F_{23} = \frac{1}{2}\nabla \cdot (h\tilde{\mathbf{u}}) \tag{2.246}$$

$$F_{22} = \frac{1}{2}\nabla \cdot \tilde{\mathbf{u}} \tag{2.247}$$

with

$$F_{21} = 2F_{23} - 2hF_{22} \tag{2.248}$$

Now, we proceed to integrate (2.242) term by term. The first term is

$$\int_{-h}^{\delta\eta} \mathbf{u}dz = \mathbf{M}_w + \mathbf{M}_r. \tag{2.249}$$

The second term is

$$\int_{-h}^{\delta\eta} \mathbf{u}\mathbf{u}dz = \int_{-h}^{\delta\eta} (\mathbf{u}_w + \mathbf{u}_r)(\mathbf{u}_w + \mathbf{u}_r)dz = I + II + III + IV \tag{2.250}$$

where

$$I \equiv \frac{\mathbf{M}_w \mathbf{M}_w}{H} + O(\mu^4) \tag{2.251}$$

$$II \equiv -\frac{\mathbf{M}_{wr} \mathbf{M}_{wr}}{r} + \mathbf{C}\mathbf{M}_{wr} + O(\mu^4) \tag{2.252}$$

$$III \equiv -\frac{\mathbf{M}_{wr} \mathbf{M}_{wr}}{r} + \mathbf{C}\mathbf{M}_{wr} + O(\mu^4) \tag{2.253}$$

with

$$\begin{aligned} \mathbf{M}_{wr} &= \int_{\delta\eta - r}^{\delta\eta} \mathbf{u}_w dz \\ &= \tilde{\mathbf{u}} r + \mu^2 (\nabla F_{21} + 2F_{22} \nabla h)(Ahr - \frac{H^2 - (H-r)^2}{2}) \\ &\quad + \mu^2 (Bh^2 r - \frac{H^3 - (H-r)^3}{3}) \nabla F_{22} \end{aligned} \tag{2.254}$$

$\mathbf{M}_{wr}$ is the wave velocity contribution of the flux in the roller.

$$IV \equiv \mathbf{C}\mathbf{C} r - 2\mathbf{C}\mathbf{M}_{wr} + \frac{\mathbf{M}_{wr} \mathbf{M}_{wr}}{r} + O(\mu^4) \tag{2.255}$$

So we have

$$II + III + IV = \frac{\mathbf{C}\mathbf{C} r^2 - \mathbf{M}_{wr} \mathbf{M}_{wr}}{r} \tag{2.256}$$

Hence the second term is now written as

$$\int_{-h}^{\delta\eta} \mathbf{u}\mathbf{u} dz = \frac{\mathbf{M}_w \mathbf{M}_{wj}}{H} + \frac{\mathbf{C}\mathbf{C} r^2 - \mathbf{M}_{wr} \mathbf{M}_{wr}}{r}. \tag{2.257}$$

The third term is

$$\int_{-h}^{\delta\eta} p dz = \frac{H^2}{2\delta} - \mu^2 H^2 \{[F_{23t} + (\frac{2H}{3} - h) F_{22t}] + \delta \tilde{\mathbf{u}} \cdot [\nabla F_{23} + (\frac{2H}{3} - h) F_{22t}]\} \tag{2.258}$$

The fourth term is

$$p|_{z=-h} = \frac{H}{\delta} - 2\mu^2 H \{[F_{23t} + (\frac{H}{2} - h) F_{22t}] + \delta \tilde{\mathbf{u}} \cdot [\nabla F_{23} + (\frac{H}{2} - h) \nabla F_{22}]\} \tag{2.259}$$

Substituting the four terms into equation (2.242), we obtain the momentum equation for the whole water column

$$\begin{aligned}\frac{\partial \mathbf{M}_w}{\partial t} &+ \frac{\partial \mathbf{M}_r}{\partial t} + \delta\nabla\cdot[\frac{\mathbf{M}_w\mathbf{M}_w}{H} + \frac{\mathbf{CC}r^2 - \mathbf{M}_{wr}\mathbf{M}_{wr}}{r}] \\ &+ \nabla[\frac{H^2}{2\delta} - \mu^2H^2\{[F_{23t} + (\frac{2H}{3} - h)F_{22t}] + \delta\tilde{\mathbf{u}}\cdot[\nabla F_{23} + (\frac{2H}{3} - h)\nabla F_{22}]\}] \\ &- \nabla h[\frac{H}{\delta} - 2\mu^2H\{[F_{23t} + (\frac{H}{2} - h)F_{22t}] + \delta\tilde{\mathbf{u}}\cdot[\nabla F_{23} + (\frac{H}{2} - h)\nabla F_{22}]\}] \\ &= 0 \end{aligned} \tag{2.260}$$

Equation (2.260) is the new Boussinesq momentum equation with clear physical meaning for every term. It has the following observed properties 1) the equation is fully nonlinear since all δ terms are kept up to $O(\mu^2)$; 2) the equation is also in terms of $\tilde{\mathbf{u}}$ which will recover Nwogu (1993), Wei et al. (1995) $\mathbf{u}_\alpha$, Kennedy et al. (2001) moving level and Gobbi et al. (2000) multi-level reference velocities; 3) the equation is more compact than equations given by previous sections; 4) the equation is written in divergence form except the bottom pressure terms; 5) the equation includes the momentum balance effect of surface roller for spilling breakers.

2.4 Final Form of Boussinesq Equation

The final second order Boussinesq equations can be summarized here.

(1) Conservation of Mass (COM)

$$\frac{\partial \eta}{\partial t} + \nabla\cdot\mathbf{M}_w + \nabla\cdot\mathbf{M}_r = 0 \tag{2.261}$$

where $\mathbf{M}_w$ is volume flux due to irrotational flow $\mathbf{u}_w$ and also defined as

$$\mathbf{M}_w \equiv \int_{-h}^{\delta\eta}\mathbf{u}_w dz \tag{2.262}$$

$$\mathbf{M}_w = H\tilde{\mathbf{u}} + \mu^2H\{(Ah - \frac{H}{2})2\nabla F_{23} + (Bh^2 - \frac{H^2}{3} - 2Ah^2 + hH)\nabla F_{22}\} \tag{2.263}$$

We see that (2.263) is exactly the same as previous Boussinesq equations.

$$\mathbf{M}_r \equiv \int_{-h}^{\delta\eta}\mathbf{u}_r dz \tag{2.264}$$

$$\begin{aligned}\mathbf{M}_r &= \int_{-h}^{\delta\eta-r} 0dz + \int_{\delta\eta-r}^{\delta\eta} (\mathbf{C}-\mathbf{u}_w)dz \\ &= (\mathbf{C}-\tilde{\mathbf{u}})r + O(\mu^2 r) \end{aligned} \tag{2.265}$$

(2) Equation of Motion (EOM)

$$\begin{aligned}\frac{\partial \mathbf{M}_w}{\partial t} &+ \frac{\partial \mathbf{M}_r}{\partial t} + \delta\nabla\cdot[\frac{\mathbf{M}_w\mathbf{M}_w}{H} + \frac{\mathbf{CC}r^2 - \mathbf{M}_{wr}\mathbf{M}_{wr}}{r}] \\ &+ \nabla[\frac{H^2}{2\delta} - \mu^2 H^2\{[F_{23t} + (\frac{2H}{3}-h)F_{22t}] + \delta\tilde{\mathbf{u}}\cdot[\nabla F_{23} + (\frac{2H}{3}-h)\nabla F_{22}]\}] \\ &- \nabla h[\frac{H}{\delta} - 2\mu^2 H\{[F_{23t} + (\frac{H}{2}-h)F_{22t}] + \delta\tilde{\mathbf{u}}\cdot[\nabla F_{23} + (\frac{H}{2}-h)\nabla F_{22}]\}] \\ &= 0 \end{aligned} \tag{2.266}$$

In dimensional form, we have

$$\begin{aligned}\frac{\partial \mathbf{M}_w}{\partial t} &+ \frac{\partial \mathbf{M}_r}{\partial t} + \nabla\cdot[\frac{\mathbf{M}_w\mathbf{M}_w}{H} + \frac{\mathbf{CC}r^2 - \mathbf{M}_{wr}\mathbf{M}_{wr}}{r}] \\ &+ \nabla[\frac{H^2}{2} - H^2\{[F_{23t} + (\frac{2H}{3}-h)F_{22t}] + \tilde{\mathbf{u}}\cdot[\nabla F_{23} + (\frac{2H}{3}-h)\nabla F_{22}]\}] \\ &- \nabla h[H - 2H\{[F_{23t} + (\frac{H}{2}-h)F_{22t}] + \tilde{\mathbf{u}}\cdot[\nabla F_{23} + (\frac{H}{2}-h)\nabla F_{22}]\}] \\ &= 0 \end{aligned} \tag{2.267}$$

$$\mathbf{M}_w = H\tilde{\mathbf{u}} + H\{(Ah - \frac{H}{2})2\nabla F_{23} + (Bh^2 - \frac{H^2}{3} - 2Ah^2 + hH)\nabla F_{22}\} \tag{2.268}$$

$$\begin{aligned}\mathbf{M}_r &= \int_{-h}^{\eta-r} 0dz + \int_{\eta-r}^{\eta} (\mathbf{C}-\mathbf{u}_w)dz \\ &= (\mathbf{C}-\tilde{\mathbf{u}})r + O(\mu^2 r) \end{aligned} \tag{2.269}$$

$$\begin{aligned}\mathbf{M}_{wr} &= \int_{\eta-r}^{\eta} \mathbf{u}_w dz \\ &= \tilde{\mathbf{u}}r + (\nabla F_{21} + 2\nabla h F_{22})(Ahr - \frac{H^2-(H-r)^2}{2}) \\ &\quad + (Bh^2 r - \frac{H^3-(H-r)^3}{3})\nabla F_{22} \end{aligned} \tag{2.270}$$

Chapter 3

SEDIMENT TRANSPORT

Up to now, most of our intermediate to large scale sediment transport models are still based on calculation of the transport rate from empirical or semi-empirical correlations between the driving flow and the sediment motion. This is due to our limited computer power and knowledge on how to estimate the forces exerted on sediments. The ultimate law that governs the motion of sediments is Newton's Second Law, which means that if we are to model sediment transport dynamically, we need to find external forces on sediments and integrate Newton's Second Law to obtain sediment transport rate. It is, however, still quite difficult to identify and quantify the forces on sediments. Roughly speaking, the forces felt by a non-cohesive sediment particle exposed in the flow and surrounded by other sediment particles include gravity, skin drag, form drag, inertial force and contact force of other particles. Skin drag is due to flow shear on the surface of sediment particles. Form drag is due to pressure of fluid on the sediments. Inertial force is due to relative acceleration between flow and sediment particles. Contact force is due to shear force and normal force between sediment particles when they impinge on each other. The only thing that's obvious and easy to estimate is gravity. Skin drag, form drag, inertial force are all related to detailed fluid flow field and the relative motion between sediments and fluid which are yet quite difficult to obtain except for very small scale problems. For suspended fine sediments, it's usually assumed that the particles follow the water flow such that no dynamic model is needed. The transport rate can be simply calculated by integration of uc, where u is flow velocity, and c is sediment volumetric concentration.

Modeling small scale sediment transport can be found in Drew (1975, 1976, 1983), Dong and Zhang (1999), Drake and Calantoni (2001), Hsu (2002), Mina and Sato (2004) and Dartevelle (2004). In the field of granular and particle laden flows, most studies are still based on one directional flows or steady flows such as pneumatic transport in pipelines and particle flows down inclined chutes (Savage, 1984). In Savage (1984), simple rheology of sediments have been proposed. In Dartevelle (2004) and Ancey (2005), very comprehensive study on granular flow rheology is presented. In Hsu (2002), detailed 1-D vertical simulation of flows are given by using a granular flow technique. In Drake and Calantoni (2001), discrete particle simulation has been done based on dynamic forces exerted on individual grains under oscillatory free stream flow condition to investigate the effects of free stream acceleration on sediment transport. These small scale simulations help gain our understanding of sediment transport substantially. However, detailed simulation of sediment motion is still not feasible for engineering practice at this time. There are also sediment models that are based on the calculation of forces on bulk sands instead of individual sand particles (Prasad and Singh, 1982; Mina and Sato, 2004). This approach should become the next generation of sediment transport model in the nearshore region.

Presently, however, sediment transport models in engineering are still mostly focused on calculating transport rates based on hydrodynamic quantities such as flow velocity and bottom shear stress, and the problem is simplified to a large extent. As a result, there exist a number of proposed formulas in the literature which are based on experiments or semi-empirical analysis. These models are effective in their suggested range of parameters, with most of them for 1-D and one directional flows. For transport rate under conditions of combined waves and currents, there is still a large amount of uncertainty. In this study we will mainly focus on testing and extending sediment transport formulas that are proposed for nearshore environment.

In this chapter, we first review some of the existing sediment transport formulas.

Then we focus on ad-hoc extensions to the Bagnold (1966) and Bailard (1981) formulas by including effects of free stream flow acceleration. Next, we discuss the use of Meyer-Peter-Müller (1948) formula with instantaneous bottom shear stress obtained from detailed simulation of the bottom boundary layer.

3.1 Various Transport Formulas

Numerous sediment transport formulas have been proposed in the literature. For steady flow, significant ones include Du Boys (1879), Schoklitsch (1930), Shields (1936), Einstein (1942), Meyer-Peter (1948, 1951), Einstein (1950), Schoklitsch (1950), Nielsen (1992), Bagnold (1966), Grass (1981) and Van Rijn (1984). For sediment transport due to waves or combined waves and currents, up to date formulas are mostly based on quasi-steady assumption, which include Madsen and Grant (1976), Bailard (1981) and Trowbridge and Young (1989). Recently developed transport formulas are also available from Dibajnia and Watanabe (1998) and Soulsby and Damgaard (2005).

3.1.1 Sediment transport formulas for steady flow

These formulas are from the investigation of rivers, channels and pipelines with which the flow are predominantly one directional and relatively steady in time. A review is available in Chanson (1999). In the following formulas, q_s is volumetric sediment transport rate per unit width (m^2/s), q is volumetric water flux (m^2/s), τ_0 is bed shear stress, τ_{0c} is critical bed shear stress for initiation of sediment transport, ρ is water density, ρ_s is dry sediment density, s is sediment specific gravity ($s = \rho_s/\rho$).

(1) Du Boys (1879)

$$q_s = \lambda \tau_0 (\tau_0 - \tau_{0c}) \tag{3.1}$$

where

$$\lambda = \frac{0.54}{(\rho_s - \rho)g} \tag{3.2}$$

or

$$\lambda \propto d_s^{-3/4}. \tag{3.3}$$

λ is called the characteristic sediment coefficient. Equation (3.2) is from laboratory experiments with uniform grains of various kinds of sand and porcelain by Schoklitsch (1914). (3.3) is for grain size $0.125\text{mm} < d_s < 4\text{mm}$ based on laboratory data of Straub (1935).

(2) Schoklitsch (1930)

$$q_s = \lambda'(\sin\theta)^k(q - q_c) \tag{3.4}$$

$$q_c = 1.944 \times 10^{-2} d_s(\sin\theta)^{-4/3} \tag{3.5}$$

with $0.305\text{mm} < d_s < 7.02\text{mm}$ from laboratory experiments,and θ being slope of an open channel. λ' and k are empirical coefficients to be calibrated.

(3) Shields (1936)

$$\frac{q_s}{q} = 10\frac{\sin\theta}{s}\frac{\tau_0 - \tau_{0c}}{\rho g(s-1)d_s} \tag{3.6}$$

with $1.06 < s < 4.25$ and $1.56\text{mm} < d_s < 2.47\text{mm}$

(4) Einstein (1942)

$$\frac{q_s}{\sqrt{(s-1)gd_s^3}} = 2.15exp(-0.391\frac{\rho(s-1)gd_s}{\tau_0}) \tag{3.7}$$

with $\frac{q_s}{\sqrt{(s-1)gd_s^3}} < 0.4$, $1.25 < s < 4.25$ and $0.315\text{mm} < d_s < 28.6\text{mm}$ for sand mixtures and $d_s \approx d_{35}$ to d_{45}.

(5) Meyer-Peter (1948, 1951)

$$\frac{q_s}{\sqrt{(s-1)gd_s^3}} = (\frac{4\tau_0}{\rho(s-1)gd_s} - 0.188)^{3/2} \tag{3.8}$$

for particle mixtures with $d_s \approx d_{50}$ from laboratory experiments and θ being slope of open channel.

(6) Einstein (1950)

$$\frac{q_s}{\sqrt{(s-1)gd_s^3}} = f(\frac{\rho(s-1)gd_s}{\tau_0}) \tag{3.9}$$

with $\frac{q_s}{\sqrt{(s-1)gd_s^3}} < 10$, $1.25 < s < 4.25$ and $0.315\text{mm} < d_s < 28.6\text{mm}$ for sand mixtures and $d_s \approx d_{35}$ to d_{45} from laboratory experiments. Function $f()$ is based on a design chart of Einstein (1950).

(7) Bagnold (1966)

$$i = i_b + i_s = \omega[\frac{\epsilon_B}{\tan\phi - \tan\beta} + \frac{\epsilon_S(1-\epsilon_B)}{(\omega/\bar{U}_s) - \tan\beta}] \tag{3.10}$$

where i is total immersed weight transport rate of sediments per unit width, i_b is bed load immersed weight transport rate, i_s is suspended load immersed weight transport rate, ω is called available fluid power, ϵ_B and ϵ_S are empirical coefficients. $\bar{U}_s$ is the mean fluid flow velocity to transport suspended sediments. ω is calculated by

$$\omega = c_r \rho u^{*3} \tag{3.11}$$

with c_r a general constant under conditions of no suspended load, and u^* is the friction velocity.

(8) Van Rijn (1984)

$$q_s(u,h) = \begin{cases} Au(|u| - u_{cr})^{2.4} \ \text{if} |u| > u_{cr} \\ 0 \end{cases} \tag{3.12}$$

where u_{cr} is the threshold current speed which is calculated by

$$u_{cr} = \begin{cases} 0.19(d_{50})^{0.1} log_{10}(\frac{2h}{d_{50}}) \ if \ 100 \leq d_{50} \leq 500 \ \mu\text{m} \\ 8.5(d_{50})^{0.6} log_{10}(\frac{2h}{d_{50}}) \ if \ 500 \leq d_{50} \leq 2000 \ \mu\text{m} \end{cases} \tag{3.13}$$

and

$$A = \frac{d_{50}(0.005(\frac{d_{50}}{h})^{0.2} + 0.012D_*^{-0.6})}{(gd_{50}(s-1))^{1.2}} \tag{3.14}$$

$$D_* = d_{50}(\frac{g}{\nu^2}(s-1))^{1/3}. \tag{3.15}$$

with u the velocity near bed and ν the kinematic viscosity of water, h is the water depth.

(9) Nielsen (1992)

$$\frac{q_s}{\sqrt{(s-1)gd_s^3}} = (\frac{12\tau_0}{\rho(s-1)gd_s} - 0.05)\sqrt{\frac{\tau_0}{\rho(s-1)gd_s}} \tag{3.16}$$

with $1.25 < s < 4.22$ and $0.69\text{mm} < d_s < 28.7\text{mm}$ from re-analysis of laboratory data.

3.1.2 Sediment transport formulas for wave current climate

(1) Madsen and Grant (1976)

$$\phi(t) = 40\psi^3(t) \tag{3.17}$$

where

$$\phi(t) = \frac{q_s(t)}{w_{fall}d} \tag{3.18}$$

and

$$\psi(t) = \frac{\tau_0(t)}{(s-1)\rho gd} \tag{3.19}$$

with w_{fall} the sediment fall velocity, d the sediment diameter, ψ the instantaneous shields parameter. $\tau_0(t)$ is instantaneous bed shear stress predicted by

$$\tau_0(t) = \frac{1}{2}f_w\rho|\mathbf{u}_b(t)|^2\frac{\mathbf{u}_{bw}(t)}{|\mathbf{u}_{bw}(t)|} \tag{3.20}$$

for pure waves,

$$\tau_0(t) = \frac{1}{2}f_c\rho|\mathbf{U}_b|^2\frac{\mathbf{U}_b}{|\mathbf{U}_b|} \tag{3.21}$$

for pure currents and

$$\tau_0(t) = \frac{1}{2}f_{cw}\rho|\mathbf{u}_b(t)|^2\frac{\mathbf{u}_b(t)}{|\mathbf{u}_b(t)|} \tag{3.22}$$

for combined waves and currents. f_w is the wave friction coefficient, f_c is the current friction coefficient and f_{cw} is the combined wave current friction coefficient given by Jonsson (1966)

$$f_{cw} = \frac{|\mathbf{U_b}|f_c + |\mathbf{u}_{bw}(t)|f_w}{|\mathbf{U_b}| + |\mathbf{u}_{bw}|(t)} \tag{3.23}$$

where $\mathbf{U}_b = \overline{\mathbf{u}_b(t)}$ is the current at bottom and $\mathbf{u}_{bw}$ is the wave velocity at the bottom. $\mathbf{u}_b(t) = \mathbf{U}_b + \mathbf{u}_{bw}$. All these calculations of bottom shear stress are under the quasi-steady assumption. The effect of wave skewness[1] to sediment transport in equation (3.17) is discussed in Madsen and Grant (1976). The effect of bottom slope was treated by modifying the instantaneous Shields parameter $\psi(t)$ to

$$\psi(t) = \frac{\tau_0(t)}{(s-1)\rho g d} - c_m \sin(\beta) \tag{3.24}$$

with β being the local bottom slope. The negative sign is introduced to reflect the fact that gravity acts in the down-slope direction.

(2) Bailard (1981)

$$\begin{aligned} < \mathbf{i}_{tot} > &= \rho c_f \frac{\epsilon_B}{\tan\phi}\left[< |\mathbf{u}_b|^2 \mathbf{u}_b > - \frac{\tan\beta}{\tan\phi} < |\mathbf{u}_b|^3 > \mathbf{l}\right] \\ &+ \rho c_f \frac{\epsilon_S}{w_{fall}}\left[< |\mathbf{u}_b|^3 \mathbf{u}_b > - \frac{\epsilon_S}{w_{fall}} \tan\beta < |\mathbf{u}_b|^5 > \mathbf{l}\right] \end{aligned} \tag{3.25}$$

where $\mathbf{i}_{tot}$ is total immersed weight sediment transport rate which can be converted to total volumetric sediment transport rate $\mathbf{q}_t$ by:

$$\mathbf{q}_{tot} = \frac{\mathbf{i}_{tot}}{g(s-1)\rho} \tag{3.26}$$

with ϵ_B and ϵ_S the same as Bagnold (1966), β the bed slope angle relative to horizontal plane, $\mathbf{l}$ the direction of upslope, i.e. direction of the gradient of bottom elevation ∇z_b, c_f is the combined wave current friction coefficient equivalent to f_{cw} of (3.23)

(3) Trowbridge and Young (1989)

In Trowbridge and Young (1989), the sheet flow transport rate is assumed to be proportional to the bed shear stress according to experiments by Horikawa et al. (1982).

[1] Note that in many publications, wave skewness is referred to as wave asymmetry, while here we use the term skewness for asymmetry of wave form about mean water level, and use the term wave asymmetry only for the asymmetry of wave form in horizontal direction or in time

$$\frac{q_s(t)}{w_{all}d} = \frac{K\tau_b(t)}{\rho g d(s-1)}. \tag{3.27}$$

A quadratic drag law with a time shift T is then used to calculate the shear stress $\tau_b(t) = f_w\rho|u_b(t+T)|u_b(t+T)$ to give

$$\frac{q_s(t)}{w_{fall}d} = \frac{Kf_w u_b(t+T)|u_b(t+T)|}{gd(s-1)}. \tag{3.28}$$

Equation (3.28) predicts sheet flow sediment transport rate with a phase lead to the free stream velocity instead of phase lag.

(4) Soulsby and Damgaard (2005)

$$\frac{q_b}{\sqrt{g(s-1)d^3}} = A_2\theta^{1/2}(\theta - \theta_{cr}) \tag{3.29}$$

with

$$A_2 = \frac{2A_1}{(n+1)(n+2)\mu} \tag{3.30}$$

and $8.2 < A_1 < 16.1$ empirically. Here q_b is bedload volumetric sediment transport rate. n is flow profile parameter about 0.75, $\mu = 0.2\tan 32°$, with $32°$ a typical angle of repose for sand. θ is Shields parameter equivalent to (3.19)

$$\theta = \frac{\tau_0(t)}{(s-1)\rho g d} \tag{3.31}$$

3.2 Ad-hoc Modifications to Bagnold (1966) and Bailard (1981) Formulas

Bailard (1981) formula (3.25) is basically a time averaged version of the Bagnold (1966) formula with bottom shear stress obtained through quadratic correlation to the free stream velocity instantaneously by using wave current bottom friction coefficient c_f.

Recent evidence (Gallagher et al., 1998, for example) indicates that the energetic transport formula (Bagnold, 1966; Bailard, 1981), derived originally under steady flow conditions, is inadequate for predicting transport in unsteady wave environment where waves provide the dominant contribution to bed shear stress. Elgar et al. (2001) have

shown several instances from the Duck94 data set, in which onshore bar migration is associated with gradients of acceleration skewness. Similar results have been noted in direct simulations of grain flows by Drake and Calantoni (2001), who have provided an extended version of the Bailard model for wave averaged transport by incorporating an acceleration skewness effect.

To date, efforts to extend the Bagnold (for instantaneous conditions) or Bailard (for wave-averaged conditions) formulations, including the present study, are ad hoc in nature and lack a clear theoretical basis for the model extensions being employed.

Here we take the Bagnold formula to calculate the instantaneous transport rate as the Boussinesq model is able to give instantaneous bottom velocity. Also an acceleration term is added to the formula in light of the findings in Drake and Calantoni (2001) as well as field observations of Elgar et al. (2001). The added term here does not correspond in a direct way to the acceleration skewness measure employed in Drake and Calantoni. The adaptation of an acceleration term raised to the first power does appear to have some correspondence with results for bed failure during rapid acceleration, as noted in recent calculations with a two-phase model of sediment transport (T.-J. Hsu, personal communication). The calibration coefficient is a dimensional coefficient which thus differs from the corresponding coefficient appearing in Drake and Calantoni.

The extended formula is presented as:

$$\begin{aligned} i_{tot} = i_b + i_s + i_a &= \rho c_f \frac{\epsilon_B}{\tan\phi}[|u_b|^2 u_b - \frac{\tan\beta}{\tan\phi}|u_b|^3] \\ &+ \rho c_f \frac{\epsilon_S}{w_{fall}}[|u_b|^3 u_b - \frac{\epsilon_S \tan\beta}{w_{fall}}|u_b|^5] \\ &+ g(\rho_s - \rho)K_a(|u_{b,t}| - u_{btcr})\mathrm{sign}(u_{b,t}) \end{aligned} \tag{3.32}$$

where i_b, i_s, i_a are immersed weight sediment transport rate for bed load, suspended load and the effect of free stream acceleration respectively, ϕ is the internal angle of friction, $\tan\beta$ is the slope of the bed level, c_f is friction coefficient, w_{fall} is sediment

fall velocity, u_b is bottom velocity. ϵ_B and ϵ_S are effectiveness coefficients for bed load and suspended load. $u_{b,t}$ is the acceleration of instantaneous free stream velocity u_b, and u_{btcr} is a threshold value. K_a is an empirical coefficient that needs calibration. When $|u_{b,t}| - u_{btcr} < 0$, the last term i_a is set to be zero.

The total volumetric sediment transport rate $q_{tot}(x,t)$ is calculated as

$$q_{tot} = \frac{i_{tot}}{g(\rho_s - \rho)} \tag{3.33}$$

3.3 Meyer-Peter Müller Formula with Shear Stress by Boundary Layer Model

The extended Bailard formula by Drake and Calantoni (2001) and equation (3.32) have no specific mechanical underpinning. Recently, using a small-scale two-phase sheet flow model, Hsu and Hanes (2004) demonstrated that the instantaneous sediment transport rate under unsteady free stream flow follows the instantaneous bed shear stress closely.

Previous work such as Ribberink (1998) and Hsu and Hanes (2004) tried to estimate such transport rate using instantaneous bed shear stress estimation through simple power laws, and their model accuracy relies strongly on the bed shear stress prediction. In the present work , we use a physically-based model for the local boundary layer structure over the vertical, integrated with the Boussinesq model in order to provide a profile evolution model.

The adopted formula for total load is written as

$$\Psi = A(\theta - \theta_c)^b \tag{3.34}$$

where Ψ is normalized transport rate, θ is the Shields parameter, θ_c is threshold value of Shields parameter for initiation of sediment transport, A and b are dimensionless constants, with typical values $A = 11$ and $b = 1.65$, which should be calibrated for specific applications.

$$\Psi = q_{tot}/(d\sqrt{(s-1)gd}) \tag{3.35}$$

$$\theta = \tau_b/((\rho_s - \rho)gd) \tag{3.36}$$

where τ_b is instantaneous bed shear stress obtained from solving wave bottom boundary layer instead of using quadratic correlations.

Chapter 4

NUMERICAL SOLUTION OF BOUSSINESQ EQUATIONS

In this chapter, we present the details of numerical solution to the Boussinesq equations for hydrodynamics. In order to create a model that can accomodate complicated nearshore bathymetry and shoreline geometry, we solve the problem using a generalized curvilinear coordinate system.

First, the continuity equation (COM) (2.261) and momentum equation (EOM) (2.267) are transformed to the generalized coordinate system. Various modeled effects such as wave breaking, bottom friction, wave maker, subgrid mixing and open boundary absorption, are added to the momentum equations.

The resulting equations are solved in the image domain by finite difference method using the 3rd order Adams-Bashforth explicit predictor and the 4th order Adams-Moulton implicit corrector scheme for time integration and 4th order difference scheme for $O(1)$ part and 2nd order difference scheme for $O(\mu^2)$ part for spatial discretization.

A staggered grid system is employed here to improve numerical stability. The boundary conditions (4.101) and (4.110) are implemented in a symmetric sense rather than using the off-centered difference scheme in FUNWAVE version 1.0. Numerical simulation experience shows that a symmetric scheme for boundary conditions gives better numerical stability (Zhen, 2004).

An efficient wet-dry scheme is implemented for wave run up and inundation.

4.1 Equations in Generalized Coordinate System

4.1.1 Vector form of equations

The dimensional form of Boussinesq equations in Chapter 2 are given by the equations of

Conservation of Mass (COM):

$$\frac{\partial H}{\partial t} + \nabla \cdot \mathbf{M}_w + \nabla \cdot \mathbf{M}_r = 0 \tag{4.1}$$

Equation of Motion (EOM):

$$\begin{aligned}
\frac{\partial \mathbf{M}_w}{\partial t} + \frac{\partial \mathbf{M}_r}{\partial t} &+ \nabla \cdot [\frac{\mathbf{M}_w \mathbf{M}_w}{H} + \frac{\mathbf{CC}r^2 - \mathbf{M}_{wr}\mathbf{M}_{wr}}{r}] \\
&+ \nabla[\frac{gH^2}{2} - H^2\{[F_{23t} + (\frac{2H}{3} - h)F_{22t}] + \tilde{\mathbf{u}} \cdot [\nabla F_{23} + (\frac{2H}{3} - h)\nabla F_{22}]\}] \\
&- \nabla h[gH - 2\{[F_{23t} + (\frac{H}{2} - h)F_{22t}] + \tilde{\mathbf{u}} \cdot [\nabla F_{23} + (\frac{H}{2} - h)\nabla F_{22}]\}] \\
&= 0
\end{aligned} \tag{4.2}$$

where

$$\mathbf{M}_w = H\tilde{\mathbf{u}} + H\{(Ah - \frac{H}{2})2\nabla F_{23} + (Bh^2 - \frac{H^2}{3} - 2Ah^2 + hH)\nabla F_{22}\} \tag{4.3}$$

$$\mathbf{M}_r = \int_{\eta - r}^{\eta} (\mathbf{C} - \mathbf{u}_w)dz = (\mathbf{C} - \tilde{\mathbf{u}})r + O(\mu^2 r) \tag{4.4}$$

$$\begin{aligned}
\mathbf{M}_{wr} &= \int_{\eta - r}^{\eta} \mathbf{u}_w dz \\
&= \tilde{\mathbf{u}}r + (\nabla F_{21} + 2\nabla h F_{22})(Ahr - \frac{H^2 - (H - r)^2}{2}) \\
&\quad + (Bh^2 r - \frac{H^3 - (H - r)^3}{3})\nabla F_{22}
\end{aligned} \tag{4.5}$$

4.1.2 Additional effects for actual implementation

In addition to the equations shown above, we need to add the following effects for an actual implementations: 1) damping /friction; 2) wave breaking; 3) wave absorbing

boundary; 4) subgrid mixing; 5) wave generation /source term; 6) wet-dry scheme for moving shoreline.

When added with the source term (Kennedy et al., 2000; Chen et al., 2003; Wei et al., 1999) the COM (4.1) becomes

$$H_t = \mathbf{E} + f_s(x, y, t) \tag{4.6}$$

where

$$\mathbf{E} = -\nabla \cdot (\mathbf{M_w} + \mathbf{M_r}) \tag{4.7}$$

When adding damping, breaking, absorbing, source term and subgrid mixing, the momentum equation(4.2) becomes:

$$\frac{\partial \mathbf{M}_{wi}}{\partial t} = +\mathbf{\Gamma}_b + \mathbf{\Gamma}_{br} + \mathbf{\Gamma}_{sg} + \mathbf{\Gamma}_{sp} - gH\nabla p_s + \mathbf{\Gamma}_{pr} + \mathbf{\Gamma}_{cv} + \mathbf{\Gamma}_{ro} \tag{4.8}$$

where $\mathbf{\Gamma}_{pr}$, $\mathbf{\Gamma}_{cv}$, $\mathbf{\Gamma}_{ro}$ represent the pressure, convection and roller terms respectively. $\mathbf{\Gamma}_b, \mathbf{\Gamma}_{br}, \mathbf{\Gamma}_{sg}, \mathbf{\Gamma}_{sp}$ and $-g\nabla p_s$ represent the bottom friction, breaking term, subgrid-mixing term, sponge layer term and source term respectively. The breaking term $\mathbf{\Gamma}_{br}$ here is from the eddy viscosity breaking model by Kennedy et al. (2000) and Chen et al. (2003). This is an alternative approach for spilling wave breakers that is parallel to the roller approach. We keep it for diagnostic and comparison purpose. The pressure gradient term is given by

$$\begin{aligned}\mathbf{\Gamma}_{pr} = & - \nabla[\frac{gH^2}{2} - H^2\{[F_{23t} + (\frac{2H}{3} - h)F_{22t}] + \tilde{\mathbf{u}} \cdot [\nabla F_{23} + (\frac{2H}{3} - h)\nabla F_{22}]\}] \\ & + \nabla h[gH - 2H\{[F_{23t} + (\frac{H}{2} - h)F_{22t}] + \tilde{\mathbf{u}} \cdot [\nabla F_{23} + (\frac{H}{2} - h)\nabla F_{22}]\}]\end{aligned} \tag{4.9}$$

In (4.9), the gradients of the time derivative terms F_{23t} and F_{22t} are found to be relatively difficult to discretize and they introduce instability. In order to cancel these terms, we define variable $\mathbf{M}_{dw} = (M_{dw1}, M_{dw2}) = M_{dwi}$, $(i = 1, 2)$:

$$\mathbf{M}_{dw} = H\tilde{\mathbf{u}} + H\{(Ah - H)2\nabla F_{23} + \frac{(Bh^2 - 2Ah^2 + hH)}{2}2\nabla F_{22}\} \tag{4.10}$$

such that

$$\mathbf{M}_w = \mathbf{M}_{dw} + H^2 \nabla F_{23} - \frac{H^3}{3} \nabla F_{22} \tag{4.11}$$

and can approximately cancel the $[F_{23t} + (\frac{2H}{3} - h)F_{22t}]$ term in Γ_{pr}. Thus, the EOM becomes:

$$\frac{\partial \mathbf{M}_{dw}}{\partial t} = \mathbf{\Gamma}_{pr} + \mathbf{\Gamma}_{cv} + \mathbf{\Gamma}_{ro} + \mathbf{\Gamma}_{b} + \mathbf{\Gamma}_{br} + \mathbf{\Gamma}_{sg} + \mathbf{\Gamma}_{sp} - gH\nabla p_s \tag{4.12}$$

with

1) Pressure term $\mathbf{\Gamma}_{pr}$

$$\begin{aligned} \mathbf{\Gamma}_{pr} = & - \nabla[\frac{gH^2}{2} - H^2\{\tilde{\mathbf{u}} \cdot [\nabla F_{23} + (\frac{2H}{3} - h)\nabla F_{22}]\}] \\ & + \nabla h[gH - 2H\{[F_{23t} + (\frac{H}{2} - h)F_{22t}] \\ & + \tilde{\mathbf{u}} \cdot [\nabla F_{23} + (\frac{H}{2} - h)\nabla F_{22}]\}] \end{aligned} \tag{4.13}$$

2) Convection term $\mathbf{\Gamma}_{cv}$

$$\mathbf{\Gamma}_{cv} = -\nabla \cdot [\frac{\mathbf{M}_w \mathbf{M}_w}{H}] \tag{4.14}$$

3) Roller term $\mathbf{\Gamma}_{ro}$

$$\mathbf{\Gamma}_{ro} = -\frac{\partial \mathbf{M}_r}{\partial t} - \nabla \cdot [\frac{\mathbf{C}\mathbf{C}r^2 - \mathbf{M}_{wr}\mathbf{M}_{wr}}{r}] \tag{4.15}$$

4) Damping term (bottom friction)

Classical quadratic damping due to bottom friction is used for wave attenuation

$$\Gamma_b = -f_b \tilde{\mathbf{u}} |\tilde{\mathbf{u}}| \tag{4.16}$$

where f_b is friction coefficient. Typical value is $f_b \approx 1.0 \times 10^{-5}$

5) Breaking term (eddy viscosity breaking model)

Breaking is simulated by the eddy viscosity approach which takes energy out of the main flow through a localized diffusion mechanism (Kennedy et al., 2000, Chen et al., 2003). Here the formula is presented in vector form.

$$\Gamma_{br} = [\nabla \cdot (\nu \tilde{\tilde{\mathbf{T}}})] \tag{4.17}$$

where

$$\tilde{\tilde{\mathbf{T}}} = \frac{1}{2}(\nabla(H\tilde{\mathbf{u}}) + \nabla(H\tilde{\mathbf{u}})^T) \tag{4.18}$$

is a second order tensor that represents the rate of strain. ν is eddy viscosity given by

$$\nu = B_b \delta_b^2 |(h+\eta)\eta_t| \tag{4.19}$$

where

$$B_b = \begin{cases} 1, & \eta_t \geq 2\eta_t^* \\ \frac{\eta_t}{\eta_t^*} - 1, & \eta_t^* \leq \eta_t \leq 2\eta_t^* \\ 0, & \eta_t \leq \eta_t^* \end{cases} \tag{4.20}$$

$$\eta_t^* = \begin{cases} \eta_t^{(F)}, & t - t_0 \geq T^* \\ \eta_t^{(I)} + \frac{t-t_0}{T^*}(\eta_t^{(F)} - \eta_t^{(I)}), & 0 \leq t - t_0 \leq T^* \end{cases} \tag{4.21}$$

$$\eta_t^{(I)} \approx C_{br}\sqrt{gh} \tag{4.22}$$

$$\eta_t^{(F)} \approx 0.15\sqrt{gh} \tag{4.23}$$

$$T^* \approx 5.0\sqrt{h/g} \tag{4.24}$$

t_0 is the time when an individual breaking event occurs. $C_{br} \approx 0.3\text{to}0.65$. $\delta_b \approx 1.0\text{to}1.5$. The process is that the eddy viscosity is turned on when η_t is greater than η_t^*, and turned off when it drops below η_t^*. The eddy viscosity given by (4.19) is filtered using a nine point numerical filter before being put into Γ_{br} in the implementation.

6) Subgrid mixing term

Subgrid mixing is based on the Smagorinsky theory (Smagorinsky, 1963).

$$\Gamma_{sg} = [\nabla \cdot (\nu_{sg}\tilde{\tilde{\mathbf{T}}})] \tag{4.25}$$

where

$$\begin{aligned} \nu_{sg} &= C_m \Delta x \Delta y |\tilde{\tilde{\mathbf{D}}}| \\ &= C_m \Delta x \Delta y (\tilde{\tilde{\mathbf{D}}} : \tilde{\tilde{\mathbf{D}}})^{1/2} \end{aligned} \tag{4.26}$$

$$\tilde{\tilde{\mathbf{D}}} = \frac{1}{2}[\nabla\overline{\mathbf{U}} + (\nabla\overline{\mathbf{U}})^T] \tag{4.27}$$

and $\overline{\mathbf{U}} = (\overline{U}, \overline{V})$ is the short-wave averaged velocity defined in (2.110). C_m is a coefficient with a typical value is about 0.2 . $\Delta x \Delta y$ represents the grid size of the mesh, and it will be substituted by $\sqrt{g_0} d\xi_1 d\xi_2$, where $\sqrt{g_0}$ is the Jacobian of coordinate transform and ξ_1 and ξ_2 are curvilinear coordinates to be addressed later.

7) Sponge layer term (absorbing term)

Two major absorbing mechanisms are included for absorbing waves at open boundary to prevent reflection

$$\Gamma_{sp} = -\omega_1 \tilde{\mathbf{u}} + \omega_2 \nabla \cdot \tilde{\tilde{\mathbf{T}}}_{sp}. \tag{4.28}$$

where the first term represents Newton cooling, the second term represents pseudo-viscous dissipation

$$\omega_i = C_i \omega f(x), (i = 1, 2). \tag{4.29}$$

For a sponge layer at down stream starting from location $x = x_s$ and ending at $x = x_e$, $f(x)$ is given as:

$$f(x) = \frac{e^{\frac{x - x_s}{x_e - x_s}} - 1}{e - 1} \tag{4.30}$$

C_1, C_2 are parameters to control the strength of sponge layer. ω is the frequency of waves to be absorbed. For random wave, it is chosen to be the peak angular frequency of the random wave spectra.

8) Source term (wave generation)

We use the Chawla and Kirby (2000) one-way numerical wave maker theory. For detailed derivations, see the appendix. The advantage of one-way wave maker is to save some grid points behind the wave maker region, otherwise we need more wave absorbing grids.

$$f_s = D_1 e^{(-\beta_s x^2)} \tag{4.31}$$

and

$$p_s = D_2 x e^{(-\beta_s x^2)} \tag{4.32}$$

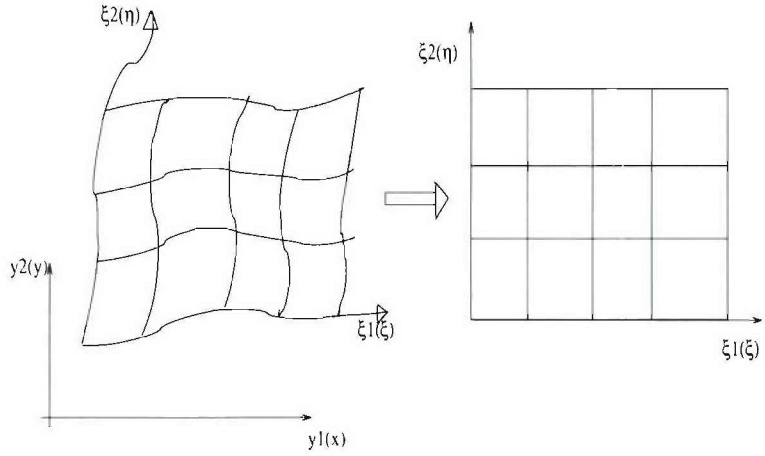

Figure 4.1: Cartesian coordinate and curvilinear coordinate

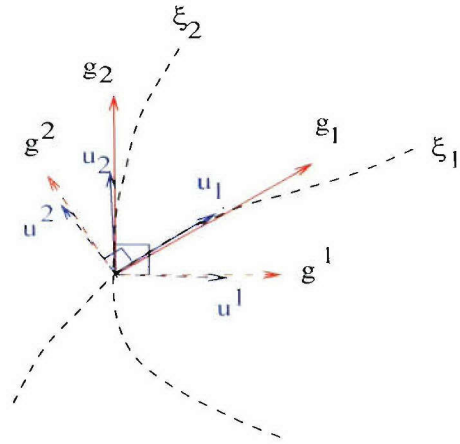

Figure 4.2: Covariant basis and contravariant basis

where D_1, D_2 are defined in appendix (A.21) and (A.10), x is local Cartesian coordinate measured from the center of source region.

4.1.3 Some notes on curvilinear coordinates

In order to write the governing equations (4.7) and (4.12) in terms of curvilinear coordinate system, we define the curvilinear coordinate system following Shi et al. (2001). As shown in figure 4.1, the usual Cartesian coordinates $(y_1, y_2) = (x, y)$ are transformed to curvilinear coordinates $(x^1, x^2) = (\xi_1, \xi_2) = (\xi, \eta)$.

For the convenience of defining inner products and cross products, covariant basis $(\mathbf{g}_1, \mathbf{g}_2)$ and contravariant basis $(\mathbf{g}^1, \mathbf{g}^2)$ are defined in figure 4.2. The velocity $\mathbf{u}$ is decomposed using these two non-orthogonal basis vectors

$$\begin{aligned} \mathbf{u} &= u^1\mathbf{g}_1 + u^2\mathbf{g}_2 \\ &= u\mathbf{g}_1 + v\mathbf{g}_2 \end{aligned} \tag{4.33}$$

and

$$\mathbf{u} = u_1\mathbf{g}^1 + u_2\mathbf{g}^2, \tag{4.34}$$

where $(u^1, u^2) \equiv (u, v)$ are called contravariant components and (u_1, u_2) are called covariant components.

In our implementation, the contravariant components are employed since they give simpler boundary conditions (Shi et al., 2001). Some basic definitions about the coordinate transform are presented in the Appendix.

4.1.4 COM and depth integrated EOM in generalized coordinate system

We choose to use contravariant velocity components $\tilde{\mathbf{u}} = (\tilde{u}^1, \tilde{u}^2)$ for all equations.

COM:

When we substitute (A.47) into COM

$$H_t = -\nabla \cdot \mathbf{M} + f_s, \tag{4.35}$$

it becomes

$$H_t = E \equiv -\frac{1}{\sqrt{g_0}}\frac{\partial}{\partial x^k}[\sqrt{g_0}(M_w^k + M_r^k)] + f_s \tag{4.36}$$

where $(x^1, x^2) = (\xi_1, \xi_2)$ is the curvilinear coordinate. M_w^k is transformed by considering (A.46) and (4.3):

$$\begin{aligned} M_w^k = H\tilde{u}^k + \quad & \{ \quad (Ah - \frac{H}{2})[\mathbf{DHU}]^{lk} \\ & + \quad (\frac{Bh^2}{2} - Ah^2 - \frac{H^2}{6} + \frac{hH}{2})[\mathbf{DU}]^{lk}\} \end{aligned} \tag{4.37}$$

where

$$\mathbf{DHU} = 2F_{23} = \frac{1}{\sqrt{g_0}}\frac{\partial}{\partial x^l}(\sqrt{g_0}h\tilde{u}^l) \tag{4.38}$$

$$\mathbf{DU} = 2F_{22} = \frac{1}{\sqrt{g_0}}\frac{\partial}{\partial x^l}(\sqrt{g_0}\tilde{u}^l) \tag{4.39}$$

with $k = 1, 2$. Calculation of $\mathbf{DHU}$ and $\mathbf{DU}$ in curvilinear coordinate is

$$\mathbf{DHU} = \frac{1}{\sqrt{g_0}}[\frac{\partial\sqrt{g_0}h\tilde{u}}{\partial\xi_1} + \frac{\partial\sqrt{g_0}h\tilde{v}}{\partial\xi_2}] \tag{4.40}$$

$$\mathbf{DU} = \frac{1}{\sqrt{g_0}}[\frac{\partial\sqrt{g_0}\tilde{u}}{\partial\xi_1} + \frac{\partial\sqrt{g_0}\tilde{v}}{\partial\xi_2}] \tag{4.41}$$

EOM:

$$\mathbf{M_{dw}}_t = \mathbf{\Gamma}_{pr} + \mathbf{\Gamma}_{cv} + \mathbf{\Gamma}_{ro} + \mathbf{\Gamma}_b + \mathbf{\Gamma}_{br} + \mathbf{\Gamma}_{sg} + \mathbf{\Gamma}_{sp} - gH\nabla p_s \tag{4.42}$$

1) $\mathbf{M_{dw}}$:

From (4.10),

$$\mathbf{M_{dw}} = H\tilde{\mathbf{u}} + H[(Ah - H)2\nabla F_{23} + (Bh^2 - 2Ah^2 + hH)\nabla F_{22}] \tag{4.43}$$

then

$$\begin{aligned} M_{dw}^k = \quad & H\tilde{u}^k + H(Ah - H)[\frac{1}{\sqrt{g_0}}\frac{\partial}{\partial x^l}(\sqrt{g_0}h\tilde{u}^l)]^{!k} \\ + \quad & H\frac{Bh^2 - 2Ah^2 + hH}{2}[\frac{1}{\sqrt{g_0}}\frac{\partial}{\partial x^l}(\sqrt{g_0}\tilde{u}^l)]^{!k} \end{aligned} \tag{4.44}$$

The first component ($k = 1$) is given as

$$M_{dw}^1 = \tilde{M}_w^1 - F_1(\tilde{v}) - F_2(\tilde{u}, \tilde{v}), \tag{4.45}$$

where

$$\begin{aligned} \tilde{M}_w^1 = H\tilde{u} \quad + \quad & H(Ah - H)g^{11}\frac{\partial[\frac{1}{\sqrt{g_0}}\frac{\partial}{\partial\xi_1}(\sqrt{g_0}h\tilde{u})]}{\partial\xi_1} \\ + \quad & H\frac{Bh^2 - 2Ah^2 + hH}{2}g^{11}\frac{\partial[\frac{1}{\sqrt{g_0}}\frac{\partial}{\partial\xi_1}(\sqrt{g_0}\tilde{u})]}{\partial\xi_1} \end{aligned} \tag{4.46}$$

$$-F_1(\tilde{v}) = H(Ah - H)g^{11}\frac{\partial[\frac{1}{\sqrt{g_0}}\frac{\partial}{\partial\xi_2}(\sqrt{g_0}h\tilde{v})]}{\partial\xi_1} + H\frac{Bh^2 - 2Ah^2 + hH}{2}g^{11}\frac{\partial[\frac{1}{\sqrt{g_0}}\frac{\partial}{\partial\xi_2}(\sqrt{g_0}\tilde{v})]}{\partial\xi_1} \tag{4.47}$$

$$-F_2(\tilde{u},\tilde{v}) = H(Ah - H)g^{21}\{\frac{\partial[\frac{1}{\sqrt{g_0}}\frac{\partial}{\partial\xi_1}(\sqrt{g_0}h\tilde{u})]}{\partial\xi_2} + \frac{\partial[\frac{1}{\sqrt{g_0}}\frac{\partial}{\partial\xi_2}(\sqrt{g_0}h\tilde{v})]}{\partial\xi_2}\} + H\frac{Bh^2 - 2Ah^2 + hH}{2}g^{21}\{\frac{\partial[\frac{1}{\sqrt{g_0}}\frac{\partial}{\partial\xi_1}(\sqrt{g_0}\tilde{u})]}{\partial\xi_2} + \frac{\partial[\frac{1}{\sqrt{g_0}}\frac{\partial}{\partial\xi_2}(\sqrt{g_0}\tilde{v})]}{\partial\xi_2}\} \tag{4.48}$$

The second component ($k = 2$) is given by

$$M^2_{dw} = V = \tilde{M}^2_w - G_1(\tilde{u}) - G_2(\tilde{u},\tilde{v}), \tag{4.49}$$

where

$$\tilde{M}^2_w = H\tilde{v} + H(Ah - H)g^{22}\frac{\partial[\frac{1}{\sqrt{g_0}}\frac{\partial}{\partial\xi_2}(\sqrt{g_0}h\tilde{v})]}{\partial\xi_2} + H\frac{Bh^2 - 2Ah^2 + hH}{2}g^{22}\frac{\partial[\frac{1}{\sqrt{g_0}}\frac{\partial}{\partial\xi_2}(\sqrt{g_0}\tilde{v})]}{\partial\xi_2} \tag{4.50}$$

$$-G_1(\tilde{u}) = H(Ah - H)g^{22}\frac{\partial[\frac{1}{\sqrt{g_0}}\frac{\partial}{\partial\xi_1}(\sqrt{g_0}h\tilde{u})]}{\partial\xi_2} + H\frac{Bh^2 - 2Ah^2 + hH}{2}g^{22}\frac{\partial[\frac{1}{\sqrt{g_0}}\frac{\partial}{\partial\xi_1}(\sqrt{g_0}\tilde{u})]}{\partial\xi_2} \tag{4.51}$$

$$-G_2(\tilde{u},\tilde{v}) = H(Ah - H)g^{12}\{\frac{\partial[\frac{1}{\sqrt{g_0}}\frac{\partial}{\partial\xi_1}(\sqrt{g_0}h\tilde{u})]}{\partial\xi_1} + \frac{\partial[\frac{1}{\sqrt{g_0}}\frac{\partial}{\partial\xi_2}(\sqrt{g_0}h\tilde{v})]}{\partial\xi_1}\} + H\frac{Bh^2 - 2Ah^2 + hH}{2}g^{21}\{\frac{\partial[\frac{1}{\sqrt{g_0}}\frac{\partial}{\partial\xi_1}(\sqrt{g_0}\tilde{u})]}{\partial\xi_1} + \frac{\partial[\frac{1}{\sqrt{g_0}}\frac{\partial}{\partial\xi_2}(\sqrt{g_0}\tilde{v})]}{\partial\xi_1}\} \tag{4.52}$$

We see that the F_1, G_1, F_2, G_2 terms are all associated with cross-derivatives. In order to solve $\tilde{u}$ and $\tilde{v}$ separately using 1-D tridiagonal solvers (see next sections), we choose to move these terms to the RHS of the equations.

2) pressure term Γ_{pr}

The pressure term $\mathbf{\Gamma}_{pr}$ given by (4.13) is now written as

$$\begin{aligned}
\mathbf{\Gamma}_{pr} &= -gH\nabla\eta + \nabla[H^2\{\tilde{\mathbf{u}}\cdot[\nabla F_{23} + (\frac{2H}{3} - h)\nabla F_{22}]\}] \\
&\quad +\nabla h[-2H\{[F_{23t} + (\frac{H}{2} - h)F_{22t}] + \tilde{\mathbf{u}}\cdot[\nabla F_{23} + (\frac{H}{2} - h)\nabla F_{22}]\}] \qquad (4.53) \\
&= -gH\eta^{,lk} + [\frac{H^2}{2}\{\tilde{u}^l[\frac{\partial \mathbf{DHU}}{\partial x^l} + (\frac{2H}{3} - h)\frac{\partial \mathbf{DU}}{\partial x^l}]\}]^{,lk} \\
&\quad +h^{,lk}[-H\{[\mathbf{DHUT} + (\frac{H}{2} - h)\mathbf{DUT}] + \tilde{u}^l[\frac{\partial \mathbf{DHU}}{\partial x^l} + (\frac{H}{2} - h)\frac{\partial \mathbf{DU}}{\partial x^l}]\}] \\
&= \left\{ \begin{array}{c} F_{pr} \\ G_{pr} \end{array} \right\} \qquad (4.54)
\end{aligned}$$

The first component (by setting $k = 1$) is

$$\begin{aligned}
F_{pr} = &- gH[g^{11}\frac{\partial \eta}{\partial \xi_1} + g^{21}\frac{\partial \eta}{\partial \xi_2}] \\
&+ g^{11}\frac{\partial[\frac{H^2}{2}\{(\tilde{u}\frac{\partial \mathbf{DHU}}{\partial \xi_1} + \tilde{v}\frac{\partial \mathbf{DHU}}{\partial \xi_2}) + (\frac{2H}{3} - h)(\tilde{u}\frac{\partial \mathbf{DU}}{\partial \xi_1} + \tilde{v}\frac{\partial \mathbf{DHU}}{\partial \xi_2})\}]}{\partial \xi_1} \\
&+ g^{21}\frac{\partial[\frac{H^2}{2}\{(\tilde{u}\frac{\partial \mathbf{DHU}}{\partial \xi_1} + \tilde{v}\frac{\partial \mathbf{DHU}}{\partial \xi_2}) + (\frac{2H}{3} - h)(\tilde{u}\frac{\partial \mathbf{DU}}{\partial \xi_1} + \tilde{v}\frac{\partial \mathbf{DU}}{\partial \xi_2})\}]}{\partial \xi_2} \\
&- [H\{\mathbf{DHUT} + (\frac{H}{2} - h)\mathbf{DUT} + (\tilde{u}\frac{\partial \mathbf{DHU}}{\partial \xi_1} + \tilde{v}\frac{\partial \mathbf{DHU}}{\partial \xi_2}) \\
&+ (\frac{2H}{3} - h)(\tilde{u}\frac{\partial \mathbf{DU}}{\partial \xi_1} + \tilde{v}\frac{\partial \mathbf{DU}}{\partial \xi_2})\}](g^{11}\frac{\partial h}{\partial \xi_1} + g^{21}\frac{\partial h}{\partial \xi_2}) \qquad (4.55)
\end{aligned}$$

The second component ($k = 2$) is

$$\begin{aligned}
G_{pr} = &- gH[g^{12}\frac{\partial \eta}{\partial \xi_1} + g^{22}\frac{\partial \eta}{\partial \xi_2}] \\
&+ g^{12}\frac{\partial[\frac{H^2}{2}\{(\tilde{u}\frac{\partial \mathbf{DHU}}{\partial \xi_1} + \tilde{v}\frac{\partial \mathbf{DHU}}{\partial \xi_2}) + (\frac{2H}{3} - h)(\tilde{u}\frac{\partial \mathbf{DU}}{\partial \xi_1} + \tilde{v}\frac{\partial \mathbf{DU}}{\partial \xi_2})\}]}{\partial \xi_1} \\
&+ g^{22}\frac{\partial[\frac{H^2}{2}\{(\tilde{u}\frac{\partial \mathbf{DHU}}{\partial \xi_1} + \tilde{v}\frac{\partial \mathbf{DHU}}{\partial \xi_2}) + (\frac{2H}{3} - h)(\tilde{u}\frac{\partial \mathbf{DU}}{\partial \xi_1} + \tilde{v}\frac{\partial \mathbf{DU}}{\partial \xi_2})\}]}{\partial \xi_2} \\
&- [H\{DHUT + (\frac{H}{2} - h)DUT + (\tilde{u}\frac{\partial \mathbf{DHU}}{\partial \xi_1} + \tilde{v}\frac{\partial \mathbf{DHU}}{\partial \xi_2}) \\
&+ (\frac{2H}{3} - h)(\tilde{u}\frac{\partial \mathbf{DU}}{\partial \xi_1} + \tilde{v}\frac{\partial \mathbf{DHU}}{\partial \xi_2})\}](g^{12}\frac{\partial h}{\partial \xi_1} + g^{22}\frac{\partial h}{\partial \xi_2}), \qquad (4.56)
\end{aligned}$$

where

$$\mathbf{DHUT} = \frac{1}{\sqrt{g_0}}\frac{\partial}{\partial x^j}(\sqrt{g_0}h\tilde{u}_t^i) \tag{4.57}$$

$$\mathbf{DUT} = \frac{1}{\sqrt{g_0}}\frac{\partial}{\partial x^i}(\sqrt{g_0}\tilde{u}_t^i). \tag{4.58}$$

Calculation of $\mathbf{DHUT}$ and $\mathbf{DUT}$ is straightforward from (4.40) and (4.41)

$$\mathbf{DHUT} = \frac{1}{\sqrt{g_0}}[\frac{\partial\sqrt{g_0}h\tilde{u}_t}{\partial\xi_1} + \frac{\partial\sqrt{g_0}h\tilde{v}_t}{\partial\xi_2}] \tag{4.59}$$

$$\mathbf{DUT} = \frac{1}{\sqrt{g_0}}[\frac{\partial\sqrt{g_0}\tilde{u}_t}{\partial\xi_1} + \frac{\partial\sqrt{g_0}\tilde{v}_t}{\partial\xi_2}] \tag{4.60}$$

3) convection term $\mathbf{\Gamma}_{cv}$

$$\begin{aligned}\mathbf{\Gamma}_{cv} &= -\nabla\cdot(\frac{\mathbf{M}_w\mathbf{M}_w}{H}) \\ &= -[\frac{1}{\sqrt{g_0}}\frac{\partial\frac{\sqrt{g_0}M_w^kM_w^j}{H}}{\partial x^j}\mathbf{g}_k + \frac{1}{H}M_w^jM_w^lC_{ji}^k\mathbf{g}_k] \\ &= \left\{\begin{array}{c} F_{cv} \\ G_{cv}\end{array}\right\}\end{aligned} \tag{4.61}$$

The first component ($k=1$) is

$$\begin{aligned}\Gamma_{cv}^1 = F_{cv} = &-\frac{1}{\sqrt{g_0}}\frac{\partial\frac{\sqrt{g_0}M_w^1M_w^1}{H}}{\partial\xi_1} - \frac{1}{\sqrt{g_0}}\frac{\partial\frac{\sqrt{g_0}M_w^1M_w^2}{H}}{\partial\xi_2} \\ &-(M_w^1M_w^1C_{11}^1 + M_w^2M_w^1C_{21}^1 + M_w^1M_w^2C_{12}^1 + M_w^2M_w^2C_{22}^1).\end{aligned} \tag{4.62}$$

The second component ($k=2$) is

$$\begin{aligned}\Gamma_{cv}^2 = G_{cv} = &-\frac{1}{\sqrt{g_0}}\frac{\partial\frac{\sqrt{g_0}M_w^2M_w^1}{H}}{\partial\xi_1} - \frac{1}{\sqrt{g_0}}\frac{\partial\frac{\sqrt{g_0}M_w^2M_w^2}{H}}{\partial\xi_2} \\ &-(M_w^1M_w^1C_{11}^2 + M_w^2M_w^1C_{21}^2 + M_w^1M_w^2C_{12}^2 + M_w^2M_w^2C_{22}^2).\end{aligned} \tag{4.63}$$

4) Roller contribution term $\mathbf{\Gamma}_{ro}$

$$\begin{aligned}\mathbf{\Gamma}_{ro} &= -\nabla\cdot(r\mathbf{CC} - \frac{\mathbf{M}_{wr}\mathbf{M}_{wr}}{r}) - \frac{\partial\mathbf{M}_r}{\partial t} \\ &= -\frac{1}{\sqrt{g_0}}[\frac{\partial\sqrt{g_0}(rC^kC^j - \frac{1}{r}M_{wr}^kM_{wr}^j)}{\partial x^j}]\mathbf{g}_k - [(rC^jC^i - \frac{1}{r}M_{wr}^jM_{wr}^i)C_{ji}^k]\mathbf{g}_k \\ &= \left\{\begin{array}{c} F_{ro} \\ G_{ro}\end{array}\right\}\end{aligned} \tag{4.64}$$

The first component ($k = 1$) is

$$\begin{aligned} F_{ro} = & - \frac{1}{\sqrt{g_0}}[\frac{\partial\sqrt{g_0}(rC^1C^1 - \frac{1}{r}M^1_{wr}M^1_{wr})}{\partial\xi_1}\frac{\partial\sqrt{g_0}(rC^1C^2 - \frac{1}{r}M^1_{wr}M^2_{wr})}{\partial\xi_2}] \\ & - [(rC^1C^1 - \frac{1}{r}M^1_{wr}M^1_{wr})C^1_{11} + (rC^1C^2 - \frac{1}{r}M^1_{wr}M^2_{wr})C^1_{12} \\ & + (rC^2C^1 - \frac{1}{r}M^2_{wr}M^1_{wr})C^1_{21} + (rC^2C^2 - \frac{1}{r}M^2_{wr}M^2_{wr})C^1_{22}]. \end{aligned} \tag{4.65}$$

The second component ($k = 2$) is

$$\begin{aligned} G_{ro} = & - \frac{1}{\sqrt{g_0}}[\frac{\partial\sqrt{g_0}(rC^2C^1 - \frac{1}{r}M^2_{wr}M^1_{wr})}{\partial\xi_1}\frac{\partial\sqrt{g_0}(rC^2C^2 - \frac{1}{r}M^2_{wr}M^2_{wr})}{\partial\xi_2}] \\ & - [(rC^1C^1 - \frac{1}{r}M^1_{wr}M^1_{wr})C^2_{11} + (rC^1C^2 - \frac{1}{r}M^1_{wr}M^2_{wr})C^2_{12} \qquad (4.66) \\ & + (rC^2C^1 - \frac{1}{r}M^2_{wr}M^1_{wr})C^2_{21} + (rC^2C^2 - \frac{1}{r}M^2_{wr}M^2_{wr})C^2_{22}]. \qquad (4.67) \end{aligned}$$

5) Bottom friction $\mathbf{\Gamma}_b$:

$$\begin{aligned} \mathbf{\Gamma}_b &= -f_b\tilde{\mathbf{u}}|\tilde{\mathbf{u}}| \\ &= -f_b\tilde{u}^k(\tilde{\mathbf{u}}\cdot\tilde{\mathbf{u}})^{1/2} \\ &= -f_b\tilde{u}^k(\tilde{u}^m\mathbf{g}_m\cdot\tilde{u}_l\mathbf{g}^l)^{1/2} \\ &= -f_b\tilde{u}^k(\tilde{u}^l\tilde{u}_l)^{1/2} \\ &= -f_b\tilde{u}^k(\tilde{u}^l g_{lm}\tilde{u}^m)^{1/2} \\ &= -f_b\tilde{u}^k[(\tilde{u},\tilde{v})\begin{pmatrix} g_{11} & g_{12} \\ g_{21} & g_{22}\end{pmatrix}\begin{pmatrix}\tilde{u}\\ \tilde{v}\end{pmatrix}]^{1/2} \end{aligned} \tag{4.68}$$

6) Breaking term $\mathbf{\Gamma}_{br}$:

$$\mathbf{\Gamma}_{br} = [\nabla\cdot(\nu_{br}\tilde{\tilde{\mathbf{T}}})] \tag{4.69}$$

$$\tilde{\tilde{\mathbf{T}}} = \frac{1}{2}(\nabla(H\tilde{\mathbf{u}}) + \nabla(H\tilde{\mathbf{u}})^T) \tag{4.70}$$

Since

$$\begin{aligned} \nabla(H\tilde{\mathbf{u}}) &= (H\tilde{u}^i)_{,j}\mathbf{g}_i\mathbf{g}^j \\ &= g^{jk}(H\tilde{u}^i)_{,j}\mathbf{g}_i\mathbf{g}_k \quad (exchange\ j.k \rightarrow) \\ &= g^{kj}(H\tilde{u}^i)_{,k}\mathbf{g}_i\mathbf{g}_j. \end{aligned} \tag{4.71}$$

we can exchange i, j in the upper equation except the basis $\mathbf{g}_i\mathbf{g}_j$ part, to obtain

$$(\nabla(H\tilde{\mathbf{u}}))^T = g^{ki}(H\tilde{u}^j)_{,k}\mathbf{g}_i\mathbf{g}_j. \tag{4.72}$$

So,

$$\tilde{\tilde{\mathbf{T}}} = T^{ij}\mathbf{g}_i\mathbf{g}_j = \frac{1}{2}[g^{kj}(H\tilde{u}^i)_{,k} + g^{ki}(H\tilde{u}^j)_{,k}]\mathbf{g}_i\mathbf{g}_j \tag{4.73}$$

or

$$T^{ij} = \frac{1}{2}[g^{kj}(H\tilde{u}^i)_{,k} + g^{ki}(H\tilde{u}^j)_{,k}]. \tag{4.74}$$

Thus, according to (A.60) we have:

$$\mathbf{\Gamma}_{br} = (\frac{1}{\sqrt{g_0}}\frac{\partial\sqrt{g_0}\nu T^{kl}}{\partial x^l} + C^k_{jl}\nu_{br}T_{jl})\mathbf{g}_k = \left\{ \begin{array}{c} F_{br} \\ G_{br} \end{array} \right\} \tag{4.75}$$

The first component ($k = 1$) is

$$\begin{aligned} F_{br} &= \Gamma^1_{br} = [\frac{1}{\sqrt{g_0}}\frac{\partial\sqrt{g_0}\nu T^{11}}{\partial\xi_1} + \frac{1}{\sqrt{g_0}}\frac{\partial\sqrt{g_0}\nu T^{12}}{\partial\xi_2} \\ &+ \nu_{br}(C^1_{11}T^{11} + C^1_{12}T^{12} + C^1_{21}T^{21} + C^1_{22}T^{22})]. \end{aligned} \tag{4.76}$$

The second component ($k = 2$) is

$$\begin{aligned} G_{br} &= \Gamma^2_{br} = [\frac{1}{\sqrt{g_0}}\frac{\partial\sqrt{g_0}\nu T^{21}}{\partial\xi_1} + \frac{1}{\sqrt{g_0}}\frac{\partial\sqrt{g_0}\nu T^{22}}{\partial\xi_2} \\ &+ \nu_{br}(C^2_{11}T^{11} + C^2_{12}T^{12} + C^2_{21}T^{21} + C^2_{22}T^{22})]. \end{aligned} \tag{4.77}$$

7) Subgrid mixing term $\mathbf{\Gamma}_{sg}$:

Since $\mathbf{\Gamma}_{sg}$ has the same structure as $\mathbf{\Gamma}_{br}$, it is easy to show that

$$\Gamma_{sg} = (\frac{1}{\sqrt{g_0}}\frac{\partial\sqrt{g_0}\nu_{sg}T^{kl}}{\partial x^l} + C^k_{jl}\nu_{sg}T_{jl})\mathbf{g}_k = \left\{ \begin{array}{c} F_{sg} \\ G_{sg} \end{array} \right\} \tag{4.78}$$

The first component ($k = 1$) is

$$\begin{aligned} F_{sg} &= \Gamma^1_{sg} = [\frac{1}{\sqrt{g_0}}\frac{\partial\sqrt{g_0}\nu_{sg}T^{11}}{\partial\xi_1} + \frac{1}{\sqrt{g_0}}\frac{\partial\sqrt{g_0}\nu_{sg}T^{12}}{\partial\xi_2} \\ &+ \nu_{sg}(C^1_{11}T^{11} + C^1_{12}T^{12} + C^1_{21}T^{21} + C^1_{22}T^{22})]. \end{aligned} \tag{4.79}$$

The second component ($k = 2$) is

$$\begin{aligned} G_{sg} &= \Gamma^2_{sg} = [\frac{1}{\sqrt{g_0}}\frac{\partial\sqrt{g_0}\nu_{sg}T^{21}}{\partial\xi_1} + \frac{1}{\sqrt{g_0}}\frac{\partial\sqrt{g_0}\nu_{sg}T^{22}}{\partial\xi_2} \\ &+ \nu_{sg}(C^2_{11}T^{11} + C^2_{12}T^{12} + C^2_{21}T^{21} + C^2_{22}T^{22})], \end{aligned} \tag{4.80}$$

where

$$\begin{aligned} \nu_{sg} &= C_m\sqrt{g_0}d\xi_1 d\xi_2(\tilde{\tilde{\mathbf{D}}} : \tilde{\tilde{\mathbf{D}}})^{1/2} \\ &= C_m\sqrt{g_0}d\xi_1 d\xi_2(D^{ij}D_{ij})^{1/2} \end{aligned} \tag{4.81}$$

and

$$\tilde{\tilde{\mathbf{D}}} = \frac{1}{2}[\nabla\overline{\mathbf{U}} + (\nabla\overline{\mathbf{U}})^T] = D^{ij}\mathbf{g}_i\mathbf{g}_j = D_{ij}\mathbf{g}^i\mathbf{g}^j. \tag{4.82}$$

D^{ij} and D_{ij} are the contravariant components and covariant components of $\tilde{\tilde{\mathbf{D}}}$ respectively. Since

$$\begin{aligned} \nabla(\overline{\mathbf{U}}) &= (\overline{U}^i)_{,j}\mathbf{g}_i\mathbf{g}^j \\ &= g^{jk}(\overline{U}^i)_{,j}\mathbf{g}_i\mathbf{g}_k \quad (exchange\ j,k \rightarrow) \\ &= g^{kj}(\overline{U}^i)_{,k}\mathbf{g}_i\mathbf{g}_j, \end{aligned} \tag{4.83}$$

we can exchange i, j in the upper equation except the basis $\mathbf{g}_i\mathbf{g}_j$ to get

$$(\nabla(\overline{\mathbf{U}}))^T = g^{ki}(\overline{U}^j)_{,k}\mathbf{g}_i\mathbf{g}_j. \tag{4.84}$$

So that

$$D^{ij} = \frac{1}{2}[g^{kj}(\overline{U}^i)_{,k} + g^{ki}(\overline{U}^j)_{,k}]. \tag{4.85}$$

Similarly, since

$$\begin{aligned} \nabla(\overline{\mathbf{U}}) &= (\overline{U}^i)_{,j}\mathbf{g}_i\mathbf{g}^j \quad (\mathbf{g}_i = g_{ik}\mathbf{g}^k \rightarrow) \\ &= g_{ik}(\overline{U}^i)_{,j}\mathbf{g}^k\mathbf{g}^j \quad (exchange\ i,k \rightarrow) \\ &= g_{ki}(\overline{U}^k)_{,j}\mathbf{g}^i\mathbf{g}^j, \end{aligned} \tag{4.86}$$

by exchanging i, j in the upper equation to get

$$(\nabla(\overline{\mathbf{U}}))^T = g_{kj}(\overline{U}^k)_{,i}\mathbf{g}^i\mathbf{g}^j. \tag{4.87}$$

So

$$D_{ij} = \frac{1}{2}[g_{ki}(\overline{U}^k)_{,j} + g_{kj}(\overline{U}^k)_{,i}] \tag{4.88}$$

Another way to calculate D_{ij} is

$$\begin{aligned}
\tilde{\tilde{\mathbf{D}}} &= D^{ij}\mathbf{g}_i\mathbf{g}_j \\
&= D^{ij}g_{il}\mathbf{g}^l g_{jm}\mathbf{g}^m \quad (exchange\ i\ with\ l\ and\ j\ with\ m \rightarrow) \\
&= g_{li}g_{mj}D^{lm}\mathbf{g}^i\mathbf{g}^j \\
&= D_{ij}\mathbf{g}^i\mathbf{g}^j.
\end{aligned} \tag{4.89}$$

Thus,

$$D_{ij} = g_{li}g_{mj}D^{lm}. \tag{4.90}$$

i.e., we can use the upper transform to get D_{ij} once we calculated D^{lm}. Substituting D^{ij} and D_{ij} into (4.81), we have

$$\nu_{sg} = C_m\sqrt{g_0}d\xi_1 d\xi_2(D^{11}D_{11} + D^{12}D_{12} + D^{21}D_{21} + D^{22}D_{22})^{1/2}. \tag{4.91}$$

8) Sponge layer term $\mathbf{\Gamma}_{sp}$:

$$\mathbf{\Gamma}_{sp} = -\omega_1 H\tilde{\mathbf{u}} + \omega_2 H\nabla\cdot\tilde{\tilde{\mathbf{T}}}_{sp} \tag{4.92}$$

with

$$\tilde{\tilde{\mathbf{T}}}_{sp} = T^{ij}_{sp}\mathbf{g}_i\mathbf{g}_k \tag{4.93}$$

Similar to (4.74), T^{ij}_{sp} can be calculated by

$$T^{ij}_{sp} = \frac{1}{2}[g^{kj}\tilde{\mathbf{u}}^i_{,k} + g^{ki}\tilde{\mathbf{u}}^j_{,k}]. \tag{4.94}$$

Then

$$\begin{aligned}\Gamma_{sp} &= -\omega_1 H\tilde{u}^k \mathbf{g}_k + \omega_2 H(\frac{1}{\sqrt{g_0}}\frac{\partial\sqrt{g_0}T^{kl}_{sp}}{\partial x^l} + C^k_{ji}T^{ji}_{sp})\mathbf{g}_k \\ &= \left\{ \begin{array}{c} F_{sp} \\ G_{sp} \end{array} \right\} \end{aligned} \tag{4.95}$$

The first component ($k = 1$) is

$$\begin{aligned} F_{sp} = \Gamma^1_{sp} = & - \omega_1 H\tilde{u} \\ & + \omega_2 H[\frac{1}{\sqrt{g_0}}\frac{\partial\sqrt{g_0}T^{11}_{sp}}{\partial\xi_1} + \frac{1}{\sqrt{g_0}}\frac{\partial\sqrt{g_0}T^{12}_{sp}}{\partial\xi_2} \\ & + (C^1_{11}T^{11}_{sp} + C^1_{12}T^{12}_{sp} + C^1_{21}T^{21}_{sp} + C^1_{22}T^{22}_{sp})]. \end{aligned} \tag{4.96}$$

The second component ($k = 2$) is

$$\begin{aligned} G_{sp} = \Gamma^2_{sp} = & - \omega_1 H\tilde{v} \\ & + \omega_2 H[\frac{1}{\sqrt{g_0}}\frac{\partial\sqrt{g_0}T^{21}_{sp}}{\partial\xi_1} + \frac{1}{\sqrt{g_0}}\frac{\partial\sqrt{g_0}T^{22}_{sp}}{\partial\xi_2} \\ & + (C^2_{11}T^{11}_{sp} + C^2_{12}T^{12}_{sp} + C^2_{21}T^{21}_{sp} + C^2_{22}T^{22}_{sp})]. \end{aligned} \tag{4.97}$$

Note that $\tilde{\tilde{\mathbf{T}}}$, $\tilde{\tilde{\mathbf{D}}}$, $\tilde{\tilde{\mathbf{T}}}_{sp}$ are similar in expression, so they can be calculated in a single procedure to save coding cost.

9) Wave maker term $-gH\nabla(p_s)$:

$$\begin{aligned} -gH\nabla(p_s) &= -gH(p_s)^{,k} \\ &= -gHg^{jk}\frac{\partial p_s}{\partial x^j}\mathbf{g}_k \\ &= \left\{ \begin{array}{c} F_{ps} \\ G_{ps} \end{array} \right\} \end{aligned} \tag{4.98}$$

where

$$F_{ps} = -gH[g^{11}\frac{\partial p_s}{\partial\xi_1} + g^{21}\frac{\partial p_s}{\partial\xi_2}] \tag{4.99}$$

$$G_{ps} = -gH[g^{12}\frac{\partial p_s}{\partial\xi_1} + g^{22}\frac{\partial p_s}{\partial\xi_2}] \tag{4.100}$$

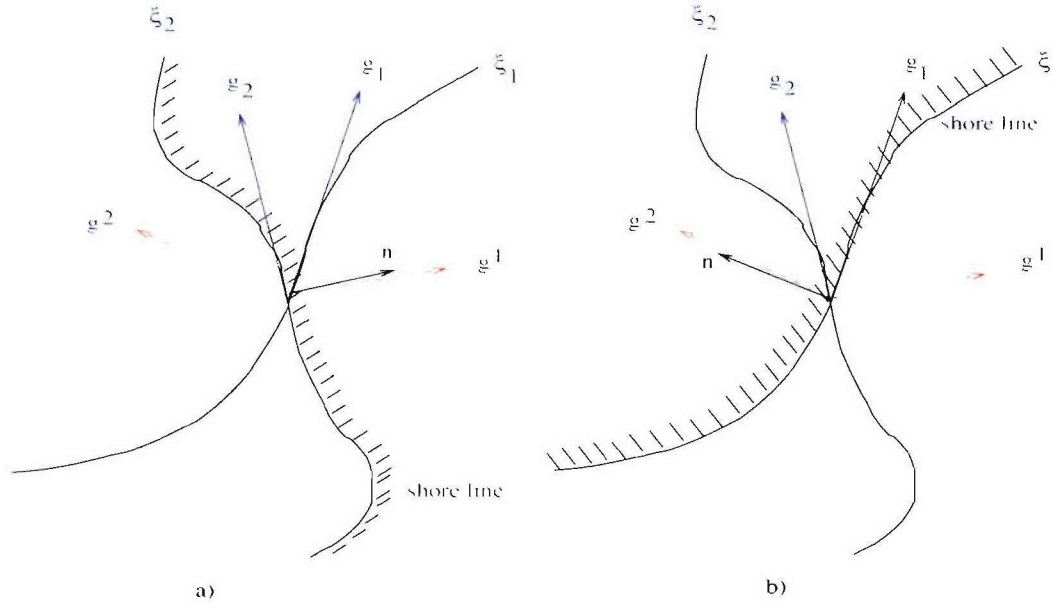

Figure 4.3: Shoreline boundary condition

4.1.5 Curvilinear representation of shoreline boundary condition

As shown in figure 4.3, at the shoreline, we require the cross boundary volume flux to be zero. Let $\mathbf{M}$ and $\mathbf{n}$ denote the volume flux and normal direction of the boundary respectively. Then we impose that

$$\mathbf{M} \cdot \mathbf{n} = 0. \qquad \text{on } \partial\Omega. \tag{4.101}$$

where

$$\begin{cases} \mathbf{M} = M^i \mathbf{g}_i \\ \mathbf{n} = n_j \mathbf{g}^j \end{cases} \tag{4.102}$$

So

$$\mathbf{M} \cdot \mathbf{n} = M^i \mathbf{g}_i \cdot n_j \mathbf{g}^j = M^i n_j \delta_i^j = M^i n_i = 0. \tag{4.103}$$

or

$$M^1 n_1 + M^2 n_2 = 0. \tag{4.104}$$

If $\mathbf{n} = n_1\mathbf{g}^1$, i.e. $n_2 = 0$ or say ξ_2 is the shoreline as in figure 4.3, then the upper equation gives

$$M^1 = 0 \tag{4.105}$$

Or, if $\mathbf{n} = n_2\mathbf{g}^2$, i.e. $n_1 = 0$ or say ξ_1 is the shoreline, we obtain

$$M^2 = 0 \tag{4.106}$$

These two equations are very simple, which is why we choose contravariant components in the implementation.

To guarantee (4.105) and (4.106) to the second order of accuracy, we require (Wei and Kirby, 1998):

$$\begin{cases} \nabla\eta \cdot \mathbf{n} = 0 \\ \tilde{\mathbf{u}} \cdot \mathbf{n} = 0 \end{cases} \tag{4.107}$$

Accordingly, if $\mathbf{n} = n_1\mathbf{g}^1$, then

$$\begin{cases} \tilde{u}^1 = \tilde{u} = 0 \\ (\nabla\eta)^1 = \eta^{11} = g^{11}\frac{\partial\eta}{\partial\xi_1} + g^{21}\frac{\partial\eta}{\partial\xi_2} = 0 \end{cases} \tag{4.108}$$

and if $\mathbf{n} = n_2\mathbf{g}^2$, then

$$\begin{cases} \tilde{u}^2 = \tilde{v} = 0 \\ (\nabla\eta)^2 = \eta^{12} = g^{12}\frac{\partial\eta}{\partial\xi_1} + g^{22}\frac{\partial\eta}{\partial\xi_2} = 0 \end{cases} \tag{4.109}$$

In addition, we impose

$$\frac{\partial\tilde{u}_T}{\partial n} = 0 \tag{4.110}$$

where $\tilde{u}_T$ is the tangential velocity component. This is not required physically, but can improve the stability of numerical simulation (Wei and Kirby, 1998).

i) If $\mathbf{n} = \mathrm{e}^1 = \frac{\mathbf{g}^1}{\sqrt{g^{11}}}$, then as shown in figure 4.3 a)

$$\tilde{u}_T = \mathbf{u} \cdot \mathbf{e}_2$$

$$
\begin{aligned}
&= \tilde{u}^i \mathbf{g}^i \cdot \frac{\mathbf{g}_2}{|\mathbf{g}_2|} \\
&= \tilde{u}^i \mathbf{g}^i \cdot \frac{\mathbf{g}_2}{\sqrt{g_{22}}} \\
&= \frac{\tilde{u}^i g_{i2}}{\sqrt{g_{22}}} \\
&= \frac{\tilde{u} g_{12} + \tilde{v} g_{22}}{\sqrt{g_{22}}}
\end{aligned} \tag{4.111}
$$

where $\mathbf{e}^i$ and $\mathbf{e}_i$ are unit contravariant and covariant basis vector. Then we have the following formula for tangential derivatives (refer to Warsi (1999) for definition of directional derivative in generalized curvilinear coordinates)

$$
\begin{aligned}
\frac{\partial \tilde{u}_T}{\partial n} &= \mathbf{n} \cdot \nabla \tilde{u}_T \\
&= \frac{\mathbf{g}^1}{\sqrt{g_{11}}} \cdot g^{jk} \frac{\partial \tilde{u}_T}{\partial x^j} \mathbf{g}_k \\
&= \frac{1}{\sqrt{g_{11}}} g^{j1} \frac{\partial \tilde{u}_T}{\partial x^j} \\
&= \frac{1}{\sqrt{g_{11}}} (\tilde{u}_T)^{|1} = 0.
\end{aligned} \tag{4.112}
$$

i.e.

$$
(\tilde{u}_T)^{|1} = 0. \tag{4.113}
$$

ii) if $\mathbf{n} = \mathbf{e}^2 = \frac{\mathbf{g}^2}{\sqrt{g^{22}}}$ then as shown in figure 4.3 b)

$$
\begin{aligned}
\tilde{u}_T &= \mathbf{u} \cdot \mathbf{e}_1 \\
&= \tilde{u}^i \mathbf{g}^i \cdot \frac{\mathbf{g}_1}{|\mathbf{g}_1|} \\
&= \tilde{u}^i \mathbf{g}^i \cdot \frac{\mathbf{g}_1}{\sqrt{g_{11}}} \\
&= \frac{\tilde{u}^i g_{i1}}{\sqrt{g_{11}}} \\
&= \frac{\tilde{u} g_{11} + \tilde{v} g_{21}}{\sqrt{g_{11}}}.
\end{aligned} \tag{4.114}
$$

then

$$
\frac{\partial \tilde{u}_T}{\partial n} = \mathbf{n} \cdot \nabla \tilde{u}_T
$$

$$
\begin{aligned}
&= \frac{\mathbf{g}^2}{\sqrt{g_{22}}} \cdot g^{jk} \frac{\partial \tilde{u}_T}{\partial x^j} \mathbf{g}_k \\
&= \frac{1}{\sqrt{g_{22}}} g^{j2} \frac{\partial \tilde{u}_T}{\partial x^j} \\
&= \frac{1}{\sqrt{g_{22}}} (\tilde{u}_T)^{!2} = 0,
\end{aligned} \tag{4.115}
$$

i.e.

$$
(\tilde{u}_T)^{!2} = 0. \tag{4.116}
$$

Note that (4.113) and (4.116) are slightly different from Shi et al. (2001) implementation, where

$$
\tilde{u}^{2(!1)} = \tilde{v}^{!1} = 0 \tag{4.117}
$$

$$
\tilde{u}^{1(!2)} = \tilde{u}^{!2} = 0 \tag{4.118}
$$

are used instead. The upper equations assume good orthogonality and homogeneity of the coordinate system (ξ_1, ξ_2) near the boundary, in which case $g_{12} = g_{21} \approx 0$ and $\sqrt{g_{11}}$ and $\sqrt{g_{22}}$ are nearly constants so that $\tilde{u}_T \approx \tilde{v}$ when the shoreline is on ξ_2 and $\tilde{u}_T \approx \tilde{u}$ when the shoreline is on ξ_1. If the mesh generator is good enough, we should use (4.117) and (4.118) for they are much simpler.

4.2 Grid System and Discretization

4.2.1 Grid system

Figure 4.4 shows the staggered grid system $(\xi_1, \xi_2) = (\xi, \eta)$ that is used as the coordinate curve. ξ_1 direction velocities are defined on – points (also called u points) , ξ_2 direction velocities are defined on | points (also called v points), while surface elevation and depth information is defined on $\times$ points(also called z points). The corner of a grid is called a node point (also called 1 point). The coordinate information is defined on node points. They all use their own independent indices.

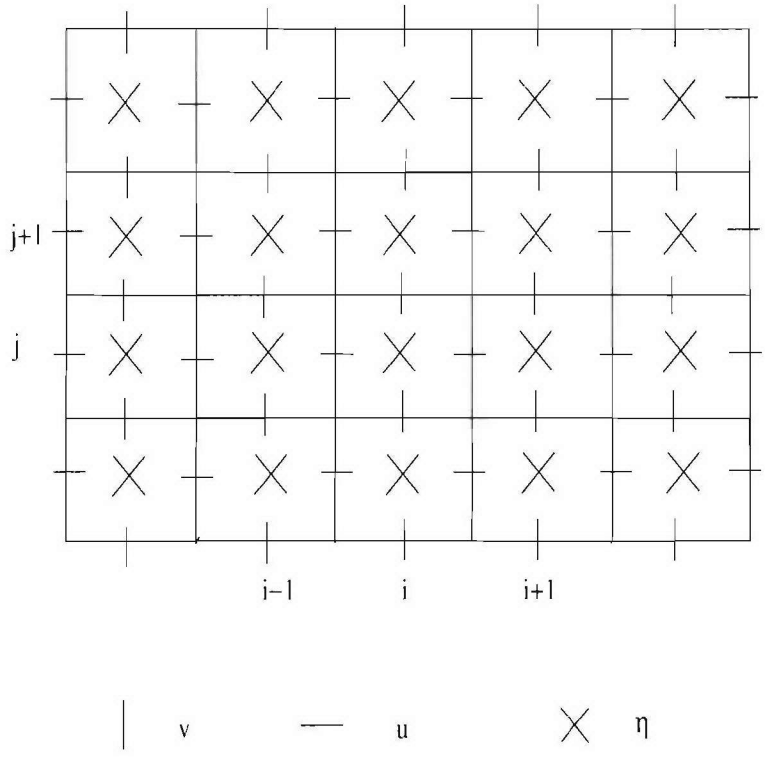

Figure 4.4: Staggered grid system

4.2.2 Spatial discretization

For example, for $\frac{\partial f}{\partial \xi}|_z$, i.e., ξ_1 derivative of function f at z points (here f is defined on u points), we employ the following finite difference scheme.

a) Second order scheme:

$$\frac{\partial f}{\partial \xi}|_z = \frac{f_{i+1} - f_i}{d\xi} + O((d\xi)^2) \tag{4.119}$$

b) Fourth order scheme

$$\frac{\partial f}{\partial \xi}|_z = \frac{8(f_{i+1} - f_i) - 0.5(f_{i+2} + f_{i+1}) + 0.5(f_{i-1} + f_i)}{6d\xi} + O((d\xi)^4) \tag{4.120}$$

where $0.5(f_{i+2} + f_{i+1})$ is an average to obtain f on $i + \frac{3}{2}$ point (note that f is defined on u points) and $0.5(f_{i-1} + f_i)$ is an average to obtain f on $i - \frac{1}{2}$ point. When i is on a left wall boundary, f_{i-1} does not exist, then it is replaced by f_{i+1} for the symmetric case or replaced by $-f_{i+1}$ for the anti-symmetric case. The same situation happens to f_{i+1} if i is on a right wall boundary. For example, for $\frac{\partial \tilde{u}}{\partial \xi}$ we should use the anti-symmetric case, since $\tilde{u} \approx 0$ at the boundary according to (4.108). An odd function satisfies this condition and it is anti-symmetric. For $\frac{\partial \tilde{v}}{\partial \xi}$, we should use the symmetric case, because $\frac{\partial \tilde{v}}{\partial \xi} \approx 0$ according to (4.117). An even function satisfies this and it is symmetric.

4.2.3 Temporal integration

4.2.3.1 Adams explicit and implicit schemes

For a simple model equation $y(t)_t = f(y,t)$, the Adams family of predictor-corrector schemes are listed below:

1) Adams 1st order explicit predictor and 2nd order implicit corrector

$$\begin{cases} \overline{y}^{p+1} = y^p + hf^p \\ y^{p+1} = y^i + \frac{h}{2}(\overline{f}^{p+1} + f^p) \end{cases} \tag{4.121}$$

where h is the time step $h = \Delta t$, p is index for current time level, $p+1$ is index for next time level, $\overline{y}$ predicted value, and $\overline{f}^{p+1} = \overline{y}_t^{p+1}$

2) Adams 2nd order explicit predictor and 3rd order implicit corrector

$$\begin{cases} \overline{y}^{p+1} = y^p + \frac{h}{2}(3f^p - f^{p-1}) \\ y^{p+1} = y^i + \frac{h}{12}(5\overline{f}^{p+1} + 8f^p - f^{p-1}) \end{cases} \tag{4.122}$$

3) Adams 3rd order explicit predictor and 4th order implicit corrector

$$\begin{cases} \overline{y}^{p+1} = y^p + \frac{h}{12}(23f^p - 16f^{p-1} + 5f^{p-2}) \\ y^{p+1} = y^i + \frac{h}{24}(9\overline{f}^{p+1} + 19f^p - 5f^{p-1} + f^{p-2}) \end{cases} \tag{4.123}$$

4.2.3.2 Implementation of Adams schemes

In our case, equation (4.36) and (4.42) are solved. The 4th order implicit corrector needs 3 previous levels of information, which is not available for the first 2 time steps. Hence the first step and the second step, 2nd order corrector (4.121) and 3rd corrector (4.122) are used to start up the simulation.

The first time step (1st order predictor, 2nd order corrector, p=1 level known)

Here, $p = 1$ level is the initial condition obtained from inputs.

Predictor stage is given by (using (4.121))

$$H_{i,j}^{p+1} = H_{i,j}^{p} + \Delta t E_{i,j}^{p} \tag{4.124}$$

$$\tilde{M}_{wi,j}^{1,p+1} = \tilde{M}_{wi,j}^{1,p} + \Delta t F_{total}^{p} \tag{4.125}$$

$$\tilde{M}_{wi,j}^{2,p+1} = \tilde{M}_{wi,j}^{2,p} + \Delta t G_{total}^{p} \tag{4.126}$$

where i, j are the spatial indices for ξ_1 and ξ_2 direction respectively, Δt is time step and

$$\begin{aligned} F_{total} &= (F_{12})_t + F_{other} \\ G_{total} &= (G_{12})_t + G_{other} \end{aligned} \tag{4.127}$$

$$\begin{aligned} F_{12} &= F_1 + F_2 \\ G_{12} &= G_1 + G_2 \end{aligned} \tag{4.128}$$

$$F_{other} = F_{pr} + F_{ro} + F_b + F_{br} + F_{sp} + F_{sg} + F_{ps}$$
$$G_{other} = G_{pr} + G_{ro} + G_b + G_{br} + G_{sp} + G_{sg} + G_{ps}. \tag{4.129}$$

F_1, F_2 and G_1, G_2 contain cross derivatives in $M^1_{wd} = \tilde{M}^1_w + F_1 + F_2$ and $M^2_{wd} = \tilde{M}^2_w + G_1 + G_2$, so they are moved to RHS of the equation. $(F_{12})_t$ is approximated by

$$(F_{12})_t = \frac{F^p_{12} - F^{p-1}_{12}}{\Delta t} \tag{4.130}$$

Since the $p-1$ level is not available, F^{p-1} is set to be same as F^p as an initial guess and this time derivative is nullified, so the upper predictor becomes

$$\tilde{M}^{1,p+1}_{wi,j} = \tilde{M}^{1,p}_{wi,j} + \Delta t F^p_{other} \tag{4.131}$$

$$\tilde{M}^{2,p+1}_{wi,j} = \tilde{M}^{2,p}_{wi,j} + \Delta t G^p_{other} \tag{4.132}$$

The corrector is given by (using (4.121))

$$H^{p+1}_{i,j} = H^p_{i,j} + \frac{\Delta t}{2}[\overline{E}^{p+1}_{i,j} + E^p_{i,j}] \tag{4.133}$$

$$\tilde{M}^{1,p+1}_{wi,j} = \tilde{M}^{1,p}_{wi,j} + \frac{\Delta t}{2}[\overline{F}^{p+1}_{total} + F^p_{total}] \tag{4.134}$$

$$\tilde{M}^{1,p+1}_{wi,j} = \tilde{M}^{2,p}_{wi,j} + \frac{\Delta t}{2}[\overline{G}^{p+1}_{total} + G^p_{total}] \tag{4.135}$$

where

$$\overline{F}_{total} = (\overline{F}_{12})_t + \overline{F}_{other}$$
$$\overline{G}_{total} = (\overline{G}_{12})_t + \overline{G}_{other} \tag{4.136}$$

and here we have

$$(\overline{F}^{p+1}_{12})_t \approx \frac{\overline{F}^{p+1}_{12} - F^p_{12}}{\Delta t}. \tag{4.137}$$

The upper corrector for $\tilde{M}^1_w$ and $\tilde{M}^2_w$ becomes:

$$\tilde{M}^{1,p+1}_{wi,j} = \tilde{M}^{1,p}_{wi,j} + (\overline{F}^{p+1}_{12} - F^p_{12}) + \frac{\Delta t}{2}[\overline{F}^{p+1}_{other} + F^p_{other}] \tag{4.138}$$

$$\tilde{M}^{2,p+1}_{wi,j} = \tilde{M}^{2,p}_{wi,j} + (\overline{G}^{p+1}_{12} - G^p_{12}) + \frac{\Delta t}{2}[\overline{G}^{p+1}_{other} + G^p_{other}] \tag{4.139}$$

The 2nd time step (2st order predictor, 3rd order corrector, p=2)

The predictor stage is given by (usin (4.122))

$$H_{i,j}^{p+1} = H_{i,j}^{p} + \frac{\Delta t}{2}[3E_{i,j}^{p} - E_{i,j}^{p-1}] \tag{4.140}$$

$$\tilde{M}_{wi,j}^{1,p+1} = \tilde{M}_{wi,j}^{1,p} + \frac{\Delta t}{2}[3F_{total}^{p} - F_{total}^{p-1}] \tag{4.141}$$

$$\tilde{M}_{wi,j}^{2,p+1} = \tilde{M}_{wi,j}^{2,p} + \frac{\Delta t}{2}[3G_{total}^{p} - G_{total}^{p-1}] \tag{4.142}$$

where

$$(F_{12}^{p})_t \approx \frac{F_{12}^{p} - F_{12}^{p-1}}{\Delta t} \tag{4.143}$$

is the same as

$$(F_{12}^{p-1})_t \approx \frac{F_{12}^{p} - F_{12}^{p-1}}{\Delta t}. \tag{4.144}$$

The upper predictor for $\tilde{M}_w^1$ and $\tilde{M}_w^2$ becomes

$$\tilde{M}_{wi,j}^{1,p+1} = \tilde{M}_{wi,j}^{1,p} + (F_{12}^{p} - F_{12}^{p-1})\frac{\Delta t}{2}[3F_{other}^{p} - F_{other}^{p-1}] \tag{4.145}$$

$$\tilde{M}_{wi,j}^{2,p+1} = \tilde{M}_{wi,j}^{2,p} + (G_{12}^{p} - G_{12}^{p-1})\frac{\Delta t}{2}[3G_{other}^{p} - G_{other}^{p-1}] \tag{4.146}$$

The corrector stage is given by (using (4.122))

$$H_{i,j}^{p+1} = H_{i,j}^{p} + \frac{\Delta t}{12}[5\overline{E}_{i,j}^{p+1} + 8E_{i,j}^{p} - E_{i,j}^{p-1}] \tag{4.147}$$

$$\tilde{M}_{wi,j}^{1,p+1} = \tilde{M}_{wi,j}^{1,p} + \frac{\Delta t}{12}[5\overline{F}_{total}^{p+1} + 8F_{total}^{p} - F_{total}^{p-1}] \tag{4.148}$$

$$\tilde{M}_{wi,j}^{2,p+1} = \tilde{M}_{wi,j}^{2,p} + \frac{\Delta t}{12}[5\overline{G}_{total}^{p+1} + 8G_{total}^{p} - G_{total}^{p-1}] \tag{4.149}$$

where

$$(\overline{F}_{12}^{p+1})_t \approx \frac{3\overline{F}_{12}^{p+1} - 4F_{12}^{p} + F_{12}^{p-1}}{2\Delta t} \tag{4.150}$$

$$(F_{12}^{p})_t \approx \frac{\overline{F}_{12}^{p+1} - F_{12}^{p-1}}{2\Delta t} \tag{4.151}$$

$$(F_{12}^{p-1})_t \approx \frac{-3F_{12}^{p-1} + 4F_{12}^{p} - \overline{F}_{12}^{p+1}}{2\Delta t} \tag{4.152}$$

Then the upper corrector for $\tilde{M}_w^1$ and $\tilde{M}_w^2$ becomes

$$\tilde{M}_{wi,j}^{1,p+1} = \tilde{M}_{wi,j}^{1,p} + (\overline{F}_{12}^{p+1} - F_{12}^{p}) + \frac{\Delta t}{12}[5\overline{F}_{other}^{p+1} + 8F_{other}^{p} - F_{other}^{p-1}] \tag{4.153}$$

$$\tilde{M}_{wi,j}^{2,p+1} = \tilde{M}_{wi,j}^{2,p} + (\overline{G}_{12}^{p+1} - G_{12}^{p}) + \frac{\Delta t}{12}[5\overline{G}_{other}^{p+1} + 8G_{other}^{p} - G_{other}^{p-1}] \tag{4.154}$$

Beyond the 3rd time step (3rd order predictor, 4th order corrector, $p \geq 3$)

In the rest of the time steps we use 3rd order predictor and 4th order corrector.

The predictor stages is given by (using (4.123))

$$H_{i,j}^{p+1} = H_{i,j}^{p} + \frac{\Delta t}{12}[23E_{i,j}^{p} - 16E_{i,j}^{p-1} + 5E_{i,j}^{p-2}] \tag{4.155}$$

$$\tilde{M}_{wi,j}^{1,p+1} = \tilde{M}_{wi,j}^{1,p} + \frac{\Delta t}{12}[23F_{total}^{p} - 16F_{total}^{p-1} + 5F_{total}^{p-2}] \tag{4.156}$$

$$\tilde{M}_{wi,j}^{2,p+1} = \tilde{M}_{wi,j}^{2,p} + \frac{\Delta t}{12}[23G_{total}^{p} - 16G_{total}^{p-1} + 5G_{total}^{p-2}] \tag{4.157}$$

where

$$(F_{12}^{p})_t \approx \frac{3F_{12}^{p} - 4F_{12}^{p-1} + F_{12}^{p-2}}{2\Delta t} \tag{4.158}$$

$$(F_{12}^{p-1})_t \approx \frac{F_{12}^{p} - F_{12}^{p-2}}{2\Delta t} \tag{4.159}$$

$$(F_{12}^{p-2})_t \approx \frac{-3F_{12}^{p-2} + 4F_{12}^{p-1} - F_{12}^{p}}{2\Delta t}. \tag{4.160}$$

The upper predictor for $\tilde{M}_w^1$ and $\tilde{M}_w^2$ becomes

$$\tilde{M}_{wi,j}^{1,p+1} = \tilde{M}_{wi,j}^{1,p} + (2F_{12}^{p} - 3F_{12}^{p-1} + F_{12}^{p}) + \frac{\Delta t}{12}[23F_{other}^{p} - 16F_{other}^{p-1} + 5F_{other}^{p-2}] \tag{4.161}$$

$$\tilde{M}_{wi,j}^{p+1} = \tilde{M}_{wi,j}^{2,p} + (2G_{12}^{p} - 3G_{12}^{p-1} + G_{12}^{p}) + \frac{\Delta t}{12}[23G_{other}^{p} - 16G_{other}^{p-1} + 5G_{other}^{p-2}] \tag{4.162}$$

The corrector stage is given by (using (4.123))

$$H_{i,j}^{p+1} = H_{i,j}^{p} + \frac{\Delta t}{24}[9\overline{E}_{i,j}^{p+1} + 19E_{i,j}^{p} - 5E_{i,j}^{p-1} + E_{i,j}^{p-2}] \tag{4.163}$$

$$\tilde{M}_{wi,j}^{1,p+1} = \tilde{M}_{wi,j}^{1,p} + \frac{\Delta t}{24}[9\overline{F}_{total}^{p+1} + 19F_{total}^{p} - 5F_{total}^{p-1} + F_{total}^{p-2}] \tag{4.164}$$

$$\tilde{M}_{wi,j}^{2,p+1} = \tilde{M}_{wi,j}^{2,p} + \frac{\Delta t}{24}[9\overline{G}_{total}^{p+1} + 19G_{total}^{p} - 5G_{total}^{p-1} + G_{total}^{p-2}] \tag{4.165}$$

where

$$(\overline{F}_{12}^{p+1})_t \approx \frac{11\overline{F}_{12}^{p+1} - 18F_{12}^{p} + 9F_{12}^{p-1} - 2F_{12}^{p-2}}{6\Delta t} + O(\Delta t^3) \tag{4.166}$$

$$(F_{12}^{p})_t \approx \frac{2\overline{F}_{12}^{p+1} + 3F_{12}^{p} - 6F_{12}^{p-1} + F_{12}^{p-2}}{6\Delta t} + O(\Delta t^3) \tag{4.167}$$

$$(F_{12}^{p-1})_t \approx \frac{-2F_{12}^{p-2} - 3F_{12}^{p-1} + 6F_{12}^{p} - \overline{F}_{12}^{p+1}}{6\Delta t} + O(\Delta t^3) \tag{4.168}$$

$$(F_{12}^{p-2})_t \approx \frac{-11F_{12}^{p-2} + 18F_{12}^{p-1} - 9F_{12}^{p} + 2\overline{F}_{12}^{p+1}}{6\Delta t}. + O(\Delta t^3) \tag{4.169}$$

Then the upper corrector for $\tilde{M}_w^1$ and $\tilde{M}_w^2$ becomes

$$\tilde{M}_{wi,j}^{1,p+1} = \tilde{M}_{wi,j}^{1,p} + (\overline{F}_{12}^{p+1} - F_{12}^{p}) + \frac{\Delta t}{24}[9\overline{F}_{other}^{p+1} + 19F_{other}^{p} - 5F_{other}^{p-1} + F_{other}^{p-2}] \tag{4.170}$$

$$\begin{aligned} \tilde{M}_{wi,j}^{2,p+1} &= \tilde{M}_{wi,j}^{2,p} + (\overline{G}_{12}^{p+1} - G_{12}^{p}) \\ &+ \frac{\Delta t}{24}[9\overline{G}_{other}^{p+1} + 19G_{other}^{p} - 5G_{other}^{p-1} + G_{other}^{p-2}] \end{aligned} \tag{4.171}$$

4.2.4 Hot-Start problem

In the predictor stage of the first time step (4.129), we need to calculate DHUT and DUT in F_{pr} and G_{pr} which are contained in F_{other} and G_{other}. But at that time, only one level of $\tilde{u}$ and $\tilde{v}$ is known from the initial condition. So we are not able to use (4.59) to calculate them. If the problem is a cold-start problem, i.e. the initial conditions are identically zero, then we can neglect these terms. Whereas, if it's a hot-start problem, we can't neglect them. They call for special treatments. One simple approach is to replace the time derivatives by spatial derivatives as follows.

From the momentum equation(4.42), we have order $O(1)$ accuracy

$$\mathbf{M}_{wt} = H[\tilde{\mathbf{u}} + O(\mu^2)]_t = -gH\nabla\eta + O(\delta) + O(\mu^2) \tag{4.172}$$

so,

$$\tilde{\mathbf{u}}_t = -g\nabla\eta + O(\mu^2) \tag{4.173}$$

Then,

$$\begin{aligned} \mathbf{DUT} &= \nabla \cdot \tilde{\mathbf{u}}_t \\ &= -g\nabla \cdot \nabla\eta + O(\mu^2) \\ &= -g\frac{1}{\sqrt{g_0}}\frac{\partial}{\partial x^i}(\sqrt{g_0}g^{ji}\frac{\partial \eta}{\partial x^j}) + O(\mu^2) \end{aligned} \tag{4.174}$$

Similarly,

$$\begin{aligned} \mathbf{DHUT} &= \nabla \cdot (h\tilde{\mathbf{u}}_t) \\ &= -g\nabla \cdot (h\nabla\eta) + O(\mu^2) \\ &= -g\frac{1}{\sqrt{g_0}}\frac{\partial}{\partial x^i}(h\sqrt{g_0}g^{ji}\frac{\partial \eta}{\partial x^j}) + O(\mu^2) \end{aligned} \tag{4.175}$$

4.3 Obtaining $\tilde{\mathbf{u}}$ from $\tilde{\mathbf{M}}_w$

In both the predictor and corrector stages, we get $\tilde{\mathbf{M}}_w = (\tilde{M}_w^1, \tilde{M}_w^2)$, then $\tilde{\mathbf{u}}$ is obtained by solving a tridiagonal matrix equation for non-periodic boundary condition case and by solving a cyclic-tridiagonal matrix equation for periodic boundary condition case.

By definition (4.46), we have

$$\begin{aligned} \tilde{M}_w^1 = H\tilde{u} &+ Hb_1\frac{g_2 2}{g_0}[\frac{1}{\sqrt{g_0}}(\sqrt{g_0}\tilde{u})_{\xi_1}]_{\xi_1} \\ &+ Hb_2\frac{g_2 2}{g_0}[\frac{1}{\sqrt{g_0}}(\sqrt{g_0}h\tilde{u})_{\xi_1}]_{\xi_1} \end{aligned} \tag{4.176}$$

where

$$b_1 = \frac{Bh^2 - 2Ah^2 + hH}{2} \tag{4.177}$$

and

$$b_2 = Ah - H. \tag{4.178}$$

(4.176) is a second order differential equation for $\tilde{u}$, which can be solved by a tri-diagonal matrix system. Since A, B are related to definitions of the multiple and moving reference level, which are functions of time. So the coefficients of the equation are time varying.

For a given u point i, the upper equation can be discretized as:

$$AA_i\tilde{u}_{i-1} + \tilde{u}_i + CC_i\tilde{u}_{i+1} = DD_i \tag{4.179}$$

where

$$\begin{aligned} AA_i &= (\sqrt{g_0})_{i-1}(\frac{g_{22}}{g_0^2})_i[b_1(\sqrt{g_0})_i + h_{i-1}b_2(\sqrt{g_0})_i \\ &+ (\frac{1}{2}b_1 + \frac{1}{2}h_{i-1}b_2)(\sqrt{g_0})_{\xi_1}]/BB \end{aligned} \tag{4.180}$$

$$\begin{aligned} CC_i &= (\sqrt{g_0})_{i+1}(\frac{g_{22}}{g_0^2})_i[b_1(\sqrt{g_0})_i + h_{i+1}b_2(\sqrt{g_0})_i \\ &- (\frac{1}{2}b_1 + \frac{1}{2}h_{i+1}b_2)(\sqrt{g_0})_{\xi_1}]/BB \end{aligned} \tag{4.181}$$

$$DD_i = \tilde{M}_{w,i}/H_i \tag{4.182}$$

$$BB = 1 - 2(\frac{g_{22}}{g_0})_i(b_1 + b_2h_i) \tag{4.183}$$

If i is on a wall boundary, then $i-1$ in AA_i is replaced by $i+1$ when the wall is at left; and $i+1$ in CC_i is replaced by $i-1$ when the wall is at right. If i is on a periodic boundary condition point and $i=1$, then $i-1$ is replaced by $mx-1$ in which mx is the last grid number. If i is on a periodic boundary condition point and $i=mx$, then $i+1$ is replaced by 2. (4.179) is a standard tridiagonal or cyclic tridiagonal matrix system, which can be readily solved. $\tilde{v}$ can be solved in the same way.

4.4 Iteration Error Control and Under-relaxation

Between iteration step k and $k+1$, the errors of iteration are defined as

$$error_z = \frac{\sum_i \sum_j |\eta_{i,j}^{k+1} - \eta_{i,j}^k|}{\sum_i \sum_j |\eta_{i,j}^{k+1}|} \tag{4.184}$$

and

$$error_{uv} = \frac{\sum_i \sum_j |\tilde{u}_{i,j}^{k+1} - \tilde{u}_{i,j}^k| + |\tilde{v}_{i,j}^{k+1} - \tilde{v}_{i,j}^k|}{\sum_i \sum_j |\tilde{u}_{i,j}^{k+1}| + |\tilde{v}_{i,j}^{k+1}|}. \tag{4.185}$$

In the very first few time steps, the denominator may be very small for a cold-start problem. In this case, if the denominator is less than $1.0E-6$ the upper errors are defined as the numerator to avoid devision by a small number. The convergence criteria is: when $\max(error_{uv}, error_z)$ is less than an designated value, the iteration is stopped. Also, an under-relaxation method is applied to get better numerical stability. It is designed as:

$$(\tilde{u}, \tilde{v}, \eta) = \omega(\tilde{u}, \tilde{v}, \eta)^{k+1} + (1-\omega)(\tilde{u}, \tilde{v}, \eta)^{k} \tag{4.186}$$

where ω is relaxation parameter chosen to be between 0.5 and 1.0 .

4.5 Calculation of Near Bottom Velocity

The near bottom velocity is of particular importance for it will be used to predict bedload sediment transport in conjunction with the bottom boundary layer model. According to the kinematics formulas (2.106) to (2.108), the near bottom velocity is calculated (by setting $h+z=0$) as

$$\begin{aligned} \mathbf{u_b}(\xi_1, \xi_2, z, t) = \tilde{\mathbf{u}} &+ (Ah)\nabla(\nabla \cdot (h\tilde{\mathbf{u}})) \\ &+ (\frac{B-2A}{2}h^2)\nabla(\nabla \cdot \tilde{\mathbf{u}}) \\ = \tilde{\mathbf{u}} &+ (Ah)(\mathbf{DHU})^{!i} \\ &+ (\frac{B-2A}{2}h^2)(\mathbf{DU})^{!i} \\ = &\quad (u_b, v_b) \end{aligned} \tag{4.187}$$

Here u_b, v_b are contravariant components in the image domain. They may be converted to Cartesian components using (A.80) and (A.81).

4.6 Wet-Dry Algorithm

With the Boussinesq wave theory development in the past two decades, we have greatly improved our modeling ability of wave dispersion and nonlinear wave wave interactions. The motion of wave run up and rundown at a moving shoreline still remains difficult to simulate. Important theoretical pursuits of wave motion on a plane sloping

beach have been made by Carrier and Greenspan (1958), Tuck and Hwang (1972), Synolakis (1987), Carrier et al. (2003) and Kanoglu (2004). In Carrier and Greenspan (1958), a hodograph transformation using Riemann invariants of the hyperbolic system is used to reduce the nonlinear shallow water wave equation to a single 2nd order linear equation. Two difficulties in the Carrier and Greenspan (1958) are present: a) derivation of equivalent initial condition in the transformed coordinate for a given initial condition in physical coordinate; b) derivation of solution for a particular time or a particular location. The first difficulty is solved by Kanoglu (2004) using a linearized form of the hodograph transformation and the second difficulty is solved by Synolakis (1987) using the Newton-Raphson iteration algorithms. In Synolakis (1987), detailed measurements of solitary wave run up are obtained. Tuck and Hwang (1972) used a slightly different transformation which gives equations that are easier to solve. Carrier et al. (2003) developed a Green's function solution using Tuck and Hwang (1972) transformation. The Carrier et al. (2003) solutions are highly singular which also require numerical integration to obtain arbitrary initial wave form propagation. Tadepalli and Synolakis (1994) presented N-wave propagation investigations commonly seen in tsunami problems. These theoretical results improved our understanding of wave run up processes. However, there are limitations associated: a) theory is based on 1D flow; b) theory is based on perfect straight beach c) only a non-breaking wave is considered. These limitations prevent their usage in real engineering applications. For systems with complicated bathymetry and shoreline layout, our modeling technique still relies on empiricism and suffers from numerical instabilities. Extensive modeling skills are required to tackle the wetting and drying of domains.

Models that include wetting and drying treatment techniques can be seen in Tao (1983, 1984), Falconer and Chen (1991) , Madsen et al. (1997), Buchard (1998), Hubbert and McInnes (1999), Kennedy et al. (2000), Brufau et al. (2002), Lynett et al. (2002), Xie et al. (2004) and Oey (2005). In Tao (1983, 1984), a slot technique is invented to deal with the swash motion through permeable bed. The technique is further discussed

by Madsen et al. (1997) and improved by Kennedy et al. (2000) and Chen et al. (2000). The method is applicable to relatively gentle beaches with small amplitude incident wave. Parameters involved in the model need calibration and spurious oscillations can be generated. In Hubbert and McInnes (1999), a comprehensive inundation scheme is developed to model the rise and fall of coastal sea level due to tides and storm surges. In the Princeton Ocean Model (POM), Xie et al. (2004) extended the Hubbert and McInnes (1999) scheme by tracking the travel distance of flooding water in partially flooded computational cells and using an iterative mass rebalancing procedure to keep total water mass conserved. This method is quite complicated to implement and the mass rebalancing procedure is applied uniformly to the whole system (uniform change of sea surface elevation in the domain) which lacks a corresponding dynamic mechanism. In Oey (2005), a simple wet and dry scheme is introduced into the POM model and analysis shows that bottom friction effect on total water depth can be represented by an advection-diffusion equation. For advection dominated shoreline change (hydraulic bores, wave breaking fronts), upwind discretization is necessary to avoid spurious oscillation in the solution. In Falconer and Chen (1991), a wetting-drying check routine is developed for shallow water system solved by ADI method. The scheme is quite stable but relatively hard to implement for models not using ADI scheme.

In Buchard (1998) and the scientific documentation of GETM (General Estuarine Transport Model), a simpler scheme is used by switching off some terms in the momentum equations plus bed friction in a thin film layer added to dry bed areas. In Lynett et al. (2002), a linear extrapolation method is proposed for discretization of spatial derivatives involved in the Boussinesq equations. The method is equivalent to upwind scheme near moving shoreline or methods using Lagrangian approach (Zelt, 1991). The procedure is much easier than extensive wet-dry checking schemes. However, it still involves issues such as which direction to extrapolate in 2D domain when complicated moving shorelines exist.

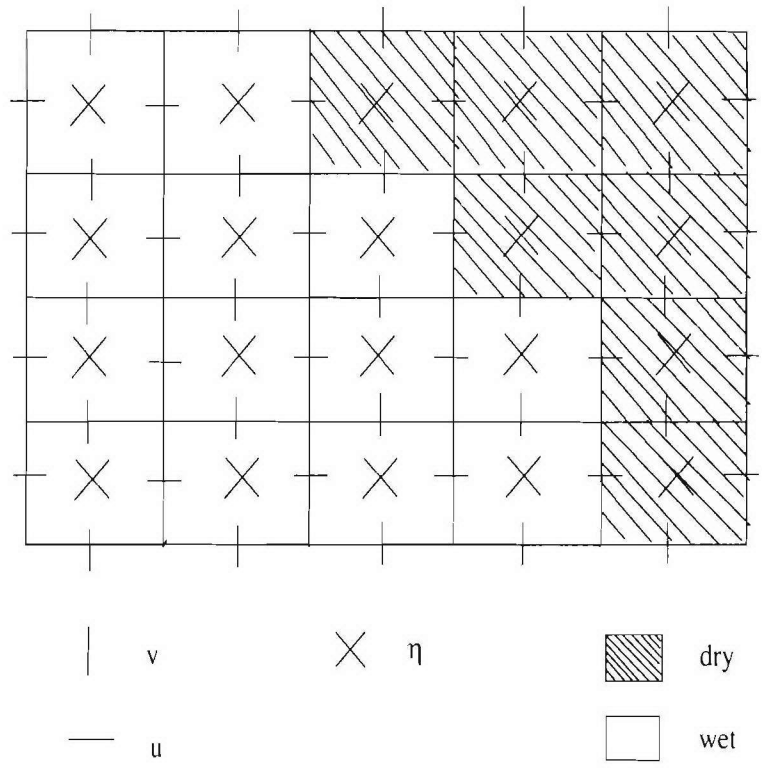

Figure 4.5: Wet-dry cells

In our approach, we use a relatively simple yet effective procedure. We modify the approach by Buchard (1998) by using a) film layer in dry grid cells; b) bottom friction dependent on total water depth; c) a smooth switching-off for source terms (gravity, nonlinearity, dispersion); d) label for dry and wet cells. In this method, no adding and deleting of cells based on velocity direction is used. No abrupt changes of parameters such as friction or gravitational acceleration are used. No checking of differentiation direction or extrapolation direction is used.

Figure 4.5 shows a sketch of new wet-dry scheme. A roughness value δ_R (also called film thickness) is defined for film thickness in dry areas. Labels $IDwetdry_u(i,j)$, $IDwetdry_v(i,j)$ and $IDwetdry(i,j)$ represent the status of wet or dry for u,v and z points respectively, in which 1 is assigned for wet points and 0 is assigned for dry points.

The bottom friction coefficient f_b is calculated as

$$f_b = f_{b0} + \frac{1}{\exp(2(\frac{H}{2\delta_R})^2) - 1} \tag{4.188}$$

where δ_R is a roughness value representing the thickness of the thin film layer and f_{b0} is physical bottom friction coefficient. When total depth $H \rightarrow 0$, the bottom friction approaches infinity. On the other hand, when $H >> \delta_R$, the friction coefficient approaches physical friction smoothly.

The assignment of wet/dry ID is given by

$$R_1 = \tanh[(\frac{\ln(\frac{\max(H_{max}, \delta_R)}{\delta_R})}{\kappa})^2] \tag{4.189}$$

$$IDwetdry(i,j) = \text{int}(R_1 + 0.1) \tag{4.190}$$

where $H_{max} = \max(H(i,j), H_u(i,j), H_u(i+1,j), H_v(i,j), H_v(i,j+1)$, i. e., the maximum depth of the four sides and the center of a grid cell, $\kappa = 0.4$ is Karman constant. int() means taking the integer value. If $IDwetdry(i,j) = 0$, then $IDwetdry_u(i,j) = 0$, $IDwetdry_u(i+1,j) = 0$, $IDwetdry_v(i,j) = 0$ and $IDwetdry_v(i,j+1) = 0$, i. e., the sides of the cell are set to be dry only when the cell is set to be dry.

RHS terms of the momentum equations except the bottom friction are multiplied by a coefficient R_f

$$R_f = \tanh[(\frac{\ln(\frac{\max(\delta_R, H)}{\delta_R})}{\kappa})^2], \tag{4.191}$$

where $H = H_u(i,j)$ for momentum equation in ξ_1 direction and $H = H_v(i,j)$ for momentum equation in ξ_2 direction. Gravitational acceleration g is also modified to be gR_f.

Figure 4.6 shows the added friction $f_b - f_{b0}$ as a function of H/δ_R. Figure 4.7 shows the transition of R_1 and $IDwetdry$ from 0 to 1 as a function of H_{max}/δ_R. Figure 4.8 shows the curve of R_f as a function of H/δ_R. We see that $IDwetdry$ distinctly labels a cell as wet when H_{max}/δ_R is larger than 1.3. R_f turns off RHS terms smoothly when H/δ_R is less than 2.

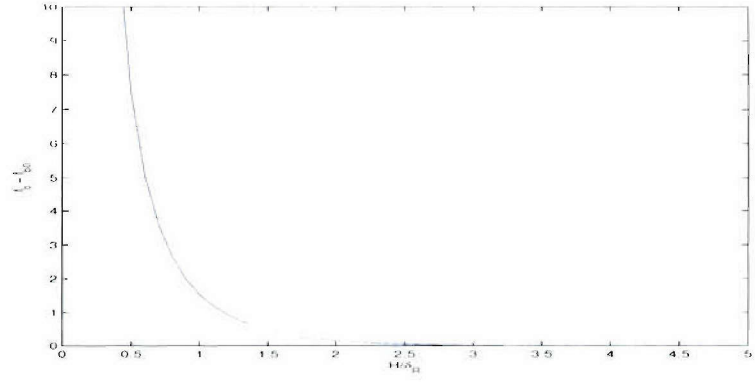

Figure 4.6: $f_b - f_{b0}$ as a function of H/δ_R

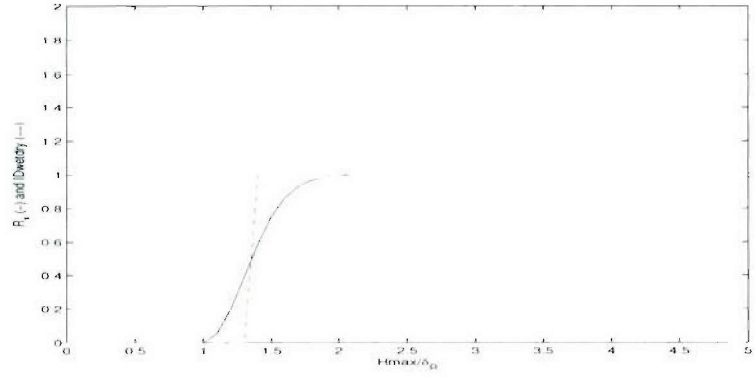

Figure 4.7: R_1 (solid) and $IDwetdry$ (dash) as a function of H_{max}/δ_R

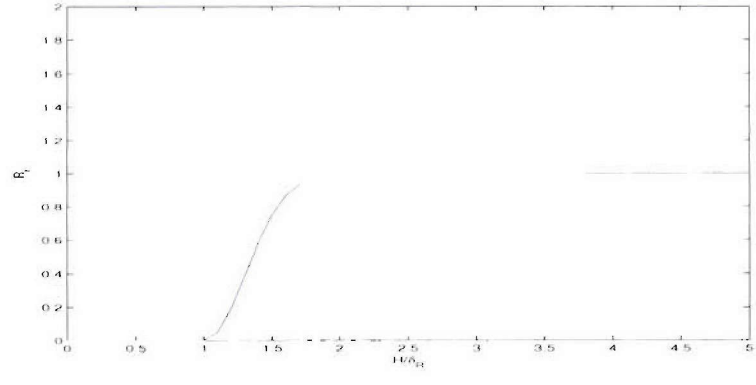

Figure 4.8: R_f as a function of H/δ_R

The overall rationale behind these treatments are: a) presence of film layer makes the discretization of equations uniform for all locations; b) strong bottom friction and switching-off of gravity within the film layer will slow down the flow rate in the film layer and prevent noise generation; c) wet/dry label can be used to assure zero velocity at the shoreline.

Model results compared to analytical results will be shown in subsequent chapters.

Chapter 5

MORPHOLOGICAL SCHEMES

The central concern of morphodynamics is to determine the evolution of bed levels for hydrodynamic systems such as rivers, estuaries, inlets, bays and other near shore regions where fluid flow interacts with the supporting bed level intensively.

Numerical morphological models involve coupling between a hydrodynamic model which provides driving forces and a sediment transport model which accounts for sediment flux and bathymetry change. Readers are directed to de Vriend et al. (1993), Nicholson et al. (1997) and Kobayashi & Johnson (2001) for examples of these models.

A large part of sediment transport formulas are based on energetics considerations, for instance, Bagnold (1966), Bailard (1981) and Meyer-Peter-Müller (1948). For steady or quasi-steady flow conditions, the transport rate of sediments is closely correlated to third power of fluid velocities near bed. Because the flow field is a nonlinear function of bed level and a number of other parameters, the transport rate is also a nonlinear function of bed level and other parameters. Hence the sediment conservation equation is physically a nonlinear conservation equation for the bed level. The same situation occurs in other physics contexts, such as mass conservation equation in hydraulics, density waves in aerodynamics as well as congestion phenomena in highway or urban transportation systems (Whitham, 1974). A common feature of these conservation laws is that shock waves, i.e. discontinuities of the respective physical quantities, will develop when particle velocity approaches celerity. Several decades of research effort have been devoted to modeling these shock waves numerically. Other important aspects of numerical methods

are stability and accuracy requirements. It is highly challenging to devise a numerical scheme which satisfies accuracy and stability requirements for long term simulation.

As reviewed in Nicholson et al. (1997), many state-of-art morphodynamic models use classical shock capturing schemes for bed level simulation. For example, Johnson and Zyserman (2002) apply a second-order accurate modified Lax-Wendroff scheme (Abbott, 1978). DH (Delft Hydraulics) model (Delft2D-MOR, Roelvink and van Banning, 1994; Roelvink et al., 1994) uses a FTCS (forward-time, central-space) explicit scheme with corrections of the transport rate to compensate negative numerical diffusion resulting from the scheme. The HR Wallingford model PISCES (Chesher et al., 1993) uses a one-step Lax-Wendroff scheme. STC (Service Technique Central des Ports Maritimes et des Voies Navigables) model uses a two-step Lax-Wendroff scheme (Tanguy et al., 1993). UL (Civil Engineering Department of the University of Liverpool) model (O'Connor and Nicholson, 1989, 1995) also uses a modified Lax-Wendroff scheme with effects of gravity on the sediment transport rate. According to Hudson (2005), the Lax-Wendroff scheme suffers from dispersion resulting in spurious oscillations occurring in the numerical results. Various techniques, including flux-limiter methods, have been used to try to eliminate the spurious oscillations. Unfortunately, spurious oscillations could not be eliminated and overpowered the numerical results for long computational run times as also pointed out by Damgaard and Chesher (1997) and Damgaard (1998).

In this research, a wave phase-resolving sediment transport model is proposed for near shore applications where waves play an important role as driving force. The wave orbital velocities are oscillatory in time and space, and the resulting sediment transport fluxes are also oscillatory. It is difficult to obtain numerical estimate of local bedform phase speed under these circumstances (See Appendix). This weakens morphological schemes (such as Lax-Wendroff type of schemes) that require decent estimates of phase speed. These complications make the demand for better schemes more urgent in bed level prediction.

In Hudson (2001), a variety of numerical schemes are discussed including modified versions of the Lax-Friedrichs (1954) scheme, the classical Lax-Wendroff scheme, MacCormack (1969) scheme and the Roe (1986) scheme based on shallow water equation for hydrodynamics and simple power law for sediment transport rate. A flux-limited version of the Roe scheme is found to be much more stable than Lax-Wendroff and Lax-Friedrichs type schemes. The disadvantage is that the Roe scheme involves calculation of eigenvectors for the so-called Roe averaged Jacobian matrix of the entire hydrodynamics and morphology system. This is feasible for shallow water systems and simple power law sediment transport rates for 1-D problems. The numerics become tedious and complex for coupled systems of more comprehensive hydrodynamic models and sediment transport models. 2-DH implementation of the Roe scheme will be practically difficult.

In this research, we investigate the stability and performance of several finite difference schemes. Comparisons are made to evaluate their applicability. The suggested Euler-WENO scheme is also applied to a phase resolving sediment transport model to study sand bar deformation under waves and bed level instabilities due to flow in a straight channel.

We present the model schemes in Cartesian grids with uniform grid spacing for the sake of convenience and clarity. Then we present the resulting Euler-WENO scheme in generalized curvilinear coordinates.

5.1 Model Equation for Bed Elevation in Sediment Transport

Bed level changes are governed by the equation of conservation of sediment mass, which can be written as

$$\frac{\partial z_b}{\partial t} = -\frac{1}{1-n_p}(\nabla \cdot \mathbf{q} + \frac{\partial}{\partial t}\int_{z_b}^{\eta} c dz) \tag{5.1}$$

where $z_b(\mathbf{x}, t)$ is the bed level elevation (defined positive upward relative to a fixed datum) at each horizontal position $\mathbf{x} = (x, y)$ and time t, n_p is the bed porosity, $\mathbf{q} = (q_x, q_y)$ is the total volumetric sediment transport rate, $c(\mathbf{x}, z, t)$ is the volumetric concentration

of suspended sediments in the water column, $\eta(\mathbf{x}, t)$ is the free surface elevation. In the following, we neglect a detailed examination of the suspended load contribution, since the numerical instabilities to be considered are apparent in the reduced flux equation given by

$$\frac{\partial z_b}{\partial t} = -\frac{1}{1-n_p}\nabla \cdot \mathbf{q} \tag{5.2}$$

The transport rate $\mathbf{q}$ is a complex function of various hydrodynamic quantities such as currents, waves and water depth as well as quantities associated with sediment properties such as sediment density and grain size. A number of formulas have been proposed for calculating $\mathbf{q}$ in the literature. Some experimental data and theory show that $\mathbf{q}$ is closely related to some power of near bed fluid velocity $\mathbf{u}$ (Grass, 1981, Van Rijn, 1984, 1993). Only in the simplest case can $\mathbf{q}$ be written as a function of z_b. Therefore, it is desirable to have a morphology updating scheme that does not depend on a particular form of the transport formula.

In this research, we consider the application of several modern shock-capturing techniques to the calculation of bedform evolution in unidirectional streams or oscillatory wave dominated flows.

Several one-dimensional examples are considered in order to evaluate the schemes and illustrate their robustness, after which a two-dimensional example of alternating bar instability in a unidirectional flow is considered. The schemes considered here are developed using finite differencing on a centered grid structure.

5.2 Classical Schemes for Shock Capturing

There are numerous finite difference schemes for spatial discretization and they can be divided into two broad categories, namely, central difference schemes and upwind schemes. Each has its own advantages and disadvantages. Here, we present several classical schemes that have been used in numerical simulation of hydrodynamics and aerodynamics for shock capturing. As far as discretization in time, many techniques have also been utilized in literature, such as simple Euler discretization, multi-level schemes,

predictor-corrector schemes and so on. We mainly focus on one and two step methods in time for sediment transport problems.

5.2.1 Central difference schemes

The simplest central difference scheme is the FTCS (forward in time, central in space) scheme. The FTCS scheme is absolutely unstable for hyperbolic conservation equations, but conditionally stable for convection diffusion problems. So, the central remedy to FTCS scheme for equation (5.2) is to introduce viscous effects. The Lax-Wendroff (1960) scheme and Lax family schemes are mostly adopted by practitioners of computational fluid dynamics. Here, we compare the Lax-Wendroff scheme, the Richtmyer (1962) scheme and the MacCormack (1969) scheme.

The basic Lax-Wendroff scheme adopted in Johnson & Zyserman (2002) and in the CBREAK model of Kobayashi & Johnson (2001) is given by

$$\frac{z_{bi}^{n+1} - z_{bi}^{n}}{\Delta t} + \frac{1}{1-n_p}\frac{(q_{i+1}^{n} - q_{i-1}^{n})}{2\Delta x} = \frac{\Delta t C_i^2}{2}\frac{(z_{bi+1}^{n} - 2z_{bi}^{n} + z_{bi-1}^{n})}{\Delta x^2} \tag{5.3}$$

where the left hand side is a simple FTCS scheme, and right hand side is an additional diffusion term which damps spurious oscillations caused by the FTCS scheme. Its accuracy is second order in time and space. The stability condition for equation (5.3) is $|C_i \frac{\Delta t}{\Delta x}| \leq 1$ where C_i is a 'bedform propagation phase speed'. Use of this scheme requires an estimate of phase speed C_i, which is not very easy to estimate in many instances (see appendix). Overestimate of C_i will over smooth the solution, while underestimate of C_i makes the scheme less stable.

In order to avoid calculating C_i, various two-step Lax schemes have been proposed. Here we examine the Richtmyer (1962) scheme and the MacCormack (1969) scheme. The Richtmyer scheme is written as

$$z_{bi}^{n+1/2} = \frac{z_{bi+1}^{n} + z_{bi}^{n}}{2} - \frac{\Delta t}{2\Delta x}\frac{1}{(1-n_p)}(q_{i+1}^{n} - q_{i}^{n}) \tag{5.4}$$

$$z_{bi}^{n+1} = z_{bi}^{n} - \frac{\Delta t}{\Delta x}\frac{1}{(1-n_p)}(q_{i}^{n+1/2} - q_{i-1}^{n+1/2}) \tag{5.5}$$

and MacCormack scheme is written as

$$\tilde{z_{bi}} = z_{bi}^n - \frac{\Delta t}{\Delta x(1-n_p)}(q_i^n - q_{i-1}^n) \tag{5.6}$$

$$z_{bi}^{n+1} = \frac{z_{bi}^n + \tilde{z_{bi}}}{2} - \frac{\Delta t}{2\Delta x(1-n_p)}(q(\tilde{z_b})_{i+1} - q(\tilde{z_b})_i) \tag{5.7}$$

The stability requirement of the Richtmyer scheme and the MacCormack scheme is $|C_i\frac{\Delta t}{\Delta x}| \leq 1$ (C_i is bed form phase speed) and accuracy is second order in time and space. They require the calculations of sediment transport rate q at intermediate bed level $z_b^{n+1/2}$ and $\tilde{z_b}$, and this requires recalculation of hydrodynamics which is costly in computation.

The common disadvantage of the second order central difference schemes is that strong spurious oscillations can be generated near shocks or steep fronts. Generally, filtering and artificial viscosity have to be added to make them more stable. In Johnson & Zyserman (2002), a filtering process suggested by Jensen et al. (1999) is used for the Lax-Wendroff scheme. The disadvantage of using a filtering process is that one may have difficulty deciding the number of filtering processes to be applied in practice.

5.2.2 Upwind schemes

Central difference schemes have higher order accuracy but more restrictive stability requirement and tend to generate spurious oscillations. Upwind schemes, on the other hand, are generally more stable due to inherent dissipation effects at the price of lower order accuracy. Here we choose the simplest first order upwind scheme FTBS (forward in time, backward in space) and the second order Warming-Beam scheme.

The FTBS scheme is written as

$$z_{bi}^{n+1} = z_{bi}^n - \frac{\Delta t}{2\Delta x(1-n_p)}[(1-\alpha)(q_{i+1}^n - q_i^n) + (1+\alpha)(q_i^n - q_{i-1}^n)] \tag{5.8}$$

with $\alpha = \text{sign}(C_i)$ This scheme is first order in time and space with strong dissipation. The scheme is conditionally stable for $|C_i\frac{\Delta t}{\Delta x}| \leq 1$, but has the disadvantage of widening the shock region excessively.

The Warming-Beam scheme adds a second order correction to the FTBS scheme, which gives higher order accuracy but still upwinding to achieve conditional stability. It can be expressed as:

$$z_{bi}^{n+1} = z_{bi}^{n} - \frac{\Delta t}{(1-n_p)\Delta x}(\hat{q}_{i+1/2} - \hat{q}_{i-1/2}) \tag{5.9}$$

where

$$\hat{q}_{i+1/2} = \frac{1}{2}(3q_i^n - q_{i-1}^n) - \frac{1}{2}C_{i-1/2}(q_i^n - q_{i-1}^n) \quad C_{i+1/2} \geq 0 \tag{5.10}$$

$$\hat{q}_{i+1/2} = \frac{1}{2}(3q_{i+1}^n - q_{i+2}^n) - \frac{1}{2}C_{i+3/2}(q_{i+2}^n - q_{i+1}^n) \quad C_{i+1/2} < 0 \tag{5.11}$$

and

$$\hat{q}_{i-1/2} = \frac{1}{2}(3q_{i-1}^n - q_{i-2}^n) - \frac{1}{2}C_{i-3/2}(q_{i-1}^n - q_{i-2}^n) \quad C_{i-1/2} \geq 0 \tag{5.12}$$

$$\hat{q}_{i-1/2} = \frac{1}{2}(3q_i^n - q_{i+1}^n) - \frac{1}{2}C_{i+1/2}(q_{i+1}^n - q_i^n) \quad C_{i-1/2} < 0 \tag{5.13}$$

with $C_{i+1/2}$, $C_{i-1/2}$, $C_{i+3/2}$ and $C_{i-3/2}$ the bed level phase speed at respective locations. Again, the second order correction requires knowledge of C which sometimes causes difficulty.

5.3 Modern Schemes for Shock Capturing

5.3.1 WENO schemes

WENO (Weighted Essentially Non-Oscillatory) schemes are based on ENO (Essentially Non-Oscillatory) schemes (Harten et al., 1983, 1987). The key idea of the ENO scheme is to use the smoothest stencil among several candidates to approximate flux q at cell boundaries ($i \pm 1/2$) to high order and at the same time to avoid spurious oscillations near shocks or discontinuities. WENO schemes go one step further by taking a weighted average of the candidate stencils. Weights are adjusted by local smoothness. More details can be found in Liu et al. (1994), Jiang et al. (1999) and Shao et al. (2004). Here we give a brief introduction for 1-D problem described by equation (5.2).

The sediment transport rate q can be split into parts associated with bedform propagation in positive x direction and in negative x direction, i.e., q^+ and q^-

$$q^+ = (1 - n_p) \int_0^{z_b} C^+(z) dz, \tag{5.14}$$

$$q^- = (1 - n_p) \int_0^{z_b} C^-(z) dz, \tag{5.15}$$

where $C^+ = \max(C, 0)$ and $C^- = \min(C, 0)$. C^+ and C^- stand for phase speed of bedform propagating in positive x direction and negative x direction respectively. Obviously, $C = C^+ + C^-$, hence $q = q^+ + q^-$. WENO scheme gives the following formula for approximating term $\frac{dq}{dx}$

$$\frac{dq}{dx} = \frac{\hat{q}_{i+1/2} - \hat{q}_{i-1/2}}{\Delta x} \tag{5.16}$$

where the remaining problem is to estimate $\hat{q}_{i+1/2}$, which is an approximation of transport rate q at grid location $i + 1/2$, and $\hat{q}_{i-1/2}$, which is an approximation of transport rate q at grid location $i - 1/2$. Again, $\hat{q}_{i+1/2}$ can be split into left-biased-flux $\hat{q}^-_{i+1/2}$ and right-biased-flux $\hat{q}^+_{i+1/2}$

$$\hat{q}_{i+1/2} = \hat{q}^-_{i+1/2} + \hat{q}^+_{i+1/2}. \tag{5.17}$$

Here, the left-biased-flux is calculated as

$$\hat{q}^-_{i+1/2} = \omega_1 q^1_{i+1/2} + \omega_2 q^2_{i+1/2} + \omega_3 q^3_{i+1/2}, \; C_{i+1/2} \geq 0 \tag{5.18}$$

$$\hat{q}^-_{i+1/2} = 0, \; C_{i+1/2} < 0 \tag{5.19}$$

where

$$q^1_{i+1/2} = \frac{1}{3} q_{i-2} - \frac{7}{6} q_{i-1} + \frac{11}{6} q_i \tag{5.20}$$

$$q^2_{i+1/2} = -\frac{1}{6} q_{i-1} + \frac{5}{6} q_i + \frac{1}{3} q_{i+1} \tag{5.21}$$

$$q^3_{i+1/2} = \frac{1}{3} q_i + \frac{5}{6} q_{i+1} - \frac{1}{6} q_{i+2} \tag{5.22}$$

are three candidate stencils for estimating q at grid location $i + 1/2$ with third order accuracy (left-biased in the sense that 3 grid points $i - 2$ to i to the left of location $i + 1/2$

are used but only 2 grid points $i+1$ and $i+2$ to the right of location $i+1/2$ are used). ω_1, ω_2 and ω_3 are carefully chosen weights such that $\hat{q}^-_{i+1/2}$ given by equation (5.18) is fifth order accurate approximate of q at grid location $i+1/2$ and near discontinuity no Gibbs phenomena occur. The calculation of weights is given by Shao et al. (2004)

$$\omega_1 = \frac{\alpha_1}{\alpha_1+\alpha_2+\alpha_3} \tag{5.23}$$

$$\omega_2 = \frac{\alpha_2}{\alpha_1+\alpha_2+\alpha_3} \tag{5.24}$$

$$\omega_3 = \frac{\alpha_3}{\alpha_1+\alpha_2+\alpha_3} \tag{5.25}$$

where

$$\alpha_1 = \frac{0.1}{(S_1+\epsilon)^2} \tag{5.26}$$

$$\alpha_2 = \frac{0.6}{(S_2+\epsilon)^2} \tag{5.27}$$

$$\alpha_3 = \frac{0.3}{(S_3+\epsilon)^2} \tag{5.28}$$

with $\epsilon \approx 10^{-6}$ a small number and

$$S_1 = \frac{13}{12}(\nu_1-2\nu_2+\nu_3)^2+\frac{1}{4}(\nu_1-4\nu_2+3\nu_3)^2 \tag{5.29}$$

$$S_2 = \frac{13}{12}(\nu_2-2\nu_3+\nu_4)^2+\frac{1}{4}(\nu_2-\nu_4)^2 \tag{5.30}$$

$$S_3 = \frac{13}{12}(\nu_3-2\nu_4+\nu_5)^2+\frac{1}{4}(3\nu_3-4\nu_4+\nu_5)^2. \tag{5.31}$$

Here, S_1, S_2 and S_3 are called smoothness measurements and

$$\nu_1 = q_{i-2} \tag{5.32}$$

$$\nu_2 = q_{i-1} \tag{5.33}$$

$$\nu_3 = q_i \tag{5.34}$$

$$\nu_4 = q_{i+1} \tag{5.35}$$

$$\nu_5 = q_{i+2}. \tag{5.36}$$

Similarly, we can calculate right-biased-flux $\hat{q}^+_{i+1/2}$ (3 grid points to the right of grid location $i+1/2$ are used and only 2 grid points to the left are used)

$$\hat{q}^+_{i+1/2} = \tilde{\omega}_1\tilde{q}^1_{i+1/2} + \tilde{\omega}_2\tilde{q}^2_{i+1/2} + \tilde{\omega}_3\tilde{q}^3_{i+1/2},\ C_{i+1/2} < 0 \tag{5.37}$$

$$\hat{q}^+_{i+1/2} = 0,\ C_{i+1/2} \geq 0 \tag{5.38}$$

$$\tilde{q}^1_{i+1/2} = -\frac{1}{6}q_{i-1} + \frac{5}{6}q_i + \frac{1}{3}q_{i+1} \tag{5.39}$$

$$\tilde{q}^2_{i+1/2} = \frac{1}{3}q_i + \frac{5}{6}q_{i+1} - \frac{1}{6}q_{i+2} \tag{5.40}$$

$$\tilde{q}^3_{i+1/2} = \frac{11}{6}q_{i+1} - \frac{7}{6}q_{i+2} + \frac{1}{3}q_{i+3} \tag{5.41}$$

$$\tilde{\omega}_1 = \frac{\tilde{\alpha}_1}{\tilde{\alpha}_1 + \tilde{\alpha}_2 + \tilde{\alpha}_3} \tag{5.42}$$

$$\tilde{\omega}_2 = \frac{\tilde{\alpha}_2}{\tilde{\alpha}_1 + \tilde{\alpha}_2 + \tilde{\alpha}_3} \tag{5.43}$$

$$\tilde{\omega}_3 = \frac{\tilde{\alpha}_3}{\tilde{\alpha}_1 + \tilde{\alpha}_2 + \tilde{\alpha}_3} \tag{5.44}$$

$$\tilde{\alpha}_1 = \frac{0.3}{(\tilde{S}_1 + \epsilon)^2} \tag{5.45}$$

$$\tilde{\alpha}_2 = \frac{0.6}{(\tilde{S}_2 + \epsilon)^2} \tag{5.46}$$

$$\tilde{\alpha}_3 = \frac{0.1}{(\tilde{S}_3 + \epsilon)^2} \tag{5.47}$$

$$\tilde{S}_1 = \frac{13}{12}(\nu_2 - 2\nu_3 + \nu_4)^2 + \frac{1}{4}(\nu_2 - 4\nu_3 + 3\nu_4)^2 \tag{5.48}$$

$$\tilde{S}_2 = \frac{13}{12}(\nu_3 - 2\nu_4 + \nu_5)^2 + \frac{1}{4}(\nu_3 - \nu_5)^2 \tag{5.49}$$

$$\tilde{S}_3 = \frac{13}{12}(\nu_4 - 2\nu_5 + \nu_6)^2 + \frac{1}{4}(3\nu_4 - 4\nu_5 + \nu_6)^2. \tag{5.50}$$

and $\nu_6 = q_{i+3}$ in addition to equations following (5.32).

Left-biased-flux $\hat{q}^{-}_{i-1/2}$ and right-biased-flux $\hat{q}^{+}_{i-1/2}$ for location $i-1/2$ can be calculated using the upper equations by simply shifting i backward for one step.

Finally, a simple Euler explicit scheme for temporal discretization can be used for updating z_b, thus, the full finite difference equation here called Euler-WENO scheme becomes

$$\frac{z_{bi}^{n+1} - z_{bi}^{n}}{\Delta t} + \frac{1}{1-n_p}\frac{\hat{q}_{i+1/2} - \hat{q}_{i-1/2}}{\Delta x} = O(\Delta t, \Delta x^5) \tag{5.51}$$

We remark that the upper Euler-WENO scheme still need information of phase speed $C_{i+1/2}$ and $C_{i-1/2}$, but it's less restrictive than Lax-Wendroff scheme and Warming-Beam scheme, for here, only the sign of $C_{i\pm1/2}$ is needed to judge the "wind" direction. Because WENO scheme is a nonlinear scheme in the sense that the coefficients w_1, w_2 and w_3 depend on the transport rate q adaptively rather than being constants, no theoretical stability criterion is available.

5.3.2 TVD schemes

TVD (Total Variation Diminishing) schemes are designed such that the total variance of the solution $TV = \int_{-\infty}^{+\infty} |\frac{\partial z_b}{\partial x}| dx$ will remain constant or only decrease in time. During the solution process, there will be no new extrema generated. Some classical schemes satisfy the TVD condition automatically, for instance the Lax-Friedrichs (1954) scheme. Harten (1983) proposed a first order TVD scheme and a second order TVD scheme. Later, many TVD schemes have been proposed based on existing schemes. For example, the Lax-Wendroff scheme has been improved to have the TVD property and is called TVD-LW scheme (Zhou and Adewumi, 2000). The MacCormack scheme has also been modified to be the TVD-MC scheme (Mingham et al., 2000) such that it also has TVD feature. For more details, please refer to Delis et al. (1998). In this research, we follow Shu & Osher (1988) and Shao et al. (2004) to apply a TVD-Runge-Kutta (TVD-RK) scheme for third order time integration of equation (5.2). The TVD-Runge-Kutta scheme (Shu & Osher 1988) is a five step algorithm with the following sequence of steps:

The first step is an Euler forward step to get time level $n+1$

$$\frac{\tilde{z}_b^{n+1} - \tilde{z}_b^n}{\Delta t} + [\frac{1}{1-n_p} q(\tilde{z}_b^n)]_x = 0 \tag{5.52}$$

The second step is a second forward step to time level $n+2$

$$\frac{\tilde{z}_b^{n+2} - \tilde{z}_b^{n+1}}{\Delta t} + [\frac{1}{1-n_p} q(\tilde{z}_b^{n+1})]_x = 0 \tag{5.53}$$

The third step uses an averaging step to obtain an approximation solution at $n+1/2$

$$\tilde{z}_b^{n+1/2} = \frac{3}{4}\tilde{z}_b^n + \frac{1}{4}\tilde{z}_b^{n+2} \tag{5.54}$$

The fourth step uses a third Euler step to get time level $n+3/2$

$$\frac{\tilde{z}_b^{n+3/2} - \tilde{z}_b^{n+1/2}}{\Delta t} + [\frac{1}{1-n_p} q(\tilde{z}_b^{n+1/2})]_x = 0 \tag{5.55}$$

For the fifth step, use another averaging step finally to get solution at time level $n+1$

$$\tilde{z}_b^{n+1} = \frac{1}{3}\tilde{z}_b^n + \frac{2}{3}\tilde{z}_b^{n+3/2} \tag{5.56}$$

where the WENO scheme is used for the spatial discretization. This scheme gives third order accuracy $O(\Delta t^3)$ in time and fifth order accuracy $O(\Delta x^5)$ in space. In the second step and the fourth step, the transport rate q has to be recalculated. It is relatively easy for the Gaussian hump test case in the next section, but it can be costly if more calls to hydrodynamic modules have to be made.

5.4 Euler-WENO Scheme for Generalized Coordinate System

Bottom elevation equation (5.2) can be written in curvilinear coordinate as

$$\frac{\partial z_b}{\partial t} = -\frac{1}{1-n_p}\nabla \cdot \mathbf{q} = -\frac{1}{1-n_p}\frac{1}{\sqrt{g_0}}\frac{\partial}{\partial x^i}(\sqrt{g_0}q^i) \tag{5.57}$$

where q^i is contravariant component of volumetric transport rate. The WENO reconstruction of left-biased flux and right biased flux are kept the same as (5.18) and (5.37) except

that q is replaced by $\sqrt{g_0}q$ to include the effect of grid density change in curvilinear grid system. Separate WENO fluxes are constructed for sediment transport in ξ_1 direction contravariant component q^1 and ξ_2 direction contravariant component q^2 of total transport vector $\mathbf{q} = q^1\mathbf{g}_1 + q^2\mathbf{g}_2 = (q^1, q^2)$. The whole Euler-WENO scheme in 2D curvilinear coordinate (ξ_1, ξ_2) becomes

$$\begin{aligned} \frac{z_{bi,j}^{n+1} - z_{bi,j}^{n}}{\Delta t} &+ \frac{1}{(1-n_p)\sqrt{g_0}_{i,j}} \frac{(\hat{q}^1_{i+1/2} - \hat{q}^1_{i-1/2})}{\Delta\xi_1} \\ &+ \frac{1}{(1-n_p)\sqrt{g_0}_{i,j}} \frac{(\hat{q}^2_{j+1/2} - \hat{q}^2_{j-1/2})}{\Delta\xi_2} \\ &= O(\Delta t, \Delta\xi_1^5, \Delta\xi_2^5) \end{aligned} \tag{5.58}$$

where $\hat{q}^1_{i+1/2}$ and $\hat{q}^1_{i-1/2}$ are WENO constructions of $\sqrt{g_0}q^1$ at location $(i+1/2, j)$ and $(i-1/2, j)$ respectively; $\hat{q}^2_{j+1/2}$ and $\hat{q}^2_{j-1/2}$ are WENO constructions of $\sqrt{g_0}q^2$ at location $(i, j+1/2)$ and $(i, j-1/2)$ respectively. The construction process is identical to (5.18) and (5.37) except that here we need to include $\sqrt{g_0}$.

5.5 Morphology Updating Scheme Tests

We use a Gaussian hump case to test the schemes described above to discuss their performance on modeling morphological change due to currents. Next, we investigate the developments of sand bars in a 1D system due to waves using the Euler-WENO scheme. This case was also studied by Yu and Mei (2000). Finally, Deformation of a 2D alternating sand bar system is studied using a 2D shallow water model and the Euler-WENO scheme to verify its applicability in multi-dimensional problems.

5.5.1 Numerical Simulation Results and Comparisons for a Gaussian Hump Test

In this section, we will apply different schemes to the Gaussian hump test case of Johnson and Zyserman (2002) and Hudson (2005). Assuming the transport rate q is

a power function of current speed (Grass, 1981; Van Rijn, 1984, 1993), and assuming a steady current with a rigid-lid, we have

$$q = au^b \tag{5.59}$$

$$u = Q/h \tag{5.60}$$

$$h = s - z_b \tag{5.61}$$

where a, b are constants, h is the water depth, s is the datum which can be set to $s = 0$, and Q is the constant volume flux. Following Johnson & Zyserman (2002), equation (5.2) can be written as

$$\frac{\partial z_b}{\partial t} + C(z_b)\frac{\partial z_b}{\partial x} = 0 \tag{5.62}$$

where $C(z_b)$ is the phase speed of bedform, and is expressed as

$$C(z_b) = \frac{1}{1-n_p}\frac{\partial q}{\partial z_b} = \frac{1}{(1-n_p)(s-z_b)}abu^b \tag{5.63}$$

$C(z_b)$ is a function of z_b, and hence equation (5.62) depicts a nonlinear propagation of the bed level $z_b(t,x)$. In most real applications, C is not as simple as a relation to z_b as above, and it can't be easily estimated (see appendix). This gives difficulty in numerical schemes that require a decent estimate of C.

The following quantities are specified to similar to values in Hudson (2005)

$$a = 0.001s^2/m \tag{5.64}$$

$$b = 3.0 \tag{5.65}$$

$$Q = 10m^2/s \tag{5.66}$$

$$n_p = 0.4 \tag{5.67}$$

and the initial condition $z_b(x,0)$ is given as a Gaussian hump,

$$z_b(x,0) = -h_0 + 2.0e^{[-\beta(x-x_c)^2]}m \tag{5.68}$$

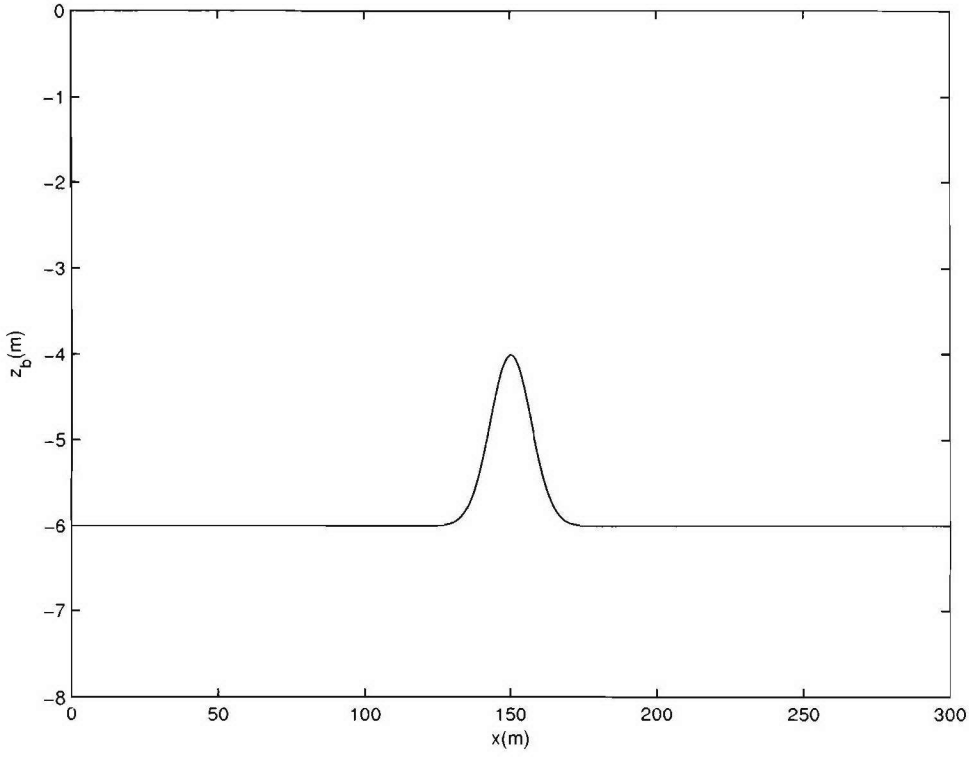

Figure 5.1: Initial bed level z_b of Gaussian hump test

with $\beta = 0.01m^{-2}$, $h_0 = 6.0m$, $0 \leq x \leq 300m$, $x_c = 150.0(m$ is the center of the Gaussian hump (See Figure 5.1). During the simulation, grid spacing is chosen to be $\Delta x = 1m$, and time step is chosen to be $\Delta t = 0.1s$ which is sufficiently small to satisfy stability conditions for the finite difference schemes.

Figure 5.2, Figure 5.3 and Figure 5.4 show results of the Lax-Wendroff scheme, the Richtmyer scheme and MacCormack scheme which are all based on central differences. Figure 5.5 shows the comparison of the Lax-Wendroff scheme, the Richtmyer and the MacCormack scheme with the exact solution obtained using characteristics according to (5.62) or (Hudson et al., 2005) for time $t = 600s$ when the shock wave of bed level starts to form. From the figure, the Lax-Wendroff scheme, the Richtmyer and the MacCormack scheme all generated oscillations at the shock front. The oscillations at the front become quite apparent at $t = 1000s$ and the solutions break down after that, generating large errors due to dispersive effects.

Figure 5.6a) and 5.6b) show the results of Lax-Wendroff scheme along with the filtering process of Johnson and Zyserman (2002) used once every 100 time steps. In figure 5.6b), bed level at time $0s$, $2000s$, $4000s$, $6000s$, $8000s$, $10000s$ are plotted together from the left to the right. We see that compared to Figure 5.2, it is more stable, and it does predict the bar migration, but there are oscillations generated at the shock location and the width of the front is not very well resolved.

Figure 5.7 and Figure 5.8 show results of the FTBS scheme and the Warming-Beam scheme. In this case, both schemes seem to be stable, but the Warming-Beam scheme generated some oscillations. Both of them has a shock front width about 5 grids wide, which is due to the strong damping effect of the schemes. A small yet visible negative peak also forms in front of the shock in the Warming-Beam scheme simulation. Figure 5.9 shows the results compared to analytical solution at $t = 600s$. It is seen that the FTBS scheme is more dissipative compared to the Warming-Beam scheme and the Lax-Wendroff scheme with filtering.

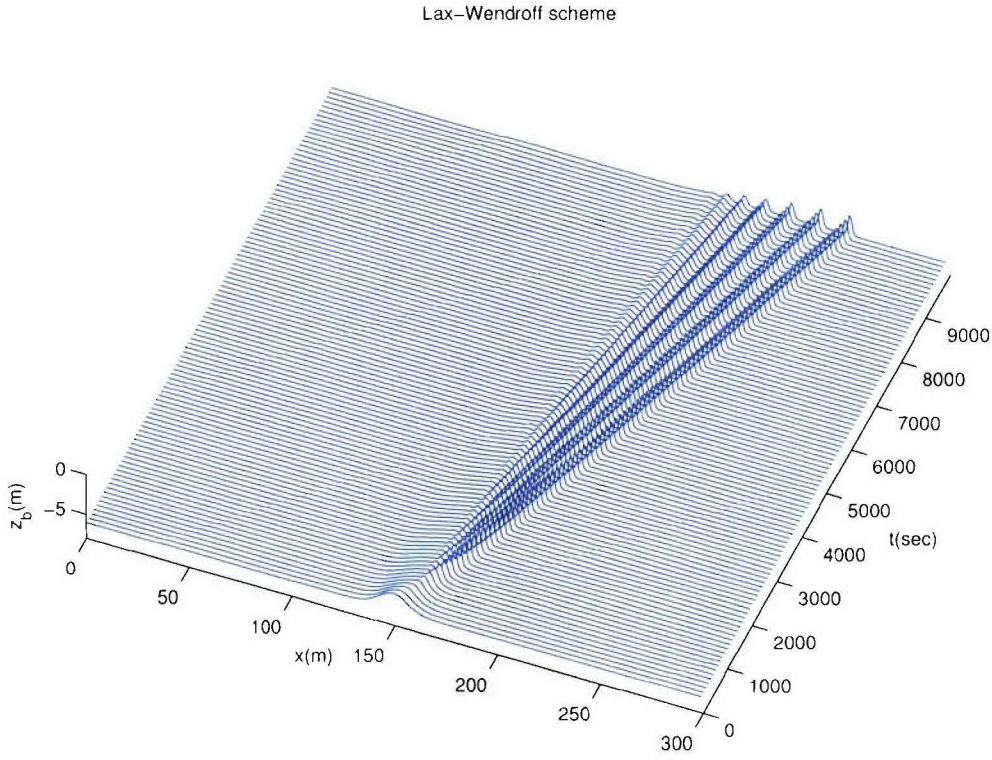

Figure 5.2: Simulation of Gaussian hump evolution using the Lax-Wendroff scheme.

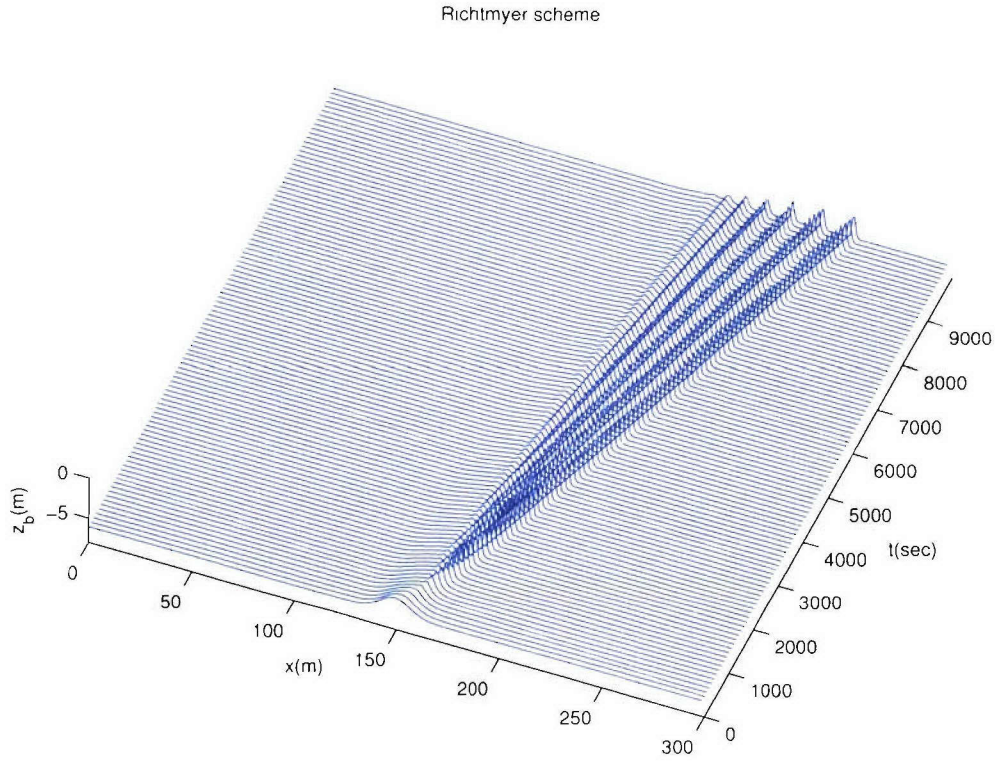

Figure 5.3: Simulation of Gaussian hump evolution using the Richtmyer scheme.

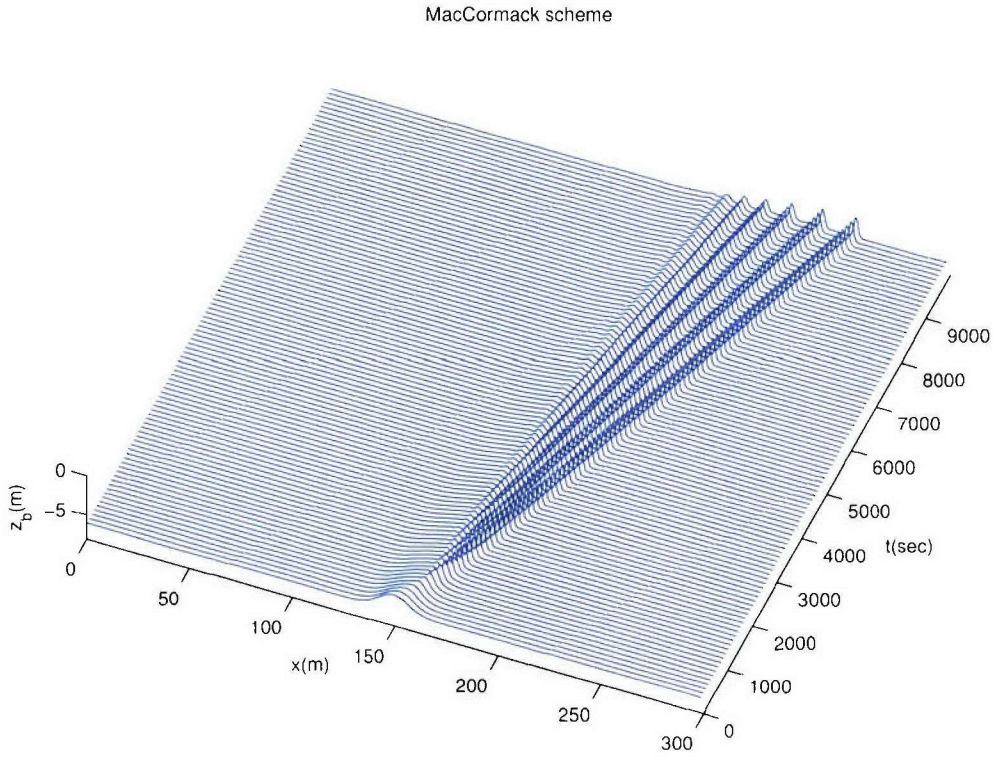

Figure 5.4: Simulation of Gaussian hump evolution using the MacCormack scheme.

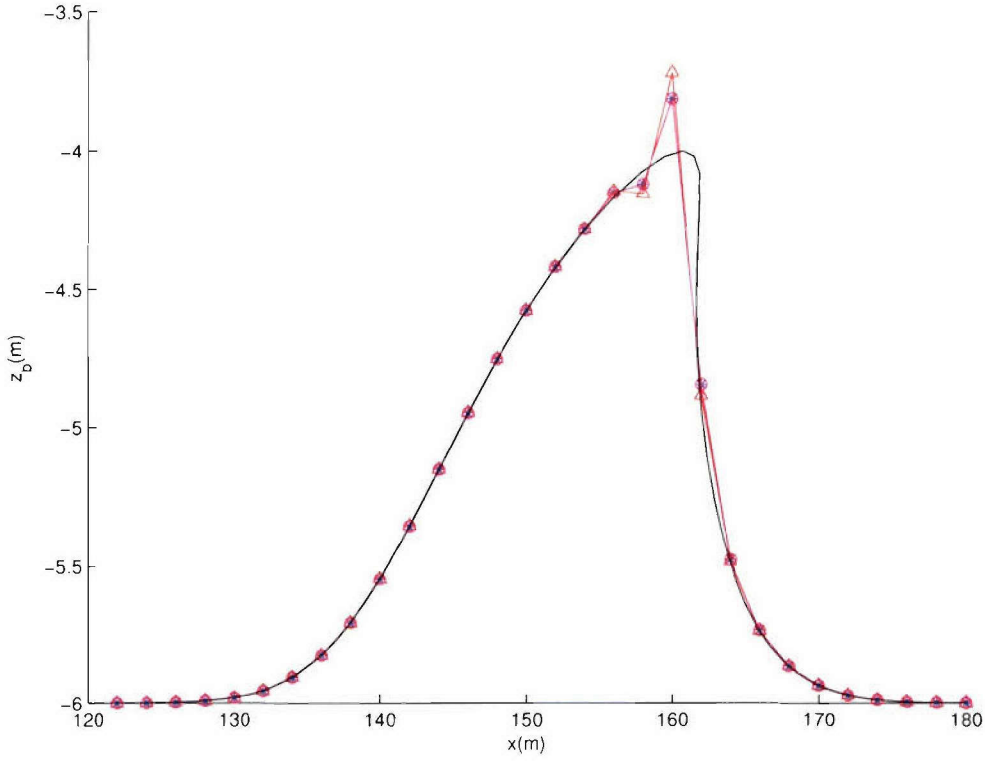

Figure 5.5: Comparison of the model results with the analytical results at $t = 600s$; Lax-Wendroff scheme (stars), Ritchmyer scheme (triangles); MacCormack scheme (circles); analytical (solid line)

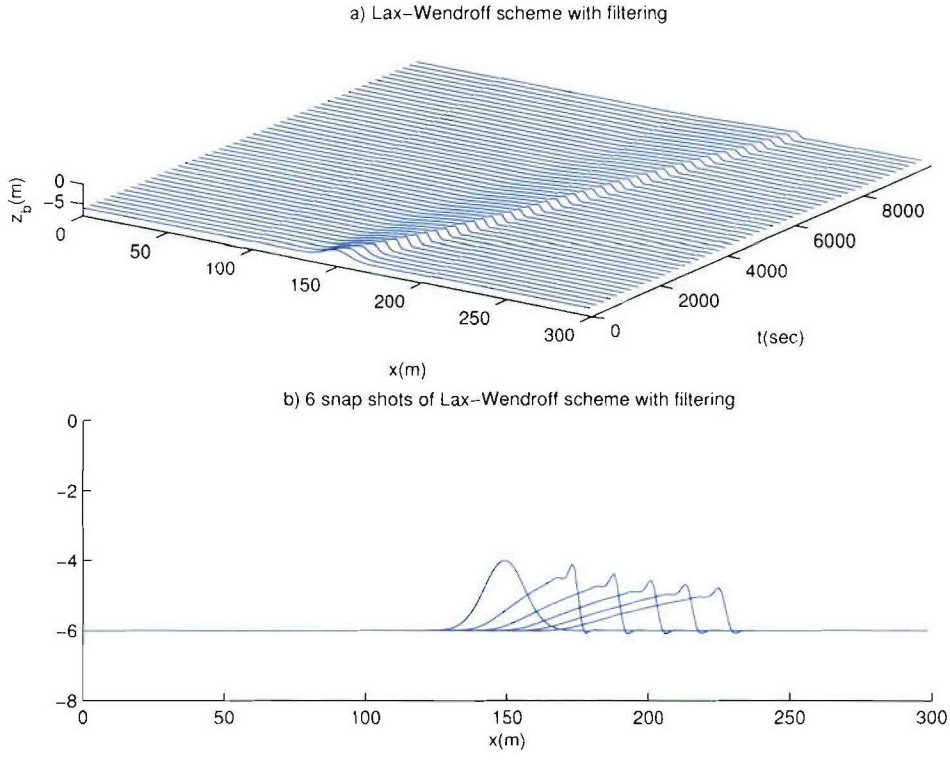

Figure 5.6: Simulation of Gaussian hump evolution using the Lax-Wendroff scheme and filtering.

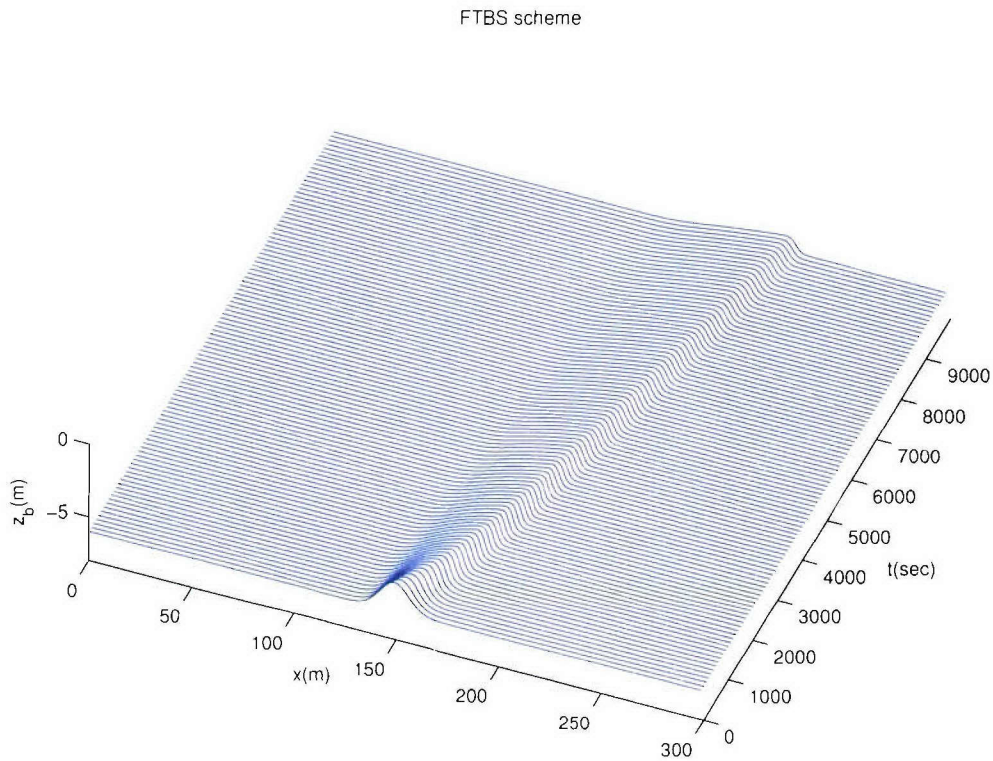

Figure 5.7: Simulation of Gaussian hump evolution using the FTBS scheme.

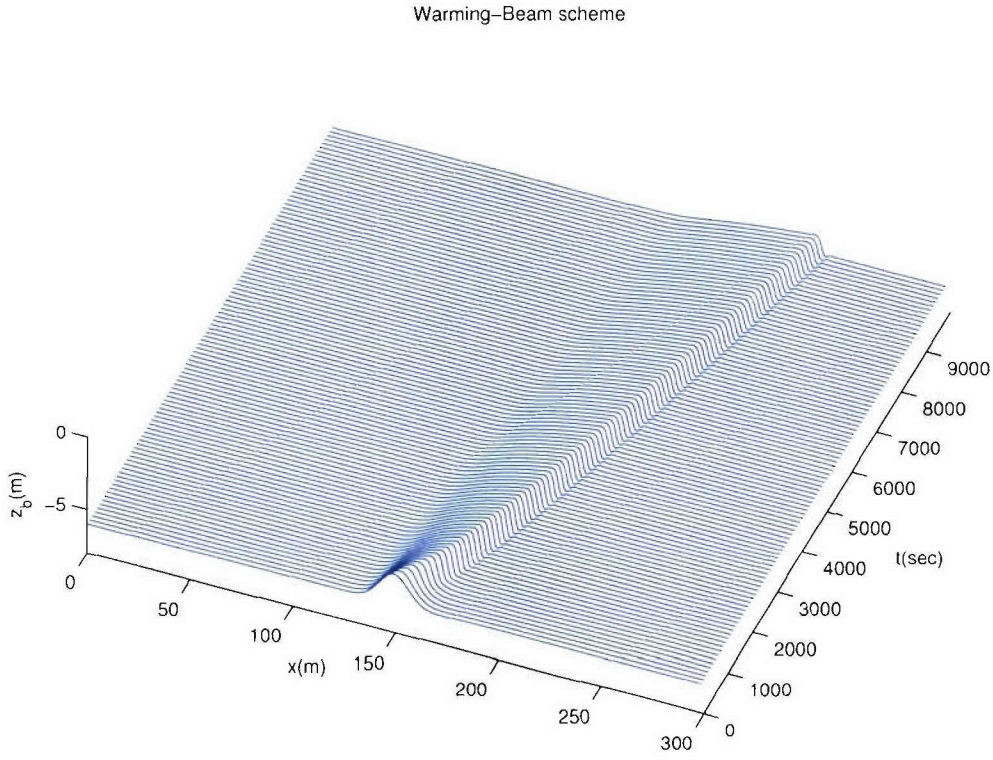

Figure 5.8: Simulation of Gaussian hump evolution using the Warming-Beam scheme

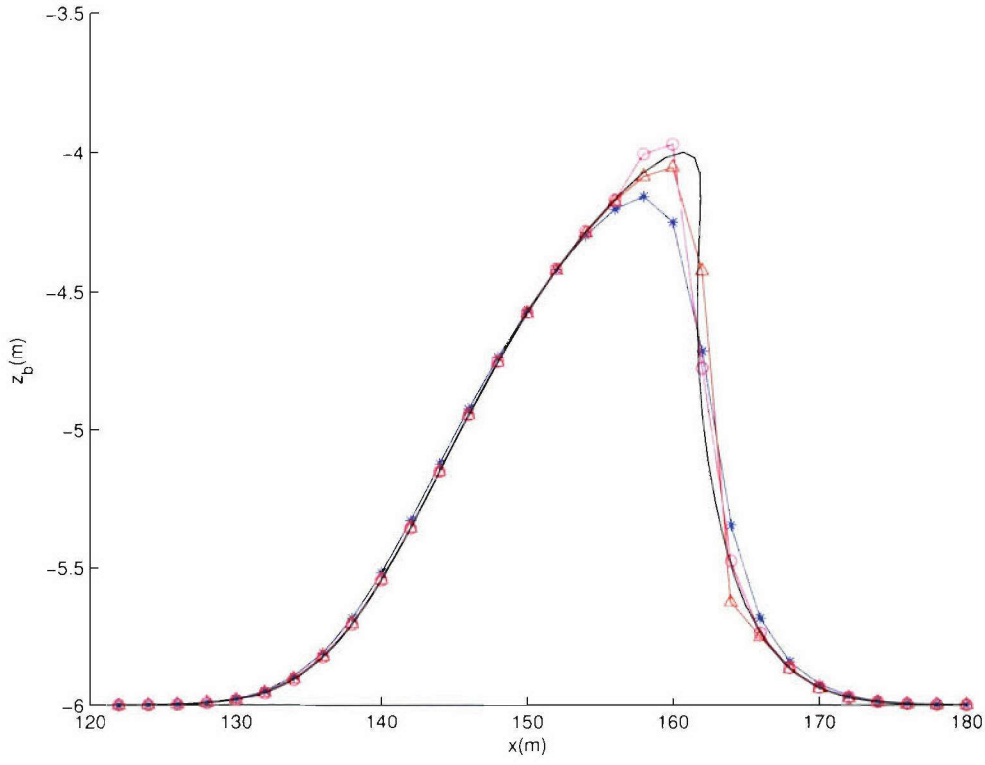

Figure 5.9: Comparison of the model results with the analytical results at $t = 600s$; FTBS (stars), Warming-Beam scheme (triangles); Lax-Wendroff scheme with filtering (circles); analytical (solid line)

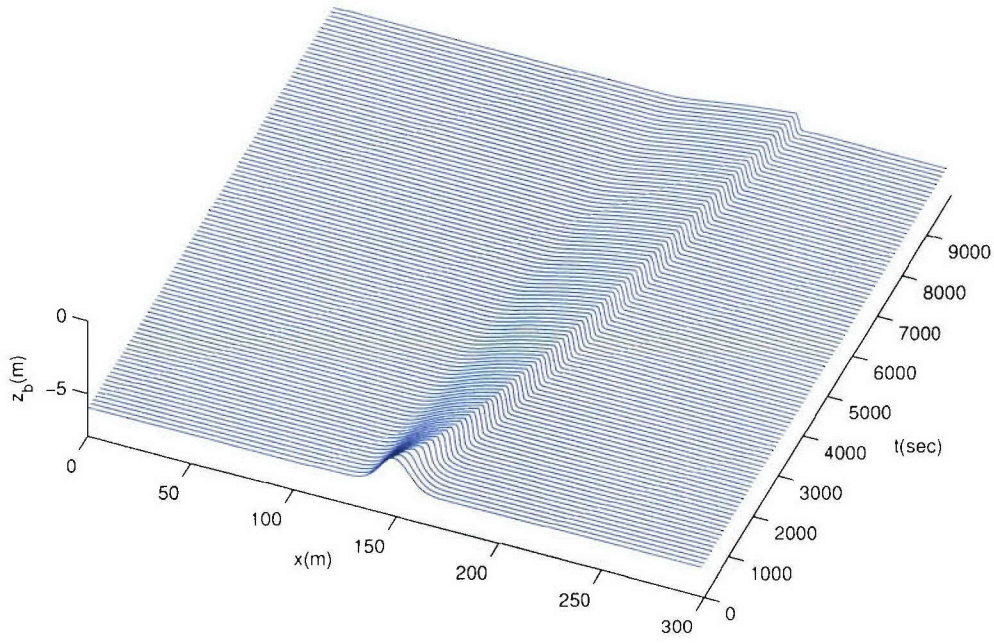

Figure 5.10: Simulation of Gaussian hump evolution using the Euler-WENO scheme.

Figure 5.10 and Figure 5.11 shows results of Euler-WENO scheme and TVD-RK-WENO scheme. Figure 5.12 shows the comparison of Euler-WENO scheme and TVD-RK-WENO scheme with the analytical solution at $t = 600s$. Here, both schemes have predicted fairly stable results with the shock front depicted in high resolution. Figure 5.13 shows the results at time $0s$, $2000s$, $4000s$, $6000s$, $8000s$, $10000s$ from left to right. The TVD-RK-WENO scheme is about 3 times slower than Euler-WENO scheme, while the results are quantitatively very close to the Euler-WENO scheme. Hence, we conclude that for sediment transport problems, Euler-WENO scheme is preferred.

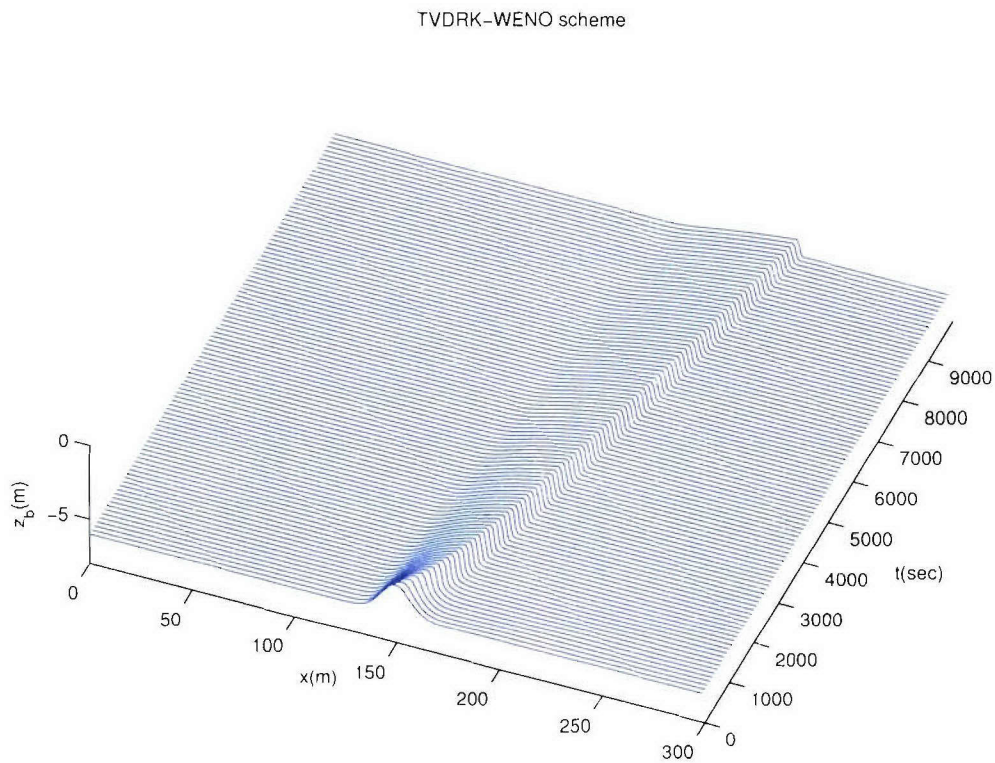

Figure 5.11: Simulation of Gaussian hump evolution using the TVD-RK-WENO scheme.

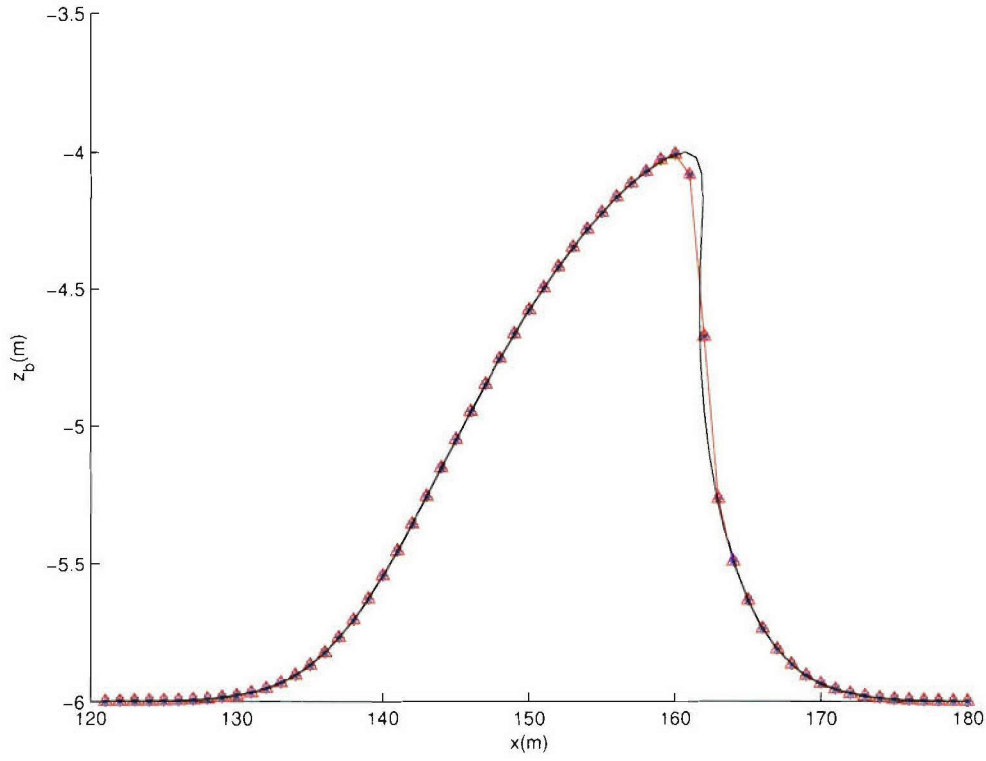

Figure 5.12: Comparison of the model results with the analytical results at $t = 600s$; Euler-WENO scheme (stars); TVD-RK-WENO scheme (triangles); analytical (solid line)

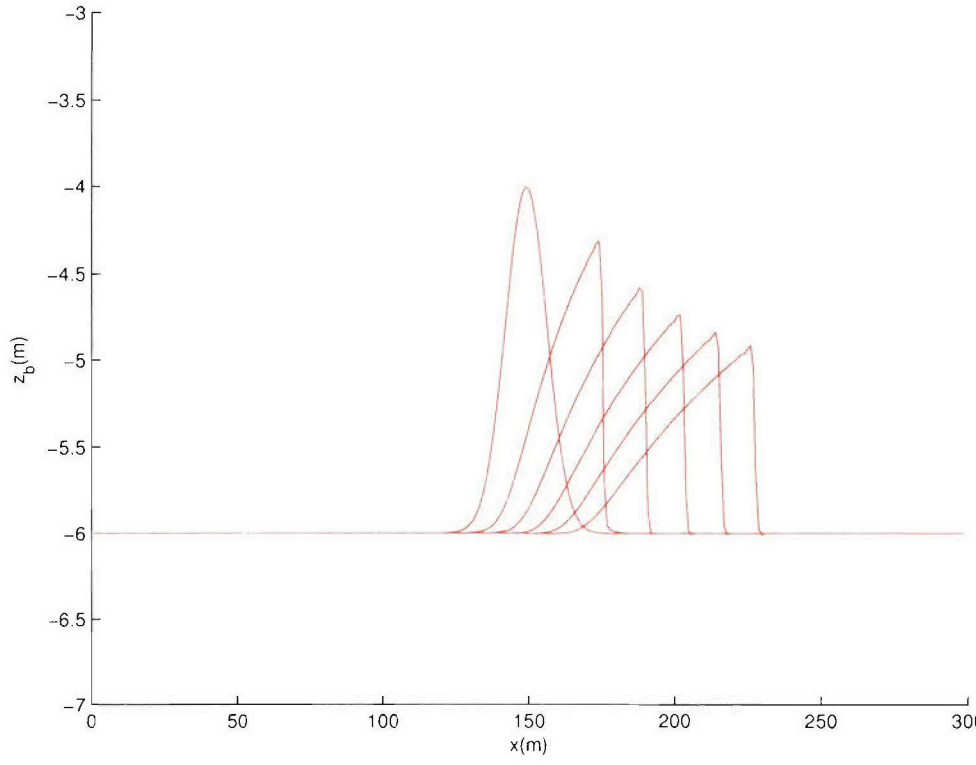

Figure 5.13: Comparison of the model results of the Euler-WENO scheme (dash) with the TVD-RK-WENO scheme (solid) at time $t = 0s$, $t = 2000s$, $t = 4000s$, $t = 6000s$, $t = 8000s$ and $t = 10000s$ from the left to the right

All of the schemes tested here have been checked for volume conservation. Expressing the total volume of sand relative to datum as

$$V(t) = \int_{-\infty}^{\infty} z_b(x,t)dx \tag{5.69}$$

we compute a relative error $(V(t) - V(0))/V(0)$ for each of the schemes. Figure 5.14 shows the relative error over time due to different schemes. All of the schemes are seen to be essentially conservative for the 10,000s of simulated time, with relative errors falling in the range of numerical roundoff.

5.5.2 Application of the Euler-WENO scheme to sand bar deformation due to waves

Periodic rows of sandbars can strongly reflect surface waves with twice the wavelength of the bar features through a process known as Bragg scattering (Mei, 1985). Partial reflection of waves by a finite patch of bars creates a partial standing wave on the upwave side of the bars. This perturbation to the incident wave field has been shown to effectively promote the formation of new bars in an initially level sand bed (Rey et al., 1995). However, Yu and Mei (2000) have shown that the sediment transport mechanisms over an existing bar itself are destructive, leading to erosion of bar crests and infilling of bar troughs. As a result, an evolving bar field would appear to march seaward over a flat bottom, with bars progressively growing on the seaward end and eroding at the landward end. This conclusion ignores the possible influence of partial standing waves in the region landward of the initial bar field, which would be a possible realistic complication if a reflective shore were present.

In this section, we apply the Euler-WENO scheme to investigate sand bar deformation under surface waves. The coupled evolution of bars and waves has been studied theoretically and experimentally by Yu and Mei (2000). When wavelengths of bars and waves are comparable, the bars are controlled by a forced diffusion process due to partially standing wave groups and gravity. In Yu and Mei (2000), wave field is solved based

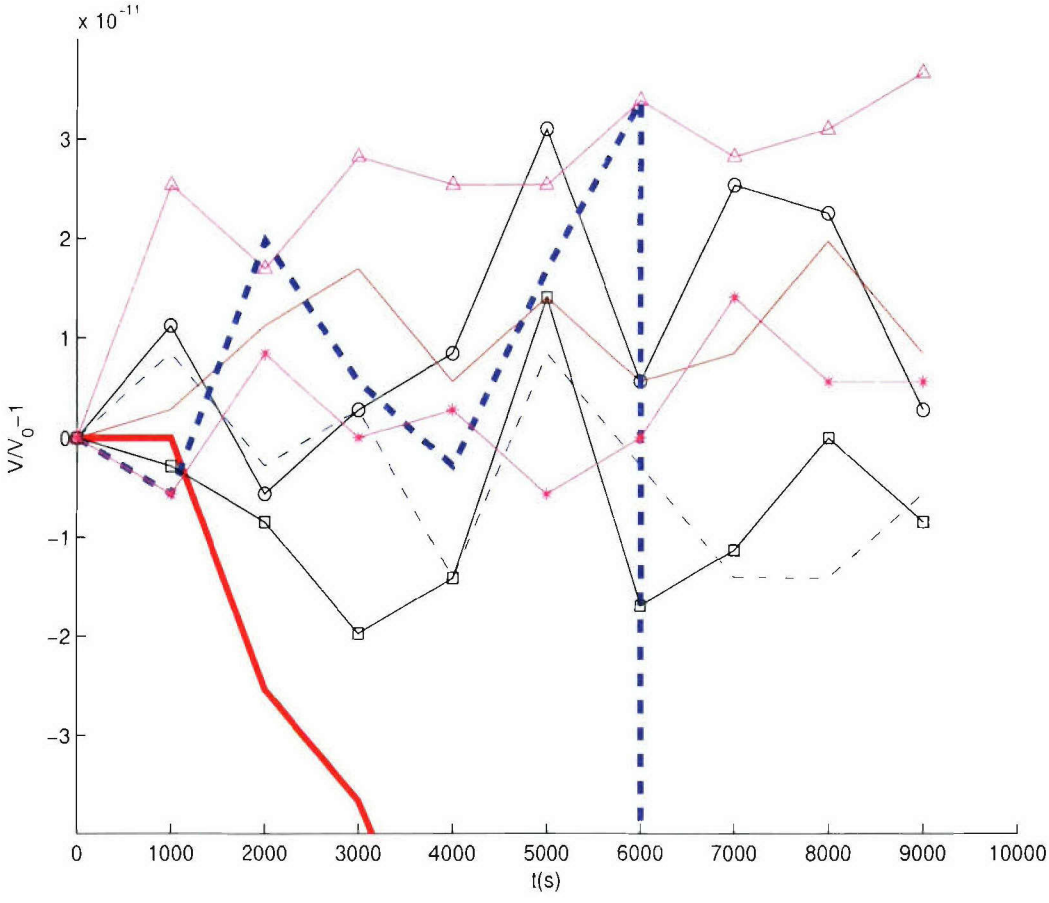

Figure 5.14: Relative error of the Gaussian hump volume by different schemes; (thin solid line: Lax-Wendroff; thin dash line: Lax-Wendroff with filtering; circles: Richtmyer; triangles: MacCormack; thick solid line: FTBS; thick dash line: Warming-Beam; squares: Euler-WENO; stars: TVD-RK-WENO)

on equations for incident and reflected wave amplitudes. The sediment transport rate is calculated by empirical bottom shear stress related to near bottom orbital velocity.

In the present study, we use the linearized Boussinesq equations to obtain the instantaneous wave field. The fluid particle velocity adjacent to the bottom wave boundary layer is obtained using the quadratic vertical variation of horizontal flow assumed in Boussinesq wave theory. The bottom shear stress is obtained by solving for the turbulent wave boundary layer with mixing length closure (Long et al., 2004). Diffusion due to gravity is not included in this model, which will result in larger growth rate of bars than seen in Yu and Mei (2000). We also point out that since the wave simulation, bed shear stress calculation and sand transport rate calculation are different both in formulation and parameters, the predicted bar morphology is not deforming quantitatively at the same rate as Yu and Mei (2000).

The sediment transport is assumed to be dominated by bedload calculated using Meyer-Peter and Müller (1948) type formula

$$\Psi(x,t) = C_1(\theta - \theta_c)^n \tag{5.70}$$

where Ψ is defined as $\Psi = q(x,t)/(d\sqrt{(s-1)gd})$, $q(x,t)$ is volumetric transport rate, d is sediment diameter, g is gravitational acceleration, $s = \rho_s/\rho$ is specific gravity of sediments, $\theta = \tau_b/(\rho(s-1)gd)$ is the Shields parameter, and θ_c is threshold value of Shields parameter for initiation of sediment transport, C_1 and n are determined empirically.

The bed elevation is simulated using the Euler-WENO scheme instantaneously. Here we consider the sandy bed evolution with pre-existing bars as also studied in Yu and Mei (2000). Initially, six sinusoidal sand bars are present in region $0 < x < 6\pi/k$ with bar amplitude equal to near bottom excursion amplitude A_b, wavelength of bars equal to half of wavelength of waves. The sea bed is initially flat elsewhere. Still water depth at the flat bed is $h = 7m$. Waves are introduced to the system from left boundary $x = -25/k$ with wave amplitude $A_0 = 0.5m$, wave period $T = 8s$ and k being the incident wave

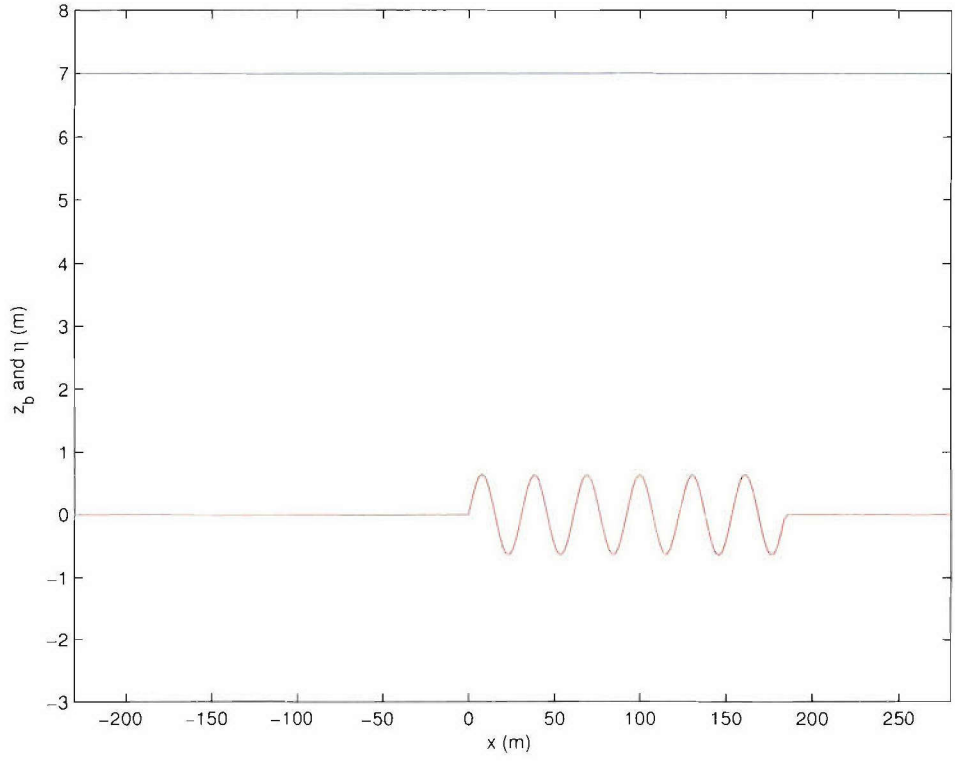

Figure 5.15: Initial bed level (red) and still water surface level (blue)

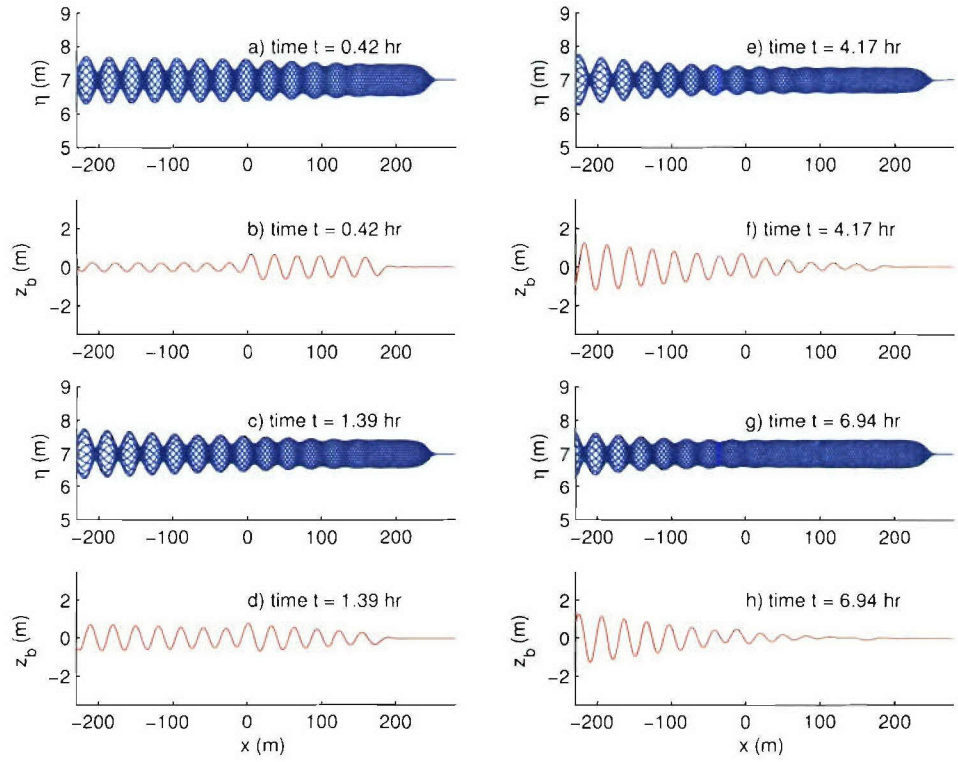

Figure 5.16: Bed level (b, f, d, h) and surface wave envelop (a, c, e, g) at different times.

number (Figure 5.15). Waves are absorbed at the right boundary $x = 25/k$ such that reflected wave energy from right boundary is nearly zero.

With the information given, we have $A_b = A_0/\sinh(kh) = 0.64$m. The time step of the simulation is chosen to be $\Delta t = 0.05s$ for waves and morphology. The spatial grid size is $\Delta x = 2m$. Other parameters are $\rho_s = 2650kg/m^3$, sediment diameter $d = 0.4$mm, still bed porosity $n_p = 0.3$, $C_1 = 11.0$, $n = 1.65$.

Figure 5.16 shows the surface elevation wave groups and the bed level at 4 chosen times. Figure 5.17 shows the entire bed level change with respect to time.

According to Yu and Mei (2000), because initially each of the bar crests is upwave of a wave node by $\pi/4$ and downwave of the next antinode by $\pi/4$ (Figure 5.16 a) and b)),

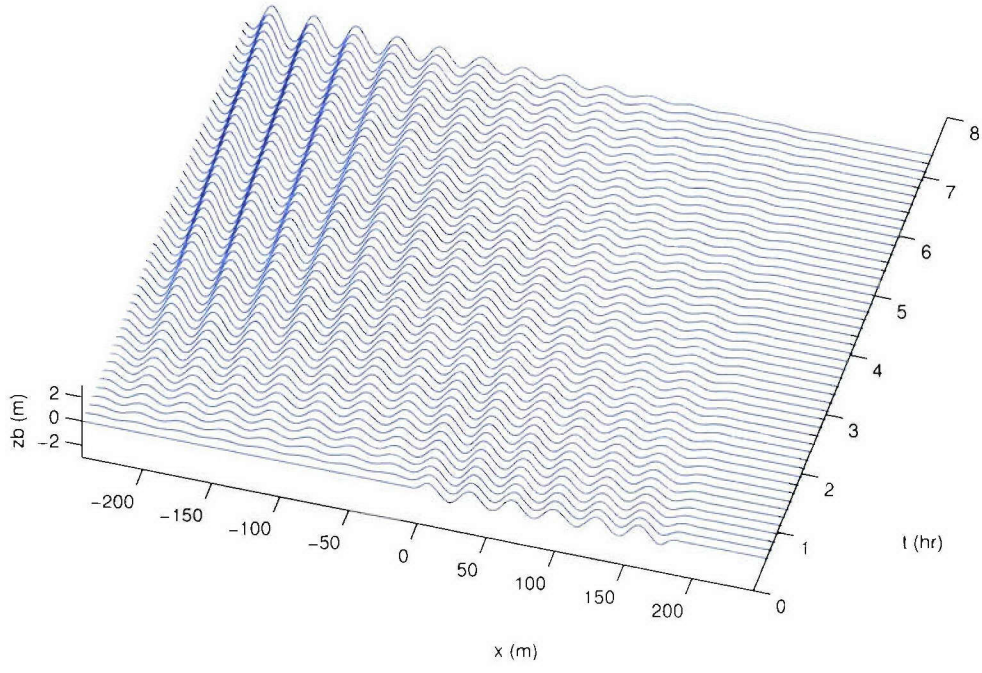

Figure 5.17: Bed level change with respect to time.

the Bragg scattered waves deposit sand into the initial bar troughs and erode the initial bar crests. Hence the bars will be be flattened by their scattered waves. New sand bars will grow offshore of the initial bars and their growth rate will be reduced as initial bars are diminishing. From figure 5.16, the above expectations are qualitatively confirmed. The growing bars on the left have larger growth rate due to the fact that waves are better sheltered on the right. Figure 5.16 and Figure 5.17 demonstrated that the Euler-WENO scheme is stable and may be used in phase resolving sediment transport models.

We also point out that since the wave simulation, bed shear stress calculation and sand transport rate calculation are different both in formulation and parameters, the predicted bar morphology is not deforming quantitatively at the same rate as predicted by Yu and Mei (2000).

5.5.3 Application of the Euler-WENO scheme to 2D channel stability problem

For 2D problems, the Euler-WENO scheme can be applied component-wise. In this section, we investigate the bed stabilities in a channel. The development of alternate bars in straight channels was investigated analytically by Colombini et al. (1987) based on a linear and weakly nonlinear stability analysis. It is shown that the initial perturbations of bed form will grow and reach an equilibrium amplitude, and the development of higher harmonics tends to cause diagonal fronts with high downstream steepness. Schielen et al. (1993) show that the nonlinear evolution of the envelope amplitude of the group of marginally unstable alternate bars satisfies a Ginzburg-Landau equation and periodic bar pattern can become unstable, exhibiting quasi-periodic behavior for realistic physical parameters and a dune covered channel bed. For increasingly unstable bars, however, pronounced oblique shocks develop in the alternating bar pattern (Chang et al., 1971). Güngördü and Kirby (2001) studied the evolution of oblique shock structures using a pseudo-spectral scheme based on the hydrodynamic model of Özkan-Haller and Kirby (1997). The pseudo-spectral results were similar to the results shown below in Figure

5.18, but were often contaminated by the presence of oscillations at the point of most rapid depth change in the down-channel direction, adjacent to channel side walls.

In this study, the channel geometry is defined as bounded by two straight walls at left ($x = 0$) and right ($x = L_x$) respectively. The flow is primarily introduced by gravitational force in y direction. Initial channel bed level perturbations are given to investigate bedform instabilities. The average water depth is h_0. The governing equations for the flow field are

$$\frac{\partial h}{\partial t} + \frac{\partial P}{\partial x} + \frac{\partial Q}{\partial y} = 0 \tag{5.71}$$

$$\frac{\partial P}{\partial t} + \frac{\partial P^2/h}{\partial x} + \frac{\partial PQ/h}{\partial y} + gh\frac{\partial h}{\partial x} = -gh\frac{\partial z_b}{\partial x} - f_b\frac{\sqrt{(P^2+Q^2)}P}{8h^2} \tag{5.72}$$

$$\frac{\partial Q}{\partial t} + \frac{\partial PQ/h}{\partial x} + \frac{\partial Q^2/h}{\partial y} + gh\frac{\partial h}{\partial y} = -gh\frac{\partial z_b}{\partial y} - f_b\frac{\sqrt{(P^2+Q^2)}Q}{8h^2} + i_0 gh \tag{5.73}$$

where $h(x, y, t)$ is total water depth, (P, Q) is depth integrated water volume flux per unit width, i_0 is the slope along the channel, f_b is bottom friction coefficient.

The transport rate formula used here is

$$\mathbf{q} = \nu_0|\mathbf{u}|^b(\frac{\mathbf{u}}{|\mathbf{u}|} - \gamma'\nabla z_b) \tag{5.74}$$

where $\mathbf{u} = (P/h, Q/h)$ is the depth averaged velocity, ν_0, b and γ' are empirical.

Periodic boundary conditions are employed in y direction. The computational domain is $0 < x < L_x$ and $0 < y < L_y$. Initial bed level is given as

$$z_b(x, y, t = 0) = a_0\cos(k_1 x)\cos(k_2 y) \tag{5.75}$$

Initial condition of the flow field is taken as still water ($P = 0$, $Q = 0$, $h = h_0 - z_b(x, y, t = 0)$)

The standard ADI (Alternating-Direction Implicit) scheme is implemented to solve the flow field, and the Euler-WENO scheme is used to update z_b for the flow field calculation of the next time step

$$\frac{z_{bi,j}^{n+1} - z_{bi,j}^{n}}{\Delta t} + \frac{1}{1-n_p}\frac{\hat{q}_{xi+1/2,j} - \hat{q}_{xi-1/2,j}}{\Delta x} + \frac{1}{1-n_p}\frac{\hat{q}_{yi,j+1/2} - \hat{q}_{yi,j-1/2}}{\Delta y} = O(\Delta t, \Delta x^5, \Delta y^5) \tag{5.76}$$

where (i, j) is grid location and $\hat{q}_x$ and $\hat{q}_y$ are x and y component of the WENO reconstructed sediment transport rate $\mathbf{q}$ at $(i \pm 1/2, j)$ and $(i, j \pm 1/2)$ respectively.

In the computation, the channel geometric parameters and the flow parameters are chosen such that the flow is subcritical, and depth averaged velocity $|\mathbf{u}|$ is about $1m/s$. The selected parameters are $h_0 = 5m$, $i_0 = 6.11 \times 10^{-5}$, $f_b = 0.024$, $\nu_0 = 0.7$, $b = 6$, $\gamma' = 0.1$, $L_x = 220m$, $L_y = 1310m$, $k_1 = \pi/L_x$, $k_2 = 2\pi/L_y$, $a_0 = 1m$, $n_p = 0.3$. Uniform spatial steps are used with $\Delta x = \Delta y = 10m$. Time step of $\Delta t = 10s$ is used.

The bed evolution in the channel is shown in Figure 5.18. The flow becomes fully developed rapidly. The bed level changes in a much slower time scale as expected. After 3 hours, the initial symmetric sinusoidal bed level has changed to be obliquely oriented. The crests start to grow and pitch forward in the flow direction, and the troughs become deeper and pitch against the flow direction. The distance between the contours indicate the gradient of the bed level is changing. These developments become more evident after 10 hours. The bed form is also moving along the flow direction. After 17 hours, the bed form becomes stable, crests and troughs are distributed as alternating bars. Similar patterns are also obtained by Güngördü and Kirby (2001).

Although more detailed experimental results are required to test the model morphology, the application of Euler-WENO scheme for morphology updating is computationally stable and successful.

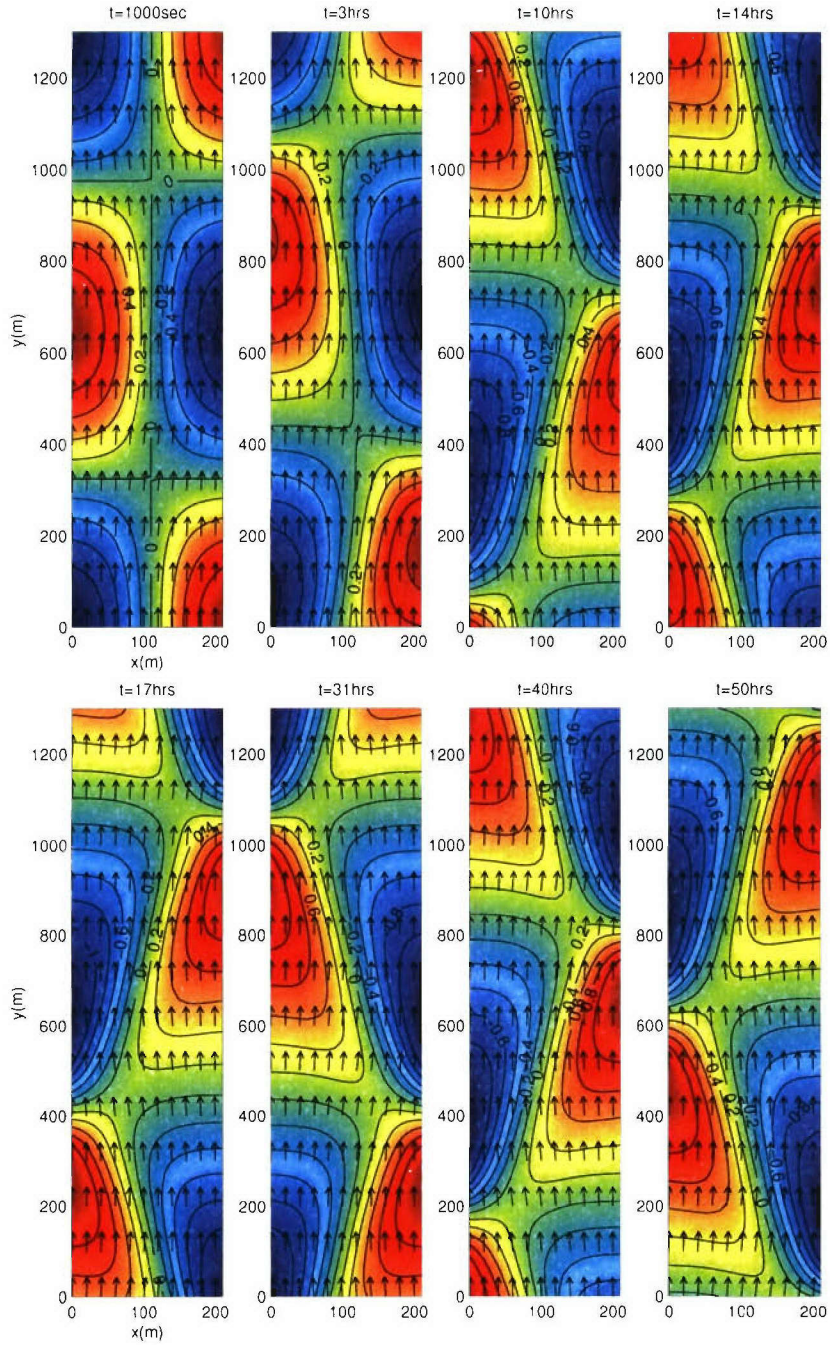

Figure 5.18: Bed evolution of a straight channel (arrow: flow field $\mathbf{u}$, averaged velocity about 1 m/s; contour: bed level)

Chapter 6

BOTTOM BOUNDARY LAYER SOLUTIONS

In this chapter, we focus on the solution of wave boundary layer in the time domain. The models in this research use numerical methods to solve turbulent wave boundary layer to obtain instantaneous bottom shear stress. We first list some analytical solutions of oscillatory boundary layer. Then, a finite difference method is used to solve 2DHV (horizontal and vertical dimensions) vertical and 3D boundary layer structure. Finally we test the 2DHV bottom boundary layer model using some analytical results and measured data.

6.1 Analytical Solutions of Oscillatory Boundary Layer Flows

In this section, a few important analytical solutions for oscillatory boundary layers are summarized briefly.

(1) Oscillating infinite plate (Stokes, 1851)

For a laminar flow introduced by an oscillating infinite plate, with oscillation velocity $u(z=0,t) = a\cos(\omega t)$ parallel to the plate plane, we have the following solution (Stokes, 1851)

$$u(x,z,t) = ae^{-\beta z}\cos(\omega t - \beta z), \tag{6.1}$$

where z is distance from the plate, $\beta = \sqrt{\frac{\omega}{2\nu}}$, and ν is constant kinematic viscosity. The shear stress on the plate becomes

$$-\rho\nu[\frac{\partial u}{\partial z}]|_{z=0} = \rho\nu\sqrt{\omega}a\cos(\omega t + \frac{1}{4}\pi). \tag{6.2}$$

We see that the shear stress has a $\frac{1}{4}\pi$ lead to the plate motion.

(2) Laminar linear wave boundary layer solution (Stokes, 1847)

For a 1-D linear sinusoidal boundary layer on flat bottom, with free stream velocity and free surface elevation given by

$$U = \frac{H}{2}ck\frac{1}{\sinh(kh)}\cos\theta \equiv U_1\cos(\theta) \tag{6.3}$$

$$W = 0 \tag{6.4}$$

$$\eta = \frac{H}{2}\cos\theta, \tag{6.5}$$

where $\theta = kx - \omega t$, H is wave height, ω is wave angular frequency, k is wave number which satisfies linear wave dispersion $\omega^2 = gk\tanh(kh)$, $c = \omega/k$ and h is still water depth, we have the following first order laminar bottom boundary layer solution

$$u(x,z,t) = U_1\cos(\theta) - U_1 e^{(-\beta z)}\cos(\theta - \beta z), \tag{6.6}$$

where $U_1 = \frac{H}{2\sinh(kh)}ck$, z is vertical coordinate from bottom. Vertical velocity w can be calculated by $w = -\int_0^z u_x dz$:

$$w(x,z,t) = -\frac{U_1 k}{\beta}[\beta z\sin\theta + \frac{1}{\sqrt{2}}(e^{-\beta z}\cos(\theta - \beta z + \frac{\pi}{4}) - \cos(\theta + \frac{\pi}{4}))] \tag{6.7}$$

This vertical velocity does not match the outer solution when $z \to \infty$, which indicates that the boundary layer flow will affect the outer flow and a two-way coupling (matching) is warranted for fully matched solution. Extended version of the solution that does account for the effect of the vertical velocity on the progressive wave can be obtained by applying bottom boundary condition $w_w + w_r = 0$ where w_w is the irrotational vertical velocity due to waves and w_r is the velocity field due to the rotational viscous boundary layer. This will lead to modification of the linear wave dispersion relationship and damping of the progressive wave field.

Shear stress is $\tau(x,z,t) = \rho\nu\frac{\partial u}{\partial z}$, i.e.

$$\tau(x,z,t) = \rho\nu\beta U_1 e^{-\beta z}\sqrt{2}\cos(\theta - \beta z + \pi/4) \tag{6.8}$$

Bottom shear stress is

$$\tau_b(x,t) = \tau(x, z = 0, t) = \sqrt{2}\rho\nu\beta U_1 \cos(\theta + \pi/4). \tag{6.9}$$

The bottom shear stress has a $\pi/4$ phase lead over the free stream velocity U.

(3) Turbulent linear wave boundary layer (Trowbridge and Madsen, 1984)

For turbulent wave boundary layer, Trowbridge and Madsen (1984) showed that close to the boundary ($z << \delta$, where δ is boundary layer thickness), the turbulent eddy viscosity can be represented by

$$\nu_t = \kappa z u_* \tag{6.10}$$

where u_* is friction velocity defined by $u_* = \sqrt{|\tau_b/\rho|}$, and the velocity field can be represented by steady turbulent flow (Townsend, 1976)

$$u(x,z,t) = \frac{u_* \text{sign}(\tau_b)}{\kappa} \ln(\frac{z}{K_s/30}) \tag{6.11}$$

where K_s is equivalent Nikuradse roughness and $\kappa = 0.41$ is the von Karman constant. Trowbridge and Madsen (1984) also argued that (6.10) is unrealistic when bottom shear stress vanishes. A modified eddy viscosity model is used to incorporate both temporal variation and a non-vanishing eddy viscosity when close to the boundary, i.e.

$$\nu_t = \nu_0(z) Re[1 + a^{(2)} e^{i2\theta}] \tag{6.12}$$

and

$$\nu_0 = \kappa \overline{u_*} \begin{cases} z & 0 \le z \le \delta_1 \\ \delta_1 & z \ge \delta_1 \end{cases}, \tag{6.13}$$

where δ_1 is a constant to be calibrated, $\overline{u_*}$ is averaged u_* over a wave period, $a^{(2)} = \overline{2e^{-i2\theta} u_*}$ and $\theta = \omega t - kx$. Since the turbulent eddy viscosity is piece-wise continuous here, solutions have to be matched at the interface $z = \delta_1$, and this is given by Trowbridge and Madsen (1984) in a Fourier series and it is not repeated here. The above theory is an important result for turbulent wave boundary layer research, but it is based on mono-chromatic waves. Further extensions of this model are produced by Foster et al. (1999)

and Zou (2002). Eddy viscosity for arbitrary free stream velocity and pressure driven boundary layer flow can be obtained from more detailed models such as $k-\epsilon$ models.

6.2 Numerical Solutions Using Finite Difference Method

In this section we discuss finite difference method for solving the vertical structure of laminar and turbulent wave boundary layer for both 2DHV (horizontal and vertical dimensions) and 3D cases.

6.2.1 Free stream velocity and pressure

The bottom boundary layer flow is driven by the free stream flow and pressure gradient. From (2.106), (2.107) and (2.108), we obtain the free stream velocity $\mathbf{u}_b$, w_b and pressure p_b by setting $\xi = 0$ (to the second order of dispersion)

$$\mathbf{u}_b = \tilde{\mathbf{u}} + \{Ah(\nabla F_{21} + 2\nabla h F_{22}) + Bh^2 \nabla F_{22}\} \tag{6.14}$$

$$w_b(x, y, t) = -F_{21} \tag{6.15}$$

$$\begin{aligned} p_b(x, y, t) &= p_a + \rho g H \\ &- \rho\{HF_{21t} + H^2 F_{22t} \\ &+ \tilde{\mathbf{u}} \cdot [\nabla F_{21} H + \nabla F_{22} H^2 + 2F_{22}\nabla h H]\} \end{aligned} \tag{6.16}$$

The bottom dynamic pressure becomes

$$\begin{aligned} p_{bd} &\equiv p_b - (p_a + \rho g h) \\ &= \rho g(H - h) \\ &- \rho\{HF_{21t} + H^2 F_{22t} \\ &+ \tilde{\mathbf{u}} \cdot [\nabla F_{21} H + \nabla F_{22} H^2 + 2F_{22}\nabla h H]\} \end{aligned} \tag{6.17}$$

6.2.2 2DHV boundary layer solution

We use coordinates (x, y, z) with z upward from the bottom and x, y for horizontal directions. The gradient of the bottom is assumed to be too small to be felt by the local boundary layer.

Here we adopt the work presented by Hsu et al. (2004) to model the flow in the wave boundary layer. The time dependent boundary layer equations are derived using boundary layer approximations from Reynolds-Averaged Naiver-Stokes equation and continuity equation:

$$\frac{\partial u}{\partial x} + \frac{\partial w}{\partial z} = 0 \tag{6.18}$$

$$\frac{\partial u}{\partial t} + u\frac{\partial u}{\partial x} + w\frac{\partial u}{\partial z} = -\frac{1}{\rho}\frac{\partial p_{bd}}{\partial x} + \frac{1}{\rho}\frac{\tau_{zx}}{\partial z} \tag{6.19}$$

Following Hsu et al. (2004), $\frac{\partial}{\partial x}$ is transformed to $-\frac{1}{c}\frac{\partial}{\partial t}$ for permanent form progressive waves nearshore, so that the upper equations become 1-D vertical in space which simplifies the problem enormously:

$$\frac{\partial w}{\partial z} = \frac{1}{c}\frac{\partial u}{\partial t} \tag{6.20}$$

$$\frac{\partial u}{\partial t} - \frac{u}{c}\frac{\partial u}{\partial t} + w\frac{\partial u}{\partial z} = -\frac{1}{\rho}\frac{\partial p_{bd}}{\partial x} + \frac{1}{\rho}\frac{\tau_{zx}}{\partial z} \tag{6.21}$$

which is slightly different from Hsu et al. (2004), since the pressure gradient term is not transformed. It is available directly from the Boussinesq model as a constant driving force through the boundary layer in vertical direction.

Turbulent Reynolds stress is essential for phase-lag effects, which are suspected to be important mechanism for sediment transport under asymmetric waves (Nielsen et al., 2002). However, Bailard (1981) sediment transport model or other free-stream velocity based parameterizations left out these effects. In present work, a turbulent eddy viscosity ν_t is used

$$\tau_{zx} = \rho(\nu_t + \nu)\frac{\partial u}{\partial z} \tag{6.22}$$

with ν_t given by mixing length theory or $k-\epsilon$ model (Justesen, 1988, Hsu et al., 2004). For mixing length theory, the eddy viscosity is taken as

$$\nu_t = \kappa|u_*| \min(z, 0.3z_0) \tag{6.23}$$

with u_* being the instantaneous friction stress estimated by assuming log law of the flow close to bed when $z = \Delta z$, $\kappa = 0.40$ being the Karman constant. For smooth wall turbulence, the log law is (Schlichting, 1968)

$$\frac{|u(z,t)|}{|u_*|} = \frac{1}{\kappa}\ln(\frac{|u_*|z}{\nu}) + 5.1 \tag{6.24}$$

and the solution this equation for $|u_*|$ requires iteration methods. For rough wall turbulence, the log law is (Trowbridge and Madsen, 1984; Foti and Scandura, 2004; Mellor, 2002; Hsu et al., 2004)

$$\frac{|u(z,t)|}{|u_*|} = \frac{1}{\kappa}\ln(\frac{z}{K_s/30}). \tag{6.25}$$

z_0 is the maximum of wave boundary layer thickness, K_s is a roughness height specified as proportional to particle diameter d, Δz is the grid size for numerical discretization[1]. Alternatively, ν_t can be obtained more accurately from a 2-equation $k-\epsilon$ turbulence model. For details about $k-\epsilon$ model, see Hsu et al. (2004), Mellor (2002), Foti and Scandura (2004) and Rodi (1993).

The boundary conditions are:

$$u(x,z,t)|_{z=\infty} = u_b(x,t) \tag{6.26}$$

$$w(x,z,t)|_{z=\infty} = w_b(x,t) \tag{6.27}$$

$$u(x,0,t) = w(x,0,t) = 0 \tag{6.28}$$

$$\tau(x,z,t)|_{z=\infty} = 0 \tag{6.29}$$

[1] Note that a distorted grid system with fine grids near the wall and coarse grids near the outer edge can be used for better resolution. Nevertheless, we use uniform girds here for simplicity.

The boundary layer equations (6.20) and (6.21) are solved numerically using finite difference method in time and space. Explicit schemes can be used to solve the equations, but the computation time is quite large due to small time step required for numerical stability. We here choose to use the well established Crank-Nicholson scheme (2nd order in time and space) to solve the diffusion and advection equation (6.21).

We will find that the boundary equation of vertical velocity w (6.27) is not satisfied, i. e. w solved from continuity equation (6.18) or (6.21) does not match free stream vertical velocity (6.15) at the outer edge of the boundary layer due to two reasons: a) Boussinesq theory does not take account of the alteration to the wave form due to the bottom boundary layer vertical velocity pumping effects; b) Here we assume the bottom boundary layer local field do not feel the gradient of bed level. Rather, we only discuss the effects of free stream velocity and pressure gradient on boundary layer, while neglecting the feed back of boundary layer effects to the outer flow. For boundary layer flow with the consideration of bottom gradient and curvature, it is difficult to solve efficiently using numerical methods due to the complexity of the geometry. Some of the aspects of the feedback of bottom boundary layer vertical velocity to the outer flow have been discussed in Liu and Orfila (2004) for ideal cases such as solitary wave damping due to bottom boundary layer.

With all the assumptions discussed above, the equations are still difficult to solve since that the upper boundary is placed at infinity. In reality, the boundary condition should be placed at the outer edge of the boundary layer which defines the thickness of the instantaneous boundary layer flow. The thickness of boundary layer can not be estimated a priori. The inclusion of an unknown boundary condition location causes more difficulty in obtaining a numerical solution. One could use a shooting-method to calculate the thickness of the boundary layer, where we could place the outer boundary condition at a certain distance z_0 from the bed level, calculate boundary layer flow, and then check if the boundary condition is satisfied. If not, we can modify the distance z_0 and do the

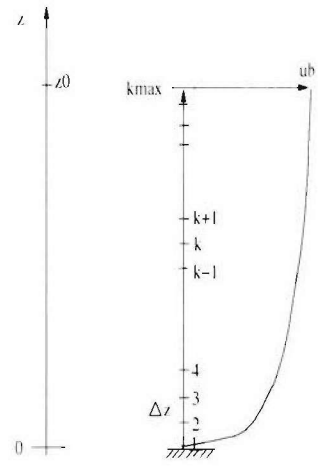

Figure 6.1: Vertical discretization grids for boundary layer

calculation again until the boundary condition is satisfied to a designated accuracy. This shooting-method takes iterations to complete, and the cost of computation time is quite demanding. An alternative way is to specify z_0 far enough from the bed level, so that the boundary layer effects is always negligible and the iterations for z_0 are not necessary. But a large z_0 will require more grid points in the vertical direction. In the numerical methods discussed below, we choose to use the latter method.

6.2.2.1 Linear wave boundary layer

For linear wave boundary layer, we entirely neglect the vertical velocity w and the convection $u\frac{\partial u}{\partial x}$. The momentum equation (6.19) becomes:

$$\frac{\partial u}{\partial t} = -\frac{1}{\rho}\frac{\partial p_{bd}}{\partial x} + \frac{1}{\rho}\frac{\partial}{\partial z}[\rho(\nu + \nu_t)\frac{\partial u}{\partial z}] \tag{6.30}$$

We discretize the 1D vertical domain $0 \leq z \leq z_0$ by uniform non-staggered grids with grid spacing Δz as shown in figure (6.1). Discretization of the equation (6.30) using Crank-Nicholson scheme results in

$$\begin{aligned}\frac{u_k^{n+1} - u_k^n}{\Delta t} &= -\frac{1}{\rho}(\frac{\partial p_{bd}}{\partial x})^{n+1/2} \\ &+ \frac{1}{2\Delta z}[(\nu + \nu_t)_{k+1/2}^{n+1}(\frac{u_{k+1}^{n+1} - u_k^{n+1}}{\Delta z}) - (\nu + \nu_t)_{k-1/2}^{n+1}(\frac{u_k^{n+1} - u_{k-1}^{n+1}}{\Delta z})]\end{aligned}$$

$$+ \quad \frac{1}{2\Delta z}[(\nu+\nu_t)^n_{k+1/2}(\frac{u^n_{k+1}-u^n_k}{\Delta z}) - (\nu+\nu_t)^n_{k-1/2}(\frac{u^n_k-u^n_{k-1}}{\Delta z})] \quad (6.31)$$

with n the current time step, $n+1$ the next time step, $k = 2, ..., k_{max}-1$. The scheme is second order in time and space. It is an implicit scheme, and large time step can be used. Re-arrangement of the upper equation leads to a linear equation system

$$A_k u^{n+1}_{k-1} + B_k u^{n+1}_k + C_k u^{n+1}_{k+1} = D_k, \quad k = 2, ..., k_{max}-1 \quad (6.32)$$

where

$$A_k = -\frac{\Delta t}{2\Delta z^2}(\nu+\nu_t)^{n+1}_{k-1/2} \quad (6.33)$$

$$B_k = 1 + \frac{\Delta t}{\Delta z^2}(\nu+\nu_t)^{n+1}_k \quad (6.34)$$

$$C_k = -\frac{\Delta t}{2\Delta z^2}(\nu+\nu_t)^{n+1}_{k+1/2} \quad (6.35)$$

$$\begin{aligned} D_k &= u^n_k - \Delta t\frac{1}{\rho}(\frac{\partial p_{bd}}{\partial x})^{n+1/2}_k \\ &+ \frac{\Delta t}{2\Delta z^2}[(\nu+\nu_t)^n_{k+1/2}(u^n_{k+1}-u^n_k) - (\nu+\nu_t)^n_{k-1/2}(u^n_k-u^n_{k-1})] \end{aligned} \quad (6.36)$$

The numerical boundary conditions at bottom and top of the boundary layer requires different approaches for different problems. For the top boundary condition, if the top free stream velocity $u_b(x,t)$ is known, then one should use

$$u_{k_{max}} = u_b(x,t) \quad (6.37)$$

and the unknown variables are $u_2, u_3, ..., u_{k_{max}-1}$. If the free stream pressure gradient $\frac{\partial p_{bd}}{\partial x}$ is known, then one can use zero shear condition

$$\tau_{k_{max}-1/2} = 0. \quad (6.38)$$

i.e.,

$$u_{k_{max}-1} = u_{k_{max}} \quad (6.39)$$

and the knowns are $u_2, u_3, ..., u_{k_{max}}$ with the upper equation (6.39) added to the equation system (6.32). Boundary condition (6.37) and (6.39) are equivalent to each other when z_0 is sufficiently large. The bottom boundary condition is simply

$$u_1 = 0. \tag{6.40}$$

The turbulent viscosity ν_t is a function of the flow itself according to (6.23), hence iteration is utilized to obtain solution. In practice, to save computation time, one may also use the turbulent viscosity obtained from the last time step and the iteration is not necessary. A tridiagonal matrix solver is used to solve equation (6.32). The pressure gradient $\frac{\partial p_{bd}}{\partial x}$ is the driving force for the boundary layer flow, and it is specified from the Boussinesq model results. Bottom shear stress is obtained through the logarithmic profile assumption within the first grid (6.24) and (6.25).

6.2.2.2 Nonlinear wave boundary layer

For nonlinear wave boundary layer, second order effects due to advection need to be considered and the full equations (6.20)-(6.21) are solved. The same Crank-Nicholson scheme is used for discretization, and the convective terms in (6.21) are moved to RHS of the equation, which gives

$$A_k u_{k-1}^{n+1} + B_k u_k^{n+1} + C_k u_{k+1}^{n+1} = D_k, \quad k = 2, ..., k_{max} - 1 \tag{6.41}$$

with

$$A_k = -[\frac{\Delta t}{2\Delta z^2}(\nu + \nu_t)_{k-1/2}^{n+1} + \frac{\Delta t}{4\Delta z} w_k^{n+1}] \frac{1}{(1 - \frac{u}{c})_k^{n+1/2}} \tag{6.42}$$

$$B_k = 1 + [\frac{\Delta t}{\Delta z^2}(\nu + \nu_t)_k^{n+1}] \frac{1}{(1 - \frac{u}{c})_k^{n+1/2}} \tag{6.43}$$

$$C_k = -[\frac{\Delta t}{2\Delta z^2}(\nu + \nu_t)_{k+1/2}^{n+1} - \frac{\Delta t}{4\Delta z} w_k^{n+1}] \frac{1}{(1 - \frac{u}{c})_k^{n+1/2}} \tag{6.44}$$

$$D_k = \{u_k^n \quad - \quad \Delta t \frac{1}{\rho} (\frac{\partial p_{bd}}{\partial x})_k^{n+1/2}$$

$$+ \quad \frac{\Delta t}{2\Delta z^2}[(\nu+\nu_t)^n_{k+1/2}(u^n_{k+1}-u^n_k)-(\nu+\nu_t)^n_{k-1/2}(u^n_k-u^n_{k-1})]$$
$$- \quad \frac{\Delta t}{4\Delta z}w^n_k(u^n_{k+1}-u^n_{k-1})\}\frac{1}{(1-\frac{u}{c})^{n+1/2}_k} \tag{6.45}$$

Vertical velocity w is integrated simply using trapezoidal rule from (6.20):

$$w^{n+1}_k - w^{n+1}_0 = \frac{1}{c}\sum_{m=1}^{k-1}(\frac{u^{n+1}-u^n}{\Delta t})_{k+1/2}\Delta z \tag{6.46}$$

where $w^{n+1}_0 = 0$ from bottom boundary condition (6.28). Again, iteration and tridiagonal solver are used to solve equation (6.41) for u^{n+1} and (6.46) for w^{n+1}. The wave speed c is estimated as $\sqrt{gh}$ within surfzone for simplicity. Note that the transform $\frac{\partial}{\partial x} \rightarrow \frac{-1}{c}\frac{\partial}{\partial x}$ is only valid for progressive waves in $+x$ direction. This method is not valid for standing waves and reflected waves near structures.

6.2.3 3D boundary layer solution

For 3D boundary layer, with free stream flow in both x and y directions, we only use the linear wave boundary layer solution.

In addition to (6.30), we have the linearized momentum equation in the y direction for solution of v

$$\frac{\partial v}{\partial t} = -\frac{1}{\rho}\frac{\partial p_{bd}}{\partial y} + \frac{1}{\rho}\frac{\partial}{\partial z}(\rho(\nu+\nu_t)\frac{\partial v}{\partial z}). \tag{6.47}$$

The discretized equation is

$$A_k v^{n+1}_{k-1} + B_k v^{n+1}_k + C_k v^{n+1}_{k+1} = E_k, \quad k = 2, ..., k_{max}-1, \tag{6.48}$$

where A_k, B_k, C_k are the same as (6.33), (6.34) and (6.35).

$$E_k = v^n_k - \Delta t\frac{1}{\rho}(\frac{\partial p_{bd}}{\partial y})^{n+1/2}_k$$
$$+ \quad \frac{\Delta t}{2\Delta z^2}[(\nu+\nu_t)^n_{k+1/2}(v^n_{k+1}-v^n_k)-(\nu+\nu_t)^n_{k-1/2}(v^n_k-v^n_{k-1})] \tag{6.49}$$

and ν_t is given by

$$\nu_t = \kappa|u_*|\min(z, 0.3z_0). \tag{6.50}$$

where for rough wall

$$|u_*| = \kappa \frac{|\mathbf{u}(\Delta z, t)|}{\ln(30\Delta z/K_s)} \tag{6.51}$$

and for smooth wall

$$\frac{|\mathbf{u}(\Delta z, t)|}{|u_*|} = \frac{1}{\kappa} \ln(\frac{|u_*|\Delta z}{\nu}) + 5.1 \tag{6.52}$$

with $|\mathbf{u}(\Delta z, t)| = \sqrt{u^2(\Delta z, t) + v^2(\Delta z, t)}|$.

6.3 Bottom Boundary Layer Model Test

In this section, we examine the solutions of the boundary layer model using a) analytical linear laminar wave boundary layer and b) data and model results provided by Jensen et al. (1989), Mellor (2002) and Foti and Scandura (2004).

6.3.1 Linear laminar wave boundary layer

Here, the laminar wave boundary layer solution (6.6) is used to test the numerical scheme given by (6.32). We choose an ideal case with free stream velocity given by the linear wave theory

$$U = \frac{H}{2} ck \frac{1}{\sinh(kh)} \cos(\omega t - kx) \equiv U_1 \cos(\omega t - kx) \tag{6.53}$$

$$W = 0 \tag{6.54}$$

$$\eta = \frac{H}{2} \cos(\omega t - kx). \tag{6.55}$$

where we choose water depth $h = 4m$, wave height $H = 0.5m$, wave period $T = 2\pi/\omega = 5sec$. The corresponding wave number is $k = 0.225m^{-1}$, angular frequency $\omega = 1.257s^{-1}$ and wave phase speed is $c = 5.589m/s$. The bottom fluid excursion velocity is $U_1 = 0.306m/s$ and the excursion radius is $a = U_1/\omega = 0.244m$. The viscosity is $\nu = 1 \times 10^{-6}m^2/s$. We assume the bottom boundary layer flow is laminar although the Reynolds number is $R_e = U_1 a/\nu = 7.46 \times 10^4$ is not small. The thickness of the boundary layer is on the order of $\delta_0 = 1/\beta = 0.0013m$ with $\beta = \sqrt{\frac{\omega}{2\nu}} = 792.666m^{-1}$. In the simulation, we use a domain of size $0 < z < z_0$ with $z_0 = 10\delta_0 = 0.013m$. 151 grids

in the vertical direction are used to obtain a vertical discretization step $\Delta z = 0.0867$mm. Time step $\Delta t = T/500 = 0.01s$ is used in the model computation. Linear equations are solved and the bottom boundary condition $u = 0$ is used instead of using logarithmic profile. Analytical solution is used as initial condition in the model simulation.

The model results are plotted against the analytical solution

$$u(x, z, t) = U_1 \cos(\omega t - kx) - U_1 e^{(-\beta z)} \cos(\omega t - kx - \beta z) \tag{6.56}$$

in figure 6.2, where x is set to be $x = 0$ without loss of generality. From the figure, the model results are in very good agreement with the analytical results. Figure 6.3 shows the comparison of model bottom shear stress and the analytical bottom shear stress

$$\tau_b(x, t) = \sqrt{2}\rho\nu\beta U_1 \cos(\omega t - kx + \pi/4) = 0.343 \cos(\omega t - kx + \pi/4)\ (p_a). \tag{6.57}$$

The model captures the bottom shear stress time history well except small errors occur at the times when the shear stress has a maximum absolute value. This is due to the fact that the bottom shear stress here for laminar boundary layer is calculated by the first order finite difference

$$\tau_b = \rho\nu \frac{u(z = \Delta z, t)}{\Delta z} + O(\Delta z), \tag{6.58}$$

although the Crank-Nicholson scheme for solving $u(z, t)$ is of second order accuracy.

6.3.2 Wave boundary layer experiment by Jensen et al. (1989)

The boundary layer model performs well in comparison to analytical results of linear theory. Here, we further test the model performance using experimental data under smooth wall turbulence and rough wall turbulence conditions. The chosen data sets are obtained from Jensen et al. (1989). Many researchers have also compared their models or analysis to these data, e.g., Mellor (2002) and Foti and Scandura (2004). In this research, we follow Foti and Scandura (2004) and show the model data comparisons of a smooth wall case (test 10 of Jensen et al., 1989, hereafter called JSF10) and rough wall case (test 13 of Jensen et al., 1989, hereafter called JSF13). The experiments were carried

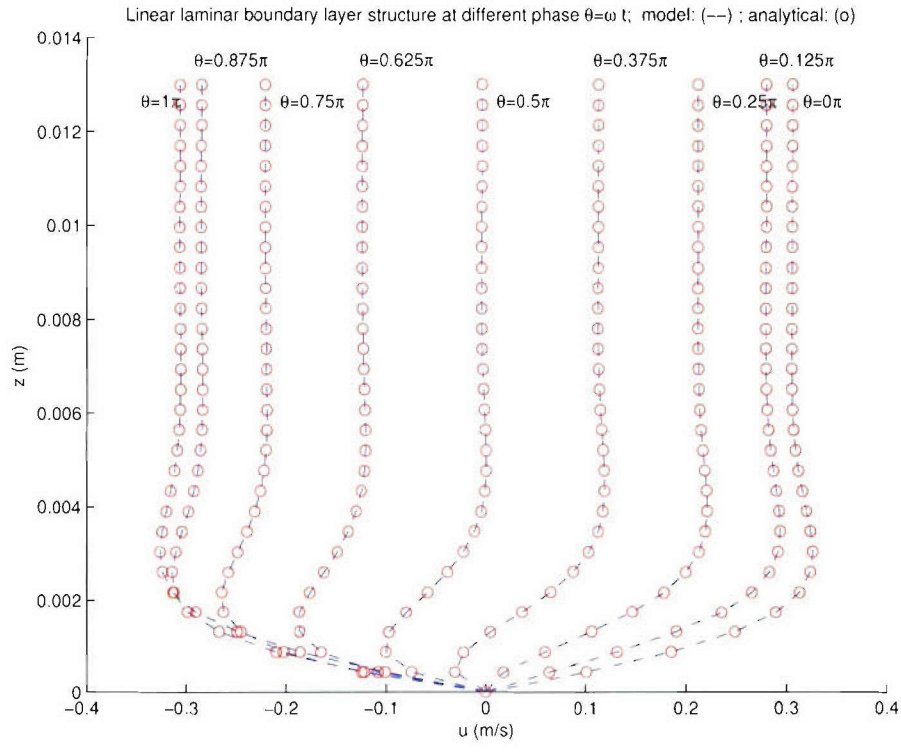

Figure 6.2: Flow structure for laminar boundary layer computation; model: dash; analytical solution: circles

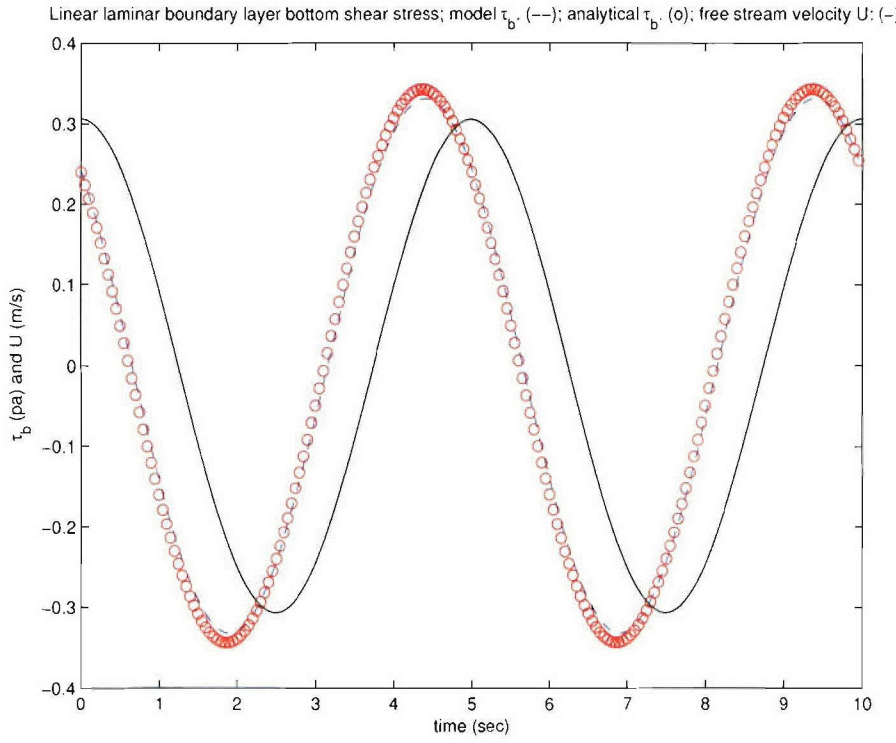

Figure 6.3: Bottom shear stress for laminar boundary layer computation; model: dash; analytical solution: circles; free stream velocity U: solid

out in a U-shaped oscillatory-flow water tunnel with a working section $10m$ long, $0.39m$ wide and $0.28m$ high for the smooth wall tests and $0.30m$ high for the rough wall tests. Period of free stream oscillatory flow is $T = 9.72s$. Reynolds number is defined as $R_e = \frac{U_{0m}a}{\nu}$ where U_{0m} is the amplitude of the free stream velocity. a is the orbital excursion amplitude. The 2DHV linear boundary model is used to simulate the two test cases because $w = 0$ and the flows in the oscillatory tunnel are uniform in the stream-wise direction. The free stream velocity is given as $u_b(t) = U_{0m}\sin(\theta)\tanh(t/T)$ with $\theta = \omega t = 2\pi t/T$. The initial condition is given as zero, and the $\tanh(t/T)$ function gives a gradual spin-up of the system from $t = 0$ to $t \approx= 5T$ when the system reaches a steadily cycling state. Ten cycles are simulated and the results of the last cycle are presented in the following paragraphs.

For the smooth wall turbulence case JSF10, the parameters are $U_{om} = 2.0m/s$, $T = 9.72s$, $a = 3.1m$, $R_e = 6 \times 10^6$, $\nu = 1.14 \times 10^{-2}cm^2/s$ and the sampling interval is $24ms$. The flow is simulated using our boundary layer model with $\Delta z = 0.0015m$, $\Delta t = T/360$. The model results of flow structure is plotted against the data and Mellor (2002) in the figure 6.4. The bottom shear stress is indicated by the friction velocity u_* and plotted in the figure 6.5. Generally speaking, the model captures the flow structure within the boundary layer. The $k-\epsilon$ model of Mellor (2002) gives better agreement than current model. This is reasonable because the $k-\epsilon$ model can give better description of the turbulence kinetic energy and the turbulent viscosity. The current model, the Foti and Scandura (2004) $k-\epsilon$ model and the Mellor (2002) $k-\epsilon$ model all agree very well with the measured bottom shear stress. The results are similar due to the fact that the same smooth wall log law is used in obtaining bottom shear stress.

For the rough wall turbulence case JSF13, the test parameters are $U_{om} = 2.0m/s$, $T = 9.72s$, $a = 3.1m$, $R_e = 6 \times 10^6$, $\nu = 1.14 \times 10^{-2}cm^2/s$, roughness $K_s = 0.84$mm and the sampling interval is $48ms$. Similar to the JSF10 case, the model uses $\Delta z = 0.0015m$ as vertical step and $\Delta t = T/360$ as time step. The modeled flow structure

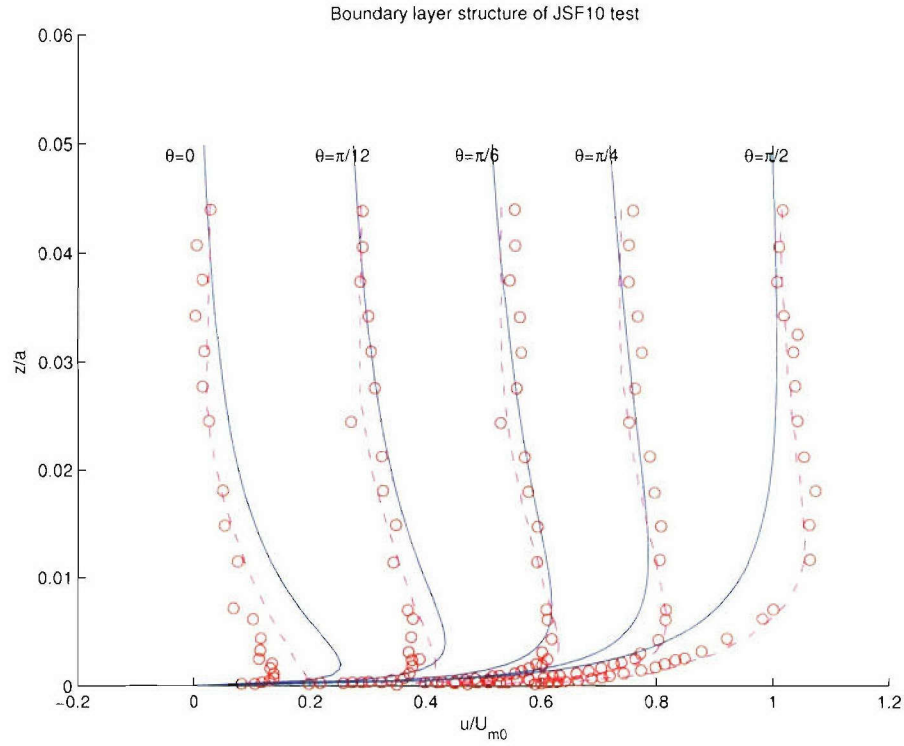

Figure 6.4: Flow structure for smooth wall boundary layer computation; model: solid; data: circles; Mellor (2002): dash

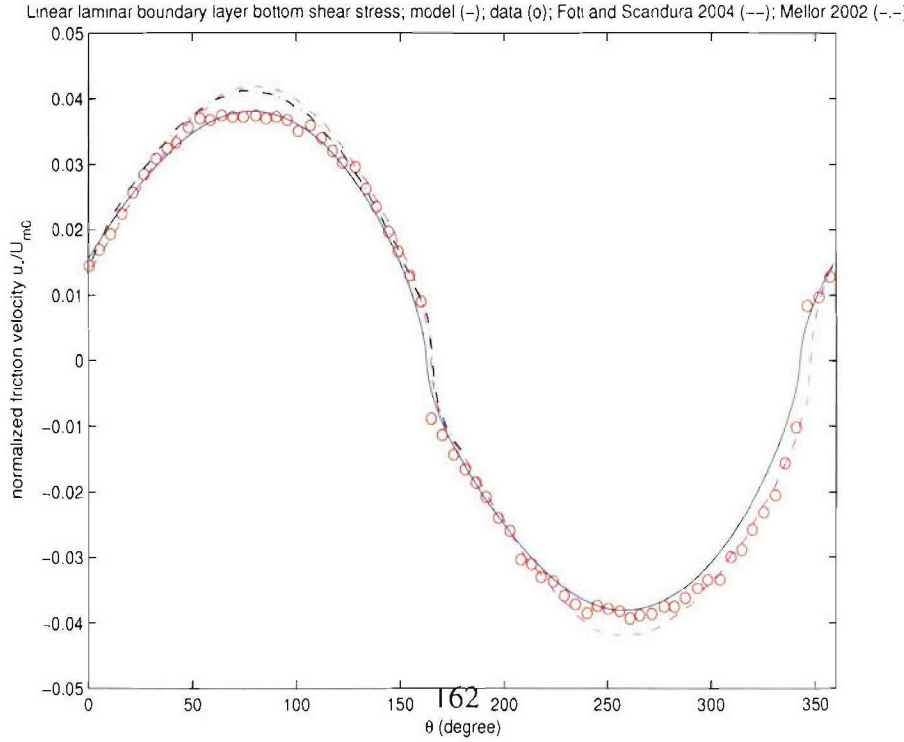

Figure 6.5: Bottom shear stress for smooth wall boundary layer computation; model: solid; data: circles; Foti and Scandura (2004): dash; Mellor (2002): dot-dash

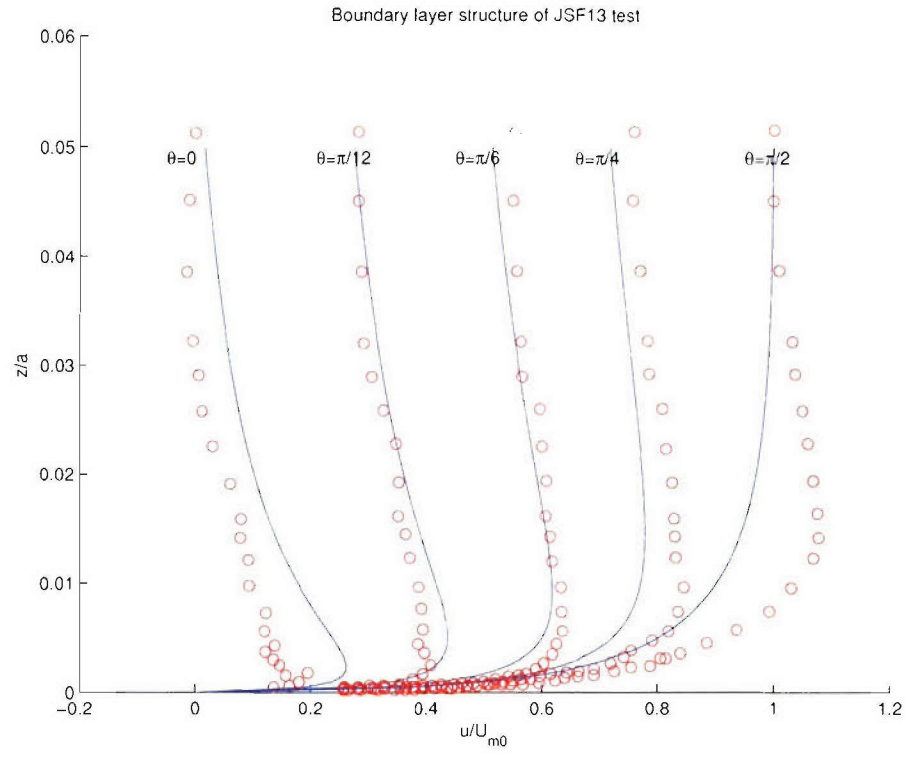

Figure 6.6: Flow structure for smooth wall boundary layer computation; model: solid; data: circles

is plotted against the data in the figure 6.6. The bottom shear stress is indicated by the friction velocity u_* and plotted in the figure 6.7. The flow structure is captured by the current model. The largest discrepancy occurs at $\theta = \pi/2$. Both the current model and the Foti and Scandura (2004) models give good agreement of shear stress. The model by Mellor (2002) underestimates bottom shear for this case.

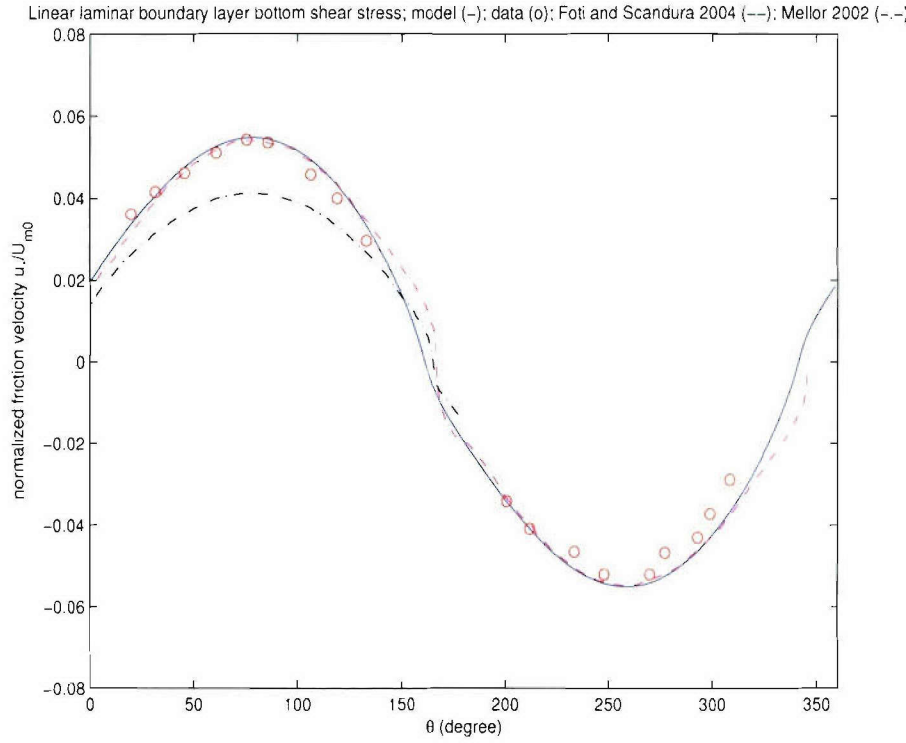

Figure 6.7: Bottom shear stress for smooth wall boundary layer computation; model: solid; data: circles; Foti and Scandura (2004): dash; Mellor (2002): dot-dash

Chapter 7

MODEL TESTS I: WAVE CURRENT SIMULATION TEST

In this chapter, we test the Boussinesq wave current model using both experimental results and analytical solutions. Both 1D model tests and 2D model tests are conducted. We cover monochromatic waves, random waves, solitary wave run up, wave breaking and undertow, wave refraction, wave diffraction and curvilinear grid system. In these tests, no sediment transport and morphology change modules are included.

In the first section, the Mase and Kirby (1992) experiments are modeled to test wave transformation and breaking on a sloping beach. Next, the Stive and Wind (1986) experiment on wave-induced undertow is simulated. Then the solitary wave run up experiments by Synolakis (1987) are compared with numerical computations to investigate the accuracy of the wet-dry scheme. In order to test the use of curvilinear coordinates, we calculate the transformation of waves in a circular channel. Finally, waves on a plane beach with groins are modeled to show the model ability of dealing with coastal structures.

7.1 Mase and Kirby (1992) Flume Test

Mase and Kirby (1992) conducted a laboratory experiment of random wave propagation over a plane beach. Figure 7.1 shows the experiment layout, where a constant depth on the left connects to a constant slope on the right. Two sets of random waves with peak frequencies 0.6Hz ($run1$) and 1.0Hz ($run2$) are generated by a wave maker on the left end and propagate over the flat bottom and then onto the slope. Starting at the toe, 12 wave gages are deployed along the slope at locations whose water depths are

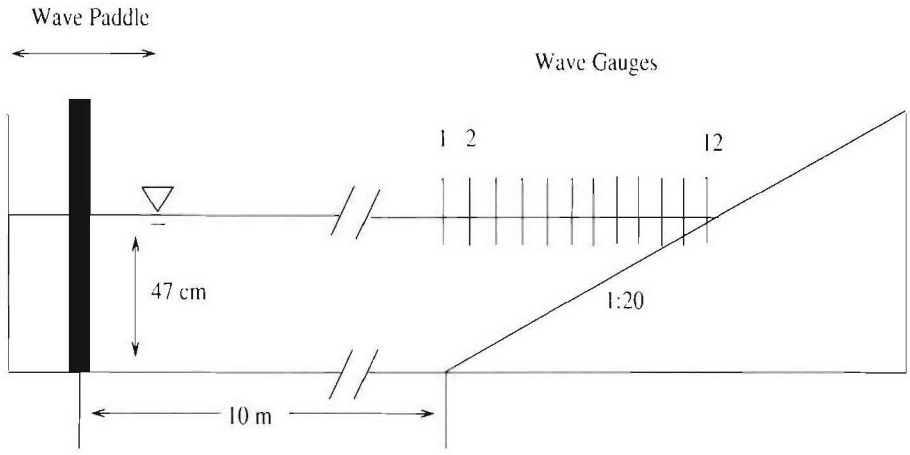

Figure 7.1: Experiment layout of Mase and Kirby (1992)

$h = 47, 35, 30, 25, 20, 17.5, 15, 12.5, 10, 7.5, 5, 2.5\ cm$. Time series of surface elevation η at these locations are collected simultaneously for about 14 minutes for $run1$ with sampling frequency of $25Hz$ and 12 minutes for $run2$ with sampling frequency of $20Hz$

.

Here we present the model results for $run2$ and compare them with the experimental data. The closest gage to the experimental wave maker is at the toe with a depth $h = 47cm$. The measured surface elevation data $\eta(t)$ at that location is used as input to the model to generate time series of source function amplitude in the numerical wave maker. In the model run, the following parameters are used; $\Delta t = 0.01$sec, $\Delta x = 0.025m$, maximum tolerance error $Error_{max} = 0.00005$. Time series comparison of η between model (solid lines) and data (dash lines) at 11 wave gage locations are shown in figure 7.2 and figure 7.3.

Figure 7.4 shows the model and data comparison of the power spectra for the 11 gages. Generally, the model reproduces a satisfactory transformation of the wave spectra over the slope. However, at gage $h = 35cm$, which is located close to the numerical wave maker, the wave energy spectra is underestimated compared to the data at frequency f about $2Hz$. This is due to the numerical wave maker transfer function D_1 (see appendix),

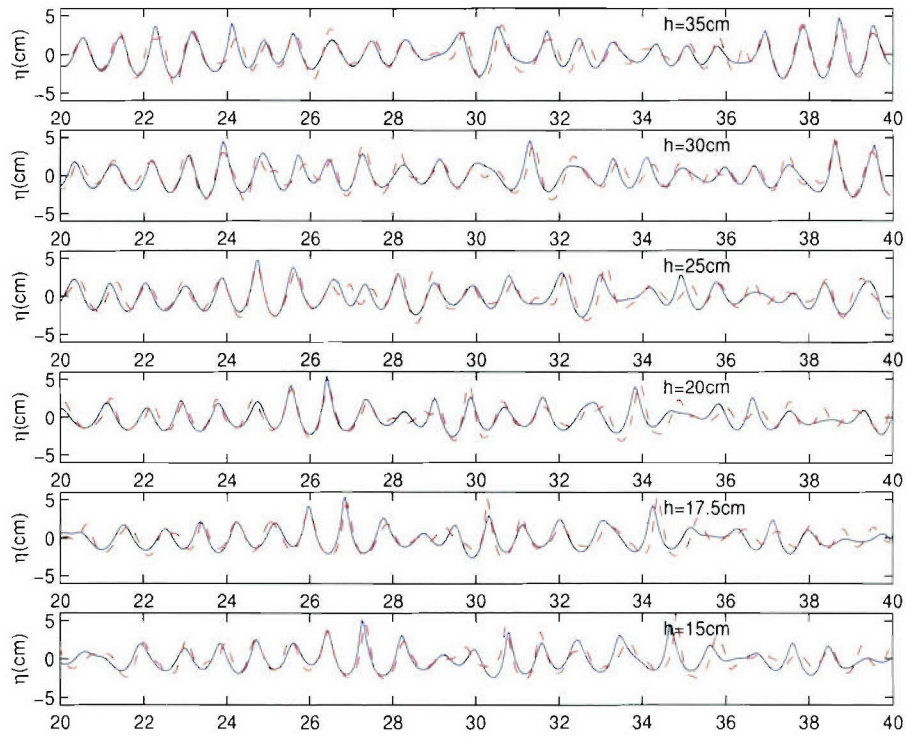

Figure 7.2: Time series comparison of gages a) $h = 35cm$ to $15cm$; dash : data; solid: model

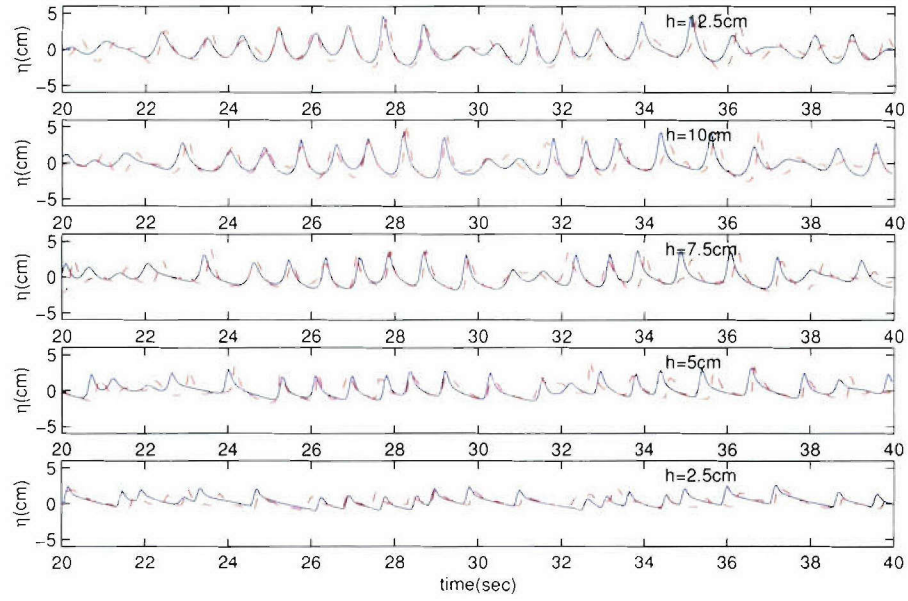

Figure 7.3: Time series comparison of gages b) $h = 12.5$ to $2.5cm$; dash : data; solid: model

which is exponentially increasing for high frequency waves. The numerical wave maker has a cut off at the high frequency end. The effect of this cut off is that the wave energy input in the numerical model is less than experiments and the model RMS wave height is further underestimated by about 5 percent, which is shown in figure 7.5. In figure 7.6, the wave set down and set up are also plotted against data values. The model seems to overestimate the set down compared to data values, but the location of maximum set down and the slope of the set up are well reproduced.

Comparison of normalized skewness ($< \eta^3(t) > /(\sqrt{< \eta^2(t) >})^3$) and asymmetry ($< H(\eta(t))^3 > /(\sqrt{< \eta^2(t) >})^3$ where $H()$ is Hilbert transform) at different water depths is shown in figure 7.7. The model captures the transform of both skewness and asymmetry well except that they are overestimated at the deep water end. In the shallow water region, both the skewness and asymmetry are well reproduced. In the surfzone ($h < 10cm$), a decay of skewness is both evident from the model run and the experiment.

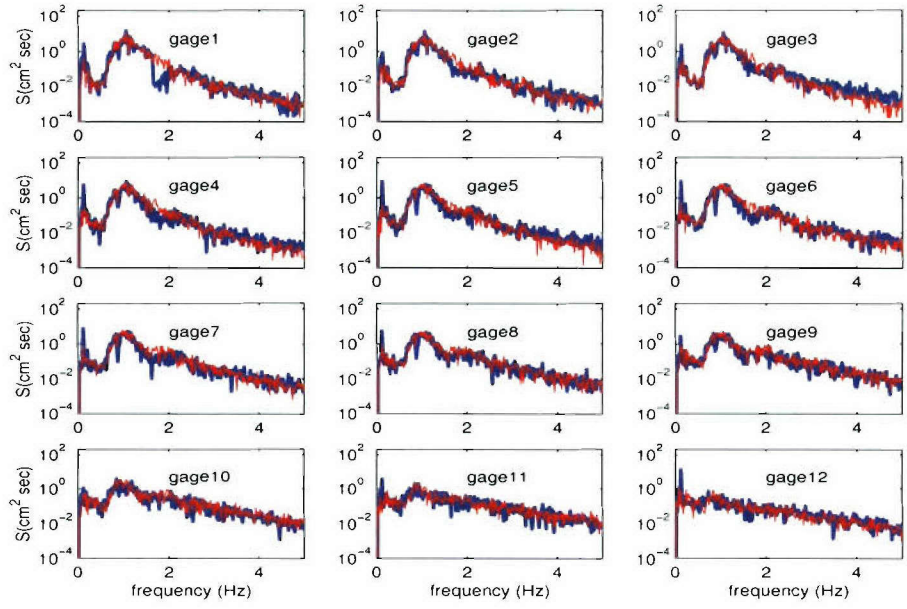

Figure 7.4: Model data comparison of wave spectra; model: thick solid line; data: thin solid line

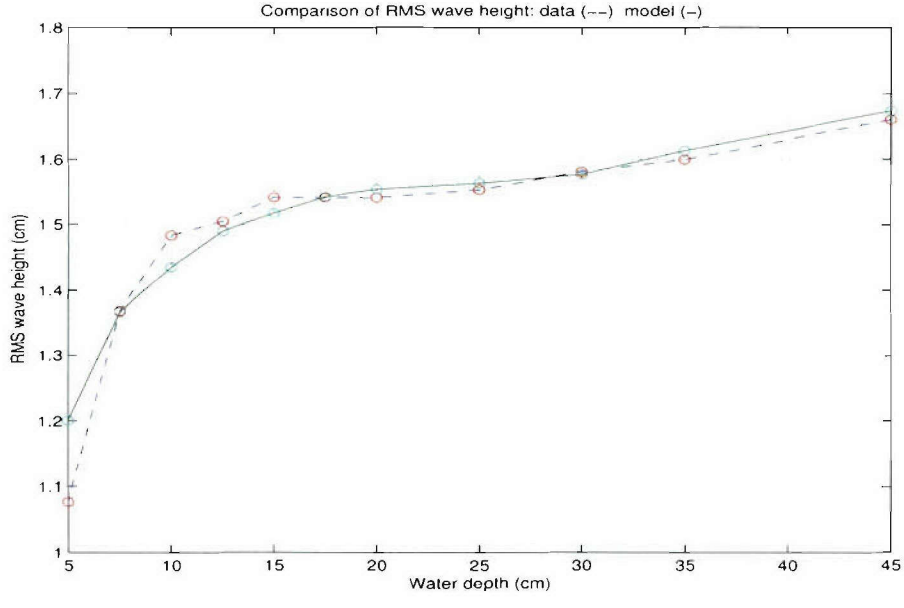

Figure 7.5: Wave height comparison

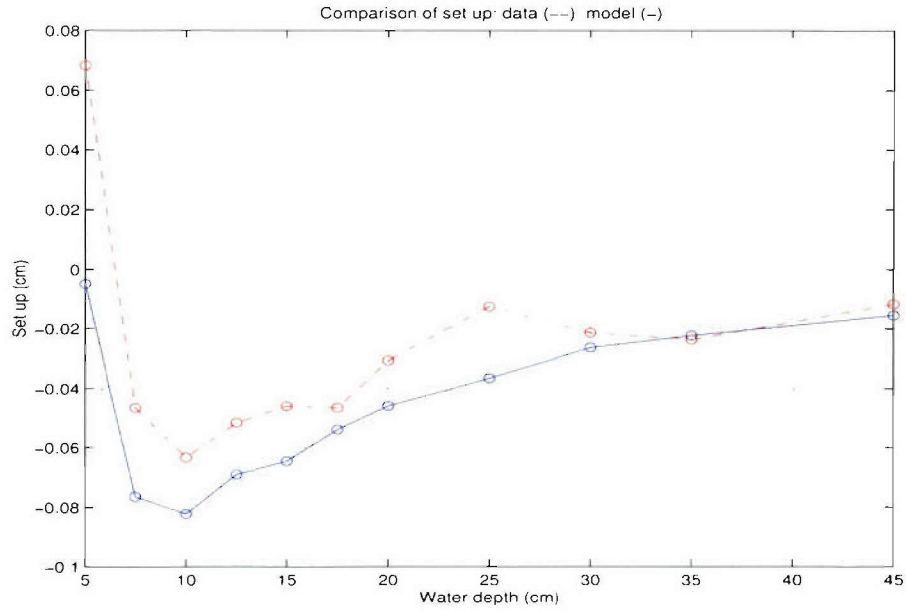

Figure 7.6: Wave set up comparison

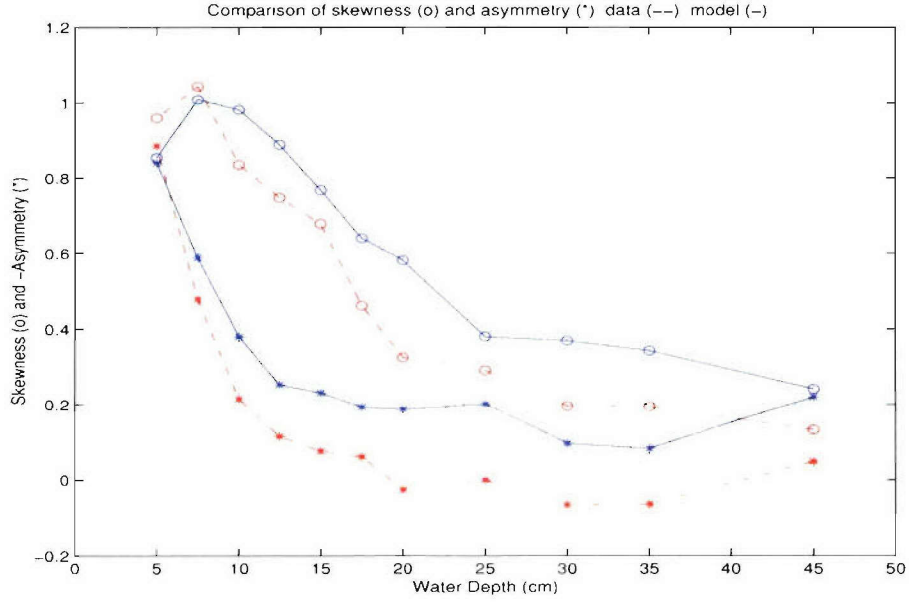

Figure 7.7: Comparison of skewness and asymmetry

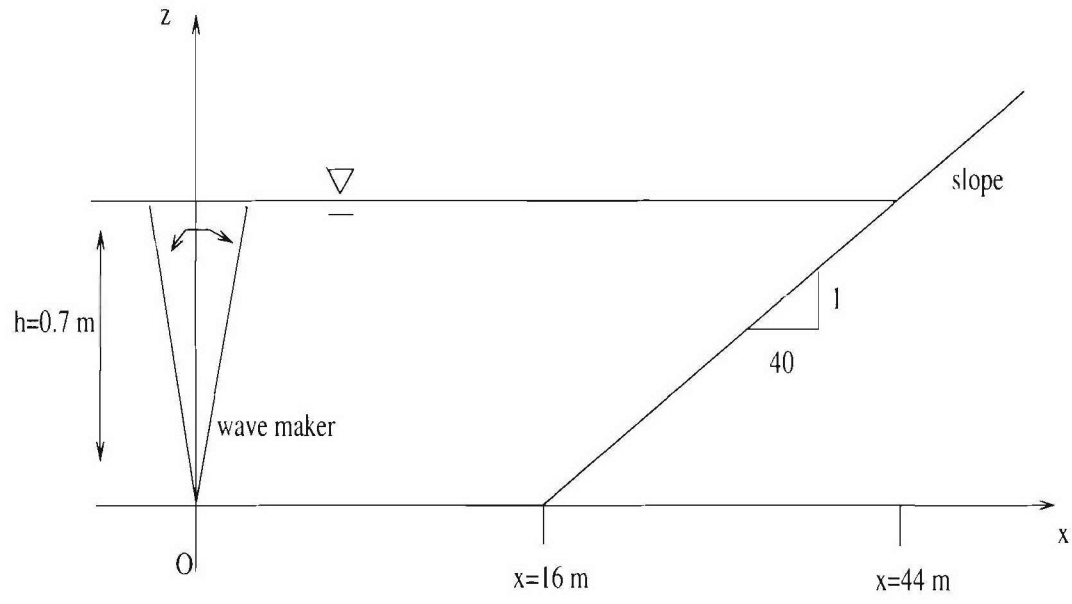

Figure 7.8: Stive and Wind 1986 undertow test

7.2 Stive and Wind (1986) Undertow Test

A test of the undertow simulation against the experiments of Stive and Wind (1996) is carried out here. The physical geometry of the experiments is shown in figure 7.8. The experiments are conducted on a sloping beach with slope of $1 : 40$, with incident wave height $H_0 = 0.145m$, period $T = 1.79$sec , deep end depth $h = 0.7m$, shore line located at $x = 44m$ and breaking point at $x_b = 34.5m$ measured from the location of the wave maker. Six experimental gages are located at ($x = 36.51m$, $37.49m$, $38.47m$, $39.45m$, $40.43m$, $41.41m$) with measured mean bottom return current velocity ($\bar{u_b} = -0.084, -0.067, -0.056, -0.053, -0.044, -0.045m/s$) (values are obtained from Stive and Wind (1986)).

In the simulation, the following parameters are used: $\Delta t = 0.01$sec, $\Delta x = 0.05m$, number of time steps $nt = 15000$, surface roller initial breaking angle $\phi_B = 16°$, roller final $\phi_0 = 10°$, surface roller transition time from $T^* = 0.8$sec, roller shape factor $f_{roller} = 1.0$ (please refer to the appendix for more details of surface roller description) and film layer thickness $\delta_R = 0.001m$ for simulation of moving shore line.

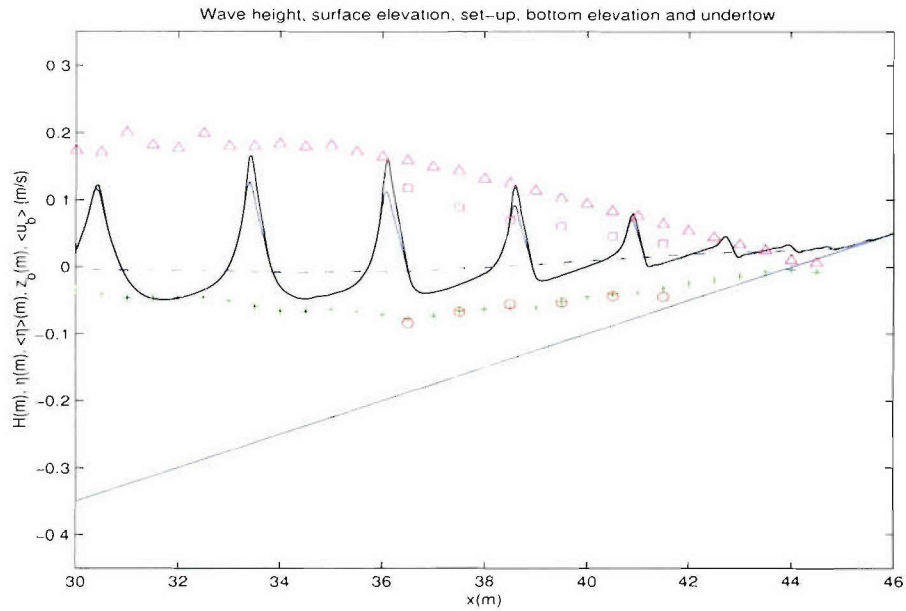

Figure 7.9: Model and data comparison of the Stive and Wind (1986) undertow test: free surface η (solid), bottom elevation z_b (solid), model undertow $< u_b >$ (plus), measured undertow $< u_b >$ (circle) model wave height (triangle), measured wave height (square) and model set up $< \eta >$ (dash-dot)

Figure 7.9 shows the simulated wave height, the measured wave height, a snap shot of wave surface elevation with roller geometry, the model wave set up, the model mean bottom velocity and the measured mean bottom velocity (undertow). The model captures the correct wave breaking location and the undertow rate well. Wave set up is also evident from the figure.

Figure 7.10 a) shows a snap shot of the bottom velocity. The predicted instantaneous bottom velocity is smooth throughout the domain. Whereas if we use the method in Long and Kirby (2003), in which the bottom velocity is obtained by subtracting roller flux contribution $MI_r/(h+\eta)$ from the bottom velocity predicted from the Wei et al. (1995) Boussinesq equation, the resulting reconstruction of instantaneous bottom velocity has non-physical negative spikes corresponding to the roller. These spikes will affect the prediction of both bottom velocity skewness and asymmetry, which are very important for bed load sediment transport prediction. Here, in the new model FUNWAVE1D2.0 we

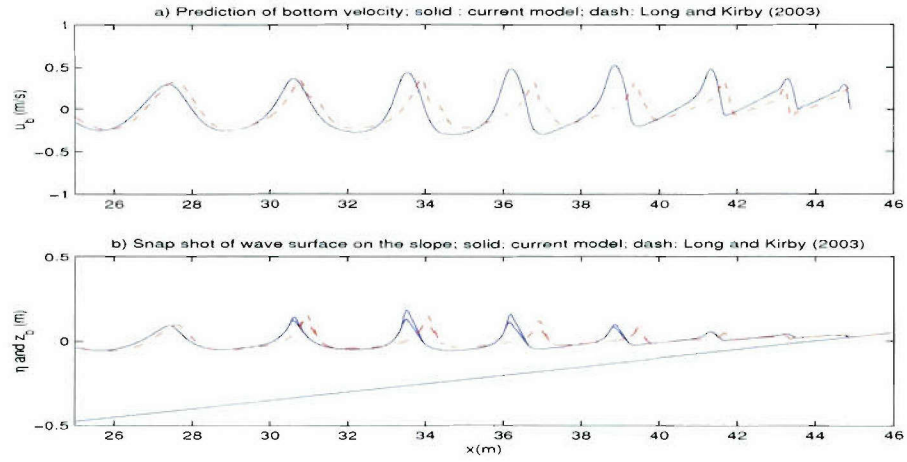

Figure 7.10: Snap shot of bottom velocity and surface elevation; solid : FUNWAVE1D2.0 model; dash: Long and Kirby (2003)

include M_r in the momentum equation directly, and it contributes to the return flow in M_w. The effect of the second order dispersion terms in the relationship between M_w and $\tilde{u}$ (equivalent to u_α in Wei et al. (1995) equation) eliminates the spikes in $\tilde{u}$ and the bottom velocity u_b. From figure 7.10 b), the new model overpredicts the wave height in the surfzone compared to Long and Kirby (2003). This is due to the inclusion of roller flux in the momentum equation and the undertow current actually modifies the dispersion relationship in the surfzone and shortens the wave length of waves. On the other hand, the effect of currents on waves is not included in Long and Kirby (2003). From figure 7.9, the model wave height is also higher than the measured data. The reason for this overprediction is probably due to the Doppler effects of undertow on waves.

7.3 Solitary Wave Run up Test

In this section, we test the wet-dry scheme using the Synolakis (1987) experimental data. Two tests corresponding Figure 6 and Figure 9 in Synolakis (1987) are conducted. The first one is a non-breaking solitary wave run up on a $1 : 19.85$ sloping beach with a constant depth ($d = 0.39m$) end. The second test is a breaking solitary wave run up on the same bathymetry where back wash breaking occurs during the downrush

phase and no breaking occurs during the uprush phase. For both of the non-breaking wave case and the breaking case, the model runs use $dt = 5.112498 \times 10^{-4}$sec, $\Delta x = 0.01m$ and film thickness $\delta_R = 0.001m$.

Figure 7.11 shows the model and data comparison of the non-breaking wave run up case corresponding to the figure 6 of Synolakis (1987). 10 snap shots of the surface elevation at different times $t/\sqrt{g/d} = 25, 30, 35, 40, 45, 50, 55, 60, 65, 70$ are shown in the figure. The dashed lines show the results given by Synolakis (1987) based on nonlinear shallow water wave theory. Figure 7.12 shows the model and data comparison of the breaking wave run up case corresponding to figure 9 of Synolakis (1987), in which 8 snap shots of the surface elevation at different times $t/\sqrt{g/d} = 20, 26, 32, 38, 44, 50, 56, 62$ are plotted. Again the dashed lines show the results given by Synolakis (1987) based on nonlinear shallow water wave theory. The figures indicate that the analytical solution of nonlinear water wave equation given by Synolakis (1987) overpredicts the wave run up and run down, i.e., the maximum run up and maximum run down are overpredicted. On the other hand the model results follow well with the experimental data except during down rush breaking time of the breaking wave case (figure 7.12 (h)). The overprediction of the run up and run down by analytical nonlinear wave theory could be due to the fact that no bottom friction is considered in the analytical solution. This is also pointed out by Lynett et al. (2002) in their simulation using an extrapolation method, in which it is found that using a friction coefficient between $f_b = 10^{-3}$ and $f_b = 10^{-2}$ is adequate for predicting the run up/run down magnitude for the experimental configuration considered. In our model, the inclusion of bottom friction is automatically considered according to the wet/dry scheme discussed in previous chapters. The largest discrepancy between the present model results and the experimental data occurs in the down rush breaking phase. This is due to the breaking wave treatment in the present model may not be accurate for down rush wave breaking events.

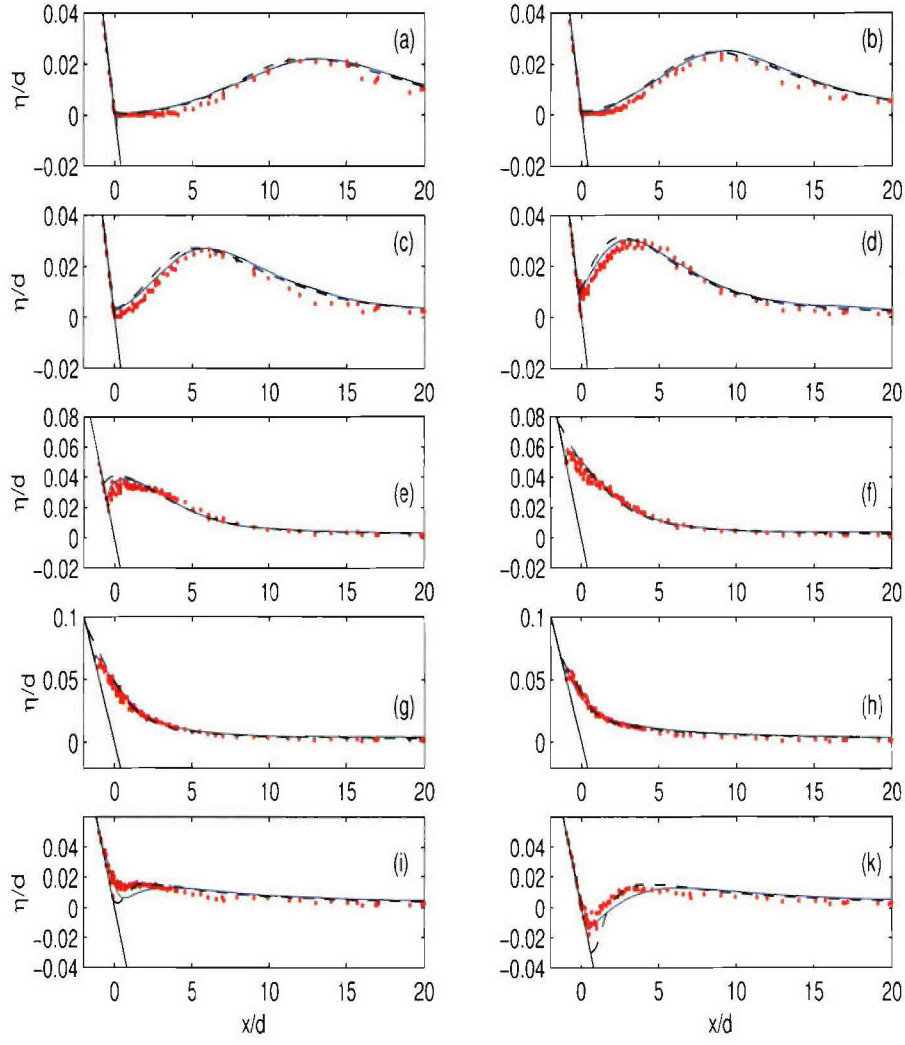

Figure 7.11: The climb of a solitary wave with $H/d = 0.019$ up a $1 : 19.85$ beach; corresponding to Synolakis (1987) figure 6; (a) $t/\sqrt{g/d} = 25$, (b) $t/\sqrt{g/d} = 30$, (c) $t/\sqrt{g/d} = 35$, (d) $t/\sqrt{g/d} = 40$, (e) $t/\sqrt{g/d} = 45$, (f) $t/\sqrt{g/d} = 50$, (g) $t/\sqrt{g/d} = 55$, (h) $t/\sqrt{g/d} = 60$, (i) $t/\sqrt{g/d} = 65$, (k) $t/\sqrt{g/d} = 70$; dots: measured value ; solid line: model value; dash-line: nonlinear shallow water wave theory by Synolakis (1987)

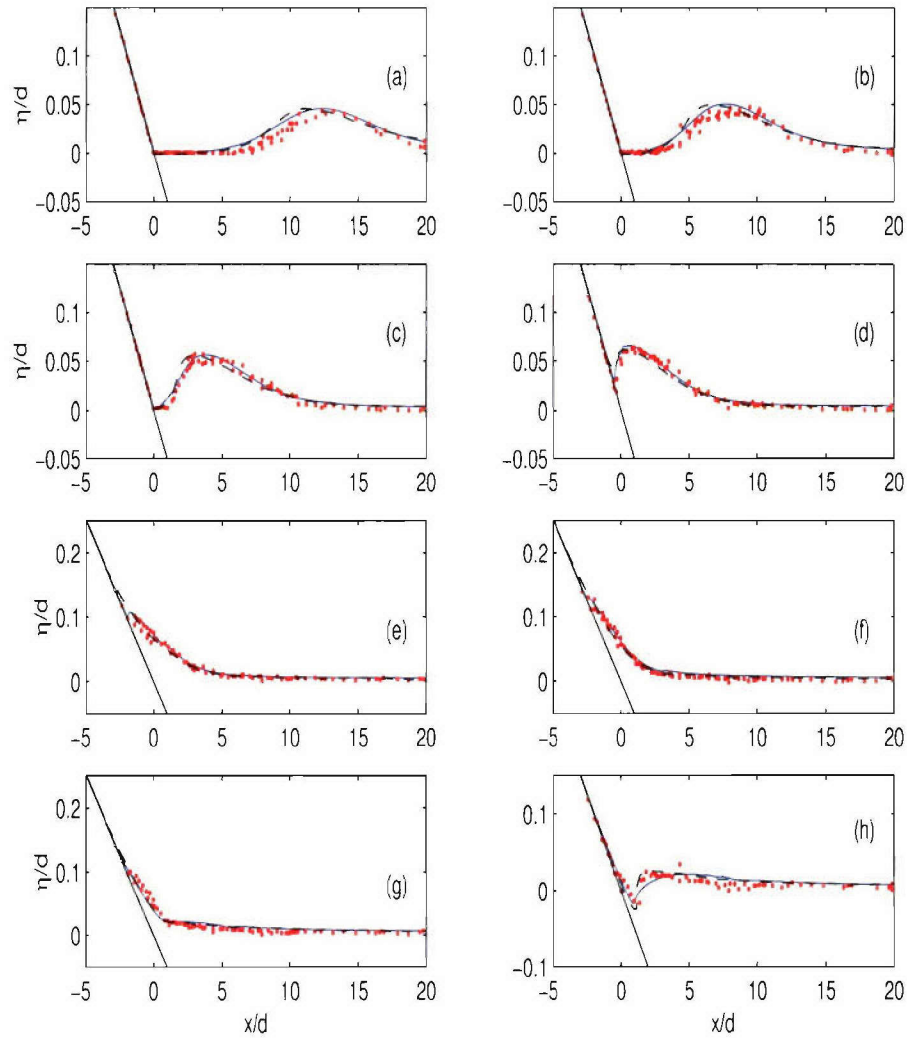

Figure 7.12: The climb of a solitary wave with $H/d = 0.04$ up a $1 : 19.85$ beach; corresponding to Synolakis (1987) figure 9; (a) $t/\sqrt{g/d} = 20$, (b) $t/\sqrt{g/d} = 26$, (c) $t/\sqrt{g/d} = 32$, (d) $t/\sqrt{g/d} = 38$, (e) $t/\sqrt{g/d} = 44$, (f) $t/\sqrt{g/d} = 50$, (g) $t/\sqrt{g/d} = 56$, (h) $t/\sqrt{g/d} = 62$; dots: measured value ; solid line: model value; dash-line: nonlinear shallow water wave theory by Synolakis (1987)

7.4 Waves in a Circular Channel

Following Shi et al. (2001) we test the model with wave propagation within a circular channel of constant depth. Let r_1 and r_2 be the inner and outer radius of the channel respectively, with $r_1 = 75m$, $r_2 = 200m$ in this case. The depth of the channel is $4m$. The coordinate transformation can be described by

$$\xi = \xi_1 = \frac{r_2 - \sqrt{x^2 + y^2}}{r_2 - r_1} \tag{7.1}$$

$$\eta = \xi_2 = \frac{\tan^{-1}(\frac{y}{x})}{\pi} \tag{7.2}$$

Then the Cartesian coordinates are given by

$$x = \pm\sqrt{\frac{(r_2 - (r_2 - r_1)\xi_2)^2}{1 + \tan^2(\pi\xi_1)}} \tag{7.3}$$

$$y = x\tan(\pi\xi_1) \tag{7.4}$$

where when $\xi_1 \leq 0.5$, use '+', otherwise use '-'.

Figure 7.13 shows the model grid system. In the simulation, grid dimensions are set to be $mx = 251$ in the along channel direction (ξ) and $ny = 51$ in the radial direction (η). Waves with period 4sec and height $H_0 = 0.4m$ are generated from right inlet of the channel and propagate to the left along the channel. The modeling time step is $\Delta t = 0.1$sec. The model grid spacing and time step is twice as coarse than the computation by Shi et al. (2001). Here, the incident wave height is finite amplitude relative to water depth hence wave nonlinearity is not negligible and direct comparison to linear theory is not justified. Sponge layers are placed both behind the wave maker (not shown) and at the downstream end of the channel.

Figure 7.14 shows a snap shot of the surface elevation. The bending of the channel causes wave diffraction along the inner circle of the channel. The wall at the outer circle of the channel generates partial standing wave pattern and reflects wave energy further down the channel. Finally, wave energy concentrates at the outer arc close to the outlet.

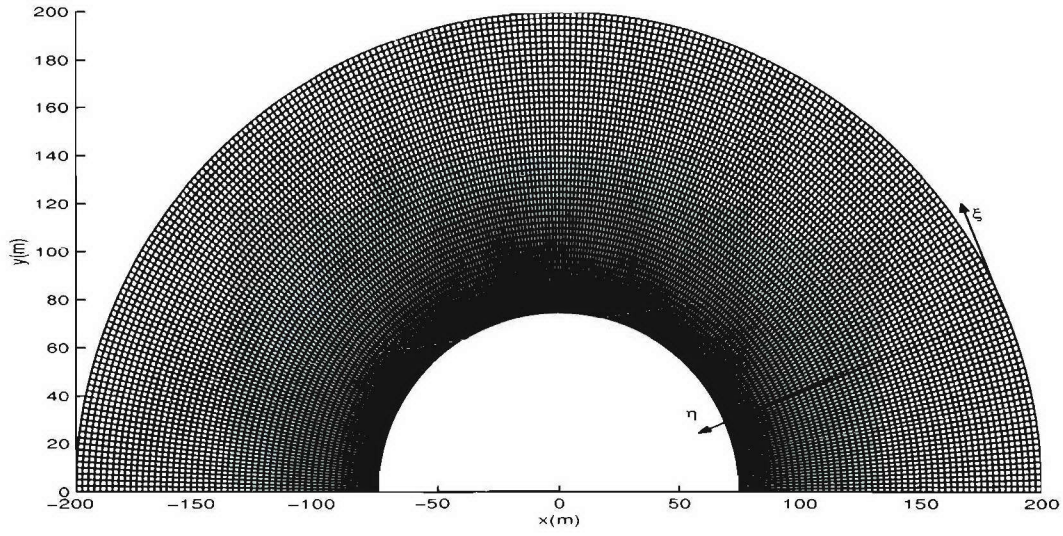

Figure 7.13: Curvilinear grid system for the circular channel test

Figure 7.15 shows the wave height distribution normalized by the incident wave height. The contours clearly show the distribution of wave energy. The area close to the top of the inner circle is well sheltered. But the area located near the outer circle and opposite to the incident waves has concentrated wave energy. The reflected wave energy reaches the outlet which is again reflected by the outer circle and the maximum normalized wave height there is about 0.8. This test demonstrates the model ability of simulating waves in domains with curved boundaries.

7.5 Wave Field on a Sloping Beach with Periodic Groins

As a last yet important example, we show the simulation of oblique wave propagation on a sloping beach with alongshore periodically placed groins (treated as vertical walls). The geometry of the bathymetry comprises a constant depth ($h = 4m$) offshore sea bed and a $1 : 20$ sloping beach with longshore uniformity and groins which are placed periodically with a distance of $50m$ from each other. Each groin extends $20m$ into the ocean from the still water shoreline. Oblique waves of period $T = 4$sec and height $H_0 = 0.5m$ are generated at $160m$ offshore. Two run cases with different approaching

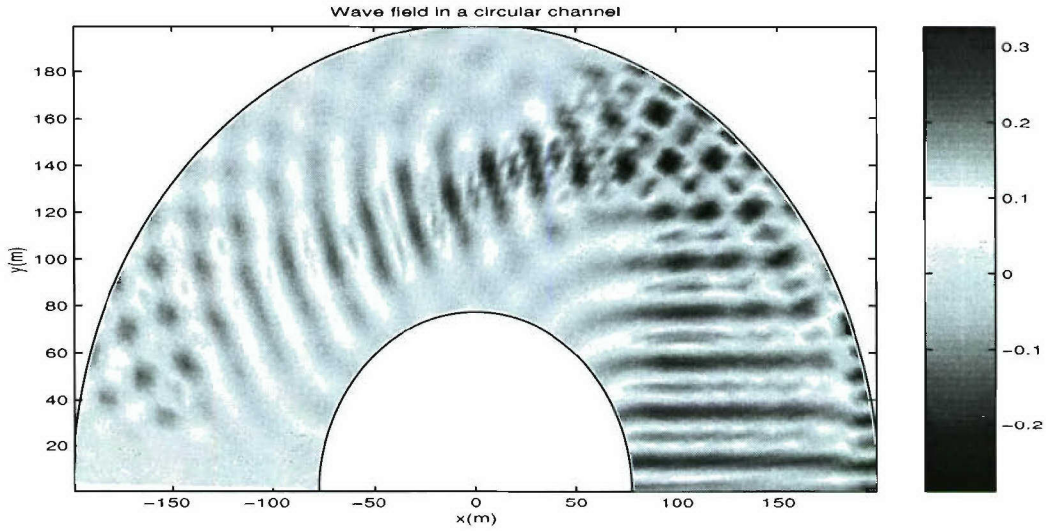

Figure 7.14: Computed surface elevation $\eta(m)$

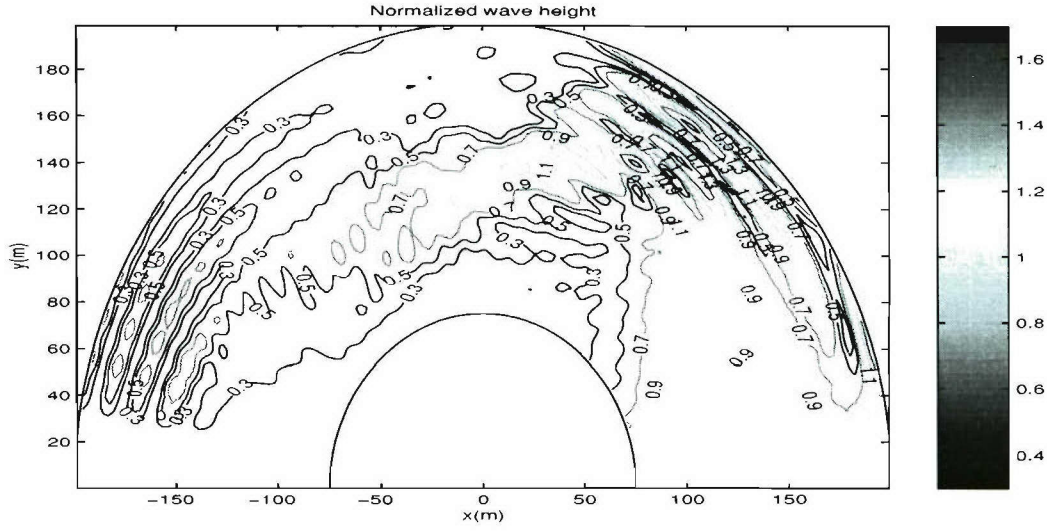

Figure 7.15: Computed wave height distribution normalized by the incident wave height (H/H_0)

angles relative to the shorenormal direction are conducted. Case a) has an approaching angle θ_0 of $30°$ and case b) has an approaching angle of $45°$. Periodic longshore boundary condition is imposed to mimic an infinitely long beach. In both cases, the model parameters are set to be $\Delta x = \Delta y = 1m$, $\Delta t = 0.1$sec. The simulation includes the shoaling, refraction, diffraction and reflection as well as swash motion of the waves.

Figure 7.16 shows a snapshot of the wave field for case a) with contours of water depth and groin layouts. Figure 7.17 shows a snapshot of the wave field for case b). 3D surface plots are also shown in figure 7.18 and 7.19 for case a) and b) respectively. The figures show clearly the wave refraction onto the beach and the diffraction and reflection close to the groins. The moving shore lines are also shown in figure 7.18 and 7.19. The waves reflected from the groins interact with the incident waves to form short-crest wave patterns. There are also noticeable wave crests (also called Mach stems) perpendicular to the groins which are due to nonlinear wave-wave interactions.

Figure 7.20 and 7.21 show the distribution of the wave height normalized by the incident wave height (H/H_0) of case a) for different horizontal (constant y coordinate) and vertical (constant x coordinate) sections respectively. In the figure 7.20, the cross section $y = 78m$ is immediately next to the second groin in the figure 7.16, and the rest of the sections are $10m$ next to each other consecutively except that the last section $y = 124m$ is immediately to the south of the third groin. The bottom slope starts from $x = 100m$ and ends at $x = 200m$ with the still water shoreline located at $x = 180m$. Waves shoal on the slope up to $x = 160m$ where the depth is $1m$ and the waves are reflected and diffracted by the groins. The shadow areas of the groins are slightly sheltered. Wave energy is dissipated by wave breaking further onshore ($x > 165m$). The cross section $y = 118m$ and $y = 124m$ are at the south side of the third groin and the waves there are reflected and the wave height is larger than the other sections. In the figure 7.21, wave height distribution of vertical cross sections clearly shows the shoaling and reflection as well as the wave dissipation as waves approach the groins and the shore line. At $x =$

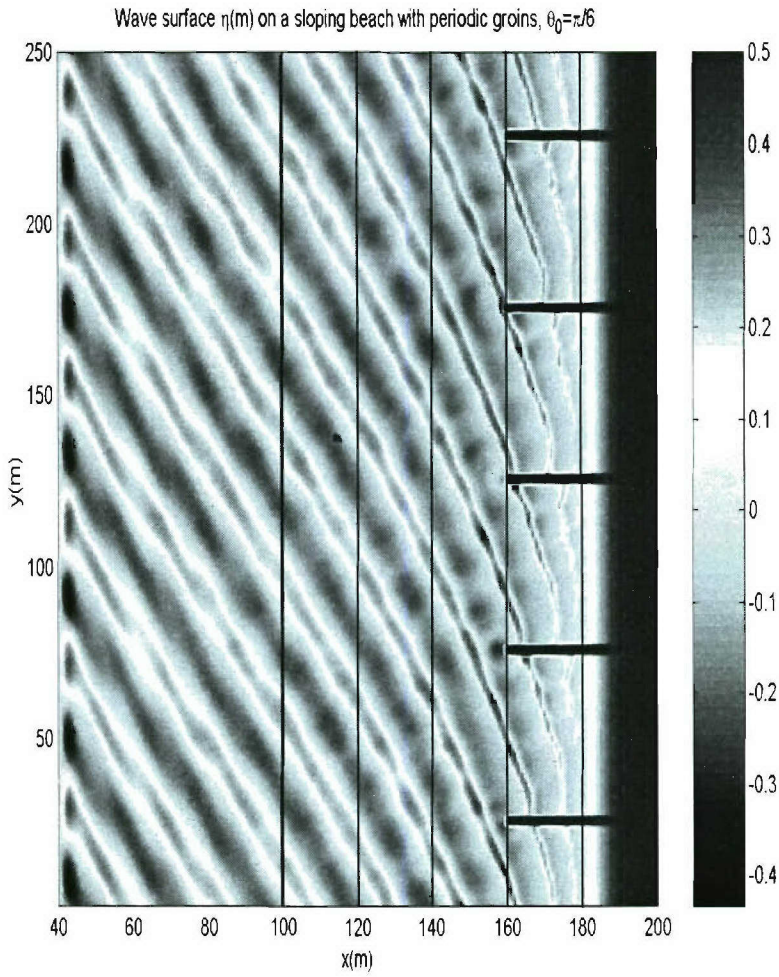

Figure 7.16: Wave field on a sloping beach with periodic groins, case a) $\theta_0 = 30°$; The shore parallel solid lines show the depth contours of $-4m$, $-3m$, $-2m$, $-1m$, $0m$ respectively from the left to the right; Still water level shoreline is located at $x = 180m$.

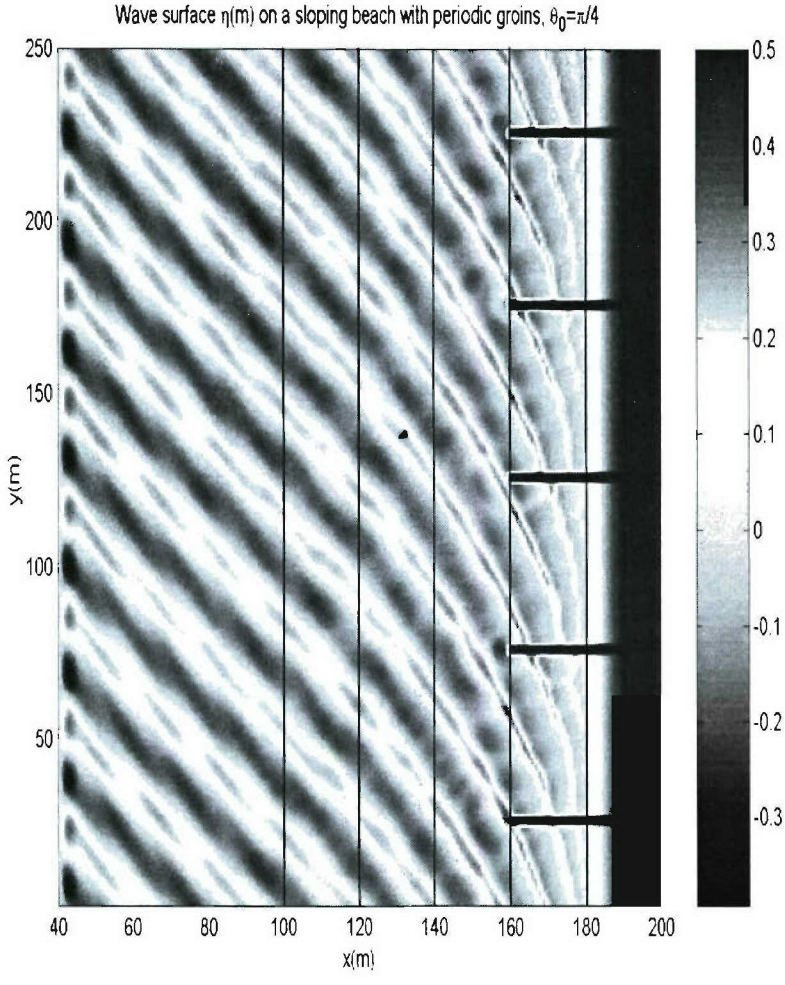

Figure 7.17: Wave field on a sloping beach with periodic groins, case b) $\theta_0 = 45°$; The shore parallel solid lines show the depth contours of $-4m$, $-3m$, $-2m$, $-1m$, $0m$ respectively from the left to the right; Still water level shoreline is located at $x = 180m$.

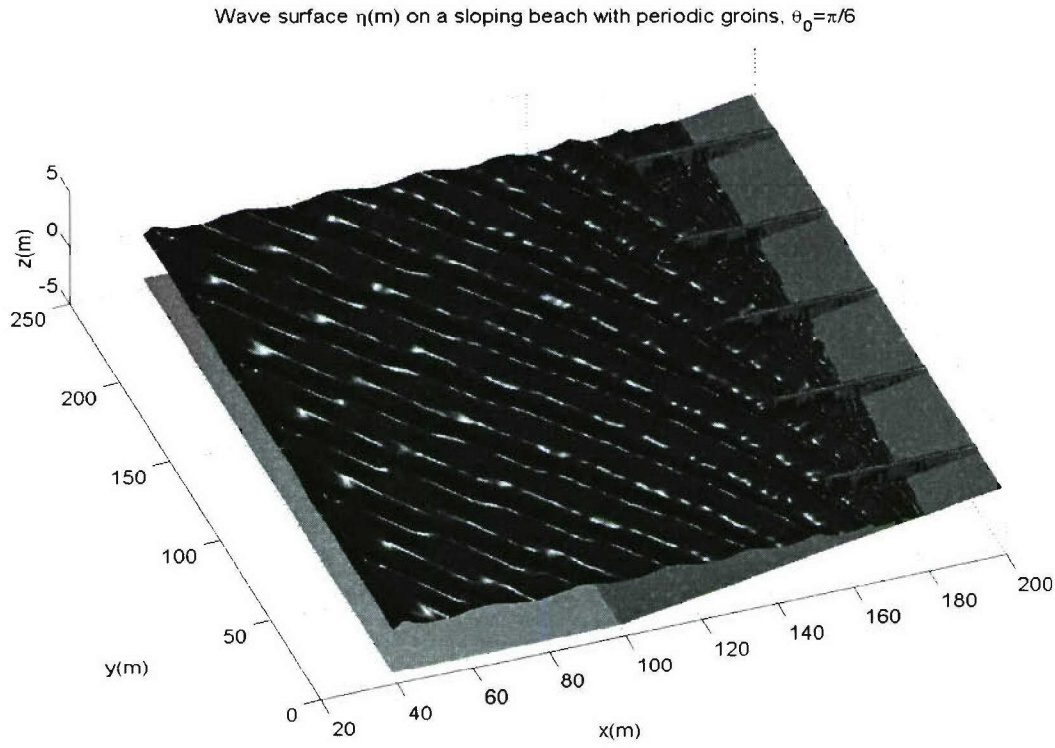

Figure 7.18: Surface elevation and bathymetry of case a) $\theta_0 = 30°$

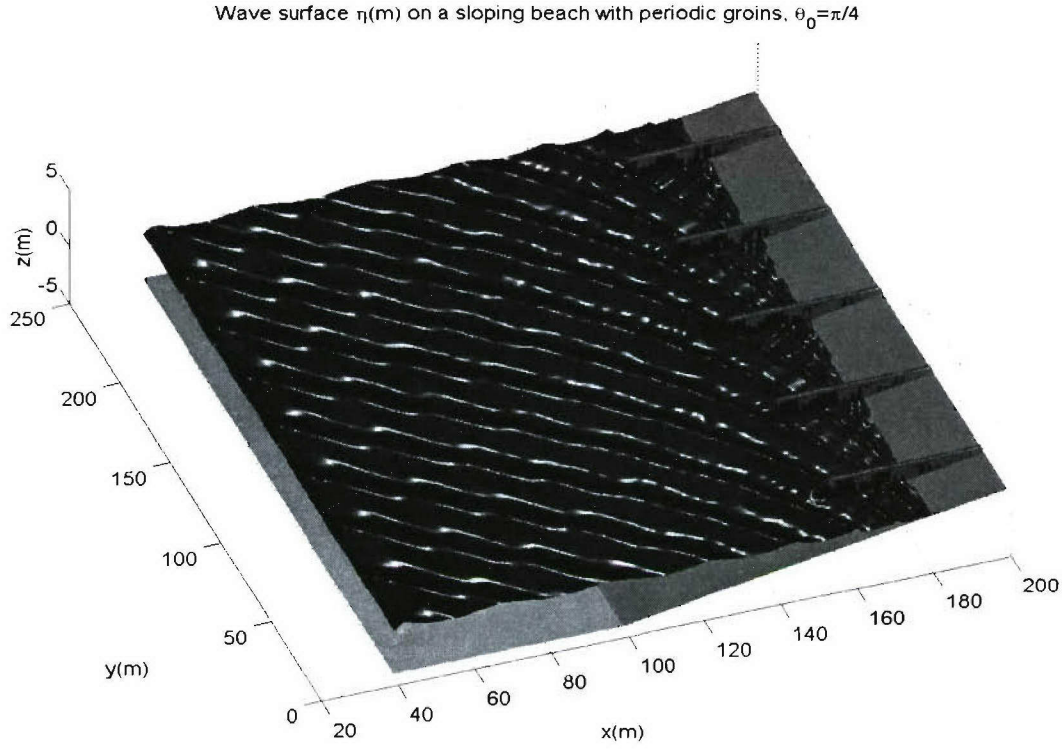

Figure 7.19: Surface elevation and bathymetry of case b) $\theta_0 = 45°$

$150m$ the wave height is dominated by shoaling effects due to the slope from $x = 100m$ to $x = 150m$ although partial standing wave patterns are also pronounced. At $x = 155m$, more clear partial standing wave pattern are evident such that the wave height distribution has more shorter scale variations. At $x = 160m$, the groins locations are shown as wave height being zero. Standing wave pattern is very well organized and there 9 anti-nodes between two adjacent groins. The wave height immediately to the south of the groin is much larger than the wave height immediately to the north of the groin due to the reflection and sheltering of the south side and the north side respectively. From $x = 165m$ to $x = 175m$, the wave energy is significantly dissipated due to wave breaking. Similar plots of case b) ares shown in figure 7.22 and 7.23. The wave height distribution is similar to case a) yet with a few noticeable differences: i) the wave shoaling from $x = 100m$ to $x = 150m$ of case b) is not as large as case a) mainly due to 45 degree incident waves experience a milder slope in the wave ray direction; ii) the number of anti-nodes between the groins is 11 for case b) and 10 for case a) due to shorter wave length in y direction for case b) than for case a).

Figure 7.24 shows the depth and time averaged velocity field between two groins for case a). There is a major cells at the south side of the groin from which waves are reflected. This circulation can possibly lead to scour. A streak of flow is also meandering offshore along the tip of the groin. In the shadowed zone, circulation is relatively weaker and sediments may deposit.

This example shows that the FUNWAVE2D2.0 model is capable of simulating waves with complex nearshore geometries.

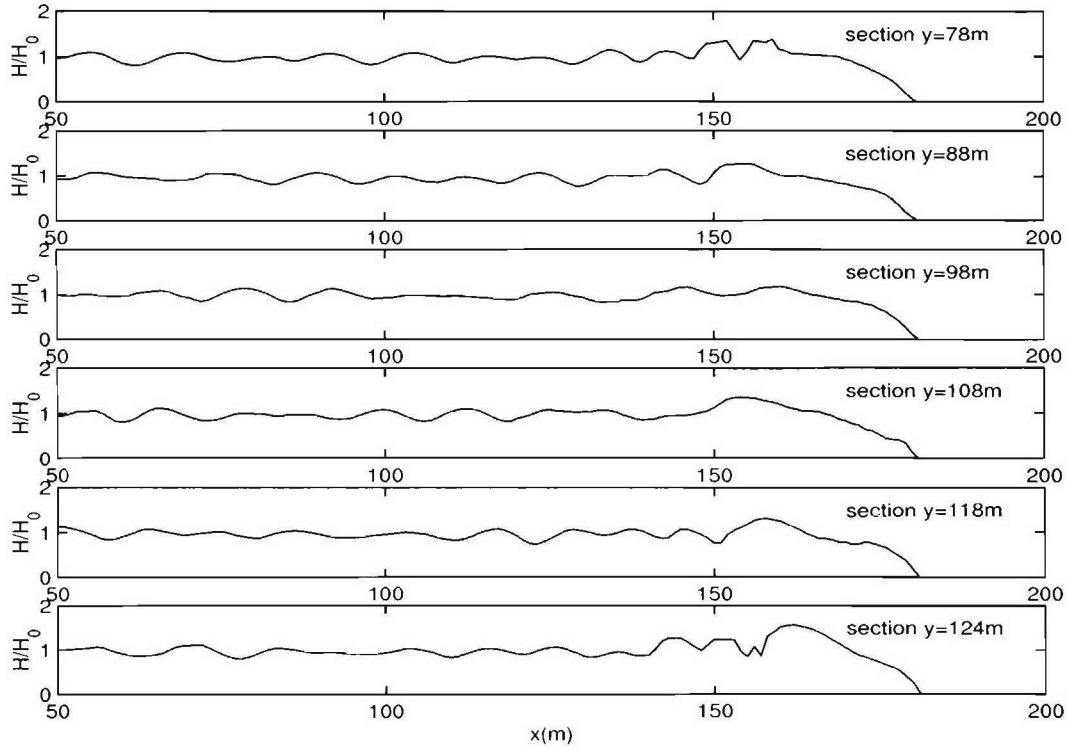

Figure 7.20: Normalized wave height distribution H/H_0 of 6 horizontal sections of case a) $\theta_0 = 30°$

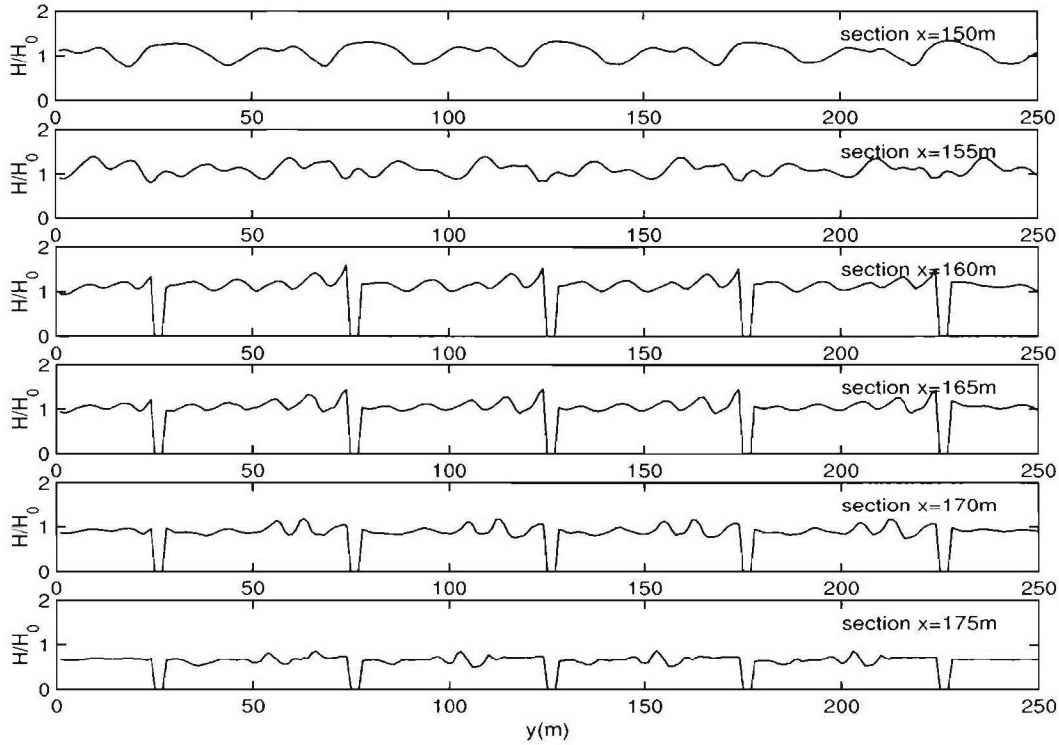

Figure 7.21: Normalized wave height distribution H/H_0 of 6 vertical sections of case a) $\theta_0 = 30°$

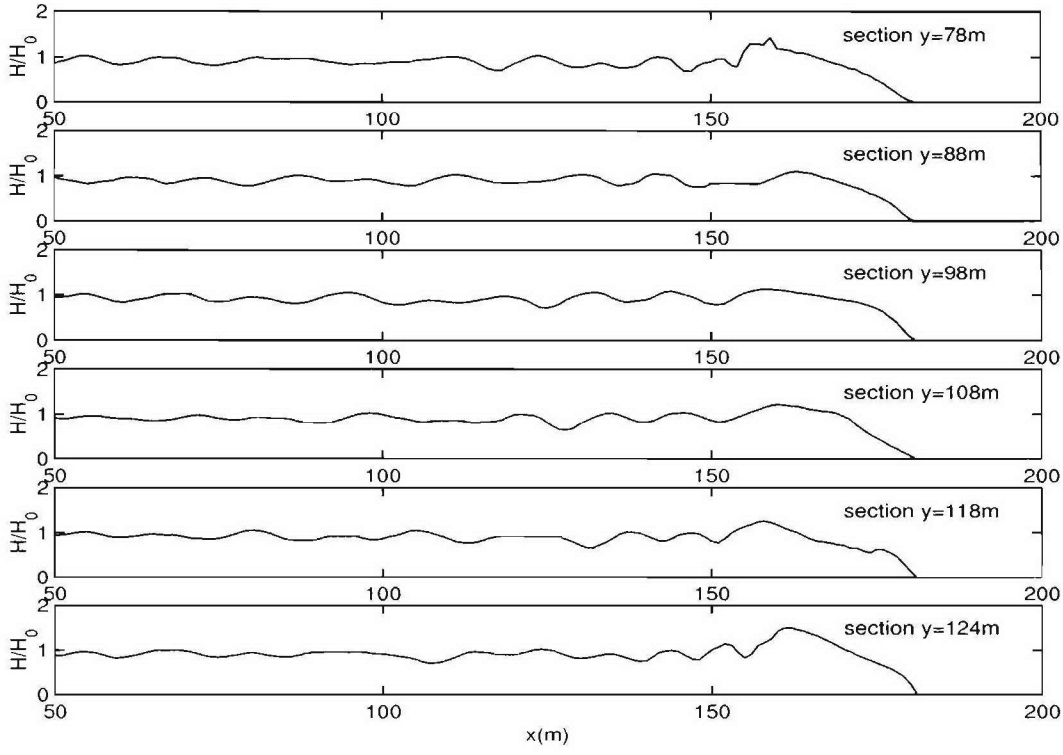

Figure 7.22: Normalized wave height distribution H/H_0 of 6 horizontal sections of case b) $\theta_0 = 45°$

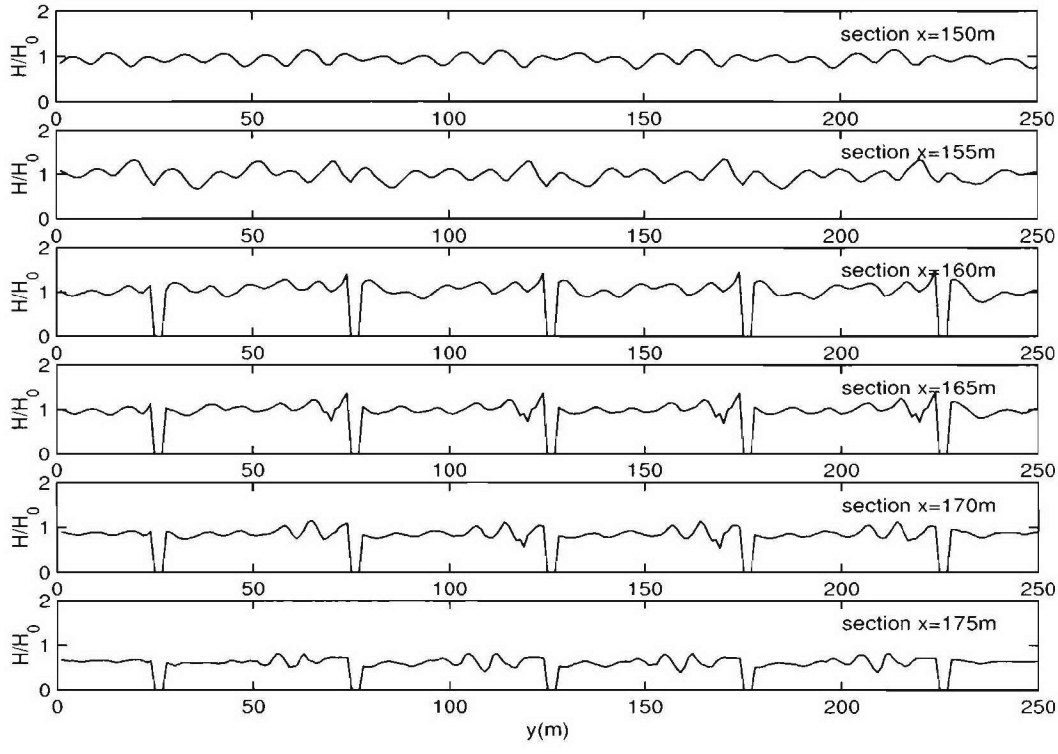

Figure 7.23: Normalized wave height distribution H/H_0 of 6 vertical sections of case b) $\theta_0 = 45°$

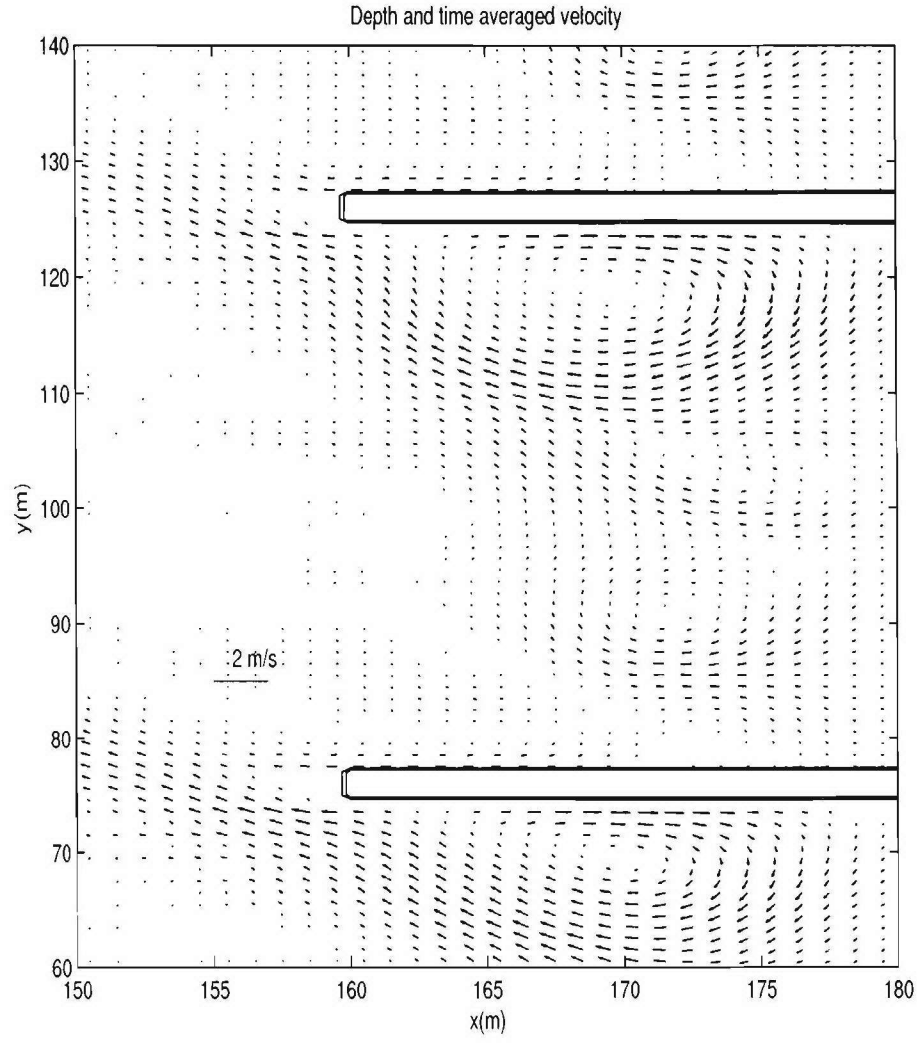

Figure 7.24: Depth and time averaged current between the groins for case a) $\theta_0 = 30°$

Chapter 8

MODEL TESTS II: SEDIMENT TRANSPORT TEST

In this chapter, we focus on testing the overall coupled hydrodynamic and sediment transport models using field data and laboratory data. First, the sand bar migration events occurring in Duck'94 field experiment are investigated in detail. Both onshore bar migration and offshore migration events are modeled using FUNSEDI1D model comprised of FUNWAVE1D2.0, bottom boundary layer model, sediment transport model using modified Bagnold formula and Meyer-Peter Müller formula and morphological model using the Euler-WENO scheme. Second, the LIP11D laboratory experiments are also modeled to assess the model applicability.

Two sets of sediment transport formulations are tested. Model A uses the coupled Boussinesq model and an un-averaged Bagnold sediment transport model based on the Boussinesq model predicted bottom velocity with the ad-hoc free stream acceleration term proposed by Long and Kirby (2003). Model B uses the coupled Boussinesq model and Meyer-Peter-Müller (1948) sediment transport model with bottom shear stress given by the boundary layer model for the wave-related transport rate and a Bailard (1981) formula for free stream mean flow related transport rate as shown in Hsu et al. (2005).

In model A, the volumetric transport rate is calculated by

$$q_{tot} = \frac{i_{tot}}{g(\rho_s - \rho)} \tag{8.1}$$

where

$$i_{tot} = i_b + i_s + i_a \quad = \quad \rho C_f \frac{\epsilon_B}{\tan\phi}[|u_b|^2 u_b - \frac{\tan\beta}{\tan\phi}|u_b|^3]$$

$$+ \quad \rho C_f \frac{\epsilon_S}{w_{fall}} [|u_b|^3 u_b - \frac{\epsilon_S \tan\beta}{w_{fall}} |u_b|^5]$$
$$+ \quad g(\rho_s - \rho) K_a (|u_{b,t}| - u_{btcr}) \text{sign}(u_{b,t}) \tag{8.2}$$

where i_b, i_s are immersed weight sediment transport rate for bed load and suspended load respectively, i_a is the accleration contribution, φ is the internal angle of friction, $\tan\beta$ is the slope of the bed level, C_f is friction coefficient, w_{fall} is the sediment fall velocity, u_b is the bottom velocity. ϵ_B and ϵ_S are effectiveness coefficients for bed load and suspended load. $u_{b,t}$ is the acceleration of instantaneous free stream velocity u_b, and u_{btcr} is a threshold value. i_{tot} is the total immersed weight sediment transport rate. K_a is an empirical dimensional coefficient. The last term is set to zero when $|u_{b,t}| - u_{btcr} \leq 0$

In model B, the volumetric transport rate is calculated by

$$q_{tot} = q_w + q_c \tag{8.3}$$

where q_w corresponding to wave-related transport rate is driven by bottom wave boundary layer shear stress, q_c is associated with mean velocity outside of the bottom boundary layer (Hsu et al., 2005). q_w is calculated according to Meyer-Peter-Müller formula

$$\Psi = A(\theta - \theta_c)^b \tag{8.4}$$

where Ψ is the normalized transport rate, θ is the Shields parameter, θ_c is the threshold value of the Shields parameter for initiation of sediment transport, A and b are dimensionless constants, with typical values $A = 11$ and $b = 1.65$ that are used below.

$$\Psi = q_w / (d\sqrt{(s-1)gd}) \tag{8.5}$$

$$\theta = \tau_b / ((\rho_s - \rho) g d) \tag{8.6}$$

where τ_b is the instantaneous bed shear stress obtained from solving the wave bottom boundary layer instead of using quadratic correlations. q_c is calculated according to the Bailard (1981) formula (Hsu et al., 2005).

$$q_c = \frac{\rho}{g(\rho_s - \rho)} C_f \frac{\epsilon_B}{\tan\phi} [|u_b|^2 \overline{u_b} - \frac{\tan\beta}{\tan\phi} |u_b|^3]$$

$$+ \quad \frac{\rho}{g(\rho_s - \rho)} C_f \frac{\epsilon_S}{w_{fall}} [|u_b|^3 \overline{u_b} - \frac{\epsilon_S \tan\beta}{w_{fall}} |u_b|^5] \tag{8.7}$$

where $\overline{u_b}$ is the mean bottom velocity based on a time average of instantaneous bottom velocity for an appropriate period of time.

8.1 Duck'94 Field Experiment Test

As an example of sand bar migration in a real coastal setting, the Duck '94 experiment is well documented and presents very informative data for testing the model in this research. A number of studies have been made on the significant bar migration processes during the 3 month experiment. Typically, onshore bar migrations were observed under intermediate wave conditions, while large offshore bar migrations were observed under strong storm wave conditions. Previous research by Gallagher et al. (1998) indicated that the offshore bar migration can be qualitatively modeled with a BBB type model. Onshore migration is associated strongly with flow acceleration (Elgar et al., 2001) and free stream pressure gradient, and the BBB models did not capture it.

8.1.1 Layout of the experiments and wave conditions

Figure 8.1 shows a basic lay out of the experiment. The contours show the bathymetry which clearly indicates the existence of a linear longshore sand bar. The open squares below profile line number 245 are the cross-shore deployed pressure gages and current meters. The open circles adjacent to the pressure gages are sonar altimeters to measure bottom elevation. Figure 8.2 shows the bar crest migration history for the most prominent nearshore bar (from Elgar et al., 2001). The top panel shows the time history of significant wave height offshore from an measurement array located at 8 meter depth isobath. It indicates that there were 4 major storms that took place at about 33, 52, 62 and 71 days respectively after August 1, 1994. In the bottom panel, the cross shore location of the bar crest is shown by the dark thick line, with the color indicating the acceleration skewness estimated from near bottom velocities. It has been pointed out by Elgar et al. (2001) that

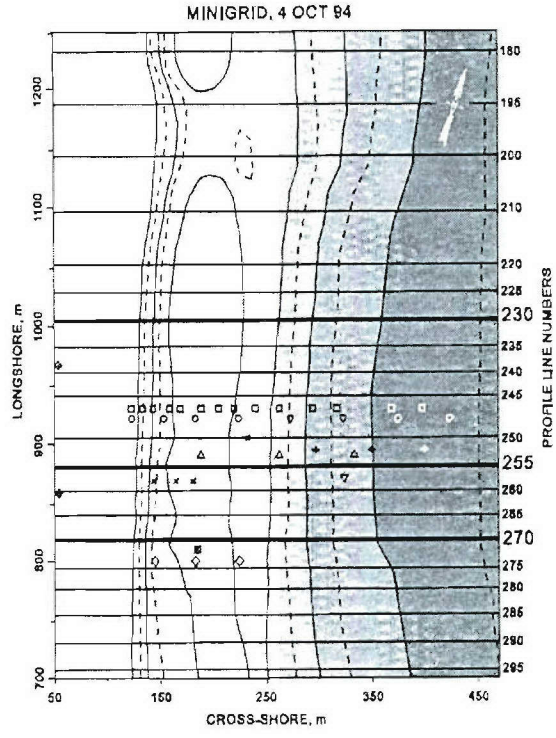

Figure 8.1: Duck 94 experiment layout (open squares: pressure gages; circles: sonar altimeters; from Stauble and Cialone, 1997)

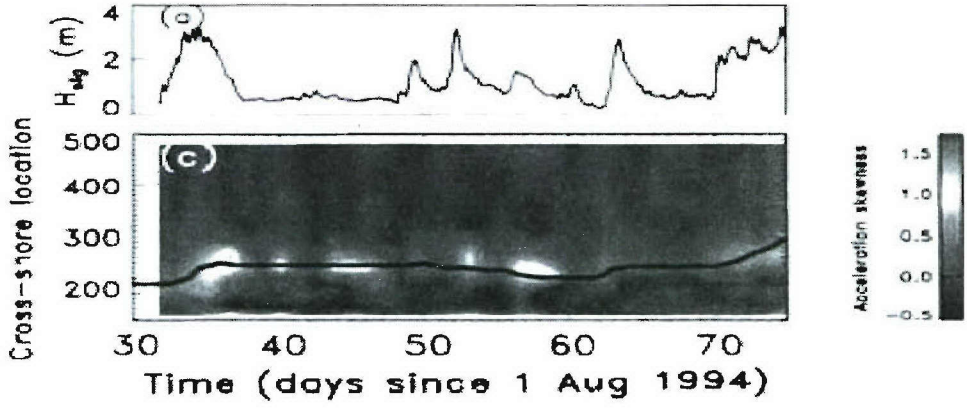

Figure 8.2: Bar migration history (bar crest location indicated by thick solid curve, modified from Elgar et al., 2001)

Gage	x(m)	y(m)	Gage	x(m)	y(m)
s02	135.07	930.06	s06	169.88	930.09
s03	145.42	930.84	s05	170.08	930.09
s04	160.76	930.64	s12	205.42	930.45
s08	168.64	930.06	s13	220.23	930.41
s11	169.47	930.87	s14	240.55	930.00
s07	169.48	930.08	s15	264.70	930.44
s09	169.49	929.47	s17	320.23	930.67
s10	169.49	929.67	s18	398.43	931.12

Table 8.1: Sonar altimeter gage locations during September 21 to September 30 and October 10 to October 16 in the Duck'94 field experiments

Gage	x(m)	y(m)	Gage	x(m)	y(m)
p1	124.94	929.82	p14	240.55	928.72
p2	135.01	928.88	p15	264.70	929.06
p3	145.42	929.56	p16	295.8	929.94
p4	160.77	929.36	p17	320.37	929.39
p5	169.50	928.44	p45	370.08	928.03
p23	190.20	929.92	p18	398.39	929.85
p26	190.20	929.92	p19	480.34	930.57
p12	205.34	929.17	p87	884.11	919.79
p13	220.23	929.13			

Table 8.2: Pressure gage locations during September 21 to September 30 in the Duck'94 field experiments

the offshore migration events were associated with strong undertow induced by breaking waves in energetic storm conditions. There was a major onshore bar migration event around September 20 to September 30 when waves were moderately energetic but the acceleration skewness was relatively high.

The 16 sonar altimeter gage locations (local Field Research Facility (FRF) coordinates) are shown in table 8.1. The pressure gage locations are shown in table 8.2 and 8.3 where gage p16 was located at $(295.80, 929.94)$ in September and moved to $(252.03, 917.26)$ during from 22:00, October 1 to 22:00, October 27. The current meters are mostly co-located with the pressure with some exceptions are shown in table 8.4.

Gage	x(m)	y(m)	Gage	x(m)	y(m)
p1	124.94	929.82	p14	240.55	928.72
p2	135.01	928.88	p16	252.03	917.26
p3	145.42	929.56	p15	264.70	929.06
p4	160.77	929.36	p17	320.37	929.39
p5	169.50	928.44	p45	370.08	928.03
p23	190.20	929.92	p18	398.39	929.85
p26	190.20	929.92	p19	480.34	930.57
p12	205.34	929.17	p87	884.11	919.79
p13	220.23	929.13			

Table 8.3: Pressure gage locations during October 10 to October 16 in the Duck'94 field experiments

Gage	x(m)	y(m)	Gage	x(m)	y(m)
u02	135.04	929.69	u16	296.40	931.31
u03	145.42	930.17	u17	320.30	930.00
u04	160.76	929.98	u18	398.41	930.46
u05	169.49	929.08	u19	480.34	930.00
u12	205.38	929.79	u22	189.87	930.74
u13	220.23	929.75	u44	370.15	928.63
u14	240.55	929.33	u87	884.11	915.44
u15	264.70	929.77			

Table 8.4: Near bed cross shore current meter (u-gage) locations during September 21 to October 16 in the Duck'94 field experiments; (alongshore current meters (v-gage) are co-located with the cross shore current meters)

Figure 8.3 and 8.4 show the peak wave period and significant wave height at gage p19 versus time in September, 1994 and October, 1994 respectively. The data are plotted every 170 minutes and connected using a solid line. On some of the days, the data were missing due to gage malfunction.

The current meters recorded both the alongshore and cross shore currents. The following figures 8.5 to 8.17 show the time history of daily averaged alongshore and cross shore currents as well as the bed level at 1:00am of each respective day during from September 21 to September 26 when a major onshore bar migration event took place and from October 11 to October 16 when a major offshore bar migration event took place (data courtesy of S. Elgar).

To show more clearly the near bottom currents landward of the bar trough, the alongshore and cross shore mean currents (averaged every 17 minutes) of gage p12 (FRF coordinate (205.38, 929.79), collocated with velocity gage u12) and p13 (FRF coordinate (220.23, 929.75), collocated with velocity gage u13) are shown in the figure 8.18 and 8.19 for September and 8.20 and 8.21 for October. From figure 8.18 and 8.19, during the period of September 21 to September 27, both the alongshore current and the cross shore current near the bottom of the bar trough are in moderate magnitude except on day September 22 when one of the major storms took place (see figure 8.2 and 8.3) and the observed cross shore undertow current (offshore near bed current) exceeded $0.4m/s$ and the alongshore current exceeded $0.8m/s$ toward north direction. The gage p13 is closer to the bar crest, and the recorded undertow currents were less than $0.3m/s$ from day 23 to 27. The alongshore currents of gage p13 were on the order of $0.2m/s$ from day 23 to 27. On the other hand, from figure 8.20 and 8.21, when a large storm struck the region and offshore bar migration was observed, both the undertow and the alongshore currents are quite large. The cross shore undertow currents exceeded $0.3m/s$ for the majority of the time from October 10 to October 17. The alongshore currents reached $1m/s$ at both gages p12 and p13 and they changed direction from toward south to toward

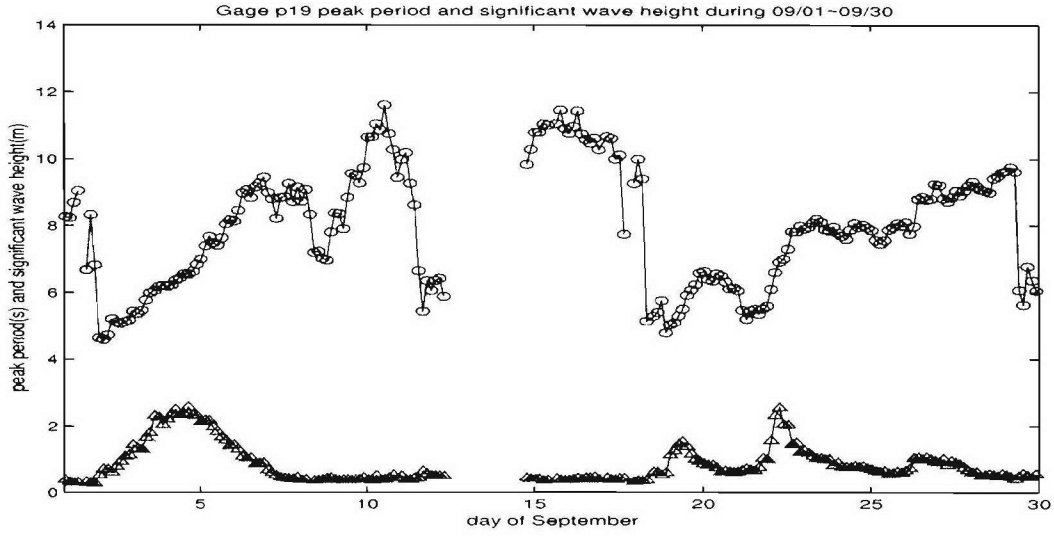

Figure 8.3: Peak wave period (circles) and significant wave height (triangles) at gage p19 in Sept., 1994

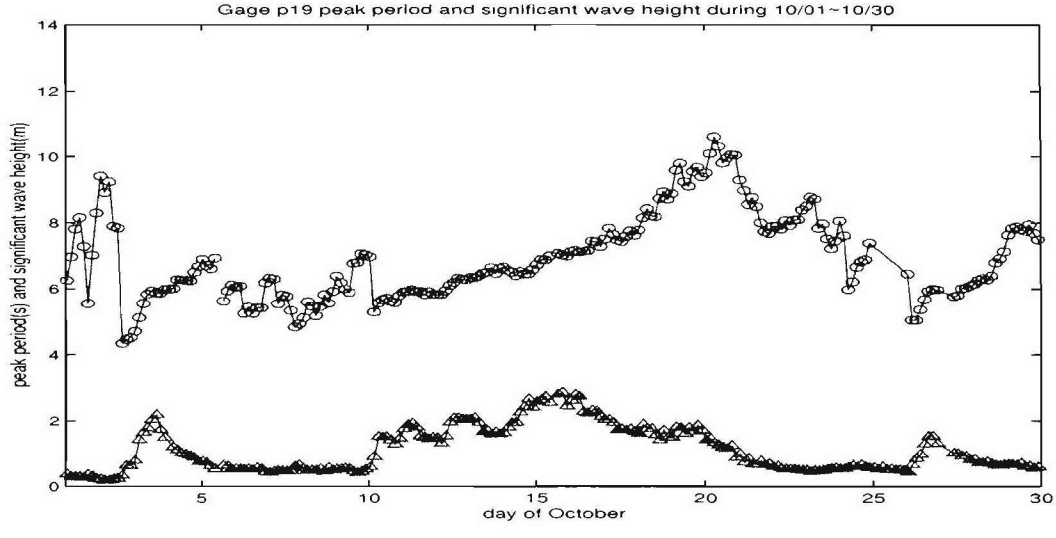

Figure 8.4: Peak wave period (circles) and significant wave height (triangles) at gage p19 in Oct., 1994

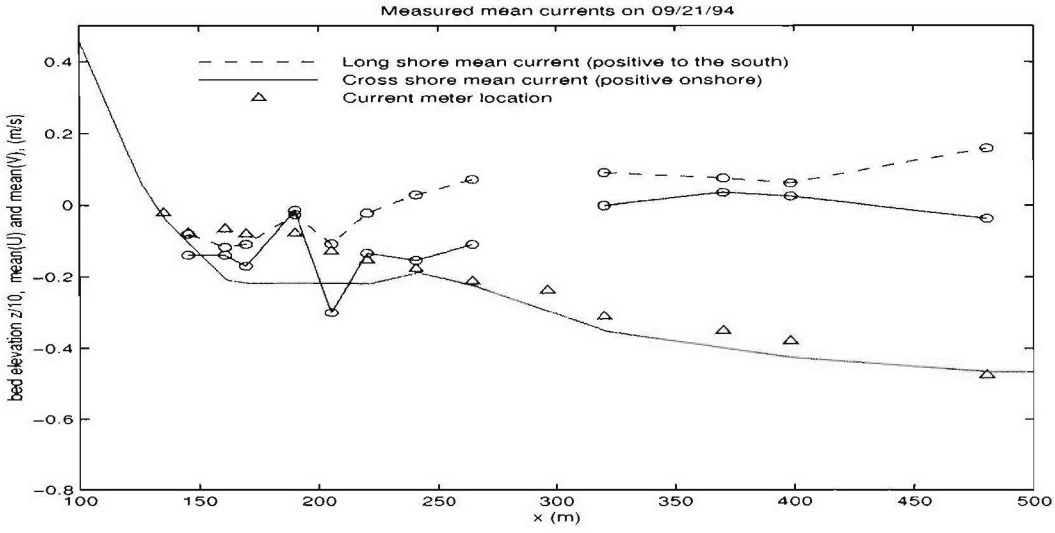

Figure 8.5: Mean current and bed elevation on day 09/21/94

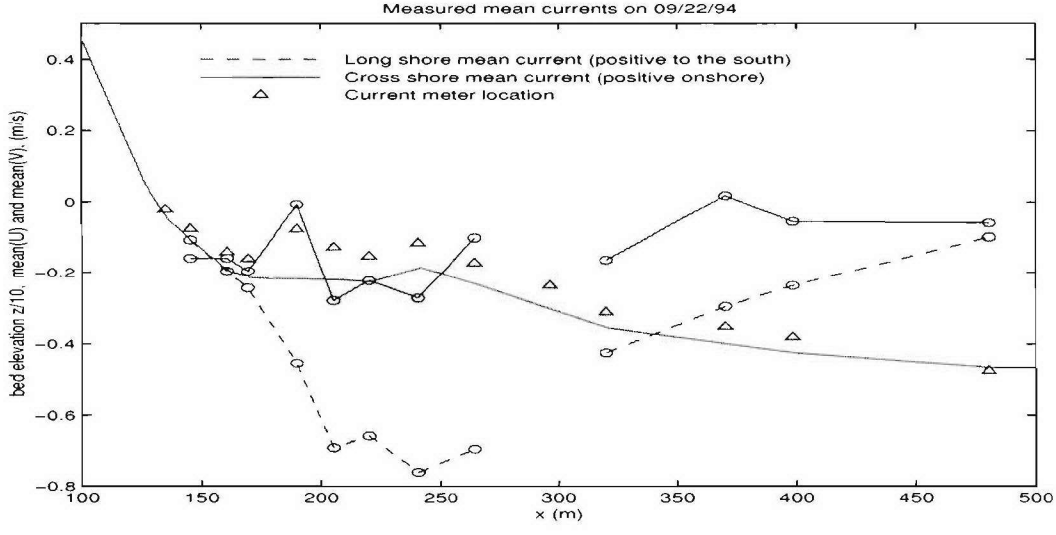

Figure 8.6: Mean current and bed elevation on day 09/22/94

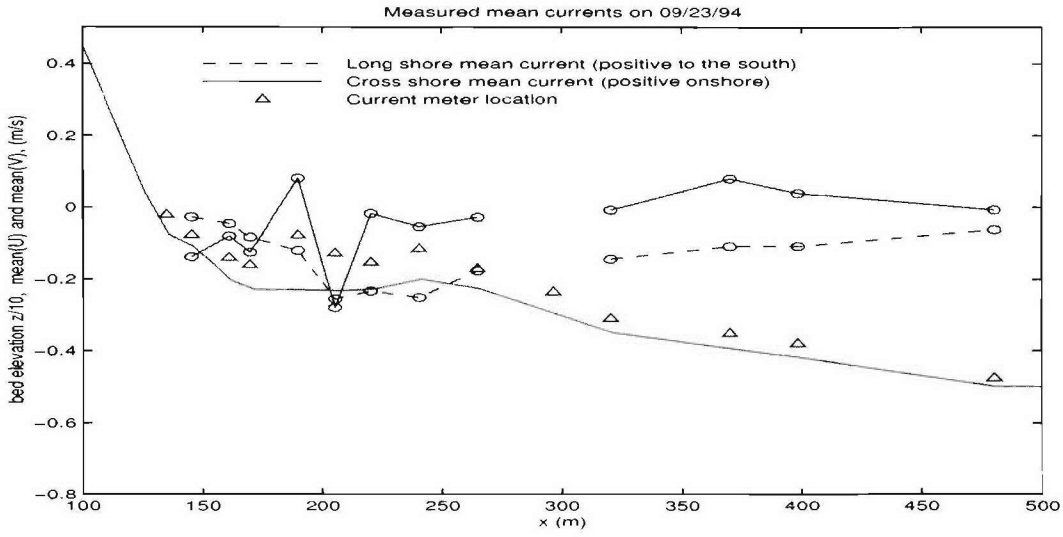

Figure 8.7: Mean current and bed elevation on day 09/23/94

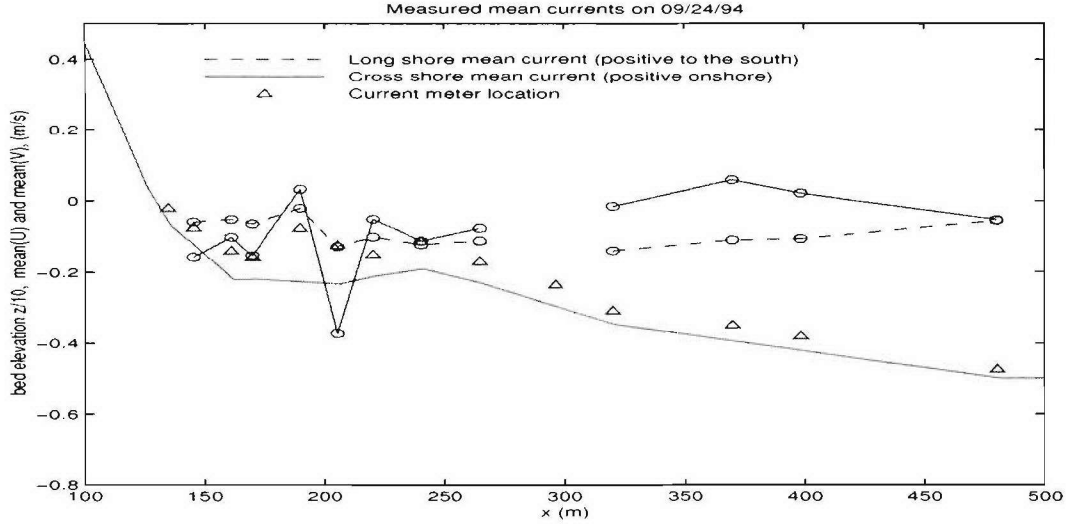

Figure 8.8: Mean current and bed elevation on day 09/24/94

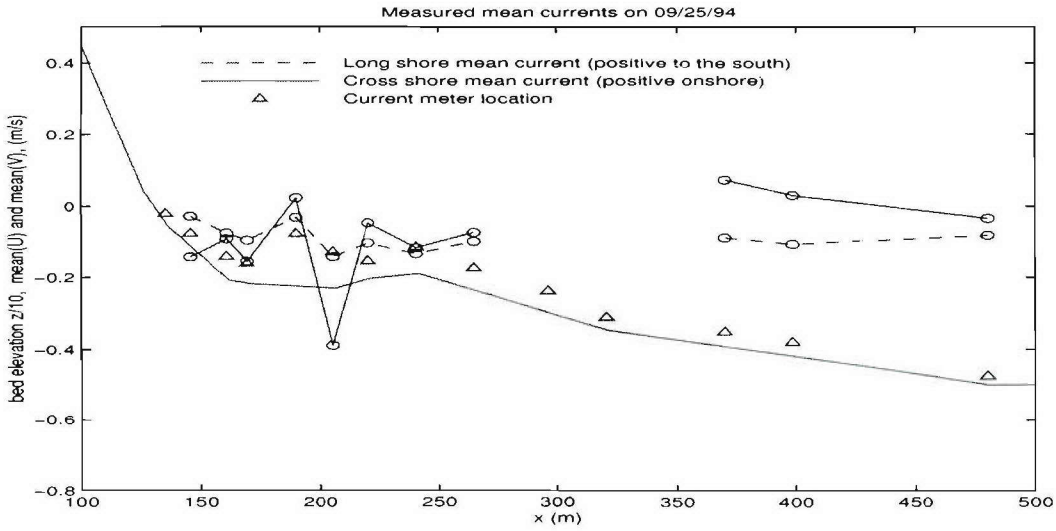

Figure 8.9: Mean current and bed elevation on day 09/25/94

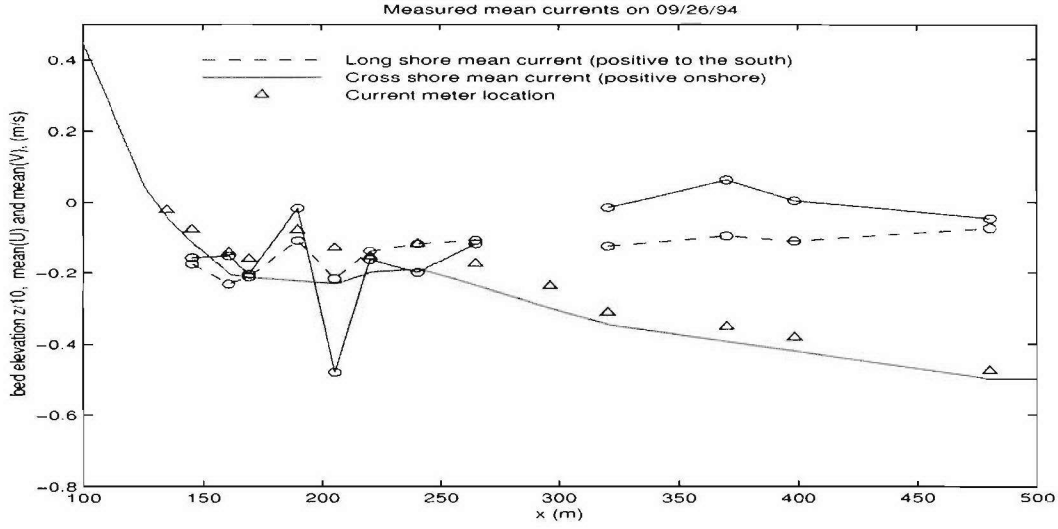

Figure 8.10: Mean current and bed elevation on day 09/26/94

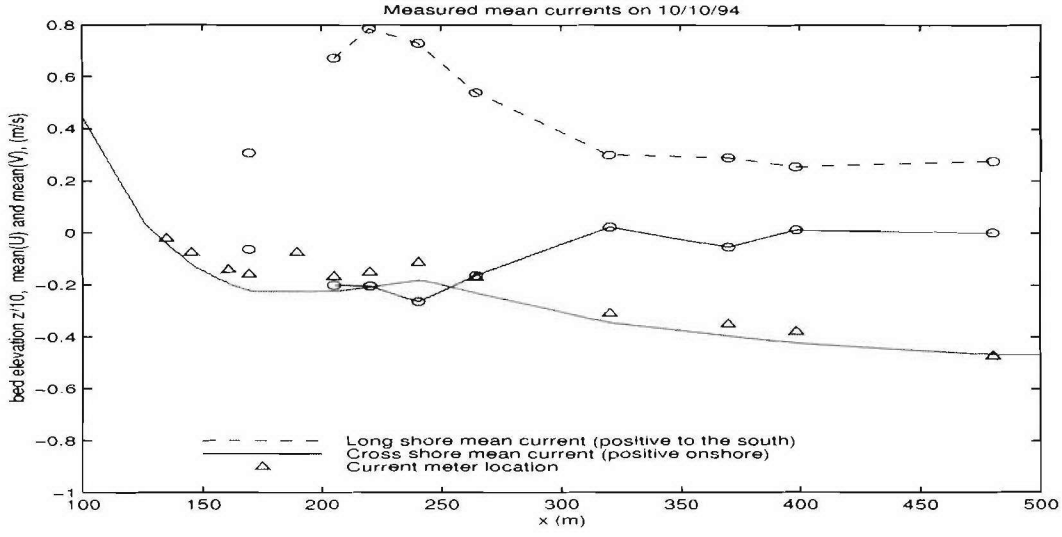

Figure 8.11: Mean current and bed elevation on day 10/10/94

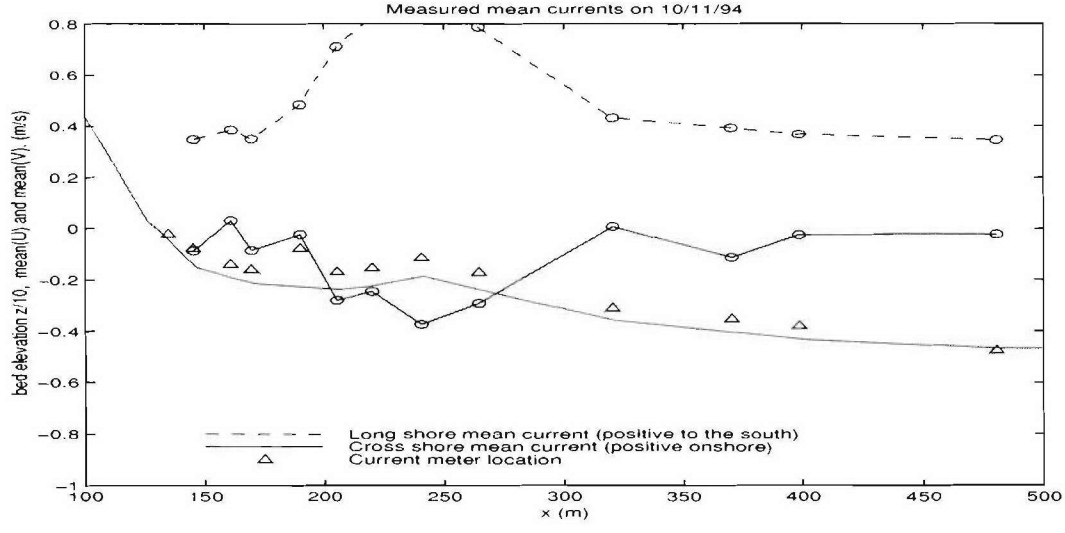

Figure 8.12: Mean current and bed elevation on day 10/11/94

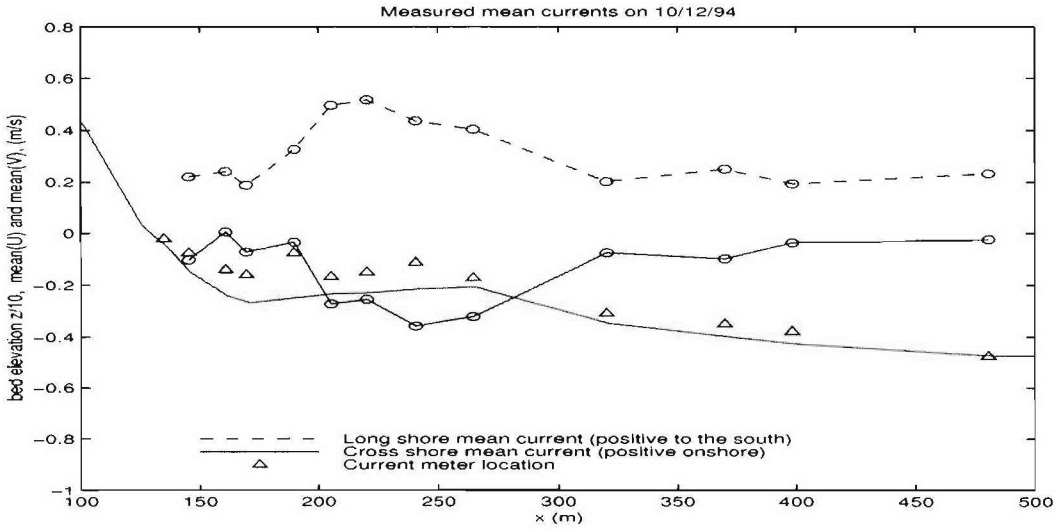

Figure 8.13: Mean current and bed elevation on day 10/12/94

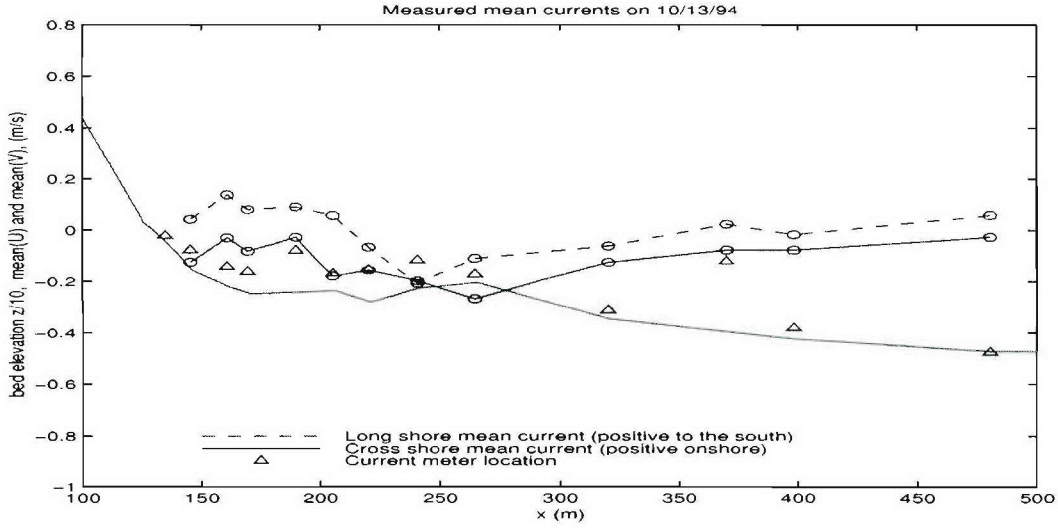

Figure 8.14: Mean current and bed elevation on day 10/13/94

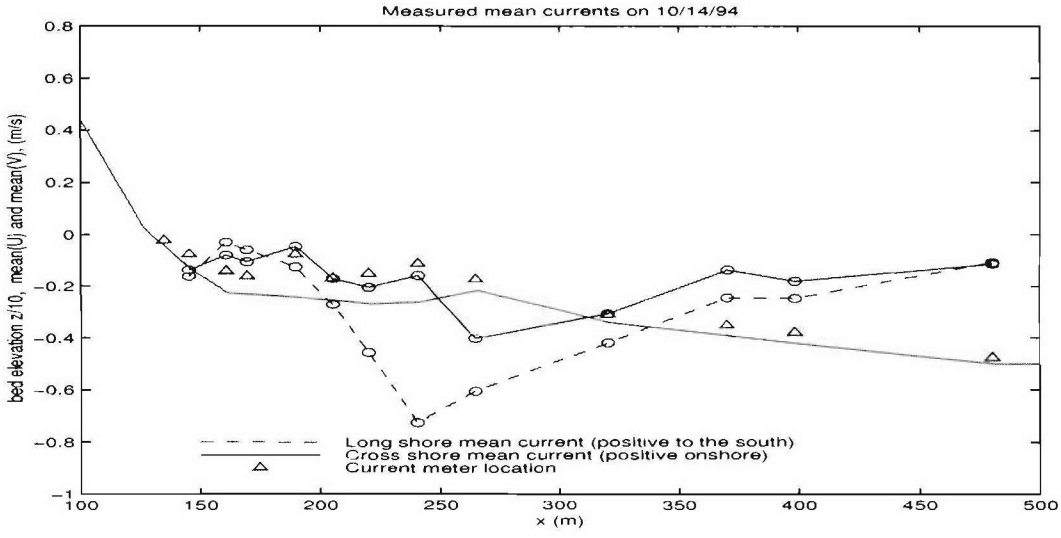

Figure 8.15: Mean current and bed elevation on day 10/14/94

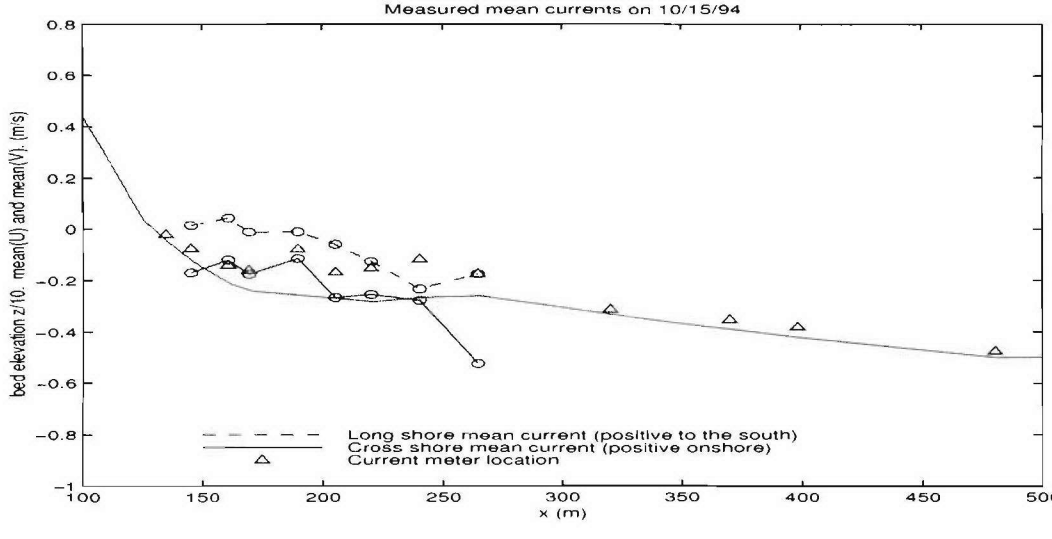

Figure 8.16: Mean current and bed elevation on day 10/15/94

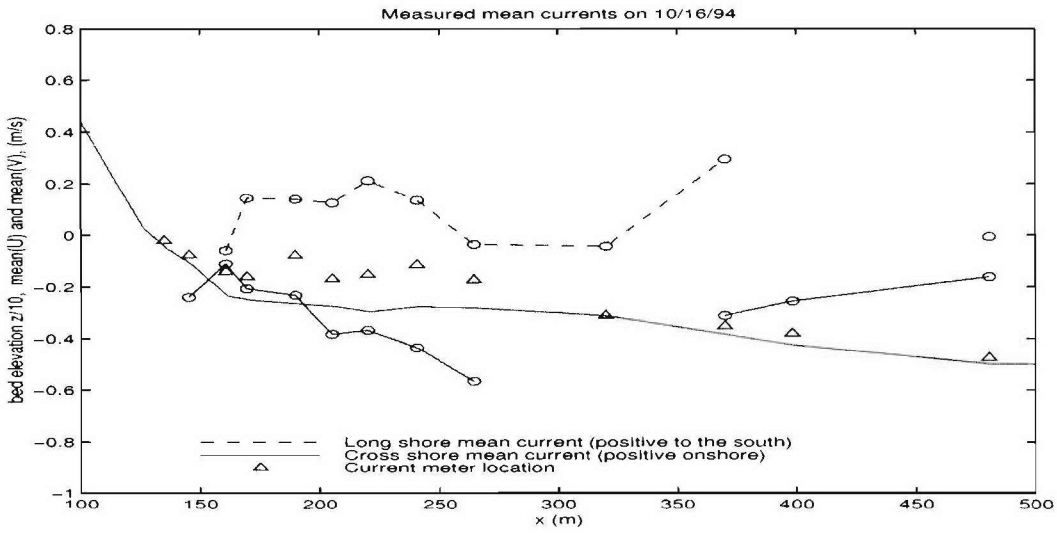

Figure 8.17: Mean current and bed elevation on day 10/16/94

north at the beginning of day 13. These observations help to qualitatively explain the onshore bar migration event when undertow was weak and offshore bar migration event when undertow was strong. The fact that weak alongshore currents were observed during September 23 to September 27 enables us to use a 1-D cross shore model to simulate the hydrodynamics and bathymetry change in great detail. Although there have been relatively strong longshore processes during the October 10 to October 16 events, we still elect to use the 1D modeling due to limited data available.

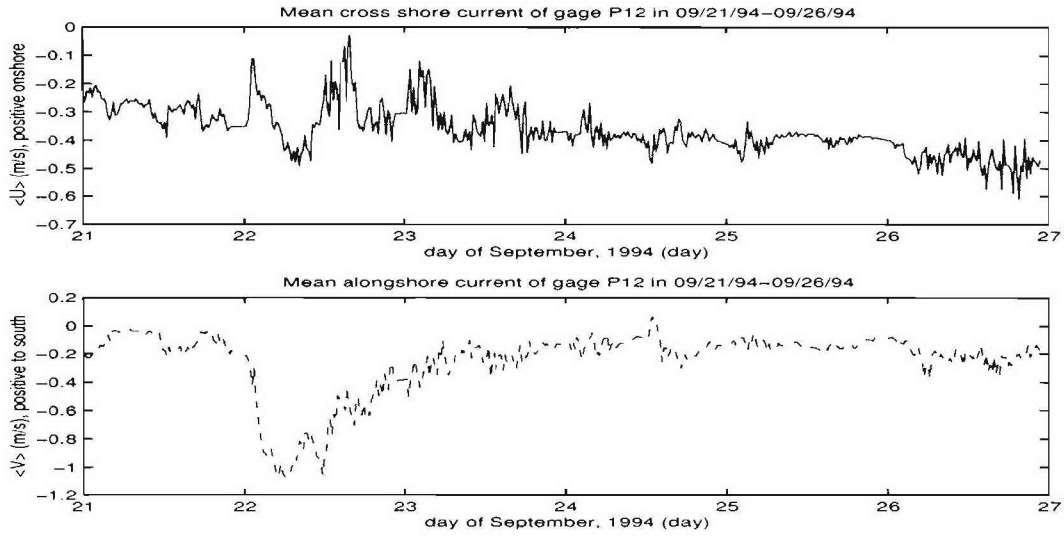

Figure 8.18: Mean current of bar trough gage p12 in September, 1994; Upper panel: cross shore mean current (positive onshore); Lower panel: alongshore mean current (positive toward south)

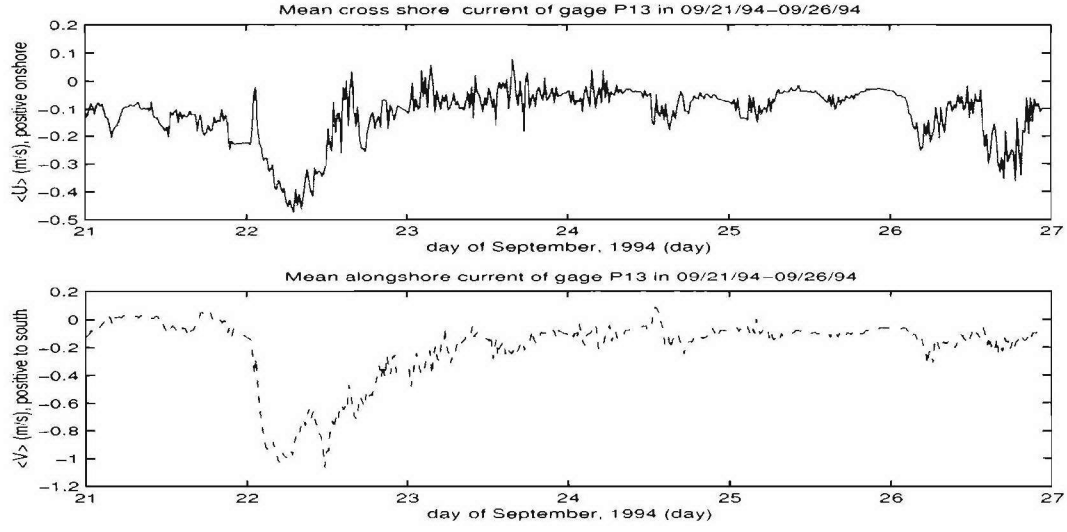

Figure 8.19: Mean current of bar trough gage p13 in September, 1994; Upper panel: cross shore mean current (positive onshore); Lower panel: alongshore mean current (positive toward south)

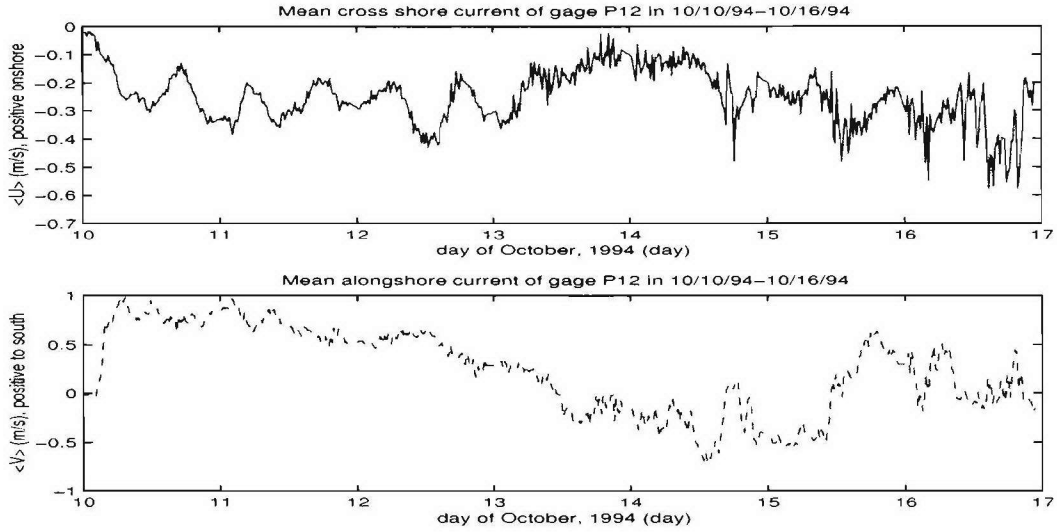

Figure 8.20: Mean current of bar trough gage p12 in October, 1994; Upper panel: cross shore mean current (positive onshore); Lower panel: alongshore mean current (positive toward south)

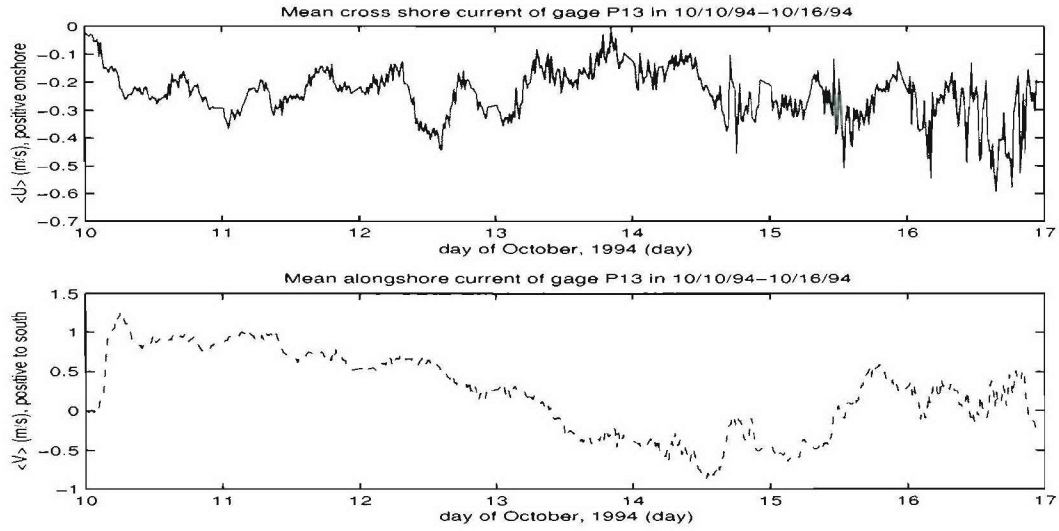

Figure 8.21: Mean current of bar trough gage p13 in October, 1994; Upper panel: cross shore mean current (positive onshore); Lower panel: alongshore mean current (positive toward south)

gage	x(m)	y(m)	gage	x(m)	y(m)
a00	0.0	930.00	s13	220.23	930.41
p01	124.94	929.82	s14	240.55	930.00
s02	135.07	930.06	s15	264.70	930.44
s03	145.42	930.84	s17	320.23	930.67
s04	160.76	930.64	s18	398.43	931.12
s05	170.08	930.09	p19	480.34	930.57
s12	205.42	930.45			

Table 8.5: Gage locations where bathymetry data are obtained

8.1.2 Model Setup

In the model runs, we use the following procedure: 1) obtain the measured pressure time series (0.5 sec interval) of the offshore gage p19; 2) convert the pressure time series into free surface elevation time series (using linear wave theory) which contain both wave signal and tidal level; 3) de-trend the free surface elevation time series into a wave time series and a tidal series; 4) use the wave time series and the tidal series as input for the FUNSEDI1D1.0 model to calculate the wave propagation and bathymetry change on a day to day basis.

The 13 gage locations (FRF coordinate) for obtaining the bathymetry are listed in table 8.5, where the gage number a00 is artificial to extend the bathymetry onshore to $x = 0$ with a beach slope corresponding to the two close-to-shoreline gages p01 and s02, gage number p01 and p19 are pressure gages which also reported the bed elevation, and gages s02, s03, s04, s05, s12, s13, s14, s15, s17, s18 are sonar altimeter gages.

The obtained time series for waves and tidal level are plotted in figure 8.22 and 8.23 for September and 8.24 and 8.25 for October respectively.

The observd bathymetry of each day are shown in figure 8.26 and 8.27.

Both the onshore bar migration (09/23/94 to 09/30/94) and offshore migration (10/10/94 to 10/16/94) events are modeled separately using the FUNSEDI1D1.0 model. The initial bathymetry data are obtained from the measured altimeters at 1:00am on September 23 for the onshore bar migration run and at 1:00am on October 10 for the offshore

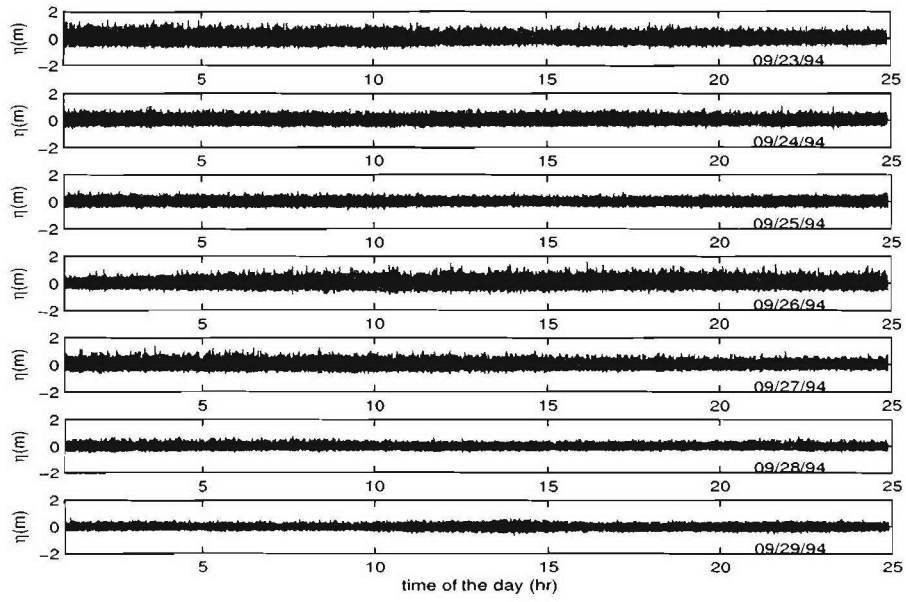

Figure 8.22: Time series of wave signal η at gage p19 from 09/23/94 to 09/29/94; The time axis is from 1:00am of each day to 1:00am of the next day

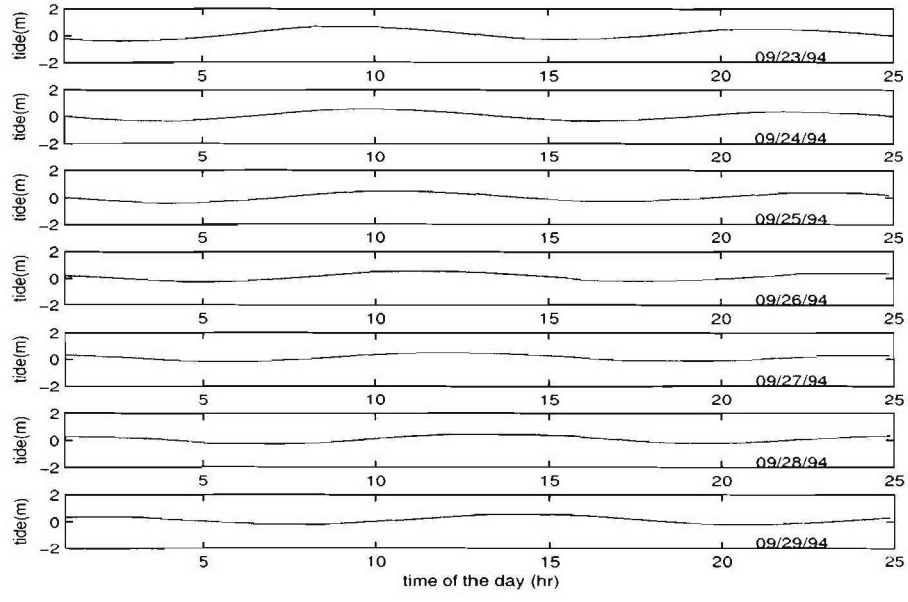

Figure 8.23: Time series of tidal level signal at gage p19 from 09/23/94 to 09/29/94 (relative to NGVD datum); The time axis is from 1:00am of each day to 1:00am of the next day

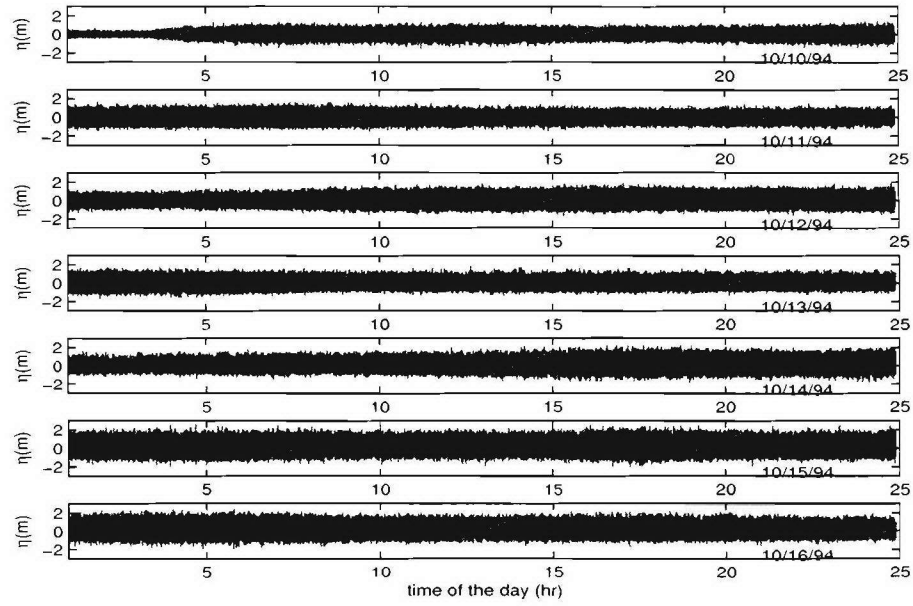

Figure 8.24: Time series of wave signal η at gage p19 from 10/10/94 to 10/16/94; Th time axis is from 1:00am of each day to 1:00am of the next day; The measurements from 13:00 to 16:00 on day 10/15/94 are missing due to gage malfunction, and they are shown as repeated signal from 10:00 to 13:00

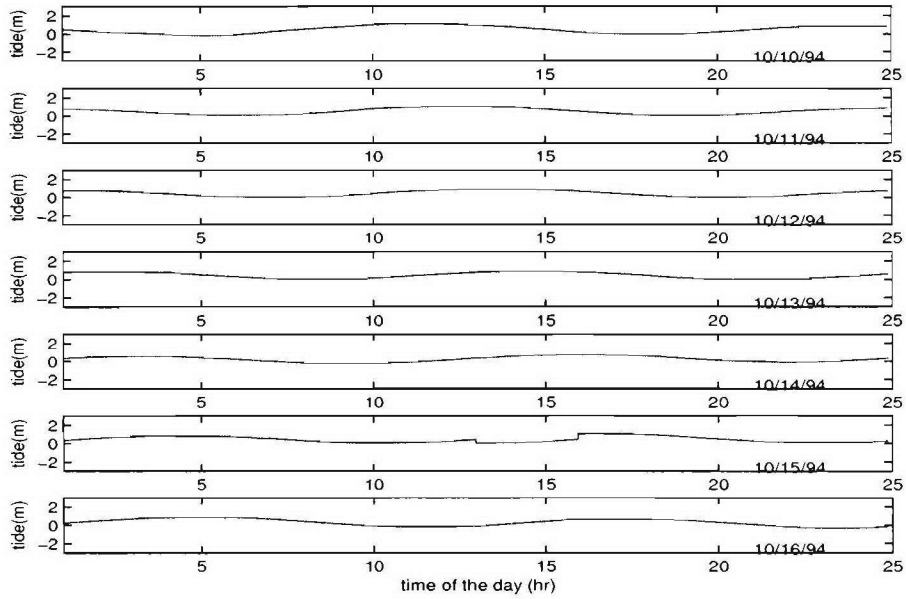

Figure 8.25: Time series of tidal level signal at gage p19 from 10/10/94 to 10/16/94 (relative to NGVD datum); The time axis is from 1:00am of each day to 1:00am of the next day; The measurements from 13:00 to 16:00 on day 10/15/94 are missing due to gage malfunction, and they are shown as repeated signal from 10:00 to 13:00

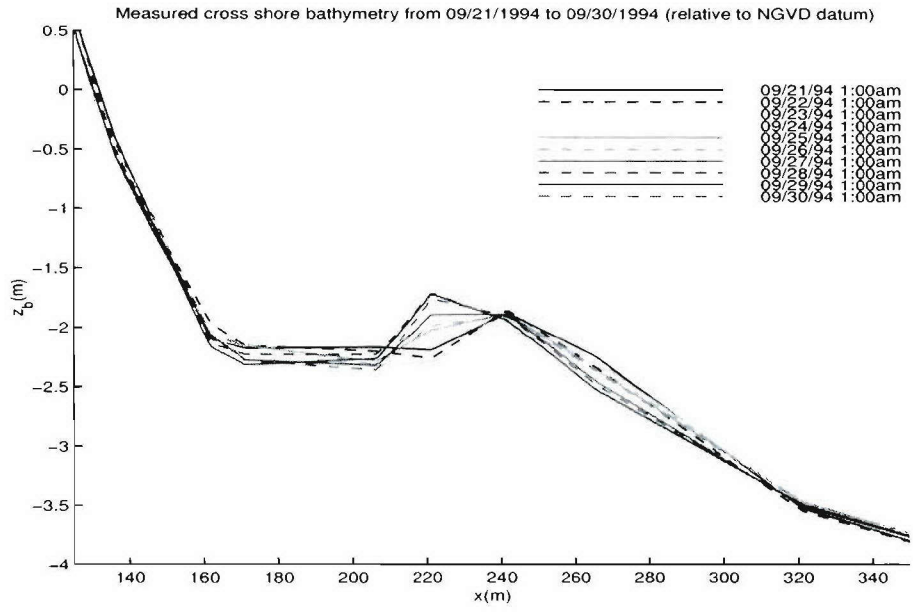

Figure 8.26: Measured cross shore bathymetry from Sept. 21 to Sept. 30 (relative to NGVD datum)

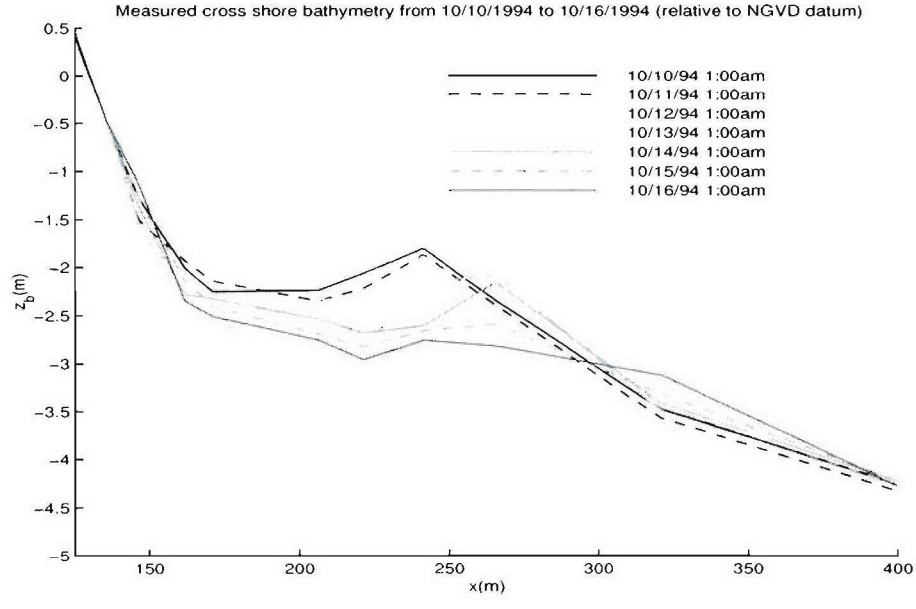

Figure 8.27: Measured cross shore bathymetry from Oct. 10 to Oct. 16 (relative to NGVD datum)

bar migration run. The bathymetry data were originally composed of only 12 points according to the altimeters and they are interpolated to be a 1-D array of bathymetry with spacing $\Delta x = 1m$.

Time step for both the wave model (FUNWAVE) is $\Delta t = 0.1s$ and the morphological model (Euler-WENO) is set to be $\Delta t_s = 30$min. The sediment transport rates are calculated instantaneously and accumulated for every 30min before being used to update the bathymetry.

8.1.3 Wave and mean Current test

A detailed comparison of the modeled bottom velocities and measured velocities is shown below. The compared quantities include power spectra, variance, mean flow and skewness. Figure 8.28 to 8.35 show the comparison of the power spectra of the modeled velocities with the measured velocities at 1:00am of day September 23 to September 30. From the figures, the modeled spectra agrees well with the measured data spectra except at the high frequency end. Figure 8.36 to 8.43 show the comparison of the variance of the modeled velocities with the measured velocities for each 3 hour period of each day from September 23 to September 30. Figure 8.44 to 8.51 show the comparison of the mean values of the modeled cross shore velocities with the measured velocities for each 3 hour period of each day from September 23 to September 30. Figure 8.52 to 8.59 show the comparison of the skewness of the modeled velocities with the measured velocities for each 3 hour period of each day from September 23 to September 30. Generally, the model gives good estimate on variance and reasonable estimate on skewness. The mean current predicted by the model is very small while the data show substantial scattering.

Figure 8.60 to 8.66 show the comparison of the power spectra of the modeled velocities with the measured velocities at 1:00am of day October 10 to October 16. Figure 8.67 to 8.73 show the comparison of the variance of the modeled velocities with the measured velocities for each 3 hour period of each day from October 10 to October 16. Figure 8.74 to 8.80 show the comparison of the mean values of the modeled cross shore

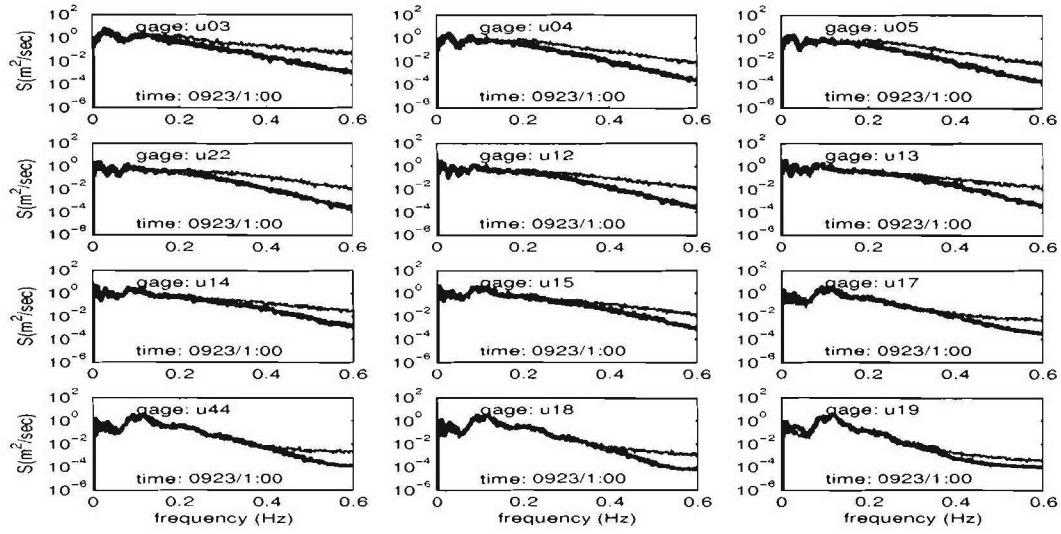

Figure 8.28: Model data comparison of velocity power spectra at different gages on 09/23/94, 1:00am (data: thin-line; model: thick-line)

velocities with the measured velocities for each 3 hour period of each day from October 10 to October 16. Figure 8.81 to 8.87 show the comparison of the skewness of the modeled velocities with the measured velocities for each 3 hour period of each day from October 10 to October 16. Again, wave spectra and variance are reproduced in reasonable accuracy. Skewness agreement is also acceptable. The mean current (undertow) is underestimated substantially. The reason of the underestimate may be due to the assumption of vertical uniformity of the return flow in the model and the sand bar is located at the depth of 2 to 4 meters which is not quite shallow compared to lab experiments. This severe underestimate of near-bottom undertow causes difficulty in modeling the offshore bar migration.

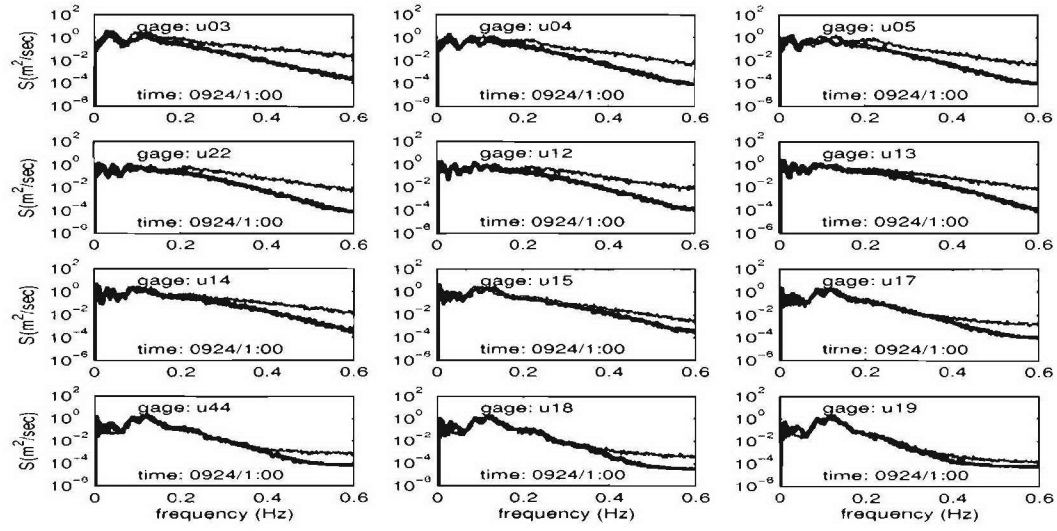

Figure 8.29: Model data comparison of velocity power spectra at different gages on 09/24/94, 1:00am (data: thin-line; model: thick-line)

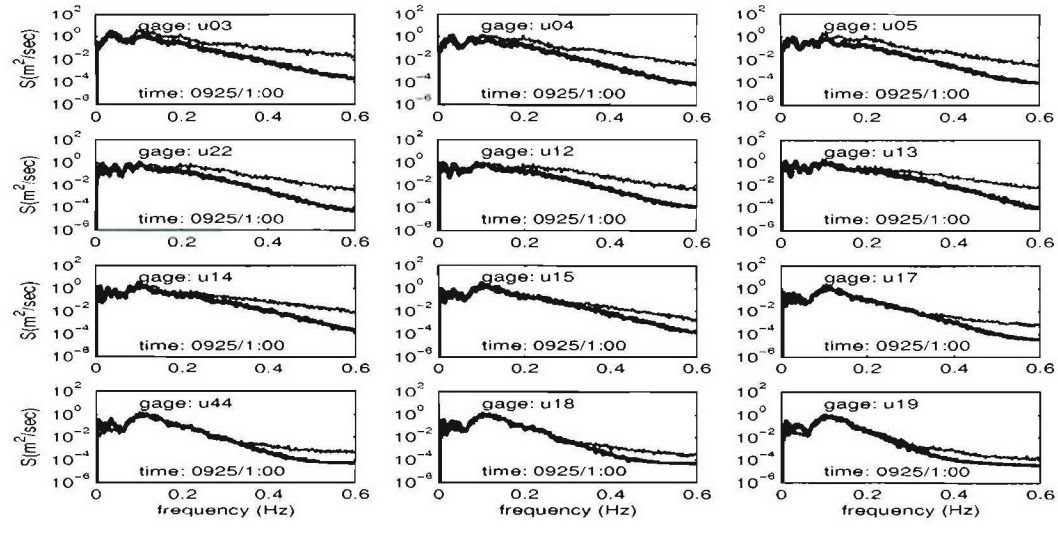

Figure 8.30: Model data comparison of velocity power spectra at different gages on 09/25/94, 1:00am (data: thin-line; model: thick-line)

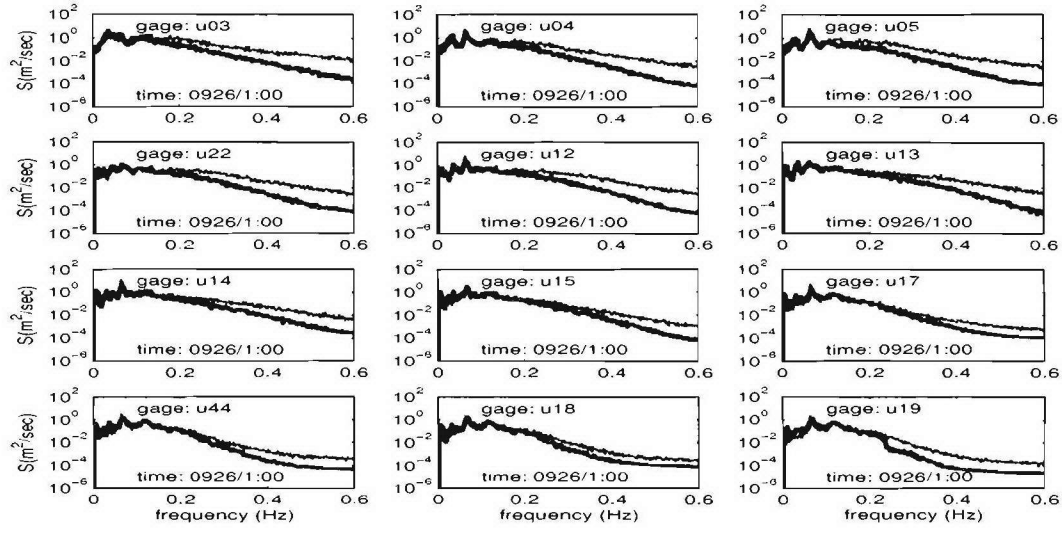

Figure 8.31: Model data comparison of velocity power spectra at different gages on 09/26/94, 1:00am (data: thin-line; model: thick-line)

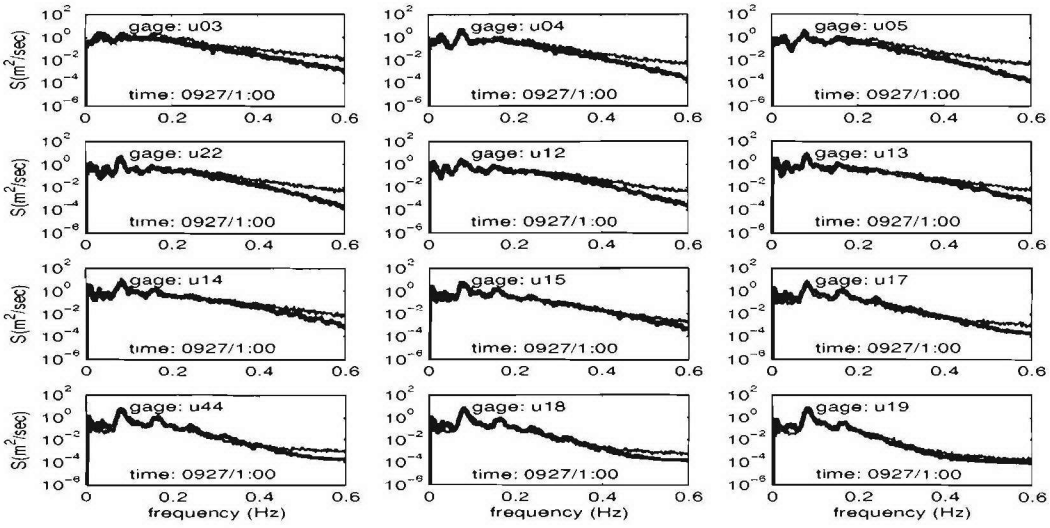

Figure 8.32: Model data comparison of velocity power spectra at different gages on 09/27/94, 1:00am (data: thin-line; model: thick-line)

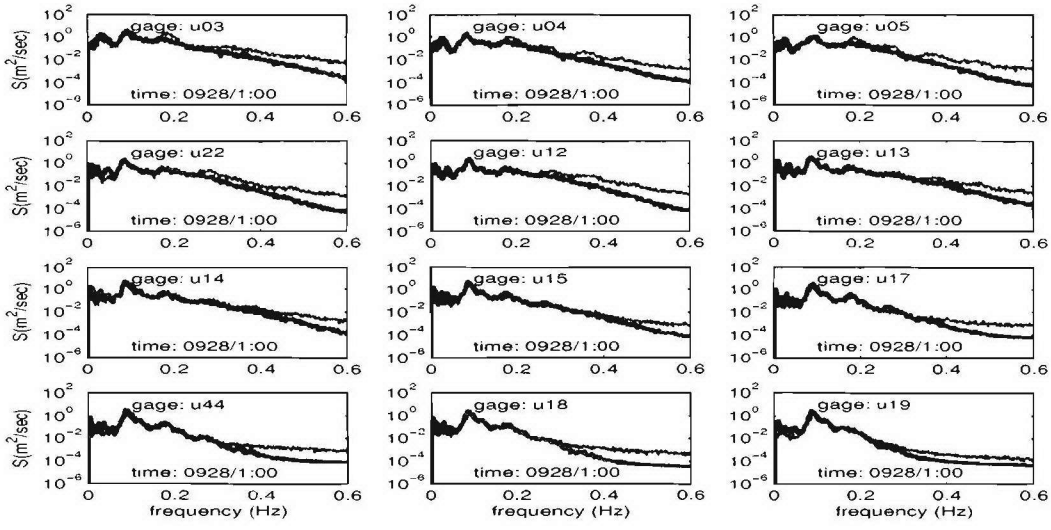

Figure 8.33: Model data comparison of velocity power spectra at different gages on 09/28/94, 1:00am (data: thin-line; model: thick-line)

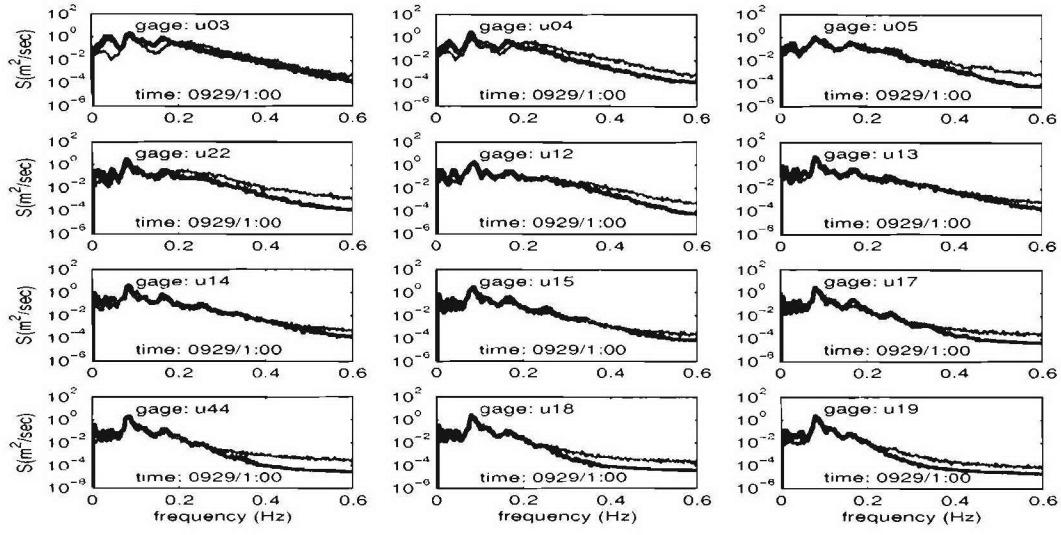

Figure 8.34: Model data comparison of velocity power spectra at different gages on 09/29/94, 1:00am (data: thin-line; model: thick-line)

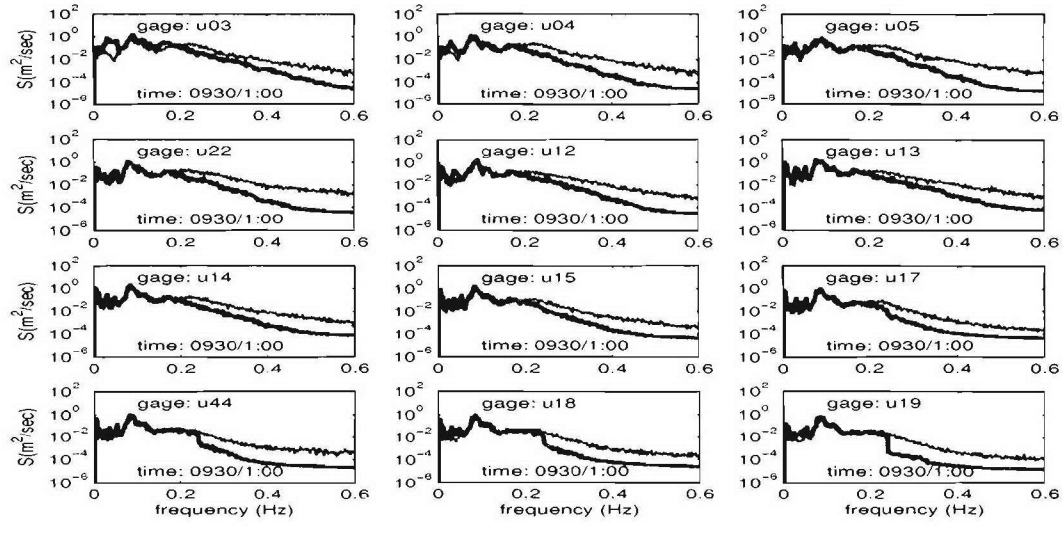

Figure 8.35: Model data comparison of velocity power spectra at different gages on 09/30/94, 1:00am (data: thin-line; model: thick-line)

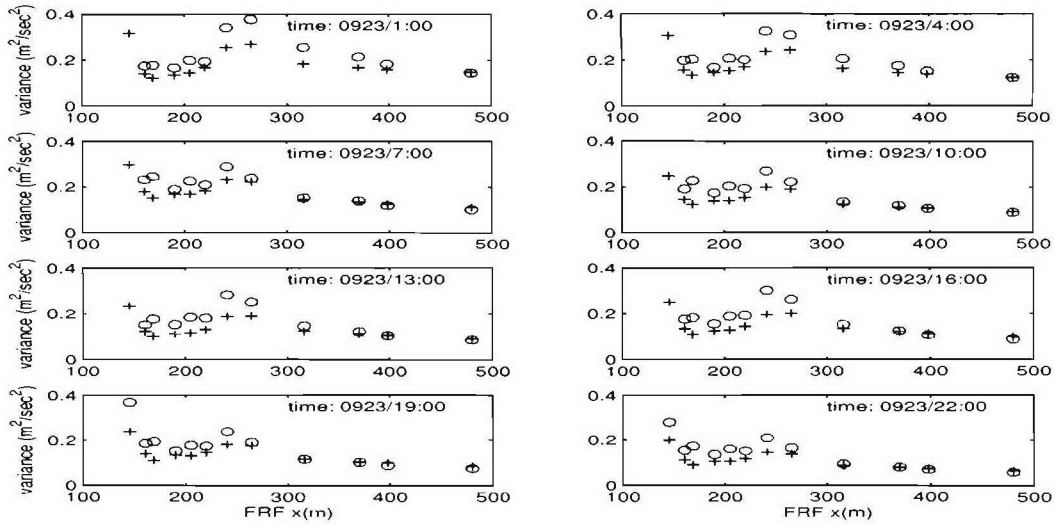

Figure 8.36: Model data comparison of velocity variance at different velocity gages on 09/23/94, (data: circles; model: pluses)

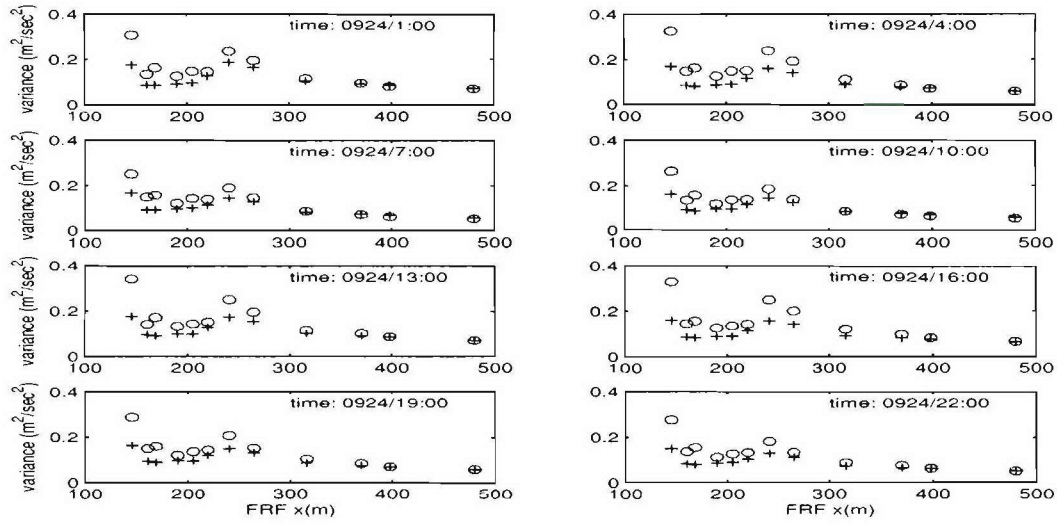

Figure 8.37: Model data comparison of velocity variance at different velocity gages on 09/24/94, (data: circles; model: pluses)

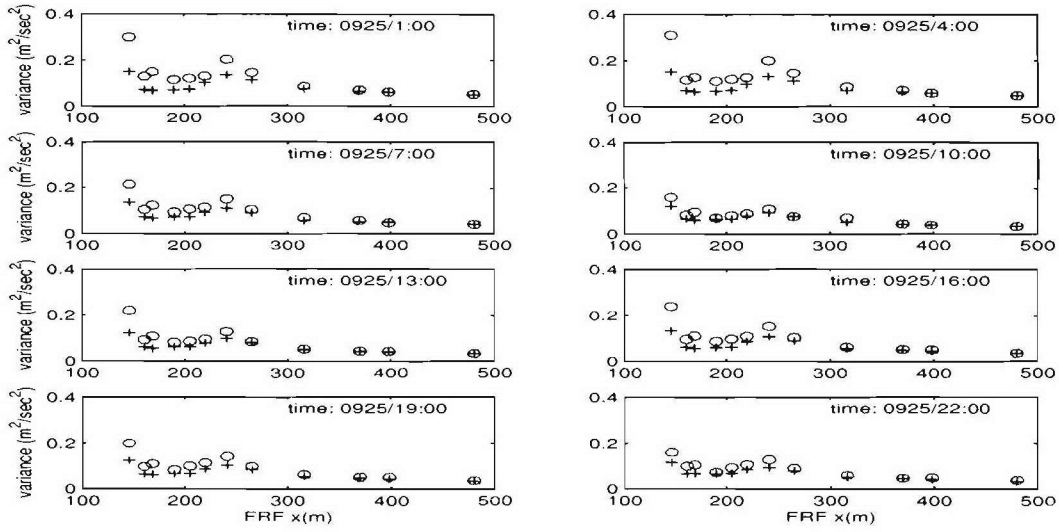

Figure 8.38: Model data comparison of velocity variance at different velocity gages on 09/25/94, (data: circles; model: pluses)

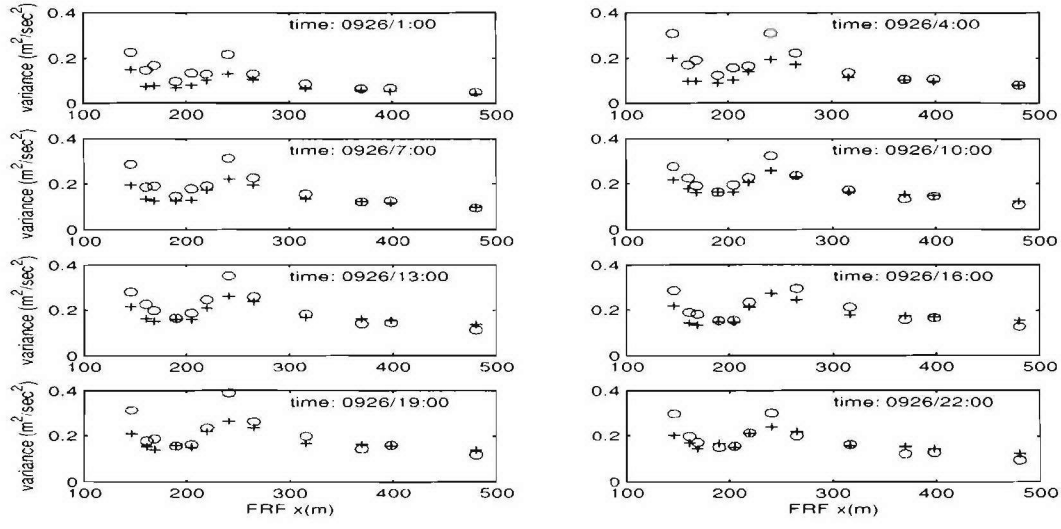

Figure 8.39: Model data comparison of velocity variance at different velocity gages on 09/26/94, (data: circles; model: pluses)

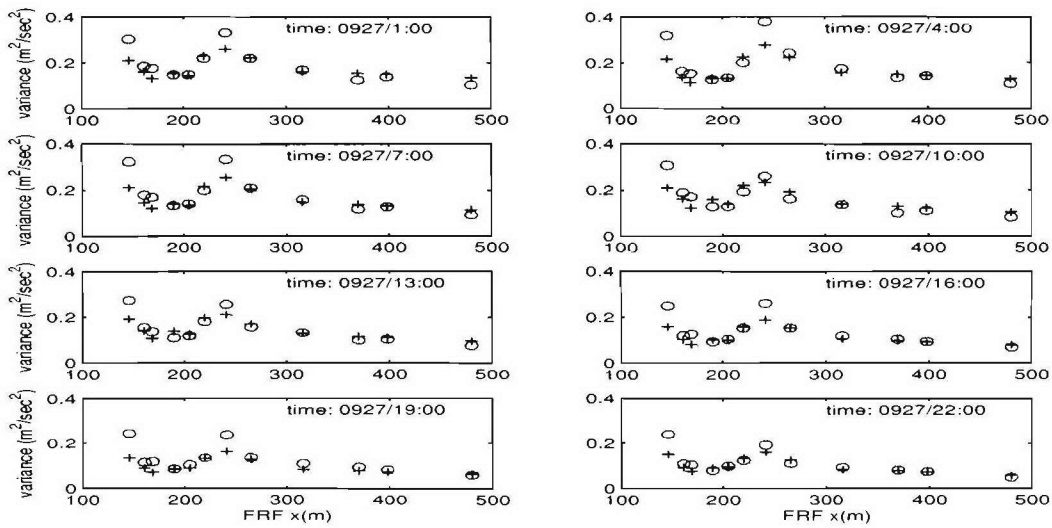

Figure 8.40: Model data comparison of velocity variance at different velocity gages on 09/27/94, (data: circles; model: pluses)

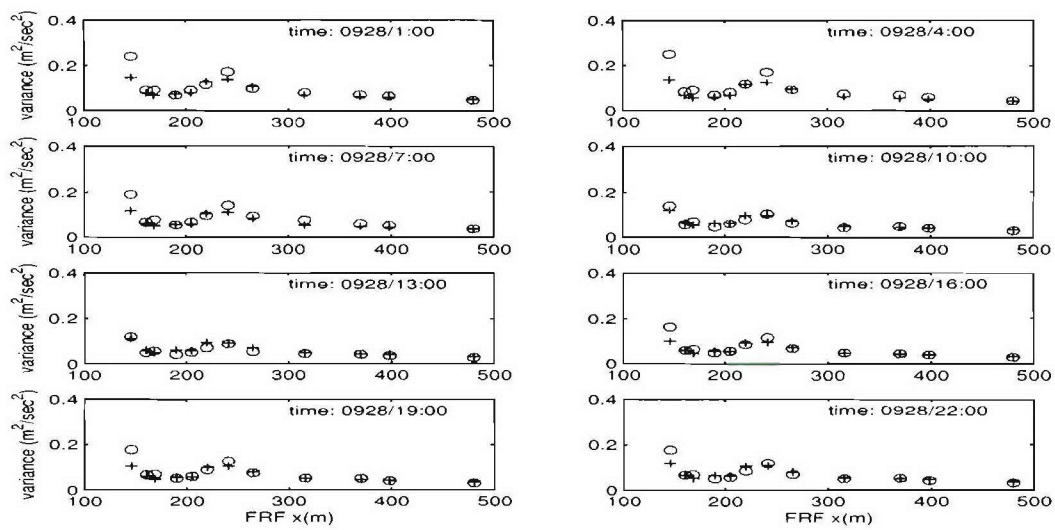

Figure 8.41: Model data comparison of velocity variance at different velocity gages on 09/28/94, (data: circles; model: pluses)

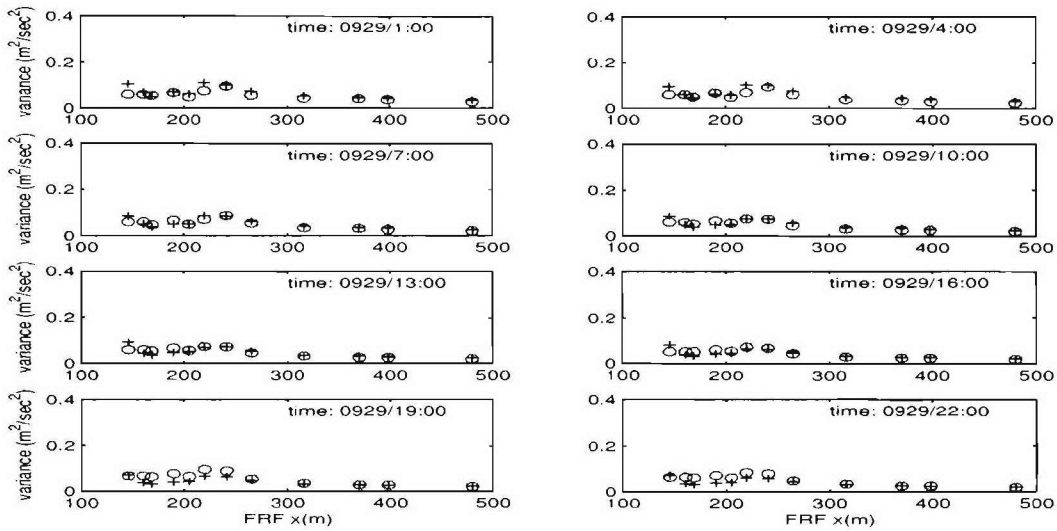

Figure 8.42: Model data comparison of velocity variance at different velocity gages on 09/29/94, (data: circles; model: pluses)

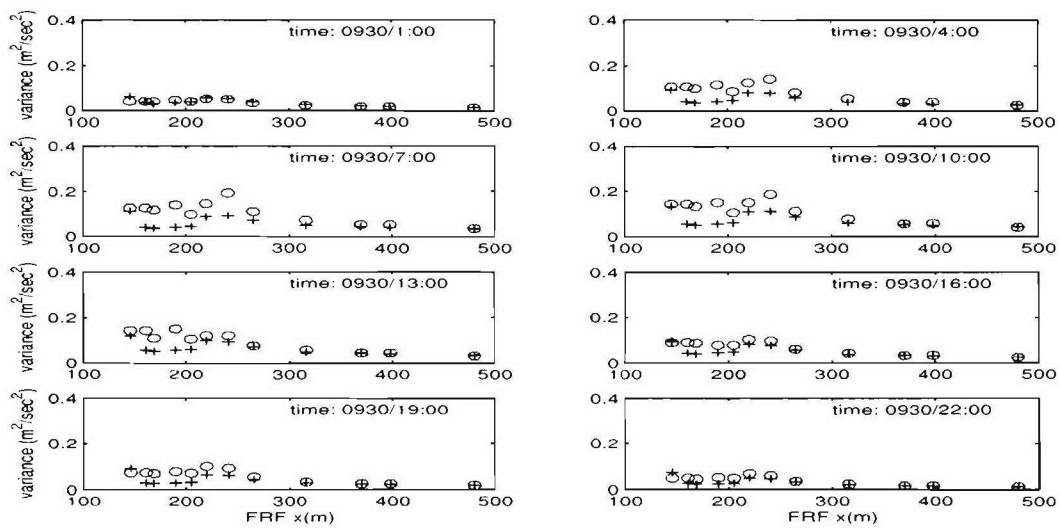

Figure 8.43: Model data comparison of velocity variance at different velocity gages on 09/30/94, (data: circles; model: pluses)

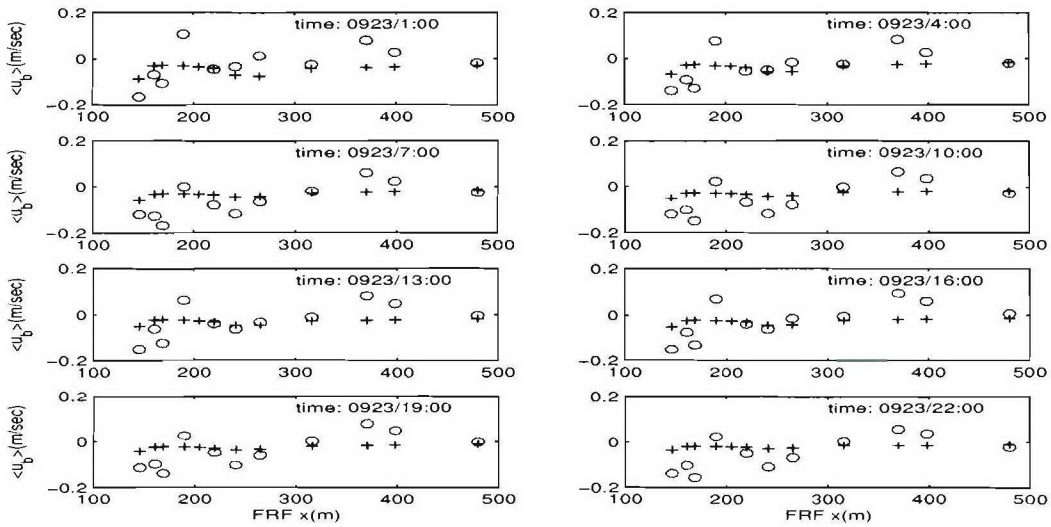

Figure 8.44: Model data comparison of velocity mean at different velocity gages on 09/23/94, (data: circles; model: pluses)

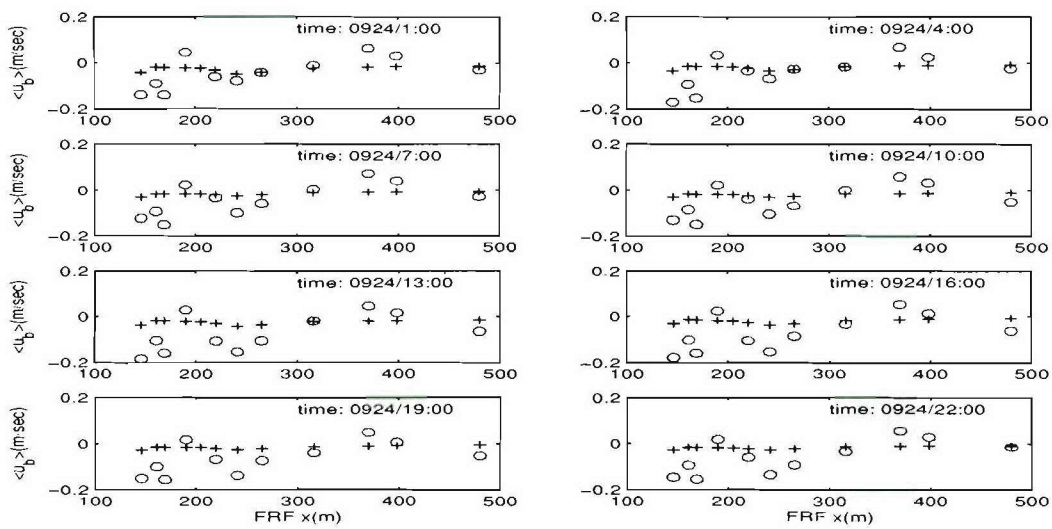

Figure 8.45: Model data comparison of velocity mean at different velocity gages on 09/24/94, (data: circles; model: pluses)

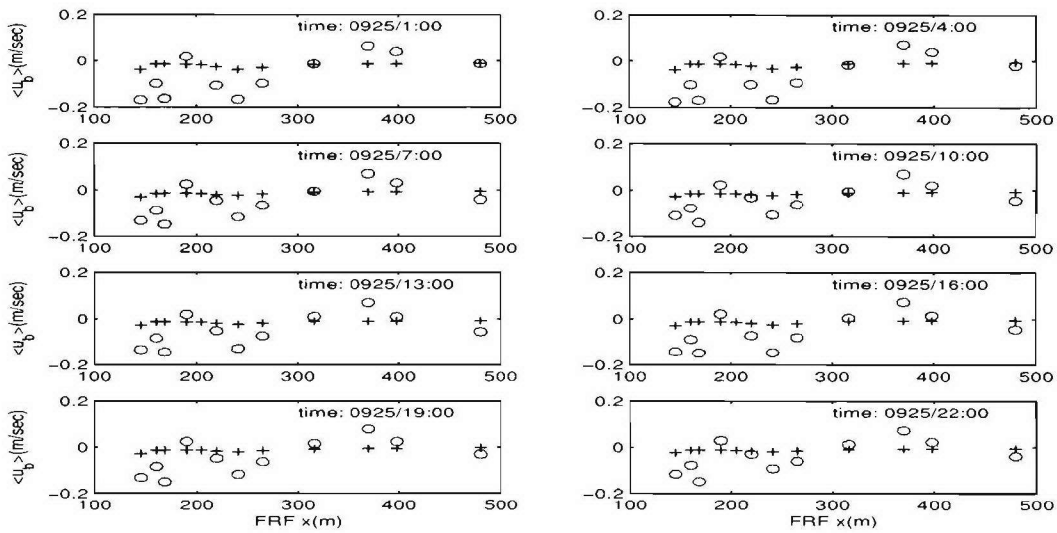

Figure 8.46: Model data comparison of velocity mean at different velocity gages on 09/25/94, (data: circles; model: pluses)

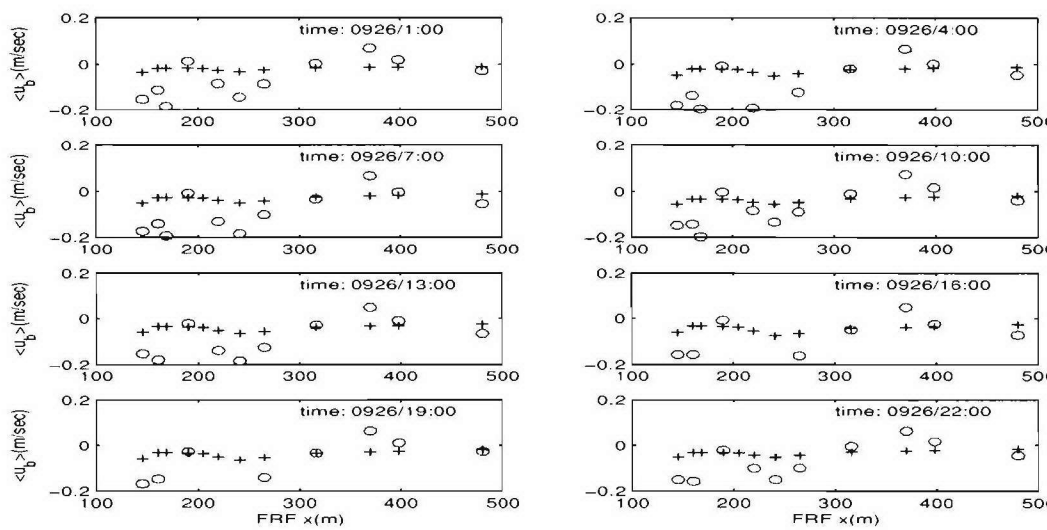

Figure 8.47: Model data comparison of velocity mean at different velocity gages on 09/26/94, (data: circles; model: pluses)

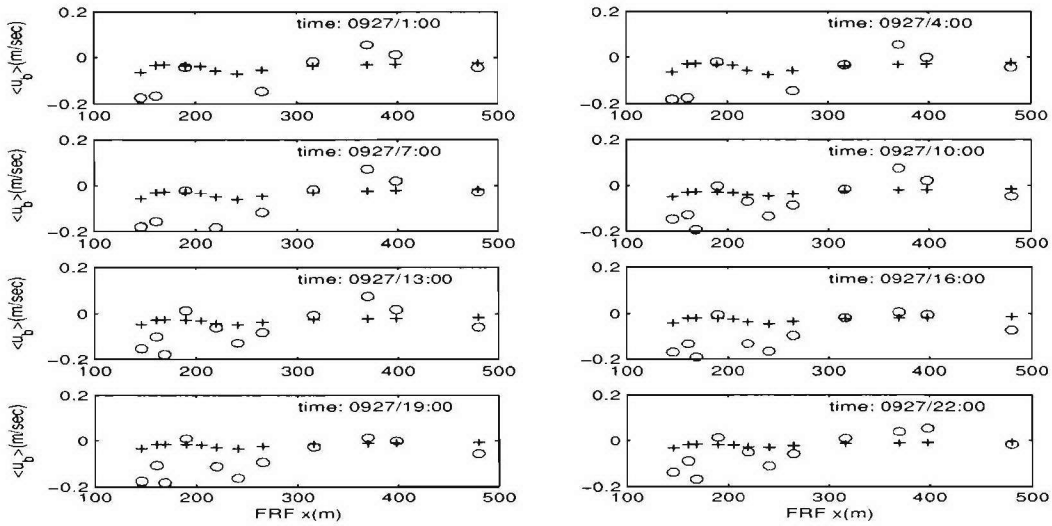

Figure 8.48: Model data comparison of velocity mean at different velocity gages on 09/27/94, (data: circles; model: pluses)

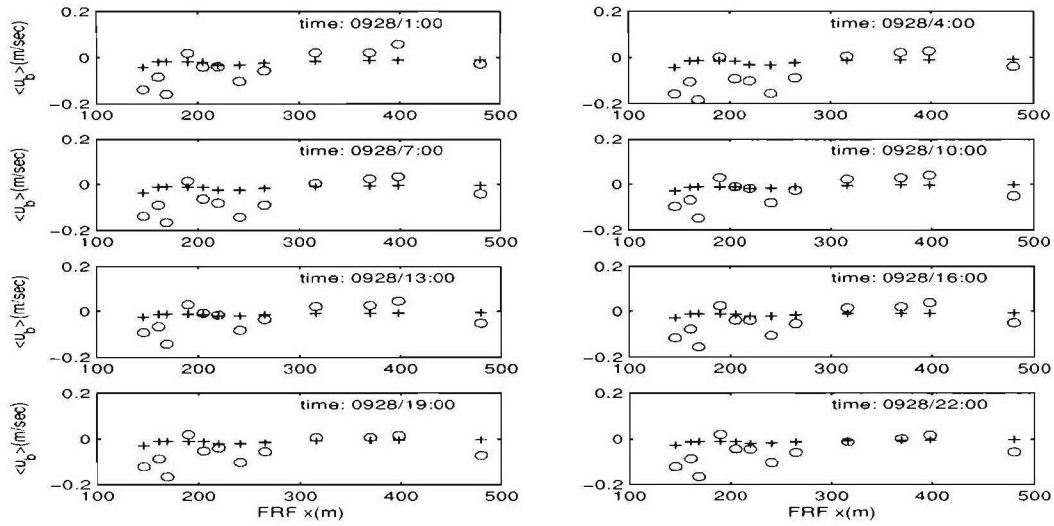

Figure 8.49: Model data comparison of velocity mean at different velocity gages on 09/28/94, (data: circles; model: pluses)

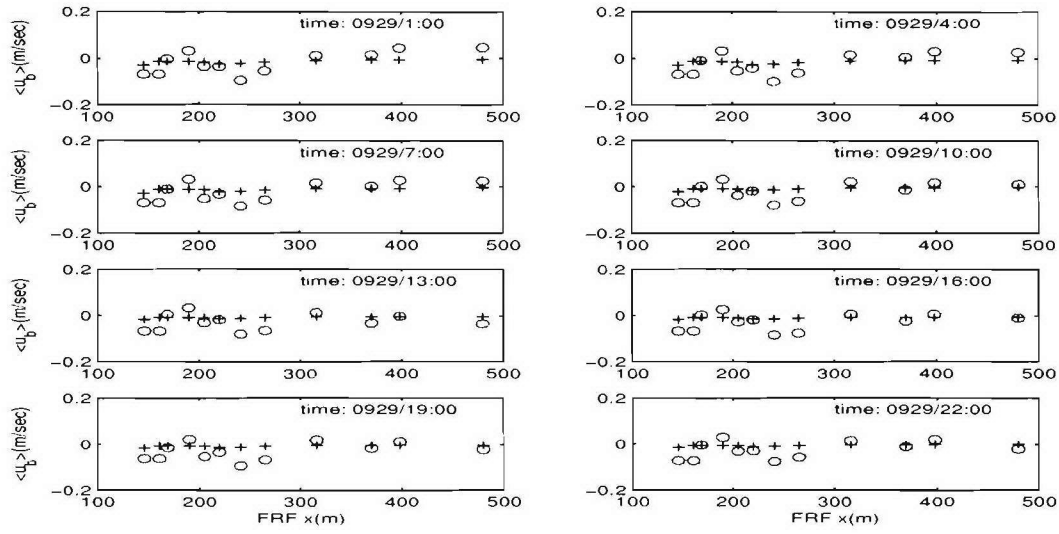

Figure 8.50: Model data comparison of velocity mean at different velocity gages on 09/29/94, (data: circles; model: pluses)

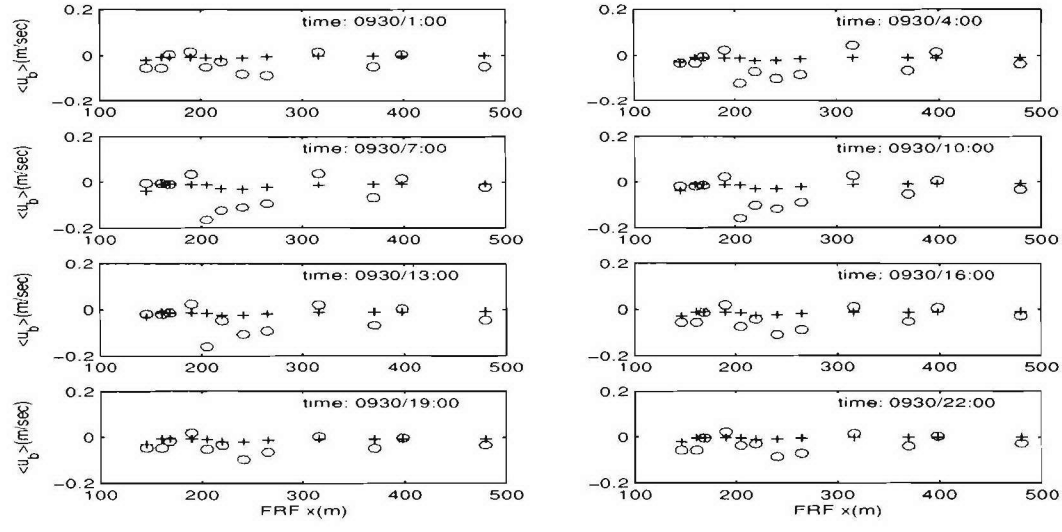

Figure 8.51: Model data comparison of velocity mean at different velocity gages on 09/30/94, (data: circles; model: pluses)

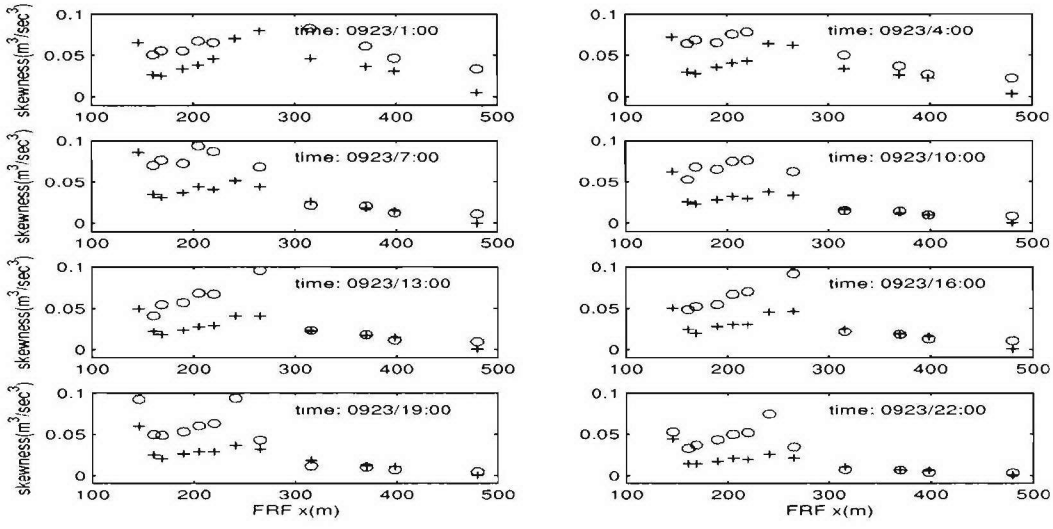

Figure 8.52: Model data comparison of velocity skewness at different velocity gages on 09/23/94, (data: circles; model: pluses)

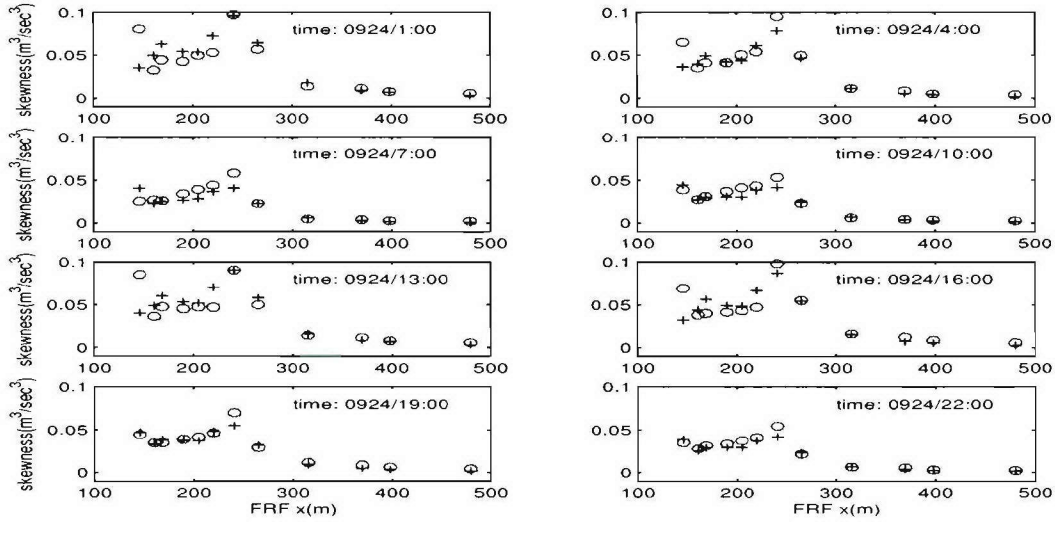

Figure 8.53: Model data comparison of velocity skewness at different velocity gages on 09/24/94, (data: circles; model: pluses)

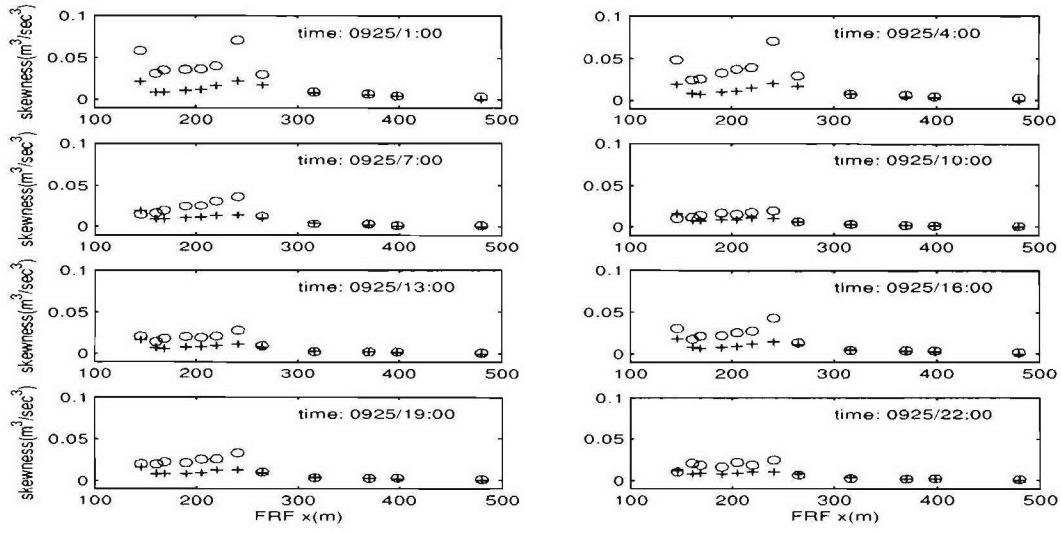

Figure 8.54: Model data comparison of velocity skewness at different velocity gages on 09/25/94, (data: circles; model: pluses)

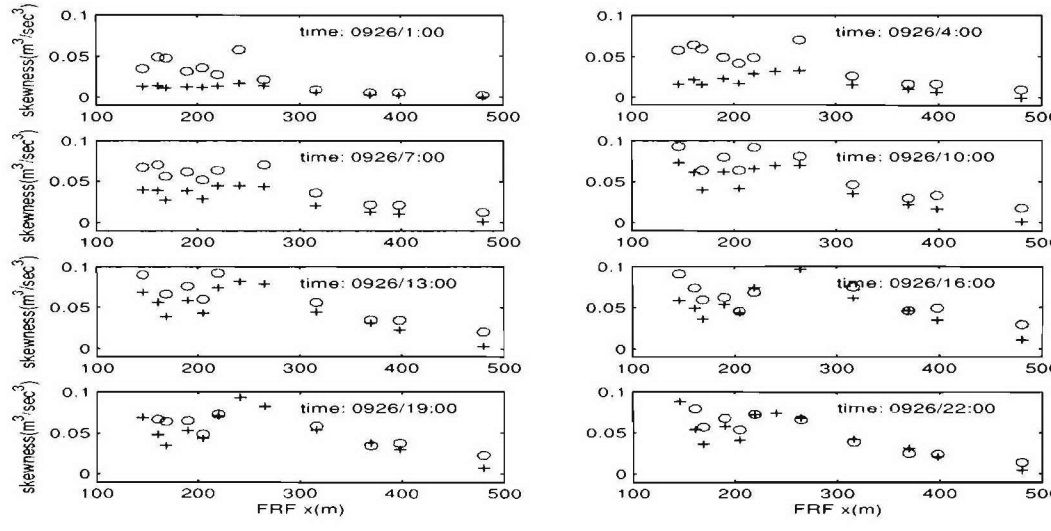

Figure 8.55: Model data comparison of velocity skewness at different velocity gages on 09/26/94, (data: circles; model: pluses)

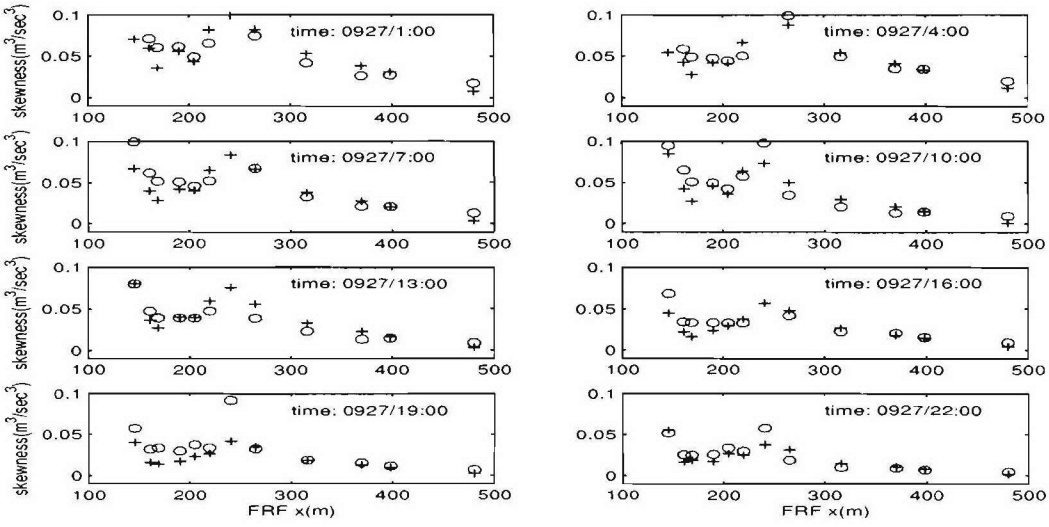

Figure 8.56: Model data comparison of velocity skewness at different velocity gages on 09/27/94, (data: circles; model: pluses)

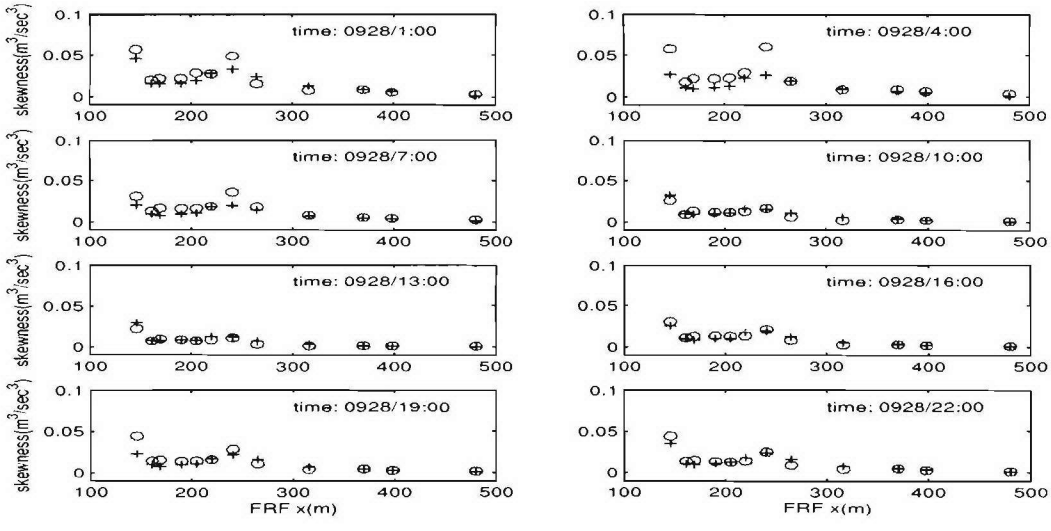

Figure 8.57: Model data comparison of velocity skewness at different velocity gages on 09/28/94, (data: circles; model: pluses)

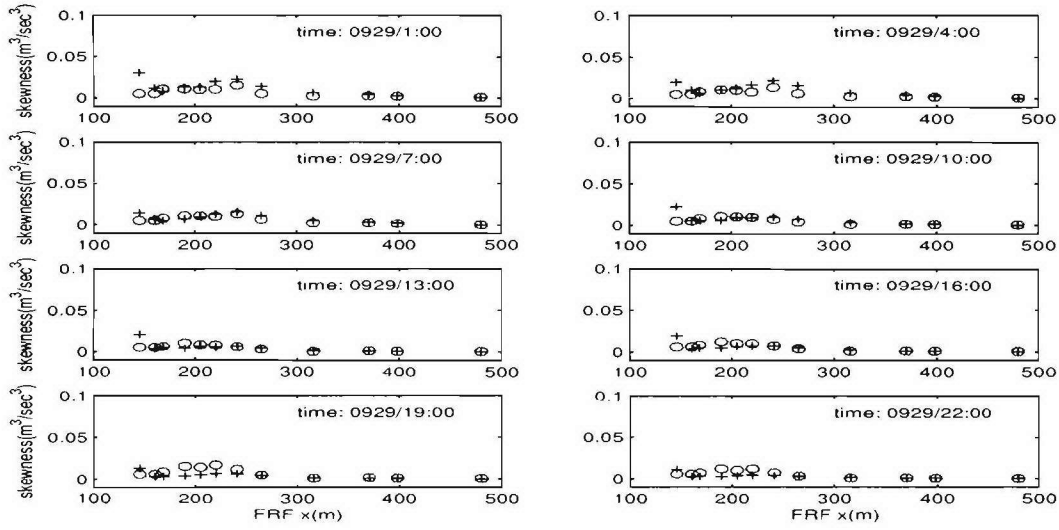

Figure 8.58: Model data comparison of velocity skewness at different velocity gages on 09/29/94, (data: circles; model: pluses)

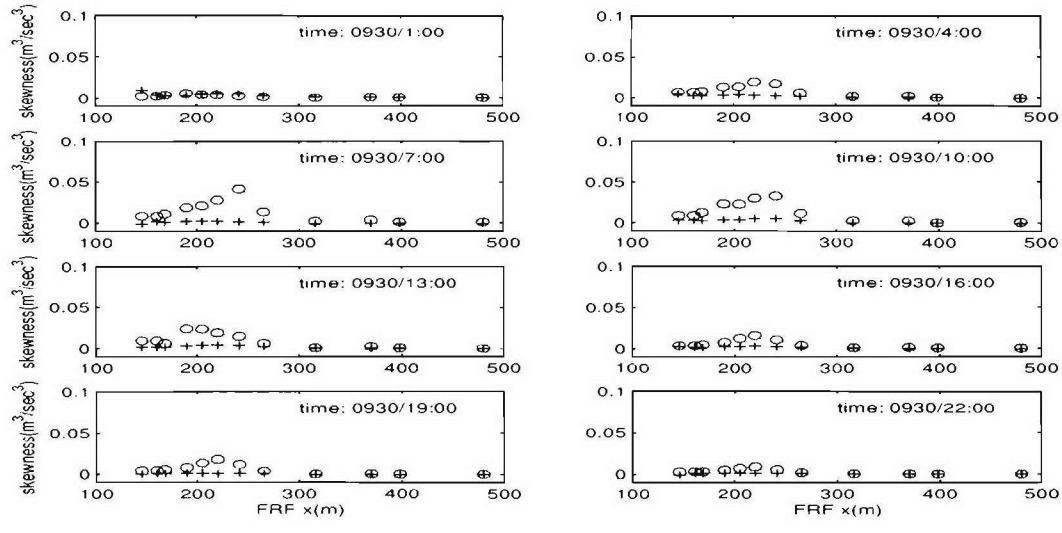

Figure 8.59: Model data comparison of velocity skewness at different velocity gages on 09/30/94, (data: circles; model: pluses)

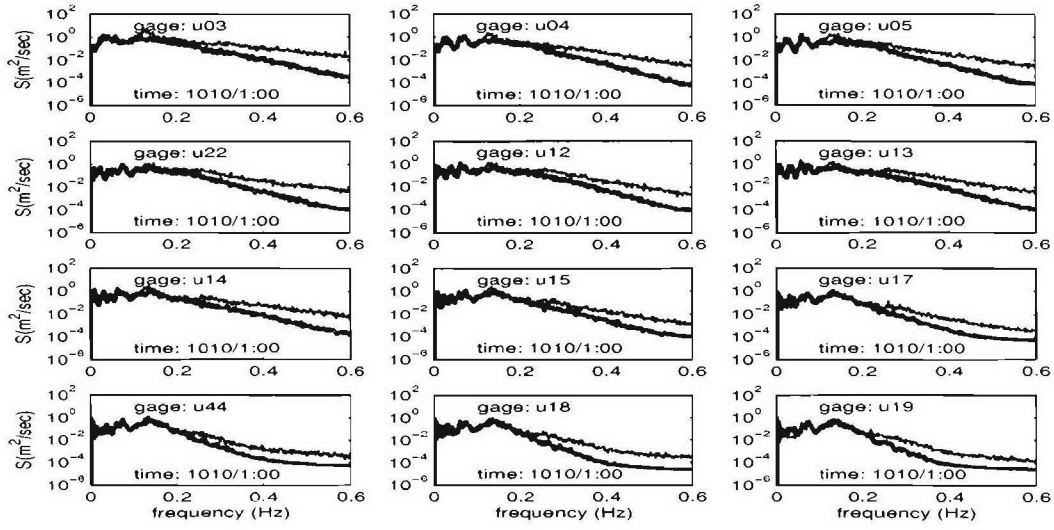

Figure 8.60: Model data comparison of velocity power spectra at different gages on 10/10/94, 1:00am (data: thin-line; model: thick-line)

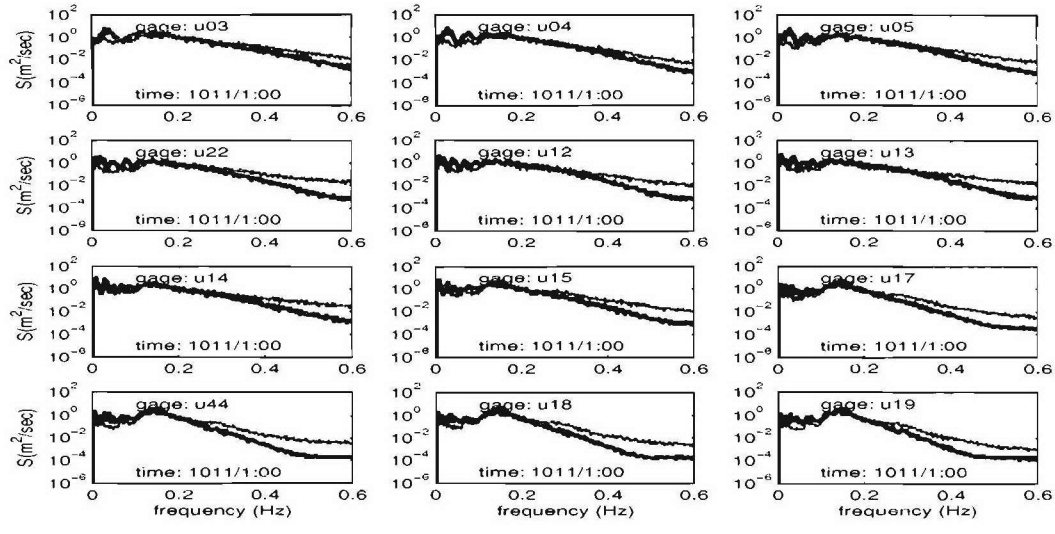

Figure 8.61: Model data comparison of velocity power spectra at different gages on 10/11/94, 1:00am (data: thin-line; model: thick-line)

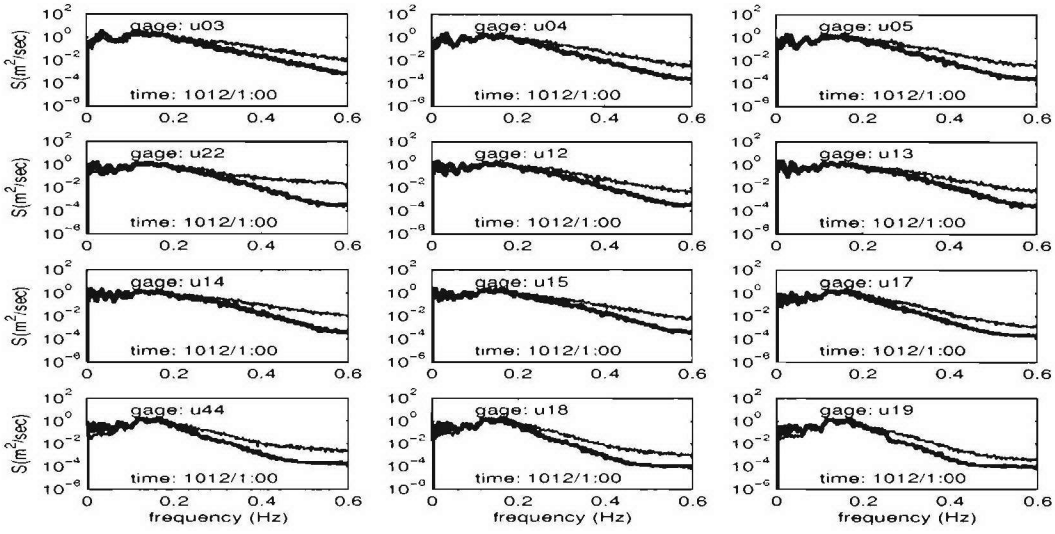

Figure 8.62: Model data comparison of velocity power spectra at different gages on 10/12/94, 1:00am (data: thin-line; model: thick-line)

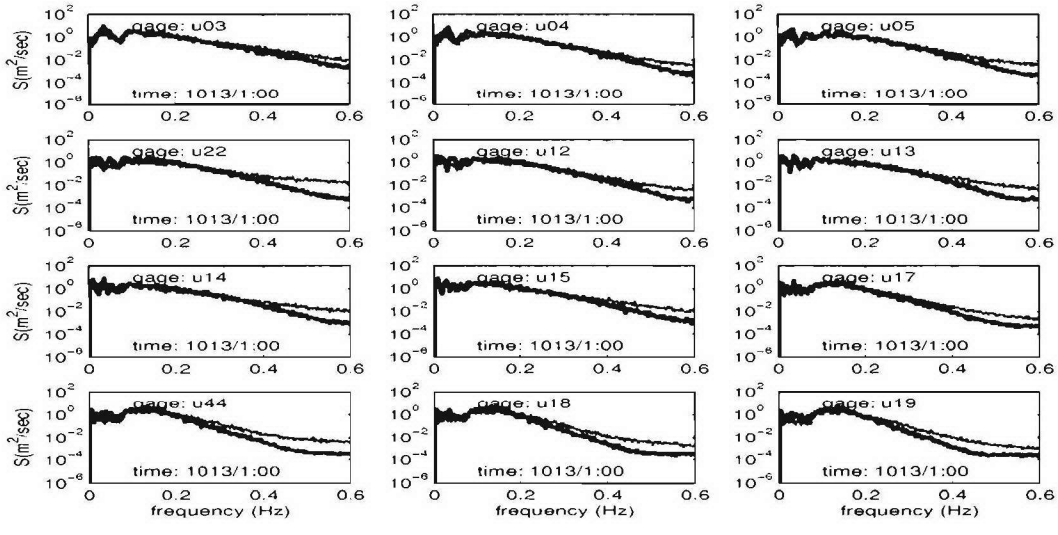

Figure 8.63: Model data comparison of velocity power spectra at different gages on 10/13/94, 1:00am (data: thin-line; model: thick-line)

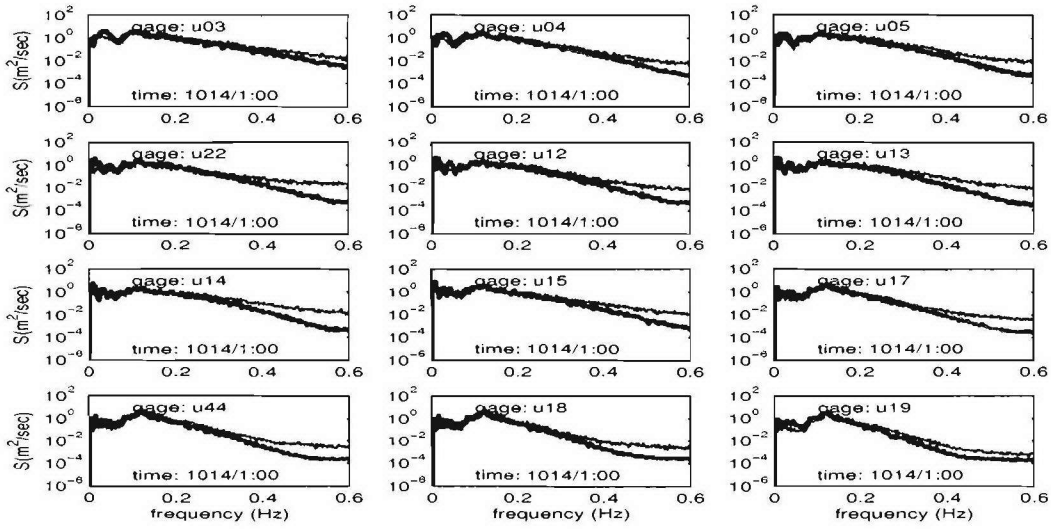

Figure 8.64: Model data comparison of velocity power spectra at different gages on 10/14/94, 1:00am (data: thin-line; model: thick-line)

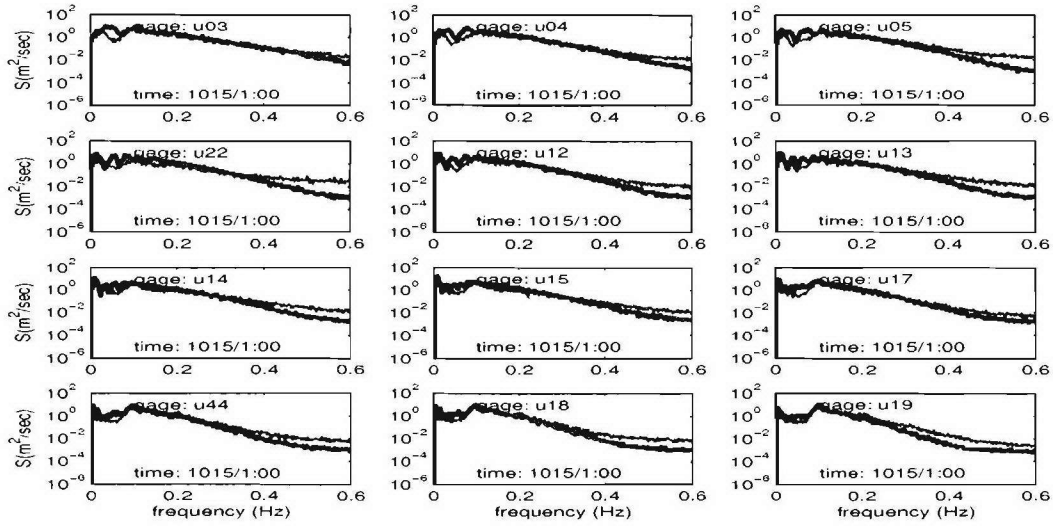

Figure 8.65: Model data comparison of velocity power spectra at different gages on 10/15/94, 1:00am (data: thin-line; model: thick-line)

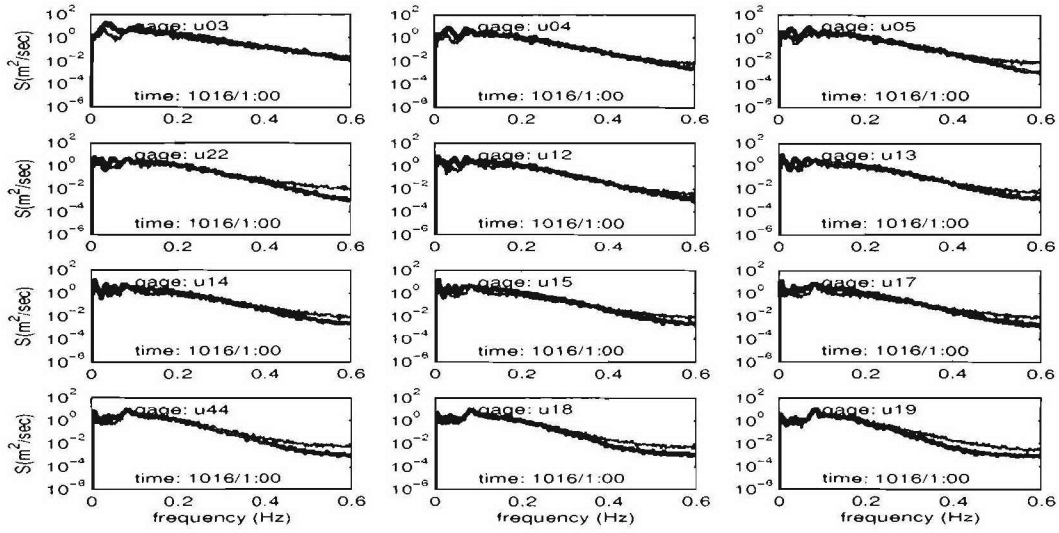

Figure 8.66: Model data comparison of velocity power spectra at different gages on 10/16/94, 1:00am (data: thin-line; model: thick-line)

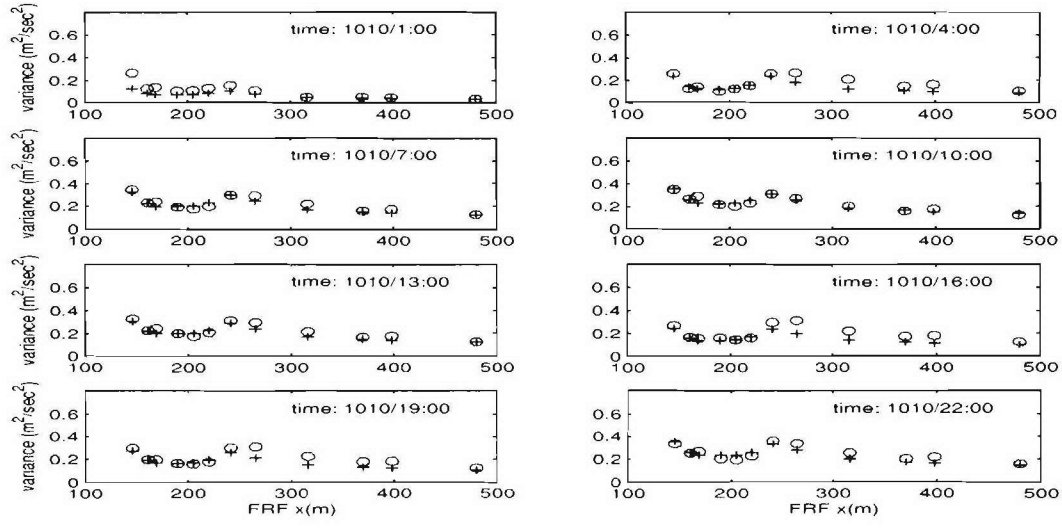

Figure 8.67: Model data comparison of velocity variance at different velocity gages on 10/10/94, (data: circles; model: pluses)

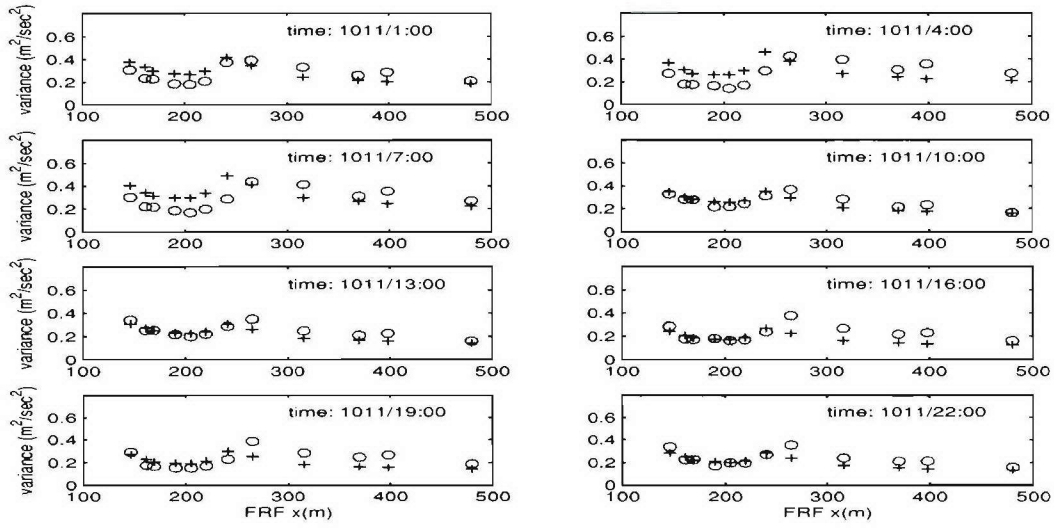

Figure 8.68: Model data comparison of velocity variance at different velocity gages on 10/11/94, (data: circles; model: pluses)

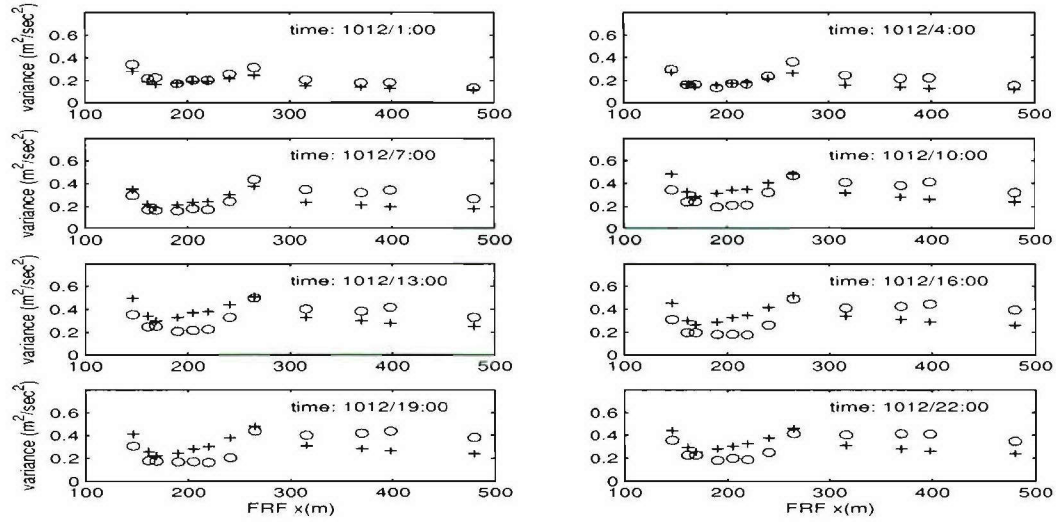

Figure 8.69: Model data comparison of velocity variance at different velocity gages on 10/12/94, (data: circles; model: pluses)

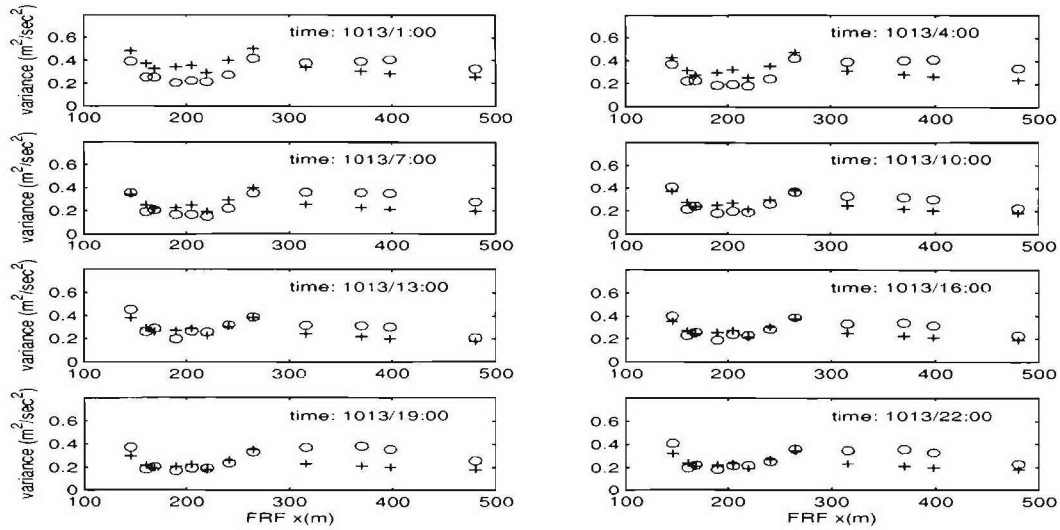

Figure 8.70: Model data comparison of velocity variance at different velocity gages on 10/13/94, (data: circles; model: pluses)

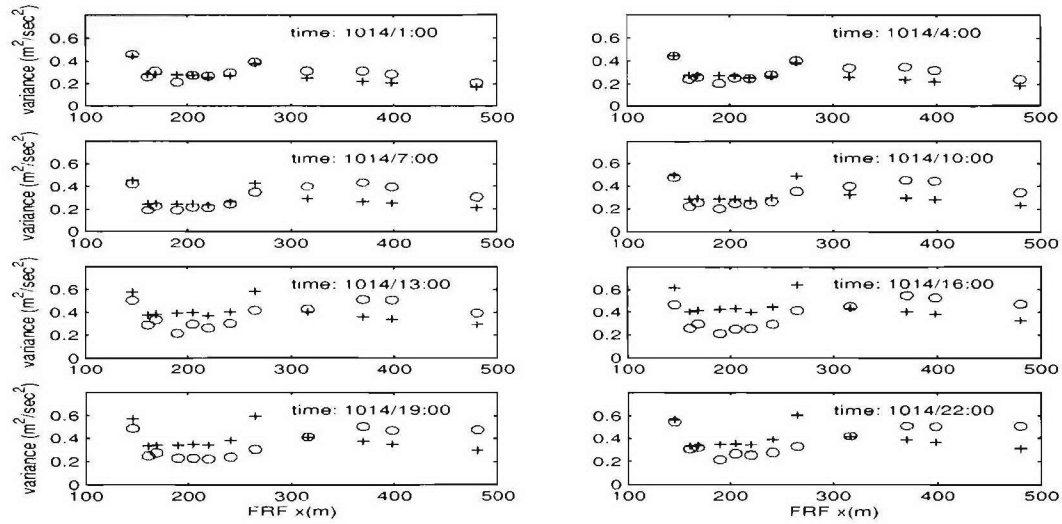

Figure 8.71: Model data comparison of velocity variance at different velocity gages on 10/14/94, (data: circles; model: pluses)

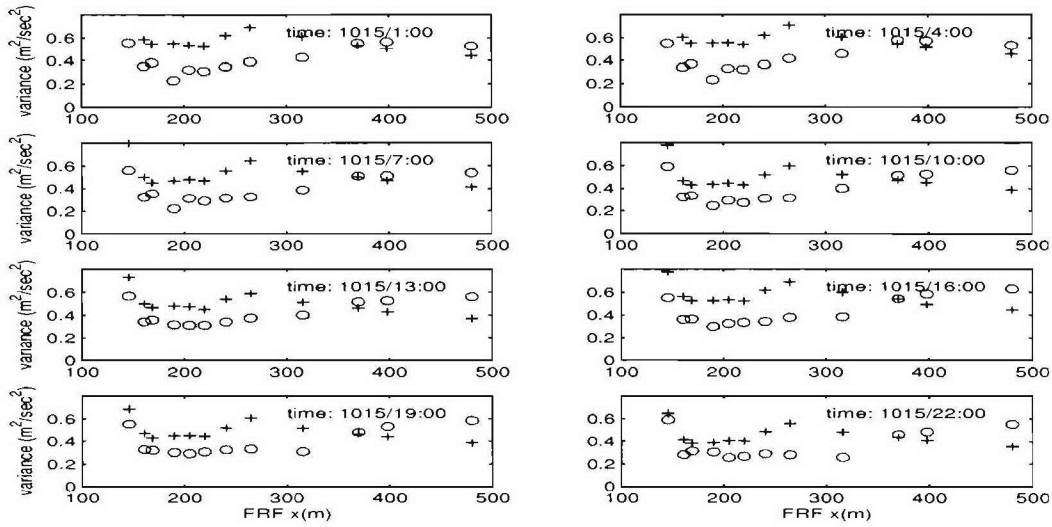

Figure 8.72: Model data comparison of velocity variance at different velocity gages on 10/15/94, (data: circles; model: pluses)

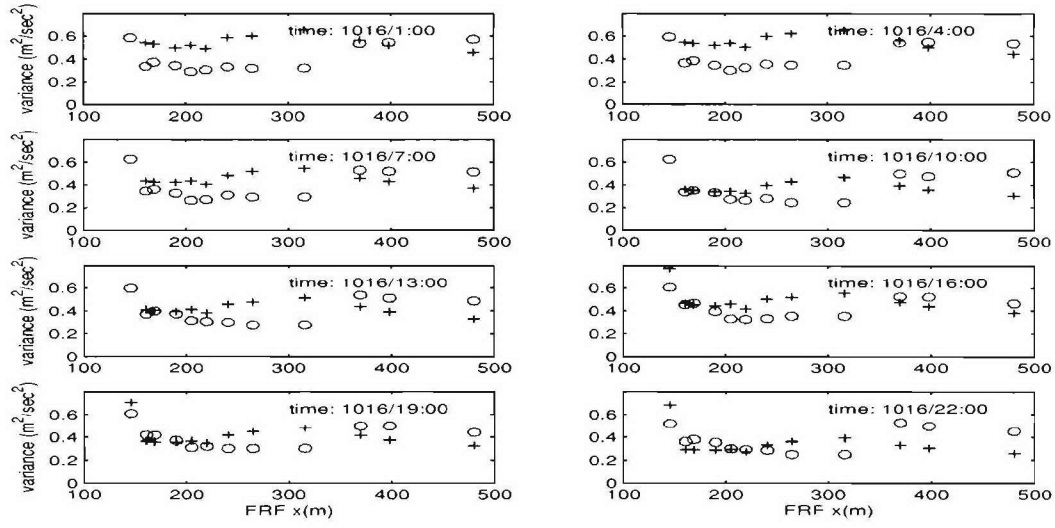

Figure 8.73: Model data comparison of velocity variance at different velocity gages on 10/16/94, (data: circles; model: pluses)

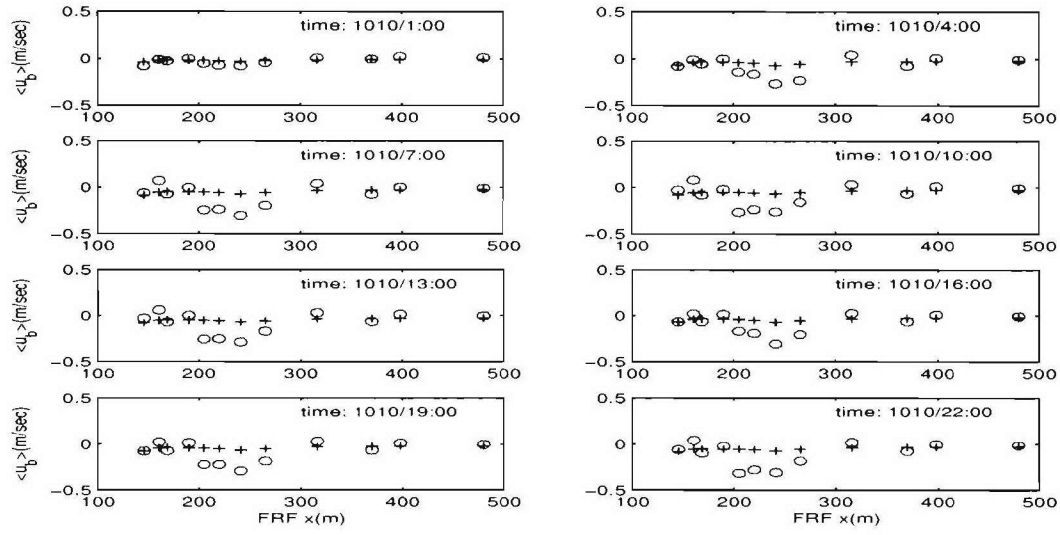

Figure 8.74: Model data comparison of velocity mean at different velocity gages on 10/10/94, (data: circles; model: pluses)

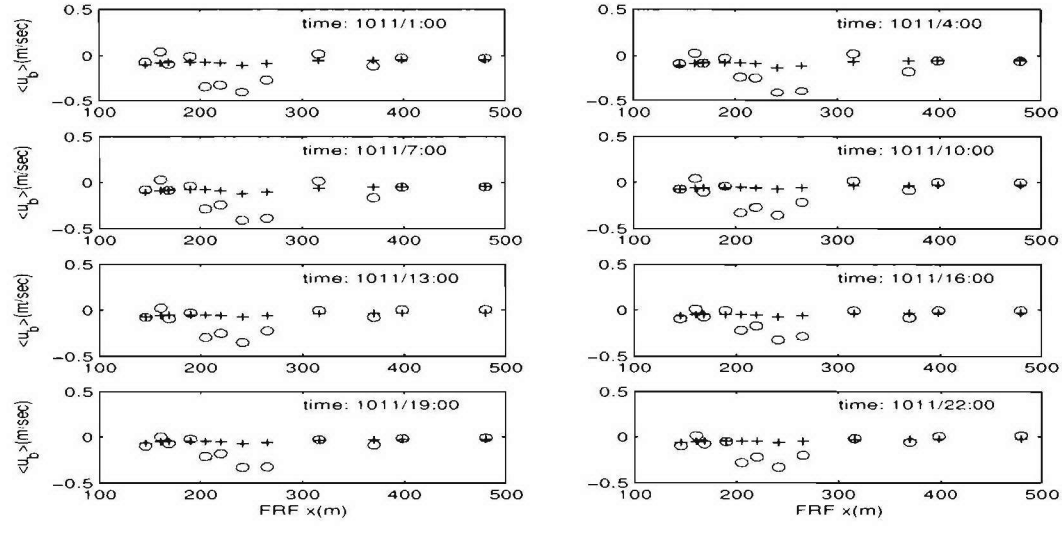

Figure 8.75: Model data comparison of velocity mean at different velocity gages on 10/11/94, (data: circles; model: pluses)

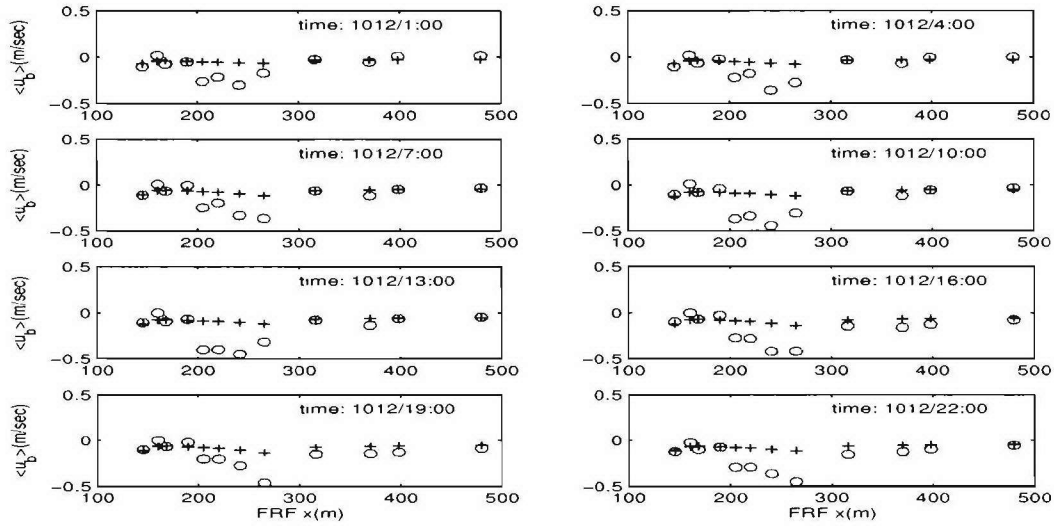

Figure 8.76: Model data comparison of velocity mean at different velocity gages on 10/12/94, (data: circles; model: pluses)

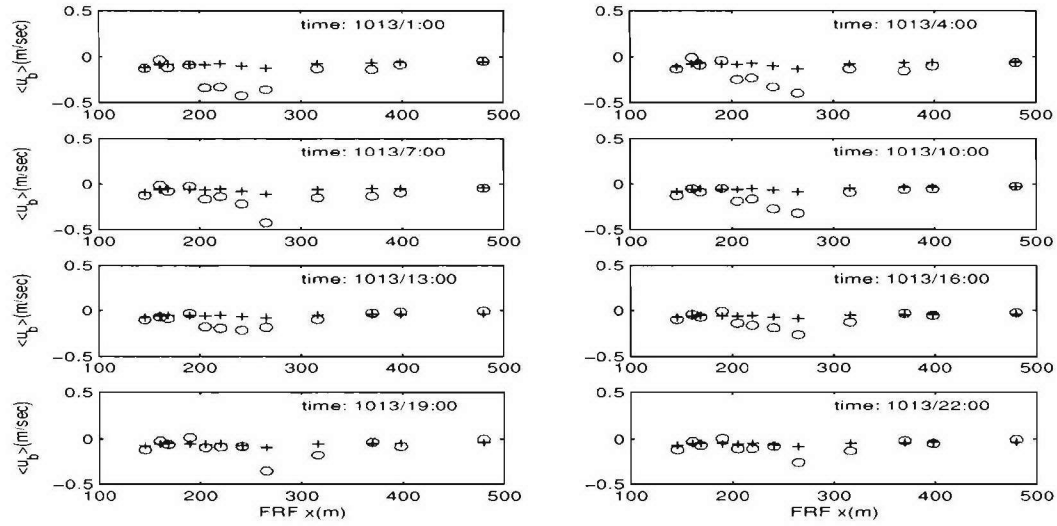

Figure 8.77: Model data comparison of velocity mean at different velocity gages on 10/13/94, (data: circles; model: pluses)

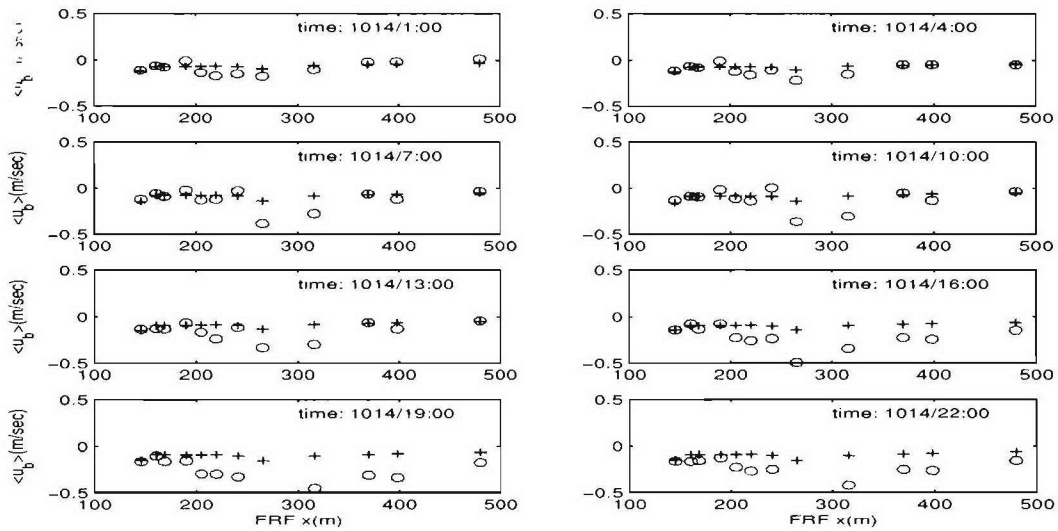

Figure 8.78: Model data comparison of velocity mean at different velocity gages on 10/14/94, (data: circles; model: pluses)

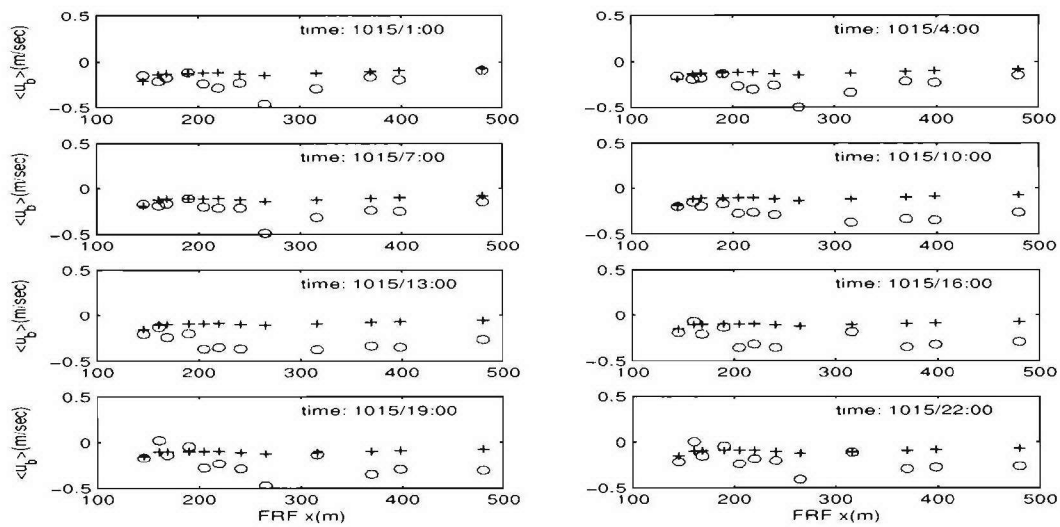

Figure 8.79: Model data comparison of velocity mean at different velocity gages on 10/15/94, (data: circles; model: pluses)

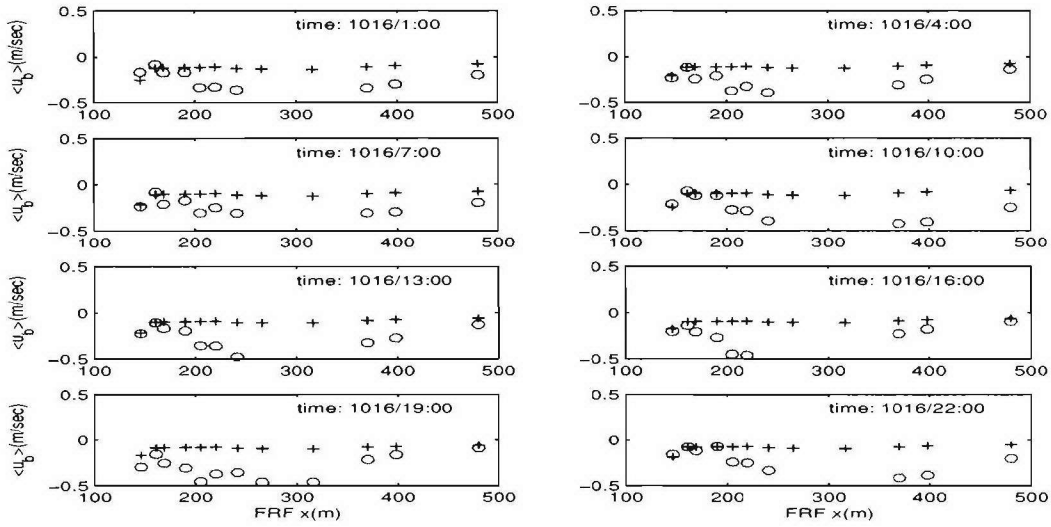

Figure 8.80: Model data comparison of velocity mean at different velocity gages on 10/16/94, (data: circles; model: pluses)

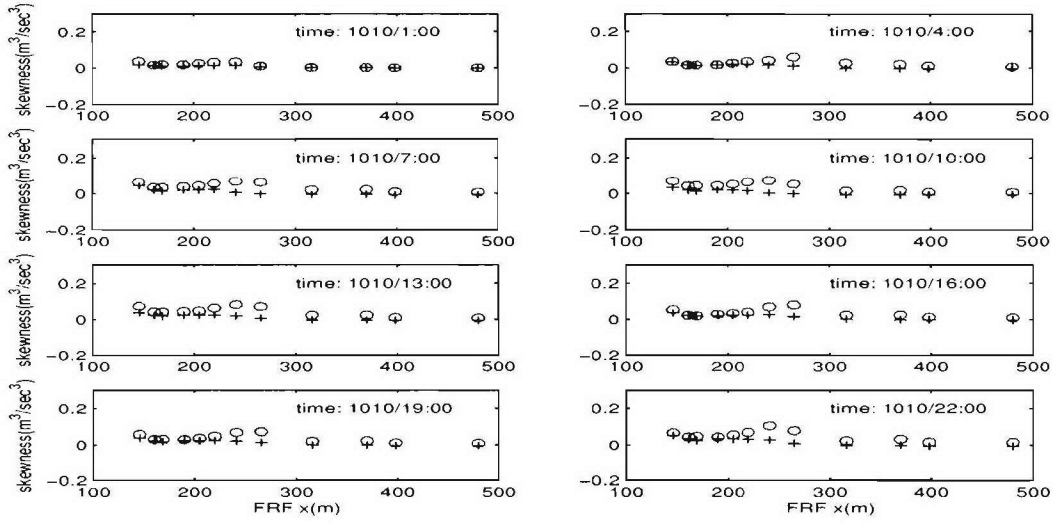

Figure 8.81: Model data comparison of velocity skewness at different velocity gages on 10/10/94, (data: circles; model: pluses)

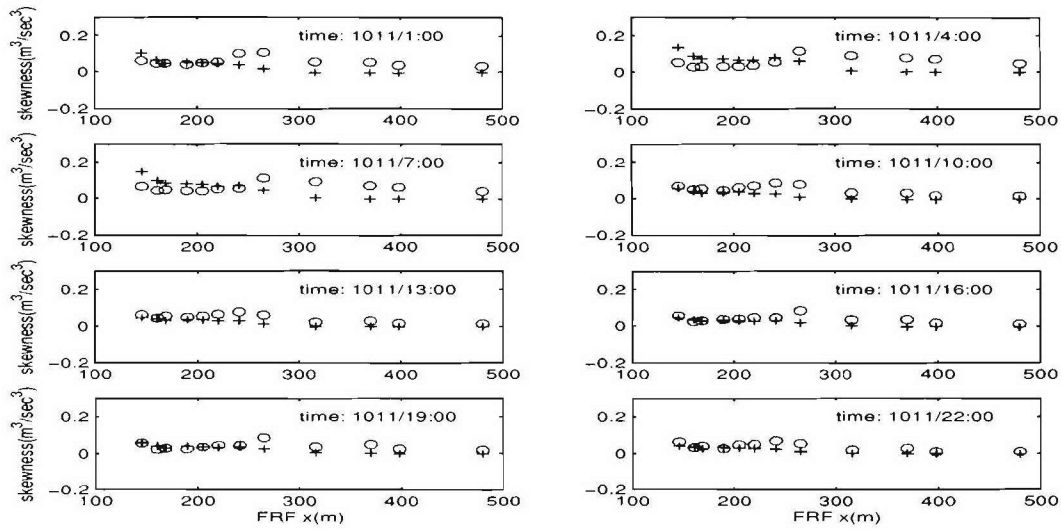

Figure 8.82: Model data comparison of velocity skewness at different velocity gages on 10/11/94, (data: circles; model: pluses)

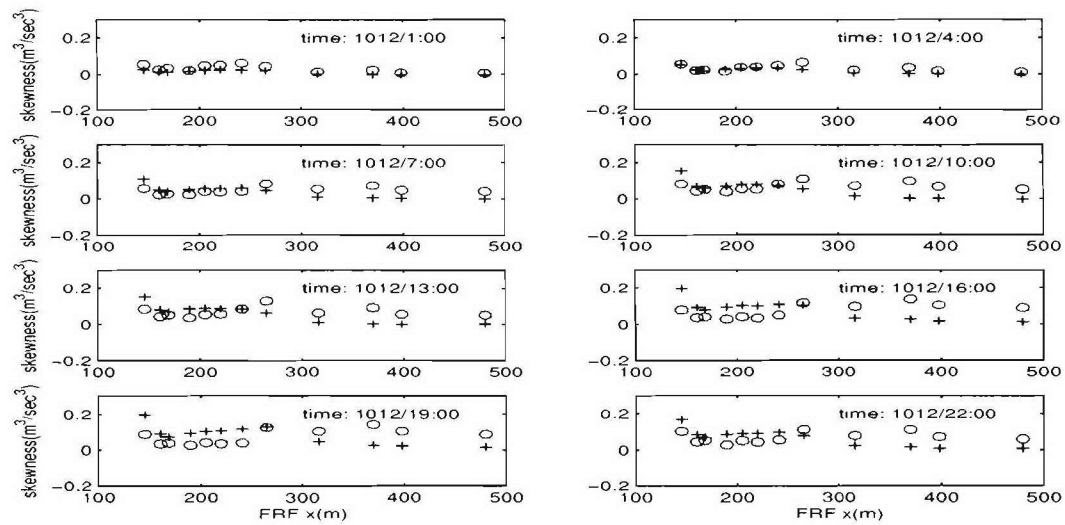

Figure 8.83: Model data comparison of velocity skewness at different velocity gages on 10/12/94, (data: circles; model: pluses)

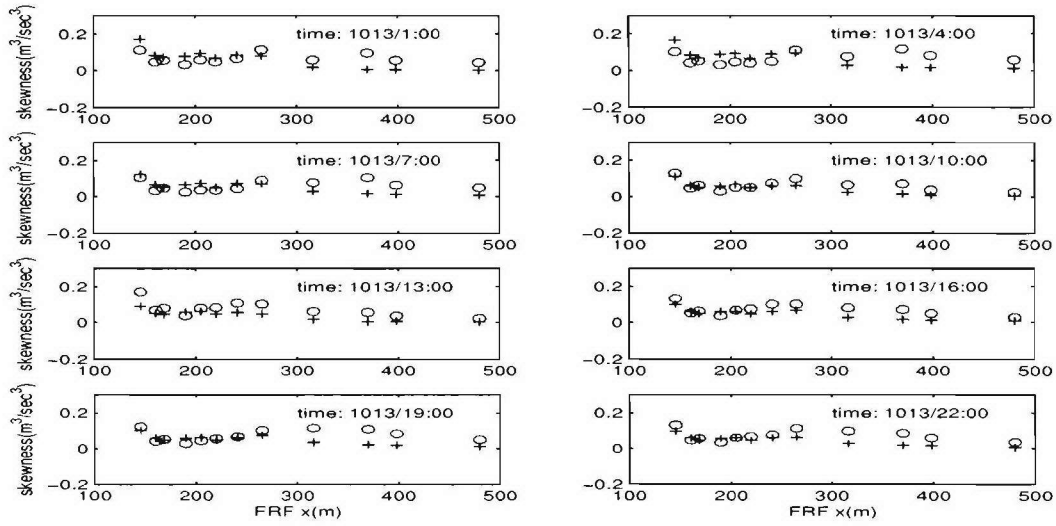

Figure 8.84: Model data comparison of velocity skewness at different velocity gages on 10/13/94, (data: circles; model: pluses)

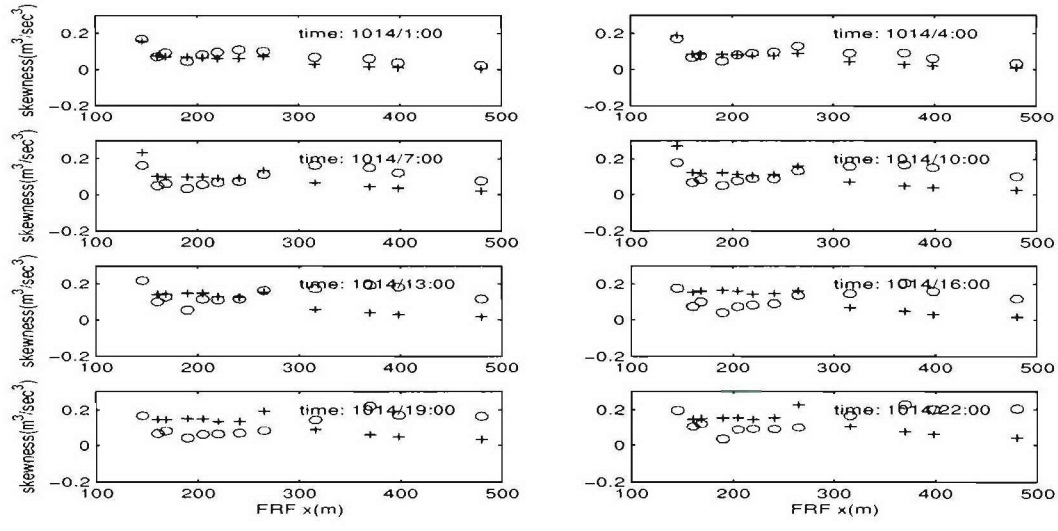

Figure 8.85: Model data comparison of velocity skewness at different velocity gages on 10/14/94, (data: circles; model: pluses)

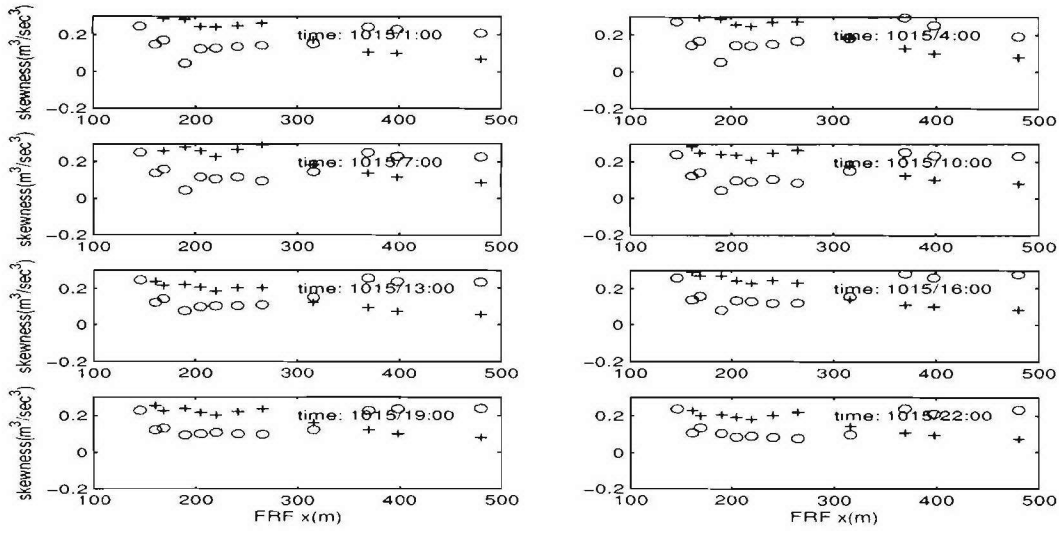

Figure 8.86: Model data comparison of velocity skewness at different velocity gages on 10/15/94, (data: circles; model: pluses)

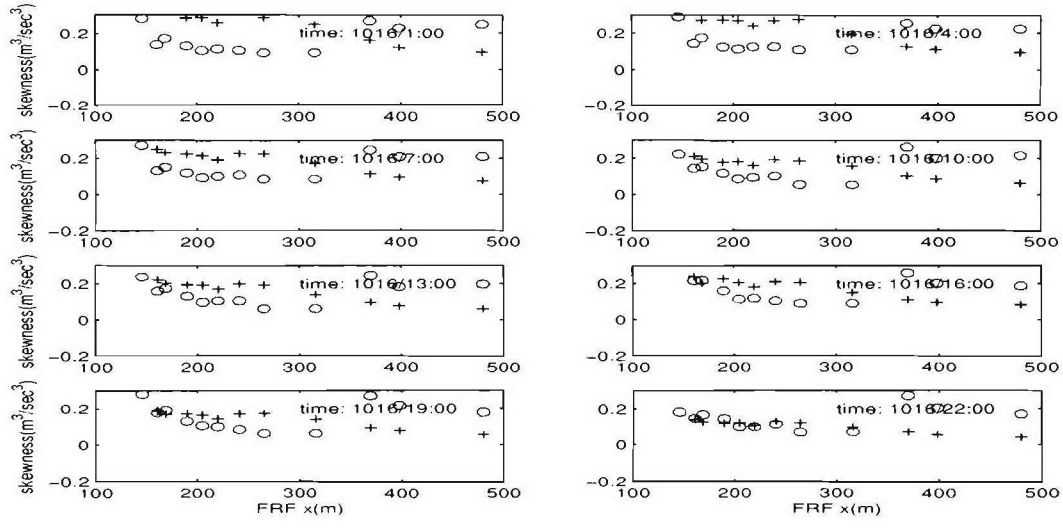

Figure 8.87: Model data comparison of velocity skewness at different velocity gages on 10/16/94, (data: circles; model: pluses)

8.1.4 Onshore bar migration events

In this section, we report the results obtained by complete simulation for 8 days from 09/23 to 09/30 when a large onshore migration event took place.

First, we reproduce the results obtained by Hsu et al. (2005) where measured near bottom velocities of 12 u-gages are used to drive a Meyer-Peter-Müller type sediment transport model. Then, the same calculations are conducted using the Boussinesq model predicted near bottom velocities (based on measured bathymetry) at the same 12 u-gages to show that the results are consistent with Hsu et al. (2005).

Then, we conduct continuous model runs using the coupled model FUNSEDI1D1.0 with the two different transport formulations: model A (8.2) and model B (8.3). Continuous predictions of surface wave elevation, bottom velocity, shear stress, and transport rates are made to predict the bathymetry change in the entire domain with a spatial resolution of $\Delta x = 1m$.

8.1.4.1 Data driven model by Hsu et al. (2005)

In Hsu et al. (2005), simulation of bedform change using measured near bottom velocities from 12 gages is carried out with the above mentioned boundary layer model. Here, we demonstrate that almost the same results are obtained using the near bottom velocities from the Boussinesq model.

In the computation, the parameters are: dry sediment density $\rho_s = 2650kg/m^3$, sediment diameter $d = 0.2$mm, bottom roughness $K_s = 14d$, still bed porosity $n_p = 0.3$. These parameters are essentially the same as in Hsu et al. (2005) and Long and Kirby (2003). The onshore bar migration event from September 23, 1:00am to September 28, 1:00am is simulated separately using modeled bottom velocities and measured bottom velocities. Note that the modeled bottom velocities here are calculated based on the measured bathymetry to be consistent with the measured velocities.

Figure 8.88 and figure 8.89 show the modeled bedform change using measured bottom velocities following Hsu et al. (2005). In figure 8.88, the predicted bathymetries

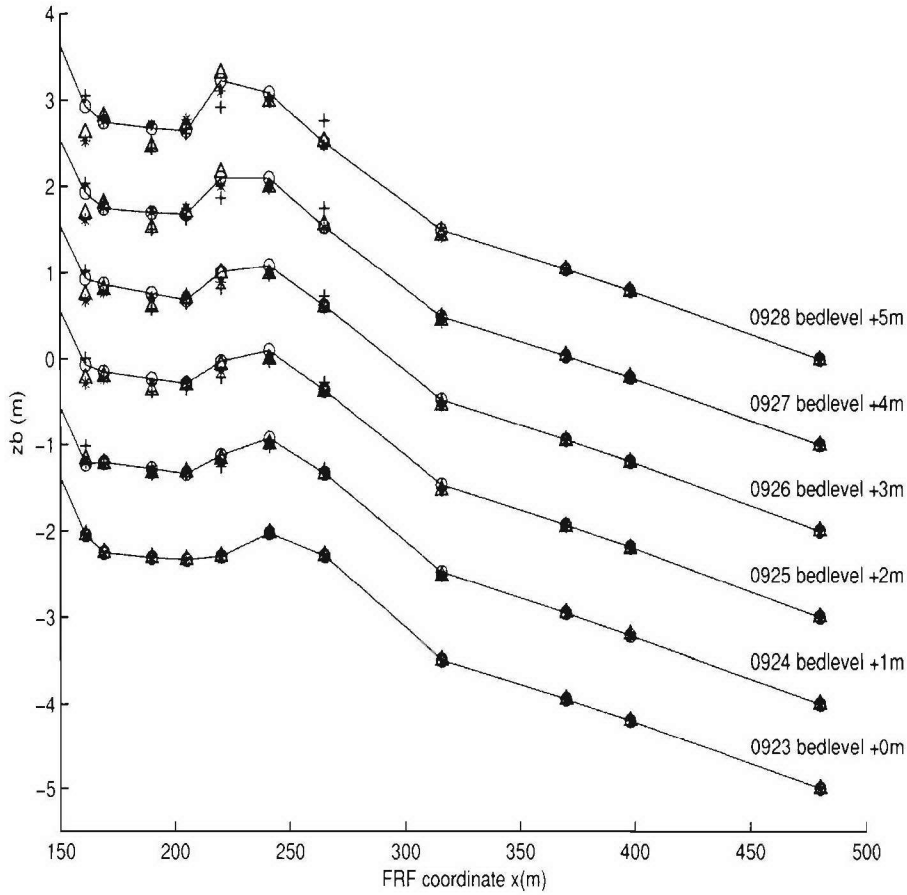

Figure 8.88: Onshore bar migration predicted using measured velocities during 09/23/1994 1:00am to 09/28/1994 1:00am; circles: measured bathymetry; triangles: predicted bathymetry using total transport q_c+q_w by (8.3); pluses: predicted bathymetry using current-related transport q_c only; stars: predicted bathymetry using wave-related transport q_w only

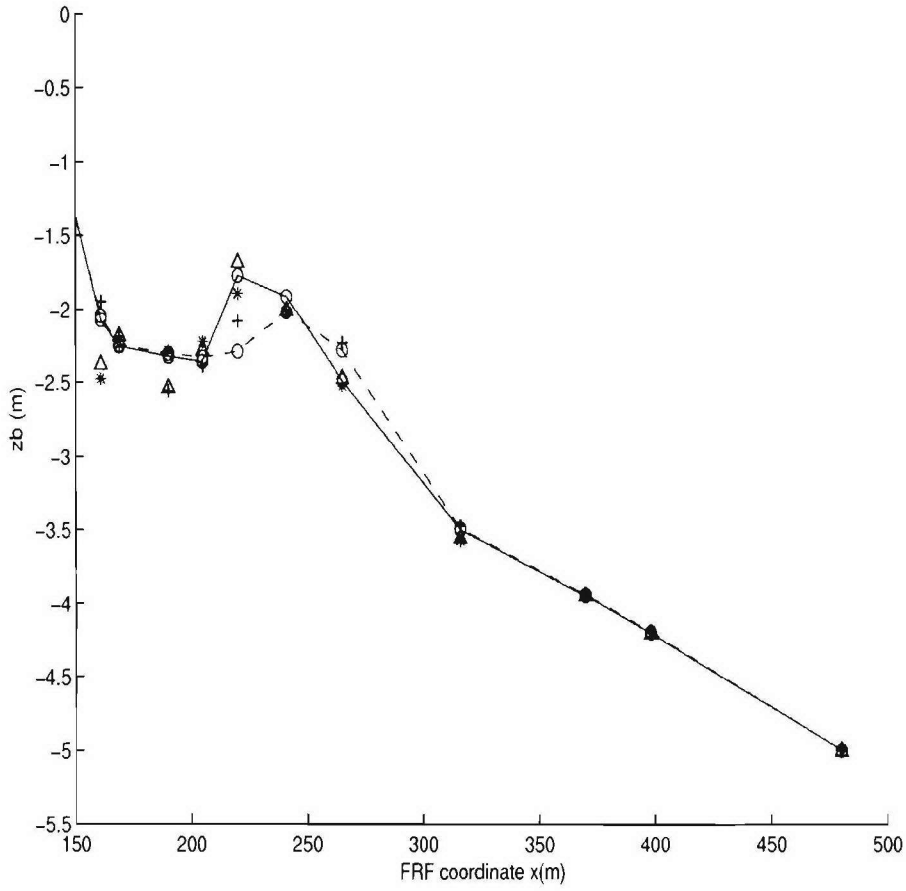

Figure 8.89: Onshore bar migration predicted using measured velocities during 09/23/1994 1:00am to 09/28/1994 1:00am; circles: measured bathymetry (dash line indicates the measured bathymetry on 09/23/1994 1:00am, solid line indicates the measured bathymetry on 09/28/1994 1:00am); triangles: predicted bathymetry using total transport $q_c + q_w$ by (8.3); pluses: predicted bathymetry using current-related transport q_c only; stars: predicted bathymetry using wave-related transport q_w only);

due to wave-related transport q_w, due to current-related transport q_c and due to the total transport $q_w + q_c$ are plotted for each day. Figure 8.89 shows the predicted bathymetries due to q_w, q_c and q_w+q_c for day 09/28/1994 1:00am compared to the measured bathymetry change. Although the mean current (undertow) is quite small during this period, the contribution of q_c contributed to slight offshore transport rate and undermines the dominant onshore transport rate due to q_w. q_w is driven by instantaneous shear stress resulted from the wave bottom boundary layer model, and it automatically incorporates wave skewness and asymmetry. The total transport rate $q_w + q_c$ by (8.3) gives a reasonable prediction of the onshore bar migration process during the five day period. This indicates that the bottom shear stress driven transport q_w gives significant onshore bar migration. The same results are also shown in Hsu et al. (2005).

Figure 8.90 and figure 8.91 shows the modeled bedform change using the Boussinesq model produced bottom velocities with the same transport rate calculations. We see that again the contribution of q_c to the bedform change is almost negligible because the mean velocities are fairly small. When the total transport rate is considered, the predicted bar migration reproduces the measured bathymetry change. This indicates that the Boussinesq model along with the bottom boundary layer model can provide reasonable predictions of wave orbital velocities and bottom shear stress.

The simulations in figure 8.89 and Hsu et al. (2005) are based on measured near bottom velocities. These velocities correctly reflect the bed deformation effects on waves. In the modeling given by figure 8.91, similarly, the near bed velocities are modeled based on measured bathymetry and used to drive sediment transport model, but no feed back is given from the computed bathymetry to the hydrodynamic model. This is referred to as one-way coupling model.

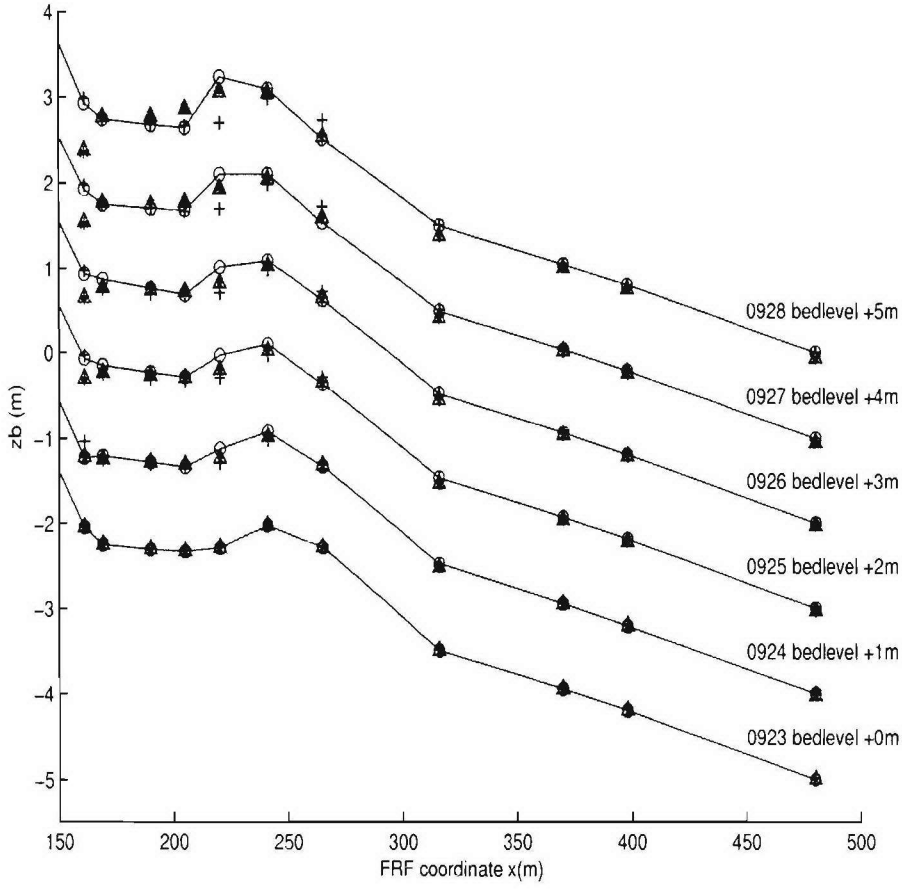

Figure 8.90: Onshore bar migration predicted using Boussinesq model velocities during 09/23/1994 1:00am to 09/28/1994 1:00am; circles: measured bathymetry; triangles: predicted bathymetry using total transport $q_c + q_w$ by (8.3); pluses: predicted bathymetry using current-related transport q_c only; stars: predicted bathymetry using wave-related transport q_w only

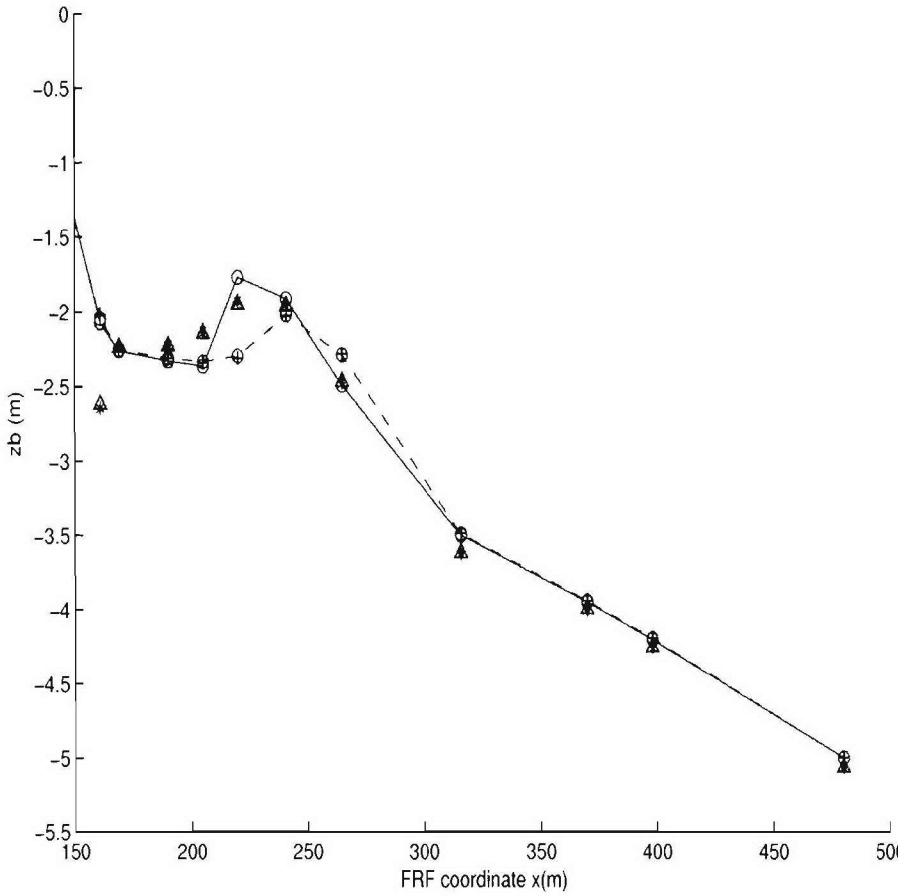

Figure 8.91: Onshore bar migration predicted using Boussinesq model velocities during 09/23/1994 1:00am to 09/28/1994 1:00am, circles: measured bathymetry (dash line indicates the measured bathymetry on 09/23/1994 1:00am, solid line indicates the measured bathymetry on 09/28/1994 1:00am); triangles: predicted bathymetry using total transport $q_c + q_w$ by (8.3); pluses: predicted bathymetry using current-related transport q_c only; stars: predicted bathymetry using wave-related transport q_w only);

8.1.4.2 Model results by FUNSEDI1D1.0

In this section, we investigate two-way coupled models, in which velocities are computed based on the evolving, numerically predicted bathymetry. This approach introduces an extra degree of freedom when we feed back the computed bathymetry into the Boussinesq model for wave simulation. This is because the computed bathymetry has some discrepancies compared to real bathymetry, and hence the near bottom velocities based on computed bathymetry will have discrepancies compared to measured bottom velocities, and in turn it will affect the bathymetry computation for the next step. Both model A and model B are utilized to simulate the event from September 23 1:00am to September 30 1:00am. The following parameters are used in the models: time step for waves $\Delta t = 0.1s$, spatial step $\Delta x = 1m$. the time step for the bottom boundary layer model $\Delta t_{bbl} = 0.1s$, vertical spatial step $\Delta z = 3$mm, bottom roughness K_s is set to be $K_s = 25d$, sediment diameter $d = 0.2$mm, $\epsilon_B = 0.135$, $\epsilon_S = 0.015$, bottom friction coefficient $C_f = 0.009$, acceleration term coefficient $K_a = 0.001ms$, acceleration threshold $u_{btcr} = 0.1m/s^2$, sediment fall velocity $w_{fall} = 2cm/s$, sediment density $\rho_s = 2650kg/m^3$, water density $\rho = 1000kg/m^3$, molecular viscosity $\nu = 1 \times 10^{-6} m^2/s$. The sediment transport rates are calculated at every wave time step, and are accumulated for 30 minutes before being used to update the bathymetry. The mean bottom velocity $\overline{u_b}$ is also obtained by a time average of u_b for 30 minutes. Critical shield stress θ_c is obtained through Shields diagram. During the simulation, a sponge layer is placed on the shoreface to suppress the bathymetry change due to large, unrealistic transport rates calculated by the model. The computation time is about 2 days for 8 days realization on a $2.4GHz$, 8-CPU, Linux platform system using the f77 compiler.

Figure 8.92 shows the simulation from September 23, 1:00am to September 30, 1:00am with Model A and Model B. Both model A and model B predicted onshore bar migration. Both models under-predicted the bar crest height, and model B is better than model A in terms of crest height. Model A is better in terms of migration distance. One

of the reason for under-prediction is due to the un-conserved mass of sand at the chosen measured cross section, possibly due to horizontally 2-D effects in the field experiment which can not be captured using a 1-D model.

Due to the computational cost, no nonlinear wave boundary layer model or $k-\epsilon$ turbulence model computation results have been shown here. Previous studies (e.g., Henderson et al., 2004; Hsu et al., 2005) suggest that the nonlinear wave boundary layer model will give a better prediction of bar crest height.

8.1.5 Offshore bar migration events

The same procedure of computation has been undertaken to simulate the offshore bar migration event from 10/10/94 to 10/15/94, which include comparison of results obtained by using the measured bottom velocity data of the 12 velocity gages and the Boussinesq model predicted bottom velocity data, as well as continuously two-way coupled model A and model B.

8.1.5.1 Data driven model by Hsu et al. (2005)

The results obtained based on the 12 gages velocity data from measurements and from the Boussinesq wave model prediction are presented below. In figure 8.93 and 8.94, the bathymetry change by model B using measured cross shore velocities are given compared to measured bathymetry change. The bathymetry change due to current-related q_c gives large erosion of the sand bar trough and bar crest is moved offshore from gage u14 ($x = 240.55m$) to u15 ($x = 264.70m$) with its height more than 1.5 meter. On the other hand, the bathymetry change due to wave-related transport q_w gives slight onshore movement of the bar crest. The overall effect of q_w and q_c resulted in offshore migration with the amount of erosion less than the measurements, i.e., the offshore bar migration is underestimated.

Figure 8.95 and 8.96 show the bathymetry change modeled by model B using near-bottom cross shore velocities provided by the Boussinesq model. The bathymetry

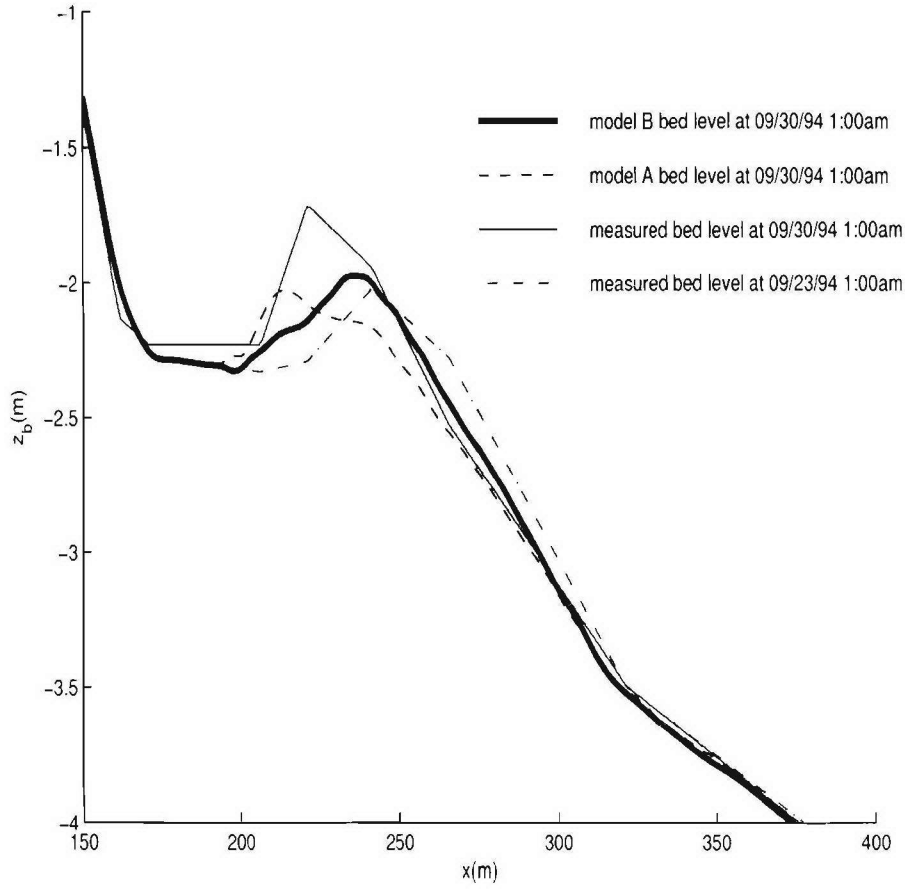

Figure 8.92: Bedform change using coupled Boussinesq model and sediment transport model (dash-dotted line: measured bathymetry at 09/23/94 1:00am; thin solid line: measured bathymetry at 09/30/94 1:00am; dash line: model A bathymetry at 09/30/94 1:00am; thick solid line: model B bathymetry at 09/30/94 1:00am)

change due to q_c also reflects offshore bar migration with the onshore side of the bar crest eroded and the offshore side of the bar crest accreted. The magnitude of offshore migration is substantially smaller than the results given by model using measured near-bottom velocity in figure 8.94. This is due to the underestimate of near-bottom mean current by the Boussineq model. The wave-related transport q_w gives slightly onshore bar migation as the same as the simulation using measured near-bottom velocity in figure 8.94. Overall results given by $q_c + q_w$ gives offshore bar migration. The overall magnitude of offshore bar migration is very limited. This agreement of these offshore migration events should be improved by an undertow model that can simulate the vertical structure of the cross shore circulation.

8.1.5.2 Model results by FUNSEDI1D1.0

For this case, the same setting of parameters as the simulation of the onshore migration events are used. There is also a sponge layer on the shoreface to suppress bathymetry change in the swash zone. The model and data comparison of the bathymetry change is shown in figure 8.97.

The measured data show a large distance of offshore movement and depression of the bar. Yet the model A and B show poor agreement with the measurement. The model results also show loss of sand due to the fact that no offshore migration is obtained, and modeled sediments are transported onshore into the swash zone and are absorbed by the sponge layer. An attempt has been made to carry out the simulation without the sponge layer onshore, but these failed due to complicated near shoreline bathymetry that is generated. The sediment transport processes within the swash zone are still highly difficult to model with the current method due to the missing of important physics such as crossshore grain size distribution. The failure of producing offshore bar migration is mainly due to severe underestimate of the near bed undertow current because the model using measured velocity series does show offshore bar migration.

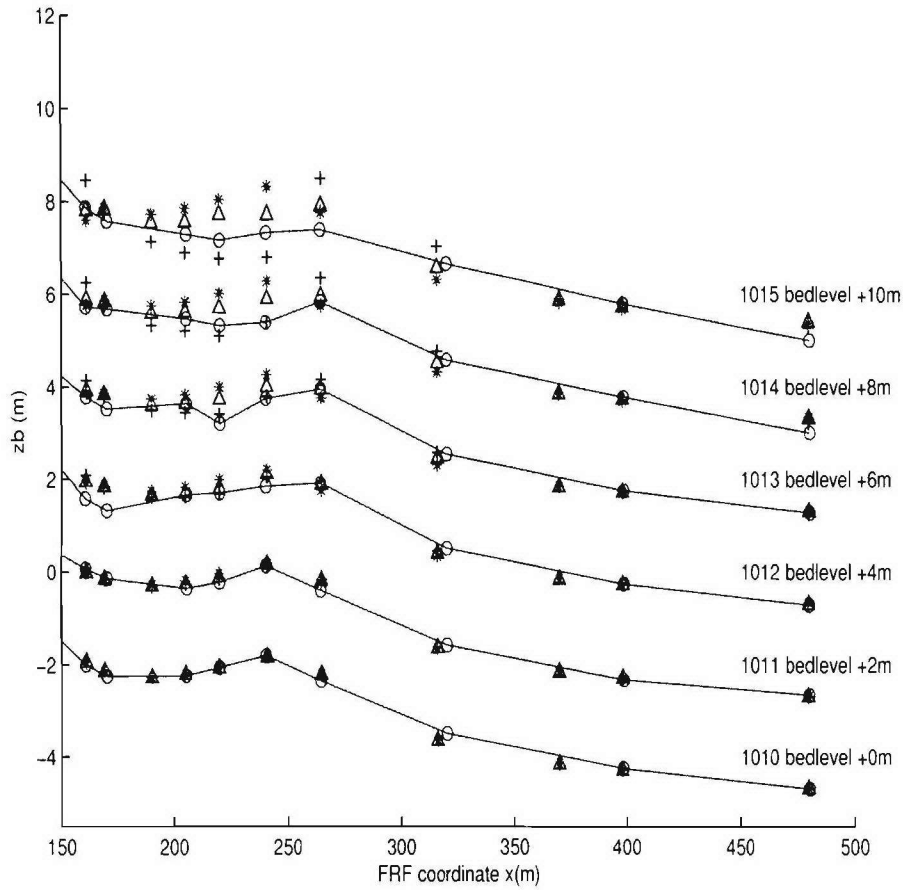

Figure 8.93: Offshore bar migration predicted using measured velocities during 10/10/1994 1:00am to 10/15/1994 1:00am; circles: measured bathymetry; triangles: predicted bathymetry using total transport q_c+q_w by (8.3); pluses: predicted bathymetry using current-related transport q_c only; stars: predicted bathymetry using wave-related transport q_w only

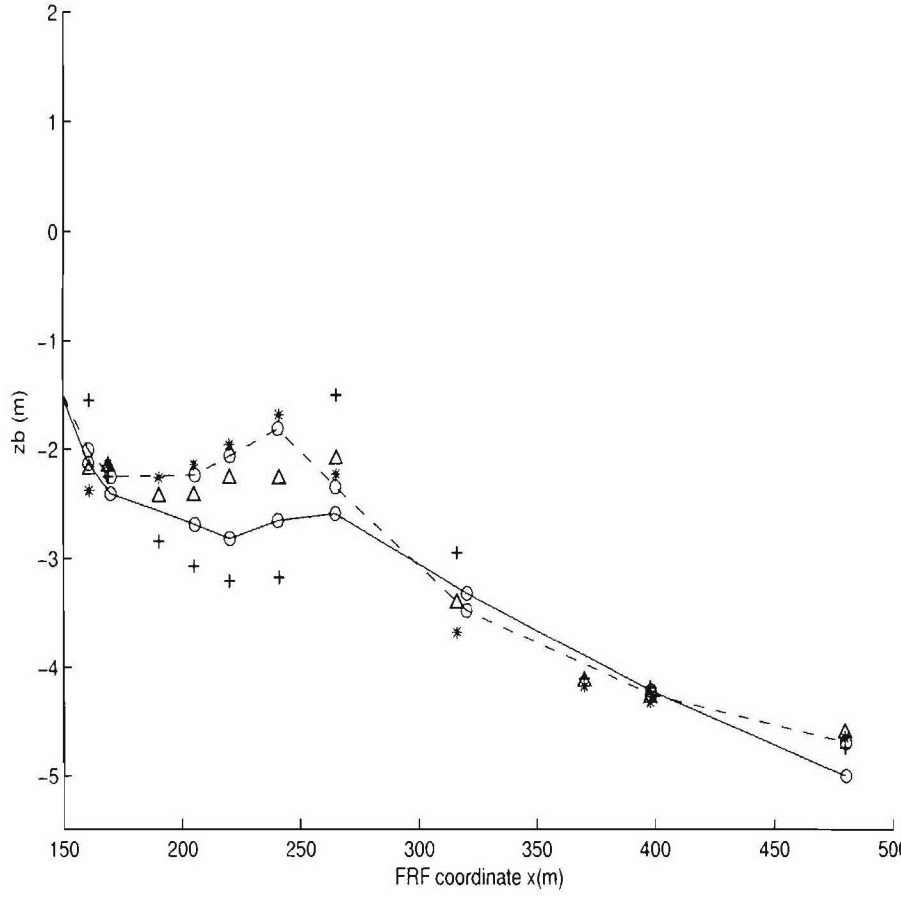

Figure 8.94: Offshore bar migration predicted using measured velocities during 10/10/1994 1:00am to 10/15/1994 1:00am, circles: measured bathymetry (dash line indicates the measured bathymetry on 10/10/1994 1:00am, solid line indicates the measured bathymetry on 10/15/1994 1:00am); triangles: predicted bathymetry using total transport $q_c + q_w$ by (8.3); pluses: predicted bathymetry using current-related transport q_c only; stars: predicted bathymetry using wave-related transport q_w only;

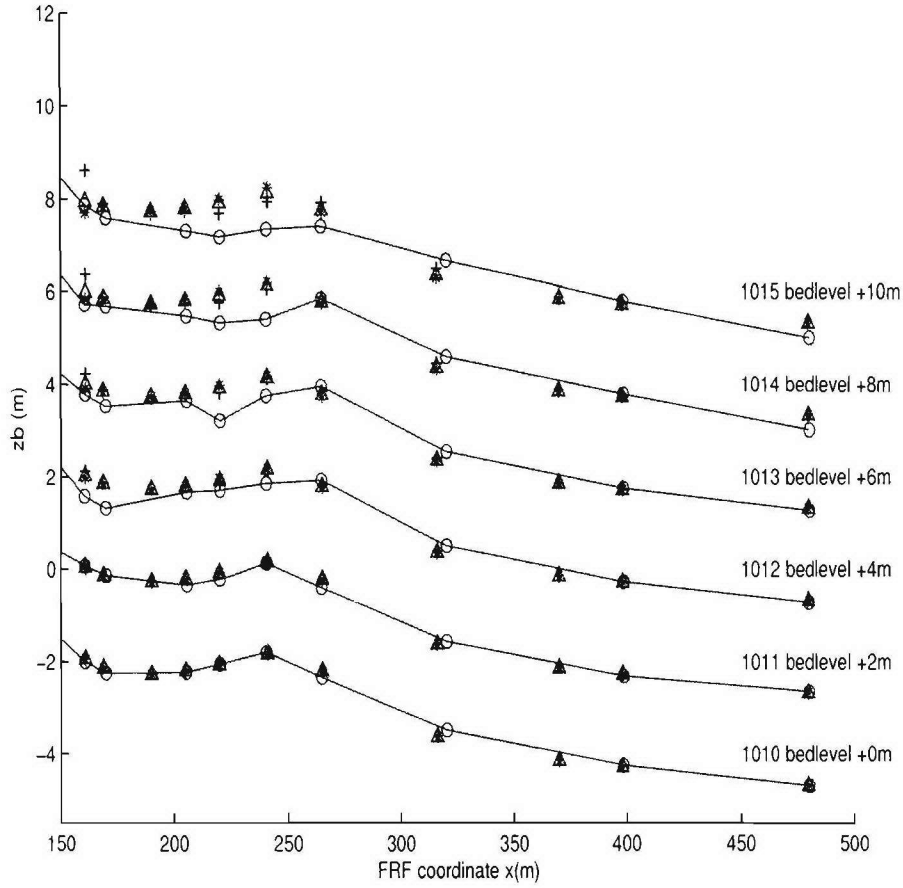

Figure 8.95: Offshore bar migration predicted using Boussinesq model velocities during 10/10/1994 1:00am to 10/15/1994 1:00am; circles: measured bathymetry; triangles: predicted bathymetry using total transport $q_c + q_w$ by (8.3); pluses: predicted bathymetry using current-related transport q_c only; stars: predicted bathymetry using wave-related transport q_w only

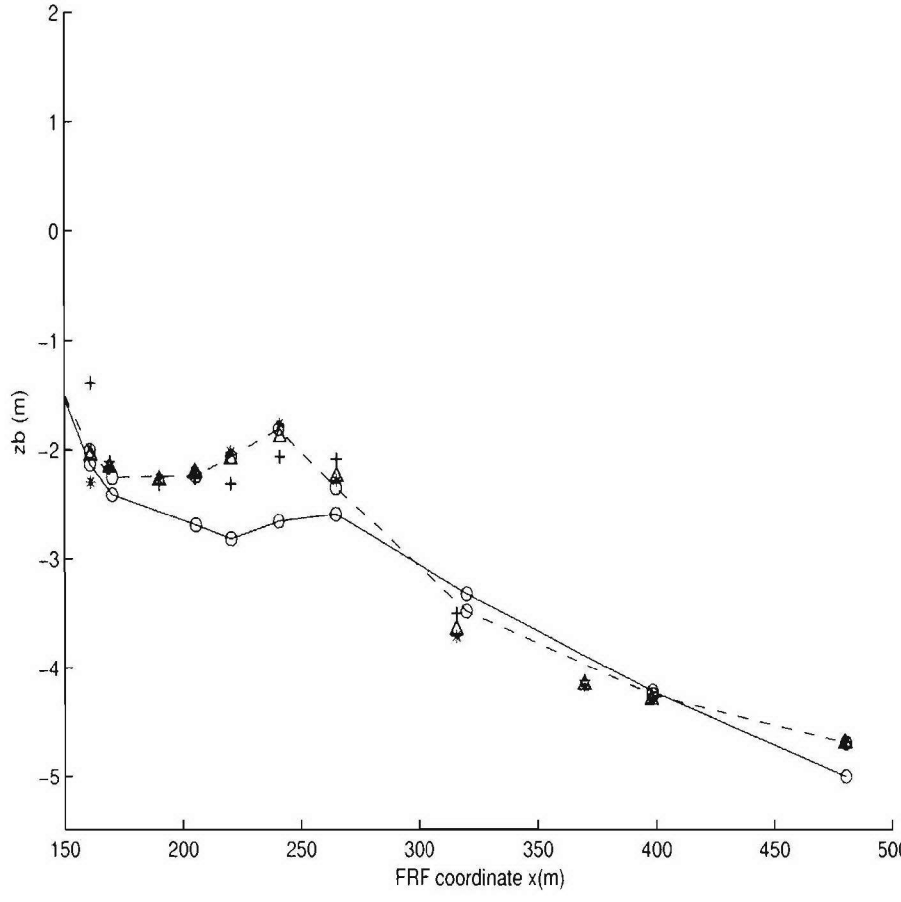

Figure 8.96: Offshore bar migration predicted using Boussinesq model velocities during 10/10/1994 1:00am to 10/15/1994 1:00am, circles: measured bathymetry (dash line indicates the measured bathymetry on 10/10/1994 1:00am, solid line indicates the measured bathymetry on 10/15/1994 1:00am); triangles: predicted bathymetry using total transport $q_c + q_w$ by (8.3); pluses: predicted bathymetry using current-related transport q_c only; stars: predicted bathymetry using wave-related transport q_w only;

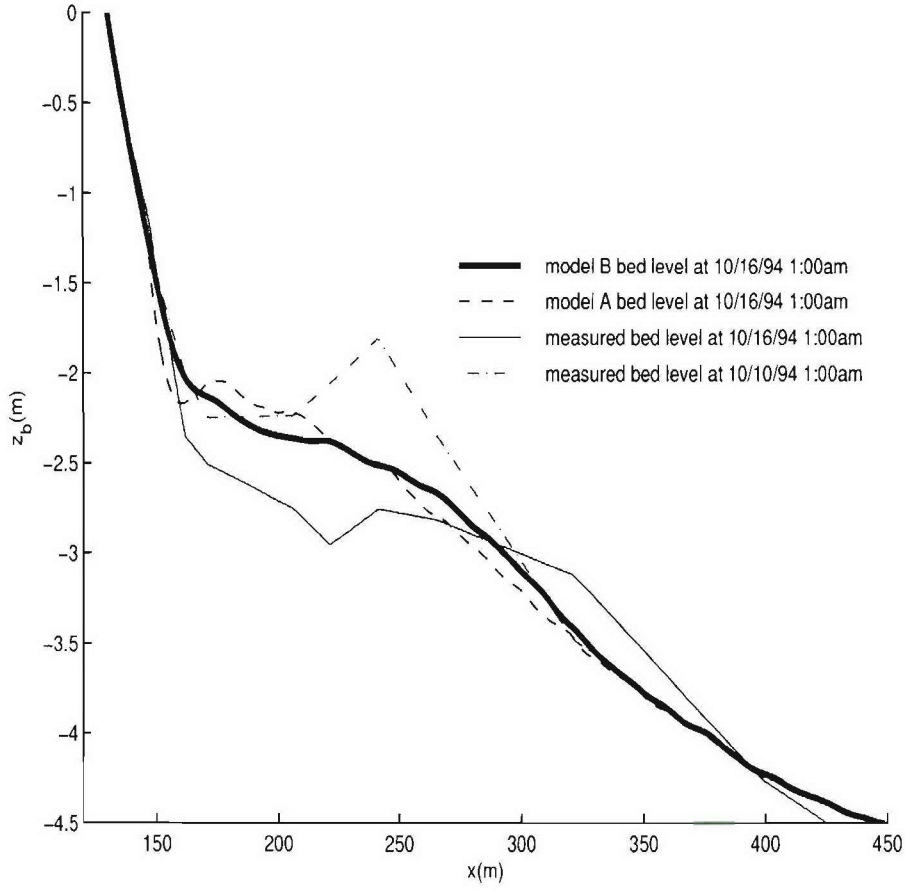

Figure 8.97: Bedform change using coupled Boussinesq model and sediment transport model (dash-dotted line: measured bathymetry at 10/10/94 1:00am; thin solid line: measured bathymetry at 10/16/94 1:00am; dash line: model A bathymetry at 10/16/94 1:00am; thick solid line: model B bathymetry at 10/16/94 1:00am)

Test	H_{m0}(m)	T_p(s)	D50(mm)	Wave Type	Duration(hr)
Test 1c	0.6	8.0	0.2	irregular	13
Test 1b	1.4	5.0	0.2	irregular	18

Table 8.6: Test conditions of LIP11D experiment

8.2 LIP11D Lab Experiment Test

Although extensive efforts have been made to model offshore bar migration events during the Duck 94 experiments, the outcome is less than satisfactory primarily due to the under-prediction of the undertow currents and also due to the fact that there is substantial amount of impact by longshore sediment transport processes during 10/10/1994 to 10/16/1994. Hence, we further test the model with LIP11D lab experiment data (Roelvink and Reniers 1995; Arcilla et al. 1994). We test the model with two tests (Test1b and Test1c) that were also selected by Rakha et al. (1997) for their model validation.

8.2.1 Layout of the experiments and wave conditions

The experiments were carried out within the framework of the European Large Installation Plan (LIP) with the purpose of obtaining detailed measurements of hydrodynamics and sediment transport in the surf zone. The experimental facility is the Delft Hydraulics' Delta Flume shown in figure 8.98. The flume is about 220 meters long, with a deep end of 4 meters still water depth. A plane beach starts at 20 meters from the wave paddles on the left.

The test conditions are listed in table 8.6, where H_{m0} is the spectral estimate of significant wave height, T_p is peak wave period, D_{50} is median sand diameter.

The bed profiles at 3 different test wavehours for Test 1b and Test 1c are shown in figure 8.99 and figure 8.100 respectively. Test 1b is a strongly breaking wave condition case and the profile is eroded. Test 1c is a moderate wave condition case and the profile is accreted.

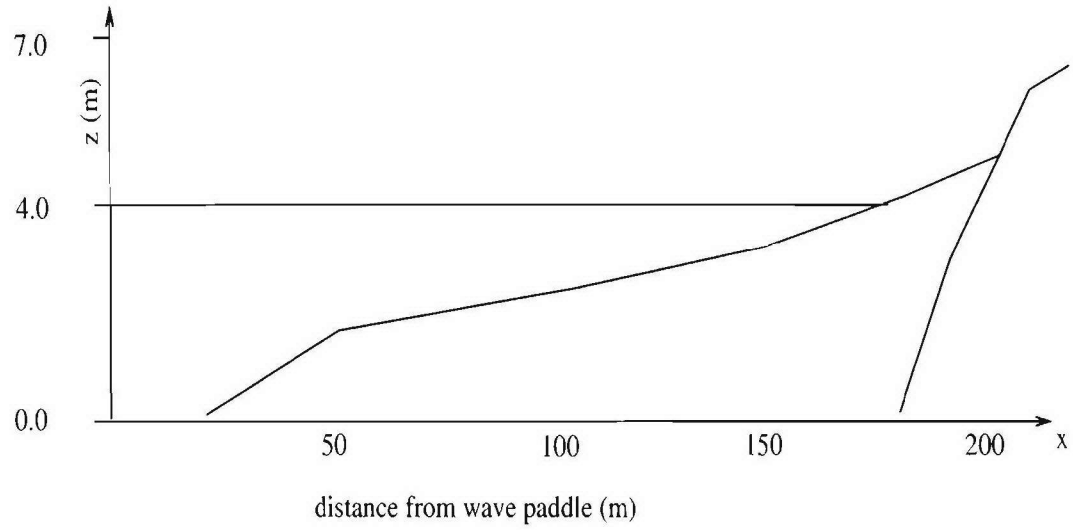

Figure 8.98: Schematic layout of the LIP11D experiments.

8.2.2 Model data comparison of waves and currents

During both Test 1b and Test 1c, 10 pressure gages are mounted at $x = 20m$, $65m$, $100m$, $115m$, $130m$, $138m$, $145m$, $152m$, $160m$ and $170m$ to measure the instantaneous pressure fluctuations, and the free surface elevation is inferred from these pressure measurements. We will show the model data comparisons of the significant wave height H_{m0} and setup for wavehour 9 of Test 1b (test code #1b0909) and wavehour 7 of Test 1c (test code #1c0706).

In addition to the model wave height and setup validation, the vertical structure of the mean current is collected through 4 different wavehour model tests for Test 1c and Test 1b separately. The vertical profiles of velocities were measured by an array of EMF current meters mounted on a carriage towed to different x locations at different wavehours shown in table 8.7.

The following parameters are used for the Boussinesq model FUNWAVE1D2.0: (1) for Test 1b, $\Delta t = 0.025sec$, $\Delta x = 0.5m$; the roller shape parameters (see Appendix) are $\phi_B = 16^\circ$ and $\phi_0 = 10^\circ$, $t^* = 3.0sec$ and $f_\delta = 1.1$; (2) for Test 1c, $\Delta t = 0.025sec$,

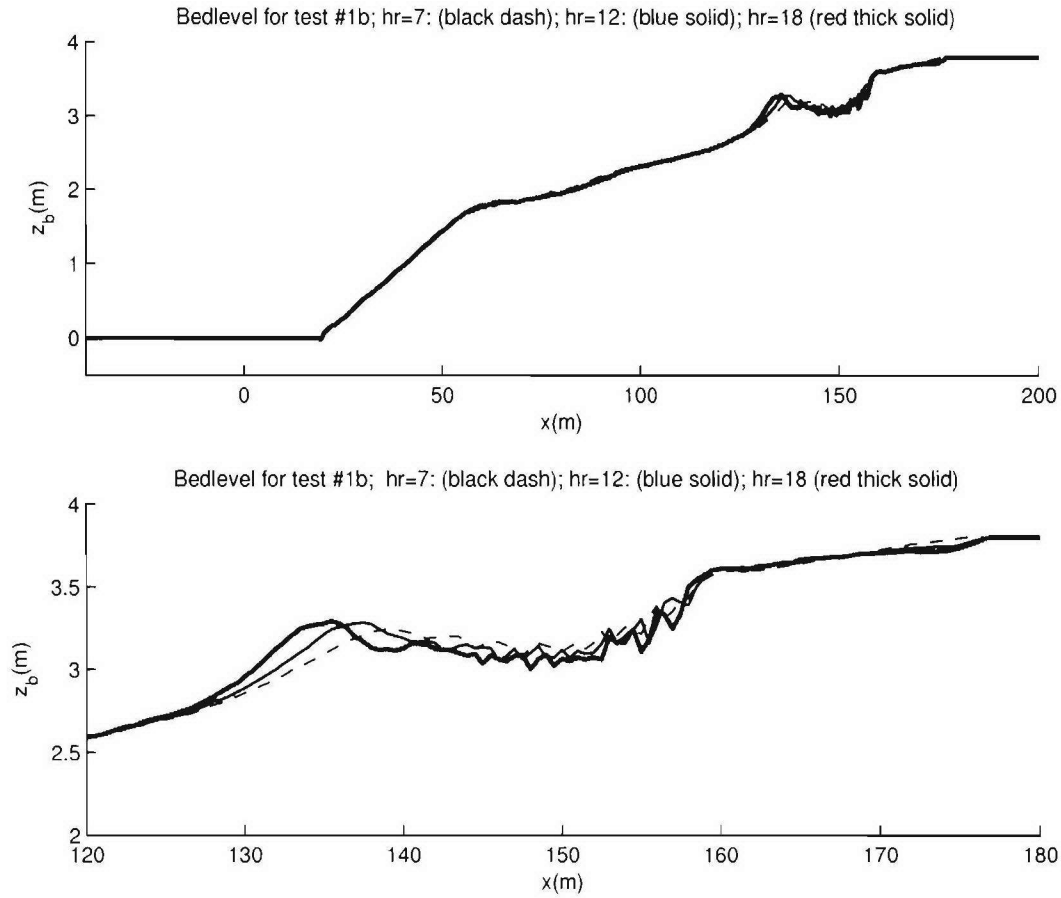

Figure 8.99: Bed profiles during Test 1b; top panel: overall bed profile; bottom panel: closer view of the offshore bar movement from wavehour 7 to wavehour 18

Testcode	Wavehour	X location (m)
#1b1102	11	65
#1b1213	12	102
#1b1706	17	138
#1b0707	7	145
#1c0102	1	65
#1c0313	3	102
#1c0706	7	138
#1c0807	8	145

Table 8.7: EMF current meter locations during different test wavehours

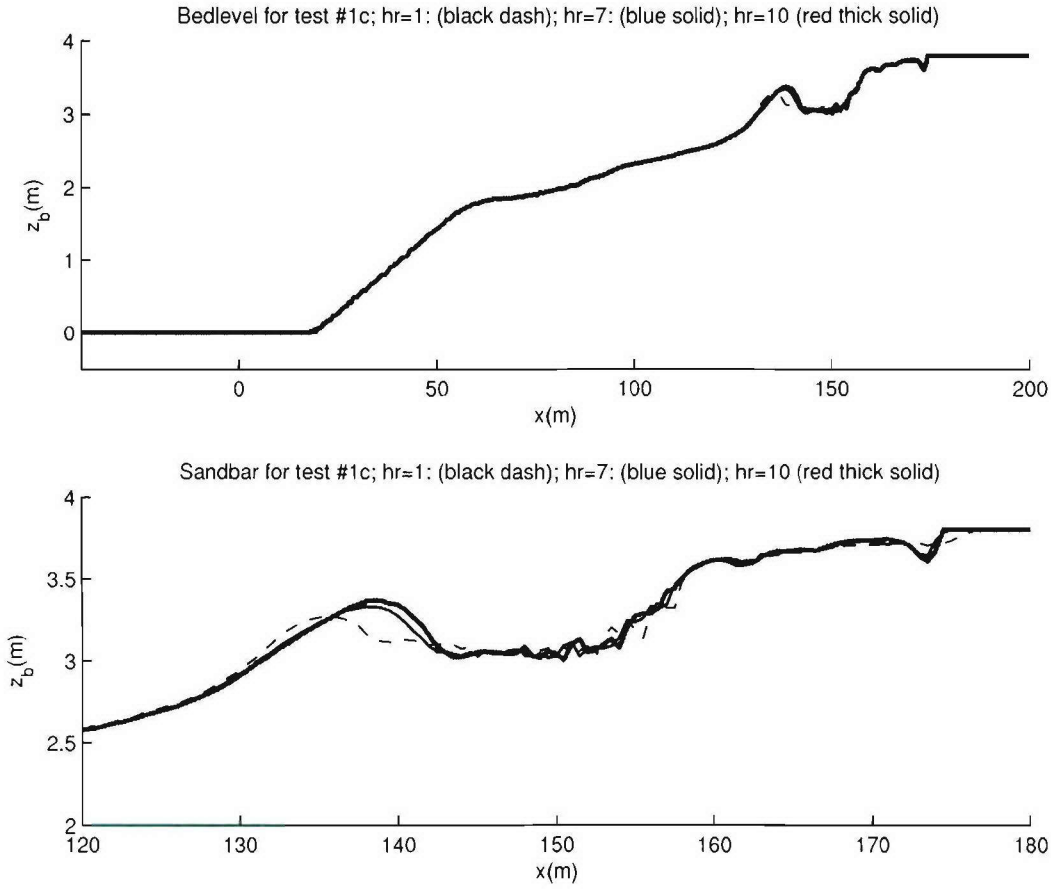

Figure 8.100: Bed profiles during Test 1c; top panel: overall bed profile; bottom panel: closer view of the onshore bar movement from wavehour 1 to wavehour 10

$\Delta x = 0.5m$; $\phi_B = 16°$ and $\phi_0 = 10°$, $t^* = 3.5sec$, $f_\delta = 1.0$.

The modeled wave height and setup are compared to measured data in figure 8.101 and figure 8.102. The model results match with the measured data very well except near the numerical wave maker due to cutoff of high frequency energy (see Appendix). For #test1b0909, waves break from the toe of the beach and wave height decreases monotonically from $x = 20m$ to $x = 180m$. The maximum wave setup is about $5cm$. For #test1c0706, waves are smaller, and wave shoaling dominated the process from offshore to the crest of the sand bar. Further inshore of the bar crest, waves break and are dissipated rapidly. The maximum wave setup is about $3cm$.

The modeled mean flow results are shown in comparison with data in figure 8.103 and figure 8.104. The undertow currents are small for Test 1c (less than $0.15m/s$). On the other hand, the undertow currents are stronger for Test 1b (maximum value is about $0.3m/s$). The model assumes a vertically constant return flow. The measurements show a large variation over the depth at $x = 138m$ and $x = 145m$ where waves break strongly. Hence the predicted value is much less than the measured maximum value that occurs near the bottom. For the Test 1b wavehour 17 (testcode #1b1706), at $x = 138m$, the upper most EMF current gage is out of water, and no measured and modeled data are plotted. The second EMF current gage is slightly below wave trough. Visual inspection of figure 8.103 shows that vertical integration of measured undertow is about $0.3m/s \times 0.7m/2 = 0.105m^2/s$, and the vertical integration of modeled undertow is about $0.17m/s \times 0.7m = 0.119m^2/s$. This indicates that although the model does not correctly predict the vertical structure of the undertow currents, it gives the overall return flow mass flux close to the measurements. For $x = 145m$ of Test 1b wavehour 7 (testcode #1b0707), the upper most EMF current gage is above the wave trough level, but not totally out of water, and it picks up onshore surface currents due to wave breaking and wave skewness. The same visual inspection also indicates that the model predicts correct return flow mass flux. For Test 1c wavehour 7 (testcode #1c0706), the beach is accreted and the bar crest is higher

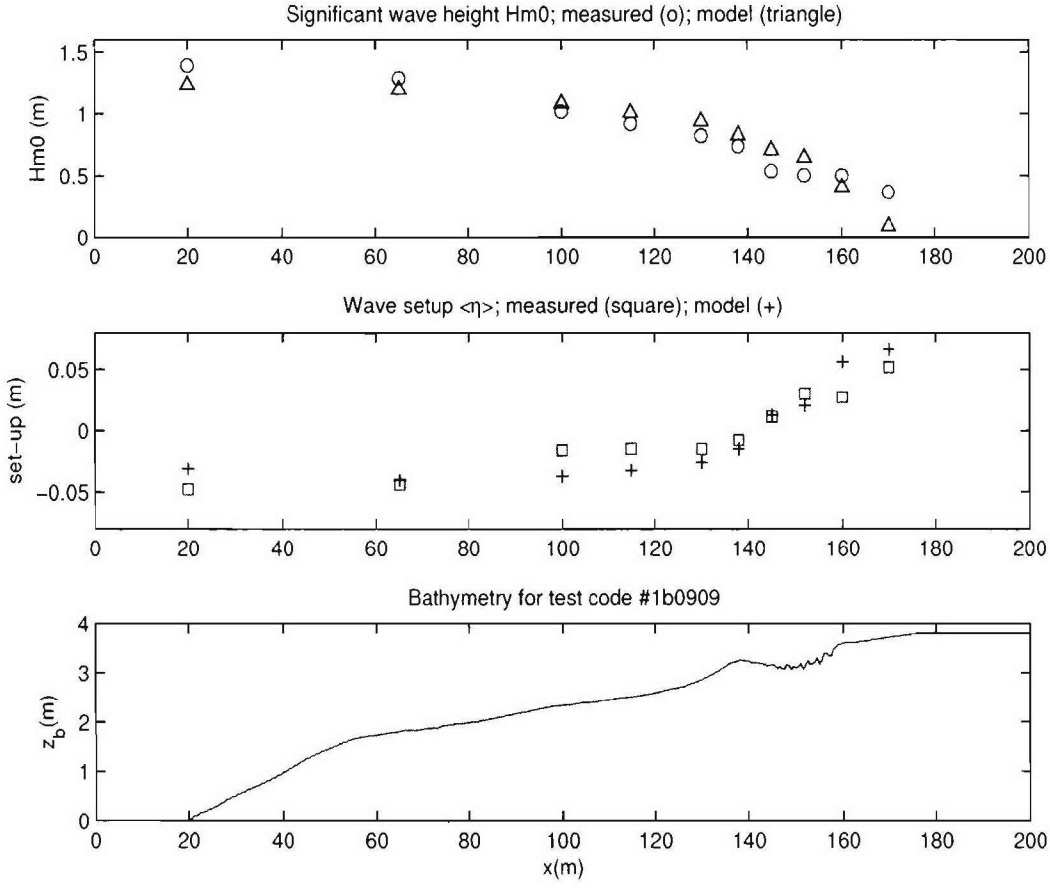

Figure 8.101: Model data comparison of wave height and setup for Test 1b

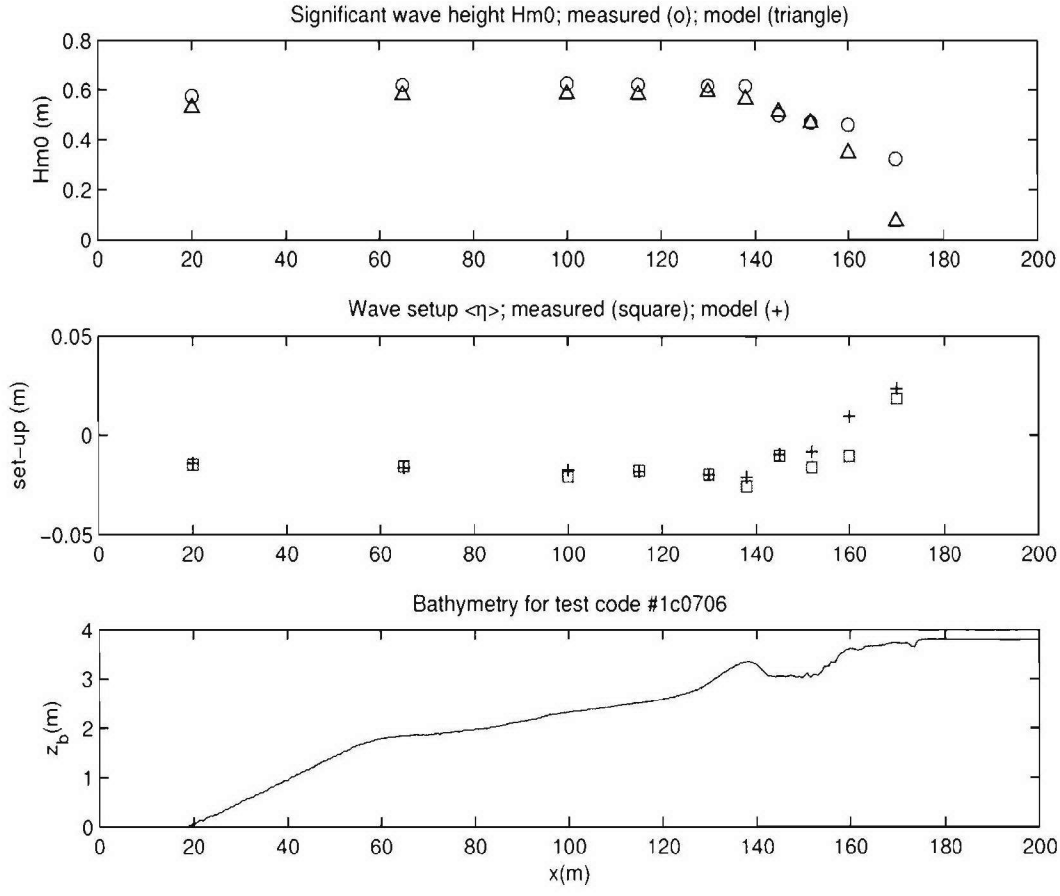

Figure 8.102: Model data comparison of wave height and setup for Test 1c

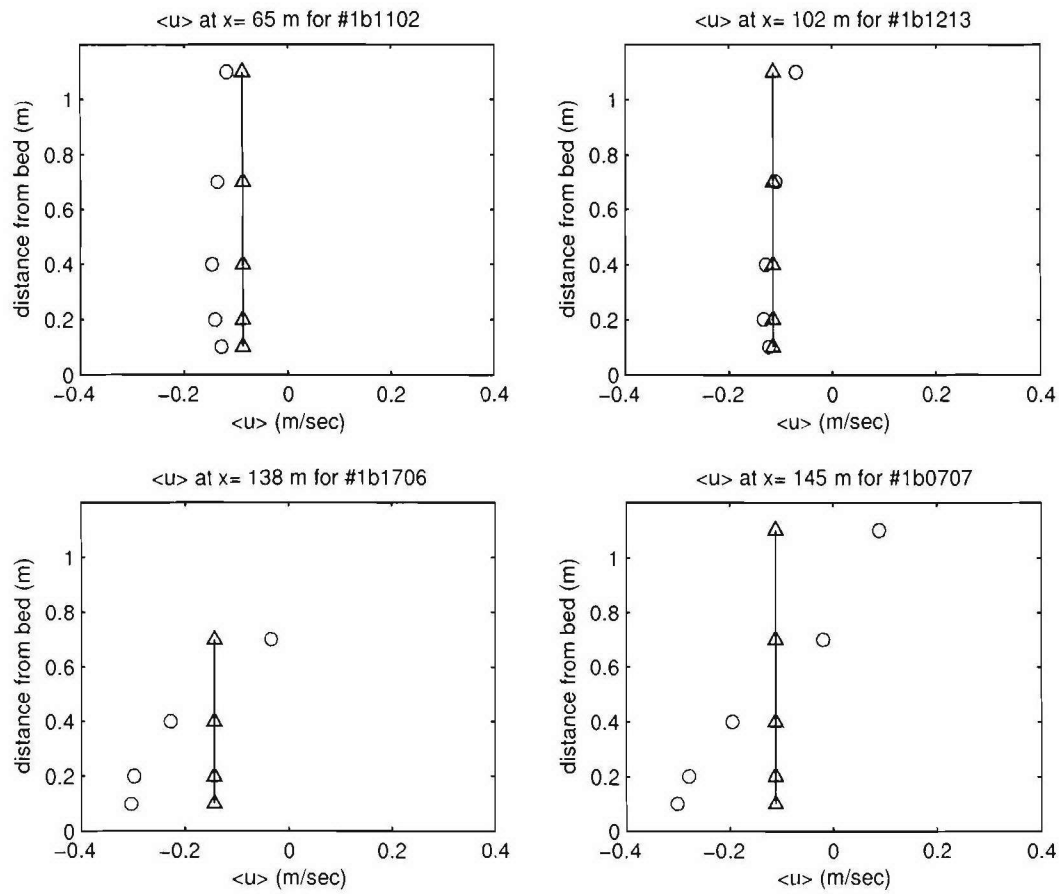

Figure 8.103: Model data comparison of the vertical structure of undertow for Test 1b; data (o); model (Δ)

compared to Test 1b, and at $x = 138m$, which is at the bar crest location, the first EMF current gage is totally above waves, and the second EMF gage ($0.7m$ from the bottom) is close to mean water level, and it picks up the onshore surface current as well. For Test 1c wavehour 8 (testcode #1c0807), The first EMF gage is also out of water level, and there are no measured and modeled data.

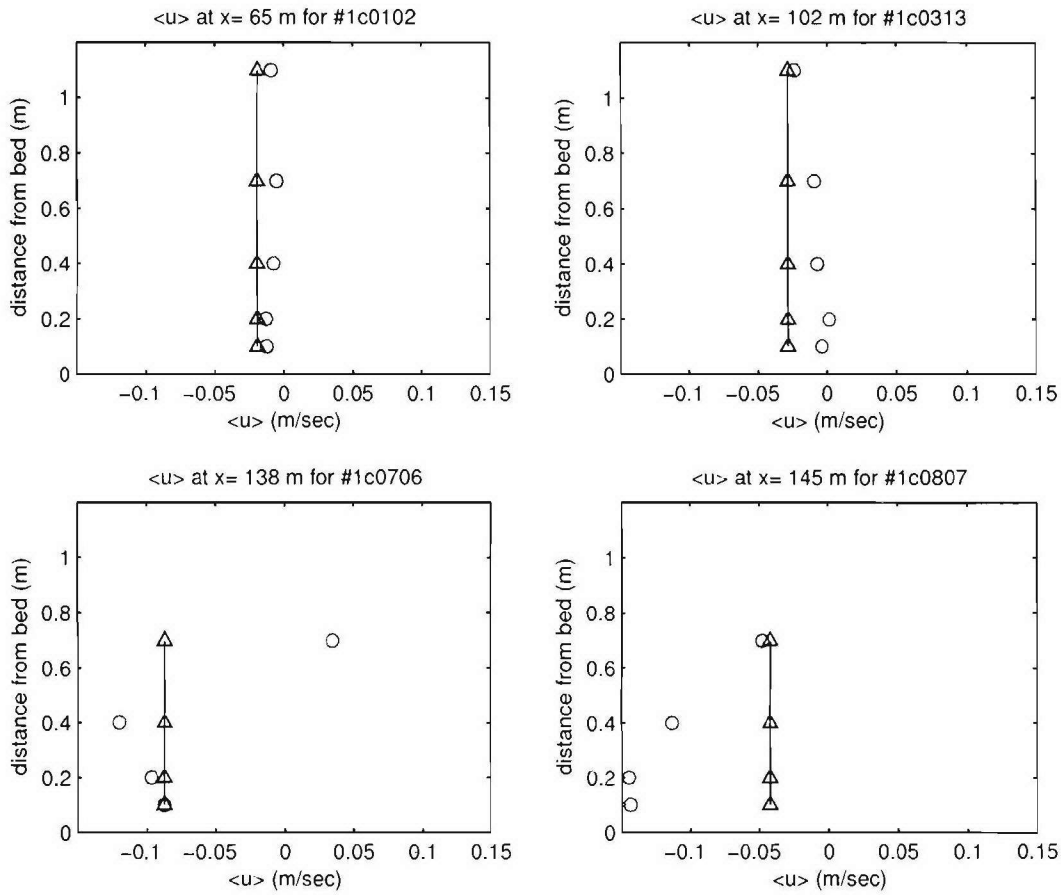

Figure 8.104: Model data comparison of the vertical structure of undertow for Test 1c; data (o); model (Δ)

8.2.3 Erosional case: Test 1b

During the Test 1b experiments, a wave gage WHM03 was placed at the toe of the slope $x = 20m$ and the surface elevation history was continuously recorded with a sampling frequency of $10Hz$ from wavehour 7 to wavehour 17. Hence, here we choose to model the hydrodynamics and the bathymetry change from wave hour 7 to wave hour 17 with both sediment model A and model B. The simulation parameters of waves for both model A and model B are set as: time step for waves $\Delta t = 0.025s$, spatial step $\Delta x = 0.5m$, surface roller geometry parameters are $\phi_B = 16°$, $\phi_0 = 10°$, $t^* = 3.0s$, $f_\delta = 1.1$. For model A sediment transport, the bottom friction coefficient $C_f = 0.003$, bedload effectiveness $\epsilon_B = 0.135$, suspended load effectiveness $\epsilon_S = 0.010$, bed porosity $n_p = 0.4$, sediment internal friction angle $\phi = 32°$, sediment median diameter $d_{50} = 0.2$mm, terminal velocity $w_{fall} = 2cm/s$, sediment density $\rho_s = 2650kg/m^3$, water density $\rho = 1000kg/m^3$, water molecular viscosity $\nu = 1.0 \times 10^{-6}m^2/s$. The acceleration term coefficient is $K_a = 0.0002ms$, and the critical acceleration threshold is $u_{btcr} = 0.5m/s^2$. For mode B sediment transport, the 2DHV linear bottom boundary layer model is used to obtain bottom shear stress τ_b. The parameters for the bottom boundary layer model are: $\Delta t_{bbl} = 0.005s$, $\Delta z = 3$mm, rough wall boundary condition for the bed boundary is used with a roughness $K_s = 25d_{50}$ (Long et al. 2004; Hsu et al. 2005) and velocity match condition for the top boundary of the boundary layer is used. The bedlevel is updated every 448 seconds using the Euler-WENO scheme. The undertow current $\overline{u_b}$ for the calculation of q_c is also by a time average of near bed velocity $u_b(x,t)$ over a period of 448 seconds.

The bedlevel predicted at the end of wavehour 17 by model A is shown along with the measured bedlevel in figure 8.105. In the figure panel (a), the modeled bedlevel is simulated using the full formula by (8.2). In the figure panel (b), the modeled bedlevel is due to the Bagnold formula. In the figure panel (c), the modeled bedlevel is due to the

acceleration term solely. From the figure, we see that the measured bedlevels show a pronounced offshore bar movement with the bar crest height increased slightly. The modeled results due to the Bagnold component show a larger distance of offshore bar migration compared to measurements and the bar height is also decreased. On the other hand, the modeled results due to the acceleration component give slight onshore bar movement. The overall model A by both the Bagnold formula and the ad hoc acceleration term gives offshore bar migration for the bar and also accretion further inshore of the bar trough. The model gives qualitative agreement of the bar migration, but the quantitative comparison is poor.

The model B results are shown in figure 8.106. Here, the transport rate consists of a wave-related component q_w by Meyer-Peter-Müller formula and a current-related component q_c by Bailard (1981) as is described in (8.3). In figure 8.106, panel (a) shows the overall prediction, panel (b) shows the prediction due to q_w and panel (c) shows the prediction due to q_c. The results show that the q_w gives offshore movement of the bar and also some accretion further inshore of the bar trough. The current-related transport q_c gives small magnitude of offshore bar movement. The overall results are similar to model A, namely, offshore bar migration is predicted, inshore bar trough accretion appears in contrast to measured bathymetry and the bar crest height is underestimated.

8.2.4 Accretional case: Test 1c

During the Test 1c experiments, a wave gage WHM01 was placed at the toe of the slope $x = 20m$ and the surface elevation history was recorded with a sampling frequency of $10Hz$ from wavehour 1 to wave hour 10. This data series can be used as the input for the numerical wavemaker in Boussinesq model. Hence, here we choose to model the hydrodynamics and the bathymetry change from wave hour 1 to wave hour 10.

The simulation parameters both model A and model B are set similar to test 1b except that here $t^* = 3.5s$, $f_\delta = 1.0$, the bottom friction coefficient $C_f = 0.001$ with less turbulent intensity for smaller wave height compared to test 1b, the acceleration term

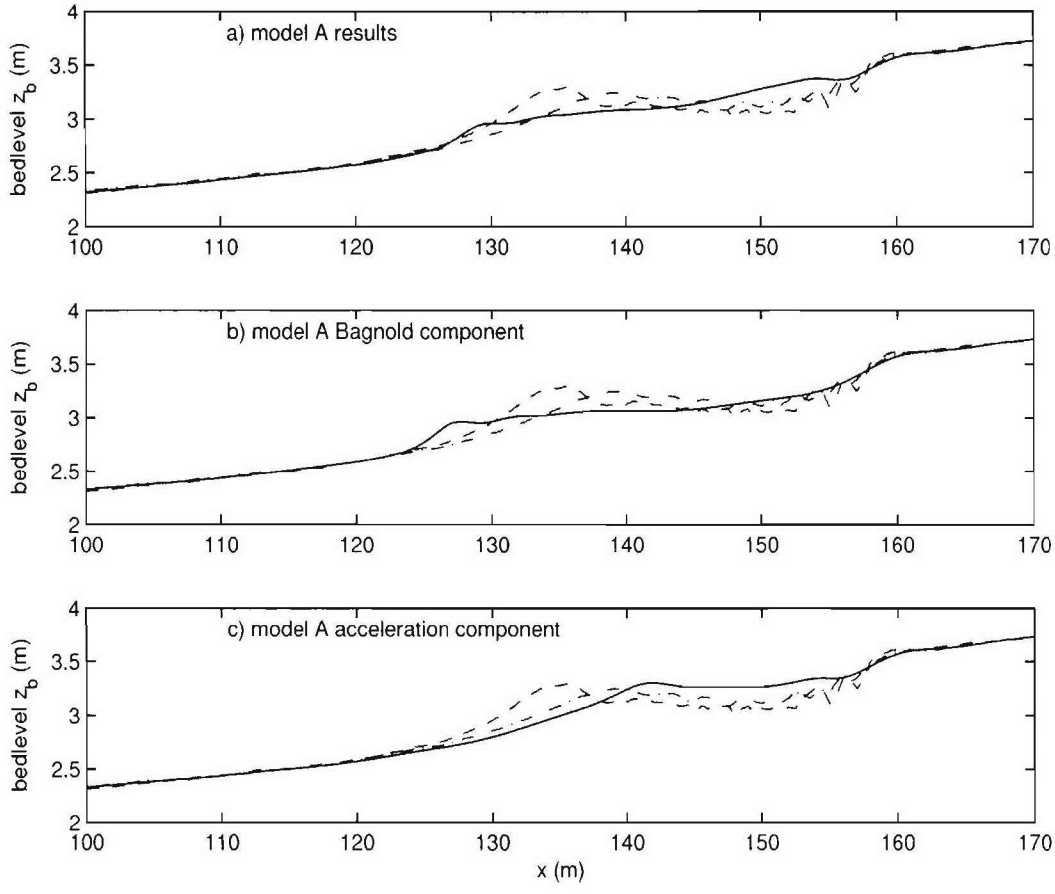

Figure 8.105: Bedlevel change by model A for test 1b; (a) bedlevel due to both Bagnold formula and acceleration term; (b) bedlevel due to Bagnold formula; (c)bedlevel due to acceleration term; model bedlevel (solid line); measured initial bedlevel (dash-dotted line); measured final bedlevel (dash line)

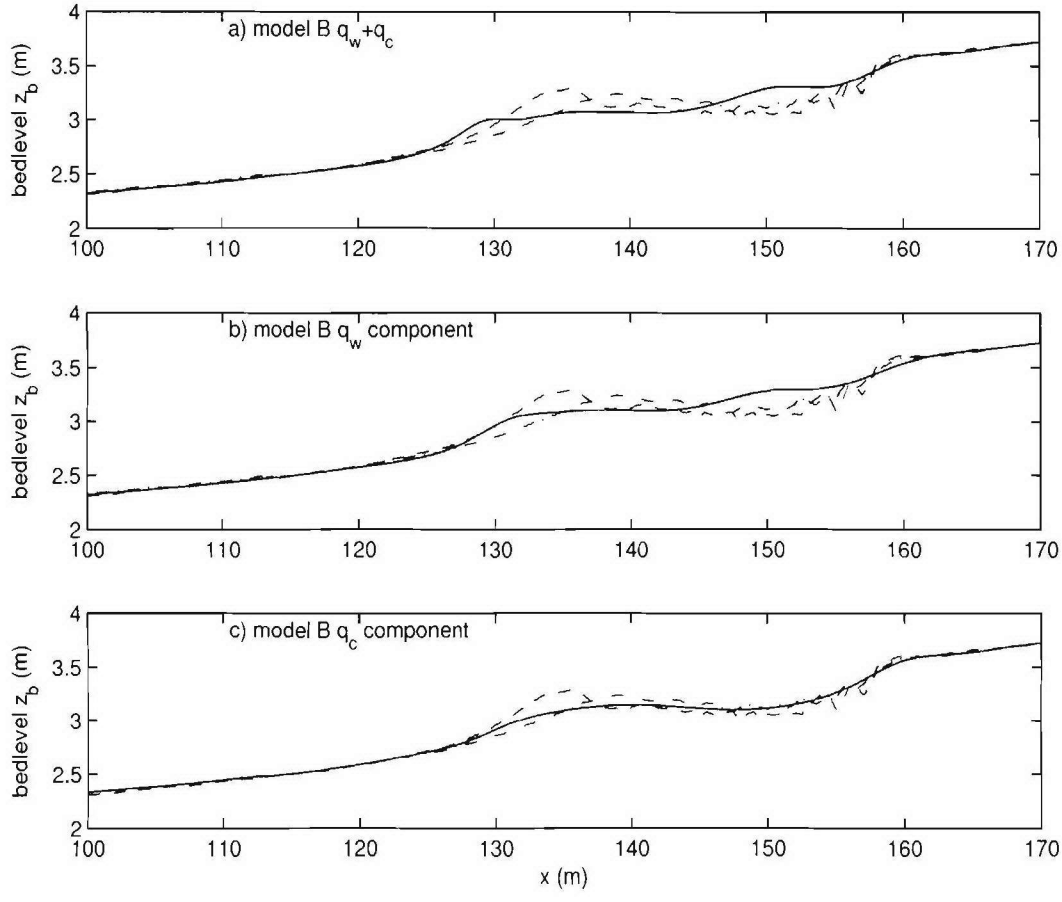

Figure 8.106: Bedlevel change by model B for test 1b; (a) bedlevel due to both q_w and q_c; (b) bedlevel due to q_w; (c)bedlevel due to q_c; model bedlevel (solid line); measured initial bedlevel (dash-dotted line); measured final bedlevel (dash line)

coefficient $K_a = 0.0004ms$, with the critical acceleration threshold $u_{btcr} = 0.3m/s^2$. The bedlevel is updated also every 448 seconds using the Euler-WENO scheme. The undertow current $\overline{u_b}$ for the calculation of q_c is again obtained by a time average of near bed velocity $u_b(x,t)$ over a period of 448 seconds.

The model A results are shown in Figure 8.107. The measurements show onshore migration of the sandbar with a increased bar height. From panel (b) of the figure, we see that the Bagnold formula show almost no change to the bedlevel. Panel (c) shows that the transport due to the acceleration term gives correct bar movement direction and distance. The overall results given in panel (a) show accretional onshore bar movement. Again, the bar crest height is underestimated by the model.

The model B results are shown in Figure 8.108. Similar to the results of model A, the current-related component predicted by the Bailard formula in panel (c) shows no effect on bathymetry. But the q_w predicted by the Meyer-Peter-Müller formula and the bottom boundary layer model shows accretion of the beach profile at the offshore side of the sand bar. There is also some erosion further inshore of the bar trough which results to a increase of the bar crest height. The onshore bar migration event is predicted but the scene is more complicated than the measurements.

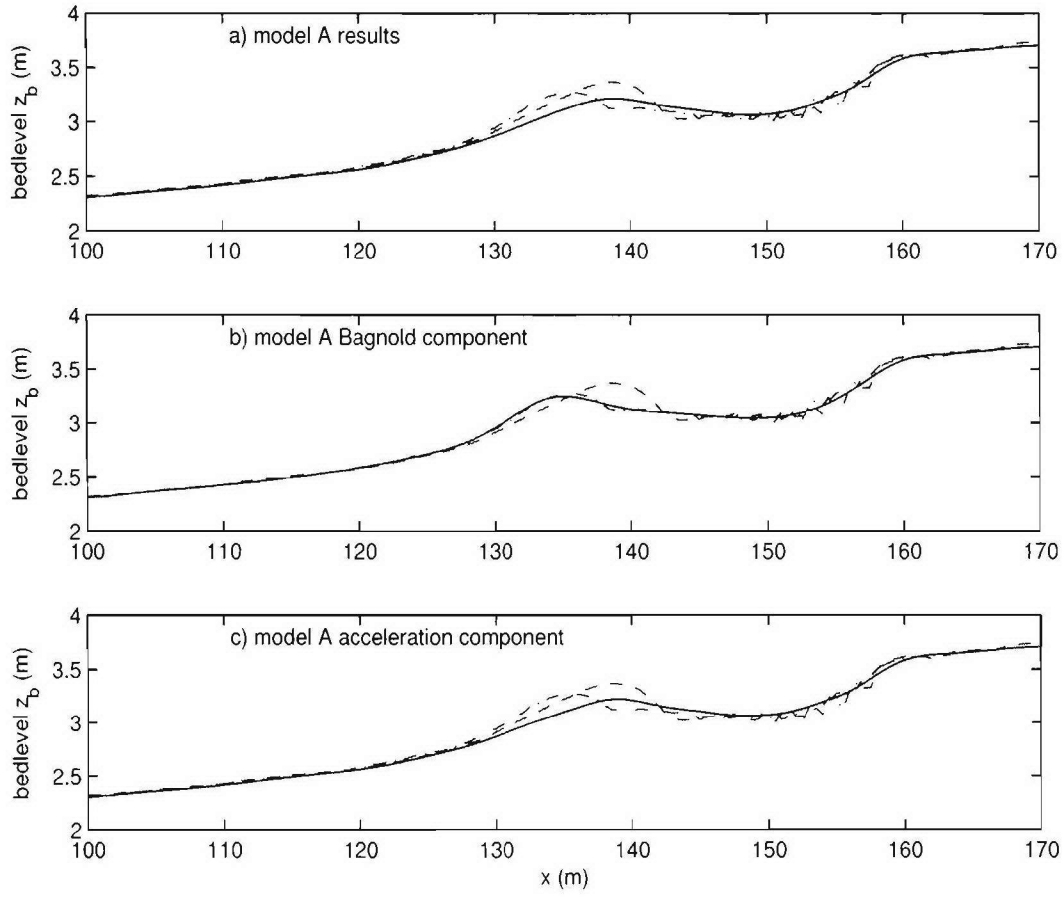

Figure 8.107: Bedlevel change by model A for test 1c; (a) bedlevel due to both Bagnold formula and acceleration term; (b) bedlevel due to Bagnold formula; (c) bedlevel due to acceleration term; model bedlevel (solid line); measured initial bedlevel (dash-dotted line); measured final bedlevel (dash line)

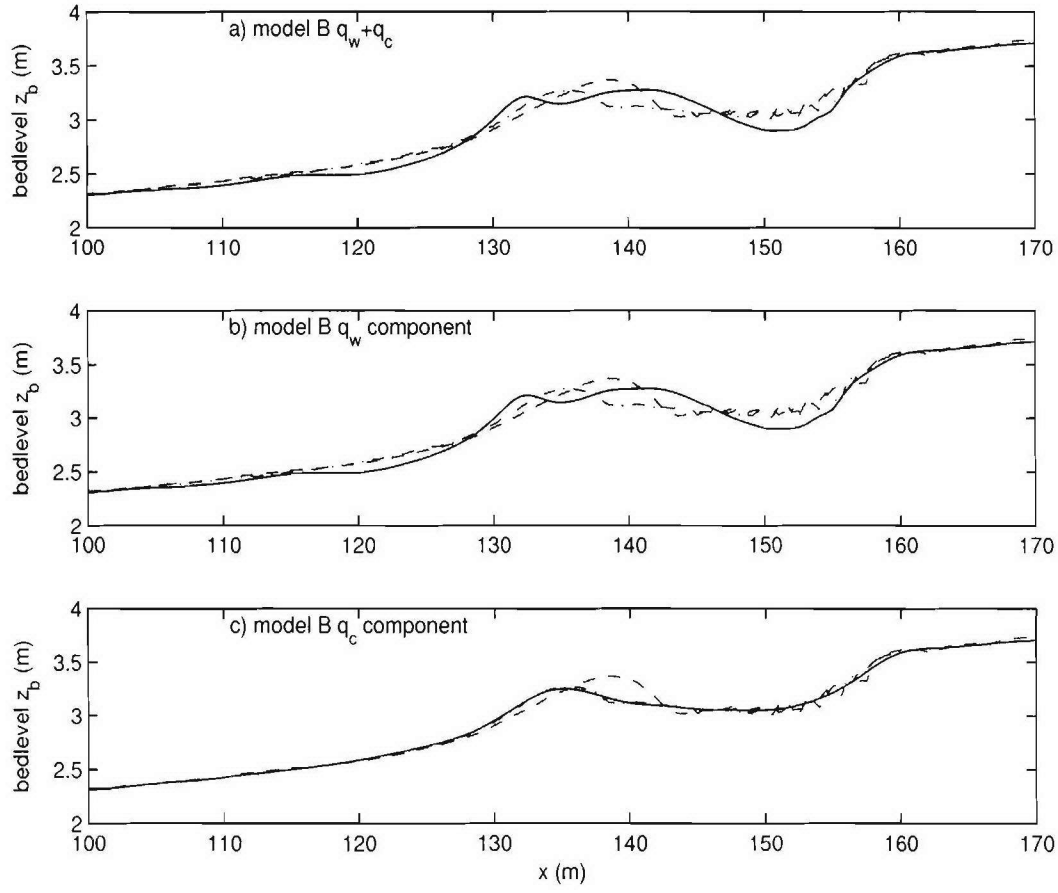

Figure 8.108: Bedlevel change by model B for test 1c; (a) bedlevel due to both q_w and q_c; (b) bedlevel due to q_w; (c) bedlevel due to q_c; model bedlevel (solid line); measured initial bedlevel (dash-dotted line); measured final bedlevel (dash line)

Chapter 9

CONCLUSION AND FUTURE DEVELOPMENT

9.1 Conclusion

1D and 2D Boussinesq wave models FUNWAVE1D2.0 and FUNWAVE2D2.0 are established based on FUNWAVE1.0 with extensions of multiple reference levels, one-way numerical wave maker, surface roller induced undertow and film layer modeling of moving shoreline. The 2D model is also based on a staggered grid system with curvilinear coordinates for complex nearshore geometries.

Finite difference schemes for bed updating in morphological modeling are systematically studied and compared. The Euler-WENO scheme is introduced to model morphology and is proved to have significant advantages over conventional schemes.

Classical turbulent wave boundary layer models based on mixing length turbulence closure are set up to model near bottom boundary layer structure due to unsteady free stream velocity and pressure gradient.

Sediment transport formulas for nearshore wave and current climate are reviewed and discussed. An ad-hoc extension to the Bagnold (1966) formula is proposed by including an acceleration term in light of Drake and Calantoni (2001). The wave boundary layer model is also coupled with Meyer-Peter-Müller formula for sediment transport coupled with the Boussinesq wave model instantaneously.

Phase-resolving sediment transport and morphology models FUNSEDI1D and FUNSEDI2D are set up by coupling the Boussinesq model, bottom boundary model, instantaneous sediment transport formulas and Euler-WENO morphology model together.

The Duck'94 field experimental data are used to test the model and investigate the onshore and offshore bar migration events due to different wave conditions. The Boussinesq model gives good agreement of wave spectra, bottom velocity variance and skewness with the data. The undertow (mean current) in the October 10 - 16 run is underestimated. Boundary layer model driven using measured near bed velocity show identical results with Hsu et al. (2004). The Boussinesq model data driven sediment transport shows good agreement with data for the onshore bar migration event, but poor agreement for the offshore bar migration event due to substantial underestimate of near-bed undertow current.

The LIP11D laboratory data are also utilized to test the phase resolving sediment transport model driven by the Boussinesq wave model. Both erosional and accretional cases are investigated with qualitative agreement to measured data. The behavior of the beach profile predicted by the model is complex and sensitive to the sediment transport formula, which indicate that much research on detailed mechanism of the sediment transport is warranted. The framework of phase-resolving coupling between the sediment transport model and the Boussinesq wave model accomplished during this research gives a unique opportunity to investigate future proposed transport formulas in great detail with affordable computation cost.

9.2 Perspective on Proposition of New Transport Formulas

The transport formulas in Chapter 3 and Chapter 8 are based on steady or quasi-steady assumptions or ad-hoc modifications to include unsteady flow effects. They are subjected to testing with modern experimental results conducted in the last decade or will be tested in the future. In this section, we share some remarks on the proposition of new transport formulas in the hope that can include unsteady flow features that are physically based that we think are significant to sediment transport near bed.

Bagnold (1966) assumed that sediments are transported along with energy loss of

free stream fluid particle kinetic energy. The kinetic energy loss is assumed to be proportional to the bottom shear stress multiplied by the velocity of particles. For steady flow, the bottom shear stress can be related to free stream velocity through the quadratic law of friction. The velocity of sediment particles is assumed to be proportional to free stream velocity. Hence the resulted transport formula is in the form of cubic power function of the free stream velocity.

Meyer-Peter and Muller (1948) formula uses purely bottom shear stress, i.e. only friction velocity u^*, which is consistent to Bagnold (1966) approach for steady flow because friction velocity u^* is related to free stream velocity linearly. When free stream velocity is replaced by u^*, and further replace u^* using shear stress $\sqrt{2\tau_b/\rho}$ according to its definition, the Bagnold (1966) formula for bedload has the form of Meter-Peter and Muller (1948).

For sediment transport under waves, it is not justified to use quadratic parameterization of friction to relate bottom shear stress to free stream velocity. Hence there is no linear correlation between bottom friction velocity and free stream velocity. Both formulas that are in the form of power function of free stream velocity u_b (Bagnold 1966) or friction velocity u^* (Meyer-Peter and Muller 1948) are not valid for wave conditions unless the quasi-steady assumption is used.

Madsen and Grant (1976) and Bailard (1981) neglected the effect of wave horizontal asymmetry and phase lag between fluid flow and bottom shear stress, because they also applied the quasi-steady assumption in calculating bottom shear stress.

Malarkey and Li (2003) presented a quasi-steady, one-dimensional, vertical model of unsteady sheet flow by using empirical assumptions for time-varying sheet-flow layer thickness for sheet flow layer and time-varying equivalent bed roughness for suspension layer. The instantaneous sheet flow layer thickness is assumed to be proportional to Shields parameter similar to Wilson (1989) and Sumer et al. (1996). The sediment

concentration within the sheet flow layer is assumed to be quadratic function of normalized vertical distance from stationary bed according to measurements by Horikawa (1982). For unsteady flows, quadratic profile of concentration seems to be more realistic than linear profile of Wilson (1989) and Pugh and Wilson (1999) for steady flow. The velocity profile of sediments within the sheet flow is assumed to be linear suggested by Sumer et al. (1996) from steady flow experiments. The erosion depth is determined by conservation of sediment in the vertical direction which may be questionable for unsteady flows.

Soulsby and Damgaard (2005) took another approach. In their study, a sheet flow sediment transport formula has been proposed based on the assumption that concentration within the sheet flow is linear, and the velocity profile of sediments is an algebraic equation of normalized vertical coordinate. It is also assumed that the top of the sheet flow velocity is proportional to friction velocity. Thickness of the sheet flow is obtained from the Coulomb friction assumption. We think that it is necessary to identify the pick-up layer and the sheet-suspension layer from the substantial observations discussed in the previous section. Since in the sheet-suspension layer, the sediment motion is dominated by turbulence instead of inter-granular collision. Especially for fine sediments, the turbulence suspension becomes more important and the total sheet flow thickness is much larger than the pick-up layer thickness, meaning that the thickness of the sheet-suspension layer is much larger than the pick-up layer. We suggest that the pick-up layer thickness can be obtained from an analysis based on Coulomb friction law, while the thickness of the sheet-suspension layer should be analyzed with considerations of the turbulent mixing and vertical velocity w especially for fine sands. Also it should be acknowledged that the velocity and concentration distribution within the pick-up layer and sheet-suspension layer is different due to different mechanisms evident from observations.

Based on the discussion from both experimental observations (Sumer et al., 1996;

Flores and Sleath, 1998; Pugh and Wilson, 1999; O'Donoghue and Wright, 2004; Dohmen-Janssen et al., 2001; Dohmen-Janssen and Hanes, 2002; Liu and Sato, 2005) and recent development of sediment transport models (Hsu, 2002; Soulsby and Damgaard, 2005), we suggestthat a new sediment transport formula for sheet flow should consider the following:

The sheet follow sediment transport should consist of two sub layers due to different mechanisms: the lower pick-up layer and the upper sheet-suspension layer. The lower pick-up layer is developed due to near bed friction and strong inter-granular collisions. The upper sheet-suspension layer is due to turbulence and vertical acceleration of flow in the bottom boundary layer. For the sheet-suspension layer, one should consider the importance of acceleration of flow especially in asymmetric sawtooth shape wave conditions nearshore. The following assumptions may be used based on the above discussions of the experimental observations (a) in the pick-up layer, assume concentration convex; (b) in the sheet-suspension layer, assume concentration concave; (c) In the pick-up layer, assume linear distribution of streamwise velocity; (d) in the sheet-suspension layer, assume logarithmic distribution of streamwise velocity; (e) assume erosion depth (pick-up layer thickness) based on Coulomb theory from grain shear; (f) obtain suspension layer thickness through the vertical balance of sand mass or turbulent diffusion; (g) assume interface concentration $0.5C_b$, where C_b is the densely packed bed volumetric concentration; (h) use matching of sand velocity to obtain roughness of suspension layer logarithmic distribution. (i) try to include phase lag in the concentration profile in the vertical direction compared to pick-up layer, and this might be quite difficult; (j) sum up the transport in the pick-up layer and the sheet-suspension layer to get total transport rate of the sheet flow.

9.3 Comments on Future Development

Although the Boussinesq model is quite powerful in predicting waves both in 1D cross shore and 2D horizontal problems, for periodic and transient waves, monochromatic and random wave field in the nearshore region, the inclusion of undertow prediction in

this research is through empirical modeling of surface roller and the vertical structure of the mean current in the vertical is not modeled through a dynamic approach. Future research on extending the Boussinesq model to incorporate undertow prediction seamlessly is needed. The research by Veeramony and Svendsen (2000) and Svendsen et al. (2000) extended Boussinesq models with inclusion of rotational flow in the vertical plane, and inclusion of this approach may enable us to provide cross shore circulation accurately.

In the swash zone, fluid velocity and bed shear stresses are large due to diminishing water depth. This can result to large sediment transport rate and quick response of the beach profile to the water motion. The speed of bed level change can be in the same magnitude of the surface water level. Hence, the fixed bottom assumption in the Boussinesq theory should be discarded. Sediment transport formulas should also take account of sediment size distribution.

This research has set up the FUNSEDI2D model framework but testing is unfinished due to limited data availability and the large computation cost. This should be tested extensively in the near future.

The majority of the difficulties are still related to developing a sediment transport formula based on hydrodynamic quantities that can be applied for unsteady wave current climate nearshore. To date, the cross shore sediment transport processes are still modeled quite empirically with transport formulas based on quasi-steady assumptions and limited experimental data for unsteady cases. The testing of model A and model B in the Duck'94 experiment case and the LIP11D experiment case certainly shows us different behavior for different formulas. Hence, much of the research effort should be devoted to investigate newly proposed transport formulas such as Soulsby and Damgaard (2005) and the approach based on the previous section. The entire system of the Boussinesq model, wave boundary layer model, and Euler-WENO morphological scheme developed in this research can be used to propose, test, and correct sediment transport formulas systematically for outside of the surf zone, inside of the surf zone and swash zone processes,

cross shore and alongshore processes through a computer modeling approach in parallel to experimental and theoretical efforts.

Appendix A

A.1 Wave Maker Theory

The wave maker mechanism for the Boussinesq model is basically done by adding a periodic forcing term to the equation. FUNWAVE 1.0 uses a two-way wave maker where a forcing term symmetric about the central line of source region is added to the continuity equation. Theory has been developed by Wei et al. (1999), basically using Fourier transform method to solve the linearized equation to obtain the transfer function between the desired wave height and source strength. Chawla and Kirby (2000) developed a one-way wave maker by further adding a forcing term anti-symmetric about the central line of source region, and Doppler effects of background current is also taken into account. Here the derivation of Chawla and Kirby (2000) is repeated for the linearized version of Boussinesq Equation, but no Doppler effect is considered for simplicity.

The 1D linearized version of Boussinesq Equation (2.261) (2.267) with constant depth h is:

COM:

$$\eta_t + h\nabla \cdot \tilde{\mathbf{u}} + \mu^2 \alpha_1 h^3 \nabla^2 (\nabla \cdot \tilde{\mathbf{u}}) = 0 \tag{A.1}$$

EOM:

$$\tilde{\mathbf{u}}_t + \nabla\eta + \mu^2 \alpha h^2 \nabla (\nabla \cdot \tilde{\mathbf{u}}_t) = 0 \tag{A.2}$$

where $\alpha = \frac{B-1}{2}$, $\alpha_1 = \alpha + 1/3 = B/2 - 1/6$. Since h is constant and equation is linearized, here B is also a constant, means that the moving part in B has been taken out, hence α and α_1 are constant too. z_c in (2.179) is also set to be constant for linearization and finally disappears here. The upper two equations are of the same form of Chawla and

Kirby (2000) equation (4a) and (4b), except that the current U there is now set to be zero and the definition of α is different. So all the derivations in Chawla and Kirby (2000) can be used here.

When introducing source functions in both the continuity and momentum equations, we get (in dimensional form):

COM:

$$\eta_t + h\nabla \cdot \tilde{\mathbf{u}} + \alpha_1 h^3 \nabla^2(\nabla \cdot \tilde{\mathbf{u}}) = f_s(x, y, t) \tag{A.3}$$

EOM:

$$\tilde{\mathbf{u}}_t + g\nabla\eta + \alpha h^2 \nabla(\nabla \cdot \tilde{\mathbf{u}}_t) = -g\nabla p_s(x, y, t). \tag{A.4}$$

Then, f_s and p_s can be rewritten by introducing Fourier transforms in time and in the spanwise direction:

$$f_s(x, y, t) = \frac{1}{4\pi^2} \int_{-\infty}^{\infty} \int_{-\infty}^{\infty} \hat{f}_s(x, \lambda, \omega) e^{i(\lambda y - \omega t)} d\lambda d\omega \tag{A.5}$$

$$p_s(x, y, t) = \frac{1}{4\pi^2} \int_{-\infty}^{\infty} \int_{-\infty}^{\infty} \hat{p}_s(x, \lambda, \omega) e^{i(\lambda y - \omega t)} d\lambda d\omega \tag{A.6}$$

where $\hat{f}_s$ and $\hat{p}_s$ are transfer function of f_s and p_s respectively. Following Chawla and Kirby (2000) derivations, we obtain:

$$\hat{f}_s = D_1 e^{-\beta_s x^2} \tag{A.7}$$

$$\hat{p}_s = D_2 x e^{-\beta_s x^2} \tag{A.8}$$

where

$$D_1 = \frac{-i\eta_0 e^{(\frac{l_1^2}{4\beta_s})}}{a_1 \sqrt{\frac{\pi}{\beta_s}}(2\omega)(1 - \alpha h^2 k^2)} \tag{A.9}$$

and

$$D_2 = \frac{-2\beta_s D_1}{l_1 \omega} \tag{A.10}$$

$$\beta_s = \frac{80}{\gamma_r^2 L^2} \tag{A.11}$$

where η_0 is the desired wave amplitude, ω is the angular frequency of a single wave component, L is typical wave length, γ_r is a parameter to control the source region width W:

$$W = \gamma_r \frac{L}{2}. \tag{A.12}$$

a_1 is given by

$$a_1 = \frac{i}{A_s(l_1 - l_2)(l_1 + l_2)2l_1} \tag{A.13}$$

where

$$l_1 = \left(\frac{C_s - \sqrt{C_s^2 - 4A_sE_s}}{2A_s}\right)^{1/2} \tag{A.14}$$

$$l_2 = \left(\frac{C_s + \sqrt{C_s^2 - 4A_sE_s}}{2A_s}\right)^{1/2} \tag{A.15}$$

and $l_1^2 + \lambda^2 = k^2$, here $l_1 = k\cos\theta$ and $\lambda = k\sin\theta$, where θ is the wave direction relative to x axis and k is the wavenumber given by dispersion relation:

$$\omega^2 = ghk^2 \frac{1 - \alpha_1 k^2 h^2}{1 - \alpha k^2 h^2} \tag{A.16}$$

A_s, C_s and E_s are given by

$$A_s = \alpha_1 gh^3 \tag{A.17}$$

$$C_s = gh + \omega^2 \alpha h^2 - 2\alpha_1 \lambda^2 gh^3 \tag{A.18}$$

$$E_s = \omega^2[1 - \alpha(\lambda h)^2] - gh\lambda^2[1 - \alpha_1(\lambda h)^2] \tag{A.19}$$

By using the dispersion relation, a_1 can be simplified to:

$$a_1 = \frac{-ik}{2(\omega^2 - \alpha_1 gh^3 k^4)\cos\theta} \tag{A.20}$$

then D_1 can be written as:

$$D_1(\eta_0, \omega, \theta) = \frac{\eta_0 \cos\theta e^{(\frac{l_1^2}{4\beta_s})}(\omega^2 - \alpha_1 gh^3 k^4)}{\omega k\sqrt{\frac{\pi}{\beta_s}}(1 - \alpha h^2 k^2)} \tag{A.21}$$

Then the source function $f_s(x, y, t)$ is calculated by inverse discrete Fourier transform for directional random waves:

$$
\begin{aligned}
f_s(x,y,t) &= \text{Real}\{\frac{1}{4\pi^2}\int_{-\infty}^{\infty}\int_{-\infty}^{\infty}\hat{f}_s(x,\lambda,\omega)e^{i(\lambda y-\omega t)}d\lambda d\omega\} \\
&= \sum_{i=1}^{M}\sum_{j=1}^{N}\frac{1}{2}\hat{f}_s(x,\lambda_j,\omega_i,\eta_{0ij})[e^{i(\lambda_j y-\omega_i t+\phi_0)}+c.c.] \\
&= \sum_{i=1}^{M}\sum_{j=1}^{N}\hat{f}_s(x,\lambda_j,\omega_i,\eta_{0ij})\cos(\lambda_j y-\omega_i t+\phi_0) \qquad \text{(A.22)}
\end{aligned}
$$

where ϕ_0 is a random phase given from 0 to 2π, η_{0ij} is the wave amplitude for the $i'th$ frequency component and the $j'th$ directional component given by selected power density spectrum

$$
\begin{aligned}
\eta_{0ij} &= \eta_0(\omega_i,\theta_j) \\
&= \sqrt{2S(\omega_i)G(\theta_j)d\omega_i d\theta_j} \\
&= \sqrt{2S(\omega_i)d\omega_i} \text{ (if only frequency spectrum exists)} \\
&= \sqrt{2G(\theta_j)d\theta_j} \text{ (if only directional spectrum exists)} \qquad \text{(A.23)}
\end{aligned}
$$

where $S(\omega_i)$, $G(\theta_j)$ are power density spectrum. $p_s(x,y,t)$ is calculated in the same way:

$$
p_s(x,y,t) = \sum_{i=1}^{M}\sum_{j=1}^{N}\hat{p}_s(x,\lambda_j,\omega_i,\eta_{0ij})\cos(\lambda_j y-\omega_i t+\phi_0) \qquad \text{(A.24)}
$$

A.2 Algorithms for Surface Roller Detection

The geometry of the free surface roller for a spilling breaker is described in Schäffer et al. (1993) and also shown in the figure A.1.

The roller thickness r is the distance between the free surface elevation η and the arc ADB in the figure A.1. The starting point A and the ending point B for the roller is found by a) locating point A through a search of the surface points where the slope angle is the same as a breaking criterion angle ϕ; b) extending the tangential line backward from A to intersect with the surface elevation at point B. The arc ADB is made by expanding

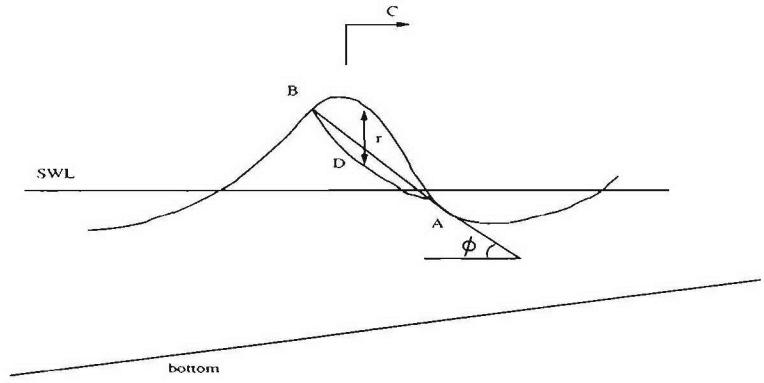

Figure A.1: Roller geometry for a spilling breaker

the thickness between the line AB and the surface elevation η by a factor of f_δ. The breaking criterion angle ϕ is given by

$$\tan\phi = \tan\phi_0 + (\tan\phi_B - \tan\phi_0)\exp[-ln2\frac{t-t_B}{t^*}], \tag{A.25}$$

where ϕ_B is the initial breaking angle, ϕ_0 is the final breaking angle, t^* is the duration of a breaking event such that the angle ϕ decreases from ϕ_B to ϕ_0 gradually. t_B is the starting time of a breaking event and $t - t_B$ is the age of a roller. Typical value of ϕ_B is on the order of 15 to 20 degree, and typical value of ϕ_0 is on the order of 7 to 15 degree. The transition time t^* is approximately $5\sqrt{d/g}$ where d is the still water depth and g is gravitational acceleration. f_δ is the roller shape factor with typical range $1.0 \leq f_\delta \leq 1.6$. In order to track the initial breaking time t_B of a breaker, a variable $ntbr(i)$ is given to keep the record of the time step that a roller initially forms for each point i in the domain. The following Fortran subroutine get_roller() is listed to obtain the roller thickness for every point $1 \leq i \leq mx - 1$.

```
      Subroutine get_roller(etas, ntbr, Mw, Roller
     &          , mx, ITMAX, Roughness, it, Cph, phi_0
     &          , phi_B, T_star)
!
!Obtain surface roller geometry    --- Roller(i)
!also phase speed Cph(i) within the roller
!
```

```
c----- dummy variables---
      INTEGER mx                    !number of grids
      INTEGER ITMAX                 !maximum number of time step
      INTEGER it                    !current time step
      DOUBLEE PRECISION etas(mx)    !free surface
     &                 ,Mw(mx)      !depth integrated flux m^2/s
     &                 ,Roller(mx) !roller thickness,>0: x+ wave
                                    !                 <0: x- wave
     &                 ,Roughness   !film layer thickness
     &                 ,ntbr(mx)    !initial breaking time
                                    !step of a roller
     &                ,Cph(mx)      !phase speed of roller

      DOUBLE PRECISION  Phi_0,      !final breaking angle
     &                  Phi_B,      !initial breaking angle
     &                  T_star      !transition time of the breaker
     &                              !criterion
c----- Local Variables----
        INTEGER i,              !temp index
     &      i1,
     &      iA,                !grid index of roller front
     &      iB,                !grid index of roller tail
     &      nage,              !the time step that the roller
                               !is generated
     &      IDRollerCheck(mx) !a flag to mark whether a point
                               !has been checked in
           !the algorithm of searching for roller
           !  IDRollerCheck(i) =1: yes, already searched,
           !                       or no need to check
           !                   =0: no, not checked yet
       DOUBLE PRECISION
     &                 ,eta_x(mx) !local slope of free
                                    !surface eta: d(eta)/dx
     &                 ,Csign     !local phase speed direction
                                    !of the free surface
                               !Csign = 1 : waves going to right
                               !Csign =-1 : waves going to left
       DOUBLE PRECISION yA, yB, yi1, yi2 !temp variables
       DOUBLE PRECISION ddd
       INTEGER ntbrmin
       DOUBLE PRECISION grav  !gravitational acceleration
```

```
c---------
      grav = 9.81
!
! before start searching for roller, set IDRollerCheck =0
! for all points except film layer also initialize thickness
!
        DO i=1, mx
           IF(h(i).GE.Roughness*2)THEN
! only search for roller out of film layer
              IDRollerCheck(i)= 0
           ELSE
! mark, not necessary to search for roller in film layer
              IDRollerCheck(i)= 1
           ENDIF
! set the roller thickness to be zero
           Roller(i)  = 0.d0
        ENDDO
!
! find the critical breaking angle phi for a roller by eqn (3.1)
! of Schaffer et al. (1993)
!
        DO i=2,mx-2
! find the initial breaking time of a roller by
! searching around neighbors
              nage=MIN(ntbr(i+1),ntbr(i-1))
              nage=MIN(nage,ntbr(i))
              IF(ntbr(i).LT.ITMAX)THEN
! already a broken wave, roller exists
                 tanphi(i)=TAN(Phi_0)+(TAN(Phi_B)-TAN(Phi_0))
     &                    *EXP(-LOG(2.0)*(it-nage)*dt/T_star)
              ELSE
! not a breaking wave yet, set as phi_B
                 tanphi(i)=TAN(Phi_B)
              ENDIF
        ENDDO
!
! Find the local free surface slope d(eta)/dx
! using forth order finite difference
!
       DO i=1,mx
           IF(i.eq.1)THEN
```

```
            eta_x(i)=1.0/(12.0*dx)
     &        *(-25.0*etas(1)+48.0*etas(2)-36.0*etas(3)
     &          +16.0*etas(4)-3.0 *etas(5))
          ELSEIF(i.eq.2)THEN
            eta_x(i)=1.0/(12.0*dx)
     &        *(- 3.0*etas(1)-10.0*etas(2)+18.0*etas(3)
     &          - 6.0*etas(4)+     etas(5))
          ELSEIF(i.eq.mx-1)THEN
            eta_x(i)=1.0/(12.0*dx)
     &        *( 3.0*etas(mx)+10.0*etas(mx-1)-18.0*etas(mx-2)
     &          +6.0*etas(mx-3)-   etas(mx-4))
          ELSEIF(i.eq.mx)THEN
            eta_x(i)=1.0/(12.0*dx)
     &       *( 25.0*etas(mx)  -48.0*etas(mx-1)+36.0*etas(mx-2)
     &        -16.0*etas(mx-3)+ 3.0*etas(mx-4))
          ELSE
            eta_x(i)=1.0/(12.0*dx)
     &       *( 8.0*etas(i+1)-8.0*etas(i-1)-etas(i+2)+etas(i-2))
          ENDIF
       ENDDO
!
! search backward from grid i=mx-1 to i= 2
! look for roller that rides on waves propagating
! in positive x direction
!
        iB= mx-1    !assume the tail of right
                    !most roller is at mx-1
50      DO i=mx-1,2,-1
!find the propagation direction of waves at i approximately
          Csign= Dsign(1.d0, ( Mw(i+1)
     &                         -Mw(i-1)
     &                        )
     &                       *(etas(i+1)-etas(i-1))
     &                 )
          IF(Csign.GE.0.and.IDRollerCheck(i).eq.0)THEN
!do the search for positive x going wave  and unsearched points
             IF(eta_x(i)  .le.-tanphi(i).AND.
     &          eta_x(i+1).gt.-tanphi(i))THEN
               iA=i          !find point A of the roller
                             !the front index of the roller
               yA=etas(i)    !record the height of A
```

```
                nage= ntbr(iA)
                IF(nage.eq.ITMAX) THEN
                  ntbr(iA) = it
                ENDIF
                ntbrmin = ITMAX
!
!search back and find corresponding roller thickness
!
                DO i1=iA,MAX(iA-mx,2),-1
!the elevation of intersection line at i1
                  yi1=yA+(iA-i1)*dx*tanphi(iA)
!the elevation of intersection line at i1-1
                  yi2=yA+(iA-(i1-1))*dx*tanphi(iA)
                  IF(etas(i1-1).ge.yi2)then
!
!the thickness of the roller  (counted as positive)
! for waves propagating in +x direction
!
                  Roller(i1)=max(0.d0,(etas(i1)-yi1)*f_delta)
!i1 is within a roller for sure,
!no need to search for it any more
                   IDRollerCheck(i1) = 1
!trying to track the minimum breaking time
                   ntbrmin = min (ntbrmin,ntbr(i1))
                 ENDIF
!try to locate the tail point B of the roller
                  iB=i1
                  IF( (etas(i1)-yi1).ge.0.and.
     &                 (etas(i1-1)-yi2).lt.0)THEN
                    iB=i1    !found point B of the roller
                    GOTO 100
                  ENDIF
                ENDDO
100           iB = max(1, iB)
                DO i1= iA+1,iB-1,-1
!record the starting breaking time of this breaker
!even this breaking changes it's location and spread (iA, iB)
                  ntbr(i1) = ntbrmin
                    IDRollerCheck(i1) = 1
                ENDDO
            ENDIF
```

```
         ENDIF
       ENDDO   !go to next search from the new iB to i=2
!
!search forward from grid i=2 to i= mx-1,
!look for roller that rides on waves propagating
!in x- direction
!
       iB= 2  !assume the tail of right most roller is at 2
       DO i=2,mx-1,1
 !find the propagatin direction of waves at i approximately
          Csign= Dsign(1.d0, (  Mw(i+1)
     &                        - Mw(i-1)
     &                      *(etas(i+1)-etas(i-1))
     &                )
!do the search for negative x going wave and unsearched points
             IF(Csign.LT.0.and.IDRollerCheck(i).eq.0)THEN
             IF(eta_x(i)  .le.tanphi(i).and.
     &          eta_x(i+1).gt.tanphi(i))then
!find point A of the roller !the front index of the roller
                iA=i
                yA=etas(i)      !record the height of A
                 nage= ntbr(iA)
                IF(nage.eq.ITMAX) THEN
                   ntbr(iA) = it
                ENDIF
                ntbrmin = mx
!
!search forward and find corresponding roller thickness
!                DO i1=iA,MIN(iA+mx,mx-1),1
!the elevation of intersection line at i1
!the elevatio of intersection line at i1+1
                  yi1=yA+(i1-iA)*dx*tanphi(iA)
                  yi2=yA+((i1+1)-iA)*dx*tanphi(iA)
                  IF(etas(i1+1).ge.yi2)THEN
 !the thickness of the roller
 !counted as negative for waves propagating in x- direction
                  Roller(i1)=-MAX(0.d0,(etas(i1)-yi1)*f_delta)
!i1 is within a roller for sure,
!no need to search for it any more
                  IDRollerCheck(i1) = 1
!trying to track the minimum breaking time
```

```
                    ntbrmin = min (ntbrmin,ntbr(i1))
                  ENDIF
!try to locate the tail point B of the roller
                  iB=i1
                  IF( (etas(i1)-yi1).ge.0.and.
     &                (etas(i1+1)-yi2).lt.0)THEN
                      iB=i1    !found point B of the roller
                      GOTO 200
                  ENDIF
                ENDDO
200           iB = min(mx-1, iB)
                DO i1= iA-1,iB+1,+1
!record the starting breaking time of this breaker
!even this breaking changes it's location and spread (iA, iB)
                  ntbr(i1) = ntbrmin
                  IDRollerCheck(i1) = 1
                ENDDO
            ENDIF
          ENDIF
       ENDDO  !go to next search from the new iB to i=mx-1
!
! Set the initial breaking
! to be infinity for points not in roller
!
       DO i=1,mx
            IF(IDRollerCheck(i).eq.0)THEN
               ntbr(i)=ITMAX
            ENDIF
       ENDDO
!
! Find local phase speed roughly
!
       Do i=2,mx-1
          Csign = Dsign(1.d0,roller(i))
          ddd   = etastill(i)-zb(i)
          ddd   = max(ddd, Roughness)
!Csign>0 , waves go x+ direction
!Csign<0 , waves go x- direction
          Cph(i) = Csign*sqrt(grav*ddd)
       ENDDO
       Cph(1)   = Cph(2)
```

A.3 Cyclically Tridiagonal Matrix Solver

When periodic boundary conditions are used in the modeling practice, such as lateral open boundaries for a domain consists of infinitely long beach, the so called cyclically tridiagonal matrix equation system will be obtained and need to be solved using a special method that involves the Sherman-Morrison formula (Sherman and Morrison, 1949).

Let the cyclically tridiagonal system be

$$\mathbf{Qx} = \psi \tag{A.26}$$

where Q is a cyclically tridiagonal matrix

$$\mathbf{Q} = \begin{pmatrix} \beta_1 & \gamma_1 & 0 & 0 & \ldots & \alpha_1 \\ \alpha_2 & \beta_2 & \gamma_2 & 0 & \ldots & 0 \\ 0 & \alpha_3 & \beta_3 & \gamma_3 & \ldots & 0 \\ \ldots & \ldots & \ldots & \ldots & \ldots & \ldots \\ 0 & 0 & \ldots & \alpha_{N-1} & \beta_{N-1} & \gamma_{N-1} \\ \gamma_N & \ldots & 0 & 0 & \alpha_N & \beta_N \end{pmatrix}, \tag{A.27}$$

$\mathbf{x} = (x_1,\ x_2,\ x_3,\ \ldots,\ x_N)^T$ is the unknowns vector, and $\psi = (\psi_1,\ \psi_2,\ \psi_3,\ \ldots,\ \psi_N)^T$. In order to solve (A.26), the following strategy can be used. Let

$$\mathbf{u} = \begin{Bmatrix} \beta \\ 0 \\ \ldots \\ 0 \\ \gamma_N \end{Bmatrix} \tag{A.28}$$

and

$$\mathbf{v} = \begin{Bmatrix} 1 \\ 0 \\ \ldots \\ 0 \\ \alpha_1/\beta \end{Bmatrix}, \tag{A.29}$$

where β can be any real number other than β_1, then we have

$$\mathbf{u} \times \mathbf{v}^T = \begin{pmatrix} \beta & 0 & \ldots & \alpha_1 \\ 0 & \ldots & \ldots & 0 \\ \ldots & \ldots & \ldots & \ldots \\ \gamma_N & 0 & \ldots & \alpha_1\gamma_N/\beta \end{pmatrix}. \tag{A.30}$$

Let $\mathbf{A} = \mathbf{Q} - \mathbf{u} \times \mathbf{v}^T$, we have

$$\mathbf{A} = \begin{pmatrix} \beta_1 - \beta & \gamma_1 & 0 & \ldots & 0 \\ \alpha_2 & \beta_2 & \gamma_2 & \ldots & 0 \\ \ldots & \ldots & \ldots & \ldots & \ldots \\ 0 & \ldots & \alpha_{N-1} & \beta_{N-1} & \gamma_{N-1} \\ 0 & \ldots & 0 & \alpha_N & \beta_N - \alpha_1\gamma_N/\beta \end{pmatrix}. \tag{A.31}$$

Here $\mathbf{A}$ is the conventional tridiagonal matrix. According to Sherman-Morrison formula, we can solve the following conventional tridiagonal systems to obtain solution for (A.26)

$$\mathbf{A}\mathbf{y} = \psi \tag{A.32}$$

$$\mathbf{A}\mathbf{z} = \mathbf{u} \tag{A.33}$$

where $\mathbf{y} = (y_1,\ y_2,\ ..., y_N)^T$ and $\mathbf{z} = (z_1,\ z_2,\ ..., z_N)^T$. Finally the solution of $\mathbf{x}$ is obtained by

$$\mathbf{x} = \mathbf{y} - (\frac{\mathbf{v} \cdot \mathbf{y}}{1 + \mathbf{v} \cdot \mathbf{z}})\mathbf{z} \tag{A.34}$$

where $\mathbf{v} \cdot \mathbf{y} = v_1y_1 + v_2y_2 + ... + v_Ny_N$ and $\mathbf{v} \cdot \mathbf{z} = v_1z_1 + v_2z_2 + ... + v_Nz_N$.

A Fortran 77 subroutine cyclic() for solving the cyclically tridiagonal system (A.26) is given here.

```
      Subroutine cyclic (alpha, beta,gamma, b, x, N)
!---solve the following cyclic tridiagonal equation---
!*********************************************************!
!*                                                       *!
!*     (B1 C1                          A1 )   (x1)      (b1)  *!
!*     (A2 B2 C2                          )   (x2)      (b2)  *!
!*     (   A3 B3 C3                       )   (x3)      (b3)  *!
!*     (      A4 B4 C4                    )   (x4)====        *!
!*     (         A5 B5  C5                )   ... ====  ...   *!
!*     (            ... ... ...           )   ...       ...   *!
!*     (                AN-1 BN-1 CN-1)   (xN-1)    (bN-1)*!
!*     (CN                    AN   BN  )   (xN)      (bN)  *!
!*                                                       *!
!*********************************************************!
!    where A's are alpha, B's are beta, C's are gamma
c----dummy variables--
        Integer N
      double precision alpha(N), beta(N),gamma(N),b(N),x(N)
c----local variables--
        double precision betaPrime(N),u(N),z(N),c,fact
c----
         c=-beta(1)     !the minus sign makes
                        !sure betaPrime(1) non zero
!the first tridiagonal element
         betaPrime(1) = beta(1) - c
         do i=2,N-1,1
            betaPrime(i)=beta(i)
         enddo
!the last tridiagonal element
         betaPrime(N) = beta(N) - alpha(1) * gamma(N)/c
!solve for u and store it in x
         call tri_ge(alpha, betaPrime, gamma, b, x, N)
!first u
         u(1) = c;
         do i=2,N-1
          u(i)=0.d0
       enddo
!last u
         u(N) = gamma(N)
!solve for z
         call tri_ge(alpha, betaPrime, gamma, u, z, N)
```

```
          fact = (x(1) + alpha(1) * x(N) / c)
     &         / (1.0 + z(1) + alpha(1) * z(N) / c)
!construct final results
          do i=1,N
             x(i) =x(i)- fact * z(i)

          enddo
    Return
    End

     Subroutine tri_ge(alpha,beta,gamma,b, x, N)
!----solve the following conventional tridiagonal system without
!----changing coefficients in A, B and C
!*************************************************************!
!*                                                           *!
!*     (B1 C1                          )   (x1)      (b1)   *!
!*     (A2 B2 C2                       )   (x2)      (b2)   *!
!*     (   A3 B3 C3                    )   (x3)      (b3)   *!
!*     (      A4 B4 C4                 )   (x4)====          *!
!*     (         A5 B5  C5             )   ... ====   ...    *!
!*     (            ... ... ...        )   ...         ...   *!
!*     (                An-1 Bn-1 Cn-1)   (xn-1)    (bn-1)*!
!*     (                     An   Bn  )   (xn)      (bn)   *!
!*                                                           *!
!*                                                           *!
!*************************************************************!
! where A's are alpha, B's are beta, C's are gamma
c----dummy variables---
        integer N
        double precision alpha(N),beta(N), gamma(N), b(N), x(N)
c-----local variables
        double precision betaPrime(N), bPrime(N)
        double precision coeff
        integer i

!Perform forward elimination
         betaPrime(1) = beta(1)
         bPrime(1) = b(1)

         do i=2,N
```

```
                coeff = alpha(i) / betaPrime(i-1)
                betaPrime(i) = beta(i) - coeff * gamma(i-1)
                bPrime(i) = b(i) - coeff * bPrime(i-1)
          enddo

! Perform back substitution
          x(N) = bPrime(N) / betaPrime(N)
          do i=N-1,1,-1
               x(i) = (bPrime(i) - gamma(i) * x(i+1))
     &                / betaPrime(i)
          enddo
    return
    End
```

A.4 Notes on Generalized Curvilinear Coordinate System

In this section, we present basic but important definitions and relations for generalized curvilinear coordinate system.

$$g_{ik} = \mathbf{g}_i \cdot \mathbf{g}_k = \frac{\partial y_i \partial y_j}{\partial x^i \partial x^k} \tag{A.35}$$

$$g^{ik} = \mathbf{g}^i \cdot \mathbf{g}^k \tag{A.36}$$

$$\delta_i^j = \mathbf{g}_i \cdot \mathbf{g}^j = \mathbf{g}^j \cdot \mathbf{g}_i = \begin{cases} 1, & i = j \\ 0, & i \neq j \end{cases} \tag{A.37}$$

$$u^i = g^{ik} u_k \tag{A.38}$$

$$u_i = g_{ik} u^k \tag{A.39}$$

$$\mathbf{g}^i = g^{ij} \mathbf{g}_j \tag{A.40}$$

$$\mathbf{g}_i = g_{ij} \mathbf{g}^j \tag{A.41}$$

$$g_{ik} g^{jk} = \delta_i^j = \begin{bmatrix} 1 & 0 & 0 \\ 0 & 1 & 0 \\ 0 & 0 & 1 \end{bmatrix} \tag{A.42}$$

$$\sqrt{g_0} = J = \begin{vmatrix} \frac{\partial y_1}{\partial x^1} & \frac{\partial y_1}{\partial x^2} & \frac{\partial y_1}{\partial x^3} \\ \frac{\partial y_2}{\partial x^1} & \frac{\partial y_2}{\partial x^2} & \frac{\partial y_2}{\partial x^3} \\ \frac{\partial y_3}{\partial x^1} & \frac{\partial y_3}{\partial x^2} & \frac{\partial y_3}{\partial x^3} \end{vmatrix} \tag{A.43}$$

The last two equations give

$$g^{ij} = (g_{rs}g_{mn} - g_{rn}g_{ms})/g_0 \tag{A.44}$$

where

$$\begin{cases} i = 1 : r = 2, m = 3; & j = 1 : s = 2, n = 3 \\ i = 2 : r = 2, m = 1; & j = 2 : s = 3, n = 1 \\ i = 3 : r = 1, m = 2; & j = 3 : s = 1, n = 2 \end{cases} \tag{A.45}$$

Gradient, Divergence and Curl

If $\phi, \mathbf{u}, \tilde{\tilde{\mathbf{T}}}$ represent scalar, vector, and second order tensor respectively, then we have the following relations for calculating gradient, divergence and curl in curvilinear coordinate system

$$\nabla\phi \equiv g^{ij}\frac{\partial\phi}{\partial x^j}\mathbf{g}_i = \frac{\partial\phi}{\partial x^j}\mathbf{g}^j \equiv \phi!^i \tag{A.46}$$

$$\nabla \cdot \mathbf{u} = u^i_{,i} = \frac{1}{\sqrt{g_0}}\frac{\partial}{\partial x^i}(\sqrt{g_0}u^i) \tag{A.47}$$

$$\nabla\mathbf{u} = u^k_{,i}\mathbf{g}_k\mathbf{g}^i, \tag{A.48}$$

where

$$u^k_{,i} = \frac{\partial u^k}{\partial x^i} + C^k_{ji}u^j \tag{A.49}$$

$$u^i_{,j} = \frac{\partial u^i}{\partial x^j} + C^i_{kj}u^k \tag{A.50}$$

and

$$C^i_{kj} = \frac{\partial^2 y_l}{\partial x^k \partial x^j}\frac{\partial x^i}{\partial y_l} \tag{A.51}$$

is called the Christoffel symbol of the second kind.

$$u_{k,j} = g_{ks}u^s_{,j} \tag{A.52}$$

$$\tilde{\tilde{\mathbf{T}}} = T^{ij}\mathbf{g}_i\mathbf{g}_j \Rightarrow \nabla \cdot \tilde{\tilde{\mathbf{T}}} = T^{ik}_{,k}\mathbf{g}_i \tag{A.53}$$

$$\tilde{\tilde{\mathbf{T}}} = T^i_j \mathbf{g}_i \mathbf{g}^j \Rightarrow \nabla \cdot \tilde{\tilde{\mathbf{T}}} = g^{jk} T^i_{j,k} \mathbf{g}_i \tag{A.54}$$

$$\tilde{\tilde{\mathbf{T}}} = T_{ij} \mathbf{g}^i \mathbf{g}^j \Rightarrow \nabla \cdot \tilde{\tilde{\mathbf{T}}} = g^{jk} T_{ij,k} \mathbf{g}^i \tag{A.55}$$

where

$$T^{ij}_{,k} = \frac{\partial T^{ij}}{\partial x^k} + C^i_{mk} T^{mj} + C^j_{mk} T^{im} \tag{A.56}$$

$$T_{ij,k} = \frac{\partial T_{ij}}{\partial x^k} - C^m_{ik} T_{mj} - C^m_{jk} T_{im} \tag{A.57}$$

$$T^i_{j,k} = \frac{\partial T^i_j}{\partial x^k} + C^i_{mk} T^m_j - C^m_{jk} T^i_m \tag{A.58}$$

Then

$$\begin{aligned} T^{ik}_{,k} &= \frac{\partial T^{ik}}{\partial x^k} + C^i_{mk} T^{mk} + C^k_{mk} T^{im} \\ &= \frac{\partial T^{ik}}{\partial x^k} + C^k_{mk} T^{im} + C^i_{mk} T^{mk} \\ &= \frac{\partial T^{ik}}{\partial x^k} + \frac{\partial ln\sqrt{g_0}}{\partial x^m} T^{im} + C^i_{mk} T^{mk} \\ &= \frac{1}{\sqrt{g_0}} \frac{\partial}{\partial x^k} (\sqrt{g_0} T^{ik}) + C^i_{mk} T^{mk} \end{aligned} \tag{A.59}$$

Then,

$$\begin{aligned} \nabla \cdot \tilde{\tilde{\mathbf{T}}} &= T^{ik}_{,k} \mathbf{g}_i \\ &= (\frac{1}{\sqrt{g_0}} \frac{\partial}{\partial x^k} (\sqrt{g_0} T^{ik}) + C^i_{mk} T^{mk}) \mathbf{g}_i \end{aligned} \tag{A.60}$$

$$\nabla \times \mathbf{u} = \frac{1}{\sqrt{g_0}} e^{inm} u_{m,n} \mathbf{g}_i \tag{A.61}$$

where e^{inm} is permutation tensor (Warsi, 1999). Also we have another permutation tensor e_{ijk} given by

$$\mathbf{g}_i \times \mathbf{g}_j = \sqrt{g_0} e_{ijk} \mathbf{g}^k \tag{A.62}$$

and

$$e^{inm} e_{ijk} = \delta^n_j \delta^m_k - \delta^n_k \delta^m_j \tag{A.63}$$

Thus,

$$
\begin{aligned}
(\nabla \times \mathbf{u}) \times \mathbf{v} &= (\frac{1}{\sqrt{g_0}} e^{inm} u_{m,n} \mathbf{g}_i) \times v^j \mathbf{g}_j \\
&= \frac{1}{\sqrt{g_0}} u_{m,n} v^j e^{inm} \mathbf{g}_i \times \mathbf{g}_j \\
&= \frac{1}{\sqrt{g_0}} u_{m,n} v^j e^{inm} \sqrt{g_0} e_{ijk} \mathbf{g}^k \\
&= u_{m,n} v^j (e^{inm} e_{ijk}) \mathbf{g}^k \\
&= u_{m,n} v^j (\delta^n_j \delta^m_k - \delta^n_k \delta^m_j) \mathbf{g}^k \\
&= (u_{k,j} v^j - u_{j,k} v^j) \mathbf{g}^k \\
&= (g_{ks} u^s_{,j} v^j - g_{js} u^s_{,k} v^j) g^{kl} \mathbf{g}_l \\
&= (\delta^l_s u^s_{,j} v^j - g_{js} g^{kl} u^s_{,k} v^j) \mathbf{g}_l \\
&= (u^l_{,j} v^j - g_{js} g^{kl} u^s_{,k} v^j) \mathbf{g}_l \qquad \text{(A.64)}
\end{aligned}
$$

This equation gives the cross product in terms of contravariant components.

For a 2-D curvilinear coordinate system, we have simplified formulas for all the basic geometric quantities g_{ij}, $\sqrt{g_0}$, C^k_{ij} as the following:

$$g_{ik} = \frac{\partial y_j \partial y_j}{\partial x^i \partial x^k} \qquad \text{(A.65)}$$

$$g_{11} = x^2_{\xi_1} + y^2_{\xi_1} \qquad \text{(A.66)}$$

$$g_{22} = x^2_{\xi_2} + y^2_{\xi_2} \qquad \text{(A.67)}$$

$$g_{12} = g_{21} = x_{\xi_1} x_{\xi_2} + y_{\xi_1} y_{\xi_2} \qquad \text{(A.68)}$$

$$g_0 = J^2 = g_{11} g_{22} - g_{12} g_{12} \qquad \text{(A.69)}$$

$$J = x_{\xi_1} y_{\xi_2} - x_{\xi_2} y_{\xi_1} = \sqrt{g_0} \qquad \text{(A.70)}$$

$$g^{11} = \frac{g_{22}}{g_0} \qquad \text{(A.71)}$$

$$g^{22} = \frac{g_{11}}{g_0} \qquad \text{(A.72)}$$

$$g^{12} = -\frac{g_{12}}{g_0} = g^{21} \tag{A.73}$$

$$C_{11}^1 = \frac{1}{2}g^{11}\frac{\partial g_{11}}{\partial \xi_1} + g^{12}\frac{\partial g_{12}}{\partial \xi_1} - \frac{1}{2}g^{12}\frac{\partial g_{11}}{\partial \xi_2} \tag{A.74}$$

$$C_{11}^2 = \frac{1}{2}g^{12}\frac{\partial g_{11}}{\partial \xi_1} + g^{22}\frac{\partial g_{12}}{\partial \xi_1} - \frac{1}{2}g^{22}\frac{\partial g_{11}}{\partial \xi_2} \tag{A.75}$$

$$C_{22}^2 = g^{12}\frac{\partial g_{12}}{\partial \xi_2} - \frac{1}{2}g^{12}\frac{\partial g_{22}}{\partial \xi_1} + \frac{1}{2}g^{22}\frac{\partial g_{22}}{\partial \xi_2} \tag{A.76}$$

$$C_{22}^1 = g^{11}\frac{\partial g_{12}}{\partial \xi_2} - \frac{1}{2}g^{11}\frac{\partial g_{22}}{\partial \xi_1} + \frac{1}{2}g^{22}\frac{\partial g_{22}}{\partial \xi_2} \tag{A.77}$$

$$C_{12}^2 = C_{21}^2 = \frac{1}{2}g^{12}\frac{\partial g_{11}}{\partial \xi_2} + \frac{1}{2}g^{22}\frac{\partial g_{22}}{\partial \xi_1} \tag{A.78}$$

$$C_{12}^1 = C_{21}^2 = \frac{1}{2}g^{11}\frac{\partial g_{11}}{\partial \xi_2} + \frac{1}{2}g^{12}\frac{\partial g_{22}}{\partial \xi_1} \tag{A.79}$$

The relationships between Cartesian velocity (u_{cart}, v_{cart}) and Contravariant velocity $(u^1, u^2) = (u, v)$ are important for interpretation of model results and they given here as

$$u_{cart} = \frac{Dx}{Dt} = u^1 x_{\xi_1} + u^2 x_{\xi_2} = u x_{\xi_1} + v x_{\xi_2} \tag{A.80}$$

$$v_{cart} = \frac{Dy}{Dt} = u^1 y_{\xi_1} + u^2 y_{\xi_2} = u y_{\xi_1} + v y_{\xi_2} \tag{A.81}$$

where $\frac{\partial x}{\partial t} = 0$ and $\frac{\partial y}{\partial t} = 0$ are utilized for non-time-varying curvilinear coordinate system (ξ_1, ξ_2).

Vice versa, we have

$$u = u^1 = \frac{y_{\xi_2} u_{cart} - x_{\xi_2} v_{cart}}{\sqrt{g_0}} \tag{A.82}$$

$$v = u^2 = \frac{x_{\xi_1} v_{cart} - y_{\xi_1} u_{cart}}{\sqrt{g_0}} \tag{A.83}$$

A.5 Numerical Estimation of Bedform Phase Speed

For the 1-D case, equations (5.2) and (5.62) give:

$$C(z_b) = \frac{\frac{\partial q}{\partial x}}{(1-n_p)\frac{\partial z_b}{\partial x}} \tag{A.84}$$

For 2D case, the upper equation can be generalized (assuming that the bedform propagation direction is collinear as the gradient direction of z_b) as:

$$\mathbf{C} = -\frac{\frac{\partial z_b}{\partial t}}{|\nabla z_b|^2}\nabla z_b = \frac{\nabla \cdot \mathbf{q}}{(1-n_p)|\nabla z_b|^2}\nabla z_b, \tag{A.85}$$

where $\mathbf{C} = (C_x, C_y)$ is a vector. Equations (A.84) and (A.85) give the calculations of phase speed in terms of the spatial derivatives. For the 1-D case, Hudson (2001) employed a central difference scheme to estimate C numerically:

$$C_i = \frac{q_{i+1} - q_{i-1}}{(1-n_p)(z_{bi+1} - z_{bi-1})}, z_{bi+1} \neq z_{bi-1}. \tag{A.86}$$

Unfortunately, the upper equation can be used only when $z_{bi+1} \neq z_{bi-1}$ and it will produce quite inaccurate approximation of the phase speed when the bed level gradient approaches zero or changes sign. For monotonic beach profile, this case doesn't occur. For bedforms with sand bars, ripples or flat sea bed, it is prone to have significant errors.

In the WENO scheme implementation of this study, it is important that upwinding is used, and the easiest and the most inexpensive way to achieve upwinding is to compute the Roe speed (Shu 1997, page 22):

$$a_{i+\frac{1}{2}} = \frac{q_{i+1} - q_i}{(1-n_p)(z_{bi+1} - z_{bi})}. \tag{A.87}$$

If $a_{i+1/2} \geq 0$, the wind blows from the left to the right, and corresponding bedform phase speed is also from left to right. Otherwise, if $a_{i+1/2} < 0$, the wind is blowing from right to left. In computer programming, since only the sign of $a_{i+1/2}$ is needed, we can simply use $\text{sign}((q_{i+1} - q_i)(z_{bi+1} - z_{bi}))$ to avoid division by a small number when $(z_{bi+1} - z_{bi})$ approaches zero. Because WENO only requires the sign of the phase speed, it is much

more stable than schemes that require accurate estimate of phase speed both in magnitude and sign.

BIBLIOGRAPHY

[1] Abbott, M. B., Computational Hydraulics, Elements of theory of free surface flows, Pitman Publishing, London, 1978

[2] Airy, G. B., On the laws of the tides on the coasts of Ireland, as inferred from an extensive series of observations made in connexion with the Ordnance Survey of Ireland [1844], *Philos. Trans. R. Soc. London*, pp 1124, 1845

[3] Ancey, C., Introduction to Fluid Rheology, manuscript, 2005

[4] Arcilla, A. S., J. A. Roelvink, B. A. O'Conner, A. Reniers and J. A. Jimenez, The Delta Flume'93 experiment. *Conference on Coastal Dynamics*, 1994, Barcelona, pp 488-502, 1994

[5] Bagnold, R. A, Experiments on a gravity-free dispersion of large solid spheres in a Newtonian fluid under shear, *Proc. R. Soc. Lond.*, **A 225**, pp 49-63, 1954

[6] Bagnold, R. A., An approach to the sediment transport problem from general physics, *U. S. Geol. Surv. Prof. Paper*, **422-I**, 1966

[7] Bagnold, R. A., The nature of saltation and of bed-load transport in water, *Proc. Roy. Soc. London A*, **332**, pp 473-504, 1973

[8] Bailard, J. A., An energetics total load sediment transport model for a plane sloping beach, *J. Geophysical Research*, **86, C11**, pp 938-954, 1981

[9] Bayram, A. and M. Larson, Wave transformation in the nearshore zone: comparison between a Boussinesq model and field data, *Coastal Engineering*, **39**, pp 49-171, 2000

[10] Bellotti, G., Shoreline boundary conditions for water wave models, Dipartimento di Idraulica, Transporti e Strade, Universita Degli Studi Di Napoli Federico II. Ph.D., 2001

[11] Berkhoff, J. C. W., Computation of combined refraction-diffraction, *Proceedings of 13th International Conference on Coastal Engineering*, **1**, pp 472- 490, 1972

[12] Berkhoff, J. C. W., N. Booy and A. C. Radder, Verification of numerical wave propagation models for simple harmonic linear water waves, *Coastal Engineering*, **6**, pp 255-279, 1982

[13] Bosboom, J., G. Klopman, J. A. Roelvink and J. A. Battjes, Boussinesq modelling of wave-induced horizontal particle velocities, *Coastal Engineering*, **32**, pp 163-180, 1997

[14] Boussinesq, J., Th'eorie des ondes et des remous qui se propagent le long d'un canal rectangulaire horizontal, en communiquant au liquide contenu dans ce canal des vitesses sensiblement pareilles de la surface au fond, *J. Math. Pures Appl.*, **17 (2)**, pp 55-108, 1872

[15] Briganti, R., R. E. Musumeci, G. Bellotti, M. Brocchini and E. Foti, Boussinesq modeling of breaking waves: description of turbulence, *Journal of Geophysical Research*, **109(C07015)**, 2004

[16] Brufau, P., M. E. Vazquez-Cendon, and P. Garcia-Navarro, A numerical model for the flooding and drying of irregular domains, *International Journal For Numerical Methods in Fluids*, **39**, pp 247-275, 2002

[17] Burchard, H. and K. Bolding, GETM, a General Estuarine Transport Model, scientific documentation, 2003

[18] Carrier, G. F. and H. P. Greenspan, Water waves of finite amplitude on a sloping beach, *Journal of Fluid Mechanics*, **17**, pp 97-109, 1958

[19] Carrier, G. F., T. T. Wu and H. Yeh, Tsunami run-up and draw-down on a plane beach, *J. Fluid Mech.*, **475**, pp 79-99, 2003

[20] Chang, H. Y., D. E. Simons and D. A. Woolhiser, Flume experiments on alternate bar formation, *J. Waterway, Port, Coastal and Ocean Engrng.*, **97**, pp 155-165, 1971

[21] Chanson, H., The Hydraulics of Open Channel Flow, Arnold, 338 Euston Road, London, NW1 3BH, UK, 1999.

[22] Chawla, A. and J. T. Kirby, A source function method for generation of waves on currents in Boussinesq models, *Applied Ocean Research*, **22**, pp 75-83, 2000

[23] Chen, Q., R. A. Dalrymple, J. T. Kirby, A. B. Kennedy and M. Haller, Boussinesq modeling of a rip current system, *Journal of Geophysical Research*, **104(C9)**, pp 20617-20637. (1999).

[24] Chen, Q., J. T. Kirby, R. A. Dalrymple, A. B. Kennedy and A. Chawla, Boussinesq modeling of wave transformation, breaking and runup. II: Two horizontal dimensions, *Journal of Waterway, Port, Coastal and Ocean Engineering*, **126**, pp 48-56, 2000

[25] Chen, Q., J. T. Kirby, R. A. Dalrymple, F. Shi and E. B. Thornton, Boussinesq modeling of longshore currents, *Journal of Geophysical Research*,**108(C11,3362)**, doi:10.1029/2002JC001308, pp 26-1-26-18, 2003

[26] Chesher, T. J., H. M. Wallace, I. C. Meadowcroft and H. N. Southgate, PISCES. A morphodynamic coastal area model, *First Annual Report, Report SR 337*, HR Wallingford, pp 27, 1993

[27] Cienfuegos, R., E. Barthelemy, and P. Bonneton, A fourth-order compact finite volume scheme for fully nonlinear and weakly dispersive Boussinesq-type equations. Part I: Model development and analysis, *International Journal for Numerical Methods in Fluids*, (in press), 2006

[28] Colombini, M., G. Seminara and M. Tubino, Finite-amplitude alternate bars, *J. Fluid Mech.*, **181**, 213-232, 1987

[29] Cox, D. and N. Kobayashi, Application of an undertow model to irregular waves on plane and barred beaches, *Journal of Coastal Research*, **14**, pp 1314-1315, 1998

[30] Damgaard, J. S., Numerical schemes for morphodynamic simulations, *HR Wallingford, Report IT 459*, March, 1998

[31] Damgaard, J. S. and T. J. Chesher, Morphodynamic simulations of Helwick Bank, *HR Wallingford, Report TR 31*, 1997

[32] Dartevelle, S., Numerical modeling of geophysical granular flows: 1. A comprehensive approach to granular rhelogies and geophysical multiphase flows, *Geochemistry Geophysics Geosystems*, **5(8)**, 2004

[33] Davies, A. G., J. S. Ribberink, A. Temperville and J. A. Zyserman, Comparisons between sediment transport models and observations made in wave and current flows above plane beds, *Coastal Engineering*, **31**, pp 163-198, 1997

[34] Dean, R.G. and R. A. Dalrymple, Coastal processes with engineering applications, Cambridge University Press, Cambridge, England, 2002

[35] De Vriend, H. J., J. A. Zyserman, J. Nicholson, J. A. Roelvink, P. Péchon, H. N. Southgate, Medium-term 2DH coastal area modeling, *Coastal Engineering*, **21**, 193-224, 1993

[36] Dean, R. G. and R. A. Dalrymple, Water Wave Mechanics for Engineers and Scientists, World Scientific, 1991

[37] Delis, A. I., C. P. Skeels, TVD schemes for open channel flow, *International Journal for Numerical Methods in Fluids*, **26**, 791-809, 1998

[38] DHI, MIKE 21 Coastal hydraulics and oceanography hydrodynamic module reference manual, DHI Water & Environment, 2002

[39] DHI, MIKE 11, A modelling system for rivers and channels, reference manual, DHI Water & Environment, 2003

[40] DHI, MIKE FLOOD 1D-2D modelling, user manual, DHI Water & Environment, 2003

[41] Dibajnia, M. and A. Watanabe, Transport rate under irregular sheet flow conditions, *Coastal Engineering*, **35**, pp 167-183, 1998

[42] Dohmen-Janssen, C. M. and D. M. Hanes, Sheet flow dynamics under monochromatic nonbreaking waves, *Journal of Geophysical Research*, **107(C10)**, doi:1029/2001JC001045, 2002

[43] Dohmen-Janssen, C. M., D. F. Kroekenstoel, W. N. Hassan and J. S. Ribberink, Phase lags in oscillatory sheet flow: experiments and bed load modelling, *Coastal Engineering*, **46**, pp 61-87, 2002

[44] Dohmen-Janssen, C. M., W. N. Hassan and J. S. Ribberink, Mobile-bed effects in oscillatory sheet flow, *Journal of Geophysical Research*, **106(C11)**, pp 27103-27115, 2001

[45] Dohmen-Janssen, C. M., and D. M. Hanes, Sheet flow and suspended sediment due to wave groups in a large wave flume, *Continental Shelf Research*, **25(3)**, pp 333-347, doi:10.1016/j.csr.2004.10.009, 2005

[46] Dong, P. and K. Zhang, Two-phase flow modelling of sediment motions in oscillatory sheet flow, *Coastal Engineering*, **36**, pp 87-109, 1999

[47] Dong, P. and K. Zhang, Intense near-bed sediment motions in waves and currents, *Coastal Engineering*, **45**, pp 75-87, 2002

[48] Drake, T. G. and J. Calantoni, Discrete particle model for sheet flow sediment transport in the nearshore, *J. Geophysical Research*, **106, C9**, pp 19,859-19,868, 2001

[49] Drew, D. A., Turbulent sediment transport over a flat bottom using momentum balance, *Journal of Applied Mechanics* , March, pp 38-44, 1975

[50] Drew, D. A., Production and dissipation of energy in the turbulent flow of a particle-fluid mixture, with some results on drag reduction, *Journal of Applied Mechanics*, December, pp 543-547, 1976

[51] Drew, D. A., Mathematical modeling of two-phase flow, *Annual Review of Fluid Mechanics* , **15**, pp 261-291, 1983

[52] Du Boys, M.P., Estudes du regime et laction exercee par les eaux sur un lit a fond de graviers indefinement affouilable, *Ann. Ponts Chaussees*, **18**, pp 141195, 1879

[53] Einstein, H. A., Formulas for the transportation of bed-load, *Transactions of the American Society of Engineers*, **107**, Paper No. 2140, pp 561-573, 1942

[54] Einstein, H. A., The bed-load function for sediment transportation in open channel flows, US Department of Agriculture Technical Bulletin No. 1026, Soil Conservation Service, Washington, DC, 71 pp, 1950

[55] Elfrink, B. and T. Baldock, Hydrodynamics and sediment transport in the swash zone: a review and perspectives, *Coastal Engineering*, **45**, pp 149-167, 2002

[56] Elgar, S., E. L. Gallagher and R. T. Guza, Nearshore sandbar migration, *J. Geophysical Research*, **106, C6**, pp 11,623-11,627, 2001

[57] Falconer, R. A. and Y. Chen, An improved representation of flooding and drying and wind stress effects in a two-dimensional tidal numerical model, *Proc. Inst. Civil Engineers, Part 2*, **91**, pp 659-678, 1991

[58] Garcez-Faria, A. F., E. B. Thornton, T. P. Stanton and C. V. Soares, Vertical profiles of longshore currents and related bed shear stress and bottom roughness, *Journal of Geophysical Research*, **103(C2)**, pp 3217-3232, 1998

[59] Feddersen, F. and R. T. Guza, Velocity moments in alongshore bottom stress parameterizations, *Journal of Geophysical Research*, **105(C4)**, pp 8673-8686, 2000

[60] Flores, N. Z. and J. F. A. Sleath, Mobile layer in oscillatory sheet flow, *Journal of Geophysical Research*, **103**, pp 12783-12793, 1998

[61] Foster, D. L., R. A. Guenther and R. A. Holman, An analytic solution to the wave bottom boundary layer governing equation under arbitrary wave forcing, *Ocean Engineering*, **26**, pp 595 - 623, 1999

[62] Foti, E. and P. Scandura, A low Reynolds number $k - \epsilon$ model validated for oscillatory flows over smooth and rough wall, *Coastal Engineering*, **51**, pp 173-184, 2004

[63] Gallagher, E. L., S. Elgar and R. T. Guza, Observations of sand bar evolution on a natural beach, *J. Geophysical Research*, **103, C2**, pp 3,203-3,215, 1998

[64] Gerstner, F. J. von, Theorie der wellen. abhand. kön. böhmischen gesel. wiss., Prague, 1802

[65] Gobbi, M. F. and J. T. Kirby, Wave evolution over submerged sills: tests of a high-order Boussinesq model, *Coastal Engineering*, **37**, pp 57-96, 1999

[66] Gobbi, M. F., J. T. Kirby and Q. J. Chen, Boussinesq wave models and vertical vorticity fields, manuscript, 2006

[67] Gobbi, M. F., J. T. Kirby and G. Wei, A fully nonlinear Boussinesq model for surface waves. II. Extension to $O(kh^4)$, *Journal of Fluid Mechanics*, **405**, pp 181-210, 2000

[68] Grass, A. J., Sediment transport by waves and currents, *SERC London Cent. Mar. Technol*, Report No. FL29, 1981

[69] Güngördü, Ö and J. T. Kirby, Evolution of coupled hydrodynamic and bed instabilities, Research Report No. CACR-01-04, Center for Applied Coastal Research, Department of Civil and Environmental Engineering, University of Delaware, Newark, 2001

[70] Harten, A., High resolution schemes for hyperbolic conservation laws, *J. Comput. Phys.*, **49**, pp 357, 1983

[71] Harten, A., B. Engquist, S. Osher, and S. Chakravarthy, Uniformly high-order accurate essentially non-oscillatory schemes, III, *J. Comput. Phys.* **71**, pp 231 1987

[72] Henderson, S. M., J. S. Allen and P. A. Newberger, Nearshore sandbar migration predicted by an eddy-diffusive boundary layer model, *J. Geophysical Research*, **109**, C06024, doi:10.1029/2003JC002137, 2004

[73] Hoefel, F. and S. Elgar, Wave-induced sediment transport and sandbar migration, *Science*, **299**, pp 1885-1887, 2003

[74] Horikawa, K., A. Watanabe and S. Katori, Sediment transport under sheet flow condition, *Proceedings of 18th International Conference on Coastal Engineering*, Cape Town, pp 1335, 1982

[75] Hsu, T.-J., A two-phase flow approach for sediment transport, Cornell University, Ph.D dissertation, 2002

[76] Hsu, T.-J. and D. M. Hanes, The effect of wave shape on sheet flow sediment transport, *J. Geophysical Research*, **109**, C06025, doi:10.1029/2003JC002075, 2004

[77] Hsu, T.-J. and S. Elgar and R. T. Guza, A phase-resolving approach for nearshore sandbar migration, *Coastal Engineering*, submitted, 2005

[78] Hubbert, G. D., and K. L. McInne, A storm surge inundation model for coastal planning and impact studies, *Journal of Coastal Research*, **15(1)**, pp 168185, 1999

[79] Hudson J., Numerical Techniques for Morphodynamic Modelling, Ph.D dissertation, Dept. of Mathematics, University of Reading, UK, 2001

[80] Hudson, J., J. Damgaard, N. Dodd, T. Chesher, A. Cooper, Numerical approaches for 1D morphodynamic modelling, *Coastal Engineering*, **52(8)**, pp 691-707, 2005

[81] Jaffe, B. E. and D. M. Rubin, Using nonlinear forecasting to learn the magnitude and phasing of time-varying sediment suspension in the surf zone, *Journal of Geophysical Research*, **101(C6)**, pp 14283-14296, 1996

[82] Jensen, B. J., B. M. Sumer and J. Fredsøe, Turbulent oscillatory boundary layers at high Reynolds numbers, *Journal of Fluid Mechanics* , **206**, pp 265-297, 1989

[83] Jensen, J. H., E. Ø. Madsen and J. Fredsøe, Oblique flow over dredged channels: II. Sediment transport and morphology. *Journal of Hydraulic Engineering*, **125(11)**, pp 1190-1198, 1999

[84] Jiang, G.-S., C.-W. Shu, Efficient implementation of weighted ENO schemes, *J. Comput. Phys.*, **126**, pp 202, 1996

[85] Jiang, G.-S., C.-C. Wu, A high-order WENO finite difference scheme for the equations of ideal magnetohydrodynamics, *Journal of Computational Physics*,**150**, pp 561-594, 1999

[86] Johnson, H. K., J. A. Zyserman, Controlling spatial oscillations in bed level update schemes, *Coastal Engineering*, **46**, pp 09-126, 2002

[87] Jonsson, I. G., Wave boundary layers and friction factors, *Proc. 10th Int. Conf. on Coastal Engineering*, Tokyo, Japan, pp 127148, 1966

[88] Justesen, P., Turbulent wave boundary layers, *Series Paper 43*, dissertation, Institute of Hydrodynamics and Hydraulic Engineering, Technical University of Denmark, 1988

[89] Kaczmarek, L. M. and R. Ostrowski, Modelling intensive near-bed sand transport under wave-current flow versus laboratory and field data, *Coastal Engineering*, **45**, pp 1-18, 2002

[90] Kaczmarek, L. M., R. Ostrowski and R. B. Zeidler, Boundary layer theory and field bedload, *Proceedings of Coastal Dynamics '95*, 1995

[91] Kanoglu, U., Nonlinear evolution and runup-rundown of long waves over a sloping beach, *Journal of Fluid Mechanics*, **513**, pp 363-372, 2004

[92] Karambas, T. V. and C. Koutitas, A breaking wave propagation model based on the Boussinesq equations, *Coastal Engineering*, **18**, pp 1-19, 1992

[93] Karambas, T. V. and C. Koutitas, Surf and swash zone morphology evolution induced by nonlinear waves, *Journal of Waterway, Port, Coastal, and Ocean Engineering*, **128(3)**, pp 102-113, 2002

[94] Kennedy, A. B., Q. Chen, J. T. Kirby and R. A. Dalrymple, Boussinesq modeling of wave transformation, breaking, and runup. I: 1D, *Journal o f Waterway, Port, Coastal, and Ocean Engineering*, **126(1)**, pp 39-47, 2000

[95] Kennedy, A. B., J. T. Kirby, Q. Chen,and R. A. Dalrymple, Boussinesq-type equations with improved nonlinear behaviour, *Wave Motion*, **33**, pp 225-243, 2001

[96] Kirby, J. T., Boussinesq models and applications to nearshore wave propagation, surfzone processes and wave-induced currents, *Advances in Coastal Engineering*, V. C. Lakhan(ed), Elsevier, 2003

[97] Kirby, J. T. and R. A. Dalrymple, Verification of a parabolic equation for propagation of weakly-nonlinear waves, *Coastal Engineering*, **8**, pp 219-232, 1984

[98] Kirby, J. T., G. Wei, Q. Chen, A. B. Kennedy and R. A. Dalrymple, FUNWAVE 1.0, Fully nonlinear Boussinesq wave model, documentation and user's manual, Report number CACR-98-06, Center for Applied Coastal Engineering, University of Delaware, 1998

[99] Kobayashi, N. and B.D. Johnson, Sand suspension, storage, advection and settling in surf and swash zones, *Journal of Geophysical Research*, **106(C5)**, pp 9363-9376, 2001

[100] Kocyigit, M. B., R. A. Falconer and B. Lin, Three-dimensional numerical modelling of free surface flows with non-hydrostatic pressure, *Int. J. Numer. Meth. Fluids*, **4**, pp 1145-1162, 2002

[101] Kuriyama, Y. and T. Nakatsukasa, A one-dimensional model for undertow and longshore current on a barred beach, *Coastal Engineering*, **40**, pp 39-58, 2000

[102] Lax, P. D., Weak solutions of nonlinear hyperbolic equations and their numerical computation, *Commun. Pure Appl. Math.* **7**, pp 159-193, 1954

[103] Lax, P. D., B. Wendroff, Systems of conservation laws, *Commun. Pure Appl. Math.*, **13**, pp 217, 1960

[104] LeVeque, R. J., High-resolution conservative algorithms for advection in incompressible flow, lecture notes, 1995

[105] Liu, H. and S. Sato, Laboratory study on sheetflow sediment movement in the oscillatory turbulent boundary layer based on image analysis, *Coastal Engineering Journal*, **47(1)**, pp 21-40, 2005

[106] Liu, P. L.-F., Model equations for wave propagations from deep to shallow water, *Advances in coastal and ocean engineering*, (ed. P. L.-F. Liu), **1**, pp 125158, Singapore, World Scientific, 1994

[107] Liu, P. L.-F. and A. Orfila, Viscous effects on transient long-wave propagation, *Journal of Fluid Mechanics*, **520**, pp 83-92, 2004

[108] Liu, X.-D., S. Osher and T. Chan, Weighted essentially non-oscillatory schemes, *J. Comput. Phys*, **115**, pp 200, 1994

[109] Long, W. and J. T. Kirby, Cross-shore sediment transport model based on the Boussinesq equations and an improved Bagnold formula, *Proceedings Coastal Sediments'03*, Clearwater Beach, May, 2003

[110] Long, W., T.-J. Hsu and J. T. Kirby, Modeling cross-shore sediment transport processes with a time domain Boussinesq model, *Proceedings 29th International Conference on Coastal Engineering*, Lisbon, Sept., 2004

[111] Long, W., J. T. Kirby and Z. Shao, Numerical schemes for bed level updating in sediment transport, submitted to *Coastal Engineering*, 2006

[112] Lynett, P. J. and P. L.-F. Liu, Linear analysis of the multi-layer model, *Coastal Engineering*, **51(6)**, pp 439-454, 2004

[113] Lynett, P. J., Wave breaking velocity effects in depth-integrated models, manuscript, 2005

[114] Lynett, P. J., T.-R. Wu and P. L.-F. Liu, Modeling wave runup with depth-integrated equations, *Coastal Engineering*, **46**, pp 89-107, 2002

[115] MacCormack, R. W., The effect of viscosity in hypervelocity impact cratering, *AIAA Paper*, New York, pp 69-354, 1969

[116] McCowan, J., On the highest wave of permanent type, *Phil. Mag.*, **5**, pp 351357, 1894

[117] Madsen, O. S., Wave climate of the continental margin: elements of its mathematical description, marine sediment transport and environmental management, D. J. Stanley and D. J. P. Swift, John Wiley & Sons, pp 65-87, 1976

[118] Madsen, O. S. and W. D. Grant, Sediment Transport in the Coastal Environment, Dept. of Civil Engineering, MIT, 1976

[119] Madsen, P. A., and O. R. Sorensen, A new form of the Boussinesq equations with improved linear dispersion characteristics part 2. a slowly-varying bathymetry, *Coastal Engineering*, **18**, pp 183-204, 1992

[120] Madsen, P. A., O. R. Sorensen and H. A. Schaffer, Surf zone dynamics simulated by a Boussinesq type model, Part I. Model description and cross-shore motion of regular waves, *Coastal Engineering*, pp 255-287, 1997

[121] Malarkey, J., A. G. Davies and Z. Li, A simple model of unsteady sheet-flow sediment transport, *Coastal Engineering*, **48**, pp 171-188, 2003

[122] Mase, H. and J. T. Kirby, Modified frequency domain KdV equation for random wave shoaling, *Proc. 23d Intl. Conf. Coastal Engrng*, Venice, pp 474-487, October 1992.

[123] McInnes, K. L., G. D. Hubbert, D. J. Abbs and S. E. Oliver A numerical modelling study of coastal flooding, *Meteorology and Atmospheric Physics*, **80**, pp 217-233, 2002

[124] Mei, C. C., Resonant reflection of surface water waves by periodic sandbars, *J. Fluid Mech.*, **152**, pp 315-337, 1985

[125] Mellor, G., Oscillatory bottom boundary layers, *Journal of Physical Oceanography*, **32(11)**, pp 30753088, doi: 10.1175/1520-0485, 2002

[126] Meyer-Peter, E. and R. Müller, Formulas for bed-load transport, *Rep. 2nd Meet. Int. Assoc. Hydraul. Struct. Res.*, Stockholm, pp 39-64, 1948

[127] Meyer-Peter, E., Transport des matires Solides en Gnral et problme Spciaux, Bull. Gnie Civil d'Hydraulique Fluviale, Tome 5 (in French), 1951

[128] Michell, J. H., The highest wave in water, *Philos. Mag.*, **36**, pp 430437, 1893

[129] Mina, K. M. and S. Sato, A transport model for sheetflow based on two-phase flow, *Coastal Engineering Journal*, **46(3)**, pp 329-367, 2004

[130] Mingham, C. G., D. M. Causon and D. M. Ingram, A TVD MacCormack scheme for transcritical flow, *Proceedings of the Institute of Civil Engineering, Water & Maritime Engineering*, **148(3)**, pp 167-175, 2000

[131] Nairn, R. B. and H. N. Southgate, Deterministic profile modelling of nearshore processes, Part 2. Sediment transport and beach profile development, *Coastal Engineering*, **19**, pp 57-96, 1993

[132] Nicholson, J., I. Broker, J. A. Roelvink, D. Price, J. M. Tanguy and L. Moreno, Intercomparison of coastal area morphodynamic models, *Coastal Engineering*, **31**, pp 97-123, 1997

[133] Nielsen, P., Coastal bottom boundary layers and sediment transport, World Scientific, 324 pp, 1992

[134] Nielsen, P., Shear stress and sediment transport calculations for swash zone modelling, *Coastal Engineering*, **45**, pp 53-60, 2002

[135] Nielsen, P., K. van der Wall and L. Gillan, Vertical fluxes of sediment in oscillatory sheet flow, *Coastal Engineering*, **45**, pp 61-68, 2002

[136] Nino, Y. and M. Garcia, Engelund's analysis of turbulent energy and suspended load, *Journal of Engineering Mechanics*, **124(4)**, pp 480-483, 1998

[137] Nwogu, O. G., An alternative form of the Boussinesq equations for nearshore wave propagation, *J. Waterway, Port, Coast., Ocean Engrg*, **119(6)**, pp 618-638, 1993

[138] O'Connor, B. A. and J. Nicholson, Modeling changes in coastal morphology, *Sediment Transport Modeling*, S. S. Y. Wang (Editor), ASCE, pp 160-165, 1989

[139] O'Connor, B. A. and J. Nicholson, Suspended sediment transport equations, *Report No. CE/3/95*, Department of Civil Engineering, University of Liverpool, pp 11, 1995

[140] O'Donoghue, T. and S. Wright, Concentrations in oscillatory sheet flow for well sorted and graded sands, *Coastal Engineering*, **50**, pp 117-138, 2003

[141] Oey, L.-Y., A wetting and drying scheme for POM, *Ocean Modelling*, **9**, pp 133-150, 2005

[142] Ozanne, F., A. J. Chadwick, D. A. Huntley, D. J. Simmonds and J. Lawrence, Velocity predictions for shoaling and breaking waves with a Boussinesq-type model, *Coastal Engineering*, **41**, pp 361-397, 2001

[143] Özkan-Haller, H. T. and J. T. Kirby, A Fourier-Chebyshev collocation method for the shallow water equations including shoreline runup, *Applied Ocean Research*, **19**, pp 21-34, 1997

[144] Pechon, P., F. Rivero, H. Johnson, T. Chesher, B. O'Connor, J.-M. Tanguy, T. Karambas, M. Mory and L. Hamm, Intercomparison of wave-driven current models, *Coastal Engineering*, **31**, pp 199-215, 1997

[145] Pedlosky, J., Geophysical fluid dynamics (2nd edition), Springer-Verlag, 710 pp, 1986

[146] Peregrine, D. H., Long waves on a beach, *Journal of Fluid Mechanics*, **27(4)**, pp 815-827, 1967

[147] Perthame, B. and C.-W. Shu, On positivity preserving finite volume schemes for Euler equations, *Numerische mathematik*, **73**, pp 119-130, 1996

[148] Prasad, S. N. and V. P. Singh, A hydrodynamic model of sediment transport in rill flows, *Exeter Symposium*, 1982

[149] Pugh, F. J. and K. C. Wilson, Velocity and concentration distribution in sheet flow above plane beds, *Journal of Hydraulic Engineering*, **125(2)**, pp 117-125, 1999

[150] Puleo, J. A., T. Butt and N. G. Plant, Instantaneous energetics sediment transport model calibration, *Coastal Engineering*, **52**, pp 647-653, 2005

[151] Radder, A. C., On the parabolic equation method for water-wave propagation, *Journal of Fluid Mechanics*, 95, pp 159-176, 1979

[152] Rakha, K. A., A quasi-3D phase-resolving hydrodynamic and sediment transport model, *Coastal Engineering*, **34**, pp 277-311, 1998

[153] Rakha, K. A., R. Deigaard and I. Broker, A phase-resolving cross shore sediment transport model for beach profile evolution, *Coastal Engineering*, **31**, pp 231-261, 1997

[154] Rey, V., A. G. Davies and M. Belzons, On the formation of bars by the action of waves on an erodible bed: a laboratory study, *J. Coastal Res.*, **11**, 1180-1194, 1995

[155] Ribberink, J. S., Bed-load transport for steady flows and unsteady oscillatory flows, *Coastal Engineering*, **34**, pp59-82, 1998

[156] Ribberink, J. S. and A. A. Al-Salem, Sheet flow and suspension of sand in oscillatory boundary layers, *Coastal Engineering*, **25**, pp 205-225, 1995

[157] Richtmyer, R. D., A survey of difference methods for nonsteady fluid dynamics, *Natl. Cent. Atmos. Res. Tech. Note 63-2*, 1962

[158] Van Rijn, L. C., Sediment transport: Part I: Bed load transport, *Proc. ASCE Journal of Hydraulics Division*, **110**, HY10, pp 1431-1456, 1984a

[159] Van Rijn, L. C., Sediment transport: Part II: Suspended load transport, *Proc. ASCE Journal of Hydraulics Division*, **110**, HY11, pp 1613-1641, 1984b

[160] Van Rijn, L. C., Sediment transport: Part III: Bed forms and alluvial roughness, *Proc. ASCE Journal of Hydraulics Division*, **110**, HY12, pp 1733-1754, 1984c

[161] Van Rijn, L. C., Principles of sediment transport in rivers, estuaries and coastal seas, Aqua Publications, ISBN 90-800356-2-9, 1993

[162] Rodi, W., Turbulence models and their application in hydraulics - a state-of-the-art review, Int. Assoc. for Hydraul. Res., A.A. Balkema, Rotterdam, Brookfield, 3rd edition, 104 pp, 1993

[163] Roe, P. L., Upwind difference schemes for hyperbolic conservation laws with source terms, *Proc. First International Conference on Hyperbolic Problems*, Carasso, Raviart and Serre (Editors), pp 41-51, Springer, 1986

[164] Roelvink, J. A. and A. Reniers, LIP 11D delta flume experiments, *Delft Hydraulics Data Rep. H2130*, Delft , 1995

[165] Roelvink, J. A. and G. K. F. M. van Banning, Design and development of Delft3D and application to coastal morphodynamics, *Hydroinformatics '94*, Verwey, Minns, Babovic and Maksimovic (eds), Balkema, Rotterdam, pp 451-455, 1994

[166] Roelvink, J. A., D. J. R. Walstra and Z. Chen, Morphological modelling of Keta lagoon case, *Proc. 24th Int. Conf. on Coastal Engineering*, ASCE, Kobe, Japan, 1994

[167] Rouse, H., Modern conceptions of the mechanics of fluid turbulence,. *Trans. ASCE*, **102**, 1937

[168] Sana, A. and E. B. Shuy, Two-equation turbulence models for smooth oscillatory boundary layers, *Journal of Waterway, Port, Coastal and Ocean Engineering*, **128(1)**, pp 38-45, 2002

[169] Sana, A. and H. Tanaka, Improvement of the full-range equation for bottom friction under three-dimensional wave-current combined motion, *Coastal Engineering*, **31**, pp 217-229, 1997

[170] Savage, S. B., The mechanics of rapid granular flows, *Advances in Applied Mechanics*, **24**, pp 289-367, 1984

[171] Schäffer, H. A., P. A. Madsen and R. Deigaard, A Boussinesq model for waves breaking in shallow water, *Coastal Engineering*, **20**, pp 185-202, 1993

[172] Schäffer, H. A. and I. A. Svendsen , Boundary layer flow under skew waves, Inst. Hydrodynamics and Hydraulic Engineering, Tech. Univ. Denmark, report, pp 13-23, 1986

[173] Schielen, R., A. Doelman and H. E. D. Swart, On the nonlinear dynamics of free bars in straight channels, *J. Fluid Mech.*, **252**, pp 325-356, 1993

[174] Schlichting, H., Boundary-Layer Theory, 6th ed., McGraw-Hill, pp748, 1968

[175] Schoklitsch, A. Über Schleppkraft un Geschiebebewegung, Engelmann, Leipzige, Germany (in German), 1914

[176] Schoklitsch, A., Handbuch des Wasserbaues, Springer, Vienna (2nd ed.), English translation by S. Shulits., The Schoklitsch Bed-load Formula, *Engineering*, London, England, June 21, 1935, pp. 644-646; and June 28, 1935, pp 687, 1930

[177] Schoklitsch, A., Handbuch des wasserbaues, Springer-Verlag, New York, 1950

[178] Schoonees, J. S. and A. K. Theron, Evaluation of 10 cross-shore sediment transport / morphological models, *Coastal Engineering*, **25**, pp 1-41, 1995

[179] Shao, Z. Y., S. Kim and S. A. Yost, A portable numerical method for flow with discontinuities and shocks, *Proceedings of 17th Engineering Mechanics Conference, ASCE*, June 13-16, University of Delaware, Newark, DE, USA, 2004

[180] Sherman, J., and W. J. Morrison, Adjustment of an inverse matrix corresponding to changes in the elements of a given column or a given row of the original matrix, *Ann. Math. Statist.*, **20**, page 621, 1949

[181] Shi, F., Dalrymple, R. A., Kirby, J. T., Chen, Q. and Kennedy, A., A fully nonlinear Boussinesq model in generalized curvilinear coordinates, *Coastal Engineering*, **42**, pp 337-358, 2001.

[182] Shi, F., J. T. Kirby, R. A. Dalrymple and Q. Chen, Wave simulations in Ponce de Leon Inlet using Boussinesq model, *Journal of Waterway, Port, Coastal and Ocean Engineering*, **129(3)**, pp 124-135, 2003

[183] Shi, F. and W. Sun, A variable boundary model of storm surge flooding in generalized curvilinear grids, *International Journal for Numerical Methods in Fluids*, **21**, pp 641-651, 1995

[184] Shi, F., I. A. Svendsen, J. T. Kirby and J. M. Smith, A curvilinear version of a quasi-3D nearshore circulation model, *Coastal Engineering*, **49**, pp 99-124, 2003

[185] Shields, A., Application of similarity principles and turbulence research to bedload movement (English translation of the original German manuscript). Hydrodynamics Laboratory, California Institute of Technology, Pub. No 167, 1936

[186] Shu, C.-W., Essentially non-oscillatory and weighted essentially non-oscillatory schemes for hyperbolic conservation laws, lecture notes, *ICASE Report No. 97-65*, NASA/CR-97-206253, November, 1997

[187] Shu, C.-W., Total-variation-diminishing time discretizations, *SIAM J. Sci. Stat. Comput.*, **9**, pp 1073-1084, 1998

[188] Shu, C.-W. and S. Osher, Efficient implementation of essentially non-oscillatory shock-capturing schemes, *J. Comput. Phys.*, **77**, pp 439-471, 1988

[189] Shu, C.-W., High order finite difference and finite volume WENO schemes and discontinuous Galerkin Methods for CFD, ICASE report, 2001

[190] Sleath, J. F. A., Bed load transport in oscillatory flow, *Sediment Transport Mechanisms in Coastal Environments and Rivers*, M. Belorgey, R. D. Rajaona, J. F. A. Sleath, (Editor), World Scientific, Singapore, 1994

[191] Sleath, J. F. A. and S. Wallbridge, Pickup from rippled beds in oscillatory flow, *Journal of Waterway, Port, Coastal, and Ocean Engineering*, **128(6)**, pp 228-237, 2002

[192] Smagorinsky, J. S., General circulation experiments with the primitive equations, *Mon. Weather Rev.*, **93**, pp 99, 1983

[193] Sorensen, O. R., H. A. Schäffer and L. S. Sorensen, Boussinesq-type modelling using an unstructured finite element technique, manuscript, 2003

[194] Soulsby, R. L. and J. S. Damgaard, Bedload sediment transport in coastal waters, *Coastal Engineering*, **52**, pp 673-689, 2005

[195] Staub, C., I. G. Jonsson and I. A. Svendsen, Sediment suspension in oscillatory flow: measurements of instantaneous concentration at high shear, *Coastal Engineering*, **27**, pp 67-96, 1996

[196] Stauble, D. K., M. A. Cialone, Sediment dynamics and profile interactions: DUCK94, *Proceedings of 25th International Conference on Coastal Engineering*, **4**, A.S.C.E., 1997

[197] Stive, M. J. F. and H. G. Wind, Cross-shore mean flow in the surf zone, *Coastal Engineering*, **10**, pp 325-340, 1986

[198] Stive, M. J. F. and H. J. De Vriend, Shear stresses and mean flow in shoaling and breaking waves, *Proceedings of International Conference on Coastal Engineering*, 1994

[199] Stokes, G. G., On the theory of oscillatory waves. *Trans. Camb. Philos. Soc.*, **8**, pp 441455. Also in Stokes 18801905, **Vol 1**, with additional Appendices and Supplement, 1847

[200] Stokes G. G., On the resistance of a fluid to two oscillating spheres. *Rep. Br. Assoc. Adv. Sci.*, Part ii, p. 6, 1847

[201] Stokes G. G., On the effect of the internal friction of fluids on the motion of pendulums *Transactions of the Cambridge Philosophical Society*, **IX**, pp 6-106, 1851

[202] Straub, L. G., Missouri River report, Appendix XV, US Serial no. 9829, House Document no. 238, 73rd Congress, 2nd Session, Washington, DC., 1935

[203] Sumer, B. M., L. H. C. Chua, N.-S. Cheng and J. Fredsøe, Influence of turbulence on bed load sediment transport, *Journal of Hydraulic Engineering*, **129(8)**, pp 585-598, 2003

[204] Sumer, B. M., A. Kozakiewicz, J. Fredsøe and R. Deigaard, Velocity and concentration profiles in sheet-flow layer of movable bed, *Journal of Hydraulic Engineering*, **122(10)**, pp 549-558, 1996

[205] Sutherland, J., A. H. Peet and R. L. Soulsby, Evaluating the performance of morphological models, *Coastal Engineering*, **51**, pp 917-939, 2004

[206] Svendsen, I. A. and P. A. Madsen, Turbulent bore on a beach, *Journal of Fluid Mechanics*, **148**, pp 73-96, 1984

[207] Svendsen, I. A. and U. Putrevu, Nearshore circulation with 3-D profiles, *Proceedings of Twendy-Second Coastal Engineering Conference*, pp 241-254, 1990

[208] Svendsen, I. A., J. Veeramony, J. Bakunin and J. T. Kirby, The flow in weak turbulent hydraulic jumps, *J. Fluid Mech.*, **418**, pp 25-57, 2000

[209] Synolakis, C. E., The runup of solitary waves, *Journal of Fluid Mechanics*, **185**, pp 523-545, 1987

[210] Tadepalli, S. and C. E. Synolakis, The run-up of N-waves on sloping beaches, *Proc. R. Soc. Lond.*, **A 445**, pp 99112, 1994

[211] Tanaka, H. and D. Y. To, Initial motion of sediment under waves and wave-current combined motions, *Coastal Engineering*, **25**, pp 153-163, 1995

[212] Tanguy, J. M., B. Zhang and L. Hamm, A new Lax-Wendroff algorithm to solve the bed continuity equation with slope effect, *Proc. 3rd Int. Conf. on Coastal Estuarine Modeling*, ASCE, 1993

[213] Tao, J., Computation of wave run-up and wave breaking, Danish Hydraulic Institute, internal report, 1983

[214] Tao, J., Numerical modeling of wave runup and breaking on the beach *Acta Oceanologica Sinica*, **6(5)**, pp 692-700, in Chinese, 1984.

[215] Tinti, S. and R. Tonini, Analytical evolution of tsunamis induced by near-shore earthquakes on a constant-slope ocean, *Journal of Fluid Mechanics*, **535**, pp 33-64, 2005

[216] Townsend, A. A., The structure of turbulent shear flow, 2nd edn., Cambridge University Press, 1976

[217] Trowbridge, J. and O. S. Madsen, Turbulent wave boundary layers. 1. Model formulation and first-order solution, *J. Geophysical Research*, **89(C5)**, pp 7989–7997, 1984

[218] Trowbridge, J. and D. Young, Sand transport by unbroken water waves under sheet flow conditions *Journal of Geophysical research*, **94 C8**, pp 10971-10991, 1989

[219] Tsay, T.-K. and P. L.-F. Liu, Numerical solution of water-wave refraction and diffraction problems in the parabolic approximation, *Journal of Geophysical Research*, **87(C10)**, pp 7932-7941, 1982

[220] Tuck, E. O. and L. S. Hwang, Long wave generation on a sloping beach, *J. Fluid Mech.*, **51**, pp 449461, 1972

[221] Veeramony, J. and I. A. Svendsen, The flow in surf-zone waves, *Coastal Engineering*, **39**, pp 93-122, 2000

[222] Walkley, M. and M. Berzins. A finite element model for the two-dimensional extended Boussinesq equations, *Int. J. for Num. Meths. in Fluids*, **39(10)**, pp 865-885, 2002

[223] Warsi, Z.U.A., Fluid Dynamics. Theoretical and Computational Approaches. 2. Boca Raton, CRC, 1999

[224] Wei, G., J. T. Kirby, S. T. Grilli and R. Subramanya, A fully nonlinear Boussinesq model for surface waves. I. Highly nonlinear, unsteady waves, *Journal of Fluid Mechanics*, **294**, pp 71-92, 1995

[225] Wei, G., J. T. Kirby and A. Sinha, Generation of waves in Boussinesq models using a source function method, *Coastal Engineering*, **36**, pp 271-299, 1999

[226] Wei, G. and J. T. Kirby, Simulation of water waves by Boussinesq models, Research Report No. CACR-98-02, Center for Applied Coastal Research, University of Delaware, Newark, Delaware, 1998

[227] Whitham, G. B., Linear and Nonlinear Waves, John Wiley and Sons, Inc., 1974

[228] Williams, J. J., C. P. Rose, P. D. Thorne, B. A. O'Connor, J. D. Humphery, P. J. Hardcastle, S. P. Moores, J. A. Cooke and D. J. Wilson , Field observations and predictions of bed shear stresses and vertical suspended sediment concentration profiles in wave-current conditions, *Continental Shelf Research*, **19**, pp 507-536, 19999

[229] Wilson, K. C., J. S. Andersen and J. K. Shaw, Effects of wave asymmetry on sheet flow, *Coastal Engineering*, **25**, pp 191-204, 1995

[230] Witting, J. M., A unified model for evolution of nonlinear water waves, *J. Comput. Phys.*, **56**, pp 203-236, 1984

[231] Wright, L. D., S.-C. Kim and C.T. Friedrichs, Across-shelf variations in bed roughness, bed stress and sediment suspension on the northern California shelf, *Marine Geology*, **154**, Feb 2, pp 99-115, 1999

[232] Xie, L., L. J. Pietrafesa, M. Peng, Incorporation of a mass-conserving inundation scheme into a tree dimensional storm surge model, *Journal of Coastal Research*, **20(4)**, pp 1209-1223, 2004

[233] You, Z.-J., The effect of wave-induced stress on current profiles, *Ocean Engineering*, **23(7)**, pp 619-628, 1996

[234] You, Z.-J., A simple model of sediment initiation under waves, *Coastal Engineering*, **41**, pp 399-412, 2000

[235] Yu, J. and C. C. Mei, Formation of sand bars under surface waves, *J. Fluid Mech.*, **416**, pp 315-348, 2000

[236] Zelt, J. A., The run-up of nonbreaking and breaking solitary waves, *Coast. Engrg.*, **15**, pp 205246, 1991

[237] Zhen, F., On the numerical properties of staggered vs. non-staggered grid schemes for a Boussinesq equation model, Master Thesis, Dept. of Civil and Environmental Engineering, University of Delaware, Newark, Delaware, 2004

[238] Zhou, J. and M. A. Adewumi, Simulation of transients in natural gas pipelines using hybrid TVD schemes, *International Journal for Numerical Methods in Fluids*, **32**, pp 407-437, 2000

[239] Zou, Q., An analytical model of wave bottom boundary layers incorporating turbulent relaxation and diffusion effects, *Journal of Physical Oceanography*, **32**, pp 2441-2456, 2002